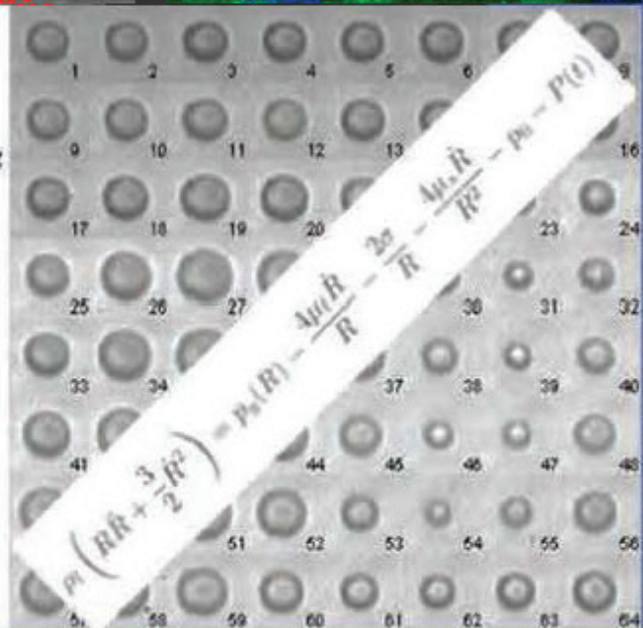
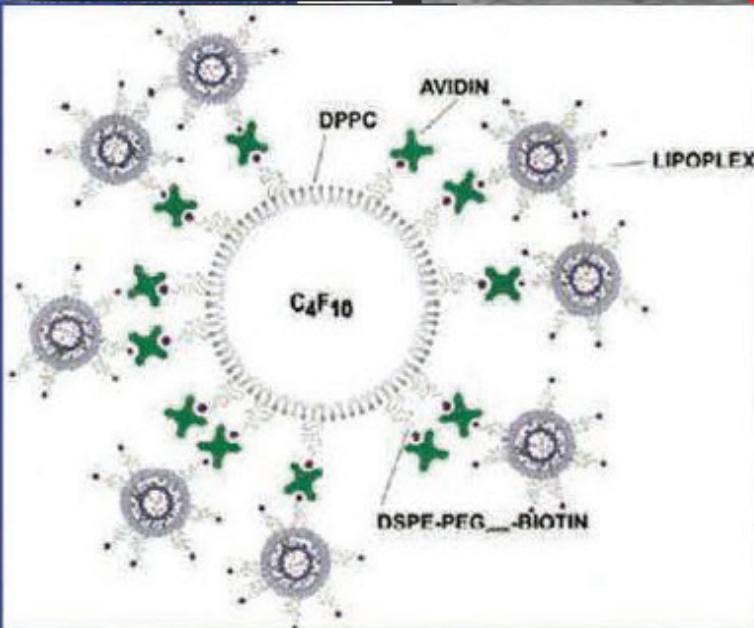
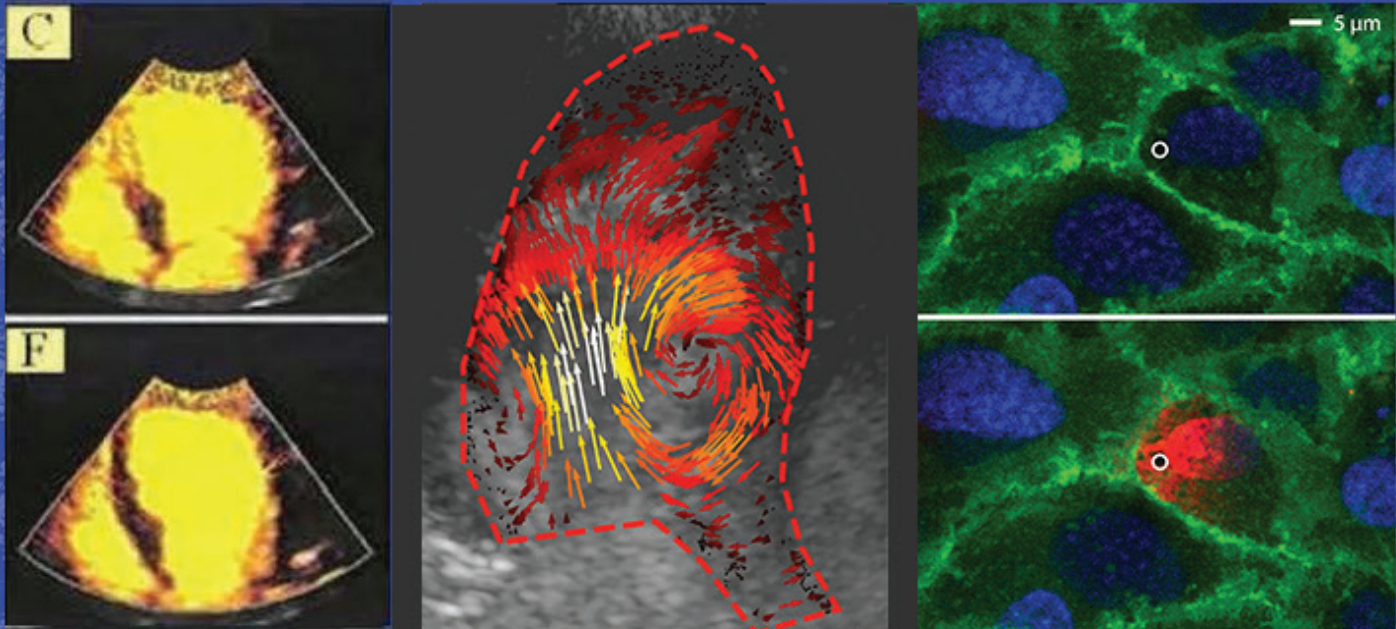


The 25th European Symposium on Ultrasound Contrast Imaging

- An ICUS Conference -



Abstract book

16-17 January 2020, Rotterdam, the Netherlands

Organised by Nico de Jong, Folkert ten Cate, Rik Vos, Klazina Kooiman,
Annemien van den Bosch, and Arend Schinkel

Erasmus MC Rotterdam



Thursday, 16 January 2020

Evening Dinner

Partyship “De Majesteit”

Maasboulevard (near by Tropicana), Rotterdam

Dinner Buffet: around 19:00

Coaches will be leaving from Hilton at 18:30 and will be back at Hilton around 22:30

25th EUROPEAN SYMPOSIUM ON ULTRASOUND CONTRAST IMAGING
16-17 JANUARY 2020, Rotterdam, The Netherlands

WEDNESDAY, 15 January 2020

- 11.30 PhD defense (Erasmus MC – Querido room) Mihai Strachinaru
 Shear wave echocardiography
- 18.00 – 21.30 Welcome Drinks + dinner buffet [1st floor, Hilton hotel Rotterdam]
 Registration

THURSDAY, 16 January 2020

Oral program

08.00 – 09.00	Registration	
09.00 – 09.10	Introduction and opening	Felix Zijlstra
09.10 – 09.25	UMB special issue: Vibrating bubbles, brilliant images and palpable therapeutics.....	Nico de Jong
09.25 – 10.15	CLINICAL THERAPY	<i>Chairpersons: Ayache Bouakaz and Folkert ten Cate</i>
Thierry Bettinger	A journey in the Bracco history of gas microbubbles: from imaging to therapy	1
Wilson Mathias	Sonothrombolysis improves myocardial dynamics and microvascular obstruction preventing left ventricular remodeling in patients with ST elevation myocardial infarction	3
Kakkhee Yeung	The application of Microbubbles and Ultrasound Accelerated Thrombolysis (MUST) for Peripheral Arterial Occlusions:..... Short-Term Results of a Phase-II Single Arm Trial.....	4
10.15 – 11.20	Coffee 10.30- 10.50: Postersessions C and D: 2 minute pitches (audience selects the winners)	
11.20 – 12.30	MOLECULAR IMAGING	<i>Chairpersons: Beat Kaufmann and Thierry Bettinger</i>
Alexander Klibanov	Targeting slow-flow tumor vasculature with lectin-decorated microbubbles.....	5
Mukesh Punjabi	Ultrasound molecular imaging of atherosclerosis: Liraglutide treatment lowers expression of endothelial vascular cell adhesion molecule 1 (VCAM-1)	7
Inés Beekers	Opening of endothelial cell-cell contacts caused by sonoporation elucidated with combined confocal microscopy and	10
Peter Burns	Brandaris 128 imaging	12
12.30 – 13.30	LUNCH	
13.30 – 14.00	DUTCH HEART FOUNDATION LECTURE	<i>Chairperson: Annemien van den Bosch</i>
Tom Porter	Transthoracic Acoustic Droplet Activation Pulse Sequence Schemes In Myocardial Ischemia And Reperfusion	13
14.00 – 15.30	THERAPY: The Basics	<i>Chairpersons: Eleanor Stride and Olivier Couture</i>
Christy Holland	NO-Microbubbles Promote Sonobactericide.....	15
Liza Villanueva	Ultrasound-Mediated Doxorubicin Delivery by Microbubble-Liposome Complexes Has Superior Anti-tumor Efficacy..... and Reduced Cardiotoxicity <i>in vivo</i>	18
Sofie Snipstad	Mechanisms and effects of nanoparticle-stabilized microbubbles designed for enhanced drug delivery	20
Kirby Lattwein	Dispersion and sonoporation of bacteria in biofilms by oscillating microbubbles	25
John Pacella	Characterization of a novel nitro-fatty acid microbubble for ultrasound-targeted microbubble cavitation	28
15.30 – 16.00	Intermission	
16.00 – 17.45	CLINICAL IMAGING	<i>Chairpersons: Steve Feinstein and Dan Adam</i>
Roxy Senior	Recent ESC Guidelines in patients with Chronic Coronary Syndrome-relevance to Contrast Echocardiography	30
Charlie Demené	Deep Transcranial Ultrasound Localization Microscopy of the adult human brain vascularization	31
Yuko Kono	CEUS LI-RADS – preliminary results on multi-center prospective validation study	32
Stephanie Wilson	Why should everybody use contrast for liver US	34
Pintong Huang	Role of Contrast-Enhanced Ultrasound in the Pre-operative Diagnosis of Cervical Lymph Node Metastasis in Patients with... Papillary Thyroid Carcinoma	37
Matthieu Toulemonde	Motion correction for high-frame-rate contrast enhanced echocardiography	38
18.30 – 22.30	EVENING PROGRAM (Incl. Dinner buffet)	

25th EUROPEAN SYMPOSIUM ON ULTRASOUND CONTRAST IMAGING
16-17 JANUARY 2020, Rotterdam, The Netherlands

FRIDAY, 17 January 2020

07.30 – 08.00 Registration

07.30 – 09.00 MODERATED POSTER SESSIONS A and B

Oral program

09.00 – 09.50	BUBBLE TECHNOLOGY <i>Chairpersons: Michel Versluis and Rik Vos</i>	
Verya Daeichin	A new Photoacoustic based Technique for Single Microbubble Characterization.....	42
Sophie Heymans	Radiation-induced vaporization of PCDA-PFB nanodroplets: a feasibility study for ultrasound-based proton range verification and dosimetry.....	45
Tim Segers	Foam-free monodisperse lipid-coated ultrasound contrast agent synthesis through multi-gas-component microbubble stabilization.....	48

09.50 – 10.55 Coffee

10.05 - 10.25: Postersessions E and F: 2 minute pitches (audience selects the winners)

10.55 – 12.40	THERAPY: Towards clinical use <i>Chairpersons: Klazina Kooiman and Arend Schinkel</i>	
Meaghan O'Reilly	Non-Invasive Ultrasound and Bubble-Mediated Blood-Spinal Cord Barrier Opening: Experiences with a Pig Model.....	52
Elvin 't Hart	Enhanced radiosensitizer extravasation across the blood-brain barrier after focused ultrasound for diffuse intrinsic pontine gliomas treatment: preliminary pharmacokinetics results.....	54
Phillip Durham	Preliminary Evaluation of Reactive Molecule Delivery for Brain Depot Capture.....	56
Jonathan Kopechek	Ultrasound and microbubble-targeted delivery of microRNA therapeutics to the heart for cardiac therapies.....	58
Anne Rix	Contrast enhanced ultrasound alters tumor pathophysiology and therapy outcome in orthotopic triple negative breast cancer in mice.....	60
Roel Deckers	Bleomycin plus ultrasound and microbubbles to treat feline oral squamous cell carcinoma, as a model for human head and neck cancer, preliminary results of the BUBBLEFISH Trial.....	

12.40 – 13.40 LUNCH

13.40 – 14.10	25th ANNIVERSARY LECTURE <i>Chairperson: Christy Holland</i>	
Ruud van Sloun	Artificial intelligence for (super-resolution) contrast agent detection.....	65

14.10 – 15.40	COMPETITION: SUPER-RESOLUTION IMAGING <i>Chairpersons: Nico de Jong and Peter Burns</i>	
Matthieu Toulemonde	Microvessel Analysis with 3D Super-resolution Ultrasound and Super-Resolved Velocity Mapping.....	68
John Hossack	Super resolution imaging combined with differential targeted enhancement for structural and functional imaging of tumor vasculature.....	71
Vincent Hingot	Ultrasound Localization Microscopy predicts ischemic stroke outcome and response to treatment in mouse model.....	74
Meng-Xing Tang	Effect of Concentrations of Contrast Agents in Ultrasound Super-Resolution Imaging.....	76
Baptiste Heiles	Whole rat brain microvasculature imaging in vivo with 3D Ultrasound Localization Microscopy.....	79
Isabel Newsome	Imaging of Cancerous Microvasculature with Acoustic Angiography and Superharmonic Ultrasound Localization Microscopy.....	82

15.40 – 16.00 CLOSING REMARKS *Nico de Jong*

16.00 FAREWELL DRINKS

ANNOUNCEMENT OF THE WINNERS OF THE COMPETITION AND POSTER PRIZES

Organised by: Nico de Jong, Folkert ten Cate, Rik Vos, Klazina Kooiman, Annemien van den Bosch, Arend Schinkel
 Scientific board: Mike Averkiou, Mark Borden, Paolo Colonna, Olivier Couture, Beat Kaufmann, Eleanor Stride.

Poster sessions Thursday - Election by the audience

Thursday 10.15-11.20		POSTER SESSION C: NEW MICROBUBBLES <i>Chairperson: Eleanor Stride</i>
C1)	Steven Machtaler	Copper-free click conjugation of P-selectin antibody to lipid-shelled microbubbles for imaging inflammation in a 84 murine model of inflammatory bowel disease.....
C2)	Patrick Koczera	CORM-1-loaded PBCA microbubbles for US- and MRI-guided light-triggered CO delivery..... 87
C3)	Alec Thomas	Design of Therapeutic Magnetic Microbubbles for the Treatment of Pseudo-aneurysms..... 89
C4)	Dragana Ristanovic	UV-responsive microbubbles as a model system for cleavage-based detection..... 92
C5)	Ugur Soysal	Generation of microfluidic monodisperse microbubbles for enhancing contrast imaging..... 95
C6)	Emma Bluemke	Magnetic Resonance Imaging of Oxygen Micro and Nanobubbles..... 99
C7)	Damien Batchelor	Nested Nanobubbles as Ultrasound Triggered Drug Delivery Vehicles 102
C8)	Simone Langeveld	Effect of lipid handling on phase behavior and ligand distribution in targeted microbubbles 106
C9)	Nicola Ingram	Towards clinically relevant therapeutic microbubbles..... 108
C10)	Anastasiia Panfilova	Acoustic characterization of antibubbles..... 109
 Thursday 10.15-11.20		 POSTER SESSION D: NEW DIRECTIONS BIOLOGY/CLINICAL <i>Chairperson: Olivier Couture</i>
D1)	Kazuo Maruyama	Theranostics with Lipid Bubbles and Ultrasound 111
D2)	Yajing Liu	Ultrasound-targeted microbubble destruction and Photoacoustic Tracking of Mesenchymal Stem Cells in Multiple 113 Myeloma Model.....
D3)	Gaio Paradossi	Trajectories Analysis before Adhesion of Microbubbles to Endothelial Cells 116
D4)	Sara Keller	Cavitation Therapy Monitoring of Commercial Microbubbles with a Clinical Scanner..... 120
D5)	Saulius Šatkauskas	Cell death dynamics after calcium delivery via sonoporation 124
D6)	Soufiane El Kadi	An in-vitro study comparing sonothrombolytic efficacy of acoustically activated perflutren nanodroplets with perflutren..... 127 microbubbles.....
D7)	Astrid Hoving	Signal intensities and velocity estimations of in vitro echoPIV measurements in a carotid artery stent..... 130
D8)	Rahul Misra	Developing a 3D tumor spheroid model for Ultrasound-microbubbles (USMB) mediated delivery of chemotherapy drugs..... 132
D9)	Majorie van Helvert	High-Frame-Rate Contrast-Enhanced Ultrasound Particle Image Velocimetry in the Stented Superficial Femoral Artery..... 133
D10)	Steven Machtaler	Contrast-enhanced perfusion imaging in a teleost model organism, rainbow trout (<i>Oncorhynchus mykiss</i>) 136

FRIDAY, 17 January 2020

07.30 – 08.00 Registration

Poster sessions Friday

07.30 – 09.00

MODERATED POSTER SESSION A: BIOLOGY/CLINICAL *Moderator: Klazina Kooiman*

A1) Ryo Suzuki	Cancer therapy by the combination of ultrasound contrast imaging agent mediated sonotherapy and immunotherapy	138
A2) Antoine Presset	Acoustically-mediated blood-brain barrier opening: investigation of neurophysiological consequences by neurotranscriptomics	139
A3) Joke Deprez	Monodisperse microbubbles as a tool to elucidate sonoporation fundamentals	142
A4) Richard Browning	Combined Sonodynamic and Chemoradiotherapy for Pancreatic Cancer	144
A5) Jordan Joiner	Low-intensity focused ultrasound and microbubbles heighten immune response in pancreatic tumors	146
A6) Alexandra Vasilyeva	Investigation of the effect of orally administered oxygen bubbles upon tumour response to sonodynamic therapy	149
A7) Veerle Brans	Investigating cell membrane modulation by microbubbles and ultrasound using confocal fluorescence microscopy	152
A8) Sara Keller	Vascular disruption and enhanced drug penetration performed in a mouse model of HCC with a clinical scanner	154

07.30 – 09.00

MODERATED POSTER SESSION B: TECHNOLOGY *Moderator: Rik Vos*

B1) Alicia Clark	Enhanced Heating with Microbubbles in High Intensity Focused Ultrasound Applications	157
B2) Dan Adam	Visualization of Vasculature by Non-Rigid Registration and Segmentation of Subharmonic Ultrasonic Images	161
B3) Peiran Chen	Investigation of the relationship between microvascular architecture and ultrasound-contrast-agent kinetics by controlled porous media.....	166
B4) Charlotte Nawijn	High-speed optical characterization of the acoustic response of protein-and-nanoparticle-stabilized microbubbles.....	170
B5) Benjamin van Elburg	Tunable viscoelastic shell properties of lipid-coated monodisperse microbubbles formed by flow-focusing	173
B6) Luxi Wei	Spatial Coherence Volumetric Beamforming of Microbubbles Using a Sparse Array	176
B7) Arthur Chavignon	Single particle localization algorithms for Ultrasound Localization Microscopy in silico and in vivo.....	179
B8) Matthieu Toulemonde	3D flow visualization with locally and acoustically activated nanodroplets and high frame rate imaging using a matrix array ...	182

Poster sessions E and F: Election by the audience

Friday 09.50-10.55

POSTER SESSION E: NANOCONTRAST *Chairperson: Mark Borden*

E1) Gazendra Shakya	Tuning vaporization by interfacial melting in endoskeletal and exoskeletal droplets.....	185
E2) Romain Melich	Determination of Acoustic Droplet Vaporization threshold for various microfluidically formed PFC-nanodroplets	187
E3) Winters Fu	Preliminary Evaluations of Safety and Efficacy of a Ultra Small Contrast Agent for Contrast-enhanced Ultrasound Imaging ...	191
E4) Fabio Domenici	DODAB-shelled microdroplets, invaluable antitumor carriers.....	193
E5) Simona Turco	Pharmacokinetic modeling of targeted ultrasound nanobubbles to quantify PSMA expression in prostate cancer	195
E6) Yosra Toumia	Towards Ultrasound-assisted Photon Radiation Dosimetry using Polymeric Phase Change Nanodroplets: A Preliminary Concept Study.....	200
E7) Adeel Shafi	Systematic Characterisation of Sub-Micron Ultrasonic Contrast Agents in their Natural Hydrated State	204
E8) Evan Unger	Novel nanoplatform for ultrasound imaging and theranostic applications using different perfluorocarbons.....	206
E9) Hongjian Chen	Targeted Hydrodynamic Cavitating Flows via Ultrasound Waves via Pickering Stabilized Perfluorodroplets	208

Friday 09.50-10.55

POSTER SESSION F: NEW TECHNOLOGY *Chairperson: Mike Averkiou*

F1) Hongjian Chen	A model-guided optimization of contrast pulse sequence for polyvinyl alcohol microbubbles	212
F2) Sara Ferri	A physical model to investigate the acoustic behaviour of microbubbles within a bone fracture	216
F3) James Bezer	Single microbubble-induced tissue deformation to estimate tissue properties	219
F4) Sarah Cleve	Different experimental patterns of microstreaming observed around acoustically excited microbubbles	221
F5) John Hossack	Controlling microbubble diameters from a flow focusing microfluidics device	223
F6) Yuta Hatano	Experimental investigation of frequency-dependent shape modes of a bubble cluster under a sound field.....	225
F7) Elliott Smith	A 3D Printed Chamber for Microbubble Acoustic Characterisation	229
F8) Vincent Hingot	Ultrasound Localization Microscopy in vivo: characterization, modelization and limits in various tissues	234
F9) Steven Machtaler	Developing a microbubble-based contrast agent for X-ray phase contrast imaging	236
F10) Krit Sujarittam	On the importance of sensor placement when recording a microbubble cloud's acoustic emissions.....	240

UMB special issue: Vibrating bubbles, brilliant images and palpable therapeutics

Nico de Jong

*Biomedical Engineering, Thorax center,
Erasmus MC university hospital Rotterdam, the Netherlands
N.deJong@erasmusMC.nl*

It all started in the late eighties of the last century. Real time 2D medical ultrasound imaging was established and color Doppler turned out to have excellent diagnostic utility in the larger vessels and cavities like the atria and ventricles of the heart. For visualising smaller vessels, however, there was a clear need for a contrast agent to rescue the Doppler signal. Microbubbles were the obvious candidates, since it was known that small bubbles reflect ultrasound strongly. Very quickly, several pharmaceutical and start-up companies introduced gas filled microbubbles for intravenous administration. Clinicians reported improved image clarity in organs like heart, liver, kidney, and brain. BUT, the fact that bubbles were echogenic, was also the only knowledge we had at that time. Nonlinearity was an unknown word in medical acoustics and we were ignorant about vibration modes of bubbles, jetting, diffusion of the gases, buckling, interaction with surrounding tissue, etc etc...

There was a clear need for understanding the fundamental physics of microbubbles, their use in other organs than the heart, their safety, and also their potential application for therapy. Thus, 1996 saw the start of the yearly European symposium on ultrasound contrast imaging, also referred to as the Rotterdam bubble meeting (www.echocontrast.nl).

The symposium will reach its 25th anniversary this coming January 2020. As always, it highlights new directions of research, early experiments and clinical applications by both established faculty and young investigators. The symposium is known for its strong interaction between different disciplines, including clinicians (cardiologists, radiologists, neurologists and others), physicists and engineers, biologists and chemists, from both academic and industrial backgrounds, and it links to worldwide initiatives through the ICUS(.org) society.

For this anniversary the organising committee has invited established groups of researchers to contribute review articles covering different aspects of the past, present, and future directions in the field. In total 12 topics have been defined in four areas; 1. Bubble technology (theoretical modelling, state of the art contrast agents, new and emerging agents), 2. Clinical (liver, heart perfusion and flow, carotid), 3. Imaging (conventional, high frame rate, super-resolution, molecular imaging, machine learning) and 4. Therapy (fundamental principles and clinical applications). The reviews will be accompanied by Special Collections of key UMB research papers, designed to offer readers an overview of timely areas of research.

On behalf of the organising committee and scientific board: Rik Vos, Klazina Kooiman, Folkert ten Cate, Arend Schinkel, Annemien van den Bosch, Mieke Pruijsten, Mike Averkiou, Mark Borden, Paolo Colonna, Olivier Couture, Eleanor Stride and Beat Kaufmann.

A journey in the Bracco history of gas microbubbles: from imaging to therapy

Thierry Bettinger¹, Samir Cherkaoui¹ and Christian Greis²

¹Bracco Suisse SA, Geneva, Switzerland

²Bracco Germany, Constanz, Germany

**Corresponding author: thierry.bettinger@bracco.com*

Introduction

We will take the opportunity of the 25th anniversary of the European Symposium on Ultrasound Contrast Imaging to underline the ongoing commitment of Bracco to gas-filled microbubbles use in medicine. We will also highlight new ongoing developments, and the recent investment of Bracco in the Geneva site.

Involvement of Bracco in the field of Contrast Enhanced Ultrasound (CEUS) has started in the late 1980', with a small group of scientists working on a new agent for this imaging modality. Little was known at this time, and innovation and creativity were key factors for a successful development. And indeed, this continuous strong effort gave rise to the SonoVue[®] agent [1], marketed since 2001 and now available in 38 countries with cardiac and radiology approved indications in adult and pediatric populations. After 2015 and its introduction in the USA (Lumason[®]), the strong sales are driven by two major geographic areas: China and indeed USA.

The use of blood-pool microbubbles to demonstrate flow in the macro- and microcirculation has become established clinical reality, although it is still significantly underused compared to clinical evidences and guidelines. However, for Bracco microbubbles were always a platform technology which allows a much broader range of applications and intensive R&D activities with increasing expertise and investments allowed to develop multiple product candidates including molecular imaging and therapeutic applications. BR55, an agent specific to mark angiogenesis in various lesions based on the expression of Vascular Endothelial Growth Factor Receptor 2 (VEGF-R2) was already tested in clinical studies in humans. There was a high correlation between biomarker expression and BR55 signal, particularly in ovary and breast cancer patients [2]. This does not only allow a molecular characterisation of lesions but also could guide therapy with angiogenesis inhibitors for targeted cancer therapy as shown in preclinical studies [3-5]. Another molecular imaging agent was investigated preclinically for detecting inflammatory condition, by detecting expression of P and E-Selectin biomarker [6-8]. More recently, use of gas microbubbles has evolved to move outside the scope of diagnostic imaging, to enter the arena of therapeutic applications. In this context, gas microbubbles are exploited for their capacity to trigger in situ cavitation for eliciting drug delivery, allowing either increase of blood vessel permeability (so-called sonopermeation) or mechanical removal of blood clots [9-10]. The beauty of this mechanism of action, is that the local delivery of the therapeutic agent is achieved non-invasively by means of external ultrasound exposure, either with focused or unfocused beam. Very promising results have been achieved in preclinical settings, but more importantly, also in human patients, showing the potential of this technology to transiently and safely open the blood barriers in various organs, and noticeably in the brain [11-13]. In that scope of activity, Bracco is developing a dedicated agent for this purpose, namely BR38 [14].

The development of microbubble products is supplemented by solutions increasing the clinical value. One example is the VueBox[®] quantification software developed by Bracco Geneva, which allows the quantification of contrast-enhanced ultrasound images based for example on Time/Intensity curves from DICOM clips [15-17]. Dedicated modules for specific clinical applications are available and further ones are in development.

Finally, innovative processes are under evaluation at Bracco, relying on the use of microfluidic technology to allow the preparation of gas microbubbles and acoustically activated nanodroplets presenting monodisperse size distribution [18]. Although these preparations are still at early stage, their high potential for imaging and therapy warrant further evaluation for assessing their respective performance compared to traditional polydisperse microbubbles formulations.

The field of CEUS has become a mature imaging modality, and Bracco is today significantly investing in its R&D and manufacturing in Geneva. This will allow to sustain the increasing demand of the imaging agent Sonovue®/Lumason®, but also support future products that we hope will emerge from the Bracco microbubble platform that the R&D team was able to develop over the years.

References

- [1]. Schneider M, Arditi M, Barrau MB, et al. BR1: a new ultrasonographic contrast agent based on sulfur hexafluoride-filled microbubbles. *Invest Radiol* 1995; 30:451-457.
- [2]. Willmann JK, Bonomo L, Testa AC, et al. Ultrasound Molecular Imaging With BR55 in Patients With Breast and Ovarian Lesions: First-in-Human Results. *J Clin Oncol* 2017; 35:2133-2140.
- [3]. Wang H, Lutz AM, Hristov D, Tian L, Willmann JK. Intra-Animal Comparison between Three-dimensional Molecularly Targeted US and Three-dimensional Dynamic Contrast-enhanced US for Early Antiangiogenic Treatment Assessment in Colon Cancer. *Radiology* 2017; 282:443-452.
- [4]. Zafarnia S, Bzyl-Ibach J, Spivak I, et al. Nilotinib Enhances Tumor Angiogenesis and Counteracts VEGFR2 Blockade in an Orthotopic Breast Cancer Xenograft Model with Desmoplastic Response. *Neoplasia* 2017; 19:896-907.
- [5]. Eschbach RS, Clevert DA, Hirner-Eppeneder H, et al. Contrast-Enhanced Ultrasound with VEGFR2-Targeted Microbubbles for Monitoring Regorafenib Therapy Effects in Experimental Colorectal Adenocarcinomas in Rats with DCE-MRI and Immunohistochemical Validation. *PLoS One* 2017; 12:e0169323.
- [6]. Bettinger T, Bussat P, Tardy I, et al. Ultrasound molecular imaging contrast agent binding to both E- and P-selectin in different species. *Invest Radiol* 2012; 47:516-523.
- [7]. Wang H, Felt SA, Machtaler S, et al. Quantitative Assessment of Inflammation in a Porcine Acute Terminal Ileitis Model: US with a Molecularly Targeted Contrast Agent. *Radiology* 2015; 276:809-817.
- [8]. Hyvelin JM, Tardy I, Bettinger T, et al. Ultrasound molecular imaging of transient acute myocardial ischemia with a clinically translatable P- and E-selectin targeted contrast agent: correlation with the expression of selectins. *Invest Radiol* 2014; 49:224-235.
- [9]. Sirsi SR, Borden MA. Advances in ultrasound mediated gene therapy using microbubble contrast agents. *Theranostics* 2012; 2:1208-1222.
- [10]. Rix A, Lederle W, Theek B, et al. Advanced Ultrasound Technologies for Diagnosis and Therapy. *J Nucl Med* 2018; 59:740-746.
- [11]. Abrahao A, Meng Y, Llinas M, et al. First-in-human trial of blood-brain barrier opening in amyotrophic lateral sclerosis using MR-guided focused ultrasound. *Nat Commun* 2019; 10:4373.
- [12]. Idubai A, Canney M, Belin L, et al. Safety and Feasibility of Repeated and Transient Blood-Brain Barrier Disruption by Pulsed Ultrasound in Patients with Recurrent Glioblastoma. *Clin Cancer Res* 2019; 25:3793-3801.
- [13]. Dimcevski G, Kotopoulos S, Bjanec T, et al. A human clinical trial using ultrasound and microbubbles to enhance gemcitabine treatment of inoperable pancreatic cancer. *J Control Release* 2016; 243:172-181.
- [14]. Schneider M, Anantharam B, Arditi M, et al. BR38, a new ultrasound blood pool agent. *Invest Radiol* 2011; 46:486-494.
- [15]. Schelker RC, Andorfer K, Putz F, Herr W, Jung EM. Identification of two distinct hereditary hemorrhagic telangiectasia patient subsets with different hepatic perfusion properties by combination of contrast-enhanced ultrasound (CEUS) with perfusion imaging quantification. *PLoS One* 2019; 14:e0215178.
- [16]. Nylund K, Saevik F, Leh S, Pfeffer F, Hausken T, Gilja OH. Interobserver Analysis of CEUS-Derived Perfusion in Fibrotic and Inflammatory Crohn's Disease. *Ultraschall Med* 2019; 40:76-84.
- [17]. Wiesinger I, Kroiss E, Zausig N, et al. Analysis of arterial dynamic micro-vascularization with contrast-enhanced ultrasound (CEUS) in thyroid lesions using external perfusion software: First results. *Clin Hemorheol Microcirc* 2016; 64:747-755.
- [18]. Segers T, Lassus A, Bussat P, Gaud E, Frinking P. Improved coalescence stability of monodisperse phospholipid-coated microbubbles formed by flow-focusing at elevated temperatures. *Lab Chip* 2018; 19:158-167.

Sonothrombolysis improves myocardial dynamics and microvascular obstruction preventing left ventricular remodeling in patients with ST elevation myocardial infarction

Miguel O. D. Aguiar MD*^a, Bruno G. Tavares*^a, Jeane M. Tsutsui^a, Agostina M. Fava^c, Bruno C. Borges^b, Mucio T. Oliveira Jr.^b, Alexandre Soeiro^b, Jose C. Nicolau^b, Henrique B. Ribeiro^b, Hsu Pochiang^a, João C. N. Sbrano^a, Andrew Goldsweig^c, Carlos E. Rochitte^b, Bernardo B.C. Lopes^b, José A. F. Ramirez^b, Roberto Kalil Filho^b, Thomas R. Porter^c, Wilson Mathias, Jr^a

**The two authors contributed equally to the study.*

^a Heart Institute (InCor)- University of São Paulo Medical School and Fleury Group, São Paulo, Brazil ^b Heart Institute (InCor)- University of São Paulo Medical School, São Paulo, Brazil

^c University of Nebraska Medical Center, Omaha, NE

Corresponding author: Wilson Mathias Junior

Heart Institute (InCor), University of São Paulo Medical School Av. Dr. Enéas de Carvalho Aguiar, 44 São Paulo (SP)- Brasil, 05403-000 E-mail: wmathias@incor.usp.br
Phone/Fax:(5511) 2661-5646

Background

It has recently been demonstrated that high energy diagnostic transthoracic ultrasound and intravenous microbubbles dissolve thrombi (sonothrombolysis) and increase angiographic recanalization rates in patients with ST segment elevation myocardial infarction (STEMI). We aimed to study the effect of sonothrombolysis on the myocardial dynamics and infarct size obtained by real-time myocardial perfusion echocardiography (RTMPE) and their value in preventing left ventricular remodeling (LVR).

Methods and Results: 100 patients with STEMI were randomized into therapy [50 patients treated with sonothrombolysis and percutaneous coronary intervention (PCI)] and control (50 patients treated with PCI). Left ventricular volumes, ejection fraction, risk area (prior to treatment), myocardial perfusion defect over time (infarct size) and global longitudinal strain (LV-GLS) were determined by quantitative RTMPE and speckle tracking imaging. Risk area was similar in the control and therapy ($19.2\pm 10.1\%$ vs $20.7\pm 8.9\%$; $p=0.56$) before treatment. The therapy group presented a behavior significantly different than control over time ($p<0.001$). The perfusion defect decreased in therapy at 48-72h even in the subgroup of patients with no recanalization at first angiography ($12.9\pm 6.5\%$ therapy vs $18.8\pm 9.9\%$ control; $p=0.015$). The LV-GLS was higher in the therapy than control immediately after PCI ($14.1\pm 4.1\%$ vs $12.0\pm 3.3\%$; $p=0.012$) and this difference was maintained over time until 6 months ($17.1\pm 3.5\%$ vs $13.6\pm 3.6\%$; $p<0.001$). The only predictor of LVR was treatment with sonothrombolysis. The control group was more likely to exhibit LVR with an odds ratio of 2.79 (95%CI=0.13-6.86; $p=0.026$).

Conclusion

Sonothrombolysis reduces microvascular obstruction and improves myocardial dynamics in patients with STEMI, and is an independent predictor of LVR over time.

Reference

- [1]. Mathias W Jr, Tsutsui JM, Tavares BG, Fava AM, Aguiar MOD, Borges BC, Oliveira MT Jr, Soeiro A, Nicolau JC, Ribeiro HB, Chiang HP, Sbrano JCN, Morad A, Goldsweig A, Rochitte CE, Lopes BBC, Ramirez JAF, Kalil Filho R, Porter TR; MRUSMI Investigators. Sonothrombolysis in ST-segment Elevation Myocardial Infarction Treated with Primary Percutaneous Coronary Intervention. *J Am Coll Cardiol*. 2019. pii: S0735-1097(19)33870-7.

The Application of Microbubbles and Ultrasound-Accelerated Thrombolysis (MUST) for Peripheral Arterial Occlusions: Short-term Result of a Phase-II Single Arm Trial

Sabrina A.N. Doelare^{1,4}, Harm P. Ebben^{1,4}, Johanna H. Nederhoed¹, Rutger J. Lely², Vincent Jongkind⁵, Willem Wisselink¹, Kak K. Yeung^{1,4} & MUST collaborators*

Departments of ¹Vascular Surgery, ²Radiology, ³Cardiology and ⁴Physiology, Amsterdam University Medical Centre location VUmc, Amsterdam, the Netherlands

Department of ⁵Vascular Surgery, Dijklander hospital, Hoorn, the Netherlands

Corresponding author: k.yeung@amsterdamumc.nl

Introduction

Acute peripheral arterial occlusions can be treated by catheter-directed thrombolysis (CDT) which can restore blood flow by a less invasive alternative in comparison to surgical thromboembolectomy. However, CDT is accompanied by a risk of haemorrhagic events in up to 10% of patients. The addition of contrast-enhanced ultrasound and microbubbles, called enhanced sonothrombolysis, could improve thrombus susceptibility for thrombolytic agents.

Methods

The MUST-trial is a phase II trial focusing on patients with acute peripheral arterial occlusions. In this study, 20 patients will receive CDT added with intravenous infusion of microbubbles and ultrasound during the first hour of the standard thrombolytic therapy (Urokinase or Alteplase). Primary endpoints are occurrence of serious adverse events such as mortality. Secondary endpoints are angiographic success, clinical success, additional interventions, 30-day mortality, conversion, thrombolysis duration, additional interventions e.g. ankle brachial index, microcirculation, VAS-score, fibrinogen concentrations, VAS-score and quality of life by SF-36 questionnaires. Outpatient follow-up will take place after 2-3 months, 6 months and 1-year including diagnostic tests.

Results

Currently, all 20 patients are included (n=10 Urokinase; n=10 Alteplase). No mortality or serious adverse events related to the experimental treatment can be reported. We are still waiting for the follow-up results of 6 months of all patients. Total therapy duration was established on 50,2 hours (range 20,0-99,5), whereas flow was observed at duplex examination after 21.8 hours (range 2.0-46.5). Revascularisation at angiography was established within 24.6 hours (range 6.0-76.5). Patients receiving rTPA had faster flow at duplex examination (6.8 hours (range 2-29.5)) than the patients receiving Urokinase (24 hours (6.3-46.5h)).

Conclusions

The short-term results of the MUST-trial are promising without any major complication occurrence. We report no treatment-related serious adverse events and no mortality. Further follow-up data are necessary to evaluate the effect of contrast-enhanced sonothrombolysis during CDT in patients with acute peripheral arterial occlusions.

Targeting slow-flow tumor vasculature with lectin-decorated microbubbles

Pingyu Zhang, Arshad A. Khan, Galina B. Diakova, Alexander L. Klibanov¹

¹*Group Cardiovascular Division and Robert M Berne Cardiovascular Research Center, Department of Medicine, University of Virginia Charlottesville VA 22908 USA*

Corresponding author: sasha@virginia.edu

Introduction

Traditionally, ultrasound contrast imaging of the malignant tumor neovasculature is achieved by targeting molecular biomarkers overexpressed on vascular endothelium. Such biomarkers may be related to hypoxia (VEGFR2) [1], inflammation (VCAM-1) [2] or other relevant (e.g., $\alpha_v\beta_3$) conditions [3]. The assessment of arrival time and retention period of microbubble contrast agents in the blood pool following intravenous bolus is often applied, with the aim to visualize the external rim of active vasculature that surrounds and feeds the tumor mass. Meanwhile, the vasculature within the tumor mass is disorganized and convoluted, with slow flow vessels, vessels with indistinct direction and even stagnant pools. In this study we propose a hybrid ultrasound contrast imaging approach, via a microbubble formulated with an endothelial carbohydrate-binding molecule, tomato lectin, that will selectively adhere to vasculature in slow flow, low shear conditions, and not in normal tissues, where vasculature is fully functional and blood velocity is high.

Methods

Decafluorobutane microbubbles were prepared by sonication of aqueous saline that contained a mixture of DSPC, PEG150 monostearate, and biotin-PEG3400-DSPE in a micellar form (2:2:0.1 mass ratio). Biotinylated and FITC-labeled Tomato Lectin (TL, from *Lycopersicon Esculentum*) was attached to the microbubble shell via a streptavidin linker [4]. First, repeated centrifugal washes of microbubbles with degassed saline, saturated with perfluorobutane gas, were used to remove unincorporated micellar lipid. The amount of biotin on the microbubble shell was confirmed spectrophotometrically, with a Quant*Tag kit. Excess streptavidin was then added and bubbles washed again, to remove free streptavidin; the amount of streptavidin attached to the bubbles was determined with time-resolved fluorescence spectroscopy, using Eu-labeled streptavidin. Biotin-FITC-TL was then added and incubated, as a final step. Following subsequent washes, fluorescence spectroscopy was used to determine the amount of adherent TL on microbubbles. Flotation was used to remove larger microbubbles and conjugates that might potentially get retained within the capillaries of the vascular bed.

Alternatively, a direct coupling technique was applied, that did not require the use of biotin-streptavidin. Fluorescent DyLight-TL was covalently coupled with NHS-PEG3400-DSPE in an aqueous micellar buffer. Decafluorobutane microbubbles were prepared by Vialmix amalgamation from aqueous medium that contained propyleneglycol (15% v/v, as a co-surfactant), DSPC and PEG150 monostearate (1:1 mass ratio) in the presence of TL-PEG-DSPE “supermicelles” and used without further purification [5]. Fluorescence microscopy following flotation was used to determine the fraction of TL attached to microbubbles. Removal of larger microbubbles was achieved by flotation at normal gravity.

Adhesion of microbubbles to murine microvascular endothelial cells (MVEC) was tested in a Glycotech parallel plate flow chamber [6]. Cells were grown in a Petri dish which was then plugged into the chamber assembly. Syringe pump was used to pull microbubble suspension through the flow deck at the controlled flow shear conditions, under video microscopy control.

In vivo contrast ultrasound imaging was performed in a murine subcutaneous tumor model. MC38 murine adenocarcinoma cells (generously provided by Dr. J. Schlom, NCI) were injected subcutaneously in C57BL/6 mice. TL-carrying microbubbles or control nonspecific IgG microbubbles were administered

intravenously, and imaging of tumors and control contralateral leg muscles was performed under isoflurane anesthesia with a Siemens Sequoia c512 system equipped with 15L8 probe (CPS mode, 7 MHz, MI 0.2). Video stream data were exported to jpg files and quantified with ImageJ. For the selected region of interest in the tumor and contralateral leg, 10 min signal intensity was normalized by the peak intensity observed at 30 sec following intravenous bolus.

Results

We determined that each biotinylated microbubble carried $\sim 3 \cdot 10^5$ biotin residues, 10^5 streptavidin molecules and $2 \cdot 10^4$ molecules of TL. Likewise, for covalent coupling approach, $\sim 2 \cdot 10^4$ molecules of TL per microbubble were attached.

TL-carrying microbubbles, but not control bubbles (carrying nonspecific IgG) were selectively attached to cultured MVEC cells in static conditions. In the flow chamber setting, adhesion from the flowing media onto the cultured cell flow deck was minimal for control microbubbles. TL microbubbles were efficiently adhering at slow flow conditions (0.25 and 0.5 dyn/cm² wall shear stress). Adhesion was drastically reduced in faster flows (1 dyn/cm² and above) and became negligible at 4 dyn/cm².

In vivo ultrasound contrast imaging had demonstrated selective accumulation and retention of TL-streptavidin-microbubbles in the tumor, but not in the contralateral leg normal muscle tissue (~ 3 - 4 -fold), observed for TL-biotin-streptavidin-microbubbles, as well as TL-PEG-DSPE-microbubbles. Control microbubbles did not show significant tumor accumulation.

Conclusions

Tomato Lectin-decorated microbubbles, unlike control microbubbles, selectively adhered to vascular endothelium in cell culture in a parallel plate flow chamber, in slower flow conditions. In faster flows, TL microbubble adhesion was drastically lower. TL-decorated microbubbles accumulated efficiently in the tumor tissues in tumor-bearing mice, but not in the control contralateral leg muscle, as observed by contrast ultrasound imaging. It may therefore be suggested that disorganized vasculature with slow flow permits selective adhesion of lectin microbubbles, which allows tumor mass delineation. This approach may provide a universal contrast imaging tool to assess and delineate tumor neovasculature, especially if particular molecular biomarkers are not known or could not be targeted due to lack of specific affinity ligands.

References

- [1]. Willmann JK, Bonomo L, Testa AC, Rinaldi P, Rindi G, Valluru KS, Petrone G, Martini M, Lutz AM, Gambhir SS. Ultrasound Molecular Imaging With BR55 in Patients With Breast and Ovarian Lesions: First-in-Human Results. *J Clin Oncol*. 2017;35(19):2133-2140.
- [2]. Hernot S, Unnikrishnan S, Du Z, Shevchenko T, Cosyns B, Broisat A, Toczek J, Caveliers V, Muyldermans S, Lahoutte T, Klibanov AL, Devoogdt N. Nanobody-coupled microbubbles as novel molecular tracer. *J Control Release*. 2012;158(2):346-353.
- [3]. Ellegala DB, Leong-Poi H, Carpenter JE, Klibanov AL, Kaul S, Shaffrey ME, Sklenar J, Lindner JR. Imaging tumor angiogenesis with contrast ultrasound and microbubbles targeted to alpha(v)beta3. *Circulation*. 2003;108(3):336-341.
- [4]. Lindner JR, Song J, Christiansen J, Klibanov AL, Xu F, Ley K. Ultrasound assessment of inflammation and renal tissue injury with microbubbles targeted to P-selectin. *Circulation*. 2001;104(17):2107-2112.
- [5]. Unnikrishnan S, Du Z, Diakova GB, Klibanov AL. Formation of Microbubbles for Targeted Ultrasound Contrast Imaging: Practical Translation Considerations. *Langmuir*. 2019;35(31):10034-10041
- [6]. Takalkar AM, Klibanov AL, Rychak JJ, Lindner JR, Ley K. Binding and detachment dynamics of microbubbles targeted to P-selectin under controlled shear flow. *J Control Release*. 2004;96(3):473-482.

Ultrasound molecular imaging of atherosclerosis: Liraglutide treatment lowers expression of endothelial vascular cell adhesion molecule 1 (VCAM-1)

Mukesh Punjabi¹, Alexandra Kosareva¹, Lifen Xu¹, Amanda Ochoa-Espinosa¹, Georg Hoffmann¹, Bidha Rolin³, Michael Nyberg³, Beat A. Kaufmann^{1,2}

¹Cardiovascular Molecular Imaging, Department of Biomedicine, University Hospital Basel, University of Basel, Basel, Switzerland, ²Department of Cardiology, University Hospital Basel, Basel, Switzerland,

³Novo Nordisk A/S, Copenhagen, Denmark

Corresponding author: mukesh.punjabi@unibas.ch

Introduction

Type 2 diabetes mellitus (T2DM) is one of the most important risk factors for the development of cardiovascular disease (CVD) because it promotes systemic atherosclerosis. The inflammatory response plays an important role in the initiation and progression of CVD and, hence, has been identified as a potential therapeutic and diagnostic target for non-invasive medical imaging. Contrast enhanced ultrasound molecular imaging (CEUMI) of endothelial expression of vascular cell adhesion molecule (VCAM-1) involved in inflammatory processes that initiate and propagate atherosclerosis is a good target for testing the adequacy of anti-inflammatory treatment effects both for preclinical research in animal models, and also in humans. Glucagon like Peptide (GLP)-1, an incretin hormone is secreted by L-cells of the distal small intestine and large bowel in response to food intake and has several systemic effects, including the glucose-dependent stimulation of insulin secretion by pancreatic beta cells [1]. GLP-1 receptor (GLP-1R), a G protein-coupled receptor, has been detected in the nervous system, heart, vascular smooth muscle cells, endothelial cells, monocytes and macrophages. Several lines of evidence suggest that incretin-based therapies suppress the development of CVD in T2DM [2]. Liraglutide, a once-daily GLP-1 derivative, is a long-acting GLP-1R agonist that shares 97% sequence identity to human GLP-1 (7–37) and has a plasma half-life of 13 hours after subcutaneous administration in contrast to a short half-life of native GLP-1. Liraglutide has been shown to prevent the onset of high glucose-induced endoplasmic reticulum stress in HUVECs [3] and also inhibit the tumor necrosis factor- α induced VCAM-1 expression, and these effects were dependent on the GLP-1R [4]. Liraglutide also inhibited the progression of atherosclerotic plaques, and improved the plaque stability in mice deficient in apolipoprotein E (ApoE^{-/-}) [5]. Some small sample sized non-randomized clinical studies have also reported that the endothelial function is improved by using GLP-1 and GLP-1-related drugs [2]. A recently concluded randomized controlled trial (LEADER) specifically showed that the rate of the first occurrence of death from cardiovascular causes, nonfatal myocardial infarction, or nonfatal stroke among patients with T2DM was lower with liraglutide than with placebo [6]. Taken together, liraglutide appears to impact upon the progression of atherosclerosis, but the precise pathways that are responsible are unclear. Thus, it is also unknown whether treatment with liraglutide leads to a downregulation of VCAM-1 *in vivo* on the vascular endothelial surface. We therefore used CEUMI to investigate whether liraglutide leads to a decrease in the VCAM-1 signal on the vascular endothelium. Specifically, we tested and compared the effects of 4, 8 and 12 weeks daily liraglutide therapy on vascular endothelial phenotype in mouse model of high burden atherosclerosis.

Methods

All experiments were performed in accordance with Swiss federal legislation and approved by the ethics committee of the veterinary office of the canton of Basel. Female ApoE^{-/-} mice aged 6-8 weeks were put on western-type (fat =41 kcal%) diet and randomly divided into two groups and subcutaneously administered either liraglutide (1 mg/kg, Novo Nordisk) or vehicle (PBS-buffer) daily for a period of 8 or

12 weeks. Body weight and animal wellbeing was monitored daily. Biotinylated, lipid-shelled decafluorobutane microbubbles were prepared by sonication of a gas saturated aqueous suspension of distearoylphosphatidylcholine (2 mg/ml), polyoxyethylene-40-stearate (1 mg/ml), and 1,2-distearoyl-sn-glycero-phosphoethanolamine-N-[biotinyl(polyethylene glycol)-3400] (0.14 mg/ml). Microbubbles targeted to VCAM-1 (MB_{VCAM-1}) were prepared by conjugation of biotinylated rat anti-mouse VCAM-1 antibody to the microbubble surface using biotin-streptavidin-biotin linking. Control microbubbles (MB_{Ctrl}) bearing a non-specific isotype control antibody were also prepared. After jugular vein catheterisation, CEUMI of the aortic arch for the expression of VCAM-1 was performed before start of treatment at 0 weeks (baseline) and after 4, 8 and 12 weeks of treatment. 1×10^6 MB_{VCAM-1} and MB_{Ctrl} were injected in random order. Eight minutes after microbubble injection, ultrasound imaging with contrast pulse sequencing at 7 MHz frequency and a mechanical index of 0.87 was performed. Offline analysis was used to derive the signal from attached microbubbles by subtracting several averaged image frames after microbubble destruction from the first image frame. Signal resulting from MB_{VCAM-1} was expressed as a fold change in relation to signal from MB_{Ctrl}. High frequency ultrasound imaging was performed to measure aorta internal diameter, peak systolic flow velocity, left ventricular mass and left ventricular ejection fraction. The mice were euthanized at 8 or 12 weeks after liraglutide or vehicle treatment, and the aortic tissue was stored for immunohistology.

Results

Body weight decreased after initiation of liraglutide treatment and remained significantly lower ($p < 0.0001$) throughout the study in comparison to vehicle treated animals by around 10%. Results from CEUMI are presented in Fig. 1. At baseline, there was no difference between MB_{VCAM-1} and MB_{Ctrl} in both treatment groups. At 4, 8 and 12 weeks there was a 3 to 4 fold increase of MB_{VCAM-1} to MB_{Ctrl} signal in vehicle treated animals ($p < 0.001$ vs. baseline at 4 and 8 weeks, $p < 0.05$ vs. baseline at 12 weeks). This did not occur in liraglutide treated animals, where MB_{VCAM-1} signal was not different from MB_{Ctrl} signal at all timepoints. Additionally, there was a 3 to 4 fold increase of MB_{VCAM-1} to MB_{Ctrl} signal in vehicle vs. liraglutide treated animals ($p < 0.0001$) at 4, 8 and 12 weeks. High frequency ultrasound data analysis showed the aorta systolic flow velocity and left ventricular ejection fraction to be similar for vehicle and liraglutide treated mice after 0, 4, 8 and 12 weeks of treatment. Aorta internal diameter was higher for vehicle as compared to liraglutide treated mice only after 8 weeks ($p < 0.01$) of treatment. The left ventricular mass was higher for vehicle as compared to liraglutide treated mice only after 8 ($p < 0.05$) and 12 ($p < 0.05$) weeks of treatment.

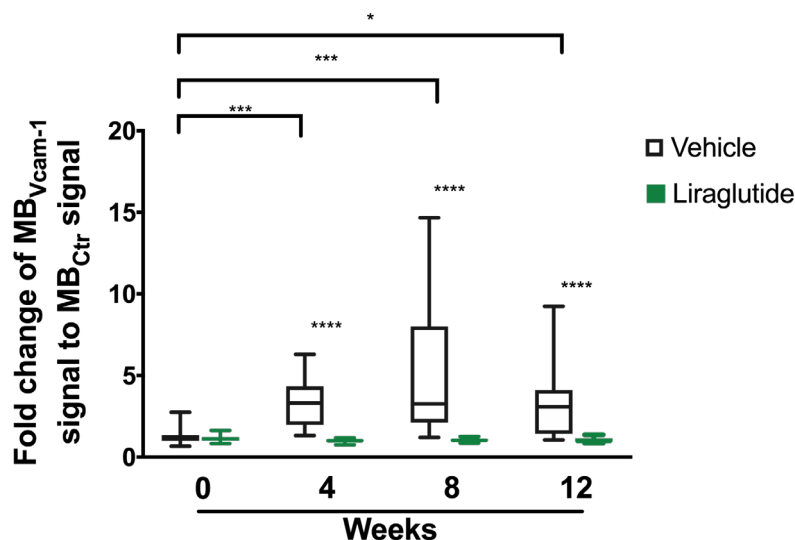


Fig. 1: Background subtracted contrast enhanced ultrasound molecular imaging signal intensity from the aortic arch 8 minutes after intravenous injection of targeted (MB_{Vcam1}) and control (MB_{Ctrl}) microbubbles in ApoE^{-/-} mice shown as fold change after 4, 8 and 12 weeks of liraglutide versus vehicle treatment (**** $p < 0.0001$, *** $p < 0.001$, * $p < 0.05$; $n = 15-20$ at each timepoint).

Conclusions

Daily long term (4, 8 and 12 weeks) liraglutide treatment leads to a reduction in the VCAM-1 expression on the vascular endothelium indicating an attenuation of vascular endothelial inflammation in a mouse model of high burden atherosclerosis. The decrease in vascular events observed in clinical trials of liraglutide treatment may therefore be related to a direct effect of liraglutide on endothelial inflammatory activation.

References

- [1]. Holst, J.J., The physiology of glucagon-like peptide 1. *Physiol Rev*, 2007. 87(4): p. 1409-39.
- [2]. Drucker, D.J., The Cardiovascular Biology of Glucagon-like Peptide-1. *Cell Metab*, 2016. 24(1): p. 15-30.
- [3]. Schisano, B., et al., GLP-1 analogue, Liraglutide protects human umbilical vein endothelial cells against high glucose induced endoplasmic reticulum stress. *Regul Pept*, 2012. 174(1-3): p. 46-52.
- [4]. Gaspari, T., et al., A GLP-1 receptor agonist liraglutide inhibits endothelial cell dysfunction and vascular adhesion molecule expression in an ApoE^{-/-} mouse model. *Diab Vasc Dis Res*, 2011. 8(2): p. 117-24.
- [5]. Gaspari, T., et al., The GLP-1 receptor agonist liraglutide inhibits progression of vascular disease via effects on atherogenesis, plaque stability and endothelial function in an ApoE^(-/-) mouse model. *Diab Vasc Dis Res*, 2013. 10(4): p. 353-60.
- [6]. Marso, S.P., et al., Liraglutide and Cardiovascular Outcomes in Type 2 Diabetes. *N Engl J Med*, 2016. 375(4): p. 311-22.

Opening of endothelial cell-cell contacts caused by sonoporation elucidated with combined confocal microscopy and Brandaris 128 imaging

Inés Beekers¹, Merel Vegter¹, Kirby R. Lattwein¹, Frits Mastik¹, Robert Beurskens¹, Antonius F. W. van der Steen^{1,2}, Nico de Jong^{1,2}, Martin D. Verweij^{2,1}, Klazina Kooiman¹

¹*Department of Biomedical Engineering, Erasmus MC, Rotterdam, the Netherlands*

²*Laboratory of Acoustical Wavefield Imaging, Delft University of Technology, Delft, the Netherlands*
Corresponding author: d.beekers@erasmusmc.nl

Introduction

The vascular endothelium constitutes a major barrier to efficient drug penetration and extravasation for localized drug delivery. Ultrasound insonification of microbubbles helps overcome this barrier by inducing cell membrane perforation (sonoporation), cell-cell contact opening, and endocytosis [1]. However, to control and maximize the therapeutic outcome, the underlying mechanisms of the microbubble-cell interaction need to be unraveled. The aim of this *in vitro* study was to elucidate the microbubble oscillation behavior required for sonoporation and opening of cell-cell contacts. To achieve the nanosecond and nanometer resolution necessary to resolve microbubble oscillation and visualize the cellular effects, a unique optical imaging system was used consisting of the Brandaris 128 ultra-high-speed camera coupled to a custom-built confocal microscope [2].

Methods

Human umbilical vein endothelial cells (HUVEC) were cultured to full confluency in a CLINiCell [3] and lipid-coated microbubbles were targeted to the $\alpha_v\beta_3$ receptor expressed during angiogenesis. To unravel the underlying biological mechanisms, we monitored the cellular effect of a single microbubble (n=152) up to 4 min after ultrasound insonification (2 MHz, 100 to 400 kPa, 10 cycles). Drug delivery was assessed by evaluating sonoporation with the fluorescent model drug Propidium Iodide (PI) and opening of cell-cell contacts with CellMask™ Green. During insonification, microbubble oscillation was recorded with the Brandaris 128 ultra-high-speed camera to determine the change in radius as a function of time.

Results

A typical example of sonoporation and opening of cell-cell contacts and the corresponding microbubble oscillation upon insonification is shown in Fig. 1A. Sonoporation occurred when microbubble excursion amplitudes exceeded 0.7 μm (difference between maximum and initial radius) and was independent of the initial microbubble size (Fig. 1B). Additionally, quantification of the PI influx profile [4] upon sonoporation showed that the size of the created pore increased for larger microbubble excursion amplitudes. Microbubble-mediated opening of cell-cell contacts did not correlate with the microbubble excursion amplitude itself and was only significantly enhanced upon sonoporation (Fig. 1C). The initial integrity of the cell-cell contacts strongly affected the susceptibility to drug delivery, since cell-cell contacts opened more often when cells were only partially attached to their neighbors (48%) than when fully attached (14%) (Fig. 1C). Finally, the drug delivery outcomes were independent of the presence of subharmonics or asymmetry in microbubble oscillation, microbubble location on the cell, and cell size.

Conclusions

Using a state-of-the-art optical imaging system, the microbubble-cell interaction was studied with high sensitivity at short timescales, while also achieving the nanosecond resolution needed to resolve microbubble oscillation. We found that larger microbubble excursion amplitudes (> 0.7 μm) correlated with the occurrence and severity of sonoporation, while the opening of cell-cell contacts could not be

predicted from microbubble behavior. Microbubble-mediated opening of cell-cell contacts only occurred upon sonoporation and was influenced significantly by the initial cell state. Therefore, our results suggest that opening of cell-cell contacts is a biological response as a consequence of sonoporation, instead of an independent drug delivery pathway. These novel insights will aid the development of safe and efficient microbubble-mediated drug delivery.

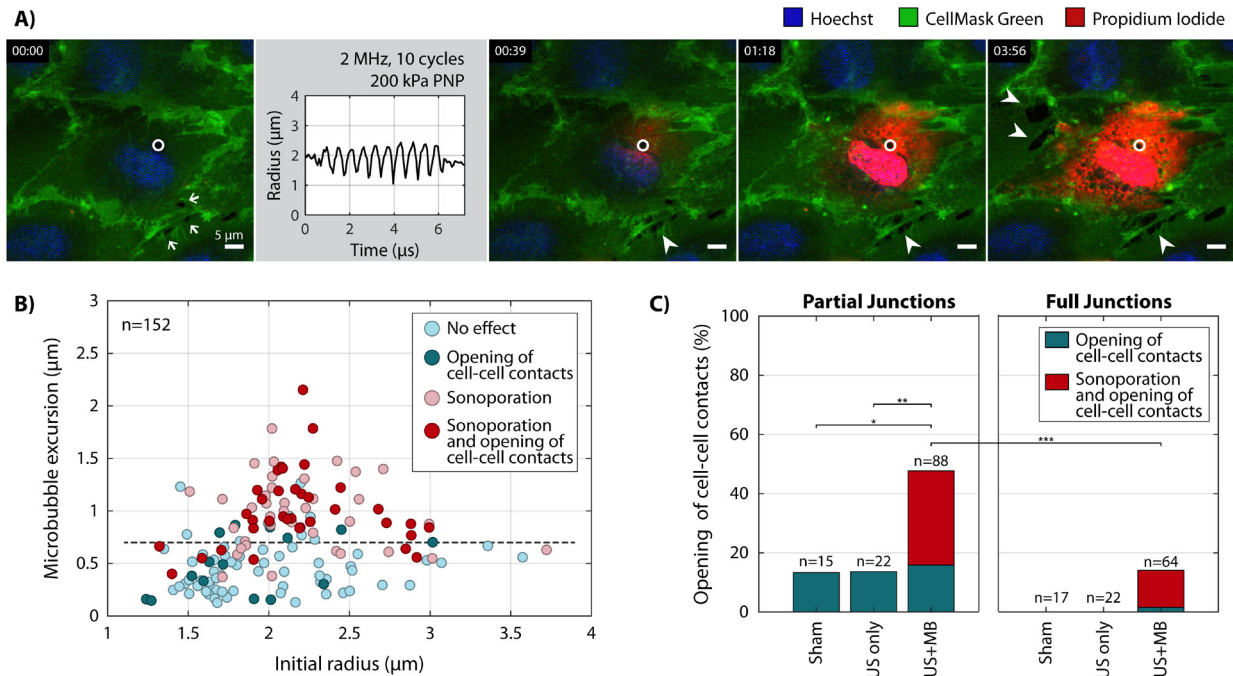


Fig. 1: A) Imaging time sequence with confocal microscopy before ultrasound, showing endothelial cells with partial initial junctions (arrows) and a single targeted microbubble (white circle; 1.9 μm in radius). The microbubble radius is shown as a function of time, as obtained from the Brandaris 128 recording. Selected frames of confocal microscopy after ultrasound show sonoporation (local PI uptake in red) and opening of cell-cell contacts (arrowheads). Scale bar 5 μm . **B)** Microbubble excursion amplitude and the induced cellular response. Dashed line indicates the 0.7 μm threshold for sonoporation. **C)** Occurrence of opening of cell-cell contacts, with or without sonoporation, and the initial integrity of cell-cell junctions before treatment. Statistical significance indicated with * $p<0.05$, ** $p<0.01$, *** $p<0.001$; US = ultrasound; MB = microbubble.

Acknowledgements

This work was supported by the Applied and Engineering Sciences TTW (Veni-project 13669), part of NWO. The authors would like to thank Phoei Ying Tang from the Department of Biomedical Engineering for assistance during experiments and cell culture and Michiel Manten and Geert Springeling from the Department of Experimental Medical Instrumentation for technical assistance, all from the Erasmus Medical Center, the Netherlands.

References

- [1]. Kooiman K, Vos HJ, Versluis M, de Jong N, Acoustic behavior of microbubbles and implications for drug delivery, *Adv Drug Deliv Rev*, vol 72, pp 28-48, 2014.
- [2]. Beekers I, Lattwein KR, Kouijzer JJP, Langeveld SAG, Vegter M, Beurskens R, Mastik F, Verduyn Lunel R, Verver E, van der Steen AFW, de Jong N, Kooiman K, Combined Confocal Microscope and Brandaris 128 Ultra-High-Speed Camera, *Ultrasound Med Biol*, vol 45, pp 2575-2582, 2019.
- [3]. Beekers I, van Rooij T, van der Steen AFW, de Jong N, Verweij MD, Kooiman K, Acoustic Characterization of the CLINicell for Ultrasound Contrast Agent Studies, *IEEE Trans Ultrason Ferroelectr Freq Control*, vol 66, pp 244-246, 2019.
- [4]. Fan Z, Liu H, Mayer M, Deng CX, Spatiotemporally controlled single cell sonoporation, *Proc Natl Acad Sci*, vol 109, pp 16486-16491, 2012.

The Rocky Road to Approval: A Bubble's story

***Peter N Burns**¹, **Christian Greis**²*

¹Professor of Medical Biophysics and Radiology, University of Toronto; Senior Scientist, Sunnybrook Research Institute, Toronto, Canada

*²Head of Global Marketing Ultrasound, Bracco Imaging
Corresponding author: Petern.burns@utoronto.ca*

All of us in biomedical research are aware of the need to satisfy our reviewers and funding agencies that the work we propose offers a reasonable expectation of translation to clinical practice. We can argue (at our peril) that translation is just around the corner, or try to reason (with equal peril) that our work is in basic science and will provide insight that should eventually benefit healthcare in some unspecified way. Both arguments have been used many times at this symposium. The pressure we feel has been referred to in a recent Nature editorial, somewhat bitterly, as 'the tyranny of translation'. But what does clinical translation really mean, and in reality, what does it take to achieve? We propose that the 25th anniversary of the European Contrast Symposium might be an appropriate time to relate the exemplary - and cautionary - tale of the clinical translation of microbubble contrast for ultrasound imaging. It begins more than four decades ago as a curiosity in fluid physics and ends today with more than 15 million patient studies worldwide and the initiation of a new era in noninvasive therapy with sound. A success story, perhaps, but one with some pretty spectacular scientific, commercial and regulatory failures on the way. As it unfolded, the story helped temper our expectations of the impact of our work, but did not prepare us for surprises that included the persistently arbitrary and capricious decisions of a US government agency, turning ultimately - and incomprehensibly - in our favour.

Transthoracic Acoustic Droplet Activation Pulse Sequence Schemes In Myocardial Ischemia And Reperfusion

T.Porter¹, S. El Kadi^{1,2}, L. Qian^{1,3}, P. Zeng¹, J. Lof¹, Jiri Sklenar, Elizabeth Stoltze¹, F. Xie¹

¹Department of Cardiovascular Medicine, University of Nebraska Medical Center, Omaha, United States

²Department of Cardiology, Amsterdam UMC – Location VUmc, Amsterdam, The Netherlands

³Department of Cardiology, The First Affiliated Hospital of Nanjing Medical University, Nanjing, China

Corresponding author: trporter@unmc.edu

Introduction Transthoracic acoustic activation of intravenously administered perfluoropropnae droplets is possible with high mechanical index (MI) diagnostic ultrasound [1,2]. Sub-micron sized liquid perfluorocarbon nanodroplets with low boiling points and can be preserved in a superheated condition without vaporization. When exposed to higher acoustic pressures, the droplets transform into gaseous microbubbles with 3-5 times the original diameter [3]. The small diameter of the nanodroplets can potentially lead to enhanced trans-endothelial passage and retention. Local activation of the accumulated nanodroplets and subsequent cavitation may result in improved detection of the developing scar zone (DSZ) during and following myocardial ischemia. The main aim of this study is to investigate the potential of droplet activation imaging using perfluorocarbon nanodroplets with two different ultrasound activation/imaging pulse schemes, when compared to microbubbles.

Methods. A diagnostic ultrasound transducer (S5-1, Philips) was used to emit intermittent high mechanical index impulses in real-time imaging with either a multi-pulse fundamental non-linear or single pulse harmonic sequence scheme. We examined the potential for each of these schemes to detect selective acoustic activation of the developing scar zone (DSZ) in a porcine model of acute anteroseptal myocardial infarction(n=6) followed by reperfusion. Definity (Lantheus) perfluorocarbon droplets (PD) were created by cooled compression of Definity microbubbles (PMB). Imaging comparisons were performed within 30 minutes of reperfusion following a 90 minute left anterior descending balloon occlusion or thrombosis, and again within 24-48 hours.

Results. At four minutes post intravenous injection (IVI), high MI harmonic imaging produced selective enhancement within the risk area, the size of which correlated with the circumferential extent of the infarct by delayed enhancement magnetic resonance imaging and post mortem TTC staining. This was not observed at any time point following the IVI of same dose of PMB (Figure 1b).

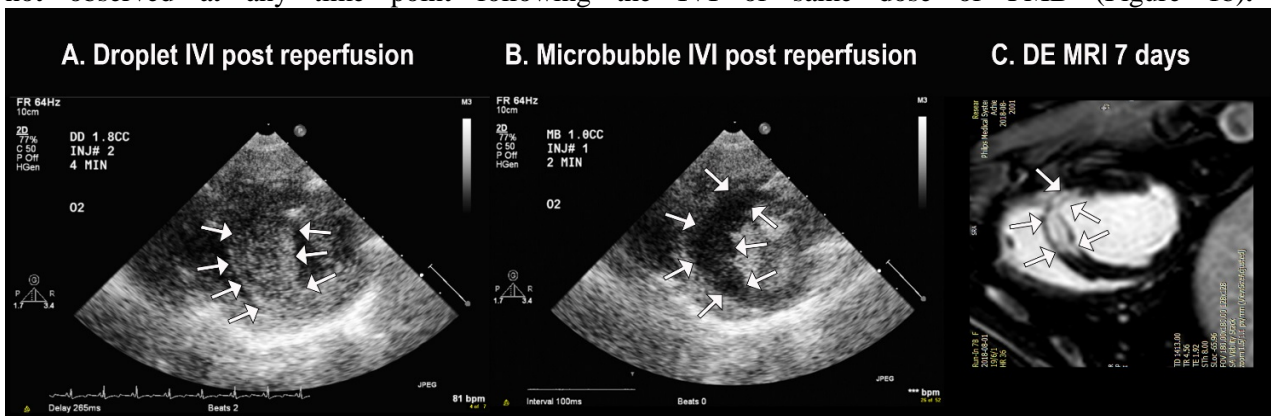


Figure 1. High MI harmonic (transthoracic imaging) following PD (Panel A) versus PMB (Panel B). Note the marked enhancement of the infarct zone following PD injection instead of a contrast defect following IVI of PMB. The enhanced area detected with PD (Panel A) developed into a scar by MRI at 7 days(C)

Transthoracic harmonic single pulse activation required a high MI (>1.0 at 1.7 MHz), but after activation formed microbubbles were still evident when returning to lower MI. On the other hand, after multipulse >1.0 MI, 40 frame, flash activation (Amplitude modulation), very low MI imaging at <0.2 MI detected the

gradual appearance of microbubbles within both the DSZ and normal zone (Figure 2). This activation was reproduced with repeated flash high MI activations up to six minutes after IVI (Figure 3).



Pre-injection background

High MI 2 min post IVI

Myocardial Background Subtracted

Figure 2. Background subtracted imaging of the DSZ (arrow) 48 hours after a 90 minute LAD balloon occlusion followed by reperfusion.



Immediate post high MI

40 sec post high MI impulse

Background-subtracted

Figure 3. Microbubble formation after high MI impulse during fundamental non-linear imaging. The arrows depict infarct zone enhancement, which was confirmed as transmural scar on post-mortem TTC staining and cardiac delayed enhancement magnetic resonance imaging.

Conclusions

Droplet activation imaging with fundamental non-linear imaging can be utilized for repeated activation of retained droplets within both normal and reperfusion-injured myocardium. This may allow selective detection, and targeted treatment, of the DSZ in acute coronary syndromes.

References

- [1]. Porter TR, Arena C, Sayyed S, Lof J, High RR, Xie F, Dayton PA. Targeted transthoracic acoustic activation of systemically administered nanodroplets to detect myocardial perfusion abnormalities. *Circ Cardiovasc Imaging*, 2016 9(1). Pii:e003770.
- [2]. Choudhury, S.A., et al., Selective infarct zone imaging with intravenous acoustically activated droplets. *PLoS One*, 2018. **13**(12): p. e0207486.
- [3]. Sheeran, P.S., et al., Decafluorobutane as a phase-change contrast agent for low-energy extravascular ultrasonic imaging. *Ultrasound Med Biol*, 2011. **37**(9): p. 1518-30.

NO-Microbubbles Promote Sonobactericide

Christy K. Holland^{1,2}, Maxime Lafond¹, Himanshu Shekhar³

¹Department of Internal Medicine, Division of Cardiovascular Health and Disease, University of Cincinnati, Cincinnati, OH, USA

²Department of Biomedical Engineering, University of Cincinnati, Cincinnati, OH, USA

³Discipline of Electrical Engineering, Indian Institute of Technology Gandhinagar, Palaj, Gandhinagar, Gujarat, India

Corresponding author: Christy.Holland@uc.edu

Introduction

Nitric oxide (NO) is a potent bioactive gas capable of inducing vasodilatory, anti-inflammatory, neuroprotectant and bactericidal effects. *In vivo* NO production is reduced in pathological conditions, such as hypertension, atherosclerosis, and chronic kidney disease [1]. The short half-life, high reactivity, and rapid diffusivity of NO make therapeutic delivery challenging. The goal of this work was to characterize NO-loaded microbubbles stabilized with a lipid shell and to assess the feasibility of antibacterial therapy *in vitro*. NO dose, acoustic response, and stability of microbubbles synthesized with either NO alone (NO-MB), or with NO and OFP at different volume fractions: 90% NO and 10% OFP (NO-OFP-MB 9:1 v/v), or 50% NO and 50% OFP (NO-OFP-MB 1:1 v/v) were quantified. The size distribution and acoustic attenuation of NO-loaded microbubbles were characterized. Imaging and release of NO and OFP from the microbubbles was demonstrated using a commercial ultrasound scanner. Finally, we evaluated the feasibility of killing the USA 300 strain of *Staphylococcus aureus* (*S. aureus*) using NO-loaded microbubbles *in vitro* [2].

Methods

Gas-loaded microbubbles were synthesized by high-shear mixing of a lipid dispersion in a vial that contained NO, and octafluoropropane (OFP) in combination [2, 3]. A Coulter counter (Multisizer 4, Beckman Coulter, Brea, CA, USA), equipped with a 30- μ m aperture, was used to measure the size distributions of NO-MB and NO-OFP-MB at room temperature. Differential interference contrast microscopy using an Axioplan 2 system (Zeiss, Thornwood, NY, USA) was performed to assess the morphology of lipid-shelled microbubbles. Broadband attenuation spectroscopy was used to measure the acoustic attenuation coefficient of NO-MB and NO-OFP-MB from 2 to 25 MHz at 37 °C as reported previously [4].

The acoustic attenuation of NO-OFP-MB was measured after exposure to either sham (no ultrasound), B-mode ultrasound at an on-screen MI of 0.04 (peak rarefactional pressure of 0.02 MPa *in situ*), or Duplex Doppler ultrasound at an on-screen MI of 1.2 (rarefactional pressure of 2.48 MPa *in situ*). The B-mode exposure was created by a clinical ultrasound scanner (EPIQ 7G, Philips Healthcare, Bothell, WA USA), which was used to drive a C5-1 transducer array (Phillips, Bothell, MA, USA) with a center frequency of 3.41 MHz. Complete attenuation loss was used to indicate gas payload release from lipid-shelled microbubbles.

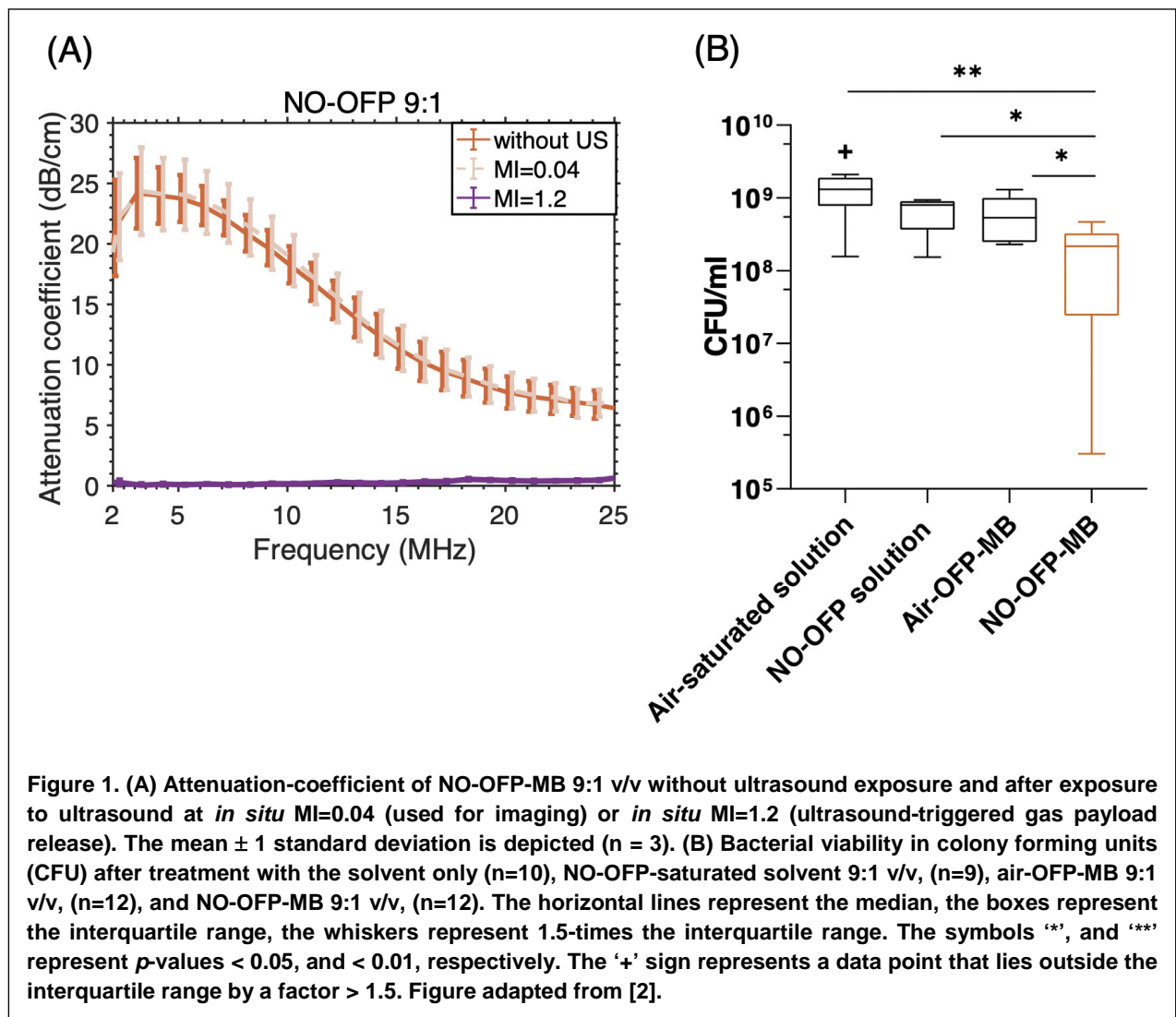
The NO dose in the microbubbles was quantified using an amperometric microelectrode sensor (Apollo 4000 with ISO-NOP electrode; World Precision Instruments, Sarasota, FL, USA), which had a response time of about 5 to 7 seconds, and compared to an NO-OFP-saturated solution. The stability of the “in vial” NO dose was assessed by successive measurements 15 min, 2, 4, and 6 h after vial activation. The NO dose in a 96-well plate was measured from 15 to 340 s. The susceptibility of *S. aureus* USA300, a methicillin-resistant strain, to NO-OFP-MB 9:1 v/v was evaluated *in vitro* in a 96-well plate. After incubation at 37 °C for 18 h, bacteria colonies were counted and reported as colony forming units

(CFU)/ml. A Kruskal-Wallis test was used to compare the CFU/ml obtained with air-saturated solution, NO-OFP 9:1 v/v saturated solution and air-OFP-MB against NO-OFP-MB. Post-hoc Dunn's multiple comparison test was used to obtain adjusted *p*-values, which were considered statistically significant if less than 0.05.

Results

Co-encapsulation of NO with OFP increased the total volume and attenuation coefficient of the microbubbles. The NO-OFP-MB were destroyed with a clinical ultrasound scanner with an output of 2.48 MPa peak negative pressure (on-screen MI of 1.2) but maintained their echogenicity when exposed to 0.02 MPa peak negative pressure (on-screen MI of 0.04), shown in Figure 1A. Ultrasound-triggered release of the encapsulated gas payload was demonstrated with 3.41-MHz pulsed Doppler ultrasound.

The NO-OFP-MB 9:1 v/v payload was 4.78 ± 1.03 mM, and the NO-OFP-MB 1:1 v/v dose was 2.96 ± 0.61 mM. The NO dose in NO-MB and NO-OFP-MB was more than 2-fold higher than an NO-OFP-saturated solution. A solution of phosphate buffered saline, polypropylene glycol, and glycerol (16:3:1 by volume) saturated with a combination of NO and OFP either at 9:1 or 1:1 v/v mixture ratio contained 1.97 ± 0.35 mM or 0.96 ± 0.11 mM NO at room temperature. The effect of NO delivery on the viability of planktonic (free living) *Staphylococcus aureus* USA 300, a methicillin-resistant strain, is shown in Figure 1B. Delivery of NO-OFP-MB increased bactericidal efficacy compared to an NO-OFP-saturated solution or air- and OFP-loaded microbubbles.



Conclusions

Loading NO into lipid-shelled microbubbles with OFP gas increased the NO dose relative to NO- and OFP-saturated solutions. The attenuation and total volume of NO-OFP-MB was higher than lipid-shelled bubbles fabricated with NO alone. The feasibility of antibacterial therapy with NO-OFP-MB against a resistant USA 300 strain was demonstrated. A statistically significant enhancement in bacterial killing over NO-OFP-saturated solution and air-OFP-MB was demonstrated *in vitro* with NO-OFP-MB. These results suggest that encapsulation of NO with OFP in lipid-shelled microbubbles enhances payload delivery.

References

- [1] A. Ahmad *et al.*, "Role of Nitric Oxide in the Cardiovascular and Renal Systems," *Int J Mol Sci*, vol. 19, no. 9, Sep 3 2018, doi: 10.3390/ijms19092605.
- [2] M. Lafond *et al.*, "Bactericidal activity of lipid-shelled nitric oxide-loaded microbubbles," *Front Pharmacol*, In Press, 2020.
- [3] H. Shekhar *et al.*, "Characterization and Imaging of Lipid-Shelled Microbubbles for Ultrasound-Triggered Release of Xenon," *Neurotherapeutics*, vol. 16, no. 3, pp. 878-890, Jul 2019, doi: 10.1007/s13311-019-00733-4.
- [4] J. L. Raymond *et al.*, "Broadband attenuation measurements of phospholipid-shelled ultrasound contrast agents," *Ultrasound Med Biol*, vol. 40, no. 2, pp. 410-21, Feb 2014, doi: 10.1016/j.ultrasmedbio.2013.09.018.

Ultrasound-Mediated Doxorubicin Delivery by Microbubble-Liposome Complexes Has Superior Anti-tumor Efficacy and Reduced Cardiotoxicity *in vivo*

Mingyu He¹, Xucui Chen¹, Francois Yu¹, Huizhu Wang¹, Linda Lavery¹, Flordeliza S. Villanueva¹

¹ Center for Ultrasound Molecular Imaging and Therapeutics, University of Pittsburgh, Pittsburgh, PA, USA

Corresponding author: villanuevafs@upmc.edu

Introduction

Doxorubicin (**Dox**) is standard of care for treatment of sarcomas; tumor response correlates with dosage. Dox is cardiotoxic in a dose-dependent manner, which can limit maximum dosing for effective therapy. Microbubbles (**MBs**) are intravenously injectable gas microspheres that are clinically used as ultrasound (**US**) contrast agents. MBs can also be used as drug or gene carriers that undergo US-triggered unloading of cargo at disease-specific sites via navigation of the US beam. We have previously shown the efficacy of liposomal-Dox-MB complexes (**DoxLPX**) and US delivery for inhibiting tumor cell growth *in vitro* equivalent to that achieved with free Dox[1]. We hypothesized that DoxLPX + US can provide targeted delivery of Dox to soft tissue sarcoma *in vivo* and increase tumor endothelium permeability, resulting in tumor growth suppression with minimal cardiotoxicity compared to equivalent doses of free Dox.

Methods

Liposomal Dox-loaded polymer MBs (**DoxLPX**) were synthesized ($\sim 6 \times 10^{-7}$ $\mu\text{g}/\text{MB}$). *In vitro* studies determined the optimal US regime for DoxLPX. Mice with xenograft sarcoma tumors (MCA205 murine sarcoma) were randomly assigned to 1 of 6 treatment groups. Treatments commenced on Day 0 (tumor volume 40 to 90 mm³). 4 Dox-containing formulations (5 mg/kg equivalent Dox dosage per treatment) were given i.v.: free Dox; liposomal Dox (**LDox**); DoxLPX; MB+LDox co-injection. MB-liposome complexes loaded with empty liposomes (**ELPX**) or saline only were also used as controls. Formulations were infused over 15 min via an internal jugular indwelling catheter on Days 0, 3, 7, and 10. Concurrent US (1 MHz, 1,000 kPa (10 μs) + 170 kPa (490 μs) followed by 500 μs off, repeated 500 times, with the pulse train repeated every 2.5 s to allow MB reperfusion to the treatment area, was delivered to tumor during infusion of DoxLPX, MB+LDox, or ELPX. Tumor volume and cardiac function were serially monitored with high-resolution US. Myocardial fibrosis and caspase-3 (apoptosis marker) in DoxLPX+US treated animals were compared with that from control hearts. To assess biodistribution, Cy5.5 was used as a fluorescent Dox analog, injected i.v. as: Cy5.5-NH₂, liposomal Cy5.5, liposomal Cy5.5+MB, Cy5.5LPX, and mice were euthanized 3.5 hrs later. Blood, tumor, spleen, kidney, liver, heart, lung, brain, skin on the back, muscle, femur (bone), and foot were imaged post-mortem and measured using a Xenogen IVIS 200 imaging system. Data were presented as mean \pm SD.

Results

DoxLPX + US and MB+LDox co-injection + US groups caused greater tumor inhibition and longer median survival time compared to free Dox and LDox in sarcoma-bearing mice ($p=0.01$). DoxLPX + US attenuated cardiotoxicity vs. other Dox-treated groups: fewer mice had a decrease in ejection fraction, fractional shortening, or increased left ventricle mass index, and these mice had less histologic fibrosis. The free Dox treated mice had a decrease in fractional shortening by Day 21 vs Day 0 baseline ($p<0.05$) whereas the other treatment groups had stable systolic function. Biodistribution data substantiated that DoxLPX + US targets Dox delivery to the tumor site, resulting in tumor growth inhibition equivalent to that achieved by free Dox, and is associated with less cardiac Dox accumulation, resulting in preservation of ventricular function. DoxLPX + US may improve cancer treatment outcome by allowing higher doses of Dox to be administered while avoiding cardiotoxicity.

Conclusions

Our DoxLPX formulation with ultrasound provides a targeted drug delivery platform with superior treatment efficacy and reduced cardiac toxicity when compared with systemic administration of free Dox or LDox+MB co-administration .

Reference

- [1]. Yu FTH, Chen X, Wang J, Qin B, Villanueva FS, Low intensity ultrasound mediated liposomal doxorubicin delivery using polymer microbubbles, *Mol Pharm* 13: 55-64, 2016.

Mechanisms and effects of nanoparticle-stabilized microbubbles designed for enhanced drug delivery

Sofie Snipstad^{1,2,3}, Tim Segers⁴, Guillaume Lajoinie⁴, Petros Yemane¹, Andreas K.O. Åslund^{1,2}, Charlotte Nawijn⁴, Einar Sulheim^{1,2,3}, Ýrr Mørch², Rune Hansen^{1,2}, Michel Versluis⁴, Catharina de Lange Davies¹, Sigrid Berg^{1,2,3}

¹Norwegian University of Science and Technology, Trondheim, Norway;

²SINTEF AS, Trondheim, Norway;

³Cancer Clinic, St. Olav's Hospital, Trondheim, Norway;

⁴Physics of Fluids group, Tech Med Center, University of Twente, Enschede, Netherlands

Corresponding author: sofie.snipstad@ntnu.no

Introduction

The delivery of drugs and nanomedicines to tumors is often insufficient resulting in limited efficacy and systemic off-target effects. Microbubbles in combination with ultrasound have been shown to improve the permeability of tumor tissue (sonopermeation) leading to enhanced accumulation of co-injected drug molecules or vesicles at the target site [1]. To further improve the therapeutic response, microbubbles that are tailored for therapeutic rather than for diagnostic purposes are needed. We developed a novel microbubble co-stabilized by protein and polymeric nanoparticles [2], which has been shown to improve the delivery and therapeutic effect of nanoparticles in solid tumors [3] and to enable drug delivery to the brain by opening the blood-brain barrier [4-6].

In the current study we aimed to investigate the effect of sonopermeation on delivery of nanoparticle-encapsulated drug to solid tumors. Based on previous experience with subgroups of responders and non-responders we aimed to evaluate if therapeutic response or variation within groups could be predicted by cavitation dose or measured tumor uptake of nanoparticles, as this could be used to predict which tumors would respond well.

To optimize ultrasound-mediated delivery of nanoparticles, an understanding of the underlying mechanisms is required. Thus, intravital microscopy was performed to study the influence of vascular parameters on extravasation, and high-speed imaging of the nanoparticle-stabilized microbubbles was performed to understand their behavior during sonication and what happens to the shell when the bubbles oscillate and burst.

Methods

A subcutaneous xenograft tumor model in mice was used to investigate the effect of ultrasound on delivery and therapeutic effect of nanoparticle-encapsulated cabazitaxel. The nanoparticle-stabilized microbubbles were injected intravenously during three consecutive weeks, and the tumors were exposed to ultrasound in a water tank with a setup that allowed for passive cavitation detection. The ultrasound treatment was performed for 15 min using ultrasound with a frequency of 1 MHz, a pulse length of 10 ms, a pulse repetition frequency of 0.25 Hz, and at a peak negative pressure of 0.5 MPa. Tumor uptake of nanoparticles was imaged by fluorescence imaging using a small animal optical imager, providing longitudinal measurements.

To obtain new knowledge on the significance of vascular parameters on extravasation and to elucidate the effect of acoustic pressure on extravasation and penetration of nanoscale particles into the extracellular matrix, real-time intravital multiphoton microscopy was performed during sonication of tumors growing in dorsal window chambers [7]. The impact of vessel diameter, vessel structure and blood flow was characterized. Fluorescein isothiocyanate (FITC) dextran was injected to visualize blood vessels, and the

nanoparticle-stabilized microbubbles were injected before insonation with ultrasound at acoustic pressures ranging from 0.2 – 0.8 MPa (1 MHz, 10 ms pulse length, pulse repetition frequency of 0.1 Hz).

In vitro high speed imaging was performed to characterize the response of bubbles to ultrasound exposure. Therefore, the bubbles were loaded in a CLINICell and their acoustic response was captured using a brightfield microscope connected to a Shimadzu HPV-X2 high speed camera operated at 10 million frames per second (fps). The bubble oscillations were driven by 5-cycle ultrasound pulses at frequencies ranging from 1 - 3 MHz and at acoustic pressures ranging from 50 kPa to 250 kPa. To study bursting bubbles and nanoparticle deposition, fluorescence high-speed imaging was performed at 500,000 fps using a laser (5W, $\lambda = 532$ nm; Cohlibri, Lightline) and a 140-cycle ultrasound driving pulse at frequencies ranging from 1 – 3 MHz and at acoustic pressure amplitudes from 100 kPa to 1.2 MPa.

Results

The results illustrate effects of sonopermeation and how the microbubbles behave on three different length and time scales; the entire tumor (uptake of nanoparticles and therapeutic effect), vascular and microdistribution (extravasation of nanoparticles), and single bubble level (deposition of nanoparticles under different conditions).

Fig. 1 shows a scanning electron microscopy (SEM) image of a nanoparticle-stabilized microbubble and their size distribution, as well as the mean broadband cavitation signal from the tumors treated with ultrasound. Ultrasound treatment resulted in improved efficacy with reduced tumor growth and prolonged survival compared to animals that did not receive ultrasound treatment (Fig. 2). The enhanced uptake of nanoparticles after ultrasound treatment lasted for several weeks, and representative images from two animals are shown in Fig. 3. Ultrasound treatment increased the tumor uptake of nanoparticles by approximately 2.5 times directly after (25 min) treatment relative to the tumors that did not receive ultrasound. In the second and third treatment, the increase was 4 and 6 times, and it further increased to 14 and 16 times 2 and 4 weeks after the last treatment. Neither cavitation dose nor the amount of uptake of nanoparticles could explain the variation in therapeutic response within groups (data not shown), emphasizing the need for a better understanding of tumor biology and the mechanisms involved in sonopermeation.

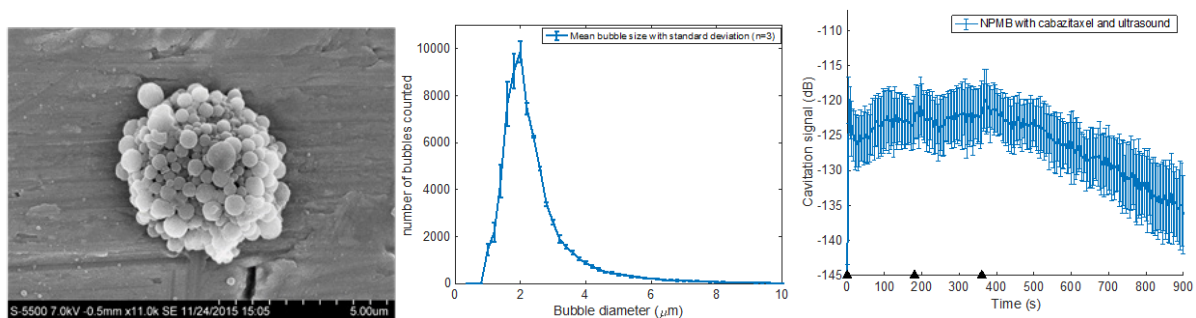


Figure 1: SEM image of nanoparticle-stabilized microbubble (left) and average size distribution of 3 batches (middle). Mean broadband cavitation signal (right) and standard deviation from bubbles circulating in the tumor bearing leg during sonication in all animals during treatment 1. The animals received three injections at time 0, 180 and 360 sec, marked with black triangles. The tumor was sonicated for 15 minutes (900 sec).

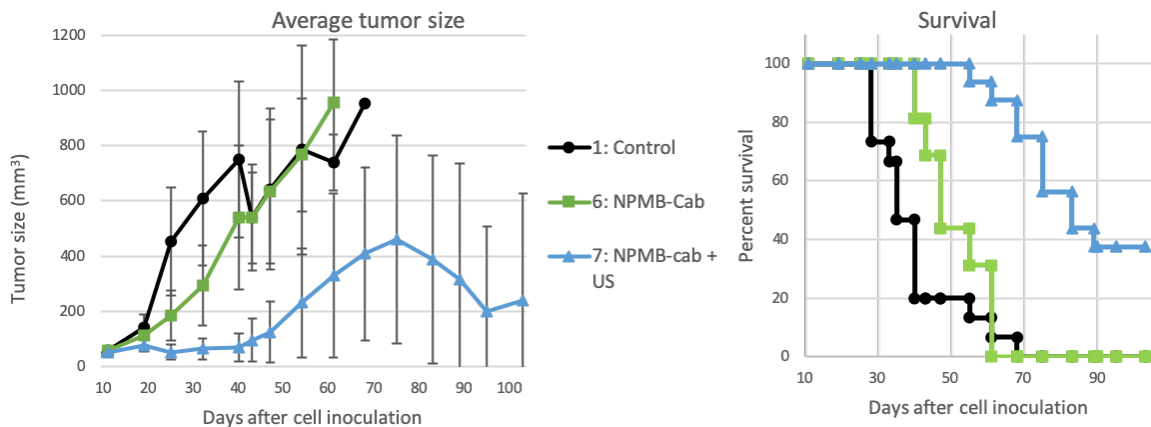


Figure 2: Tumor growth and survival plot for the different groups. Control – untreated animals, NPMB-Cab – animals treated with nanoparticle-stabilized microbubbles, and NPMB-Cab + US – animals treated with nanoparticle-stabilized microbubbles and ultrasound. Data points are group means with time, and treatments were performed on day 11, 18 and 25. N=14-16 animals per group.

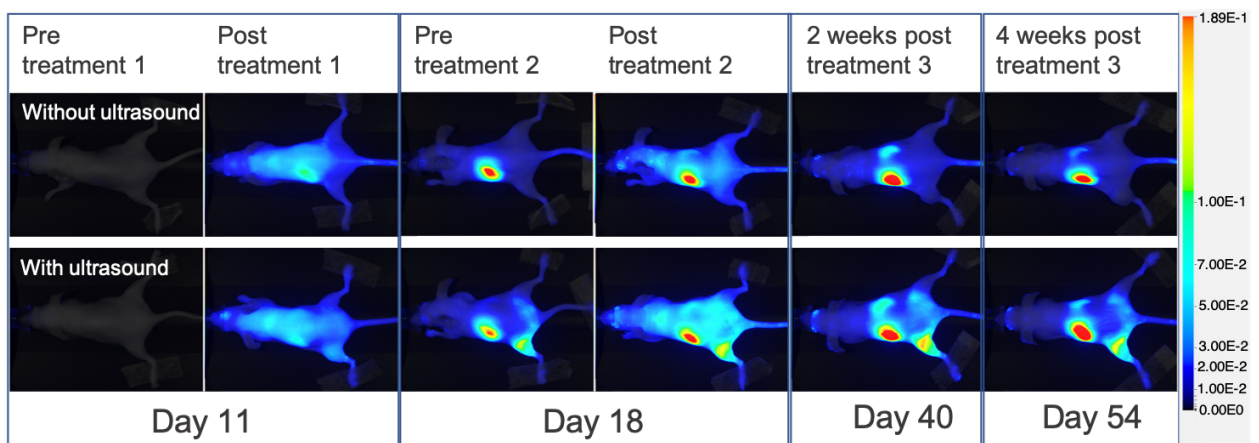


Figure 3: Representative images showing tumor accumulation of nanoparticles (imaged by fluorescence) with and without ultrasound treatment. The tumor is on the left hind leg and the nanoparticles were injected intravenously.

From intravital microscopy it was shown that the rate and extent of penetration into the extracellular matrix increased with increasing acoustic pressure, see Fig. 4. However, to achieve extravasation, smaller vessels required higher acoustic pressure amplitudes than blood vessels with larger diameters. The majority of extravasations occurred at vessel branching points. In addition, ultrasound was observed to change the blood flow rate and direction. Extravasation occurred throughout the 5 min ultrasound treatment, which corresponded to the long lasting cavitation signal that was observed from the subcutaneous tumors.

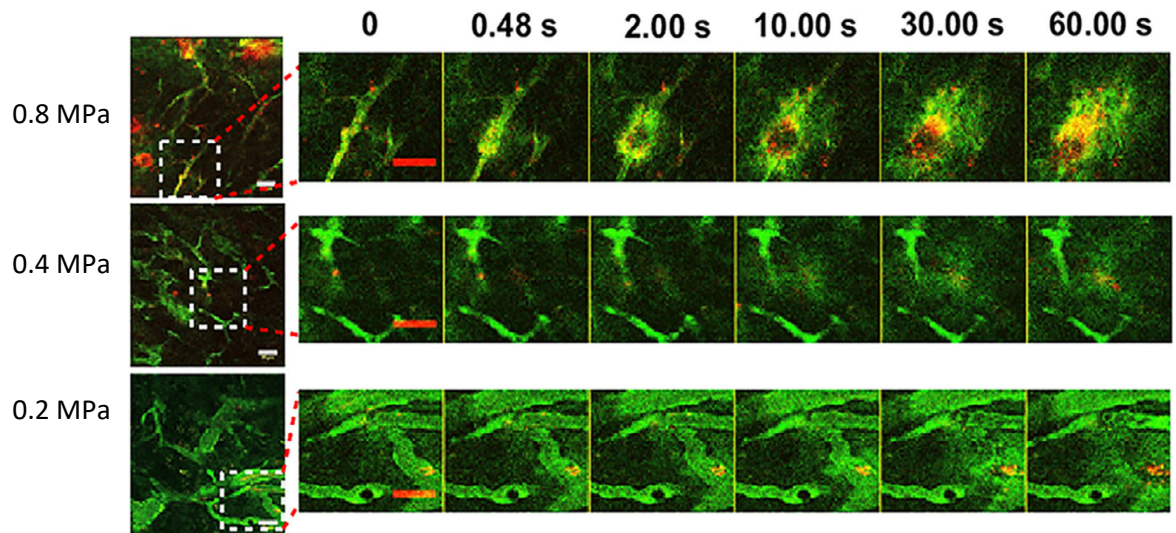


Figure 4: Intravital microscopy showed that the rate and extent of penetration of dextran (green) and nanoparticles (red) into the extracellular matrix increased with increasing acoustic pressure [7]. The scale bar is 50 μm .

High speed imaging showed that depending on bubble size and ultrasound parameters, the shell of the nanoparticle-stabilized microbubble ruptured and the nanoparticles were deposited on the membrane of the CLINicell. The probability for nanoparticle delivery on the membrane as a function of the ultrasound frequency and the bubble radius is shown in the top row of Fig. 5. A typical high-speed recording of a single bubble that ruptured and deposited its shell during a 140 cycle sonication at 1 MHz and 175 kPa is shown in the bottom row. A large variation in bubble behavior was observed at the same ultrasound parameters; some bubbles did not respond, some bubbles were volumetrically oscillating, and some bubbles ruptured rapidly, releasing a free gas bubble that oscillated more pronounced.

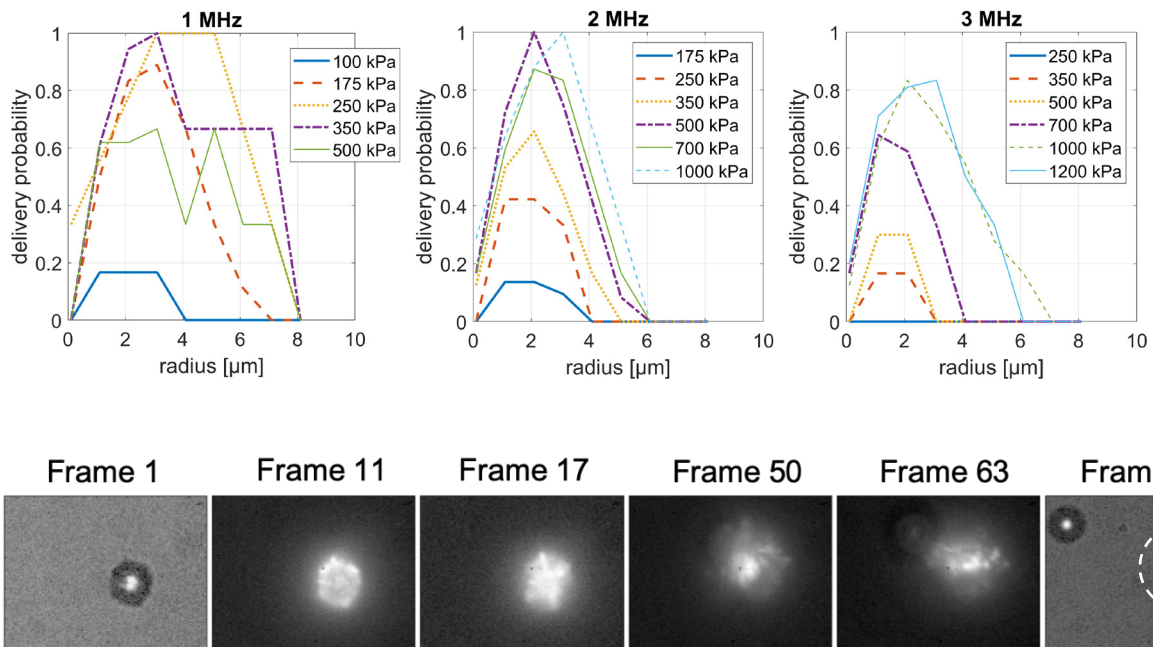


Figure 5: Top row: The probability that a bubble in the sonication field bursts during a 140 cycle pulse at a range of frequencies and pressures. Bottom row: Example of a bubble (diameter 6 μm) with a shell of fluorescent nanoparticles before, during and after sonication of 140 cycles at 1 MHz and 175 kPa. The laser was turned on during frames 10-86 and the ultrasound pulse lasted from frame 17 to 87. The shell breaks during the first cycles (frame 17), but the free gas bubble keeps oscillating for the entire duration of the ultrasound pulse (frames 50 and 63), leaving the nanoparticles scattered in the liquid. The first and last frames are plain bright field images, where frame 1 shows a bubble with nanoparticles on the shell, whereas the bubble in frame 115 has deposited the nanoparticles (circle) and probably is a free gas bubble.

However, the general trend was that the probability of release of nanoparticles was less at the lowest acoustic pressures, and a certain pressure threshold was needed. Furthermore, increasing the frequency increased the probability of release from smaller bubbles, and larger pressures were required to release the nanoparticles at higher frequencies. Thus, a clear resonance behavior was observed showing that at a specific ultrasound frequency and acoustic pressure, the delivery probability is at maximum for bubbles in a relatively narrow size range.

Conclusions

Ultrasound treatment induced cavitation in the tumors, which increased the overall uptake of nanoparticles resulting in reduced tumor growth and prolonged survival compared to animals which were not exposed to ultrasound. Intravital microscopy demonstrated that ultrasound treatment induced extravasation of nanoparticles into the interstitium, and high-speed imaging of single bubbles demonstrated how the nanoparticles were released from the bubble shell upon ultrasound treatment. Both intravital microscopy and high-speed imaging helped to elucidate the temporal and spatial behavior of microbubbles and nanoparticles during ultrasound exposure, which is useful in understanding the mechanisms underlying sonopermeation and for optimizing such technologies.

References

- [1]. Snipstad et al., Sonopermeation to improve drug delivery to tumors: from fundamental understanding to clinical translation, *Exp Opin Drug Deliv* 15: 1249-1261 (2018)
- [2]. Ý. Mørch et al., Nanoparticle-stabilized microbubbles for multimodal imaging and drug delivery, *Contrast Media Mol Imaging* 10: 356–366 (2015)
- [3]. S. Snipstad et al., Ultrasound improves the delivery and therapeutic effect of nanoparticle-stabilized microbubbles in breast cancer xenografts, *Ultrasound Med Biol* 43: 2651-2669 (2017)
- [4]. A. Åslund et al., Nanoparticle delivery to the brain – by focused ultrasound and selv-assembled nanoparticle-stabilized microbubbles, *J Control Release* 220 (Pt A): 287-294 (2015)
- [5]. Baghirov et al., Ultrasound-mediated delivery and distribution of polymeric nanoparticles in the normal brain parenchyma of a metastatic brain tumour model, *PLoS One* 13: e0191102 (2018)
- [6]. Sulheim et al., Therapeutic effect of cabazitaxel and blood-brain barrier opening in a patient-derived glioblastoma model, *Nanotheranostics* 3: 103-112 (2019)
- [7]. P. Yemane et al., Effect of Ultrasound on the Vasculature and Extravasation of Nanoscale Particles Imaged in Real Time, *Ultrasound Med Biol* 45: 3028-3041 (2019)

Dispersion and sonoporation of bacteria in biofilms by oscillating microbubbles

***Kirby R. Lattwein¹, Inés Beekers¹, Joop J.P. Kouijzer¹,
Mariël Leon-Grooters¹, Antonius F.W. van der Steen^{1,2}, Nico de Jong^{2,1},
Willem J.B. van Wamel³, and Klazina Kooiman¹***

¹ Dept. of Biomedical Engineering, Thorax Center, Erasmus MC, Rotterdam, the Netherlands

² Laboratory of Acoustic Wavefield Imaging, Delft University of Technology, Delft, the Netherlands

³ Dept. of Medical Microbiology and Infectious Diseases, Erasmus MC, Rotterdam, the Netherlands

Corresponding author: k.lattwein@erasmusmc.nl

Introduction

Biofilm infections compromise approximately 60% of all bacterial infections [1]. Bacteria encased in a biofilm pose significant challenges to successful treatment because both the immune system and antibiotics are often ineffective [2,3]. *Staphylococcus aureus* (*S. aureus*) leads to more infections than most other bacteria along with a higher associated mortality [4,5]. A potential treatment strategy is sonobactericide, which uses ultrasound and cavitation nuclei to increase the effectiveness of current antimicrobial therapeutics or directly impacts biofilm-associated bacteria [6]. Several papers have suggested that sonobactericide could be causing bacterial dispersion [7,8] or sonoporation [9]. However, these studies lack real-time observations performed during insonification and/or high resolution imaging to distinguish individual bacteria. Therefore, in this *in vitro* study we utilized ultrasound and microbubbles, in combination with an antibiotic, to investigate in real-time and with high resolution microscopy the effects of microbubble oscillation on *S. aureus* biofilms.

Methods

S. aureus, isolated from an infective endocarditis patient, was used to grow biofilms in an OptiCell culture system for 24 h under constant agitation. To visualize both living and dead/membrane-compromised bacteria, the fluorophores SYTO 9 and propidium iodide (PI) were used, respectively. Microbubbles consisted of a C₄F₁₀ gas core and a DSPC-based coating fluorescently-labelled with the lipid dye DiD [10]. Biofilms were exposed to ultrasound (2 MHz, 100-400 kPa, 100-1000 cycles, every second for 30 s) with either an antibiotic (oxacillin; 0.016 or 1 µg/mL), microbubbles alone, or both antibiotic and microbubbles. Time-lapse confocal microscopy recordings of 10 min were performed to detect bacterial responses to the different exposure conditions. Post-hoc image analysis was performed in MATLAB using particle counting as a quantitative measure of dispersion and sonoporation.

Results

The imaging control (N=6), i.e. in the presence of microbubbles without ultrasound insonification, led to minimal dispersion and PI uptake. Increasing the acoustic pressure from 100 kPa (N=4) to 200 kPa (N=4) at 100 cycles led to observable dispersion of 5% (interquartile range (IQR) 3 – 6%; Fig. 1B) and an 8% (IQR 2 – 18%) increase in PI stained cells (Fig. 1D). Further increasing the acoustic pressure to 400 kPa (N=4) resulted in a much higher percentage of cells being dispersed from the biofilm, namely 77% (IQR 72 – 82%) as shown in Fig 2. When increasing from 100 (N=4) to 1000 (N=4) cycles at 100 kPa, bacterial dispersion increased to 46% (IQR 23 – 60%). PI uptake was not quantifiable when dispersion was predominant, i.e. at pressures > 200 kPa and/or > 100 cycles due to the high amounts of cells leaving the field of view. When the total PI uptake was quantifiable but placed in the context of the ~7,000 cells

present in a field-of-view, the overall increase was close to negligible (<0.5%). The addition of the antibiotic oxacillin led to a wider range of values for both dispersion and PI uptake at pressures ≤ 400 kPa at 100 cycles. At 100 kPa, 1000 cycles antibiotic presence resulted in more dispersion and less variable outcome.

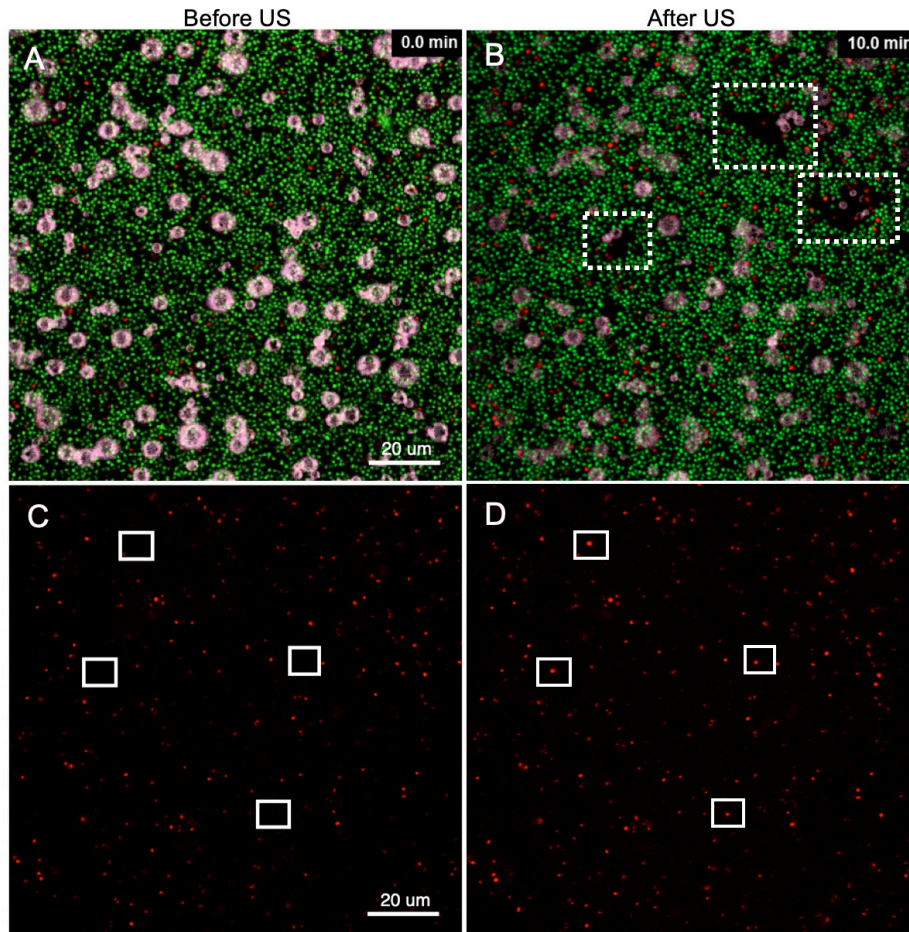


Figure 1. Confocal microscopy images of *S. aureus* biofilm during sonobactericide. Living bacteria are stained with SYTO 9 (green), dead/membrane compromised bacteria with propidium iodide (red), and microbubbles fluorescently-labelled with DiD lipid dye (pink). Biofilm images (A) before ultrasound and (B) after ultrasound (US; 2 MHz, 200 kPa, 100 cycles, every sec for 30 sec) at the end of the 10 min time-lapse recording, with dashed white squares indicating regions of dispersion. Same field-of-view biofilm images of the red channel only, i.e. propidium iodide, (C) before US and (D) after US at end of 10 min time-lapse recording with solid white squares denoting examples of cellular propidium iodide uptake.

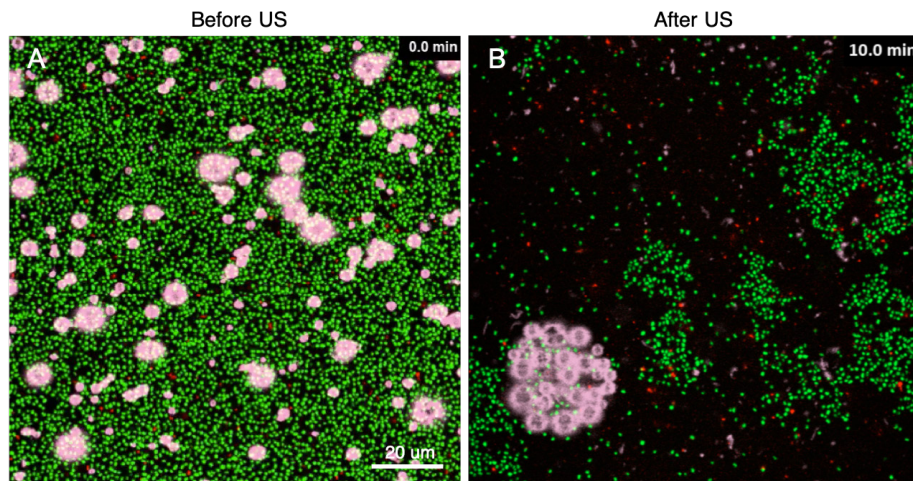


Figure 2. Confocal microscopy images of *S. aureus* biofilm during sonobactericide. (A) Before and (B) after ultrasound (US; 2 MHz, 400 kPa, 100 cycles, every sec for 30 sec) images at the end of the 10 min time-lapse recording, with living bacteria in green (SYTO 9), dead/ membrane compromised in red (propidium iodide), and microbubbles in pink (DiD lipid dye).

Conclusions

This study suggests bacterial dispersion as the more dominant effect over sonoporation resulting from oscillating microbubbles for these *S. aureus* biofilms and acoustical settings. These findings demonstrate the potential of sonobactericide to aid in biofilm infection treatment. At the same time further investigations are necessary to establish dispersion of bacteria as a safe therapeutic strategy.

This study was financially supported by the Erasmus MC Foundation (fellowship to K.K.).

References

- [1]. Fux CA, Stoodley P, Hall-Stoodley L, Costerton JW, Bacterial biofilms: a diagnostic and therapeutic challenge, *Expert Rev Anti-infect Ther*, 1:667-683, 2013.
- [2]. Moser C, Pedersen HT, Lerche CJ, Kolpen M, Line L, Thomsen K, Høiby N, Jensen PO, Biofilms and host response – helpful or harmful, *APMIS*, 125: 320-338, 2017.
- [3]. Algburi A, Comito N, Kashtanov D, Dicks LMT, Chhikindas ML, Control of biofilm formation: antibiotics and beyond, *Appl Environ Microbiol*, 83(3):e02508-16, 2017.
- [4]. Tong SYC, Davis JS, Eichenberger E, Holland TL, Fowler VG, Staphylococcus aureus infections: epidemiology, pathophysiology, clinical manifestations, and management, *Clin Microbiol Rev*, 28(3):603-661, 2015.
- [5]. Cahill TJ, Prendergast BD, Infective endocarditis, *The Lancet*, 387(10021):882-893, 2016.
- [6]. Lattwein KR, Shekhar H, Kouijzer JJP, van Wamel WJB, Holland CK, Kooiman K, Sonobactericide: an emerging treatment strategy for bacterial infections, *Ultrasound Med Biol*, article in press, 2019.
- [7]. Ronan E, Edjiu N, Kroukamp O, Wolfaardt G, Karshafian R, USMB-induced synergistic enhancement of aminoglycoside antibiotics in biofilms, *Ultrasonics*, 69:182–190, 2016.
- [8]. Lattwein KR, Shekhar H, van Wamel WJB, Gonzalez T, Herr AB, Holland CK, Kooiman K, An in vitro proof-of-principle study of sonobactericide. *Sci Rep* 8:3411, 2018.
- [9]. Han YW, Ikegami A, Chung P, Zhang L, Deng CX, Sonoporation is an efficient tool for intracellular fluorescent dextran delivery and one step double-crossover mutant construction in *Fusobacterium nucleatum*, *Appl Environ Microbiol* 73:3677–3683, 2007.
- [10]. Klibanov AL, Rasche PT, Hughes MS, Wojdyla JK, Galen KP, Wible JH, Brandenburger GH, Detection of individual microbubbles of ultrasound contrast agents: imaging of free-floating and targeted bubbles, *Investig Radiol*, 39(3):187-195, 2004.

Characterization of a novel nitro-fatty acid microbubble for ultrasound-targeted microbubble cavitation

Gary Yu¹, Marco Fazzari², Thiruganesh Ramasamy¹, Xucai Chen¹, Bruce Freeman², John Pacella¹

¹ Center for Ultrasound Molecular Imaging and Therapeutics, Department of Medicine, University of Pittsburgh, Pittsburgh, PA, USA

²Department of Pharmacology and Chemical Biology, University of Pittsburgh, Pittsburgh, PA, USA
Corresponding author: pacellaj@upmc.edu

Introduction

Microvascular obstruction (MVO) is a highly prevalent problem following percutaneous coronary intervention for the treatment of acute myocardial infarctions. It arises from a variety of mechanisms including downstream microembolization resulting in mechanical obstruction, myocardial edema, inflammation, and a milieu of oxidative stress accompanying ischemia-reperfusion injury; and it leads to worse clinical outcomes.

Although we have previously demonstrated the potential of ultrasound-targeted microbubble cavitation (UTMC) for relieving the microvascular mechanical obstructions contributing to MVO, the various biological sequelae of MVO, and in particular oxidative stress, have yet to be addressed by this therapy.

Nitro-fatty acids (NFAs) are therapeutic lipids that have potent anti-inflammatory effects and potentiation of nitric oxide. Their long hydrocarbon tail structure is compatible with the phospholipids found in lipid-shelled microbubbles used in ultrasound-targeted microbubble cavitation. Therefore, rather than loading a therapeutic agent onto the microbubble surface or via encapsulation, in the present study, we have developed a novel lipid microbubble agent with a directly functionalized NFA-incorporated shell. This novel NFA microbubble (NFAB) will not only retain the mechanical properties of standard lipid MBs for mechanical fragmentation of microthrombi but will also offer immediate delivery of NFA to the microvascular bed, offering pleiotropic effects for diminishing oxidative stress and inflammation.

Methods

NFA microbubbles (NFABs) were synthesized in-house using a mixture with various other phospholipids. Size, distribution, and stability of the NFABs were evaluated through Coulter counter measurements repeated up to 6 days post-synthesis with storage at 2-4° Celsius. Quantification of microbubble NFA content was performed with liquid chromatography and mass spectrometry, as well as subtraction of bubble solution supernatant free NFA content to control for unincorporated NFA.

NFABs were then injected arterially for UTMC in a healthy rat hindlimb model with therapeutic ultrasound delivered using a 1 MHz single-element transducer for 2 consecutive 10 minute treatments (5 ms bursts every 3 seconds at a peak negative pressure of 1.5 MPa). Treatment groups included a free NFA infusion, infusion of NFA with normal microbubble UTMC, and NFAB UTMC. NFA given in all groups was adjusted to the equivalent amount loaded onto the NFABs delivered in the NFAB UTMC group. Burst-replenishment perfusion imaging was performed at baseline and following each 10 minute treatment.

After completion of the treatments, all animals sacrificed with saline perfusion prior to tissue collection from the treatment site and an off-target control site. Tissue samples were homogenized and prepared for liquid chromatography and mass spectrometry for quantification of NFA content.

Results

Post-synthesis characterization of NFAB stability and size showed similar size distributions to normal lipid microbubbles and no significant loss of concentration or change in distribution shape up to 6 days.

Quantification of NFA loading showed approximately 100 nmol of NFA per 1E9 microbubbles with no significant change up to 4 days post-synthesis. Preliminary analysis of burst-reperfusion cineloops shows increased blood volume and blood flow over baseline for the two UTMC groups, with non-inferiority of the NFAB UTMC group to the free NFA with normal UTMC co-infusion group. Collected tissue samples showed a significant increase in NFA concentration between the target and off-target sites with UTMC, with NFAB UTMC having the greatest average increase in NFA concentration.

Conclusions

We have shown that synthesis of a novel bioactive microbubble with an NFA shell is not only feasible but also shows strong potential for therapeutic, targeted applications of UTMC in treatment of pathologies involving inflammation and oxidative stress injury. Future work will involve application of NFABs to various animal disease models for further validation of therapeutic efficacy.

Recent ESC Guidelines in patients with Chronic Coronary Syndrome-relevance to Contrast Echocardiography

Roxy Senior

Imperial College and Royal Hospital, London, UK

The recent European Guidelines on Chronic syndrome has been released. It has several new updates. The diagnostic pathway has upgraded CT to Class1 indication for the assessment of patients with suspected angina. This has major implications for stress imaging including stress echo. However, it also has statements pertaining to the use of microbubbles for LV opacification and myocardial perfusion. These will be discussed.

Deep Transcranial Ultrasound Localization Microscopy of the adult human brain vascularization

Charlie Demene¹, Justine Robin¹, Mathieu Pernot¹, Fabienne Perren², Mickael Tanter¹

¹Physics for Medicine Paris, Inserm, ESPCI Paris, CNRS, PSL Research University, 17 rue Moreau, 75012, Paris

²Clinical Neuroscience Department, LUNIC (Laboratory of Ultrafast-ultrasound Neuroimaging in Clinics), Université de Genève, Hôpitaux Universitaires de Genève, Switzerland

Corresponding author: charlie.demene@espci.fr

Introduction

Human brain vascular imaging is key for management of cerebrovascular and neurological pathologies. Challenging across modalities, it requires contrast injection, ionizing (CT) or expensive (MRI) imaging devices, overlooks blood dynamics and gives limited resolution. Ultrasound (US), conversely, is poorly used for neuroimaging due to limited sensitivity and resolution. US Localization Microscopy (ULM) has proven increased sensitivity and sub-resolution precision in the rat brain [1]. Transposed for the first time to human brain, we show that ULM is a game changer for clinical neuroimaging.

Methods

Experiments complied with the Declaration of Helsinki, patients gave informed and written consent (protocol 2017-00353 Geneva CCER). They were injected IV boluses of 0.3 mL of Sonovue before imaging through the temporal window with a 3-MHz phased array and an ultrafast scanner. Ultrafast US sequences consisted in diverging waves fired at 4800 Hz during 1s, looped every 2s, during 2 minutes. Tissue was filtered out using spatiotemporal SVD filtering [2], aberration corrections were calculated for isoplanatic patches thanks to local coherence optimization on isolated bubbles RF signatures before beamforming and motion compensation. Bubbles geometric centers were estimated using quadratic fitting, tracked and assigned to super-resolution trajectories using Hungarian algorithm

Results

Aberration corrections enabled to detect more bubbles and to refine the position of their geometric center. At typical f-numbers >4 in transtemporal imaging, theoretical ultrasonic lateral resolution is diffraction-limited to ~3 mm, while axial resolution is of the order of 0.8 mm. We show here that, with only 2 minutes of examination, vascular bed with diameters of the order 0.1 mm can be delineated, largely beating the diffraction limit and resolution of other clinical modalities, at depth up to 120 mm (~whole brain), with quantitative data on blood flow dynamics at a sub-resolution level. Vortex flow in a 1.5 mm-wide aneurysm and parabolic speed profile on a 0.8 mm vessel section could be observed, which is impossible with any other neuroimaging modality. We quantified the resolution to be at least 62 μ m. Complex flow pattern in a Moya-Moya syndrome could be observed, overstepping the partial information given by luminal-only clinical vascular imaging modalities.

Conclusions

By combining ULM with ultrafast diverging wave transmissions, skull aberration corrections and tissue motion compensation, we showed that we can redefine the reachable boundaries of cerebrovascular imaging, with 62 μ m resolution and very local blood flow dynamics assessment. This world premiere is a breakthrough for the management of cerebro-vascular diseases.

References

[1]. Errico et al, *Nature*, 2015

CEUS LI-RADS – preliminary results on multi-center prospective validation study-

***Yuko Kono¹, Fabio Piscaglia², Stephanie R, Wilson³, Andrej Lyshick⁴,
on behalf of CEUS LI-RADS Working Group***

¹Medicine & Radiology, University of California San Diego, San Diego, USA

²Internal Medicine, University of Bologna, Bologna, Italy

³Radiology, University of Calgary, Calgary, Canada

⁴Radiology, Thomas Jefferson University, Philadelphia, USA

Corresponding author: ykono@health.ucsd.edu

Introduction

Hepatocellular carcinoma (HCC) is the sixth most common cancer and fourth leading cause of cancer mortality world wide. Majority of HCC is diagnosed by imaging without histological examination. However, liver imaging is not simple especially because approximately 90% of HCC would develop in the setting of cirrhosis. Cirrhotic liver is filled with regenerative nodules, which undergo multistep carcinogenesis, making imaging diagnosis challenging. LI-RADS (Liver Imaging Reporting and Data System) was created to standardize terminology, technique, reporting and data collection for HCC diagnosis, originally for CT and MRI, and CEUS was added in 2016 [1, 2]. LI-RADS consists of 8 categories with different probability of HCC and malignancy. LR-5 is the most important category, which is a “definite HCC”, with expected specificity of near 100%. The aim of this prospective multi-center study is to validate the CEUS LI-RADS and determine the diagnostic performance of CEUS for HCC diagnosis.

Methods

Eleven international centers are participating in the study, goal is to enroll total of 640 patients. Those at risk for HCC, with focal liver observations are included in this study. They are required to have multiphaseic CT or MRI within 30 days before or after CEUS. Final diagnosis were made either by tissue diagnosis, CT or MRI, and follow up for one year.

Results

This is a preliminary data, with 402 subjects, 439 nodules. There were 101 (25.1%) female and 301 (74.9%) male. The size of the nodule was 2.4 ± 1.1 cm. The quality of CEUS was adequate in 419 (95.2%), not adequate in 21 (4.8%). The final diagnosis includes 231 (69%) HCC, 45 (13.4%) benign, 43 (13.7%) indeterminate and 13 (3.9%) other malignancy. Table 1 shows the number and percentage of HCC and malignancy in each LI-RADS category. LR-5 had high specificity for HCC at 97.9% (138/141), and moderate sensitivity for HCC at 59.7 % (138/231). There were 3 false positive LR-5 cases, including 1 ICC (MRI LR-5), 1 ICC-HCC (MRI LR-M) and 1 high grade dysplastic nodule (MRI LR-5).

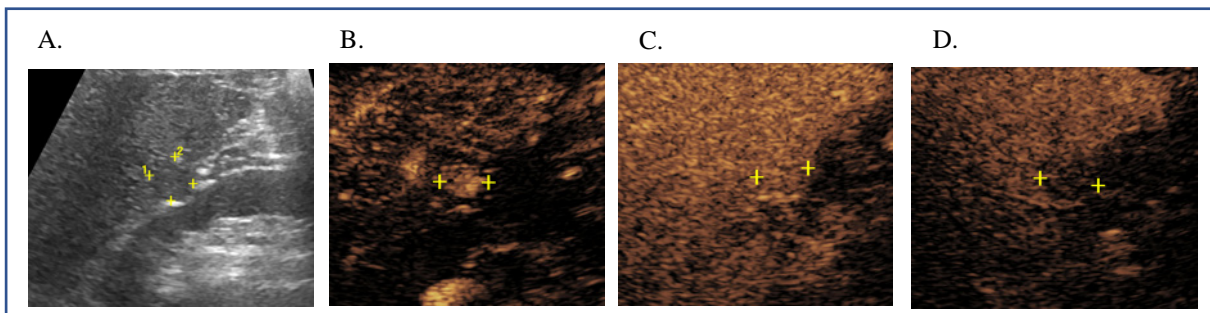
Conclusions

The CEUS LR-5 classification is highly specific for HCC, confirming high clinical value of CEUS for non-invasive HCC diagnosis.

Table 1. HCC and malignancy in LI-RADS categories

LI-RADS category	CEUS		MRI	
	HCC	Malignancy	HCC	Malignancy
LR-1	0%	0%	0%	0%
LR-2	0%	0%	16%	18%
LR-3	50%	0%	37%	39%
LR-4	89%	91%	74%	81%
LR-5	98%	99%	95%	98%
LR-M	61%	89%	37%	94%

Figure 1. CEUS LR-5 lesion: definitely HCC. A. Gray scale image showing a 15mm hypoechoic lesion in the liver. B. The nodule shows arterial phase hyperenhancement. C. The nodule shows iso-enhancement at one minute. D. Late and mild washout at 4 minutes.



References

- [1]. S. R. Wilson, A. Lyshchik, F. Piscaglia, D. Cosgrove, H. J. Jang, C. Sirlin, C. F. Dietrich, T. K. Kim, J. K. Willmann, and Y. Kono, "CEUS LI-RADS: algorithm, implementation, and key differences from CT/MRI," *Abdom Radiol (NY)*, vol. 43, no. 1, pp. 127-142, Jan, 2018.
- [2]. A. Lyshchik, Y. Kono, C. F. Dietrich, H. J. Jang, T. K. Kim, F. Piscaglia, A. Veziridis, J. K. Willmann, and S. R. Wilson, "Contrast-enhanced ultrasound of the liver: technical and lexicon recommendations from the ACR CEUS LI-RADS working group," *Abdom Radiol (NY)*, vol. 43, no. 4, pp. 861-879, Apr, 2018.

Liver: Why CEUS?

Stephanie R Wilson¹, Peter N Burns²

¹Radiology, University of Calgary, Calgary, Canada

²Imaging Research, University of Toronto, Toronto, Canada

Corresponding author: Stephanie.wilson@ahs.ca

Introduction

An epidemic of fatty liver disease and increasing incidence of liver cancer worldwide have given a new importance to non-invasive liver imaging. Contrast-enhanced ultrasound (CEUS), using microbubble contrast agents, provides unique advantages over the well accepted techniques of CT and MRI.

Methods

Established algorithms for the diagnosis of focal liver masses on CEUS are based on arterial phase enhancement patterns and assessment of the timing and intensity of washout. Not surprisingly these algorithms are similar to those established for CT and MR scan.

Fundamental interpretation of CEUS examinations includes the following critical points. Common benign tumors, hemangioma, focal nodular hyperplasia (FNH), and adenoma, are diagnosed based on their specific enhancement patterns shown in the arterial phase (AP). These are more sensitively shown on CEUS than on CT and MR scan related to the dynamic real-time method of image acquisition on CEUS as compared to the snapshot in time, characteristic of imaging on CT and MR scan.

The most valuable observation to determine malignancy on CEUS is identification of washout, whereby the enhancement of the tumor drops below the enhancement of the adjacent liver, following arterial phase enhancement of any type. Although CT and MR scan also evaluate for washout, CEUS additionally evaluates for intensity and timing of washout further differentiating hepatocellular from nonhepatocellular malignancy.

Nonhepatocellular malignant tumors comprise especially metastases and cholangiocarcinoma (ICC). Unlike benign tumors which are predicted on the basis of their arterial phase enhancement patterns, metastases and ICC are predicted instead by their rapid washout at less than one minute. Detection of metastases is improved by scanning in the portal venous phase when the tumors are black relative to the surrounding enhanced parenchyma. The technique of sweeping the entire liver in the PVP will increase the number and size of detected metastatic tumors. If solitary, cholangiocarcinoma (ICC) is frequently virtually identical to metastatic disease on CEUS and history is highly contributory to differentiation of tumors. Further, purely intravascular microbubble contrast agents will show washout in all malignant tumors whereas interstitial contrast agents for CT and MR scan may frequently show instead increasing pseudoenhancement as contrast agent passes through permeable endothelium of some malignant tumors, especially cholangiocarcinoma (ICC).

Hepatocellular carcinoma (HCC) is most accurately diagnosed on imaging with demonstration of arterial phase hyperenhancement (APHE), and late (greater than 1 minute) and weak washout, within a nodule of greater than 1 cm size. The recently introduced Liver Reporting & Data System (LI-RADS) for CEUS is available on the American College of Radiology (ACR) website. CEUS LI-RADS is a standardized system for technique, interpretation, reporting, and data collection for contrast-enhanced ultrasound exams in patients at risk for developing HCC. It includes a probabilistic scale from LR-1, a definitely benign nodule, through to LR-5, a confident hepatocellular carcinoma. LR-5 nodules require strict adherence to the described three CEUS features of size greater than 1 cm, APHE and late and weak

washout to provide a method of noninvasive diagnosis of HCC. This allows for treatment without biopsy. LI-RADS emphasizes high specificity for LR-5, as close to 100% as possible.

Results

CEUS provides determination of malignancy and allows excellent differential diagnosis of a focal liver mass. CEUS regularly resolves indeterminate result on MR imaging and is exceptional as a problem solving tool in liver imaging. CEUS has many similarities to contrast enhanced CT/MRI but also unique and valuable differences, most showing the additional benefit of inclusion of CEUS with CT and MR for liver imaging.

Conclusion

Today, increased use of CEUS provides safe and rapid diagnosis of incidentally detected liver masses, improved multi-disciplinary management of nodules in a cirrhotic liver, facilitates ablative therapy for liver tumors, and permits diagnosis of hepatocellular carcinoma without biopsy. Unique benefits of CEUS include its dynamic real-time depiction of tumor vascularity and perfusion, and the use of a purely intravascular contrast agent, accurately reflecting tumoral and inflammatory blood flow.

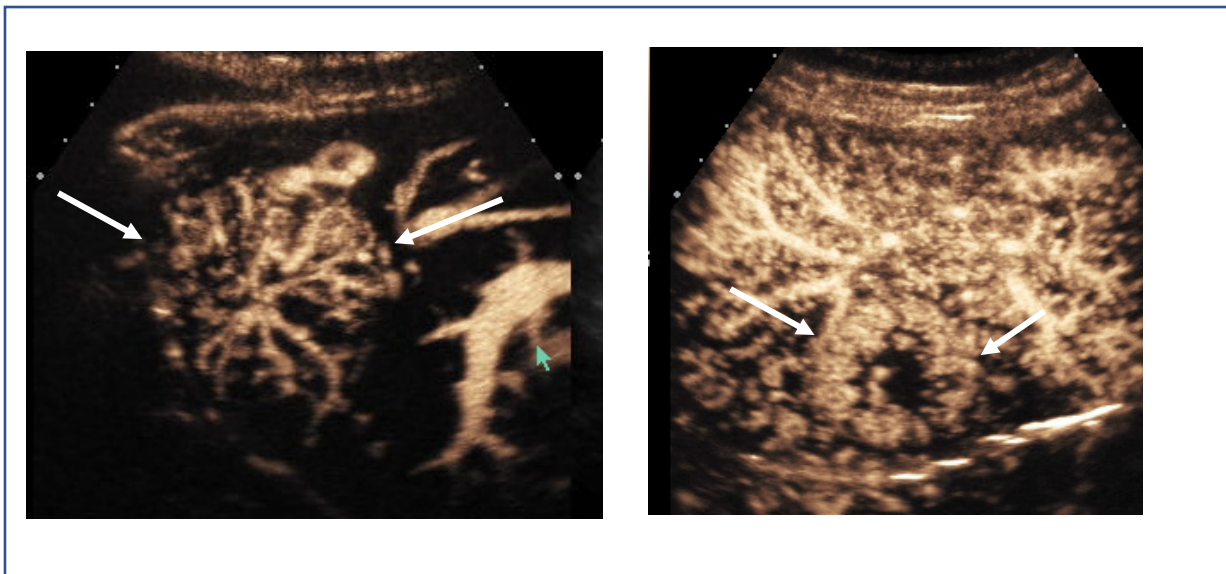


Figure 1. Benign liver tumors, with bubble tracking, in two patients. The left image shows linear stellate vessels in a classic FNH (arrows). The right image shows peripheral puddles and no linear vascularity in a classic hemangioma (arrows). Dynamic real-time ultrasound offers superior delineation of tumor vascularity as compared with either CT or MR scan.

References

- [1]. Albrecht T, Blomley MJ, Burns PN, Wilson S, et al. Improved Detection of Hepatic Metastases with Pulse-Inversion US during the Liver-specific Phase of SHU 508A: Multicenter Study. *Radiology*. 2003;227(2):361-370
- [2]. Burrowes DP, Medellin A, Harris AC, Milot L, Wilson SR. Contrast-enhanced US Approach to the Diagnosis of Focal Liver Masses. *Radiographics*. 2017;37(5):1388-400.

- [3]. Wilson SR, Kim TK, Jang HJ, Burns PN. Enhancement patterns of focal liver masses: discordance between contrast-enhanced sonography and contrast-enhanced CT and MRI. *AJR Am J Roentgenol.* 2007;189(1):W7-W12.
- [4]. Yu H, Jang HJ, Kim TK, Khalili K, Williams R, Lueck G, Hudson J, Burns PN. Pseudoenhancement within the local ablation zone of hepatic tumors due to a nonlinear artifact on contrast-enhanced ultrasound. *AJR Am J Roentgenol.* 2010;194(3):653-9.
- [5]. Terzi E, Iavarone M, Pompili M, Veronese L, Cabibbo G, Fraquelli M, Fraquelli M, Riccardi L, De Bonis L, Sangiovanni A, Leoni S, Zocco MA, Rossi S, Alessi N, Wilson SR, Piscaglia F. Contrast ultrasound LI-RADS LR-5 identifies hepatocellular carcinoma in cirrhosis in a multicenter retrospective study of 1,006 nodules. *J Hepatol.* 2018;68(3):485-92.
- [6]. Sporea I, Martie A, Bota S, Sirlu R, Popescu A, Danila M. Characterization of focal liver lesions using contrast enhanced ultrasound as a first line method: a large monocentric experience. *J Gastrointestin Liver Dis.* 2014;23:57-63
- [7]. Jo PC, Jang HJ, Burns PN, Burak KW, Kim TK, Wilson SR. Integration of Contrast-enhanced US into a Multimodality Approach to Imaging of Nodules in a Cirrhotic Liver: How I Do It. *Radiology.* 2017;282(2):317-31.

Role of Contrast-Enhanced Ultrasound in the Pre-operative Diagnosis of Cervical Lymph Node Metastasis in Patients with Papillary Thyroid Carcinoma

Pintong Huang¹

*¹Department of Ultrasound, The Second Affiliated Hospital of Zhejiang University, HanZhou, China
Corresponding author: huangpintong@126.com*

Introduction

The objective of this study was to prospectively evaluate the diagnostic accuracy of contrast-enhanced ultrasonography (CEUS) in differentiating between benign and metastatic cervical lymph nodes in patients with papillary thyroid cancer (PTC).

Methods

Three hundred nineteen cervical lymph nodes (162 metastatic from PTC and 157 benign) were evaluated using conventional ultrasonography (US) and CEUS before biopsy or surgery.

Results

Metastatic lymph nodes more often manifested centripetal or asynchronous perfusion, hyper-enhancement, heterogeneous enhancement, perfusion defects and ring-enhancing margins than benign lymph nodes at pre-operative CEUS (all p values < 0.001). The area under the receiver operating characteristic curve (AUC) for the combination of conventional US and CEUS (0.983, 95% confidence interval [CI]: 0.971-0.994) was higher than that of conventional US alone (0.929, 95% CI: 0.899-0.958) and CEUS (0.911, 95% CI: 0.876-0.947).

Conclusions

CEUS is a promising tool in conjunction with conventional US for the pre-operative prediction of metastatic cervical lymph nodes in patients with PTC

Motion correction for high-frame-rate contrast enhanced echocardiography

Matthieu Toulemonde¹, Meng-Xing Tang¹

¹*Department of Bioengineering, Imperial College London, London, United Kingdom*
Corresponding authors: m.toulemonde@imperial.ac.uk, mengxing.tang@imperial.ac.uk

Introduction

High frame rate (HFR) or ultrafast echocardiography imaging using unfocus diverging wave transmission, multiline transmission and/or acquisition, have shown their great benefit in non-contrast cardiac imaging to improve B-Mode images [1-4], Doppler for tissue or left ventricle (LV) imaging [1] [3], blood flow dynamics [5] [6], and also for shear waves and tissue velocities [4] [7]. For contrast imaging using ultrasound contrast agent, non-focus diverging transmission has shown potential for myocardium perfusion [8] [9] or flow imaging in the LV chamber [8-10]. However it suffers from motion artefacts which impact the coherent compounding or the sum of the coded transmission such as pulse-inversion (PI) [4] [11] [12]. Several research groups proposed different methods either in non-contrast mode using doppler-based motion compensation named MoCo [4] or in contrast-mode using an image registration algorithm adapted from magnetic resonance imaging [12] or a two-stage motion estimation based on cross-correlation [11]. Both registration-based methods in contrast mode have shown great potential but their computation time is high, limiting their application for the clinical purpose for quick feedback. Doppler-based motion compensation is promising as it is a fast process based on the autocorrelations along the compounding angles, however the technique only accounts for axial motion and Doppler aliasing could happen in the LV, influencing the motion compensation [4] [11].

In this study, we investigated the MoCo method for contrast enhanced echocardiography and evaluate its potential compared to the image registration method. We also proposed an adapted MOCO to reduce visual artefacts.

Methods

The HFR contrast enhanced (CE) imaging proposed here is formed by the compounding the echoes of PI diverging waves [8]. A HFR CE system based on a 128-Verasonics platform (Verasonics Inc., Kirkland, USA) mounted with an ATL P4-1 (Philips, Seattle, USA) phased-array transducer is used during in-vivo experiment. Data on a healthy human volunteer were acquired with continuous infusion of 1.2 ml/min of Sonovue approved by the Imperial College Research Ethics Committee. For each angle, two successive pulses in the opposite phase were transmitted, recorded and combined to form the PI image. The dataset has been acquired using a linear angle transmission sequence (negative to positive angles) and the transmitted parameters are provided in Table 1. Moreover, because of a possible non-perfect cancellation of the fundamental component, a high pass zero phase 5-th order Butterworth filter with a cut-off frequency at 2.7 MHz was used to extract the second-harmonic signal of the PI images.

Table 1. In-vivo acquisition parameters

Parameter	Value	Parameter	Value
Frequency (cycles)	1.5 MHz (3)	MI	0.08
Angle range	60	Frames	260
Number of angles	11 (x2 PI)	Pulse repetition frequency	5500 Hz
Transmitted sequence [Poree]	Linear	Frame rate	250 Hz

Two motion correction methods used are the image registration and the MoCo. In the case of the image registration method, the motion is compensated using a registration framework adapted from MRI [13-15]. Non-rigid transformations approach is applied to register each radio frequency beamformed PI data to the central angle of the same frame and then coherently summed. For the MoCo method, two approaches are investigated. The first one is similar to the initial MoCo proposed by [4] but applied to contrast acquisition. After beamforming, PI images are filtered with a second-harmonic filter (described above), then complex envelope images are obtained by demodulation centered on the second-harmonic frequency. Slow-time autocorrelations along the compounding angles return the phase delays due to the microbubbles' motion. The phase delays are used to rephase the beamformed images and obtain motion-corrected beamformed complex images. The final compounded image is obtained by coherently summing the motion-corrected images. The second MoCo approach, named adapted MoCo, is similar to the previous one but it is the fundamental (or negative) beamformed image which is used to estimate the motion. No filter was applied to the image. The phase delays obtained are then used to rephase the beamformed non-demodulated PI images before to be summed.

To improve the signal-to-noise ratio, 7 consecutive compounded images have been incoherently averaged before log compression, giving a frame rate comparable to standard focus CE (~30Hz) [9] [12]. The image quality is evaluated by the contrast-to-tissue ratio (CTR) between the LV chamber and 6 myocardial segments obtained using a non-rigid image registration algorithm [9]. CTR highlights the contrast ratio between the chamber and the cardiac muscle for each region of interest (ROIs) and it is a measure of our ability to remove motion artefacts.

Results

The images in Fig. 1 show the acquisition realized on healthy volunteers at two different heart phase (Top) and (Bottom) for several approaches: (a, e) without motion correction and with (b, f) image registration, (c, g) MoCo and (d, h) adapted MoCo motion correction methods. Top images of Fig. 1 highlight that artefacts inside the LV chamber can be visually important, such as in Fig. 1a, impacting the feedback of the HFR CE method. Thanks to image registration, artefacts are removed as well as with the adapted MoCo. The standard MoCo corrects the top of the LV chamber and improves the delineation of the chamber but new artefacts are created in the bottom part of the chamber because of the fast flow coming from the valves, Fig. 1c. Bottom images of Fig. 1 show that most of the motion correction methods work when there is a slow flow inside the chamber.

Fig. 2 highlights the ROIs where the CTR is calculated and the CTR quantification is provided in the chart. After motion-correction the improvement in CTR is at least about 3.6dB with image registration, 0.7dB for adapted MoCo and null with MoCo.

The image registration method provides the best visual feedback however it comes with an important computational time (Table 2). It takes less than a second for both MoCo approaches while it takes more than a minute to the image registration method.

Table 2. Computation time for each motion correction method (Intel Core i7-5820K, 4.50 GHz)

	Computation time
Image registration	71s±10s [A. Stanziola, 2018]
MoCo	0.50s±0.12s
Adapted MoCo	0.72s ± 0.11s

Conclusions

In this paper, the Doppler-based motion correction developed for standard B-Mode images has been evaluated for high frame rate contrast echocardiography imaging to correct motion artefact in the LV chamber. Even if the dataset used in this paper was not using the optimal transmission for the MoCo

(linear instead of triangle [4]), the method shown its potential to correct motion artefact in the LV chamber with a much lower computational time than the image registration method. However, artefacts were also created inside the chamber because of Doppler aliasing when motion is estimated. By using an adapted version of the MoCo, estimating the motion on the beamformed fundamental images and not the PI images, it was possible to reduce the visual artefacts inside the chamber and improve the CTR still with a low computational time compared to the image registration.

Motion correction for cardiac contrast imaging is then a trade-off between best image quality and computational time for clinical purposes. Our future work will focus to use the correct transmission sequence in-vivo for the MoCo method and implement it for real-time feedback.

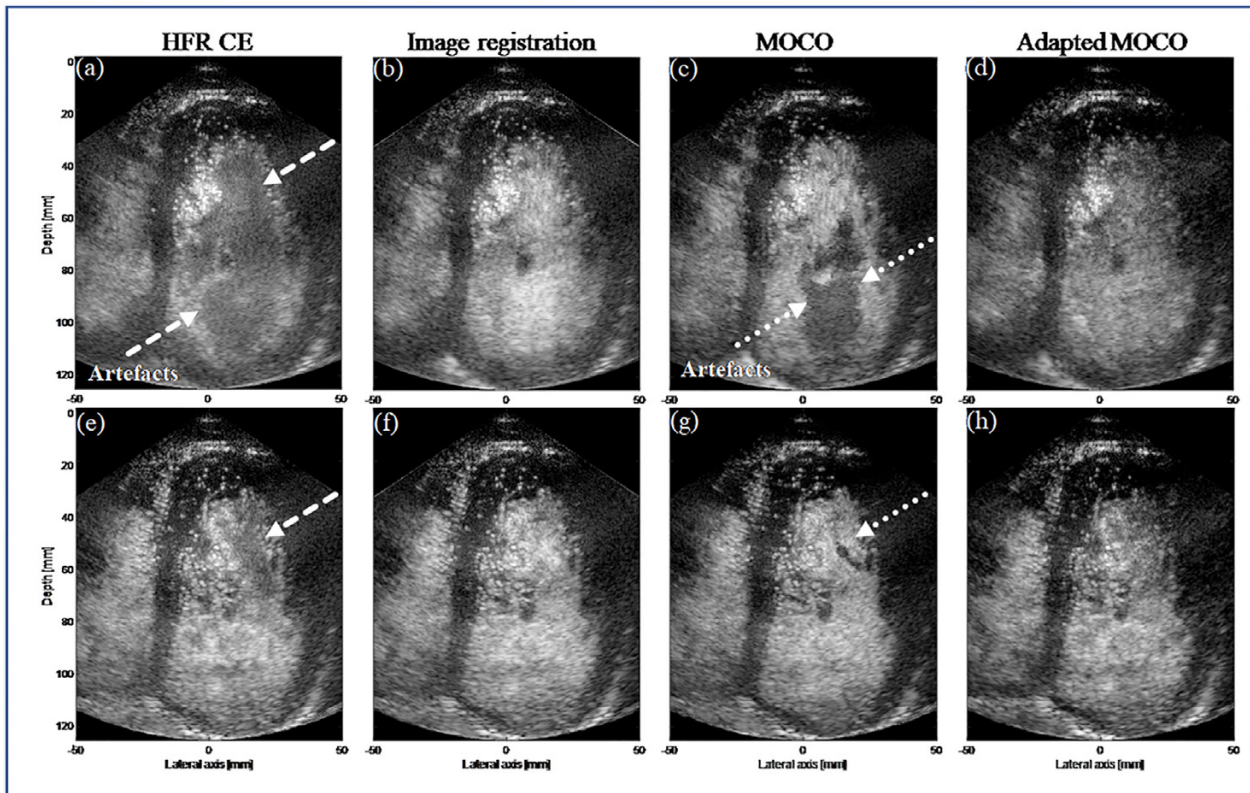


Figure 1. HFR CE images using temporal average of seven frames of the left ventricular heart chamber of a human volunteer without (a, e) and with motion correction: image registration (b, f), MoCo (c, g) or adapted MoCo (d, h). The top and the bottom show two different frames. Dashed arrows highlight initial motion artefacts and dot arrows highlight artefacts created by the MoCo method.

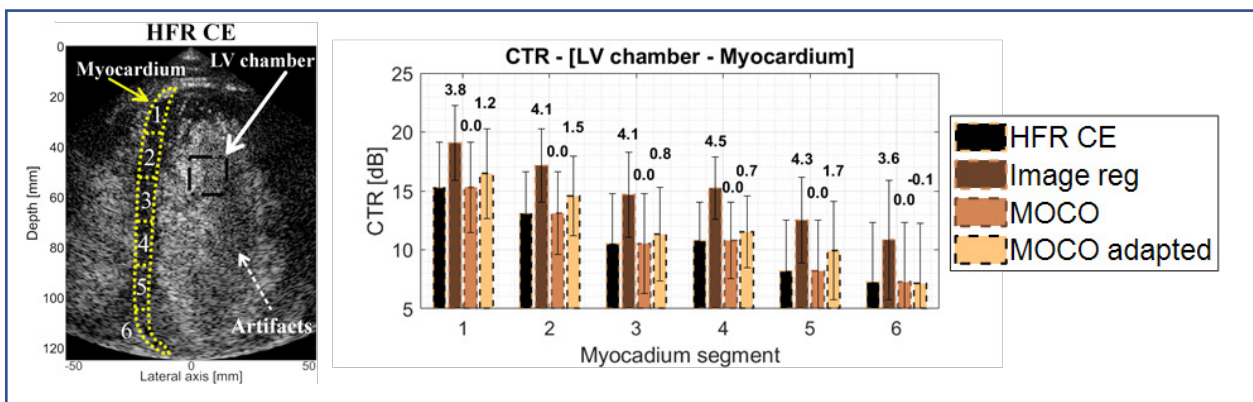


Figure 2. CTR corresponding to the diffretens ROIS shown in the left image. The bold values are the dB improvement of each technique compared to HFR CE without motion correction.

Acknowledgement

We would like to thank Antonio Stanziola, Yuanwei Li, Viginie Papadopoulou, Richard Corbett, Neill Duncan and Robert J Eckersley for their help for collecting data and their feedback.

This work was supported by an Engineering and Physical Sciences Research Council (EPSRC) grant EP/M011933/1 and grant EP/M010961/1, EPSRC Impact Acceleration Account EP/R511547/1 and by the British Heart Foundation Centre of Research Excellence grant RE/13/4/30184. We gratefully acknowledge the support of NVIDIA Corporation with the donation of the Titan Xp GPU used for this research.

References

- [1]. L. Tong, A. Ramalli, R. Jasaityte, P. Tortoli, and J. D'hooge, "Multitransmit beam forming for fast cardiac imaging—Experimental validation and in vivo application," *IEEE Trans. Med. Imag.*, vol. 33, no. 6, pp. 1205–1219, 2014.
- [2]. H. Hasegawa and H. Kanai, "High-frame-rate echocardiography using diverging transmit beams and parallel receive beamforming," *J. Med. Ultrason.*, vol. 38, no. 3, pp. 129–140, 2011.
- [3]. C. Papadacci, M. Pernot, M. Couade, M. Fink, and M. Tanter, "Highcontrast ultrafast imaging of the heart," *IEEE Trans. Ultrason., Ferroelectr., Freq. Control*, vol. 61, no. 2, pp. 288–301, Feb. 2014.
- [4]. J. Porée et al., "High-Frame-Rate Echocardiography Using Coherent Compounding With Doppler-Based Motion-Compensation", *IEEE Trans. On Medical Imaging*, vol. 35, no.7, 2016.
- [5]. J. Faurie et al., "Intracardiac vortex dynamics by high-frame-rate Doppler vortography—In vivo comparison with vector flow mapping and 4-D flow MRI," *IEEE Trans. Ultrason., Ferroelectr., Freq. Control*, vol. 64, no. 2, pp. 424–432, Feb. 2017
- [6]. S. Fadnes, S. A. Nyrnes, H. Torp, and L. Lovstakken, "In vivo intracardiac vector flow imaging using phased array transducers for pediatric cardiology," *IEEE Trans. Ultrason., Ferroelectr., Freq. Control*, vol. 64, no. 9, pp. 1318–1326, Sep. 2017.
- [7]. M. Correia, J. Provost, S. Chatelin, O. Villemain, M. Tanter, and M. Pernot, "Ultrafast harmonic coherent compound (UHCC) imaging for high frame rate echocardiography and shear-wave elastography," *IEEE Trans. Ultrason., Ferroelectr., Freq. Control*, vol. 63, no. 3, pp. 420–431, Mar. 2016.
- [8]. M.E.G. Toulemonde, and al., "High Frame-Rate Contrast Echocardiography: In-Human Demonstration", *JACC Cardiovasc. Imaging*, vol. 11, no. 6, pp. 923-924, 2018.
- [9]. M. Toulemonde, and al., "High-Frame-Rate Contrast Echocardiography Using Diverging Waves: Initial In Vitro and In Vivo Evaluation", *IEEE Trans. on UFFC*, vol. 65, no. 12, pp. 2212 – 2221, 2018.
- [10]. J. Voorneveld, and al., "High-Frame-Rate Echo-Particle Image Velocimetry Can Measure the High-Velocity Diastolic Flow Patterns", *Circ Cardiovasc Imaging*, vol. 12, no. 4, 2019.
- [11]. L. Nie et al., "High-Frame-Rate Contrast-Enhanced Echocardiography Using Diverging Waves: 2-D Motion Estimation and Compensation", *IEEE Trans. on UFFC*, vol. 66, no. 2, pp. 359-371, 2019.
- [12]. A. Stanziola et al., "Motion Artifacts and Correction in Multipulse High-Frame Rate Contrast-Enhanced Ultrasound", *IEEE Trans. On UFFC*, Vol. 66, no. 2, pp. 417-420, 2019.
- [13]. D. Rueckert et al., "Nonrigid registration using free-form deformations: application to breast MR images.", *IEEE Trans. Med. Imag.*, vol. 18, no. 8, pp. 712–21, 1999.
- [14]. D.-J. Kroon, "[online]." [Online]. Available: <https://uk.mathworks.com/matlabcentral/fileexchange/20057-b-spline-grid-image-and-point-based-registration>.
- [15]. S. Lee, G. Wolberg, and S. Y. Shin, "Scattered data interpolation with multilevel B-splines," *IEEE Trans. Vis. Comput. Graphics*, vol. 3, no. 3, pp. 228–244, Jul./Sep. 1997.

A new photoacoustic based technique for single microbubble characterization

Verya Daeichin^{1,2}, **Jordan S. Lum**¹, **Mark A. Borden**^{1,3} and **Todd W. Murray**^{1,3}

¹ Department of Mechanical Engineering, University of Colorado, Boulder, CO 80309, USA

² Department of Acoustic Wavefield Imaging, Delft University of Technology, 2628 CJ Delft, The Netherlands

³ Material Science and Engineering Program, University of Colorado, Boulder, CO 80309, USA

Corresponding author: v.daeichin@tudelft.nl

Introduction

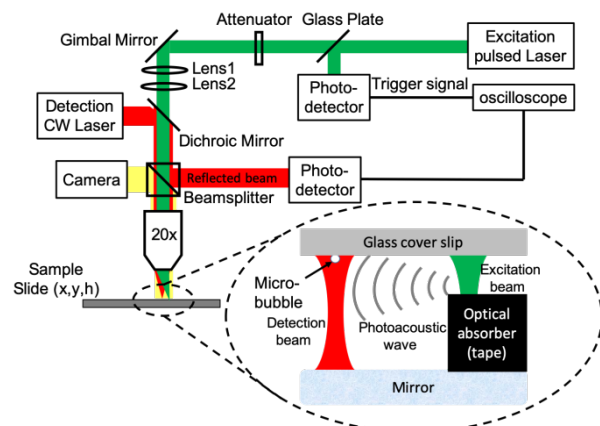
Microbubbles (MB) have been used for decades as ultrasound contrast agents (UCA) and more recently as carrier vehicles for drugs and genes in therapeutic applications. With recent developments in the field, novel MB formulations and manufacturing techniques are advancing. Accurate acoustic characterization of MBs is an essential prerequisite for optimized imaging sequences and/or optimized driving pulses when using MBs as carriers and delivering agents. Several methods have been proposed for MB characterization including high-speed cameras, acoustic cameras and laser-based techniques. A majority of the existing single MB characterization techniques, whether they are acoustically or optically probing the MB oscillations, are limited in capturing the full dynamics of the MB. Current techniques generally suffer from limited bandwidth of the excitation pulse and the detection systems; have unknown phase of the excitation pulse relative to the MB oscillation phase; have limited sensitivity and therefore require high pressure excitations to detect the MB oscillation; and are time consuming, complex and require high averaging. In order to capture the full dynamics of MB oscillation, a MB should ideally be excited with an acoustic impulse and its entire volumetric oscillation (impulse response) should be captured at once with sufficient sensitivity. Recently, Lum *et al.*[1] and Dove *et al.*[2] reported on laser-induced thermoacoustic excitation of single MBs. Besides the limited bandwidth of excitations in the first method, the amplitude of oscillation in both methods is very low (<10 nm). High data averaging is required to provide sufficient signal-to-noise ratios (~100000 averages) or narrow-bandwidth detection using a lock-in amplifier is necessary. Moreover, the MB excitation in Dove *et al.* was mentioned to be mainly due to the heat transfer into the gas core, causing a thermal expansion rather than an acoustically induced excitation. In this work, we introduce a sensitive photoacoustic (PA) based technique to capture the full dynamics of MB oscillation at once (no averaging) in response to a single broadband PA pulse.

Methods

The optical system used in this study is based on the prototype described by Murray *et al.*[3]. A schematic representation of the optical setup is shown in Fig. 1.

FIG 1. Schematic of the experimental setup used to excite and detect the microbubble oscillations with a zoomed in depiction of a single microbubble illuminated by the detection laser during excitation by a photoacoustic wave.

The PA signal was generated with a pulsed microchip laser operating at a wavelength of 532 nm, a pulse width of 400 ps, and a repetition rate of 1 kHz (PNP-M02010 PowerChip™, Meylan, France). The excitation laser pulse was sent through a relay lens system, a variable attenuator and a long working distance microscope objective (numerical aperture of 0.42) to illuminate the sample. A continuous wave detection laser (Flamenco laser, Cobalt AB, Solna, Sweden) operating at a wavelength of 660 nm (red) and an optical power of 30 mW was sent to the sample



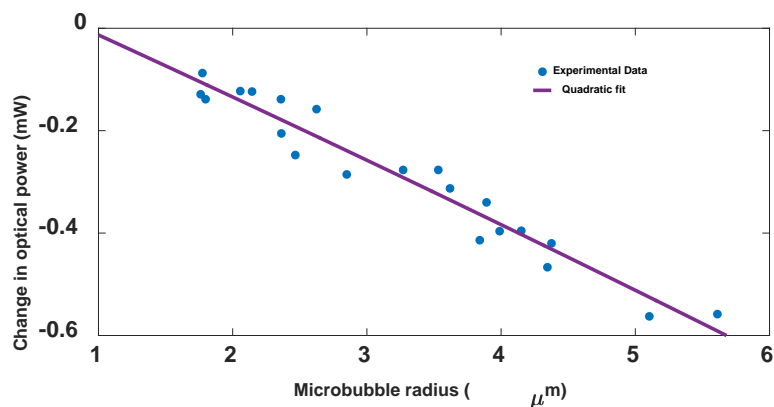
through the same objective to illuminate the single MB. After passing through the MB once, the detection beam was then reflected off the bottom mirror surface, passed through the MB again and the scattered light was then directed to a photodetector to be recorded. The output from the photodetector was digitized and processed by a high-speed oscilloscope (National Instruments PXIe 5162) and a computer. An additional optical port on the microscope housed a CCD camera which was used to locate and size microbubbles within the field of view of the microscope. The optical system allowed for precise three-dimensional positioning of the sample within the field of view of the objective, as well as control over the excitation laser position, spot size and laser fluence. The excitation laser x-y position at the sample was controlled by the gimbal mirror and relay lens system. The focal depth was controlled by adjustment of the lens relay system, and the output energy was adjusted and increased up to 50 nJ per pulse by use of the attenuator.

For the experimental measurements, DPPC-coated MBs (see [1] for exact formulation) were diluted in a 0.01 M NaCl phosphate buffered saline solution and injected between a mirror (same mirror used to reflect the detection beam) surface and a thin glass cover slip separated by a 280- μm thick adhesive seal. The sample was placed at the focal plane of the microscope objective, and an individual MB was positioned at the center of the detection beam. The MB was excited with the acoustic impulse generated by shining the pulsed excitation laser on an optical absorber next to the MB (black tape in the sample attached to the surface of the mirror). The MB volumetric oscillation was detected using light scattering. The relationship between the scattered light signal and the MB radial displacement was found using a calibration procedure similar that described in Dove *et al.*[2].

Results

A MB was first identified within the field of view of the microscope. A computer-controlled positioning stage was then used move the MB to the center of the detection beam, and the reduction in optical power associated with scattering was recorded. This procedure was repeated for a population of MBs with radii in the 1-6 μm size range to obtain a profile of light power associated with scattering for each MB size (Fig. 2).

FIG 2. The profile of light intensity associated with scattering for each bubble size. Since the bubble oscillations are small, the derivative of a quadratic fit to the light intensity profile can be used to convert the recorded optical power of the detection beam to the bubble radial oscillation.



The temporal dynamics of the generated PA signal was detected by measuring the acoustic impulse passing through the detection beam in the absence of a MB. The PA signal causes an optical phase shift of the detection beam proportional to the PA pressure integrated along the laser path, resulting in modulation of the light intensity [4,5]. The principal interaction between light and an acoustic pulse (with wavelength much smaller than the light) in water is due to the perturbations of the refractive index of water induced by the acoustic pressure field as described by Pitts and Greenleaf [6]. The bandwidth of the measured PA signal corresponds well with the expected PA signal generated from a short pulse laser (Fig. 3a and 3b). The amplitude of the PA signal can be controlled with the pulse laser energy (Fig. 3c). Such a tuneable PA signal in the vicinity of a MB can drive the MB into resonance (Fig. 3d and 3e). To confirm the linearity of the system, the amplitude of the MB radial oscillations was measured as a function of laser pulse energy (Fig. 3f).

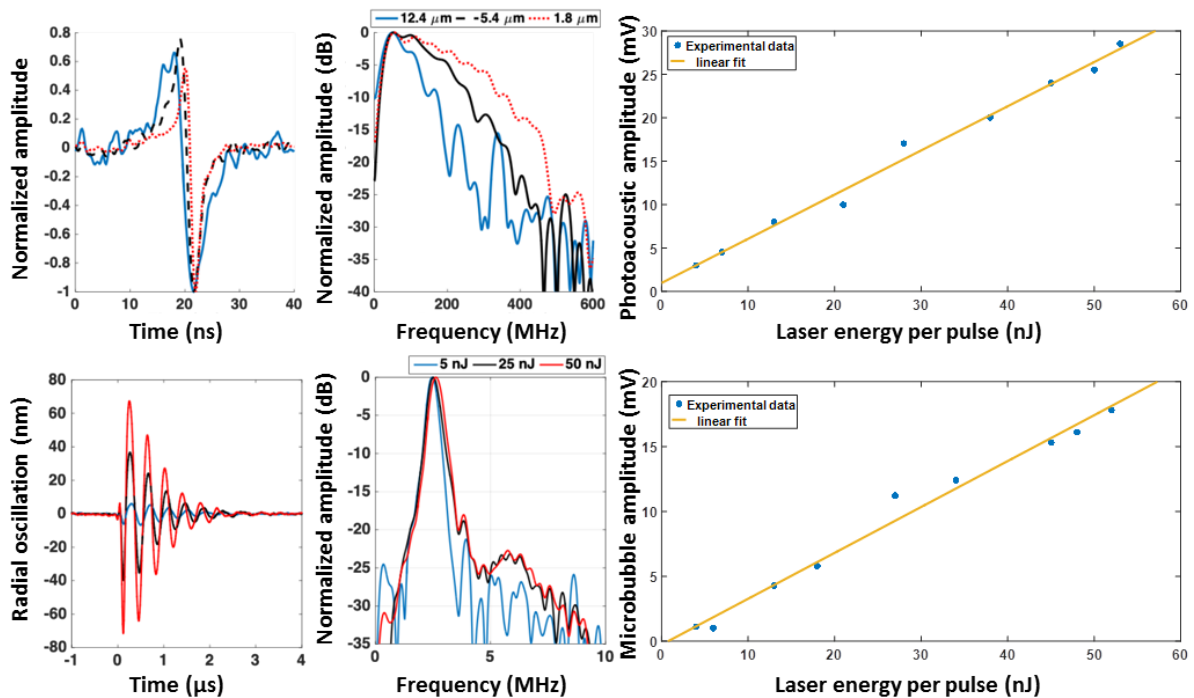


FIG 3. a and b) Measured photoacoustic wave from the absorber for 3 different pulse laser spot sizes ($1/e$ radii of $1.8 \mu\text{m}$, $5.4 \mu\text{m}$ and $12.4 \mu\text{m}$) in time domain and frequency domain. c) peak-to-peak amplitude of the photoacoustic wave as a function of the laser energy per pulse and a linear fit to the measurements. d and e) Radial oscillation of a microbubble with radius of $2.66 \mu\text{m}$ excited by the photoacoustic wave generated with three different laser pulse energies in d) time domain and e) frequency domain. f) peak-to-peak amplitude of the microbubble radial oscillation as function of laser energy per pulse and a linear fit to the measurements.

Conclusions

We have developed and tested a new PA based technique to measure the impulse response of individual MBs in single shot measurements. MB volumetric oscillations were tracked as a function of time using light scattering. The ability to probe single MB larger amplitude oscillations with high fidelity and sensitivity using PA excitation and optical detection offers a potentially powerful technique for the study of MB dynamics and modelling the observed behaviours. The validity of any model has to be established by comparison with independent experimental observations which fulfils the system identification requirements. We have developed a technique which is, for the first time, capable of offering such an experimental procedure for single MB system identification. High spatiotemporal control of an applied excitation pulse is possible using focussing optics to adjust the spot size and distance between the excitation point and MB. In this context, conventional piezoelectric acoustic source applications could be surpassed. In addition, it is possible to increase the amplitude of the excitation by matching the excitation laser wavelength with the absorption peak wavelength of the absorbing material. The application of such a technique could open a cache of opportunities for characterization of MBs used as contrast agents and as carrier vehicles for drugs and genes in therapeutic applications.

References

- [1]. J.S. Lum, D.M. Stobbe, M.A. Borden, and T.W. Murray, *Appl. Phys. Lett.* 112, 111905 (2018).
- [2]. J.D. Dove, M.A. Borden, and T.W. Murray, *Opt. Lett.* 39, 3732 (2014).
- [3]. T.W. Murray, A. Bakir, D.M. Stobbe, M.J. Kotelyanskii, R.A. Mair, M. Mehendale, X. Ru, J.D. Cohen, M.T. Schulberg, P. Mukundhan, T.J. and Kryman, *Journal of Microelectronics and Electronic Packaging*, 13(2), 58 (2016).
- [4]. X. Jia, G. Quentin and M. Lassoued, *IEEE transactions on ultrasonics, ferroelectrics, and frequency control*, 40(1), 67, (1993).
- [5]. T.A. Pitts, A. Sagers and J.F. Greenleaf, *IEEE transactions on ultrasonics, ferroelectrics, and frequency control*, 48(6), 1686, (2001).
- [6]. T.A. Pitts and J.F. Greenleaf, *The Journal of the Acoustical Society of America*, 108(6), 2873 (2000).

Radiation-induced vaporization of PCDA-PFB nanodroplets: a feasibility study for ultrasound-based proton range verification and dosimetry

Sophie V. Heymans¹, Bram Carlier^{2,3}, Sjoerd Nooijens⁴, Yosra Toumia⁵, Marcus Ingram⁴, Gaio Paradossi⁵, Emiliano d'Agostino⁶, Uwe Himmelreich^{3,7}, Jan D'hooge⁴, Edmond Sterpin^{2,3}, Koen Van Den Abeele¹

¹Department of Physics, KU Leuven Campus KULAK, Kortrijk, Belgium

²Department of Oncology, KU Leuven, Leuven, Belgium

³Molecular Small Animal Imaging Center, KU Leuven, Leuven, Belgium

⁴Department of Cardiovascular Sciences, KU Leuven, Leuven, Belgium

⁵Department of Chemical Sciences and Technology, University di Roma Tor Vergata, Rome, Italy

⁶DoseVue, Philips Open Manufacturing Campus, Turnhout, Belgium

⁷Department of Imaging & Pathology, KU Leuven, Leuven, Belgium

Corresponding author: koen.vandenabeele@kuleuven.be

Introduction

Nanodroplets, or phase-change contrast agents, are attractive candidates for ultrasound imaging and therapy, owing to their capability to extravasate and locally vaporize into microbubbles upon activation by an external energy source. While Acoustic [1] and Optical [2] Droplet Vaporization have been reported on extensively, the vaporization of nanodroplets induced by exposure to ionizing radiation remains, to our knowledge, unexplored. Yet, radiation-sensitive, injectable nanodroplets could pave the way for new applications, such as the ultrasound-based verification of treatment delivery during radiation therapy (*in vivo* dosimetry). Additionally, they might offer an innovative solution to reduce range uncertainty margins currently adopted in proton therapy [3], provided that nanodroplet vaporization profiles can be related to the proton range *in vivo*. According to the semi-empirical theory of radiation-induced nucleation, developed for superheated drop detectors and bubble chambers [4], the degree of superheat required for droplet vaporization is inversely related to the radiation linear energy transfer (LET), i.e. the energy transferred by a charged particle per unit track length. In this contribution, superheated nanodroplets were exposed to a proton beam, and the phase transition was confirmed with ultrasound imaging. Experimental results were compared to predictions obtained by applying the theory of radiation-induced nucleation.

Methods

The nanodroplets employed in this study were made of a polymerized fatty acid monolayer of 10,12-pentacosadiynoic acid (PCDA) encapsulating a perfluorobutane (C₄F₁₀, boiling point of -2°C) liquid core [5]. Gelatin phantoms with entrapped nanodroplets were irradiated from two opposing sides, at 25°C, by a monoenergetic proton beam at different energies (46.8 MeV and 62 MeV) and doses (2, 10 and 20 Gy, measured at the Bragg Peak) in the research facility of UCLouvain (Louvain-la-Neuve, Belgium). The phantoms were imaged before and after irradiation with a 7.5 MHz linear array (Vermon, France) driven by an experimental ultrasound scanner (DiPhAS, Fraunhofer IBMT, Germany). Plane wave imaging at an acoustic pressure below the threshold for droplet vaporization was employed. Bubbles were detected with an algorithm developed in-house, and bubble counts in different regions of interest were compared for irradiated (n=3) and control (n=3) phantoms using Student's t-tests. Bubble count profiles were derived from the ultrasound images and compared to the proton range (measured independently).

Results

Ultrasound images of gelatin phantoms with dispersed nanodroplets are displayed in Fig. 1 for an irradiated phantom (Fig.1a,c) and a control phantom (Fig.1b,d). After irradiation from both sides, the irradiated phantoms exhibited distinct zones of high bubble density, separated by a region of low bubble

density in the middle (Fig. 1c). In contrast, control phantoms only displayed a small amount of uniform, spontaneous vaporization over time (Fig. 1d). The increase in bubble count between pre and post images was significantly higher ($p < 0.01$) for irradiated phantoms than for control phantoms in the two irradiated regions (10 Gy and 20 Gy) and no significant difference was observed for the middle region, distal to both Bragg peaks. The number of bubbles was found to be linearly related to the proton fluence ($R^2 = 0.97$). The analysis of the bubble count profiles of irradiated phantoms (Fig. 1e) revealed that the sharp drop in bubble count occurred on average 2.60 ± 0.26 mm proximal to the proton range ($n=3$).

For perfluorobutane nanodroplets employed at 25°C, an LET threshold of 370 keV/ μ m was calculated. As protons only reach maximal LET values of 70-90 keV/ μ m at the Bragg Peak, this implies that the nanodroplets did not respond to the primary proton beam, but were vaporized by secondary particles (recoil ions) created from non-elastic reactions with the primary protons. Indeed, the LET of these recoil ions ranges between several hundreds and a thousand keV/ μ m [6]. These theoretical considerations explain the absence of enhanced response at the Bragg peak as well as the flat shape of the obtained bubble profiles (Fig. 1e), and the shift between the drop in bubble count and the proton range was related to nuclear interaction models with excellent agreement.

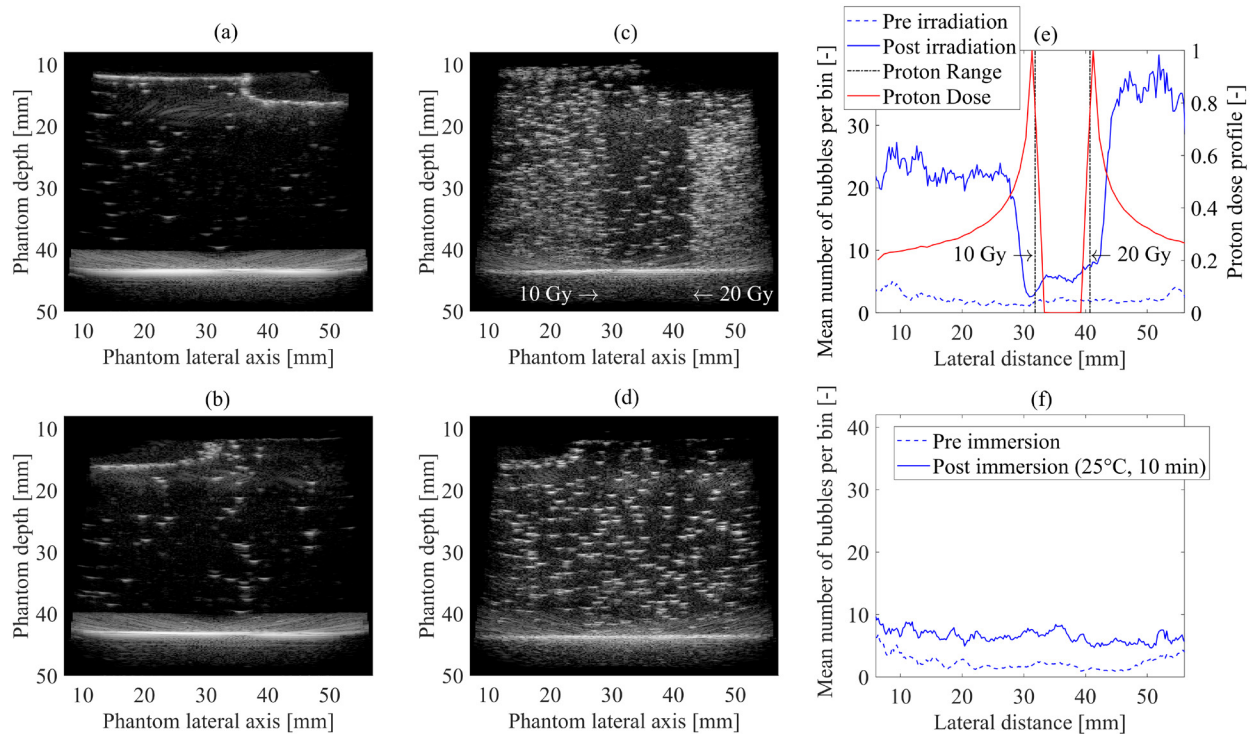


Figure 1. Top: Ultrasound images of a gelatin phantom with dispersed nanodroplets before (a) and after (c) exposure to 62 MeV protons (10 Gy dose in the forward position, 20 Gy in the reverse position). (e) Bubble count profile across the phantom, averaged over eleven images. Bottom: Images acquired before (b) and after (d) immersion at 25°C and profiles (f), for a control phantom with dispersed nanodroplets (no irradiation).

Conclusions

We evaluated the potential use of perfluorobutane nanodroplets coated with PCDA for ultrasound-based proton dosimetry and range verification. The theory of radiation-induced nucleation predicted nanodroplet vaporization triggered by high-LET nuclear reaction products. Uniformly vaporized regions proximal to the proton Bragg peak were observed experimentally with ultrasound imaging. The signal shifts between the bubble count profiles and the proton range were retrieved with sub-millimeter precision. Future work will focus on the translation towards *in vivo* applications, by evaluating the nanodroplets radiation response at physiological temperature, and optimizing the nanodroplets degree of superheat to achieve sensitivity to the primary proton beam. Additionally, the passive detection with an

ultrasound array of acoustic signals emitted by vaporizing nanodroplets during proton irradiation will be investigated.

References

- [1]. Sheeran PS, Luois SH, Mullin LB, Matsunaga TO, and Dayton PA, Design of ultrasonically-activatable nanoparticles using low boiling point perfluorocarbons, *Biomaterials*, 33(11):3262–3269, 2012.
- [2]. Dove JD, Mountford PA, Murray TW, and Borden MA, Engineering optically triggered droplets for photoacoustic imaging and therapy, *Biomedical Optics Express*, 5(12):4417-4427, 2014.
- [3]. Paganetti H, Range uncertainties in proton therapy and the role of Monte Carlo simulations, *Physics in Medicine and Biology*, 57(11):99-117, 2012.
- [4]. D'Errico F, Fundamental properties of superheated drop (bubble) detectors, *Radiation Protection Dosimetry*, 84(1–4):55–62, 1999.
- [5]. Toumia Y et al., Phase Change Ultrasound Contrast Agents with a Photopolymerized Diacetylene Shell, *Langmuir*, 35:10116–10127, 2019.
- [6]. Grassberger C and Paganetti H, Elevated LET components in clinical proton beams, *Physics in Medicine and Biology*, 56(20):6677–6691, 2011.

Acknowledgements

This project has received funding from the European Union's Horizon 2020 research and innovation Programme under grant agreement 766456 (AMPHORA).

Foam-free monodisperse lipid-coated ultrasound contrast agent synthesis through multi-gas-component microbubble stabilization

Tim Segers¹, Emmanuel Gaud², Kim Bruil¹, Pablo Peñas¹, Gilles Casqueiro², Anne Lassus², Michel Versluis¹, Peter Frinking³

¹ *Physics of Fluids group, TechMed Centre, MESA+ Institute for Nanotechnology, University of Twente, Postbus 217, 7500 AE Enschede, The Netherlands*

² *Bracco Suisse S.A., Geneva, Switzerland*

³ *Tide Microfluidics B.V., Capitool 41, 7521 PL Enschede, The Netherlands*

Corresponding author: t.j.segers@utwente.nl

Introduction

Narrowing down the size distribution of ultrasound contrast agents (UCA) is currently considered as a means to unlock the full potential of microbubbles for medical applications. Microbubbles are resonators with a characteristic resonance frequency that is inversely proportional to the microbubble size. At resonance, the relative amplitude of oscillation and the nonlinear echo are at maximum. Thus, the sensitivity of contrast-enhanced (molecular) ultrasound imaging and the efficacy of theranostic applications that rely on ultrasound-driven volumetric microbubble oscillations, such as drug and gene delivery, sonoporation, blood-brain-barrier opening, and sonothrombolysis, can be dramatically increased through the use of resonant monodisperse bubbles.

Monodisperse lipid-coated bubbles can be formed directly in a flow-focusing device (Fig. 1A). We recently fully characterized the parameter space for stable monodisperse microbubble synthesis by flow-focusing [1,2]. We found that the lipid monolayer shell around the freshly formed bubbles is initially always loosely packed resulting in a high surface tension, and thereby in a Laplace pressure-driven dissolution of the freshly formed bubbles until their stable size is reached. The ratio of the initial to the stable bubble radius practically ranges from 2 to 3 [1,2]. Thus, roughly 90% of the initial gas volume has to diffuse out of the freshly formed bubbles during the stabilization process. However, UCAs are typically filled with a gas with low aqueous solubility and once released it rapidly saturates the aqueous environment. Consequently, the stabilization process proceeds through Ostwald ripening thereby forming not only stable bubbles but also large and unstable thrombogenic foam bubbles [3] (Figs. 1D-E) that will limit a safe passage of the contrast agent through the entire circulation.

Here, we show that by forming monodisperse multicomponent bubbles filled with a mixture of a low and a high aqueous solubility gas, readily injectable, highly stable, and perfectly monodisperse microbubble suspensions can be synthesized at clinically relevant concentrations while preventing the formation of foam bubbles. The ideal volume fraction of the low solubility gas and the gas composition of the stable bubbles are modeled and in good agreement with the measurements. The present work may boost the clinical introduction of novel monodisperse agents.

Methods

The employed lipid mixture consisted of DSPC and DPPE-PEG5000 mixed at a 9:1 molar ratio to a total concentration of 10 mg per mL of air saturated saline. To minimize on-chip bubble coalescence, the flow-focusing device was placed in a thermostatic bath controlled at 55°C (Fig. 1B) [2]. The bubbles were filled with a mixture of the low solubility gas C₄F₁₀ and the high solubility gas CO₂. The composition of the gas mixture was accurately controlled by two mass-flow controllers (Bronkhorst, The Netherlands). For optimal flow stability, the liquid flow-rate was also mass-flow controlled. To drive the liquid flow, the reservoir with the lipid dispersion was pressurized by the low solubility gas. The driving pressure of the C₄F₁₀ gas was increased to 5 bar by controlling the temperature of the gas bottle and the mass-flow

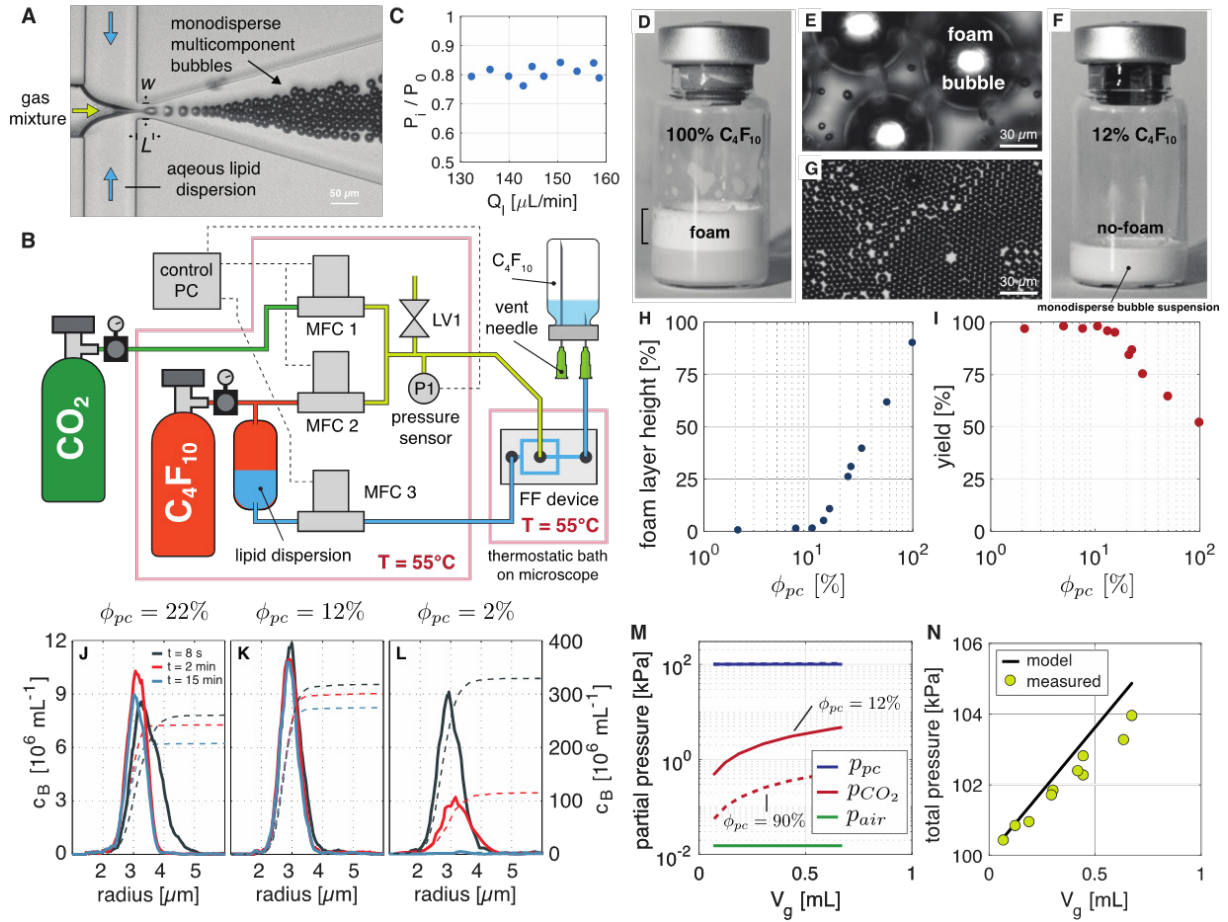


Figure 1. (A) Monodisperse multicomponent bubble formation by flow-focusing (B) Monodisperse multicomponent bubbles were formed at 55°C in a flow-focusing device. The bubbles were filled with a gas mixture of C₄F₁₀ and CO₂ and collected in a vial with a C₄F₁₀ headspace. (C) Pressure in the bubbles at pinch-off normalized to atmospheric pressure as a function of the liquid flow-rate (D&E) Large foam bubbles are formed during the stabilization of monodisperse lipid-coated microbubbles filled with pure C₄F₁₀. (F&G) Perfectly monodisperse bubble suspensions without foam can be synthesized by forming multicomponent bubbles filled with a gas mixture of C₄F₁₀ and CO₂. (H) Relative foam layer height and (I) bubble yield as a function of C₄F₁₀ volume fraction. Number and cumulative size distributions of bubble suspensions formed at (J) $\phi_{pc} = 22\%$, (K) $\phi_{pc} = 12\%$, and (L) $\phi_{pc} = 2\%$. (M) Modeled partial pressures in the stable bubbles. (N) Modeled and measured absolute pressure the headspace of bubble suspension collected in a sealed vial.

controllers at 55°C in an oven to allow bubble formation at a high production rate of 400.000 bubbles/s. The bubbles were collected in a sealed glass vial that was pre-filled with pure C₄F₁₀ gas to keep the PFC gas in the bubbles during their stabilization. Ten bubble samples of 1 mL in volume (400 s production time) were collected at PFC volume fractions of 2 to 100%. For each collected bubble suspension, the size distribution and total bubble concentration c_B were measured within 2 hours after bubble collection using a coulter counter (Multisizer 3, Beckman Coulter). A size distribution was measured 8 s, 2 mins, and 15 mins after dilution and these were used to quantify the yield and the stability of the microbubbles when diluted.

Results

Figure 1D shows a picture of a bubble suspension of which the bubbles were initially filled with pure C4F10. The photograph was taken within 10 mins after collection. Note that a thick layer of foam is formed on top of the bubble suspension. The micrograph in Fig. 1E shows that the foam bubbles were on the order of 100 μm in diameter. However, note from Fig. 1F that when the volume fraction of the PFC gas ϕ_{pc} was decreased to 12%, no foam layer was formed. Indeed, the micrograph in Fig. 1G demonstrates that at $\phi_{pc} = 12\%$ a perfectly monodisperse bubble suspension can be synthesized without thrombogenic foam bubbles. The height of the foam layer relative to that of the liquid was measured 2 hours after bubble collection and it is plotted in Fig. 1H. The figure shows that no foam is formed for $\phi_{pc} \leq 12\%$. The microbubble yield (total concentration in the vial / concentration in the flow-focusing device) is plotted in Fig. 1I. The figure shows that the yield was limited to 50% for bubbles filled with pure C4F10. Nevertheless, when the bubbles were initially filled with $\phi_{pc} \leq 12\%$, the yield increased to its maximum value of 100% meaning that all freshly formed bubbles stabilized to their final size.

Figures 2J-L show the number and cumulative size distributions of the bubble suspensions formed at $\phi_{pc} = 22\%$, 12%, and 2%, respectively. Note that over a time span of 15 mins the bubbles filled with 22 v% of PFC gas decreased in size by approx. 15% and that their monodispersity increased upon dilution. This shows that the bubbles did not fully stabilize in the collection vial. The excess C4F10 gas diffused out of the bubbles upon dilution until the stable bubble size was reached after 2 mins. On the other hand, note that the bubbles filled with $\phi_{pc} = 12\%$ were readily stable meaning that the mode and the width of the size distribution changed by less than 3% over a time window of 15 min in dilution. Also note that the total bubble concentration of 3×10^8 bubbles/mL is very similar to that of SonoVue. The bubble suspensions filled with less than 12 v% of PFC gas were not stable in dilution. Figure 2L shows a typical example, the bubble concentration decreases to nearly zero within 15 min after dilution. This shows that bubbles filled with less PFC gas than their final volume dissolve more rapidly in solution as they contain the small molecular weight CO₂ molecules with a high aqueous solubility and high diffusivity.

The optimal volume fraction of 12 v% of PFC gas in the freshly formed lipid coated microbubbles is exactly predicted by the following equation:

$$\phi_{pc} = \frac{P_0 T_i}{P_i T_0} \left(\frac{R_i}{R_f} \right)^{-3} \times 100\%.$$

In above equation, T_i is the temperature during bubble formation, P_i the pressure in the bubble at pinch-off (Fig. 1C), R_i the bubble radius at pinch-off, T_0 room temperature, P_0 atmospheric pressure, R_f the stable bubble radius. Thus, in order to avoid foam formation, the freshly formed bubble with initial radius R_i needs to be filled precisely with the amount of low aqueous solubility gas corresponding to the volume of the stable bubble V_f ($4/3\pi R_f^3$). The ratio of the initial bubble size to the stable bubble size can be calculated using the universal stabilization equation for lipid-coated bubbles obtained in our previous work [1,2], as follows:

$$\frac{R_i}{R_f} = 1.4 + 1.6 \times 10^{-3} (1 + 30\lambda_{PG}^2) M_w \phi_{PEG},$$

with λ_{PG} the propylene glycol mass fraction in the liquid, M_w the molecular weight of the PEG chain, and ϕ_{PEG} the molar fraction of the PEGylated lipid. For the present lipid mixture ($\lambda_{PG} = 0$, $M_w = 5000$, $\phi_{PEG} = 0.1$) the ratio R_i/R_f equals 2.2.

Questions may arise as to the gas composition of the stable bubbles. Using Henry's law and the ideal gas law, the composition of the gas in the stable bubbles is calculated at equilibrium, i.e. when all gasses are perfectly mixed such that the gas composition in the headspace equals that of the bubbles. The calculated partial pressures are plotted in Fig. 1M as a function of the total gas volume that diffused out of the freshly formed bubbles during stabilization. The figure shows that the amount of air in the air-saturated co-flow is negligible. It also shows that the molar amount of C4F10 dissolved in the liquid under the 5 bar C4F10 driving pressure P_d is negligible since the curves for zero P_d are indistinguishable from those calculated for $P_d = 5$ bar. Thus, the amount of C4F10 in the headspace is much larger than that dissolved in the liquid. Furthermore, Fig. 1M shows that p_{CO_2} increases with V_g since more CO_2 gas is injected in the system at a higher V_g . On the other hand, p_{ppc} is independent of V_g due to the fact that the molar amount of C4F10 in the bubbles is negligible as compared to that in the headspace. Finally, note that the stable bubbles were filled by at least 95 v% of C4F10, which explains their high stability in dilution. Figure 1N shows that the modeled and measured total pressure in the headspace ($p_{ppc} + p_{CO_2} + p_{air}$) exceeded atmospheric pressure by up to 4.5 kPa. The pressure rise results from diffusion of CO_2 dissolved in the water into the headspace. An overpressure of 4 kPa results in a 1.4% increase in bubble volume when the bubbles are taken out of the vial. This volume increase may seem negligible, however, it has been shown that the viscoelastic shell properties can change as a result of these small surface area expansions [4]. Future work will focus on the potential change in the acoustic response of bubbles collected as in the present work once taken out of the vial and on the role of under- and overfilling of the freshly formed bubbles with C4F10 on their acoustic response.

Conclusions

We have shown that perfectly monodisperse suspensions of lipid-coated microbubbles with concentrations similar to SonoVue and at a yield of 100% can be formed microfluidically by filling the microbubbles with a gas mixture of a high- and a low aqueous solubility gas. The present work therefore allows for bedside production of readily stable monodisperse UCAs without hazardous thrombogenic foam bubble formation.

References

- [1]. Segers, T., Lohse, D., Versluis, M., & Frinking, P. (2017). Universal Equations for the Coalescence Probability and Long-Term Size Stability of Phospholipid-Coated Monodisperse Microbubbles Formed by Flow Focusing. *Langmuir*, 33(39), 10329-10339.
- [2]. Segers, T., Lassus, A., Bussat, P., Gaud, E., & Frinking, P. (2019). Improved coalescence stability of monodisperse phospholipid-coated microbubbles formed by flow-focusing at elevated temperatures. *Lab on a Chip*, 19(1), 158-167.
- [3]. Segers, T., De Rond, L., de Jong, N., Borden, M., & Versluis, M. (2016). Stability of monodisperse phospholipid-coated microbubbles formed by flow-focusing at high production rates. *Langmuir*, 32(16), 3937-3944.
- [4]. Segers, T., Gaud, E., Versluis, M., & Frinking, P. (2018). High-precision acoustic measurements of the nonlinear dilatational elasticity of phospholipid coated monodisperse microbubbles. *Soft matter*, 14(47), 9550-9561.

Non-Invasive Ultrasound and Bubble-Mediated Blood-Spinal Cord Barrier Opening: Experiences with a Pig Model

Stecia Fletcher^{1,2}, Min Choi¹, Elizabeth S. Douglas¹, Ranjith Ramesh¹, Viva Chan¹, Shawna Rideout-Gros¹, Natalia Ogrodnik¹, Meaghan A. O'Reilly^{1,2}

¹Physical Sciences Platform, Sunnybrook Research Institute, Toronto, Ontario, Canada

²Department of Medical Biophysics, University of Toronto, Toronto, Ontario, Canada

Corresponding author: moreilly@sri.utoronto.ca

Introduction

Ultrasound in combination with microbubbles has been shown to transiently permeabilize the blood-brain barrier (BBB) to allow a broad range of therapeutics to be delivered from the vasculature to the brain. This technique has now reached clinical investigations for the treatment of brain tumors^{1,2} and neurodegenerative diseases^{3,4}. However, the use of ultrasound to modulate the functionally equivalent blood-spinal cord barrier (BSCB) has received less attention, despite the potential benefit to patients suffering from spinal cord diseases and disorders. In rodent models it has been shown that the BSCB can be manipulated in a similar manner to the BBB^{5,6,7} and we have shown a potential therapeutic effect in a metastatic disease model⁷. Non-invasive, clinical-scale implementation requires the development of devices and methods to deliver the ultrasound energy through the complex vertebral bone to the spinal canal and robust methods to monitor and control microbubble activity. We have previously developed Short Burst Phase Keying (SBPK) as a method to reduce focal depth of field and mitigate standing waves in the vertebral canal^{8,9}. In this talk we will present our preliminary findings testing this approach in a clinically-relevant large animal model.

Methods

A pig model was chosen for this study due to the comparable vertebral bone geometry to humans¹⁰. Pigs (Yorkshire, n=5, 30-40kg) were anesthetized with ketamine and atropine, intubated and maintained under anesthesia using isoflurane (2%) and medical air with mechanical ventilation. To prevent an adverse reaction to the microbubbles, diphenhydramine (0.5 mg/kg) was administered prior to the experiment. Animals were placed on top of an MRI compatible FUS system (LP-100, FUS Instruments) in the bore of a 3T MRI (Siemens mMR). A custom transducer holder was mounted in the FUS system, holding two 500 kHz, 5cm diameter, FN=2 piezo-composite transducers co-focused with 60° separation between the transducers. Under MRI-guidance, the lower thoracic spinal cord was targeted at multiple locations. The transducers were driven using 10 ms sinusoidal bursts or 10 ms SBPK pulse trains incorporating pulse inversion as described in⁹. In n=3 pigs, sinusoidal bursts and SBPK fixed pressure exposures were tested up to 2.1 MPa non-derated pressure at 1 Hz PRF for 2 or 5 minutes. In n=2 animals, SBPK exposures were ramped from a starting pressure of 1.7 MPa in 50 kPa increments to a maximum of 2.3 MPa non-derated pressure for 5 minutes. Definity microbubbles (0.005-0.01 ml/kg) were administered intravenously as a slow bolus at the start of the ultrasound exposure. Two receivers, a PZT receiver tuned to the subharmonic and a PVDF receiver, were used to record the acoustic emissions. Detection of subharmonic activity during the ramped exposures would trigger a reduction in pressure, similar to the control method described in¹¹ for BBB opening. Following the final treatment Evans blue (2 ml/kg, 4%) was administered and allowed to circulate for 1.5 hrs prior to sacrifice under deep anesthesia via transcardial perfusion with saline followed by formalin. The cord tissue was sent for histology and the vertebral arch from the treated region was extracted for benchtop measurements of insertion loss.

Results

The BSCB was successfully modified using both sinusoidal pulses and the SBPK exposures. Qualitatively, the SBPK exposures applied through the intact spine resulted in highly localized BSCB

modification, as assessed by Evans blue extravasation, while the 10 ms sinusoidal pulses resulted in widespread opening with damage observed at bone/tissue interfaces, likely due to reflections and standing waves. During the ramped exposures changes in bubble activity were observed although were insufficient to trigger a pressure drop by the controller before the controller pressure limit was reached. At necropsy in one animal treated with ramped exposures evidence of opening was observed at 3/4 targeted locations but without macroscopic evidence of damage, suggesting the upper limit of the controller ramp should be increased in future studies. Histological analysis will be used to assess microdamage. Benchtop measurements of ultrasound transmission through the vertebral arch from one animal found a mean transmission of $50\pm 6\%$. Additional losses through the back muscle are expected to derate the pressure further.

Conclusions

These results provide the first evidence of non-invasive opening of the BSCB in a large animal model and demonstrate that SBPK exposures can modify the barrier and suppress standing waves to generate localized opening. Future work will extend these studies to additional animals, refining the ramped treatment approach to demonstrate active treatment control prior to progressing to chronic treatments.

References

- [1]. Carpentier A, Canney M, Vignot A, Reina V, Beccaria K, Horodyckid C, Karachi C, Leclercq D, Lafon C, Chapelon JY, Capelle L, Cornu P, Sanson M, Hoang-Xuan K, Delattre JY, Idbah A. Clinical trial of blood-brain barrier disruption by pulsed ultrasound. *Sci Transl Med*. 2016 Jun 15;8(343):343re2.
- [2]. Mainprize T, Lipsman N, Huang Y, Meng Y, Bethune A, Ironside S, Heyn C, Alkins R, Trudeau M, Sahgal A, Perry J, Hynynen K. Blood-Brain Barrier Opening in Primary Brain Tumors with Non-invasive MR-Guided Focused Ultrasound: A Clinical Safety and Feasibility Study. *Sci Rep*. 2019 Jan 23;9(1):321.
- [3]. Lipsman N, Meng Y, Bethune AJ, Huang Y, Lam B, Masellis M, Herrmann N, Heyn C, Aubert I, Boutet A, Smith GS, Hynynen K, Black SE. Blood-brain barrier opening in Alzheimer's disease using MR-guided focused ultrasound. *Nat Commun*. 2018 Jul 25;9(1):2336
- [4]. Abrahao A, Meng Y, Llinas M, Huang Y, Hamani C, Mainprize T, Aubert I, Heyn C, Black SE, Hynynen K, Lipsman N, Zinman L. First-in-human trial of blood-brain barrier opening in amyotrophic lateral sclerosis using MR-guided focused ultrasound. *Nat Commun*. 2019 Sep 26;10(1):4373
- [5]. Weber-Adrian D, Thevenot E, O'Reilly MA, Oakden W, Akens MK, Ellens N, et al. Gene delivery to the spinal cord using MRI-guided focused ultrasound. *Gene Ther*. 2015;.
- [6]. Payne AH, Hawryluk GW, Anzai Y, Odéen H, Ostlie MA, Reichert EC, et al. Magnetic resonance imaging-guided focused ultrasound to increase localized blood-spinal cord barrier permeability. *Neural regeneration research*. 2017;12(12):2045.
- [7]. O'Reilly MA, Chinnery T, Yee ML, Wu SK, Hynynen K, Kerbel RS, Czarnota GJ, Pritchard KI, Sahgal A. Preliminary Investigation of Focused Ultrasound-Facilitated Drug Delivery for the Treatment of Leptomeningeal Metastases. *Sci Rep*. 2018 Jun 13;8(1):9013
- [8]. Fletcher SMP, O'Reilly MA. Analysis of Multi-Frequency and Phase Keying Strategies for Focusing Ultrasound to the Human Vertebral Canal. *IEEE Trans Ultrason Ferroelectr Freq Control*. . 2018 Dec;65(12):2322-2331 2018
- [9]. Fletcher SMP, Ogrodnik N, O'Reilly MA. Enhanced detection of bubble emissions through the intact spine for monitoring ultrasound-mediated blood-spinal cord barrier opening. *IEEE transactions on bio-medical engineering*. 2019 Aug 22. doi: 10.1109/TBME.2019.2936972
- [10]. Busscher I, Ploegmakers JJW, Verkerke GJ, Veldhuizen AG. Comparative anatomical dimensions of the complete human and porcine spine. *Eur Spine J*. 2010;19(7):1104–1114.
- [11]. O'Reilly MA, Hynynen K. Blood-brain barrier: real-time feedback-controlled focused ultrasound disruption by using an acoustic emissions-based controller. *Radiology*. 2012 Apr;263(1):96-106

Enhanced radiosensitizer extravasation across the blood-brain barrier after focused ultrasound for diffuse intrinsic pontine gliomas treatment: preliminary pharmacokinetics results

E 't Hart¹, M Derieppe¹, MAC Bruin², HC Besse³, R Haumann⁴, EW Hoving¹, ADR Huitema^{2,5}, MG Ries³, DG van Vuurden¹

¹Princess Maxima Center for Pediatric Oncology, Utrecht, The Netherlands

²Department of Pharmacy and Pharmacology, the Netherlands Cancer Institute, Amsterdam, The Netherlands

³Center for Imaging Sciences, University Medical Center Utrecht, Utrecht, The Netherlands

⁴Department of Pediatric Oncology, Amsterdam University Medical Center location Vrije Universiteit Medical Center, Amsterdam, The Netherlands

*⁵Department of Clinical Pharmacy, University Medical Center Utrecht, Utrecht, The Netherlands
Corresponding author: E.tHart-6@prinsesmaximacentrum.nl*

Introduction

Diffuse intrinsic pontine gliomas (DIPG) are lethal brain tumours located in the pons with an median survival of 11 months [1]. Poor prognosis is mainly due to low efficacy of current treatment strategies, which is partly explained by the limited drug delivery caused by a mostly intact blood-brain barrier (BBB). In addition, radioresistance is potentially associated with the upregulation of multiple DNA repair genes, such as poly(ADP-ribose) polymerase (PARP) [2]. Advances in the field of microbubble (MB) mediated focused ultrasound (FUS) create new possibilities to improve drug delivery of anticancer agents, like radiosensitizers, across the BBB [3]. The aim of this study was to demonstrate enhanced extravasation of the radiosensitizer olaparib, a PARP inhibitor, by MB mediated FUS in the pons of the mice.

Methods

All in vivo experiments were approved by the Dutch ethical committee (license permit number AVD114002017841), and the Animal Welfare Body of Vrije Universiteit Amsterdam. Female athymic nude Foxn1^{-/-} mice (Charles River, The Netherlands) were randomised in three groups; (1) no intervention, (2) MBs and (3) MBs + FUS. Stable MB (Sonovue®, Bracco, Italy) cavitation was induced by a 1 MHz mono-element transducer (Precision Acoustics, United Kingdom) delivering a tone-burst pulse (10 ms duration, 400 kPa pressure, PRF 1.6 Hz). The mouse pons was targeted using stereotactic neuro-navigation by X-ray, with a six-point hexagon-shaped coverage with 40 cycles for 240 seconds. Concomitant intravenous injection (i.v.) of 120 µL MBs was performed in 2 boli in the tail vein, and cavitation signal was monitored with a needle hydrophone (NH4000 Precision Acoustics, United Kingdom). To validate BBB opening, 50 µL of 4% Evans Blue (EB) was i.v. injected 5 minutes after sonification, followed by intraperitoneal injection of 10 mg/kg olaparib (Medchem express, USA). Thirty minutes after olaparib injection, mice were sacrificed by cardiac perfusion; subsequently blood, brain and organs were collected. Olaparib concentration was assessed by LC-MS/MS (limit of detection - LOD: 0.3 ng/ml, lower limit of quantification - LLOQ: 1 ng/ml, upper limit of quantification - ULOQ: 5000 ng/ml). Results were expressed as median (interquartile range 25-75 IQR). Statistical analysis was performed using a non-parametric Mann-Whitney U test, with significance defined as *p < 0.05.

Results

X-ray guided stereotactic neuro-navigation allowed precise targeting of the pons with FUS (Fig. 1). Mice treated with FUS + MBs showed EB-conjugated albumin extravasation in the pons, unlike the no intervention and MBs only group (Fig. 1). The cavitation signal (integrated spectral power ± 50 kHz around the 2nd and 3rd harmonic) collected by the needle hydrophone evidenced stable cavitation after

each MBs injection (Fig. 2). In the pons and cerebellum a significant increase in absolute olaparib concentrations and ratio between tissue-blood concentration after FUS + MBs intervention, were observed, compared to no intervention and only injection of MBs ($p < 0.05$) (Fig. 3A). No intervention and FUS + MBs treatment resulted in an absolute olaparib concentration in the pons of 25.5 ng/g (13.5) vs 130.8 ng/g (199.8), respectively, corresponding to 58 nM and 299 nM. No significant differences were detected in brain regions outside the ultrasound focus and organs. A high olaparib concentration measured in the liver most likely indicated drug metabolism by CYP3A (Fig 3B).

Conclusions

This *in vivo* study demonstrated a 5.1 fold median increase of olaparib and an increased EB-conjugated albumin extravasation in the mouse pons after BBB permeabilization by MB mediated FUS. Future studies will assess the therapeutic effects of olaparib in combination with radiotherapy in *in vivo* orthotopic patient-derived xenograft mouse models. Besides PARP, other upregulated DNA repair genes/pathways can be promising targets for radiosensitization in DIPG.

Acknowledgments

This project is supported by the KWF Young Investigator Award (KWF 10911, DG van Vuurden). These data have been collected at the Radionuclide Center, Department of Radiology and Nuclear Medicine, Amsterdam University Medical Center, Amsterdam, The Netherlands (Dr. Wissam Beaino).

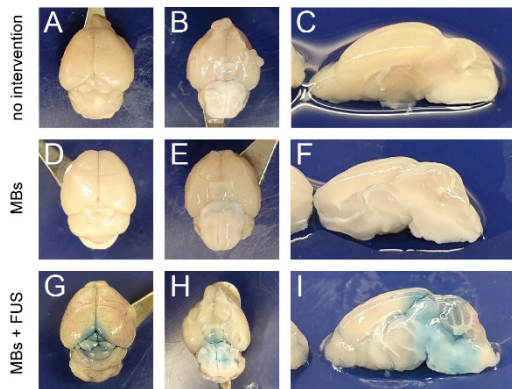


Figure 1: BBB permeability based on EB conjugated albumin extravasation.

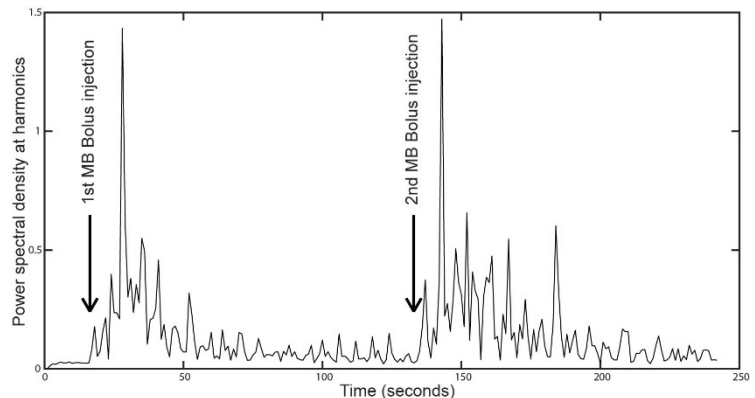


Figure 2: Cavitation time profile after i.v. injection of MBs.

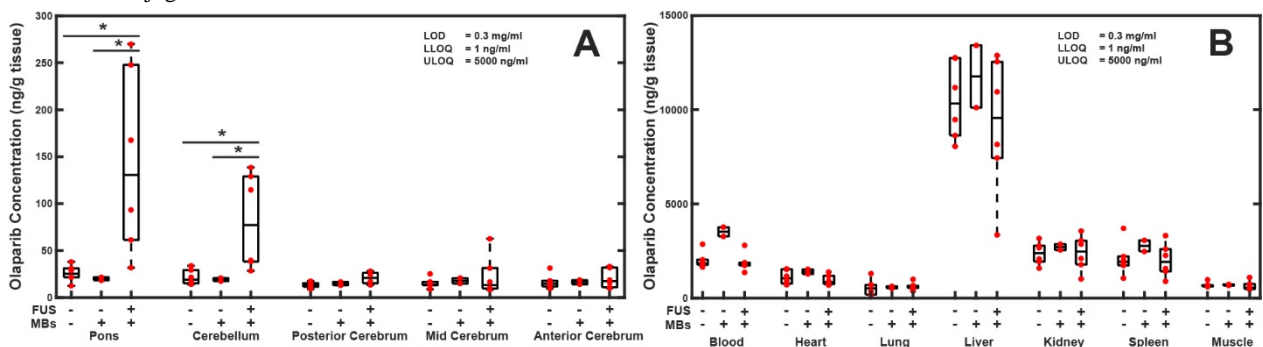


Figure 3: Extravasation of olaparib, with brain region collection after 30 minutes of injection. **A:** Significant increase of olaparib (ng/g tissue) in the pons and cerebellum after FUS and MBs treatment. **B:** Olaparib (ng/g tissue) in organs outside the brain.

References

- [1]. Hoffman LM, et al, Clinical, radiologic, pathologic, and molecular characteristics of long-term survivors of diffuse intrinsic Pontine Glioma (DIPG): a collaborative report from the international and European Society for Pediatric Oncology DIPG registries, *Journal of Clinical Oncology*, 36-19: 1963, 2018
- [2]. van Vuurden DG, et al, PARP inhibition sensitizes childhood high grade glioma, medulloblastoma and ependymoma to radiation, *Oncotarget*, 2: 984-996, 2011
- [3]. Alli S, et al, Brainstem blood brain barrier disruption using focused ultrasound: A demonstration of feasibility and enhanced doxorubicin delivery, *Journal of controlled release*, 281: 29-41, 2018

Preliminary Evaluation of Reactive Molecule Delivery for Brain Depot Capture

Phillip G. Durham¹, Christopher Moody², Yevgeny Brudno², Paul A. Dayton²

¹Eshelman School of Pharmacy, UNC Chapel Hill, NC, USA

²Joint Department of Biomedical Engineering, UNC/NCSU, Chapel Hill NC, USA

Corresponding author: pgdurham@email.unc.edu

Introduction

Glioblastoma represents the most common type of brain cancer in adults. Even patients receiving a comprehensive treatment regimen including surgical resection, radiation, and chemotherapy only have a median survival time of around 16 months due to almost universal recurrence. The blood brain barrier (BBB) limits systemic drug delivery, but local drug delivery in the form of drug-releasing implants have been evaluated clinically. While these devices do seem to improve patient survival in the short term (6-8 months), long term survival is the same. This can be attributed to the implants releasing their entire payload within weeks of the initial implantation.

A reloadable drug reservoir would enable systemically administered drugs to be captured by the depot and released over a long period of time. Chemically functionalized hydrogels have been developed that can react exclusively with a labeled drug to create high local concentrations of drug that can be sustained over time. Evaluations of such a depot in intradermal tumors have demonstrated better tumor control over conventional systemic dosing [1]. To extend this benefit to the treatment of brain cancer, we are evaluating the ability to reload a drug reservoir in the brain via the application of cavitation enhanced focused ultrasound to temporarily open the BBB. Towards this aim, we here demonstrate (a) that a chemically reactive depot can capture DBCO-Cy7 from an IV administration, (b) that DBCO-Cy7 does not enter the brain substantially on its own, and (c) cavitation enhanced ultrasound can enhance brain uptake of DBCO-Cy7.

Methods

An 8 element, 80 mm focused annular array (Therapy and Imaging Probe System [TIPS], Philips) was used to deliver low intensity ultrasound at a center frequency of 1 MHz at a peak negative pressure of 500 kPa, 10% duty cycle and a pulse repetition frequency of 100 Hz. Perfluorocarbon microbubbles were prepared via methods published previously [2]. For each ultrasound treatment, animals were anesthetized via 1.5-2.5% isoflurane inhalation using 100% oxygen as the carrier gas. The treatment location was shaved and depilated. To evaluate proof of concept, a first experiment was conducted using Evans Blue (EB) dye, which was administered simultaneously with microbubbles via tail vein injection immediately before receiving 5 minutes of ultrasound therapy. Evans Blue dye binds tightly to albumin, which has a long circulation half-life. Further, this experiment was repeated to assess the ability to deliver the experimental fluorophore DBCO-Cy7 to the brain, which will be used for depot capture in future studies. Notably, this molecule has different pharmacokinetic and physicochemical properties to Evans Blue.

3 hours after ultrasound treatment, animals were perfused with phosphate buffered saline (pH 7.4) prior to perfusion fixation with 10% formalin. Brains were removed and imaged via whole organ fluorescence imaging (IVIS Kinetic, PerkinElmer).

Results

Evans Blue dye delivery was evaluated by radiant efficiency ($[p/s]/[\mu W/cm^2]$) in a circular region of interest (ROI) around the treatment area in the right hemisphere and compared to a contralateral ROI in the untreated left hemisphere.

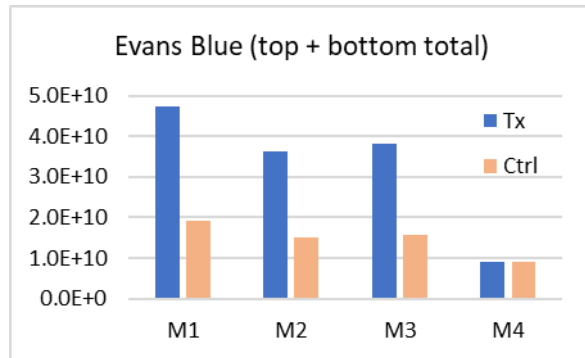
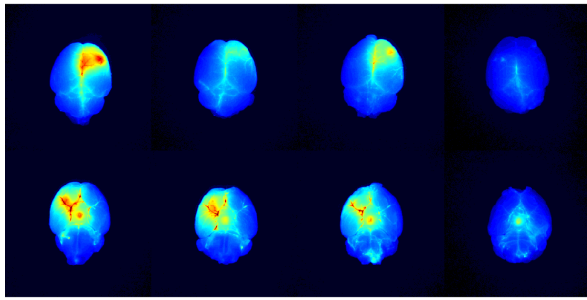


Figure 1. Enhancement can be seen in the front right hemisphere for the 3 treated animals.

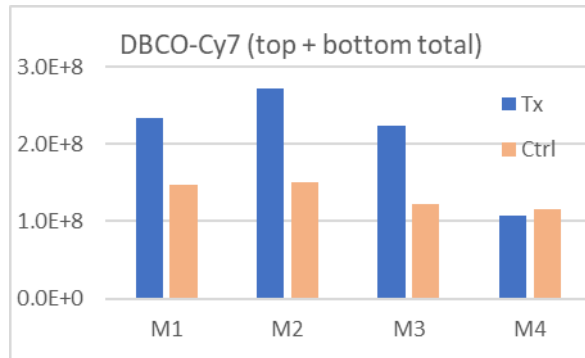
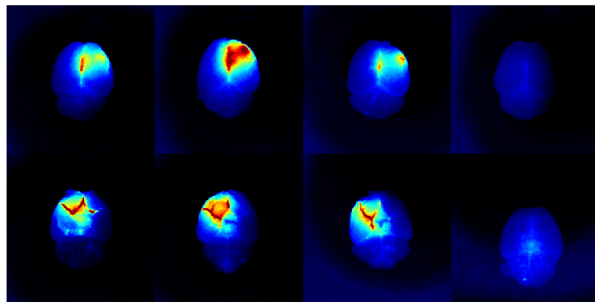


Figure 2. Animals treated with focused ultrasound show increased DBCO-Cy7 extravasation at the target site (right hemisphere) compared to the contralateral site (left hemisphere). Fluorescence images show the top view of the brain across the top row, the bottom view across the bottom.

Fluorescence enhancement was observed in the treated right hemisphere (right on the top, left on the bottom view), demonstrating increased delivery at the focus of the ultrasound beam. A control animal receiving the same microbubble and EB injection showed minimal fluorescence enhancement, as expected, due to the large size of albumin (66 kDa) and its inability to cross the BBB. There is additional enhancement localized near large blood vessels. This is possibly due to cell sonoporation in which dye may be taken up into vessel endothelial cells.

Fluorescence was also visible at the focal target spot for the delivery of DBCO-Cy7. Distribution of DBCO-Cy7 in the treated brains is consistent, though overall weaker, than EB administration. This could be attributed to the difference in dose/fluorophore performance between the two, or to the faster elimination kinetics of DBCO-Cy7.

Conclusions

For the long term treatment of glioblastoma, a refillable drug depot in the brain has many advantages over systemic chemotherapy. We show here that the chemically reactive fluorophore DBCO-Cy7 does not cross the blood brain barrier natively, but with the application of focused ultrasound and microbubbles, DBCO-Cy7 can be delivered to the brain. Future studies will evaluate the ability to refill a chemically reactive depot located in the brain via an intravenous dose, facilitated by cavitation-enhanced focused ultrasound.

References

- [1]. Brudno, Y. et al. Replenishable drug depot to combat post-resection cancer recurrence. *Biomaterials* 178, 373–382 (2018).
- [2]. Fix, S. M. et al. Accelerated Clearance of Ultrasound Contrast Agents Containing Polyethylene Glycol is Associated with the Generation of Anti-Polyethylene Glycol Antibodies. *Ultrasound Med. Biol.* 44, 1266–1280 (2018).

Ultrasound and microbubble-targeted delivery of microRNA therapeutics to the heart for cardiac therapies

Jonathan A. Kopechek^{1,2}, Mariah C. Priddy¹, Rafey Feroze², Xucai Chen², Flordeliza S. Villanueva²

¹Department of Bioengineering, University of Louisville, Louisville, KY, USA

²Center for Ultrasound Molecular Imaging and Therapeutics, Heart and Vascular Institute, Pittsburgh Heart, Lung, Blood and Vascular Medicine Institute, University of Pittsburgh, Pittsburgh, PA, USA

Corresponding author: jonathan.kopechek@louisville.edu

Introduction

MicroRNAs (miRNAs) are small endogenous RNAs that can regulate multiple genes and have a major impact on physiologic function. miRNA levels have been shown to significantly change in diseased human hearts and modulation of miRNAs to treat cardiovascular disease is seen as a potentially powerful clinical tool. However, the lack of effective non-viral methods for delivery of miRNA mimics or inhibitors limits clinical translation. Therefore, we are investigating the use of ultrasound targeted microbubble cavitation (UTMC) as an attractive non-immunogenic, theranostic delivery strategy to locally modulate miRNA levels in the heart [1]. The objective of these studies was to evaluate the efficacy of UTMC targeted delivery of miRNA mimics and inhibitors (“antimiRs”) to cardiac cells *in vitro* and to the heart *in vivo* for treatment of hypertension-induced cardiac hypertrophy and other cardiovascular conditions such as myocardial infarction.

Methods

Cationic lipid microbubbles were loaded with miR-302b/c mimics, negative control scrambled sequence (NC mimic), antimiR-23a, antimiR-34a, or negative control antimiR (antimiR-NC). For *in vitro* studies, neonatal rat cardiomyocytes or mouse coronary artery endothelial cells were exposed to microbubbles loaded with miRNA therapeutics and treated with ultrasound pulses (1.3 MHz or 2.5 MHz). Cells were harvested at 6 h, 24 h, or 48 h after treatment and miRNA levels were quantified with qPCR.

In vivo studies of hypertension-induced cardiac hypertrophy were conducted in mice which received continuous phenylephrine infusion via implanted osmotic minipumps. UTMC treatments were conducted with intravenously injected antimiR-23a loaded microbubbles at 0, 3, and 7 days later. Echocardiography was conducted weekly to assess left ventricular (LV) mass and function. At 2 weeks, hearts were harvested and miR-23a levels were measured.

Results

UTMC treatment *in vitro* with antimiR-34a significantly reduced miR-34a levels in cardiomyocytes and cardiac endothelial cells compared to antimiR-NC ($p < 0.05$). In addition, UTMC treatment *in vitro* with miR-302b/c mimics significantly increased miR-302b/c levels and knocked down target protein levels in cardiac endothelial cells ($p < 0.05$). UTMC treatment *in vivo* with antimiR-23a decreased cardiac miR-23a levels by $41 \pm 8\%$ compared to UTMC + antimiR-NC controls ($p < 0.01$). Furthermore, LV mass after 1 week of phenylephrine treatment was $17 \pm 10\%$ lower following UTMC + antimiR-23a treatment compared to UTMC + antimiR-NC controls ($p = 0.02$). At 2 weeks, fractional shortening was 23% higher in the UTMC + antimiR-23a mice compared to UTMC + antimiR-NC controls ($p < 0.01$, Fig. 1).

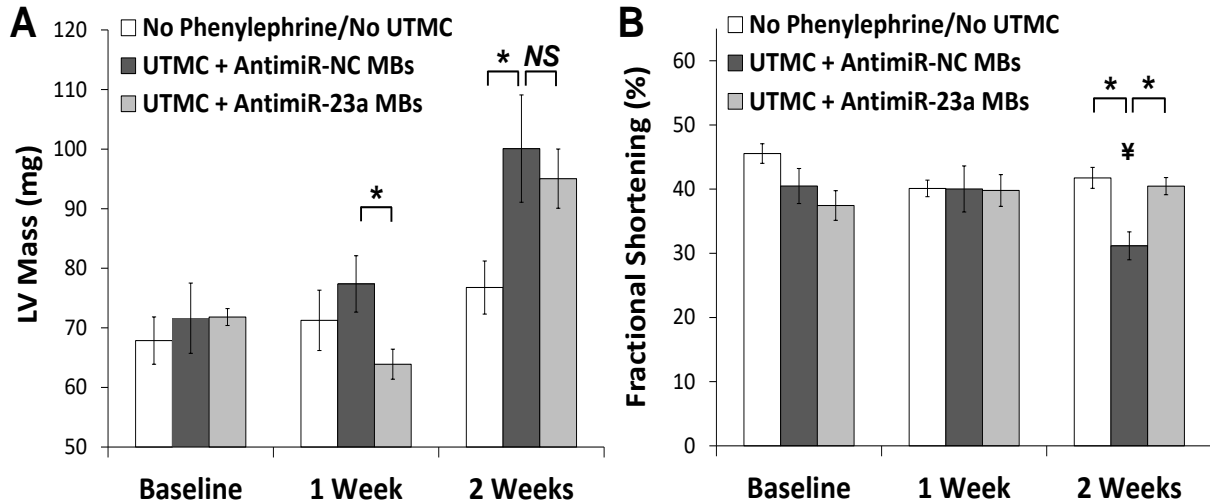


Figure 1: Ultrasound delivery of antimiR-23a reduces cardiac hypertrophy and improves cardiac function in vivo. Echocardiographic analysis indicating suppression of phenylephrine-induced left ventricular hypertrophy and preservation of systolic function with UTMC targeted delivery of antimiR-23a compared to UTMC delivery of antimiR-NC. The “no phenylephrine/no UTMC” group received neither phenylephrine nor ultrasound. Compared to UTMC + antimiR-NC microbubbles, UTMC + antimiR-23a microbubble treatment (A) blunted development of LV hypertrophy at 1 week (*p=0.02), and (B) preserved fractional shortening at 2 weeks (*p<0.01, ‡ p<0.02 vs baseline, n=5-9 animals/group).

Conclusions

These results demonstrate that UTMC is a promising non-invasive, theranostic modality for targeted functional delivery of miRNA therapeutics to the heart. In addition, UTMC delivery of antimiR-23a was shown to suppress cardiac hypertrophy and preserve systolic function in mice. This approach could represent a revolutionary therapy for patients suffering from pathological cardiac hypertrophy and other cardiovascular conditions.

References

- [1]. Kopechek JA, McTiernan CF, Chen X, Zhu J, Mburu M, Feroze R, Whitehurst DA, Lavery L, Cyriac J, Villanueva FS. "Ultrasound and Microbubble-targeted Delivery of a microRNA Inhibitor to the Heart Suppresses Cardiac Hypertrophy and Preserves Cardiac Function," *Theranostics*, 9:7088-7098 (2019).

Contrast enhanced ultrasound alters tumor pathophysiology and therapy outcome in orthotopic triple negative breast cancer in mice

Anne Rix¹, Jasmin Baier¹, Natascha Drude¹, Maike Baues¹, Jan-Niklas May¹, Susanne Koletnik¹, Milita Darguzyte¹, Rene H. Tolba², Fabian Kiessling¹

¹*Institute for Experimental Molecular Imaging, Medical Faculty, RWTH Aachen International University, Germany*

²*Institute for Laboratory Animal Science and Experimental Surgery, Medical Faculty, RWTH Aachen International University, Aachen, Germany*
Corresponding author: arix@ukaachen.de

Introduction

Contrast-enhanced ultrasound (US) is an established imaging technique in preclinical routine for the characterization of tumor vascularization and expression of molecular markers on the tumor endothelium. It is known that US contrast agents can be used to permeabilize vessels during sonoporation¹, but no data are available to exclude an influence of diagnostic contrast enhanced US on tumor biology. Therefore, this study evaluated the possible influences of diagnostic contrast-enhanced US on tumor pathophysiology and therapy outcome after antiangiogenic and antitumoral treatment.

Methods

Female orthotopic 4T1-tumor bearing BALB/c mice (n=100) were allocated randomly to the following groups: (i) no imaging, (ii) isoflurane anesthesia alone, (iii) ultrasound with destructive sequence (destructive US), (iv) contrast-enhanced ultrasound without destruction of the contrast agent (non-destructive CEUS) or (iv) contrast-enhanced ultrasound with destruction of the contrast agent (destructive CEUS). Animals of each group were subdivided to either receive 10 mg/kg regorafenib or vehicle solution daily by oral gavage. US measurements were performed on days 7, 10 and 14 after tumor cell injection using phospholipid MB for non-destructive US and VEGFR2-targeting phospholipid MB for destructive US. Impact of anesthesia and US imaging on animal welfare (heartrate, motor coordination, fecal corticosterone) and tumor size were evaluated daily. Before euthanization, blood samples were collected and a complete blood count was performed. Fluorescently labelled lectin was injected intravenously to depict perfused tumour vessels and a histological characterization of tumors concerning vascularization and immune cell infiltration was performed.

Results

Longitudinal contrast enhanced ultrasound examinations had no impact on heartrate, motor coordination or fecal corticosterone levels of the animals. No influence of the different imaging protocols on the tumor size could be detected. However, histological characterization of tumors showed a significant increase in vascularization, perfusion and angiogenesis in vehicle treated tumors exposed to non-destructive CEUS (Fig. 1). Furthermore, macrophage infiltration was significantly increased in vehicle and regorafenib treated tumors after non-destructive CEUS (Fig. 1). Surprisingly, both, non-destructive and destructive CEUS induced systemic immune reaction reflected by decreased white blood cell counts and spleen sizes in 4T1-tumor bearing mice (Fig. 2).

Conclusions

Although longitudinal US imaging did not increase the burden of the animals during the experiment, diagnostic CEUS imaging influenced 4T1-tumor vascularization, perfusion, angiogenesis and induced a local and systemic immune response. Further investigations are ongoing to characterize the tumor

microenvironment (e.g. immune cell populations, collagen content, matrix metalloproteinases, etc.) and to unravel the biological mechanisms behind these unexpected findings.

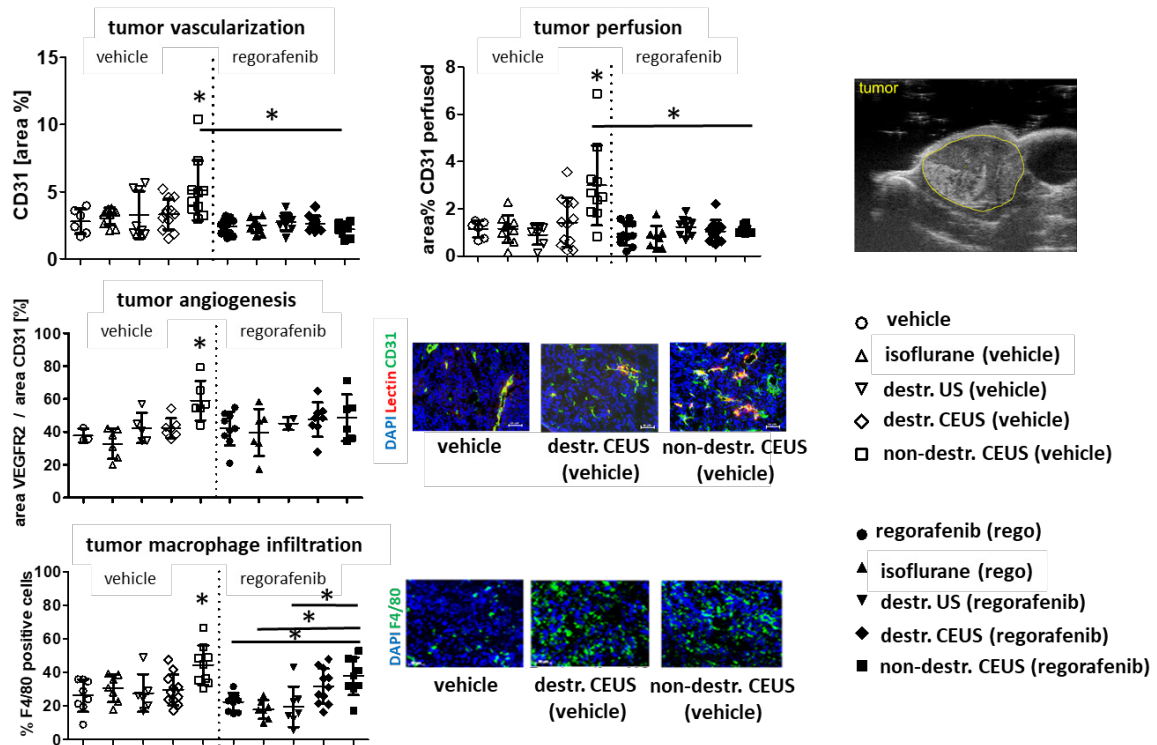


Figure 1. Influence of (contrast-enhanced) ultrasound on 4T1-tumor pathophysiology: non-destructive CEUS significantly increased tumor vascularization, perfusion and angiogenesis in vehicle treated tumors. Furthermore, macrophage infiltration into the tumor is increased after non-destructive CEUS in vehicle and regorafenib treated animals (* p < 0.05).

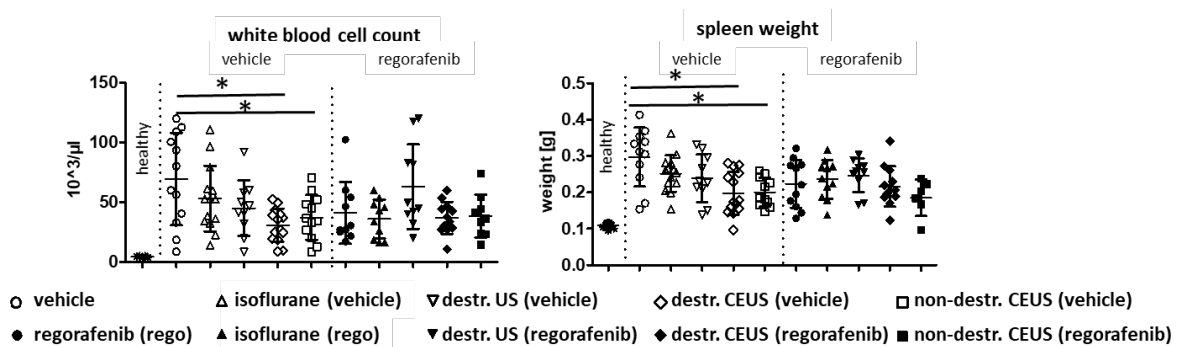


Figure 2. Influence of CEUS on systemic immune reaction: non-destructive and destructive CEUS resulted in a systemic immune response of 4T1-tumor bearing BALB/c mice (* p < 0.05).

References

[1] Theek B, Baues M, Ojha T et. al. Sonoporation enhances liposome accumulation and penetration in tumors with low EPR J Control Release. 2016 Jun 10; 231: 77–85.

Bleomycin plus ultrasound and microbubbles to treat feline oral squamous cell carcinoma, as a model for human head and neck cancer, preliminary results of the BUBBLEFISH Trial.

*Josanne S. de Maar¹, Maurice M.J.M. Zandvliet², Stefanie Veraa²,
Mauricio Tobón Restrepo², Chrit T.W. Moonen¹, Roel Deckers¹*

¹*Imaging Division, University Medical Center Utrecht, Utrecht, The Netherlands*

²*Department of Clinical Sciences of Companion Animals, Faculty of Veterinary Medicine, Utrecht, The Netherlands*

Corresponding author: j.s.demaar@umcutrecht.nl

Introduction

Head and Neck Squamous Cell Carcinoma (HNSCC) is a common group of malignancies in humans. Most patients present with locally advanced disease (~60%), where primary surgery is often not an option. Despite combination treatment existing of surgery, radiotherapy and systemic therapy, around half of the patients develop (often incurable) local recurrences. This stresses the clinical need for improved local therapy.

Sonopermeation with ultrasound and microbubbles (USMB) has been shown to increase local tumour uptake and efficacy of several drugs[1]. In particular, the nonpermeant drug bleomycin may benefit from combination with USMB. *In vitro*, USMB increased bleomycin cytotoxicity[2,3], while *in vivo*, adding USMB to bleomycin improved growth inhibition of HNSCC in mice[2].

Feline Oral Squamous Cell Carcinoma (FO SCC) is a valuable model to translate HNSCC treatment from preclinical to clinical research. Moreover, these cats have a short life expectancy (~1 month) and could benefit from a low-burden treatment alternative.

We present the first results of our veterinary study which evaluates safety, feasibility and efficacy of bleomycin plus USMB using a clinically available ultrasound contrast agent and ultrasound imager.

Methods

A single-arm prospective study in cats with spontaneously arisen FO SCC without other suitable treatment options except for palliative care is currently ongoing. During general anaesthesia, the cats receive intravenous bleomycin (10.000 IU/m²) combined with USMB treatment of the oral tumour using intravenous injections of SonoVue (Bracco, conc. 1-5x10⁸ bubbles/mL). They are treated with ultrasound on an EPIQ5 (Philips) in Pulse Wave doppler mode and parameters were optimized during the treatment of the first two cats (Table 1). Each cat is treated three times, once per week. Feasibility, adverse events, clinical performance and body condition score are monitored and questionnaires are used to evaluate quality of life. Tumour response is evaluated by clinical (caliper) and ultrasound measurement of the tumour, at 1, 2 and 5 weeks after the first treatment session.

Table 1. Parameters for USMB plus bleomycin in the first 2 FOSCC patients

	SonoVue dosage	CEUS performed?	Transducer, frequency	Cycli/pulse (sample volume)	PRF (Scale)	Indicated MI (relative I)	Sonopermeation pattern
Patient 1							
Session 1	6 boluses of 0.05ml/kg (incl 2 for CEUS)	Tried, but no bubbles visible	S5-1, 1.6 MHz	34 (SV 20mm)	1kHz (-30 – 30 cm/sec)	0.5 (0 dB)	5s PW/ 10s CEUS, repeat 15 times/bolus
Session 2	2 boluses of 0.05mL/kg (incl 1 for CEUS) 3 boluses of 0.1mL/kg	Yes, before (CEUS not feasible with 0.05ml/kg)	C9-2, 2.9 MHz	21 (SV 7.5mm)	0.4 kHz (-4 – 4 cm/sec)	1.0 (0 dB)	15s PW, 5s CEUS, after bolus 0.05mL/kg 3 times repeated, after bolus 0.1mL/kg 2.5-3min repeated.
Session 3	5 boluses of 0.1ml/kg (incl 1 for CEUS)	Yes, only before	C9-2, 2.9 MHz	21 (SV 7.5mm)	0.4 kHz (-4 – 4 cm/sec)	1.0 (0 dB)	15s PW, 5s CEUS, repeat 3-4 times/bolus
Patient 2							
Session 1	6 boluses of 0.1ml/kg (incl 2 for CEUS)	Yes (before and after)	C9-2, 2.9 MHz	21 (SV 7.5 mm)	0.4 kHz (-4 – 4 cm/sec)	1.2 (0 dB)	15s PW, 5s CEUS, repeat 2-3 times/bolus
Session 2	idem	idem	idem	idem	idem	0.3 (-10 dB)	15s PW, 5s CEUS, repeat ~6 times/bolus
Session 3	idem	idem	idem	idem	idem	0.4 (-10 dB)	15s PW, 5s CEUS, repeat 5 times/bolus

Results

So far, two feline patients, respectively with sublingual and right maxillary SCC, have been enrolled and treated. Both had T2 tumours, patient 1 had locoregional lymph node metastases and patient 2 was suspected of pulmonary metastasis.

Safety In both patients, treatment was well tolerated. The only grade 3 adverse event was anorexia in patient 1, which worsened to grade 3 at 26 days after the first study treatment. Adverse events were considered to be related to anaesthesia (lethargy, mild vomiting, constipation, hypotension and hypothermia), comorbidity (untreated hyperthyroidism in both patients) or (progressive) tumour growth in case of patient 1 (anorexia, drooling, grade 1 tumour bleeding and grade 2 soft tissue necrosis of the tongue). Quality of life, clinical performance score and body condition score did not change.

Contrast enhanced ultrasound

In patient 2 contrast-enhanced ultrasound was performed before and after sonopermeation and showed a clearly visible increase of perfusion, especially after treatment session 2 and 3, performed at a low MI (Fig 1.).

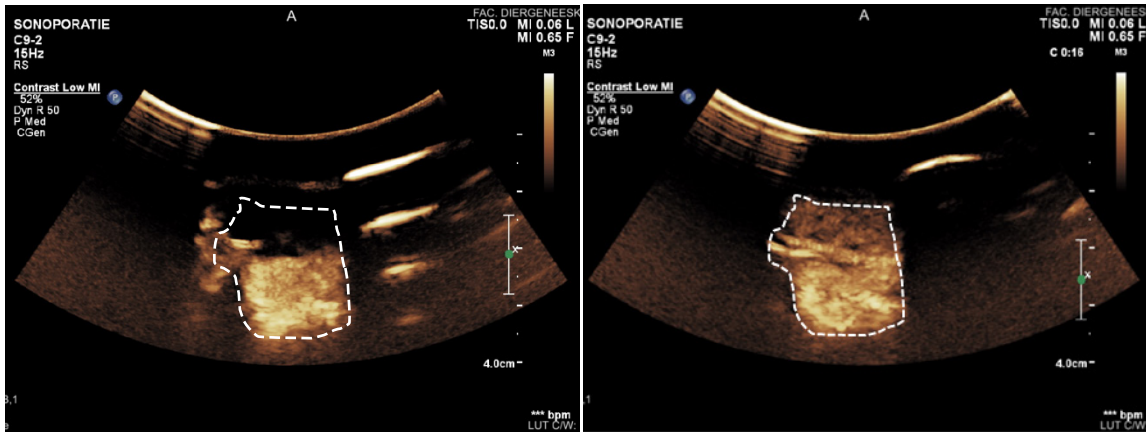


Figure 1. Contrast enhanced ultrasound in patient 2, during treatment session 2 Left: Before sonopermeation only the deep part of the tumour is perfused. Right: After sonopermeation the tumour is also perfused superficially.

Tumour response

Upon clinical examination patient 1 showed progressive disease (Fig 2.), developed soft tissue necrosis of the tongue and was euthanized 46 days after the first session, while patient 2 had stable disease at follow-up both clinically and on ultrasound (Table 2, Fig. 2) and is currently still alive 56 days after the first session.

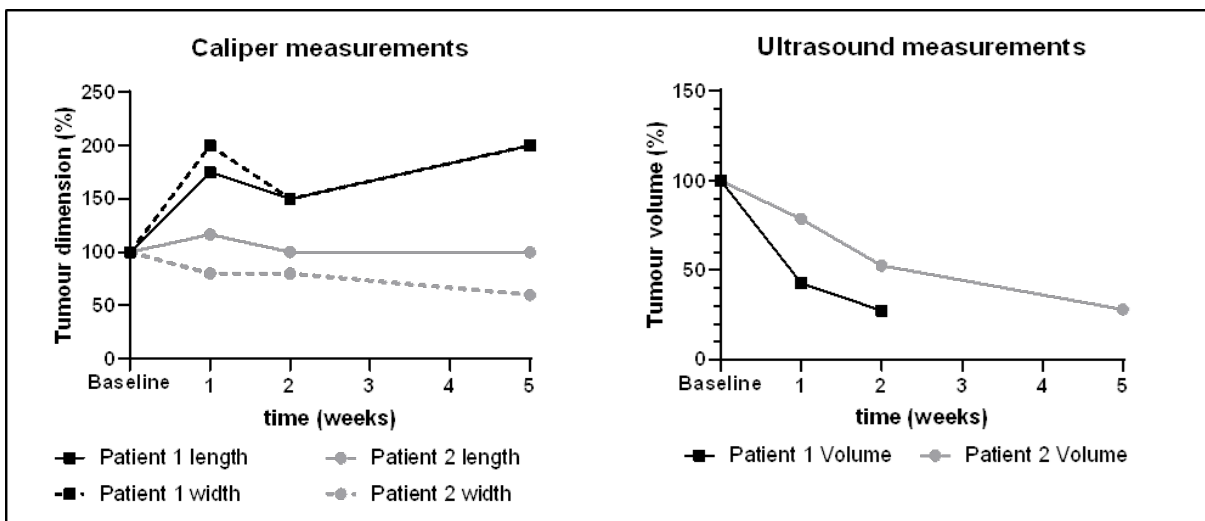


Figure 2. Left: Caliper measurements, percentages relative to baseline. Right: Ultrasound measurement based tumour volume (0.5*length*width*width), percentages relative to baseline.

	Patient 1			Patient 2		
	Sagittal, longest diameter (mm)	Sagittal, shortest diameter (mm)	Transversal, shortest diameter (mm)	Sagittal, longest diameter (mm)	Sagittal, shortest diameter (mm)	Transversal, shortest diameter (mm)
Baseline	29	17,6	12.7	32*	28.2	n.a.
1 week	29	11,5	10.1	39.2	22.6	24.4
2 weeks	17.4	11.9	10.8	26.9	22.3	n.a.
5 weeks	n.a.	n.a.	n.a.	25.3	16.8	17.9

* For patient 2, the baseline ultrasound measurement of the longest diameter is not reliable, because the margins were not visible on the image due to loss of skin contact. The longest diameter on baseline CT was 41.7 mm.

Table 2. Ultrasound tumour measurements

Conclusions

After treating two feline patients, bleomycin combined with USMB on a clinical US system using EMA/FDA approved microbubbles seems a feasible palliative treatment for FOSCC patients. Preliminary results suggest that tumour perfusion increases after sonopermeation at MI levels corresponding to stable cavitation.

References

- [1]. Lammertink BHA, Bos C, Deckers R, Storm G, Moonen CTW, Escoffre J-M, Sonochemotherapy: from bench to bedside, *Frontiers in Pharmacology*, 6(138): 1-17, 2015.
- [2]. Iwanaga K, Tominaga K, Yamamoto K, Habu M, Maeda H, Akifusa S, Tsujisawa T, Okinaga T, Fukuda J, Nishihara T, Local delivery system of cytotoxic agents to tumors by focused sonoporation, *Cancer Gene Therapy*, 14: 354-363, 2007.
- [3]. Lamanuskas N, Novell A, Escoffre J-M, Venslauskas M, Šatkauskas S, Bouakaz A, Bleomycin delivery into cancer cells in vitro with ultrasound and SonoVue® or BR14® microbubbles, *Journal of Drug Targeting*, 21(4): 407-414, 2013.

Artificial intelligence for (super-resolution) contrast agent detection

Ruud J.G. van Sloun

*Biomedical diagnostics lab, Department of Electrical Engineering,
Eindhoven University of Technology, Eindhoven, the Netherlands
Corresponding author: r.j.g.v.sloun@tue.nl*

Deep high-resolution microvascular ultrasound imaging has historically been hampered by the fundamental trade-off between resolution and penetration depth, governed by the diffraction limit. Recent advances in ultrasound localization microscopy (ULM) have allowed surpassing this diffraction limit, circumventing these long-standing trade-offs by adapting a Nobel-prize winning concept from optics (super-resolution fluorescence microscopy) to ultrasound imaging [1, 2, 3]. In optics, stochastic ‘blinking’ of subsets of fluorophores is exploited to provide sparse point sources that can subsequently be localized with high precision. In ULM, intravascular lipid-shelled gas microbubbles fulfil this role. By accumulating many of such localizations, this approach permits achieving a resolution that is up to 10 times smaller than the wavelength.

The fidelity of ULM depends on the number of localized microbubbles and the localization accuracy. This gives rise to a new trade-off that balances the required microbubble sparsity for accurate localization and acquisition time. Standard ULM methods rely on dilute microbubble solutions (to minimize point-spread-function overlap) as well as carefully-tuned tissue suppression strategies to accommodate sufficiently accurate localization. The full sensing and image reconstruction pipeline is however typically not specifically optimized to the downstream task at hand (i.e. super-localization of microbubbles). In this talk, we will discuss how artificial intelligence and deep learning methods may play a compelling role in this process.

Deep learning has been shown remarkably able to perform end-to-end optimization of predictive models for downstream tasks under a given data distribution [4]. We will show how these learning strategies can indeed be effectively absorbed into these ultrasound imaging chains, improving key components along the processing pipeline [5]. Examples include (sparse array) sampling [6], beamforming [7], tissue suppression and microbubble detection [8, 9], and super-localization [5, 10] (see figure 1). We aim to provide a broad understanding of the possible impact of deep learning on a variety of ultrasound imaging aspects, placing particular emphasis on methods that exploit both the power of data and signal structure to yield robust and data-efficient solutions.

The promise that deep learning holds for ultrasound imaging is significant; empowered by deep learning, next-generation (contrast) ultrasound imaging may become a much stronger modality with devices that provide better images and clinical insight, leading to improved and more widely accessible diagnostics.

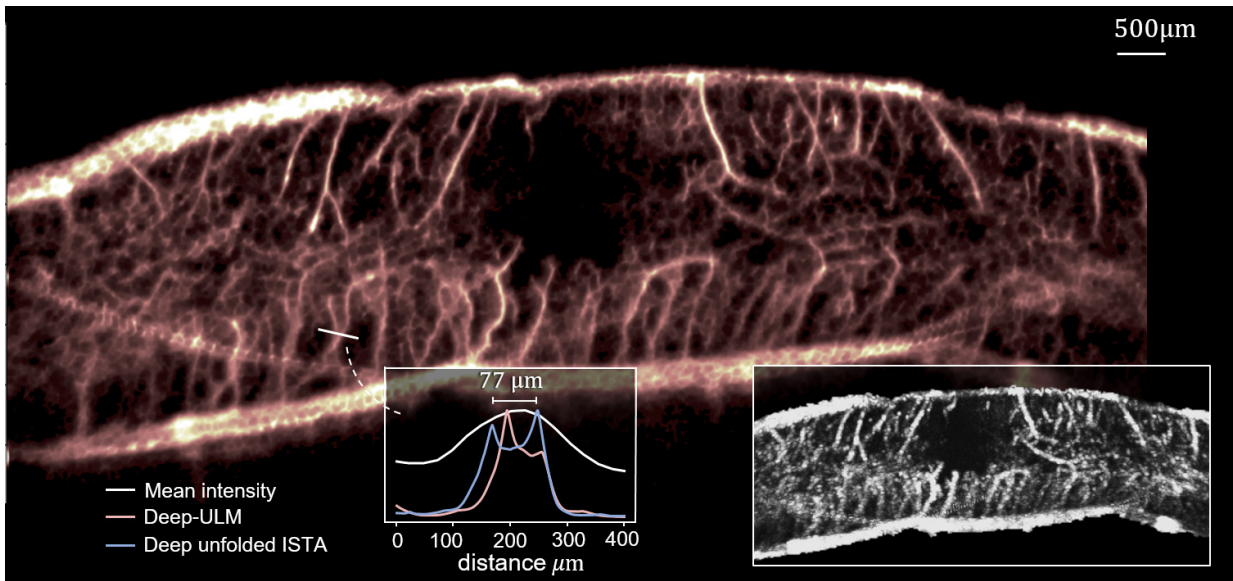


Figure 1. Super-resolution ultrasound image of a rat spinal cord by deep learning. Image adapted from [5].

References

- [1]. O.M. Viessmann, R.J. Eckersley, K. Christensen-Jeffries, M.X. Tang, and C. Dunsby. Acoustic super-resolution with ultrasound and microbubbles. *Physics in Medicine & Biology*, 2013
- [2]. C. Errico, J. Pierre, S. Pezet, Y. Desailly, Z. Lenkei, O. Couture, and M. Tanter, Ultrafast ultrasound localization microscopy for deep super-resolution vascular imaging. *Nature*, 2015.
- [3]. T. Opacic, S. Dencks, B.Theek, M. Piepenbrock, D. Ackermann, A. Rix, T. Lammers, E. Stickeler, S. Delorme, G. Schmitz, et al. Motion model ultrasound localization microscopy for preclinical and clinical multiparametric tumor characterization. *Nature communications*, 2018
- [4]. Y. LeCun, Y. Bengio, G. Hinton, Deep Learning, *Nature*, 2015.
- [5]. R.J.G. van Sloun, R. Cohen, Y.C. Eldar, Deep learning in ultrasound imaging, *Proceedings of the IEEE*, 2019
- [6]. I.A.M. Huijben, B.S. Veeling, K. Janse, M. Mischi, R.J.G. van Sloun, arXiv preprint ArXiv:1908.05764, 2019
- [7]. B. Luijten, R. Cohen, F.J. de Bruijn, H.A. Schmeitz, M. Mischi, Y.C. Eldar, R.J.G. van Sloun, Deep learning for fast adaptive beamforming, *IEEE International Conference on Acoustics, Speech and Signal Processing (ICASSP)*, 2019
- [8]. O. Solomon, R. Cohen, Y. Zhang, Y. Yang, Q. He, J. Luo, R.J.G. van Sloun, Y. Eldar, Deep unfolded robust PCA with application to clutter suppression in ultrasound, *IEEE Transactions on Medical Imaging*, 2019.
- [9]. K. Brown, J. Dormer, B. Fei, K. Hoyt, Deep 3D convolutional neural networks for fast super-resolution ultrasound imaging, *Proc. SPIE 10955, Medical Imaging 2019: Ultrasonic Imaging and Tomography*, March 2019.
- [10]. R.J.G. van Sloun, O. Solomon, M. Bruce, Z.Z. Khaing, H. Wijkstra, Y. Eldar, M. Mischi, Super-resolution ultrasound localization microscopy through deep learning, ArXiv preprint ArXiv: 1804.07661, 2019.

Microvessel Analysis with 3D Super-resolution Ultrasound and Super-Resolved Velocity Mapping

Sevan Harput^{1,2}, Matthieu Toulemonde¹, Alessandro Ramalli^{3,4}, Kirsten Christensen-Jeffries⁵, Enrico Boni³, Piero Tortoli³, Christopher Dunsby^{6} and Meng-Xing Tang^{1*}*

¹*Dept. of Bioengineering, Imperial College London, UK*

²*Div. of Electrical and Electronic Engineering, London South Bank University, London, UK*

³*Dept. of Information Engineering, University of Florence, 50139 Florence, IT*

⁴*Lab. on Cardiovascular Imaging & Dynamics, Dept. of Cardiovascular Sciences, KU Leuven, Belgium*

⁵*Dept. of Biomedical Eng., School of Biomedical Eng. & Imaging Sciences, King's College London, UK*

⁶*Dept. of Physics and Centre for Pathology, Imperial College London, London, UK*

**These authors contributed equally to this work*

Email: Harputs@lsbu.ac.uk, Mengxing.Tang@imperial.ac.uk

Introduction

Super-resolution ultrasound (SR US) imaging has been demonstrated in 3D by several research groups using different methods, such as: mechanically scanning a volume with a linear probe, by co-aligning multiple linear probes, by using multiplexed 3D clinical US systems, or by using 2D ultrasound arrays with research systems [1-9]. With the implementation of 3D SR US imaging using a 2D array [6,8-9], existing limitations of 2D super-resolution imaging such as lack of full volumetric observations [1,8-9], poor elevational resolution [1-2,5,8-9] and impossibility of out-of-plane motion compensation [10-11] were overcome. In this study, we performed 3D SR US imaging with plane waves using a 2D array on an *in vitro* phantom and tracked microbubbles to identify and separate microvessels for further analysis.

Methods

Two ULA-OP 256 systems [12-13] were synchronized to control 512 elements out of a 32x32 matrix array as described in [9]. A 1:2,000 diluted Sonovue solution was flowed through two 200 μm cellulose tubes arranged in a double helix shape as shown in the Figure. The flow in both tubes generated a mean microbubble velocity of 44 mm/s in opposing directions. 3-cycle Gaussian pulses with a 3.7 MHz centre frequency and an approximate bandwidth of 60% were used for imaging the tubes. A total of 12,000 volumetric ultrasound frames were acquired in 24 seconds at an MI of 0.055.

Velocities of super-resolved microbubbles were traced by pairing microbubbles with the minimum Euclidean distance between consecutive frames. A 3D Frangi filter was used to embody the microvessels for positive and negative velocity values separately [14]. After this, the filtered microvessel images were skeletonized for further analysis.

Results

Figure (B) shows the 3D power Doppler image of the two cellulose tubes arranged in a double helix shape with the optical image of the experimental setup given in Figure (A). In the 3D power Doppler image two touching tubes appears as one with a full-width-half-maximum (FWHM) of 495 μm , where the imaging wavelength is 404 μm . After processing 12,000 compounded ultrasound volumes, a total of 9,469 microbubbles were localized and 4,742 microbubble-pairs were tracked from consecutive frames. Tracked microbubbles were superimposed in a single frame, Figure (C), to show the 3D super-resolved velocity map where two touching 200 μm tubes can be separated. By using the direction and velocity information the microvessels are separated as shown in Figure (D). After this separation stage, crucial information can be extracted, such as the number of microvessels and microvessel density.

The velocity tracks of the microbubbles were plotted using Bezier curves as shown in Figure (E), where only one microvessel is plotted for clarity. Traced microbubbles velocities are used to calculate the mean and median velocities inside the microvessel, which are 49.1 and 47.2 mm/s, respectively. Figure (F) shows the microvessel after skeletonization, which can be used to calculate the tortuosity. In this case the length of the microvessel is measured as 7.49 mm and the distance between its ends is measured as 6.89 mm, which gives a tortuosity value of 1.087.

Conclusions

In this study, the structure of two 200 μm tubes -smaller than half the wavelength- arranged in a double helix shape were super resolved and flow velocities within these tubes were estimated in 3D. In comparison to multiplexed 3D clinical ultrasound systems, high-frame rate 3D plane wave acquisition provided a higher microbubble localization rate and improved the velocity estimations due to more frequent sampling. 3D SR US and super-resolved velocity mapping is a promising method for microvessel analysis. Future work will focus on reducing the acquisition time of super-resolution images for clinical translation by using acoustically activated nanodroplets [15-17].

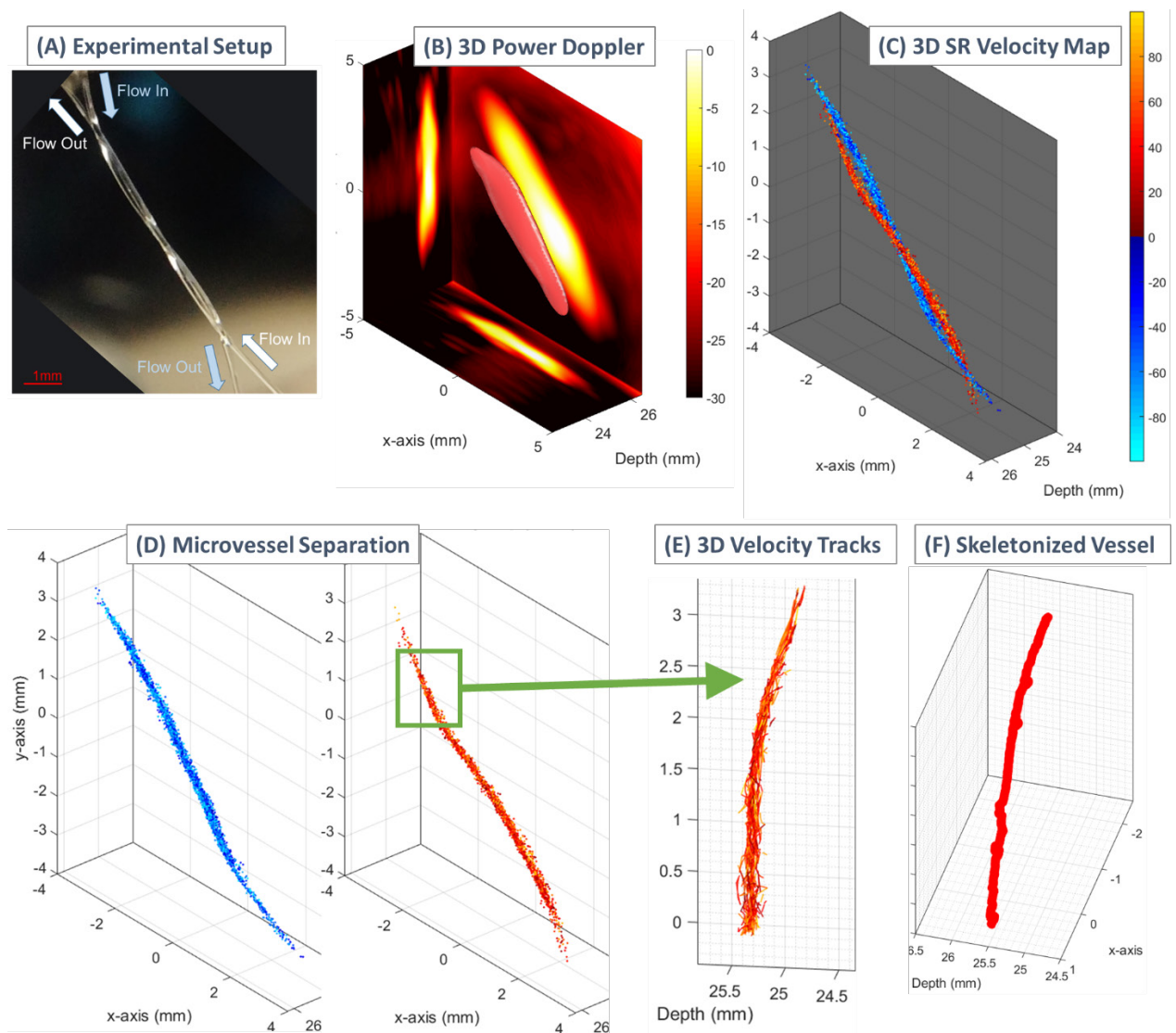


Figure (A) Optical image of the 200 μm cellulose tubes arranged in a double helix shape. **(B)** 3-D power Doppler image. **(C)** 3D velocity maps generated by tracked super-localized microbubbles with positive velocity values towards increasing y-direction. **(D)** Microvessel separation according to velocity values and direction. **(E)** Velocity tracks of the traced microbubbles. **(F)** Skeletonized tracks for microvessel analysis.

References

- [1]. M. A. O'Reilly and K. Hynynen, "A super-resolution ultrasound method for brain vascular mapping," *Medical Physics*, vol. 40, no. 110701, 2013.
- [2]. Y. Desailly, O. Couture, M. Fink, and M. Tanter, "Sono-activated ultrasound localization microscopy," *Applied Physics Letters*, vol. 103, no. 174107, 2013.
- [3]. C. Errico, J. Pierre, S. Pezet, Y. Desailly, Z. Lenkei, O. Couture, and M. Tanter, "Ultrafast ultrasound localization microscopy for deep superresolution vascular imaging," *Nature*, vol. 527, pp. 499–507, 2015.
- [4]. F. Lin, S. E. Shelton, D. Espindola, J. D. Rojas, G. Pinton, and P. A. Dayton, "3-D ultrasound localization microscopy for identifying microvascular morphology features of tumor angiogenesis at a resolution beyond the diffraction limit of conventional ultrasound," *Theranostics*, vol. 7, no. 1, pp. 196–204, 2017.
- [5]. K. Christensen-Jeffries, J. Brown, P. Aljabar, M.-X. Tang, C. Dunsby, and R. J. Eckersley, "3-D in vitro acoustic super-resolution and superresolved velocity mapping using microbubbles," *IEEE Trans. Ultrason., Ferroelectr., Freq. Control*, vol. 64, no. 10, pp. 1478–1486, 2017.
- [6]. S. Harput, K. Christensen-Jeffries, J. Brown, J. Zhu, G. Zhang, C. H. Leow, M. Toulemonde, A. Ramalli, E. Boni, P. Tortoli, R. J. Eckersley, C. Dunsby, and M.-X. Tang, "3-d super-resolution ultrasound imaging using a 2-d sparse array with high volumetric imaging rate," in *IEEE International Ultrasonics Symposium (IUS)*, 2018, pp. 1–4.
- [7]. J. Zhu, E. Rowland, S. Harput, K. Riemer, C.H. Leow, K. Cox, A. Lim, K. Christensen-Jeffries, G. Zhang, J. Brown, C. Dunsby, R.J. Eckersley, P.D. Weinberg and M-X. Tang, "3-D Super-Resolution Ultrasound Imaging of Rabbit Lymph Node Vasculature In Vivo using Microbubbles," *Radiology*, vol. 291, no. 3, pp. 642 - 650, 2019.
- [8]. B. Heiles, M. Correia, V. Hingot, M. Pernet, and J. Provost, M. Tanter and O. Couture, "Ultrafast 3D Ultrasound Localization Microscopy Using a 32×32 Matrix Array," *IEEE T. Med. Imaging*, vol. 38(9), pp. 2005–2015, 2019.
- [9]. S. Harput, K. Christensen-Jeffries, A. Ramalli, J. Brown, J. Zhu, G. Zhang, C.H. Leow, M. Toulemonde, E. Boni, P. Tortoli, R.J. Eckersley, C. Dunsby and M-X. Tang, "3-D Super-Resolution Ultrasound Imaging with a 2-D Sparse Array," *IEEE Trans. Ultrason., Ferroelectr., Freq. Control*, pre-print available online.
- [10]. S. Harput, K. Christensen-Jeffries, Y. Li, J. Brown, R. J. Eckersley, C. Dunsby, and M.-X. Tang, "Two stage sub-wavelength motion correction in human microvasculature for CEUS imaging," in *IEEE International Ultrasonics Symposium (IUS)*, 2017, pp. 1–4.
- [11]. S. Harput, K. Christensen-Jeffries, J. Brown, Y. Li, K. J. Williams, A. H. Davies, R. J. Eckersley, C. Dunsby, and M. Tang, "Two-stage motion correction for super-resolution ultrasound imaging in human lower limb," *IEEE Trans. Ultrason., Ferroelectr., Freq. Control*, vol. 65, no. 5, pp. 803–814, 2018.
- [12]. E. Boni, L. Bassi, A. Dallai, F. Guidi, V. Meacci, A. Ramalli, S. Ricci, and P. Tortoli, "Ula-op 256: A 256-channel open scanner for development and real-time implementation of new ultrasound methods," *IEEE Trans. Ultrason., Ferroelectr., Freq. Control*, vol. 63, no. 10, pp. 1488–1495, 2016.
- [13]. E. Boni, L. Bassi, A. Dallai, V. Meacci, A. Ramalli, M. Scaringella, F. Guidi, S. Ricci, and P. Tortoli, "Architecture of an ultrasound system for continuous real-time high frame rate imaging," *IEEE Trans. Ultrason., Ferroelectr., Freq. Control*, vol. 64, no. 9, pp. 1276–1284, 2017.
- [14]. A.F. Frangi, W.J. Niessen, K.L. Vincken, M.A. Viergever, "Multiscale vessel enhancement filtering", in *Medical Image Computing and Computer-Assisted Intervention - MICCAI'98*, 1998, pp. 130-137.
- [15]. G. Zhang, S. Harput, S. Lin, K. Christensen-Jeffries, C.H. Leow, J. Brown, C. Dunsby, R.J. Eckersley, and M-X. Tang, "Acoustic Wave Sparsely-Activated Localization Microscopy (AWSALM): Super-Resolution Ultrasound Imaging using Acoustic Activation and Deactivation of Nanodroplets," *Applied Physics Letters* 113, 014101, 2018.
- [16]. S. Harput, G. Zhang, M. Toulemonde, J. Zhu, K. Christensen-Jeffries, J. Brown, R. J. Eckersley, C. Dunsby, and M.-X. Tang, "Activation and 3D Imaging of Phase-change Nanodroplet Contrast Agents with a 2D Ultrasound Probe," in *IEEE International Ultrasonics Symposium (IUS)*, 2019, pp. 1–4.
- [17]. G. Zhang, S. Harput, H. Hanyu, K. Christensen-Jeffries, J. Zhu, J. Brown, C.H. Leow, R.J. Eckersley, C. Dunsby, and M-X. Tang, "Fast Acoustic Wave Sparsely Activated Localization Microscopy (fast-AWSALM): Ultrasound Super-Resolution using Plane-Wave Activation of Nanodroplets," *IEEE Trans. Ultrason., Ferroelectr., Freq. Control*, vol. 66, no. 6, pp. 1039 - 1046, 2019.

Super resolution imaging combined with differential targeted enhancement for structural and functional imaging of tumor vasculature

*Feifei Zhao¹, Sunil Unnikrishnan¹, Elizabeth B. Herbst¹, Alexander L. Klibanov^{1,2},
F. William Mauldin Jr. ¹, John A. Hossack¹*

*1Department of Biomedical Engineering 2Division of Cardiovascular Medicine, University of Virginia,
Charlottesville, VA 22908, USA*

jh7fj@virginia.edu

Introduction

In ultrasound molecular imaging (USMI), targeted microbubbles (MBs) become bound to the vascular endothelial cells via ligand-receptor pairing. This approach allows the detection of a signature of biological change occurring at molecular level. In addition, a technique known as ultrasound localization microscopy (ULM) can reveal the microvessel structure beyond the conventional limits of ultrasonic wave diffraction. In this presentation, we propose to combine super resolution anatomical imaging and molecular imaging techniques to show fine scale vasculature structure in conjunction with the signature of disease at molecular level. In this way, we anticipate providing complementary diagnostic information of evolving vasculature disease. We applied this method to image mouse tumor vasculature as a preliminary proof-of-principle study.

Methods

Experiments were performed using a Verasonics Vantage system (Verasonics Inc., Kirkland, WA, USA) equipped with an L12-5 linear array transducer. Laboratory-made lipid-shelled microbubbles were prepared including non-targeted MBs and VEGF-R2-targeted microbubbles [1]. All animal studies followed a protocol approved by the University of Virginia Animal Care and Use Committee. A murine hindlimb tumor model was used in this study. Three C57 BL/6 female mice were injected subcutaneously with murine colon adenocarcinoma cells (MC38, 1×10^6 cells, Kerfast, Boston, MA, USA) in the right hindlimb. A comparison study between the tumors and normal left legs was also performed.

Using a ULM technique with non-targeted microbubbles (a bolus of 5×10^7 MBs injected over 4 min), the map of microvessels were resolved at super resolution. Specifically, angled plane waves with 9 inclination angles between -4° and 4° with a step of 1° were transmitted at a pulse repetition frequency of 1 kHz and compounded (effective frame rate = 100 Hz). Singular value decomposition (SVD) was used for clutter removal [2]. Center positions of microbubbles were localized and accumulated from all the frames (2000 frames) to create a mapping of the tumor vasculature.

Differential targeted enhancement (dTE) was employed for targeted MB signal extraction [3]. MBs were injected into the systemic circulation via a tail vein catheter (1×10^7 VEGFR-2 targeted MBs). After 6 min waiting time, high intensity destruction pulses were administered to destroy all MBs in the field of view. Pre-burst images were used to measure the late enhancement signals from adherent and circulating MBs. Post-burst images were used to measure only the circulating MB signals. The difference image, referred to as the dTE image, between the pre- and post-burst revealed the signal intensity derived only from adherent MBs. Each dTE image was thresholded to eliminate signals below 95% of maximum intensity value. A combined dTE image was derived by summing up the 3 thresholded dTE images. The result of compounding the responses of 22 virtual sources, using a pulse inversion sequence, was used for dTE [4-6].

The dTE intensity profiles were measured as the mean value within a manually selected ROI (2×2 mm located at tumor or leg center) and plotted over time. The vasculature mapping from super resolution

processing was shown with targeted MBs intensity values overlapping, and vessel diameters were quantified. Within the ROI, vascular density was quantified as vessel index (VI), defined as the area of super-resolution blood vessel signals divided by the total area of the ROI. A higher VI means more dense vessels. In the same ROI, molecular targeting was quantified as the molecular intensity index (MII), calculated as the area of MB signals from dTE images divided by the total area within the ROI. A higher MII means more MBs are targeting the vessels.

Results

Figure 1 shows the dTE profiles and super resolution + USMI images corresponding to a mouse hindlimb tumor (a, b, c) and healthy leg (d, e, f). (c) and (f) show the super resolution zoom-in region indicated as white solid box in (b) and (e), respectively. In (a) the dTE curves show the difference in MBs signal intensity after administration of high intensity destruction pulses in different burst trials. In dTE profiles of the leg (d), no significant difference in was found pre-burst and post-burst MB signal intensity. Correspondingly, (e) shows much less signal from targeted MBs (in green color) for the healthy leg, compared to those in a tumor.

Measurements of vessel diameter showed that output super-resolution images had a resolution in the range of 50~100 microns. The VI and MII for tumors are (0.52, 0.47, 0.67) and (0.51, 0.41, 0.45), while for legs are (0.3, 0.42, 0.26) and (0.01, 0.01, 0.02) in the three mice, respectively.

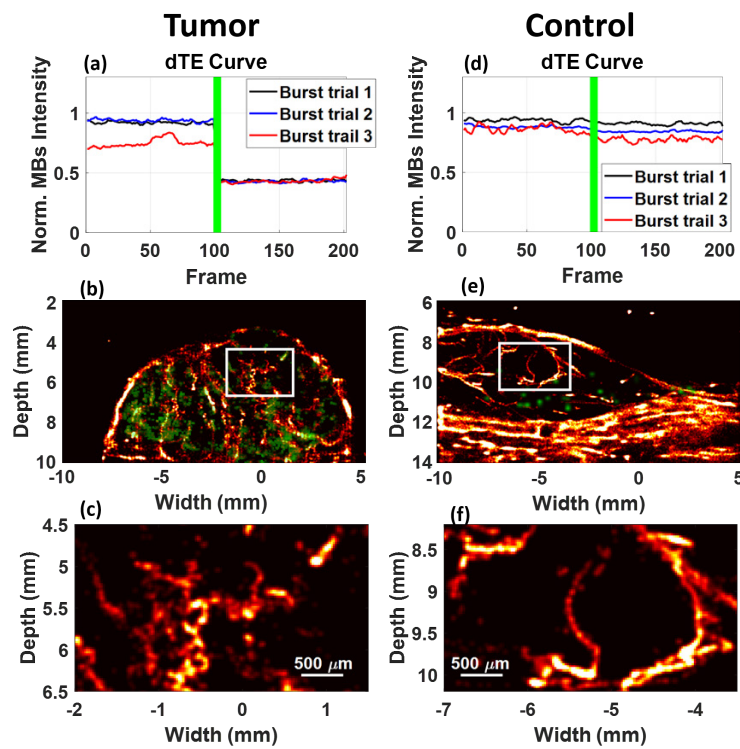


Figure 1. dTE curves and full vasculature with adherent MBs overlapping for tumor and leg respectively.

Conclusions

Overall, this preliminary study validated the feasibility of the proposed approach combining super resolution imaging of microvessels and detection of targeted MBs using USMI. The results demonstrated that normal mouse legs had lower vascular density and less MB adhesion than mouse hindlimb tumors. Using this method, the binding behavior of targeted MBs can be interrogated in relation to individual vessels, enabling simultaneous structural and molecular analysis in future disease models.

References

- [1]. Klibanov et al., "Targeting and ultrasound imaging of microbubble-based contrast agents," *Magn. Reson. Mater. Phys. Biol. Med.*
- [2]. C. Errico et al., "Ultrafast ultrasound localization microscopy for deep super-resolution vascular imaging," *Nature*, vol. 527, no. 7579, pp. 499–502, Nov. 2015.
- [3]. K. Ferrara, R. Pollard, and M. Borden, "Ultrasound microbubble contrast agents: fundamentals and application to gene and drug delivery.," *Annu. Rev. Biomed. Eng.*, vol. 9, no. 1, pp. 415–447, 2007.
- [4]. S. Wang, E. B. Herbst, F. W. Mauldin, G. B. Diakova, A. L. Klibanov, and J. A. Hossack, "Ultra-Low-Dose Ultrasound Molecular Imaging for the Detection of Angiogenesis in a Mouse Murine Tumor Model: How Little Can We See?," *Invest. Radiol.*, vol. 51, no. 12, pp. 758–766, Dec. 2016.
- [5]. C. H. Frazier and W. D. O'Brien, "Synthetic aperture techniques with a virtual source element," *IEEE Trans. Ultrason. Ferroelectr. Freq. Control*, vol. 45, no. 1, pp. 196–207, Jan. 1998.
- [6]. C.-C. Shen, Y.-H. Chou, and P.-C. Li, "Pulse Inversion Techniques in Ultrasonic Nonlinear Imaging," *J. Med. Ultrasound*, vol. 13, no. 1, pp. 3–17, 2005.

Ultrasound Localization Microscopy predicts ischemic stroke outcome and response to treatment in mouse model

V. Hingot^{1,*}, C. Brodin^{2,*}, B. Heiles¹, A. Chagnot², M. Yetim², M. Gauberti³, C. Orset², M. Tanter¹, O. Couture⁴, T. Deffieux^{1,**}, D. Vivien^{2,5**}

¹Institute Physics for Medicine Paris, Inserm U1273, CNRS FRE 2031, PSL University, Paris, France

²Normandie Univ, UNICAEN, Inserm, GIP Cyceron, UMR-S U1237, PhIND, Caen, France

³CHU Caen, Department of Radiology, Caen, France

⁴Laboratoire d'Imagerie Biomedicale, Sorbonne Université, CNRS, Inserm, F-75006, Paris, France

⁵CHU Caen, Department of Clinical Research, Caen, France

*,** these authors corresponding equally

Corresponding author: Vincent Hingot, vincenathingot@gmail.com

Introduction

In the field of ischemic cerebral injury, precise characterization of perfusion is required to select candidates for reperfusion treatments. It is admitted that advanced imaging based approaches able to diagnose and prognose patients would improve clinical care. Because of poor resolution and sensitivity, transcranial ultrasound imaging is not often used and MRI and CT are always preferred. The development of Ultrasound Localization Microscopy (ULM) improved sensitivity and resolution of ultrasound imaging and could provide new insights on tissue perfusion during stroke with a system that could be easily available for emergency imaging, bedside, non invasive, quantitative and repeatable.

Methods

When translating preclinical research to human patients, the question of precise animal modeling is crucial, even for imaging method. A thromboembolic model of ischemic stroke have been developed and validated in a multi-centric study that it accurately reproduce the physiopathology of ischemic stroke in human patients. A fibrine clot is formed in the Middle Cerebral Artery (MCA) through local injection of 1 UI of murine thrombin. 10 mice were injected with tPA which is the gold standard thrombolytic treatment for ischemic stroke whereas a control group of 10 mice received similar saline injection.

ULM was performed through the intact skull at given coronal plane for each mice and at key times of the ischemic episode: just before and just after MCA occlusion, after 1 and 2 hours, and after 24 hours. For each image, 100 µL of Sonovue microbubbles were injected in the tail vein while ultrasound images were acquired. 80 000 images were acquired in 150s by blocs of 800 compounded frames (-5°, 0°, 5°) at 1000 Hz. Microbubbles signals were filtered using a combination of high pass Butterworth and Singular Value Decomposition filters, localized using a radial symmetry based algorithm and tracked using the Hungarian method for assignment. Density images were reconstructed on a 10 µm grid.

Results

Before MCA occlusion, ULM reveals a normal vasculature through the mice skull. Some shadowing can be seen under the thicker central and lateral skull suture but the overall vasculature can be described with good precision. After MCA occlusion, ULM reveals that a large part of the contralateral cortex is hypoperfused. In the saline treated group, reperfusion is slow and ineffective and the ischemic lesion as seen in T² MRI matches the hypoperfused areas seen in ULM. In the tPA treated group, some reperfusion can be seen and the ischemic lesion at 24 h is reduced. The outcome and response to treatment can be estimated from early ULM alone and validated by T² MRI.

Conclusions

In this study, we demonstrate the ULM can be used through the intact skull of mice and can predict ischemic stroke outcome and response to treatment. The translation to human patients using lower

frequency probes could improve patients selection and access to thrombolysis and thrombectomy as well as the monitoring of response to treatment and recovery.

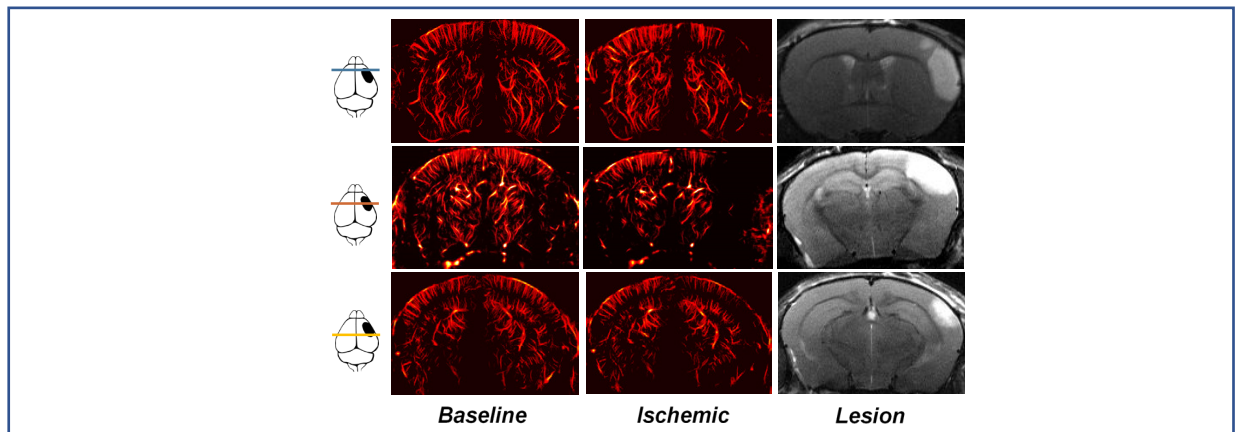


Figure 1. Ultrasound Localization Microscopy allows fine imaging of the hypoperfusion following occlusion of the Middle Cerebral Artery and predicts ischemic lesion as seen at 24 h on MRI

References

- [1]. M. Wintermark et al, Comparative Overview of Brain Perfusion Imaging Techniques, *Stroke* 36:e83–e9, 2005
- [2]. C. Orset et al, Mouse Model of In Situ Thromboembolic Stroke and Reperfusion, *Stroke* 38, 2771-2778, 2007
- [3]. C. Orset et al. Efficacy of Alteplase in a Mouse Model of Acute Ischemic Stroke: A Retrospective Pooled Analysis, *Stroke*, 1312-1318, 2016
- [4]. Errico C, et al, Ultrafast Ultrasound Localization Microscopy for deep super-resolution vascular imaging 2015, *Nature*, Nov 26;527(7579):499-502, 2015
- [6]. O. Couture et al, Ultrasound Localization Microscopy and Super Resolution: A state of the art. 2018, *IEEE TUFFS*, 2018 Aug;65(8):1304-1320, 2018

Effect of Concentrations of Contrast Agents in Ultrasound Super-Resolution Imaging

Ge Zhang¹, Fan Mo¹, Sevan Harput^{1,2}, Kirsten Christensen-Jeffries³, Jiaqi Zhu¹, Chee Hau Leow¹, Matthieu Toulemonde¹, Chris Dunsby⁴, Meng-Xing Tang¹

¹ULIS group, Department of Bioengineering, Imperial College London, London, United Kingdom

²Division of Electrical and Electronic Engineering, London South Bank University, London, UK

³Biomedical Engineering Department, Kings College London, London, United Kingdom

⁴Department of Physics and Centre for Pathology, Imperial College London, London, United Kingdom
Corresponding author: mengxing.tang@imperial.ac.uk

Introduction

Localisation-based super-resolution imaging using microbubbles has shown its capability of achieving sub-diffraction resolution in vitro [1] and in vivo [2-4]. Concentration of the contrast agents used is a key parameter in such localisation based approaches, and most existing studies used a relatively low concentration of microbubbles so that only the spatially isolated microbubble signals are localized for generating super-resolution images. Recently developed acoustic wave sparsely activated localization microscopy (AWSALM) has shown that spatially isolated signals can also be obtained after sparse acoustic activation of high concentration nanodroplets [5, 6]. It has been shown that real-time super-resolution imaging can be achieved by fast switching the agents. In this study, a comparison of the microbubble and droplets based approaches on a cross micro-tube flow phantom with different agent concentrations was made, in order to evaluate the effect of concentrations of contrast agents in the two types of localization-based ultrasound super-resolution approaches.

Methods

The preparation of decafluorobutane (DFB) microbubble and nanodroplet solutions were adapted from previous study [7]. Five different concentrations of contrast agents were used to perform the experiments (1.2×10^8 , 2.4×10^7 , 6.0×10^6 , 1.5×10^6 , and 6.0×10^5 particles/mL respectively). A $200 \mu\text{m}$ cellulose crossed micro-tube flow phantom was fabricated as illustrated in Figure 1. A phase array probe P4-1 was connected to an ultrasound research platform Verasonics 256 system. The center of the cross-tube center was held 50 mm below the surface of phase array probe. A syringe pump was used to establish a constant flow so that the contrast agent solution can be drawn from the beaker and refill the syringe. The refill rate was set as $1000 \mu\text{L}/\text{min}$. The temperature of water was controlled at 37 degrees in the water tank.

A customized Verasonic script was used to acquire the data in this study. One cycle 3.5 MHz imaging plane-waves were transmitted at a frame rate of 500 Hz for 1.6 s. For droplet vaporisation 128 two cycle 3.5 MHz focus-wave pulses was transmitted to activate the nanodroplets through the focal depth at a depth of 50 mm.

After the image acquisition, the data was beamformed using delay-and-sum (DAS) beamforming to generate the image data. After that, singular value decomposition (SVD) processing was used to remove the background noise and retain the contrast signals. Then the super-localization processing was applied to each image frame. The final super-resolution image was generated by the superposition of all the detected localizations through all the image frames.

To evaluate the resolution between bubble- and droplet-based super-resolution imaging, the minimum distance between the two micro-tubes and the full-width-half-maximum measurements were evaluated.

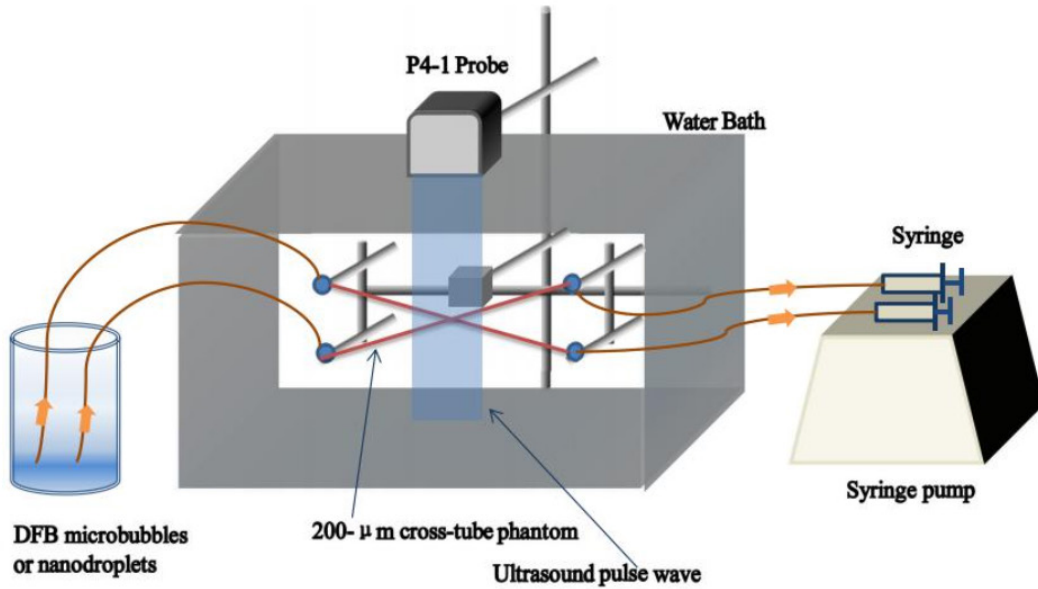


Figure 1. Experimental set-up

Results

Figure 2 shows (a) droplet- and (b) bubble-based super-resolution imaging at 3 different concentrations. Figure 3 shows the resolution measurement of bubble- and droplet-based super-resolution imaging at a high concentration of 1.2×10^8 particles/mL. It can be seen that, at a high concentration of contrast agents, the nanodroplet-based super-resolution imaging can resolve the microstructure whereas the microbubble-method cannot.

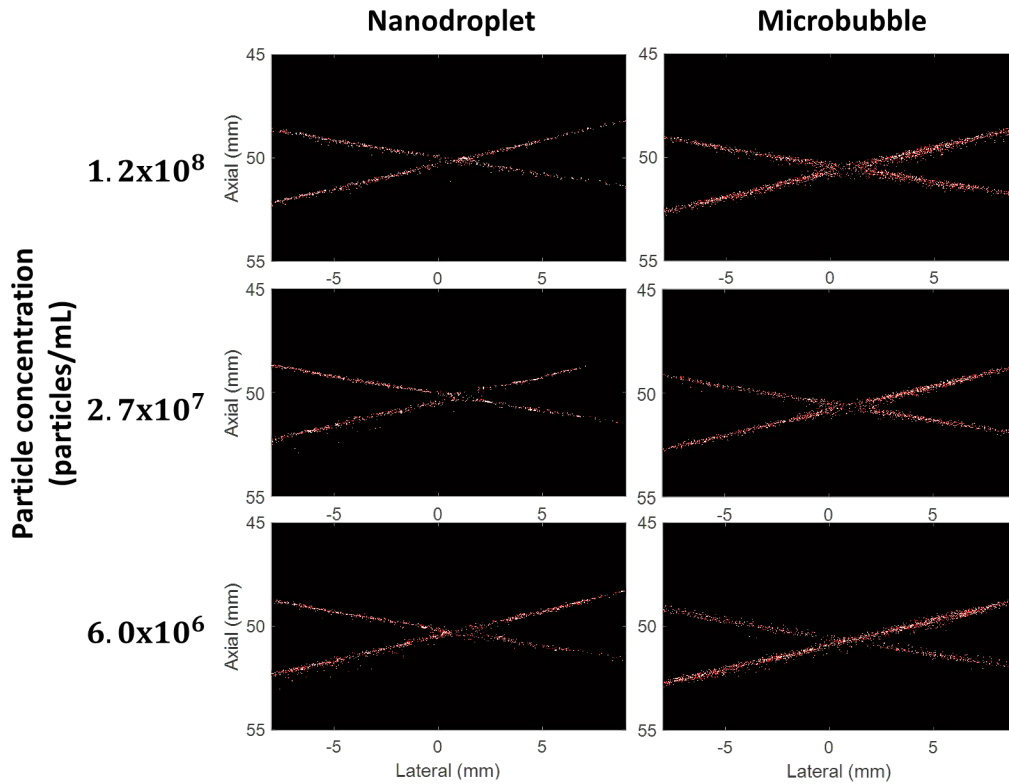


Figure 2. (a) Droplet- and (b) bubble-based super-resolution imaging at 3 different concentrations of contrast agents.

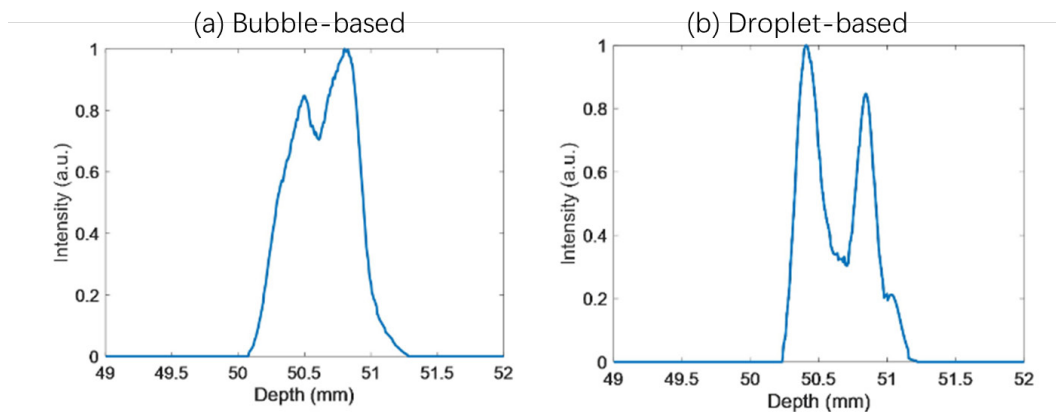


Figure 3. Resolution measurement of bubble- and droplet-based super-resolution imaging at a high concentration of 1.2×10^8 particles/mL.

Conclusions

In this study, initial results suggest that comparing with microbubble based localisation approach, droplet based super-resolution imaging approach AWSALM is less affected by contrast agent concentration and even at a high concentration (1.2×10^8 particles/mL) it can still clearly resolve two closely spaced tubes whereas the microbubble-based method cannot.

References

- [1]. OM Viessmann, RJ Eckersley, K Christensen-Jeffries, MX Tang, C Dunsby, Acoustic super-resolution with ultrasound and microbubbles, *Physics in medicine and biology* 58 (18), 6447, Sept 2013
- [2]. Christensen-Jeffries, K., et al., In Vivo Acoustic Super-Resolution and Super-Resolved Velocity Mapping Using Microbubbles. *Ieee Transactions on Medical Imaging*, 2015. 34(2): p. 433-440.
- [3]. Errico C, Pierre J, Pezet S, Desailly Y, Lenkei Z, Couture O, Tanter M., Ultrafast ultrasound localization microscopy for deep super-resolution vascular imaging. *Nature*. 2015 Nov 26;527(7579):499-502. doi: 10.1038/nature16066.
- [4]. Zhu, J., et al., 3D Super-Resolution US Imaging of Rabbit Lymph Node Vasculature in Vivo by Using Microbubbles. *Radiology*, 2019. 291(3): p. 642-650.
- [5]. Zhang, G., et al., Acoustic wave sparsely activated localization microscopy (AWSALM): Super-resolution ultrasound imaging using acoustic activation and deactivation of nanodroplets. *Applied Physics Letters*, 2018. 113(1): p. 014101.
- [6]. Zhang, G., et al., Fast Acoustic Wave Sparsely Activated Localization Microscopy: Ultrasound Super-Resolution Using Plane-Wave Activation of Nanodroplets. *IEEE Transactions on Ultrasonics, Ferroelectrics, and Frequency Control*, 2019. 66(6): p. 1039-1046.
- [7]. Zhang, G., et al., Quantification of Vaporised Targeted Nanodroplets Using High-Frame-Rate Ultrasound and Optics. *Ultrasound in Medicine & Biology*, 2019. 45(5): p. 1131-1142.

Whole rat brain microvasculature imaging *in vivo* with 3D ultrasound localization microscopy

B. Heiles¹, A. Chavignon², A. Bergel¹, V. Hingot², O. Couture²

¹*Institute Physics for Medicine, CNRS, INSERM, ESPCI Paris, PSL Research University,
17 rue Moreau, 75012, Paris*

²*Laboratoire d'Imagerie Biomédicale, Sorbonne Université – Campus des Cordeliers
15 rue de l'École de Médecine, 75006 Paris*

Corresponding author: baptiste.heiles@gmail.com

Introduction

To ensure proper functionality, the brain has to be continuously provided with oxygen and nutrients which are transported through the circulatory system. The blood supply of the brain is ensured by four arteries, and the blood is carried out from the brain from three main veins. In between these main structures, specific arteries and veins go deep in the brain with decreasing diameters (down to a few micrometers) forming a complex architecture. Several studies have described the microvasculature of the rodent brain but are usually *post mortem* and as such do not image vascular function [4]–[7].

Inspired by FPALM in optics and exploiting ultrafast ultrasound imaging, ultrafast Ultrasound Localization Microscopy (ULM) allows the reconstruction of a full velocity map of the rat brain vasculature with a micrometric resolution (8 μm) [1] [2]. Recently ported for large field of view imaging in 3D *in vitro* [3], it shows great potential for microvasculature imaging of large organs.

We present here the application of the ULM process *in vivo* to image the whole rat brain microvasculature and provide an accurate morphological description with labelling and haemodynamic characterization.

Methods

Sprague Dawley rats underwent craniectomy surgery under Isofluran anesthesia (5% with 40% O₂ and 60% air) after a preliminary induction intraperitoneously with Ketamin-Xylazin (40-80 mg/kg and 5-10 mg/kg respectively). The whole skull was removed in 5 steps from over the olfactory bulb to the cerebellum, forming a very large window allowing aberration free ultrasound imaging. The sides of the skull were also removed to prevent reflection and to allow aberration-free imaging of the lateral main arteries of the brain. The surgery took in between 4 to 7 hours to complete including the catheter placement.

The 2D matrix array with 1024 elements arranged in a 32x32 isotropic plane was controlled by the customised programmable 1024-channel system presented in [8]. The probe was driven at 9 MHz to transmit plane waves at 12 different angles to achieve a compounded volume rate of up to 500Hz. It was decided to repeat 400 blocs of 185 volumes with a pause in between to allow for data transfer. The acquisition was performed in 7 to 9 volumes to map the entire rat brain by translating the probe over the different areas. Significant overlap between the volumes was left, around 1 mm for the lateral and elevational direction, while taking into account the reduced borders to perform accurate localization. The size of the beamformed volume was larger than the probe's imprint to minimize the number of volumes required to reconstruct the whole brain.

A 3D ULM process with localization based on radial symmetry was applied to determine the position of the bubbles, track them and perform velocimetry in each of the volumes. For each of the volumes, a density based rendering was obtained. Each of these renderings was registered with respect to the other using a Mattes mutual information metric [10] implemented in Amira® (FEI®). The volumes were then stitched together to form the final rendering. The velocimetry data was registered in the same way to have access to the full velocity mapping of the brain. Vascular structures were identified based on the Waxholm space atlas described in [9].

Results

After implementation of this technique on 592,000 volumes, a volumetric rendering of the whole rat's brain microvasculature was obtained (figure 1.). At 9 MHz, the conventional resolution with this 2D array is around 250 μm . The maximum theoretical microbubble localization precision obtainable with volumetric ULM was calculated to be less than 1 μm in the axial direction and around 5 μm in the lateral and elevational directions.

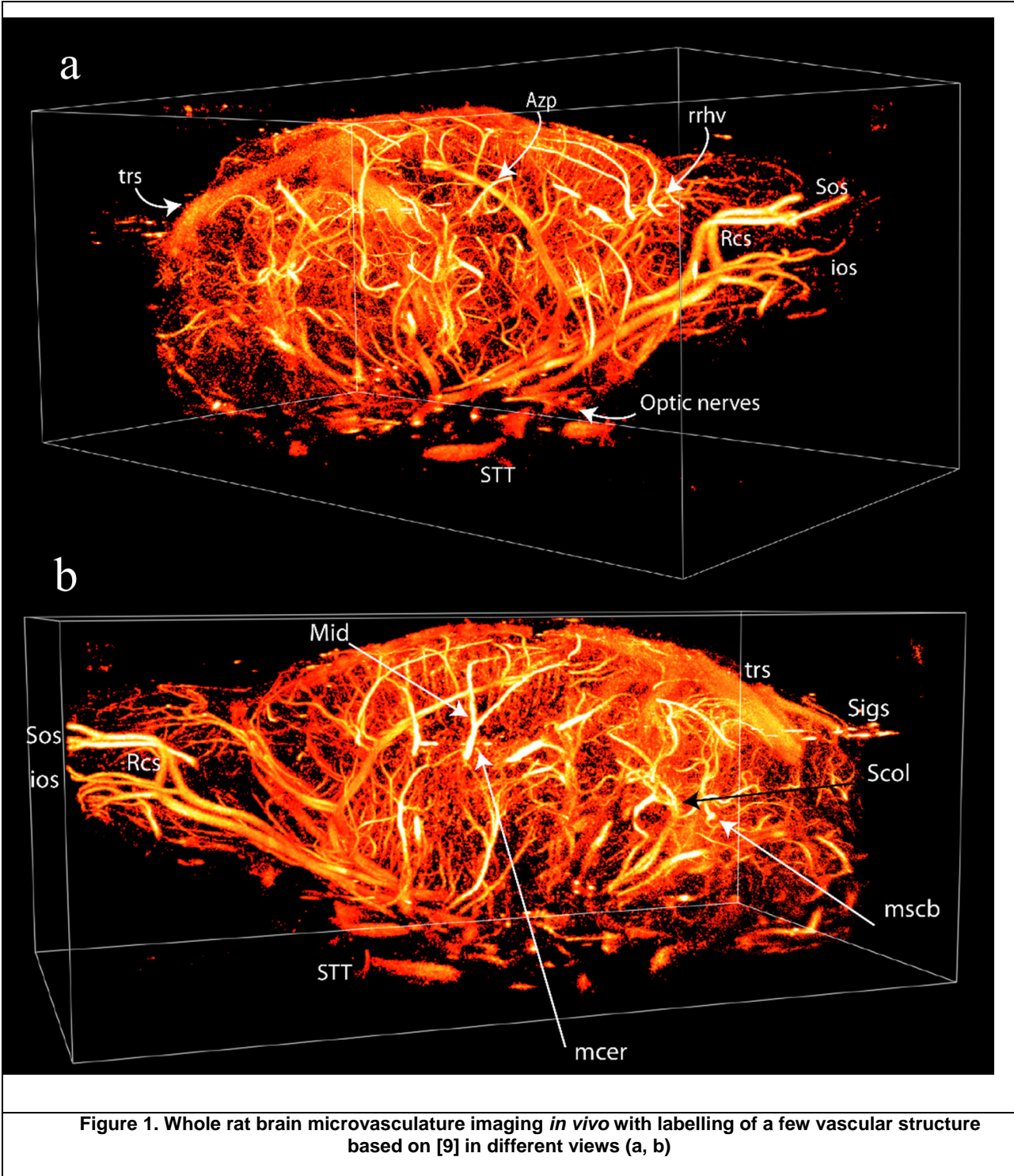


Figure 1. Whole rat brain microvasculature imaging *in vivo* with labelling of a few vascular structure based on [9] in different views (a, b)

Velocimetry was performed to yield a large range of velocity fields in microvessels from a few tens of micrometers to a few centimeters per second. The main vessels were identified based on the vascular atlas in the Sprague-Dawley rat provided by Papp, et al [9]. The smaller structures not present in this previous

work are part of the scientific deficit regarding a proper rat brain vascular atlas. The distinction in between veins and arteries were propagated from the cortex were they are arranged by ascending or descending vessels and from the main arteries and veins referenced in the Waxholm space atlas.

Conclusions

The total size of the acquired volume was 7,4 To and was achievable thanks to the high versatility of our 4D capable system. The time for post-processing was estimated to be in between a day to a day and a half using Matlab but can be considerably reduced using other programming languages. With the additional registration step, the possibility to complete large organ imaging is enabled without having to design specific probes requiring a large number of transducers. Volumetric ULM was successfully demonstrated *in vivo* on the whole rat brain revealing whole microvascular imaging *in vivo* for the first time. Velocimetry was also performed yielding haemodynamic mapping of the vasculature. In the end, the first step towards delivering an *in vivo* anatomical, haemodynamic and morphological world brain reference of the rat brain was achieved on 3 rats.

References

- [1]. C. Errico et al., "Ultrafast ultrasound localization microscopy for deep super-resolution vascular imaging," *Nature*, vol. 527, no. 7579, pp. 499–502, Nov. 2015.
- [2]. O. Couture, V. Hingot, B. Heiles, P. Muleki-Seya, and M. Tanter, "Ultrasound localization microscopy and super-resolution: a state-of-the-art," *IEEE Transactions on Ultrasonics, Ferroelectrics, and Frequency Control*, pp. 1–1, 2018.
- [3]. B. Heiles, M. Correia, V. Hingot, M. Pernot, J. Provost, and O. Couture, "Ultrafast 3D Ultrasound Localization Microscopy using a 32x32 Matrix Array," *IEEE Transactions on Medical Imaging*, p. 13, 2019.
- [4]. J. Yuan et al., "Visible rodent brain-wide networks at single-neuron resolution," *Frontiers in Neuroanatomy*, vol. 9, May 2015.
- [5]. B. Xiong et al., "Precise Cerebral Vascular Atlas in Stereotaxic Coordinates of Whole Mouse Brain," *Front. Neuroanat.*, vol. 11, p. 128, Dec. 2017.
- [6]. N. Renier, Z. Wu, D. J. Simon, J. Yang, P. Ariel, and M. Tessier-Lavigne, "iDISCO: A Simple, Rapid Method to Immunolabel Large Tissue Samples for Volume Imaging," *Cell*, vol. 159, no. 4, pp. 896–910, Nov. 2014.
- [7]. R. Tomer, L. Ye, B. Hsueh, and K. Deisseroth, "Advanced CLARITY for rapid and high-resolution imaging of intact tissues," *Nat Protoc*, vol. 9, no. 7, pp. 1682–1697, Jul. 2014.
- [8]. J. Provost et al., "3D ultrafast ultrasound imaging *in vivo*," *Physics in Medicine and Biology*, vol. 59, no. 19, pp. L1–L13, Oct. 2014.
- [9]. E. A. Papp, T. B. Leergaard, E. Calabrese, G. A. Johnson, and J. G. Bjaalie, "Waxholm Space atlas of the Sprague Dawley rat brain," *NeuroImage*, vol. 97, pp. 374–386, Aug. 2014.
- [10]. D. Mattes, D.R. Haynor, H. Vesselle, T. Lewellen, and W. Eubank. "Non-rigid multimodality image registration." (Proceedings paper). *Medical Imaging 2001: Image Processing*. SPIE Publications, 3 July 2001. pp. 1609–1620.

Imaging of Cancerous Microvasculature with Acoustic Angiography and Superharmonic Ultrasound Localization Microscopy

Isabel G. Newsome¹, Thomas M. Kierski¹, Jianhua Yin², Emmanuel Cherin², David Espindola^{1,3}, Guofeng Pang⁴, Claudia Carnevale⁴, F. Stuart Foster^{2,5}, Gianmarco F. Pinton¹, Christine E.M. Demore^{2,5}, Paul A. Dayton¹

¹ Joint Department of Biomedical Engineering, University of North Carolina and North Carolina State University, Chapel Hill, NC, USA

² Sunnybrook Research Institute, Toronto, ON, Canada

³ Instituto de Ciencias de la Ingeniería, Universidad de O'Higgins, Rancagua, Chile

⁴ Fujifilm VisualSonics, Inc., Toronto, ON, Canada

⁵ Department of Medical Biophysics, University of Toronto, Toronto, ON, Canada

Corresponding author: padayton@email.unc.edu

Introduction

In many diseases, including cancer, microvascular structure is altered during disease progression [1]. Monitoring the microvascular morphology may provide improved detection and diagnosis of malignant disease, especially for cancers which suffer low diagnostic specificity by current modalities. Contrast-enhanced ultrasound (CEUS) imaging offers an affordable, real-time, and portable alternative to computed tomography or magnetic resonance imaging for assessing microvasculature. Superharmonic techniques, which utilize echoes above the third harmonic produced by microbubble contrast, provide improved contrast-to-tissue ratio (CTR) and resolution compared to traditional second harmonic techniques for CEUS [2]. Here, we present the latest developments in two techniques based on superharmonic imaging: 1) acoustic angiography, a real-time, volumetric microvascular imaging modality, and 2) superharmonic ultrasound localization microscopy (SH-ULM), a super-resolution technique.

Methods

Acoustic angiography was performed with a novel dual-frequency array containing a 32-element 2 MHz linear array for transmit stacked behind a 256-element 20 MHz linear array for receive. The probe was driven by two synchronized Vantage 256 scanners (Verasonics, Kirkland, WA, USA) in a focused line-by-line imaging scheme with MI = 0.48. Data acquisition for SH-ULM was performed with a prototype hybrid dual-frequency device, described by [3], with 1.7 MHz plane wave transmit, 20 MHz receive, and MI = 0.24 on a Vantage 256 scanner. To form super-resolved images, SH-ULM data was thresholded to remove background noise, bubbles were localized with peak detection, and localized bubbles were tracked between frames by a nearest-neighbors approach. SH-ULM methods are described in more detail in [4]. All animal imaging was approved by the UNC Institutional Animal Care and Use Committee. Healthy or fibrosarcoma tumor-bearing female Fischer 344 rats (Charles River Laboratories, Durham, NC, USA) were anesthetized via isoflurane and shaved for imaging, and an in-house formulation of microbubble contrast (phospholipid shell, C₄F₁₀ core, 1 μm mean diameter) was administered via tail-vein catheter. For 3D data acquisition, each transducer was attached to a linear motion stage (Velmex, Inc., Bloomfield, NY, USA) controlled by a custom LabVIEW program (National Instruments, Austin, TX, USA) and translated over the tumor.

Results

A sagittal acoustic angiography maximum intensity projection (MIP) of a rat fibrosarcoma tumor is shown in Fig. 1A. As expected in a malignant tumor, the image shows highly dense and tortuous microvasculature. This scan was collected over 15 mm with 0.1 mm steps. With the dual-frequency array, vessels of 100 – 200 μm diameter are detected (Fig. 1B – 1D), CTR of 15 dB is achieved, and depth of

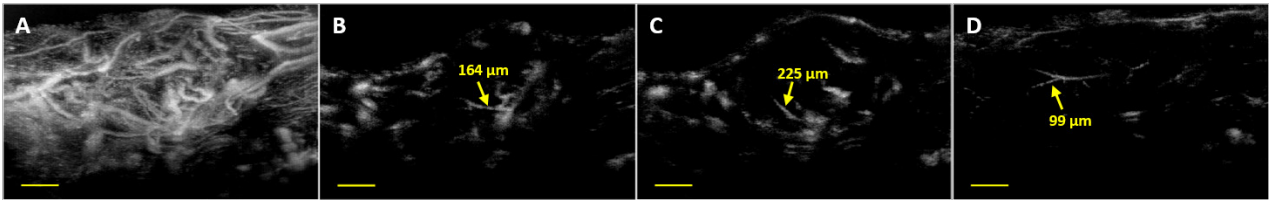


Figure 1. Acoustic angiography images of a fibrosarcoma tumor: A) sagittal maximum intensity projection through 15 mm scan, single slices at B) 3.5 mm, C) 6.9 mm, and D) 14.6 mm. Scale bar = 3 mm. Images displayed at 20 dB dynamic range.

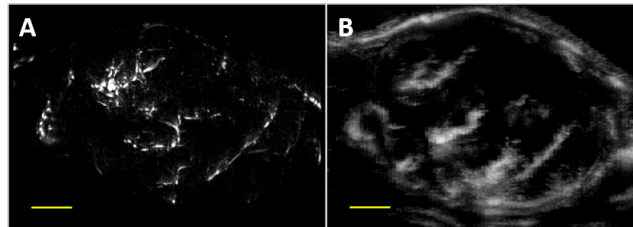


Figure 2. Comparison of A) 3D SHULM and B) acoustic angiography in a fibrosarcoma tumor. Images are maximum intensity projections through 5 mm scan near the center of the tumor. Scale bar = 2 mm.

field is improved by 5 mm over previous dual-frequency wobblers used for acoustic angiography. Here, we present the first attempt at imaging tumor microvasculature in 3D with SH-ULM. Fig. 2A presents a MIP of 3D SH-ULM data over a 5 mm scan with 0.5 mm steps near the center of the same rat fibrosarcoma tumor shown in Fig. 1. The image shown in Fig. 2A was produced from 10,000 frames at a PRF of 500 Hz and reconstructed on a 2- μ m grid. Fig. 2B shows an acoustic angiography MIP of approximately the same tumor region for comparison. These images show that the diffraction-limited resolution of acoustic angiography can be recovered with ULM processing. In the current study, no correction was applied for tissue motion in the SH-ULM data; the motion correction algorithm utilized in [4] will be applied to these data in future work.

Conclusions

Superharmonic imaging allows improved separation between microbubble contrast within vasculature and the surrounding tissue, providing excellent CTR. With acoustic angiography, high-resolution volumetric images of microvasculature can be created in real-time, while ultrafast superharmonic imaging with ULM processing can produce super-resolved images for the analysis of finer features. Here, we have applied the latest dual-frequency transducers, including the first stacked dual-frequency array and hybrid array probes, which will enable improved clinical translation of these novel imaging methods. Notably, the main limitation of superharmonic imaging is the wide bandwidth required to separate transmit and receive frequencies, and transducer development will continue to be a key role in the advancement of these techniques.

References

- [1]. Jain RK, Normalizing tumor vasculature with anti-angiogenic therapy: a new paradigm for combination therapy, *Nature Medicine*, 7(9):987-989, 2001.
- [2]. Bouakaz A, Frigstad S, Ten Cate FJ, and de Jong N, Super harmonic imaging: a new imaging technique for improved contrast detection, *Ultrasound in Medicine & Biology*, 28(1):59-68, 2002.
- [3]. Cherin E, Yin J, Forbrich A, White C, Dayton PA, Foster FS, and Demore CEM, In vitro superharmonic contrast imaging using a hybrid dual-frequency probe, *Ultrasound in Medicine & Biology*, 45(9):2525-2539.
- [4]. Kierski TM, Espindola D, Newsome IG, Cherin E, Yin J, Foster FS, Demore CEM, Pinton GF, and Dayton PA, Super harmonic ultrasound for motion-independent localization microscopy: applications to microvascular imaging from low to high flow rates, *IEEE Transactions on Ultrasonics, Ferroelectrics, and Frequency Control*, in press, 2019.

Copper-free click conjugation of P-selectin antibody to lipid-shelled microbubbles for imaging inflammation in a murine model of inflammatory bowel disease

Una Goncin¹, Wendy Bernhard², Ron Geyer², Steven Machtaler¹

¹Department of Medical Imaging, ²Department of Pathology and Laboratory Medicine, University of Saskatchewan, Saskatoon, Saskatchewan, Canada
Corresponding author: ung039@usask.ca

Introduction

Inflammatory bowel disease (IBD) is characterized by inflammation and ulceration of bowel segments within the gastrointestinal tract [1]. It is a life-long chronic disease with no cure, where the primary goal of therapy is maintenance of remission [1]. Screening patients for regions of active or recurrent IBD and monitoring regions over time present different problems for molecular imaging. Screening is generally a one-time imaging session where increased costs (MRI, CT, SPECT, PET) or radiation (CT, SPECT, PET) is acceptable. However, IBD patients require monitoring of diseased bowel over their entire lives, where the use of expensive modalities and contrast agents is not financially sustainable. We lack a low-cost contrast agent and molecular imaging approach that can be used to monitor regions of active IBD over time. Microbubbles (MBs) and ultrasound (US) are an ideal contrast agent/modality for repeated imaging of patients with active IBD due to its low construction and imaging costs, wide availability, and the ability to add targeting agents to the MB shell for molecular imaging of active inflammation [2,3]. Current clinical-grade targeted MBs make use of a maleimide-thiol reaction to add targeting agents to the surface [pochon]. Though effective, this requires use of a reducing agent and can have a negative effect on antibody-based targeting agents, and between 2-4 hours of ligation time at room temperature. Copper-free (Cu-free) click chemistry is an alternative approach to adding a targeting agent to the surface of a microbubble by exploiting the interaction between a cyclooctyne (eg. DBCO) and an azide. This reaction is quick, happens at room temperature, and is suitable for *in vivo* applications. Our goal is to make use of Cu-free click chemistry for quickly conjugating a targeting agent (commercial P-selectin) to the surface of lipid-shelled MBs and test its effectiveness for detecting inflammation in a murine model of acute inflammation.

Methods

Antibody labeling: Rat anti-Mouse α P-selectin was conjugated to a bifunctional linker (DBCO-PEG4-NHS) for 1 hour at room temperature. Excess DBCO-PEG4-NHS was removed using a desalting column. Degree of labelling was calculated using UV to be 4.2 DBCO-PEG4 per α P-selectin. The α P-selectin-DBCO was characterized by microcapillary electrophoresis (Agilent Bioanalyzer 2100; 93% pure).

MB production, labeling, and imaging: MBs were produced by sonicating perfluorobutane (C₄F₁₀)-sparged solution containing 85:5:5:5 molar ratio of DSPC, PEG40S, DSPE-PEG2000, DSPE-PEG2000-Azide (Avanti Polar Lipids) at a concentration of 1 mg lipid/ml. After synthesis, Azide-functionalized MBs were incubated with the DBCO-functionalized α P-selectin antibody for up to 2 hours. Validation that the DBCO-Azide click reaction took place on the surface of the MBs was carried by incubating labeled MBs with Goat anti-Rat IgG-Alexa555 overnight at 4°C. After incubation, MBs were washed and imaged using confocal microscopy. For *in vivo* US molecular imaging, acute bowel inflammation was induced orally by administering 4% dextran sulfate sodium (DSS) over 4 - 8 days in 5 of 8 female FVB mice until weight loss was observed. The remaining mice received normal drinking water. Mouse bowels were imaged using non-linear contrast mode on a small animal ultrasound system (Vevo3100; Visual Sonics; MX250 Transducer) following *i.v.* bolus injection of 5x10⁷ MBs. MBs were allowed to circulate for 4 minutes before the molecular imaging signal was collected (destruction-replenishment).

Each mouse received a bolus of P-selectin targeted MBs and non-targeted MBs (unlabeled; negative control), allowing for clearance in between (20 min). The resulting acoustic signal was analyzed using VEVOQC. Following imaging, mice were euthanized, and bowels were harvested.

Results

Validation of successful MB-antibody labelling using the DBCO-Azide click reaction was carried out using confocal microscopy, where a positive fluorescent signal was detected (Figure 1B). α P-selectin-targeted MBs were then generated and used to image inflammation in mice with acute IBD. A very low differential targeted enhancement (dTE) signal was detected using both targeted MBs (0.05 ± 0.08 a.u; n=3) and non-targeted MBs (0.01 a.u; n=3) in control mice (no inflammation) (Figure 1C, top). There was no significant increase in the dTE signal observed in mice with acute bowe inflammation that were imaged with non-targeted MBs (0.65 ± 0.66 a.u; n=4), but there was a significant increase in the dTE signal observed in mice with acute bowel inflammation that were imaged with targeted MBs (2.02 ± 0.44 a.u; n=5) (Figure 1C, Bottom).

Conclusions

These data show that the Azide-DBCO Cu-free click is a promising approach for quick, cost-efficient labelling of lipid-shelled MBs. Using this approach, we were able to create a targeted MB to the vascular inflammatory marker P-selectin, which generated a detectable US molecular imaging signal. This labelling approach has to potential to be is clinically translatable and may provide an alternative tool for identifying and monitoring disease progression in IBD patients.

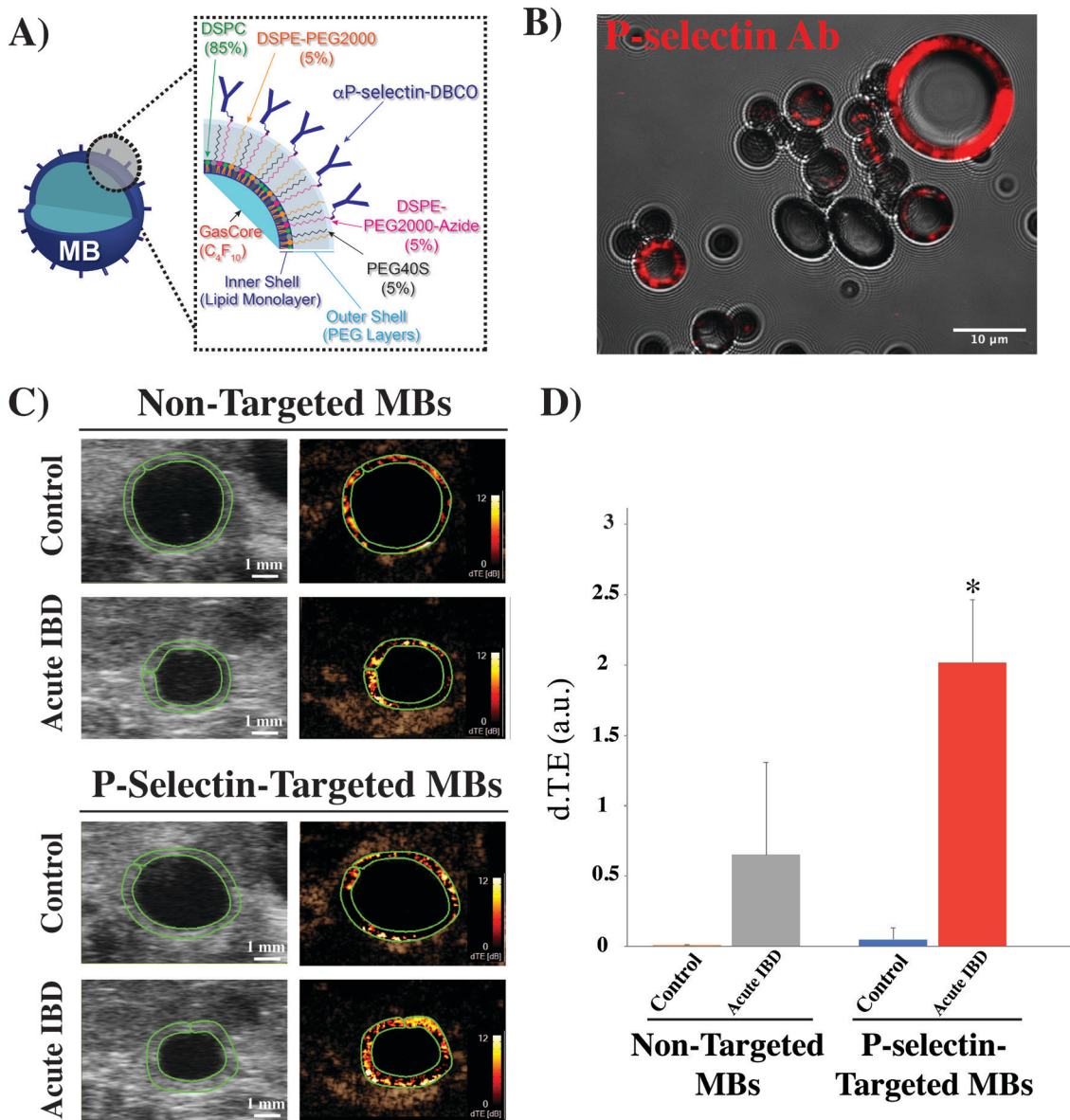


Fig. 1. Copper-free click ligation of α P-selectin antibody to microbubbles (MBs) for ultrasound (US) molecular imaging of inflammation in murine model of inflammatory bowel disease (IBD). **A)** Schematic of perfluorobutane(C₄F₁₀)-filled lipid shelled MBs containing four components (DSPC, PEG40S, PEG2000, PEG2000-Azide) and labelled with α P-selectin-DBCO. **B)** Fluorescent visualization of MBs successfully labeled with α P-selectin (red). **C)** Transverse US imaging with both non-targeted MBs and P-selectin targeted MBs in both control mice and mice with acute IBD (B-mode: left; ultrasound molecular imaging signal: right; green ROI highlights the cross section of bowel). **D)** Bar graph summarizes mean \pm standard deviations of the differential targeted enhancement (d.T.E; a.u.) signal using non-targeted MBs and P-selectin targeted MBs in control mice (n=3) and mice with acute IBD (n=4).

References

- [1]. Bailey, Rocchi, A., et al. Inflammatory bowel disease: A Canadian burden of illness review. 2012. *Can J Gastroenterol*, 26, 811-817.
- [2]. Deshpande, N., et al. Quantification and Monitoring of Inflammation in Murine Inflammatory Bowel Disease with Targeted Contrast enhanced US. 2012. *Radiology*, 262, 172-180.
- [3]. Machtaler, S., Knieling, F., Luong, R., Tian, L. & Willmann, J.K. Assessment of Inflammation in an Acute on Chronic Model of Inflammatory Bowel Disease with Ultrasound Molecular Imaging. 2015. *Theranostics* 5, 1175-1186.
- [4]. Alam, M.K., et al. Synthetic Modular Antibody Construction by Using the SpyTag/SpyCatcher Protein-Ligase System. 2017. *Chembiochem*, 18, 2217-2221.

CORM-1-loaded PBCA microbubbles for US- and MRI-guided light-triggered CO delivery

Vertika Pathak¹, Sandra Schipper^{1,2}, Nicolas Groß-Weege¹, Teresa Nolte¹, Marek Weiler¹, Volkmar Schulz¹, Fabian Kiessling¹, Twan Lammers^{1,3}, Patrick Koczera^{1,4}

¹ *Institute for Experimental Molecular Imaging, Medical Faculty, RWTH Aachen International University, Aachen, Germany*

² *Department of General, Visceral and Transplantation Surgery, Medical Faculty, RWTH Aachen International University, Aachen, Germany*

³ *Department of Targeted Therapeutics, University of Twente, Enschede, The Netherlands*

⁴ *Department of Intensive Care Medicine, Medical Faculty, RWTH Aachen International University, Aachen, Germany*

Corresponding author: pkoczera@ukaachen.de

Introduction

Scientists have started to explore the microbubble (MB) platform for delivering therapeutic gases like O₂, NO, Xe or H₂S in disease models for myocardial infarction and cardio/neuro-protection and for enhancing drug delivery to breast- and pancreatic-tumors in humans [1-3]. Carbon monoxide (CO) as signaling molecule bears the potential to modulate inflammation, cell survival and vascular tone in cardiovascular disease. In order to simplify handling and to avoid toxic gas inhalation, carbon monoxide releasing molecule-1 (CORM-1) was developed as 'pro-drugs' with carbon monoxide as an 'active compound', which shows light-triggered CO release [4]. Furthermore, the manganese central atoms bear the potential for utilization as an MRI contrast agent. However, the highly hydrophobic nature of CORM-1 requires utilization of drug delivery systems or potentially harmful organic solvents. To exploit the beneficial effects of CO for myocardial infarction, we developed CORM-1-loaded poly(butyl cyanoacrylate) (PBCA) MB (COMB), which release CO upon light irradiation, for US- and MR-imaging-guided triggered delivery of CO to coronary arteries (Figure 1).

Methods

COMB were synthesized based on a previously established 'one-step' loading protocol [3]. For this, an aqueous solution of the monomer n-butyl cyanoacrylate (BCA) with 1% Triton-X at pH 2.5 and CORM-1 in dimethylformamide was emulsified at 10 000 RPM for 1 hour. Characterization of the MB was performed in terms of sized-distribution, drug-loading, US- and MR-imaging contrast enhancement. Cell toxicity was tested for J774A.1-, A549- and NIH/3T3-cells. To evaluate CO delivery upon light irradiation under physiological conditions, the hemoglobin assay was used to spectrophotometrically quantify the saturation of hemoglobin with CO.

Results

For all tested cell lines, we did not observe relevant CORM-1-related toxicity. Generation of unloaded MB and COMB showed high yield per synthesis with a narrow-size distribution in the range of 1-4 micrometers. Successful loading of CORM-1 in microbubbles was confirmed (0.37 mM CORM-1 with 10⁹ COMB per mL). Quantification of contrast enhancement in US imaging revealed no significant differences in the acoustic behavior of unloaded and CORM-1-loaded MB. Upon white light irradiation, COMB released approximately one molecule of CO per molecule CORM-1, whereas no release was detected in the dark. Accordingly, light irradiation induced significant enhancement of T₁ and T₂ relaxation rates in MR imaging. Incubation of whole human blood with COMB and subsequent light irradiation increased percentage of hemoglobin saturated with CO significantly.

Conclusions

We developed a one-pot synthesis protocol for generation of CORM-1-loaded PBCA MB called COMB. These MB were suitable for US imaging and enabled white light-triggered delivery of CO. MRI was feasible for monitoring of CO release. The potential of COMB for adjuvant therapy in myocardial infarction was demonstrated by light-triggered delivery of CO to human blood. These promising results need further validation *in vivo* to explore the feasibility of COMB for CO delivery in myocardial infarction. For clinical applications COMB could improve recanalization therapy after myocardial infarction by (I) displaying recanalization success by US imaging, by (II) light-triggered CO delivery and by (III) MRI monitoring of CO delivery to the dilated arteries and inflammatory cells in order to enhance vascular healing and myocardial recovery, and reduce the rate of in-stent restenosis.

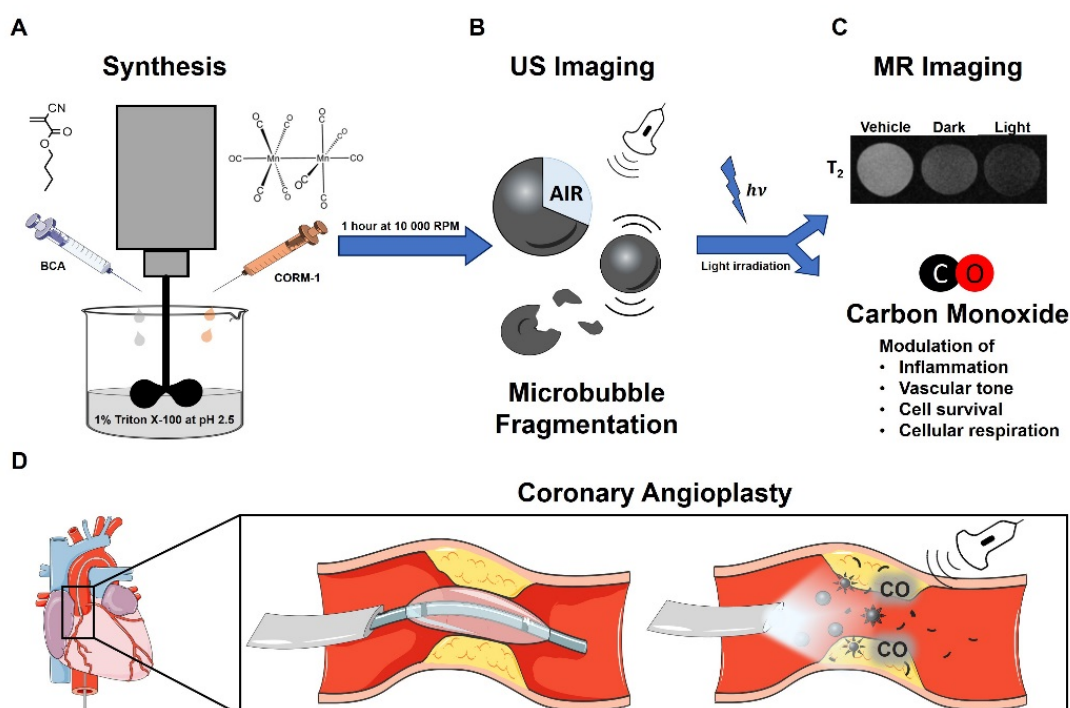


Figure 1. Schematic illustration of synthesis of CORM-1-loaded microbubbles (COMB) (A) for ultrasound (US) - and magnetic resonance (MR) imaging-trackable light-triggered delivery of CO (B,C) during coronary recanalization for therapy of myocardial infarction (D).

References

- [1]. Fix SM, Borden MA, Dayton PA, Therapeutic gas delivery via microbubbles and liposomes, *Journal of Controlled Release*, 209: 139-149, 2015.
- [2]. Snipstad S, Sulheim E, de Lange Davies RC, Moonen C, Storm G, Kiessling F, Schmid R, Lammers T, Sonopermeation to improve drug delivery to tumors: from fundamental understanding to clinical translation, *Expert opinion on drug delivery* 15: 1249-12611, 2018.
- [3]. Koczera P, Appold L, Shi Y, Liu M, Dasgupta A, Pathak V, Ojha T, Fokong S, Wu Z, van Zandvoort M, Iranzo O, Kuehne A, Pich A, Kiessling F, Lammers T, PBCA-based polymeric microbubbles for molecular imaging and drug delivery, *Journal of controlled release* 259: 128-135, 2017.
- [4]. Ling K., Fang M, Wei-Ci W, Zhou Y, Zhang H, Ye D, Carbon Monoxide and Its Controlled Release: Therapeutic Application, Detection, and Development of Carbon Monoxide Releasing Molecules (CORMs) Miniperspective, *Journal of medicinal chemistry* 61, 2611-2635, 2017.
- [5]. Otterbein LE, Zuckerbraun BS, Haga M, Liu F, Song R, Usheva A, Stachulak C, Bodyak N, Smith RN, Csizmadia E, Tyagi S, Akamatsu Y, Flavell RJ, Billiar TR, Tzeng E, Bach FH, Choi AMK, Soares MP, Carbon monoxide suppresses arteriosclerotic lesions associated with chronic graft rejection and with balloon injury, *Nature medicine* 9: 183-190, 2003.

Design of Therapeutic Magnetic Microbubbles for the Treatment of Pseudo-aneurysms

Alec N. Thomas¹, Luca Bau¹, Bernard Shieh¹, Lester Barnsely² Regent Lee³, Ashok Handa³, Eleanor Stride¹

¹*Institute of Biomedical Engineering, University of Oxford, Oxford, UK*

²*Jülich Centre for Neutron Science at Heinz Maier-Leibnitz Zentrum, Garching, Germany*

³*Nuffield Department of Surgical Sciences, Oxford, UK*

Corresponding author: alec.thomas@eng.ox.ac.uk

Introduction

The frequency of femoral artery puncture to access the vasculature has steadily increased worldwide due to the popularity of minimally invasive surgery in the area of interventional cardiology and interventional radiology.¹ While minimally invasive procedures have led to shorter post-operative hospital stays, as high as 8% of patients experience an iatrogenic pseudoaneurysm (PSA).² Perforation to the vessel combined with the influence of arterial pressure can form a perfused blood sac that communicates with the vessel lumen. Diagnosis of the condition is done by conventional angiography or duplex Doppler ultrasonography. The current standard of care is ultrasound-guided thrombin injection to the perfused sac of the PSA.² The injection of thrombin initiates blood coagulation that indirectly seals the ruptured vessel. However, a PSA must have an architecture such that the possibility of the injected thrombin to enter the arterial system is sufficiently low to avoid the risk of downstream intra-arterial thrombosis; otherwise, the treatment option is open surgery. Consequently, not all patients are eligible for thrombin injection, many of whom are high risk for surgery.

Magnetic microbubbles (MMs) are being investigated as a vehicle for targeted thrombin delivery to PSAs. This delivery scheme may increase the range of patients suitable for noninvasive ultrasound-guided thrombin injection preventing open surgery. MMs serve a dual role; firstly, to provide contrast for ultrasound imaging and secondly, they enable targeted delivery of the therapeutic. By designing thrombin conjugated MMs (TcMMs), the coagulation of blood can be spatially controlled and more easily imaged with ultrasound.

Methods

Thrombin conjugated magnetic microbubbles were produced by combining DBPC and DSPE-PEG2000-Biotin to a 9:1 molar ratio, evaporating the chloroform overnight, and dispersing the lipid in phosphate buffered saline by heating the solution to 85°C for one hour under constant mixing. Microbubbles were made by tip sonication and washed three times by centrifugation. To add magnetic material to the bubble, super paramagnetic iron oxide nanoparticles (SPION) were biotinylated and then slowly mixed with an avidin (NeutrAvidin) solution. Excess avidin was removed by buffer exchange. Next, the SPIONs coated with avidin were mixed with the freshly prepared microbubble suspension and then washed to remove any unbound SPIONs. Finally, thrombin was biotinylated to facilitate attachment to the MMs by targeting the surface exposed primary amines. Modified thrombin was then mixed with the MMs and washed once to remove free thrombin. The microbubble design is illustrated in Figure 1B with corresponding TEM images of a bubble free of SPIONs, a MM and a TcMM (Fig. 1C-E, respectively).

Magnetic retention experiments were performed in an agar channel under flow and exposed to a magnetic field. A custom built magnet, consisting of 5 concentrically stacked permanent magnetic disks of decreasing diameter housed in an aluminum bracket (Figure 2C), was positioned 3.5 cm below the center of the agar channel. Microbubbles were visualized using a Philips iU22 clinical scanner operating at an MI of 0.04. Image analysis was performed over 25 frames by calculating the average pixel intensity within

the region of interest (ROI) with and without the magnet and compared against the background measurement, as described by Beguin et al.³

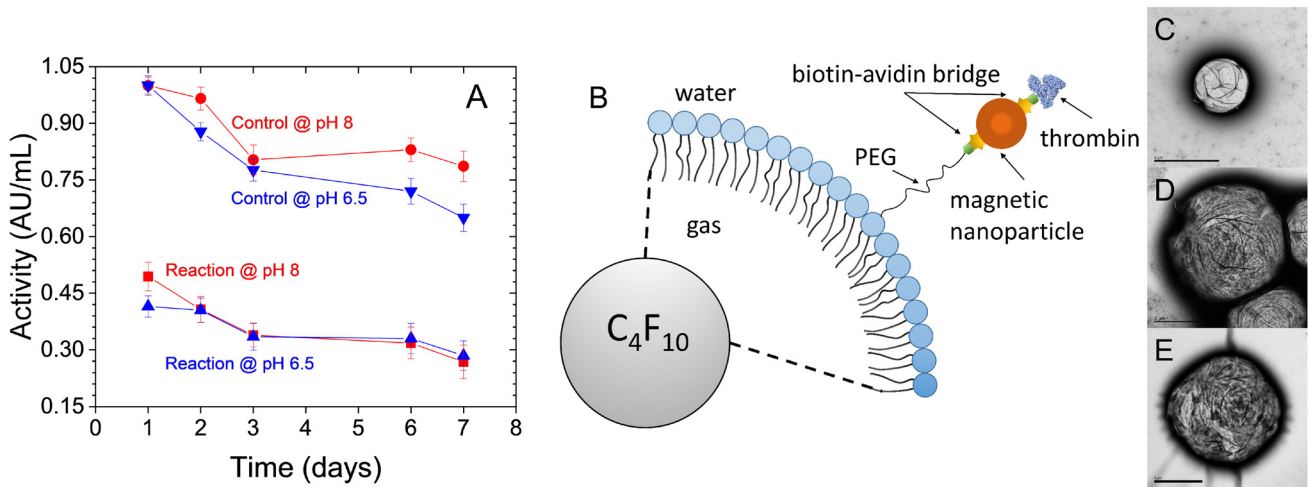


Figure 1 | (A) Longitudinal therapeutic activity measurements of modified thrombin. **(B)** Therapeutic microbubble construct filled with perfluorobutane (C_4F_{10}) gas and encapsulated with a lipid shell. The PEGylated fraction links the magnetic nanoparticle (orange) to the bubble via a biotin-avidin bridge (green and yellow). At the distal end, thrombin is bound to the nanoparticle by the same coupling mechanism. **(C-E)** TEM images of **(C)** clean microbubbles i.e. no conjugated SPIONs, **(D)** MM and **(E)** TcMM.

Results

The therapeutic activity of modified thrombin decreased by $59 \pm 3.8\%$ and $51 \pm 2.8\%$ at pH 6.5 and pH 8, respectively (Fig. 1A). The reaction conditions between the two groups (red and blue) differ by pH only; however, this has a significant effect on the number of available binding sites for the heterobifunction PEG-Biotin derivative. At lower pH, the N-terminus amine group is the preferred site of the NHS-ester reaction, which enables single biotinylation of thrombin. The long term stability profile of the protein for both reaction conditions are similar to the controls. Both the MMs and TcMMs showed strong retention compared to microbubbles with no SPIONs (clean MB) under flow when exposed to a magnetic field (Fig. 2A).

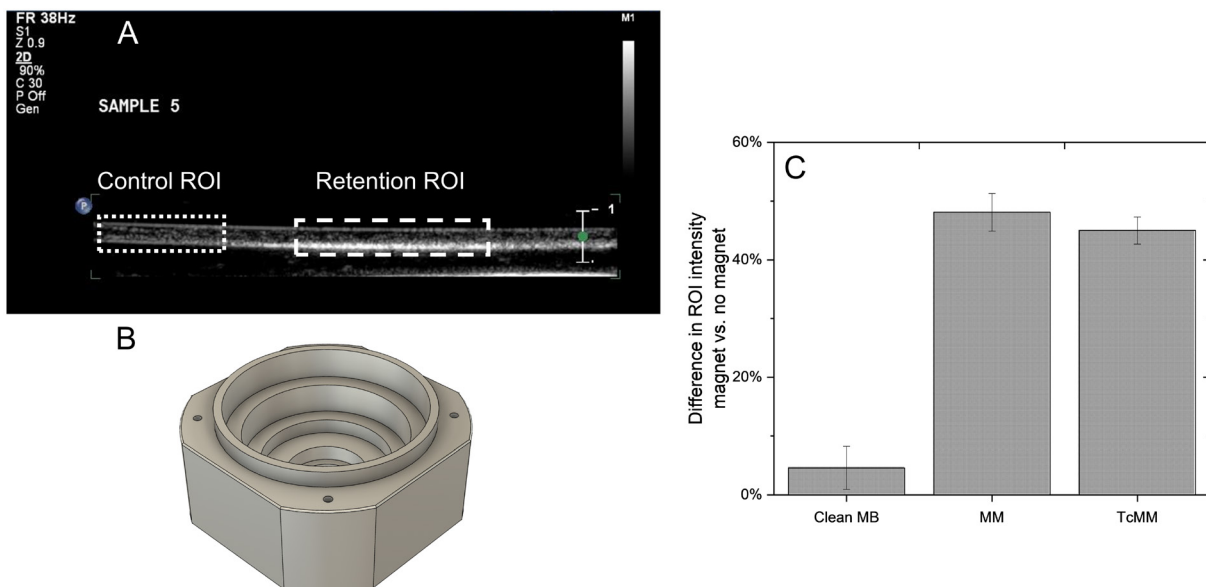


Figure 2 | (A) Example ultrasound image acquired after 1 minute of continuous flow of magnetic microbubbles. **(B)** CAD rendering of the aluminium brace that houses 5 concentrically stacked disc magnets. **(C)** Magnetic retention experiments comparing the ability of magnetic microbubbles (MM) and thrombin conjugated MM (TcMM) to be retained in a magnetic field under continuous flow.

Conclusions

The results indicate successful design of magnetically susceptible microbubbles loaded with thrombin. Modifying thrombin at a lower pH enabled a greater population of mono-biotinylated protein preventing microbubble aggregation. We demonstrated that with our custom built magnet there was significant retention of microbubbles when exposed to a magnetic field at a depth of 3.5 cm. This depth is necessary for clinical translation, as PSA can range in both subcutaneous depth and size of the the perfused blood sac.

References

- [1]. Tisi PV, Callam MJ, Treatment for femoral pseudoaneurysms. *Cochrane Database Syst Rev*, CD0004981, 2013.
- [2]. Kurzawski J, Sadowski M, Janion-Sadowska A, Complication of percutaneous thrombin injection in patients with postcatherization femoral pseudoaneurysm, *Journal of Clinical Ultrasound*, 188-195, 2015.
- [3]. Beguin E, Bau L, Shrivastava S, Stride E, Comparing strategies for magnetic functionalization of microbubbles, *Applied Materials and Interfaces*, 11, 1829-1840, 2019

UV-responsive microbubbles as a model system for cleavage-based detection

Dragana Ristanovic¹, Samuel Gebhardt¹, Michael G. Christiansen¹, Simone Schürle¹

*¹Responsive Biomedical Systems Lab, ETH Zürich, Zürich, Switzerland
Corresponding author: simone.schuerle@hest.ethz.ch*

Introduction

Assessing site-specific chemical activity within the body has the potential to supplement or improve current disease diagnostics. For instance, this principle has motivated the development of magnetic resonance imaging contrast agents that detect local chemical stimuli such as pH or the activity of biomolecules [1]. By analogy, chemically responsive ultrasound contrast agents could provide a comparatively straightforward, economical, and readily available means to non-invasively reveal information about local biomarkers or disease cues. Chemical modification of established ultrasound contrast agents may provide a route for incorporating responsiveness. In particular, targeted microbubbles are an appealing building block, due to their tunable acoustic properties, biocompatibility, and demonstrated translation into clinical trials [2]. Aptamer-crosslinked microbubbles have been shown to change their acoustic behaviour upon decrosslinking of the microbubble shell [3]. Despite this promising approach, comparable schemes for detecting pH, redox potential or enzymatic activity remain to be explored.

Here, we report on the development of a model system for responsive microbubbles based on irreversible cleavage of crosslinkers incorporated into their lipid shells. We demonstrated chemical crosslinking with 4-arm PEG on the shell of carboxylic acid-functionalized, perfluorobutane-filled microbubbles and detected corresponding changes in their acoustic properties. We subsequently extended the crosslinker with a photocleavable unit and demonstrated its UV-responsiveness. Our findings offer a step towards the development of UV-responsive microbubbles as a model system for cleavage-based detection (Figure 1A).

Methods

Microbubbles were prepared from liposome solutions containing different ratios of DSPC and DSPE-PAA which was synthesized via carbodiimide chemistry as described elsewhere [3]. Rehydration was performed in acetate buffered saline (ABS) and the head space of the samples was exchanged with perfluorobutane (PFB). Finally, microbubbles were formed by shaking. Size distribution and concentration was measured using a Multisizer 4e (Beckman Coulter). Acoustic characterization between 0.3 and 8.5 MHz was performed using an in-house built ultrasound attenuation measurement setup at a constant bubble concentration (Figure 1B).

Crosslinking of microbubbles was achieved by transferring a fresh bubble solution to a vial containing EDC and a non-responsive 4-arm PEG amine crosslinker (Figure 1A). The reaction was performed at room temperature under PFB atmosphere during several hours. To verify incorporation of the crosslinker onto the microbubble surface, an amine reactive Cy3 dye was added to the bubble solution and the resulting dye labelled microbubbles were washed by centrifugation and then imaged using confocal microscopy.

Synthesis of the UV-responsive crosslinker was performed by reacting photocleavable azido-PEG3-NHS carbonate ester with PEG-diamine. Subsequently, the intermediate product was reacted via Cu catalyzed click reaction with a 4-arm PEG alkyne. The final product was purified using size exclusion chromatography and lyophilized to obtain a yellow oil.

UV-responsiveness of the crosslinker was tested by exposing it to UV light of 365 nm wavelength for different amounts of time and two light intensities. The extent of cleavage was estimated from changes in absorbance between 400 and 450 nm relative to the unexposed control. To assess the detachment of the responsive unit from the crosslinker, the exposed product was labelled with an amine-reactive Cy3 dye and the size exclusion chromatogram was compared to the one of the Cy3-labelled uncleaved crosslinker.

Results

Figure 1C shows a confocal micrograph of fluorescently-labelled free amine groups of the 4-arm PEG crosslinker on the microbubble shell. This suggests that the crosslinker has been successfully linked to the microbubble surface, however, not all four of the sites have reacted to the PAA chains on the shell. Analysis of attenuation spectra, shown in Figure 1D, revealed that the attenuation of the crosslinked bubbles is decreased, implying that their acoustic cross section must be smaller than the one of the control sample. This indicated that the crosslinked shell is restraining the bubble from freely oscillating.

Figure 1E shows the comparison of size exclusion chromatograms of the UV-responsive crosslinker before and after UV exposure. The results show a decrease in the first and increase in the second peak. This is a clear indication that the responsive unit has been cleaved from the heavier crosslinker fragment and therefore resides longer within the size exclusion column. The inset in Figure 1E shows the change of absorbance of the UV-responsive crosslinker as a function of time and light intensity. These results indicate that even after 5 min exposure at 45 mW/cm², more than 90% of the units have been cleaved.

Conclusions

We have reported on progress towards a UV-responsive microbubble model system for cleavage-based responsive ultrasound contrast agents. In addition to establishing generalizable chemical strategies for the incorporation of other linkers, this model system provides possibilities to investigate and optimize physical characteristics, e.g. in designing microbubbles for prolonged stability or tuning harmonic response. Robust, responsive model systems are needed as a basis for comparison in future experiments and allow for selection of appropriate detection techniques.

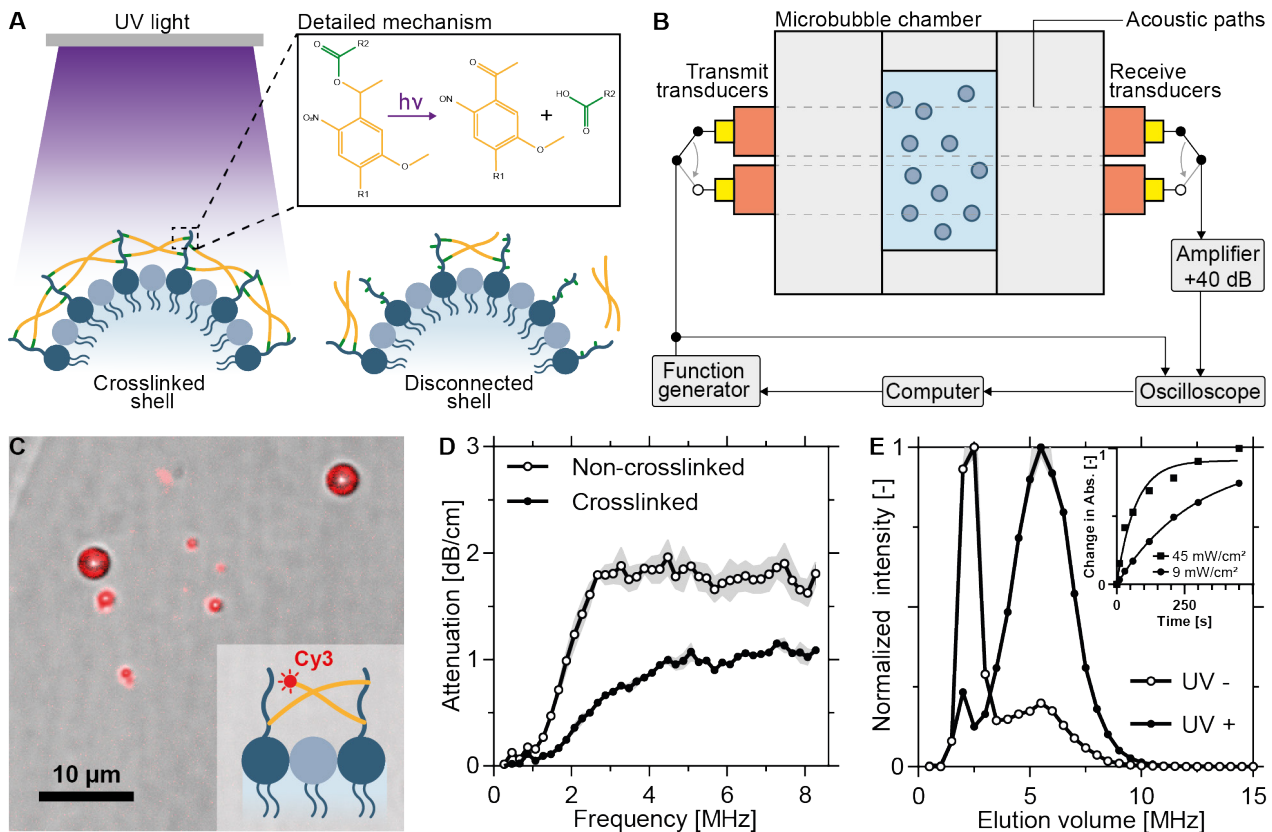


Figure 1. Underlying mechanism and ultrasound attenuation results of UV-responsive microbubbles. (A) Schematic representation of the UV responsiveness mechanism on the microbubble shell. (B) Acoustic characterization set up used to measure the ultrasound attenuation behaviour of microbubbles between 0.3 and 8.5 MHz. A signal is produced by the function generator and is sent to one of the two transmitting transducers, which have different resonance frequencies. The ultrasound waves then travel through the glass chamber, in presence or absence of the microbubbles, and are received by one of the two receiving transducers. The signal is amplified by 40 dB and digitised by an oscilloscope. (C) Overlay of bright field and fluorescence confocal microscopy images of Cy3 labelled crosslinked microbubble shells. (D) Comparison of ultrasound attenuation spectra of the non-crosslinked microbubble shells (control) and the crosslinked microbubble shell. (E) Comparison of size exclusion chromatograms of the UV-responsive crosslinker before and after UV exposure. Insert shows the relative change in absorbance between 400 and 450 nm of the crosslinker solution as a function of time and light intensity.

References

- [1]. Gallagher F.A., An introduction to functional and molecular imaging with MRI, *Clinical Radiology*, 65: 557-566, 2010.
- [2]. Wang S., Hossack J.A., Klivanov A.L., Targeting of microbubbles: contrast agents for ultrasound molecular imaging, *Journal of Drug Targeting*, 29: 420-434, 2018.
- [3]. Nakatsuka M.A., Mattrey R.F., Esener S.C., Cha J.C., Goodwin A.P., Aptamer-Crosslinked Microbubbles: Smart Contrast Agents for Thrombin-Activated Ultrasound Imaging, *Advanced Materials*, 24: 6010-6016, 2012.

Generation of microfluidic monodisperse microbubbles for enhancing contrast imaging

Ugur Soysal¹, Pedro N. Azevedo ^{1,2}, Marcio S. Carvalho², Amanda C. S. N. Pessoa³, Lucimara G. de la Torre³, Patrick Tabeling¹

¹Laboratoire de Microfluidique, MEMS et Nanostructures, ESPCI Paris, France

²Department of Mechanical Engineering, PUC-Rio, Brazil

³School of Chemical Engineering, University of Campinas, Brazil

Corresponding author: ugur.soysal@espci.fr; pedro.nieckele.azevedo@espci.fr

Introduction

Diagnosing disease in early stages prevents many people to unnecessary suffering and early death. Thereby, early disease diagnosis saves lives, reduce treatment costs. Ultrasound molecular imaging is a non-invasive method to be used for early diagnosis of many diseases. Today, the microbubbles utilized as ultrasonic contrast agents (CEUS - Contrast Enhancer Ultra Sounds). Historically, first generation microbubbles were composed of unencapsulated free gas bubbles (i.e. saline injection) as contrast enhancer, which was first used in 1968 [1]. Lack of shell material around gas led to very unstable and short life-time of bubbles *in vivo*. This was overcome with the second generation ultrasound contrast agents, which are composed of various shell materials (protein, lipid, polymer etc.) encapsulating different less soluble gases (air, SF₆, PFC etc.) in aqueous solutions where microbubbles are floating, and fall into the market more than 20 years ago. With the recent developments, monodisperse microbubbles show their potential to be used as a new generation contrast agents.

In the literature, the advantage of working with monodisperse populations of bubbles as CEUS has been discussed. *In vivo* and *in vitro* studies have already showed that using monodisperse microbubbles result in promising enhancements in ultrasound molecular imaging sensitivity [2][3][4][5].

Among the shell materials, polymer-shelled microbubbles such as poly(vinyl alcohol) (PVA), which is FDA-approved polymer, gain growing interest due to their promising echogenicity and prolonged sonographic time in comparison with commercial lipid microbubbles [6][7]. PVA-shelled microbubbles have been shown non-cytotoxic *in vivo* [8] and demonstrated its echogenic properties [9][10]. To this respect, PVA microbubbles as contrast agent holds a great potential, and therefore its monodispersity should be improved for increasing the sensitivity of molecular imaging. Besides, their external surface can be functionalized with many biologically relevant molecules [11], which leads PVA bubbles to be used as theranostic agents, and microfluidic technology has already demonstrated its capacity to produce monodisperse bubbles, echogenic and/or functionalized bubbles [12].

We hereby, for the first time, present a stable microfluidic generation of PVA-shelled monodisperse microbubbles with a diameter of 5 μm .

Methods

Monodisperse polymer-shelled bubbles encapsulating PFC or SF₆ gas were produced with a typical PDMS-based microfluidic chip which consists of a top PDMS mold and a bottom glass slide, which are bonded by UV-plasma, to tune its inner surface hydrophilicity (see Fig.1). The microfluidic channel is designed as the combination of flow focusing geometry, whose width and height is 5 μm , and step-emulsification which enlarges the dimension with an upward step-like channel whose height is around 20

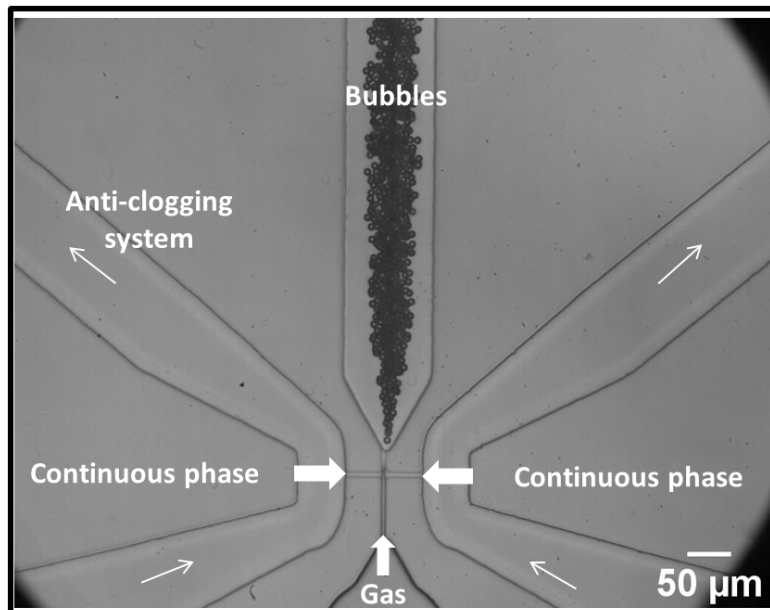


Figure 1. Generation of polymer-shelled monodisperse microbubbles encapsulating PFC or SF₆ gas by microfluidics (top view).

μm, in order to reduce the hydrodynamic resistance (see Fig.1). This in turn enables to generate 5 μm diameter of microbubbles with up to 10 kHz generation frequency. To ensure a prolonged stable generation, anti-clogging system (so-called river channels) is designed to avoid large aggregates or contaminants to clog the channels (see Fig.1).

Results

We generate (see Fig.1) and collect (see Fig.2) polymer-shelled monodisperse (CV= 6.8%) microbubbles with a diameter of 5 μm to be used as a contrast agent in the future. While this microfluidic system enables precise control of the bubble size and provide relatively high throughput (~60×10⁴ bubbles/min), which can be increased with 1000-fold parallelization, it avoids any coalescence either in the microchannels nor during the collection. In Fig. 3, PVA microbubbles are observed as hollows due to vacuum environment in SEM that ruptures the shells during the evacuation.

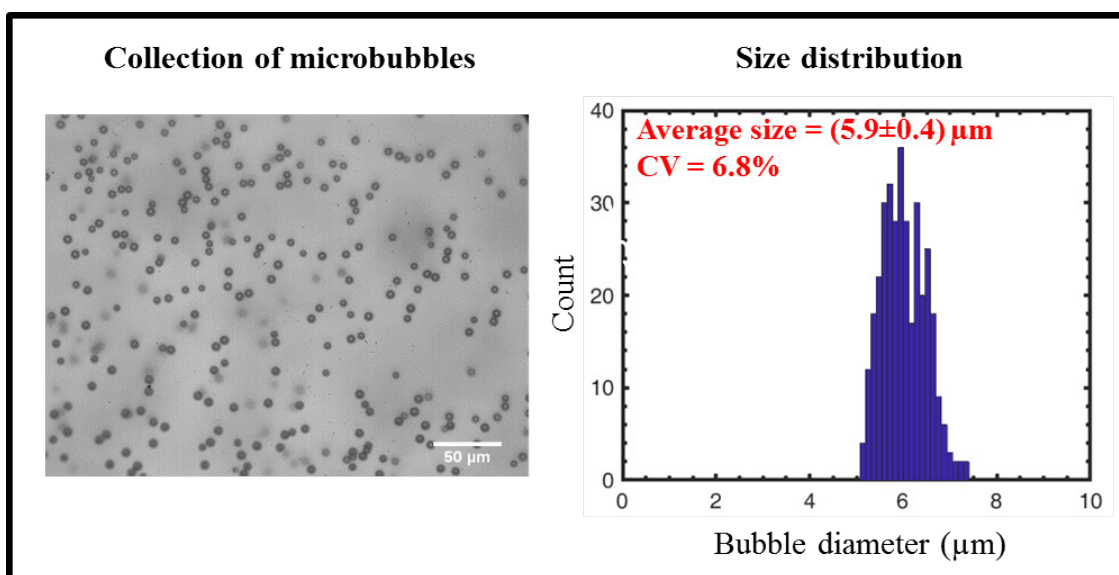


Figure 2. An optical image of collected bubbles and their size distribution. Scale bar is 50 μm.

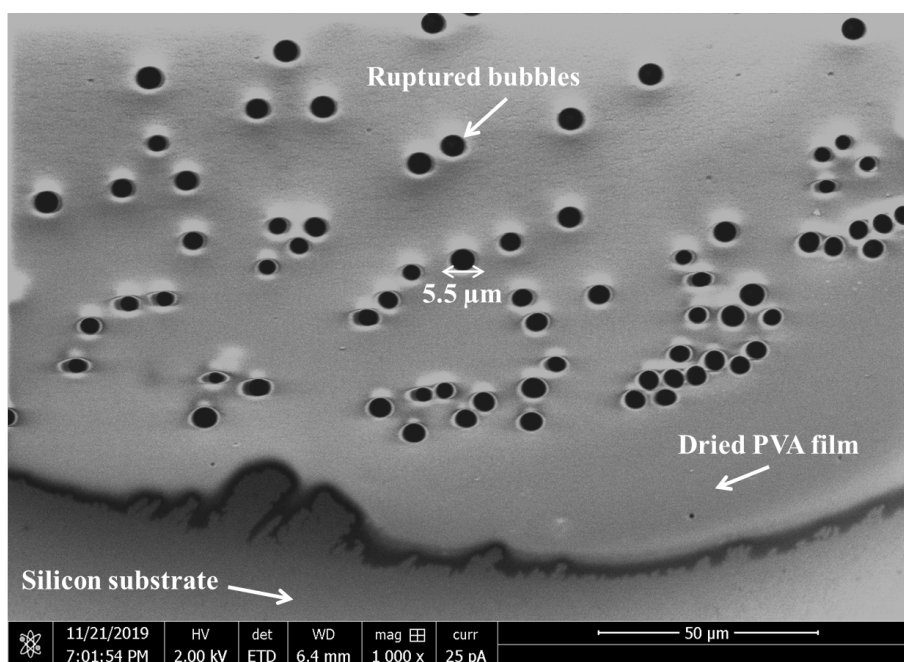


Figure 3. SEM image of PVA microbubbles. Scale bar shows 50 μm .

Conclusions

This work presents generation of monodisperse PVA-shelled microbubbles encapsulating PFC or SF_6 gas with a diameter down to 5 μm . The stable generation and collection without any coalescence have been maintained thanks to the developed microfluidic system. Microfluidic offers an excellent platform to precisely control the size of bubbles and tune its surface properties, which can be applied for the development of PVA microbubbles as theranostic agents.

Acknowledgments

The authors thank to IPGG-ESPCI-CNRS, CAPES, and São Paulo Research Foundation (FAPESP) (process no. 2018/05278-0) for their financial support.

References

- [1]. Gramiak, R., Shah, P., Echocardiography of the Aortic Root, *Invest. Radiol.* 3, 356–366, 1968.
- [2]. Parrales, M.A., Fernandez, J.M., Perez-Saborid, M., Kopechek, J.A., Porter, T.M., Acoustic characterization of monodisperse lipid-coated microbubbles: Relationship between size and shell viscoelastic properties. *J. Acoust. Soc. Am.* 136, 1077–1084, 2014.
- [3]. Segers, T., Kruizinga, P., Kok, M.P., Lajoinie, G., de Jong, N., Versluis, M., Monodisperse Versus Polydisperse Ultrasound Contrast Agents: Non-Linear Response, Sensitivity, and Deep Tissue Imaging Potential. *Ultrasound Med. Biol.* 44, 1482–1492, 2018.
- [4]. Sirsi, S., Feshitan, J., Kwan, J., Homma, S., Borden, M., Effect of Microbubble Size on Fundamental Mode High Frequency Ultrasound Imaging in Mice. *Ultrasound Med. Biol.* 36, 935–948, 2010.
- [5]. Streeter, J.E., Gessner, R., Miles, I., Dayton, P.A., Improving Sensitivity in Ultrasound Molecular Imaging by Tailoring Contrast Agent Size Distribution: In Vivo Studies. *Mol. Imaging* 9, 87–95, 2010.
- [6]. Oddo, L., Cerroni, B., Domenici, F., Bedini, A., Bordi, F., Chiessi, E., Gerbes, S., Paradossi, G., 2017. Next generation ultrasound platforms for theranostics. *Journal of Colloid and Interface Science* 491, 151–160.
- [7]. Song, R., Peng, C., Xu, X., Wang, J., Yu, M., Hou, Y., Zou, R., Yao, S., 2018. Controllable Formation of Monodisperse Polymer Microbubbles as Ultrasound Contrast Agents. *ACS Appl. Mater. Interfaces* 10, 14312–14320.

- [8]. Cerroni, B., Cicconi, R., Oddo, L., Scimeca, M., Bonfiglio, R., Bernardini, R., Palmieri, G., Domenici, F., Bonanno, E., Mattei, M., Paradossi, G., 2018. In vivo biological fate of poly(vinylalcohol) microbubbles in mice. *Heliyon* 4.
- [9]. Grishenkov, D., Pecorari, C., Brismar, T.B., Paradossi, G., 2009a. Characterization of Acoustic Properties of PVA-Shelled Ultrasound Contrast Agents: Linear Properties (Part I). *Ultrasound in Medicine & Biology* 35, 1127–1138.
- [10]. Grishenkov, D., Pecorari, C., Brismar, T.B., Paradossi, G., 2009b. Characterization of Acoustic Properties of PVA-Shelled Ultrasound Contrast Agents: Ultrasound-Induced Fracture (Part II). *Ultrasound in Medicine & Biology* 35, 1139–1147.
- [11]. Cavalieri, F., El Hamassi, A., Chiessi, E., Paradossi, G., 2005. Stable Polymeric Microballoons as Multifunctional Device for Biomedical Uses: Synthesis and Characterization. *Langmuir* 21, 8758–8764.
- [12]. Lin, H., Chen, J., Chen, C., 2016. A novel technology: microfluidic devices for microbubble ultrasound contrast agent generation. *Med Biol Eng Comput* 54, 1317–1330.

Magnetic Resonance Imaging of Oxygen Micro and Nanobubbles

Emma Bluemke¹, Daniel Bulte¹, Paul Kinchesh², Sean Smart², Eleanor Stride¹

¹Institute of Biomedical Engineering, University of Oxford, Oxford, UK

²Department of Oncology, University of Oxford, Oxford, UK

Corresponding author: emma.bluemke@new.ox.ac.uk

Introduction

It is well established that tumour hypoxia is a strong predictor of disease progression, treatment failures, and metastatic potential. To date, methods for reducing tumour hypoxia have delivered limited success owing to either a lack of proven efficacy, unwanted side effects, or logistical limitations. Therefore, there remains an urgent requirement for an effective hypoxia reduction mechanism that is safe, cost effective, biocompatible, and easy to use. To address this, oxygen-filled micro and nanobubbles have been investigated as a method of oxygen delivery and have shown promising results at improving response to ultrasound mediated therapy (Owen 2016).

For optimisation and clinical translation of oxygen bubbles for hypoxia reduction, consistent methods for measuring changes in tissue oxygenation need to be established. The ideal method should be noninvasive and quantitative, allowing tumour oxygen measurements to be obtained before, during, and after treatment. As magnetic resonance imaging (MRI) is a widely clinically available, non-ionizing, non-invasive imaging technique, it is ideal for determining tissue oxygenation noninvasively. In MRI, the rate at which the longitudinal magnetization recovers depends on the nearby environment, and the presence of paramagnetic moments nearby (such as dissolved oxygen) can greatly shorten the longitudinal relaxation (Young 1981). Thompson et al (2019) demonstrated the feasibility of using MRI to measure changes in oxygenation in vitro with microbubbles, however the nanobubbles, composed of different materials, have not yet been studied. In this study, we examined the effect of oxygen nanobubbles on the longitudinal relaxation times (represented by the T1 time constant) in an imaging phantom.

Methods

To measure the longitudinal relaxation time of solutions with varying oxygen content, five vials containing nanobubble solutions with different levels of oxygenation were prepared: nitrogen filled nanobubbles, air filled nanobubbles, half O2NB and half N2NB mixture, and two oxygen filled nanobubble solutions with differing levels of oxygenation. In addition, as a control, one vial containing water and one vial containing oxygenated water were prepared. All nanobubble solutions were prepared according to the oral nanobubble solution published in Owen et al (2016). To produce the mixture of half O2NB and half N2NB, a vial of O2NB was produced and a vial of N2NB were produced separately and then mixed. To produce a vial of oxygenated water, filtered deionized water was sparged with O2 gas for 3 minutes.

The imaging experiments were performed using a 7.0 tesla 210 mm horizontal bore VNMRS preclinical imaging system equipped with 120 mm bore gradient insert (Varian Inc. Palo Alto, CA, USA). One 0.5 ml syringe was filled per solution and sealed using Cristaseal wax (ProSciTech Pty Ltd, Australia). A 7-chamber custom built holder was used to hold seven 0.5 ml syringes in the scanner for the duration of the phantom experiment. For the phantom experiments, images for the construction of a variable flip angle (VFA) T1 map were acquired with a 3D gradient echo sequence (TR = 3.2ms, TE = 0.664ms, FA = 1, 1.2, 1.4, 1.6, 1.8, 2, 2.2, 2.4, 2.7, 3.1, 3.7, 4.4, 5.2, 6.1, 7, 8). T1 values were measured

and averaged lengthwise across each syringe to produce a mean T1 value for each syringe. Following the scans, the remaining solution in each of the 7 larger vials was measured using the fiber optic oxygen sensor (OXY Mini, PreSens Precision Sensing GmbH, Regensburg, Germany).

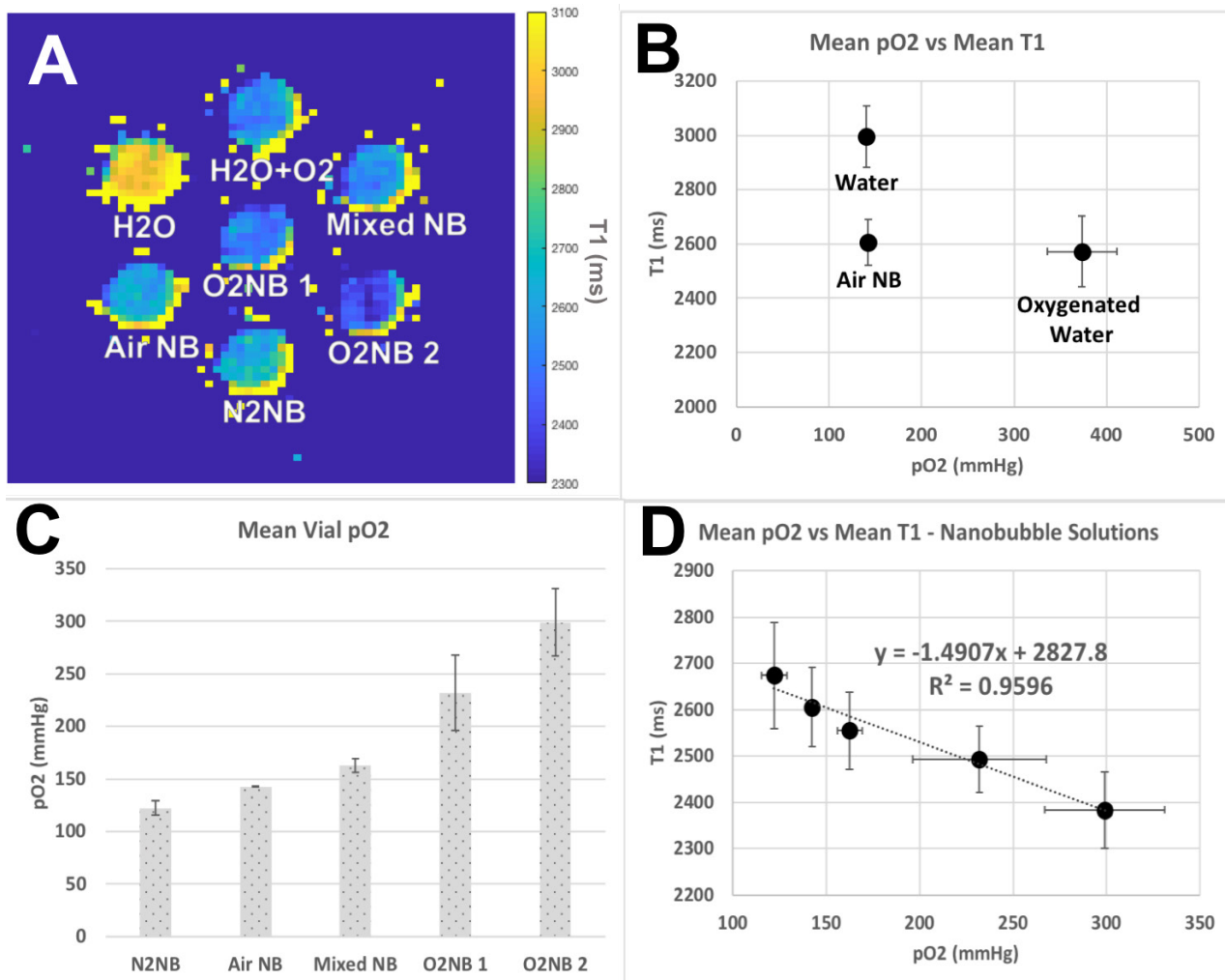


Figure 1. (A) The resulting T1 map through a section of the vials. (B) The mean T1 and pO₂ values of the vials of water and oxygenated water. (C) The mean vial pO₂ of the nanobubble solutions, showing a gradual increase in the pO₂ levels created by sparging with different gases. (D) The mean T1 values and mean pO₂ values in the nanobubble solutions, plotted with a linear line of best fit ($R^2=0.96$). The resulting relationship suggests a change in T1 of -1.5ms per mmHg change in pO₂ in the nanobubble solution.

Results

A slice of the resulting VFA T1 map of the vials is shown in Figure 1(A), where a large contrast can be seen between the vials. The longitudinal relaxation is affected by the chemical composition of the solution, with pure water containing the longest T1, thus the nanobubble solution, at a set pO₂, would be expected to have a shorter T1 than water. This was observed: when comparing the nanobubble solution at a similar pO₂ to pure water, the T1 of the nanobubble solution was shorter by 389 ms (shown in Figure 1(B)). The presence of dissolved oxygen is also expected to shorten the T1 of a solution, and this shortening was observed in the oxygenated water vial (also shown in Figure 1(B)).

Sparging the nanobubble solution with different gases resulted in 5 vials with varying pO₂ levels, plotted in Figure 1(C). Note that there are two oxygenated nanobubble solutions at different pO₂ levels due

to opening the lid of the vial of “O2NB 1”, resulting in a lower pO₂ value in that vial. The relationship between the pO₂ and T1 of the nanobubble solutions was a strong linear relationship (Figure 1(D), R²=0.96), and suggests a change in T1 of -1.5ms per mmHg change in pO₂ in the nanobubble solution when using a 7T scanner.

Conclusions

In this abstract, we measured a strong linear relationship between pO₂ and longitudinal relaxation in nanobubble solutions in vitro at 7T. This relationship describes a change in T1 of -1.5ms per mmHg change in pO₂, suggesting that T1 mapping could provide a noninvasive method of measuring oxygen delivery from oxygenated nanobubbles in therapy, depending on the oxygen delivery effect size that is expected and signal-to-noise ratio of the T1 map acquisition.

References

- [1]. Owen, J. et al. Reducing Tumour Hypoxia via Oral Administration of Oxygen Nanobubbles. PLoS ONE 11,e0168088 (2016).
- [2]. Young et al. Enhancement of relaxation rate with paramagnetic contrast agents in NMR imaging. The Journal of computed tomography 543–7 (1981). doi:10.1016/0149- 936X(81)90089-8
- [3]. Thompson, E, Smart, S, Kinchesh P, Bulte D, Stride E. Magnetic Resonance Imaging of Oxygen Microbubbles. Healthcare Technology Letters (2019).

Nested Nanobubbles as Ultrasound Triggered Drug Delivery Vehicles

Damien V. B. Batchelor¹, Sally A. Peyman¹, Louise P. Coletta², James R. McLaughlan³, Stephen D. Evans¹

¹ Department of Physics and Astronomy, University of Leeds, Leeds, UK

² Leeds Institute of Medical Research, Wellcome Trust Brenner Building, St James' University Hospital, Leeds, UK,

³ School of Electronic and Electrical Engineering³, University of Leeds, Leeds, UK

Corresponding author: S.D.Evans@leeds.ac.uk

Introduction

Chemotherapy, in combination with surgery or radiotherapy, is one of the primary treatment methods for malignant tumours and can significantly increase patient survival rates. However, treatment effectiveness is currently limited by the negative side effects and drug resistance present during systemic delivery. [1] The ability to target and locally deliver chemotherapeutics would not only reduce toxicity but also increase drug efficacy and treatment effectiveness. Methods for mechanical and thermal release triggers such as ultrasound [2] and near-infrared lasers [3] are being currently developed for controlled local release. The use of ultrasound is especially appealing due to its availability, non-invasive nature and potential for image guidance during therapeutic treatment. Microbubbles driven by an ultrasound field have been shown to increase cell membrane permeability, known as sonoporation, which when co-delivered with a therapeutic can increase drug uptake and efficacy. [4-6] Therapeutics can also be incorporated with microbubbles either in the form of therapeutic gas [7], attachment of drug-filled liposomes [8-10] or by gene-loading [11,12] and increasing ultrasound intensity can induce inertial cavitation, triggering release of the microbubble payload. [13,14] However due to microbubble size they are confined to the vasculature, limiting drug penetration to the tumour site. As such, the enhanced tumour uptake and increased stability of nanobubbles (NBs) (< 1 μm), compared to traditional ultrasound contrast agents makes them an attractive prospect for triggered drug delivery [15,16]

In this study we have produced and functionalised nanobubbles for triggered drug delivery by encapsulation within drug-loaded liposomes. These "Nested-Nanobubbles" are ~ 300 nm in size and combine the acoustic properties of nanobubbles with the drug-loading capability and stability of liposomes. During exposure to a high intensity ultrasound field, bubbles situated close to a boundary can generate shear stresses due to the no-slip fluid flow conditions imposed by the boundary. [17] In our system, the liposome bilayer surrounding the NB acts as a source for these conditions, allowing generation of shear stresses to porate the liposome membrane and provide subsequent drug release. Here we have investigated the effects of high intensity focused ultrasound (HIFU) on Nested-NBs and observed acoustic emissions and model - drug release profile.

Methods

Microbubbles were produced microfluidically in a microspray regime as previously described [15] and NBs separated via flotation due to intrinsic microbubble buoyancy. Nested-Nanobubbles were produced by passively encapsulating NBs within self-quenched Calcein loaded liposomes. Free Calcein and non-encapsulated NBs were removed via centrifugation.

NB encapsulation was visualised using Transmission Electron Microscopy and Nested-Nanobubble populations characterised using Nanoparticle Tracking Analysis (NanoSight, Malvern Panalytical, UK). Clinical frequency B-Mode imaging (3-8 MHz Linear Array, V-Scan, GE Healthcare, US) was used to confirm echogenicity of both NBs and Nested-Nanobubbles in a wall-less agar flow phantom [18] before and after ultrasound release trigger. The ultrasound release trigger was provided by a 1.1 MHz centre frequency HIFU transducer (H102, Sonic Concepts, US) and acoustic emissions monitored using a

broadband focused detector (Y-102, Sonic Concepts, US) co-aligned in the central aperture of the HIFU transducer. HIFU exposures consisted of a 5 second total duration with a pulse repetition frequency of 1 kHz, 50 % duty cycle and in situ peak negative pressure of ~ 3 MPa. Total Inertial Cavitation Dose was calculated by integrating detected broadband emissions over the total duration of the exposure. [19] After HIFU exposure, fluorescence spectroscopy was used to quantify drug release compared to positive and negative controls.

Results

NBs were produced microfluidically at a concentration of $5.79 \pm 0.66 \times 10^{11} \text{ mL}^{-1}$ with a modal size of $106.6 \pm 4.2 \text{ nm}$. NBs were imaged using clinical frequency B-mode imaging, demonstrating echogenicity, which significantly decreased after exposure to a HIFU destruction pulse.

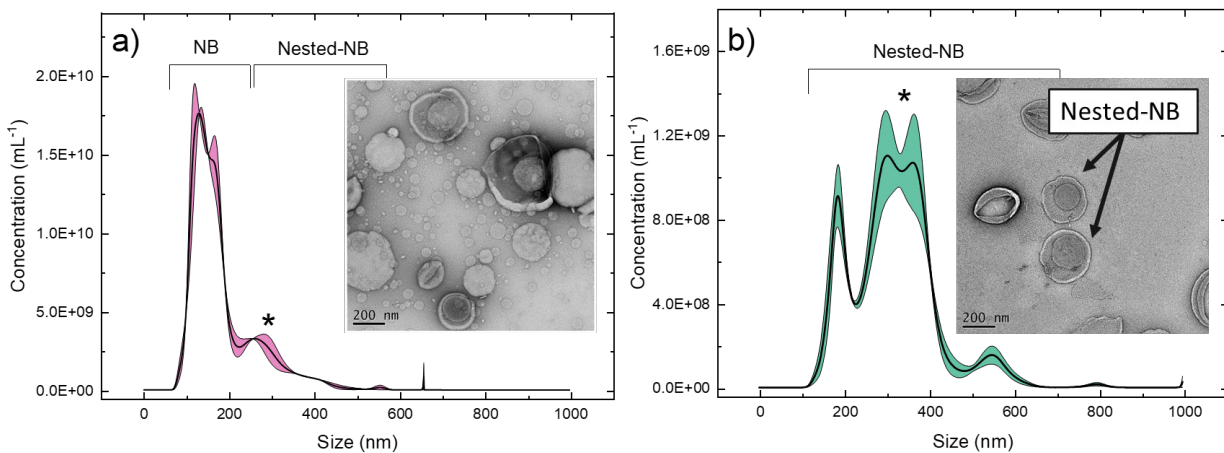


Figure 1 – Size and concentration distribution of Nested-Nanobubbles before (a) and after (b) cleaning of un-encapsulated NBs. * Signifies common population between samples. Inset: Transmission Electron Microscopy images of the corresponding samples.

NBs were successfully encapsulated within Calcein-loaded liposomes, with free NBs and Calcein removed via centrifugation demonstrated by TEM images and NTA population characterisation. (Figure 1), showing a shift in modal size from 129 nm to 305 nm and concentration decrease from $(1.82 \pm 0.09) \times 10^{12}$ to $(2.45 \pm 0.1) \times 10^{11} \text{ mL}^{-1}$ respectively. The percentage of liposomes containing a NB post cleaning was $21.8 \pm 2.4 \%$. Clinical frequency B-mode imaging show that Nested-Nanobubbles demonstrated echogenicity and after HIFU exposure, grayscale intensity decreased by 92.36 % suggesting destruction of NBs in the sample. Acoustic emissions from Nested-NBs during HIFU exposures were monitored and total inertial cavitation dose calculated to quantify inertial cavitation activity. Compared to liposome-only controls, Nested-Nanobubbles showed an increase of 77 % in inertial cavitation. [Fig. 2a]

This, in combination with B-mode imaging suggests that NBs within the liposomes have been destroyed by inertial cavitation induced by the HIFU pulse. However, no model drug release was measured after exposure compared to controls [Fig. 2b] suggesting that although NBs are experiencing inertial cavitation, the shear stress produced is not capable of sufficient membrane poration for drug release.

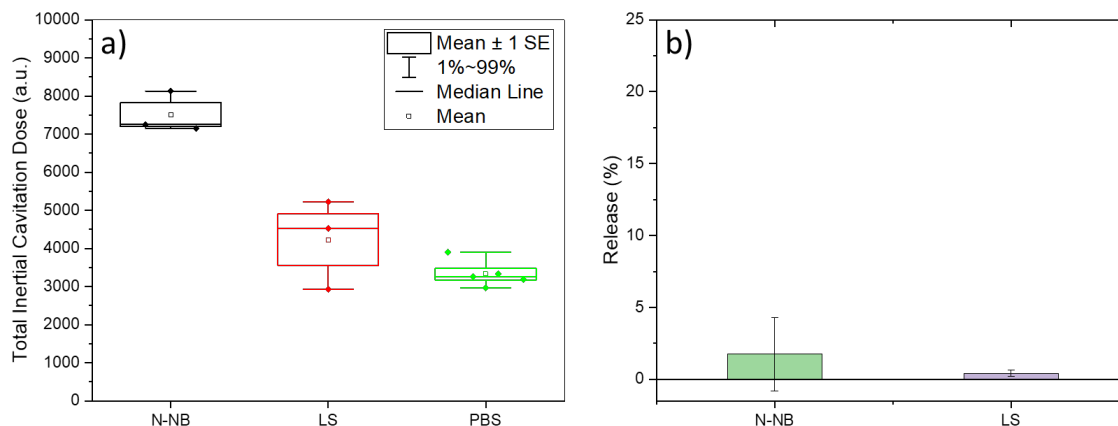


Figure 2 – a) Total Inertial Cavitation Dose of Nested-Nanobubbles (N-NBs), Liposome only controls (LS) and PBS buffer. b) Measured Calcein release for N-NBs and LS after HIFU exposure.

Conclusion

Encapsulation of Nanobubbles within model drug-loaded liposomes has been achieved, with Nested-Nanobubbles demonstrating echogenicity at clinical frequencies. During HIFU exposure, Nested-Nanobubbles experience inertial cavitation characterised by passive cavitation detection and B-mode imaging. However, no model drug release was observed suggesting that the shear forces produced by nanobubble inertial cavitation are insufficient to trigger liposome membrane poration.

References

- [1]. Shapiro, C.L., and A. Recht. 2001. Side Effects of Adjuvant Treatment of Breast Cancer. *N. Engl. J. Med.* 344: 1997–2008.
- [2]. Klibanov, A.L., T.I. Shevchenko, B.I. Raju, R. Seip, and C.T. Chin. 2010. Ultrasound-triggered release of materials entrapped in microbubble-liposome constructs: A tool for targeted drug delivery. *J. Control. Release.* 148: 13–17.
- [3]. Wu, G., J.A. Zasadzinski, A. Mikhailovsky, H.A. Khant, C. Fu, and W. Chiu. 2008. Remotely triggered liposome release by near-infrared light absorption via hollow gold nanoshells. *J. Am. Chem. Soc.* 130: 8175–8177.
- [4]. Kooiman, K., M. Foppen-Harteveld, A.F.W. Van Der Steen, and N. De Jong. 2011. Sonoporation of endothelial cells by vibrating targeted microbubbles. *J. Control. Release.* 154: 35–41.
- [5]. van Rooij, T., I. Skachkov, I. Beekers, K.R. Lattwein, J.D. Voorneveld, T.J.A. Kokhuis, D. Bera, Y. Luan, A.F.W. van der Steen, N. de Jong, and K. Kooiman. 2016. Viability of endothelial cells after ultrasound-mediated sonoporation: Influence of targeting, oscillation, and displacement of microbubbles. *J. Control. Release.* 238: 197–211.
- [6]. Lentacker, I., I. De Cock, R. Deckers, S.C. De Smedt, and C.T.W. Moonen. 2014. Understanding ultrasound induced sonoporation: Definitions and underlying mechanisms. *Adv. Drug Deliv. Rev.* 72: 49–64.
- [7]. Fix, S.M., M.A. Borden, and P.A. Dayton. 2015. Therapeutic gas delivery via microbubbles and liposomes. *J. Control. Release.* 209: 139–149.
- [8]. Peyman, S.A., R.H. Abou-Saleh, J.R. McLaughlan, N. Ingram, B.R.G. Johnson, K. Critchley, S. Freear, J.A. Evans, A.F. Markham, P.L. Coletta, and S.D. Evans. 2012. Expanding 3D geometry for enhanced on-chip microbubble production and single step formation of liposome modified microbubbles. *Lab Chip.* 12: 4544.
- [9]. Malik, R., K. Pancholi, and A. Melzer. 2016. Microbubble–liposome conjugate: Payload evaluation of potential theranostic vehicle. *Nanobiomedicine.* 3: 1–8.
- [10]. Yan, F., L. Li, Z. Deng, Q. Jin, J. Chen, W. Yang, C.K. Yeh, J. Wu, R. Shandas, X. Liu, and H. Zheng. 2013. Paclitaxel-liposome-microbubble complexes as ultrasound-triggered therapeutic drug delivery carriers. *J. Control. Release.* 166: 246–255.
- [11]. 2004. On spray formation. *J. Fluid Mech.* 498: 73–111.
- [12]. Unger, E.C., T. Porter, W. Culp, R. Labell, T. Matsunaga, and R. Zutshi. 2004. Therapeutic applications of lipid-coated microbubbles. *Adv. Drug Deliv. Rev.* 56: 1291–1314.

- [13]. Chen, W.S., A.A. Brayman, T.J. Matula, and L.A. Crum. 2003. Inertial cavitation dose and hemolysis produced in vitro with or without Optison®. *Ultrasound Med. Biol.* 29: 725–737.
- [14]. Tomita, Y., T. Matsuura, and T. Kodama. 2015. Temporal effect of inertial cavitation with and without microbubbles on surface deformation of agarose S gel in the presence of 1-MHz focused ultrasound. *Ultrasonics*. 55: 1–5.
- [15]. Peyman, S.A., J.R. McLaughlan, R.H. Abou-Saleh, G. Marston, B.R.G. Johnson, S. Freear, P.L. Coletta, A.F. Markham, and S.D. Evans. 2016. On-chip preparation of nanoscale contrast agents towards high-resolution ultrasound imaging. *Lab Chip*. 16: 679–687.
- [16]. Wu, H., E.C. Abenojar, R. Perera, A.C. De Leon, T. An, and A.A. Exner. 2019. Time-intensity-curve Analysis and Tumor Extravasation of Nanobubble Ultrasound Contrast Agents. *Ultrasound Med. Biol.* 00.
- [17]. Stoddard, R. J. & Arielle, L. Mechanisms of microbubble-facilitated sonoporation for drug and gene delivery Therapeutic. *Ther. Deliv* 7, 117–138 (2016).
- [18]. Nie, L., J.R. McLaughlan, D.M.J. Cowell, T.M. Carpenter, and S. Freear. 2018. Subharmonic Plane Wave Imaging of Liposome-Loaded Microbubbles. *IEEE Int. Ultrason. Symp. IUS*. 2018-Janua.
- [19]. McLaughlan, J.R., D.M.J. Cowell, and S. Freear. 2018. Gold nanoparticle nucleated cavitation for enhanced high intensity focused ultrasound therapy. *Phys. Med. Biol.* 63

Effect of lipid handling on phase behavior and ligand distribution in targeted microbubbles

Simone A.G. Langeveld¹, Christian Schwieger^{2,3}, Inés Beekers¹, Tom van Rooij¹, Alfred Blume², Klazina Kooiman¹

¹Department of Biomedical Engineering, Erasmus MC, Rotterdam, the Netherlands

²Department of Physical Chemistry, Martin Luther University Halle-Wittenberg, Halle, Germany

³Institute for Biochemistry and Biotechnology, Martin Luther University Halle-Wittenberg, Halle, Germany

Corresponding author: s.a.g.langeveld@erasmusmc.nl

Introduction

Phospholipid-coated targeted microbubbles are ultrasound contrast agents that can be used for molecular imaging and localized drug delivery [1,2]. However, a better understanding of the microstructures and ligand distribution in the microbubble coating is needed to elucidate the underlying mechanisms of targeting. Here we investigated the lipid phase behavior and the ligand distribution in microbubbles of clinically relevant sizes, coated with a ternary mixture of phospholipids and emulsifiers. Furthermore we investigated the effect of lipid handling prior to microbubble production. In addition, phospholipid monolayer experiments at the air/water interface were performed to study the phase behavior of the individual components and the ternary mixtures used as microbubble coating.

Methods

Monolayer experiments at the air/water interface were performed using a Langmuir trough to obtain surface pressure/area isotherms of ternary mixtures containing DPPC or DSPC (59.4 mol%), PEG-40 stearate (35.7 mol%), DSPE-PEG2000 (4.9 mol%, of which 16% contains a biotin label for conjugation of a ligand). Rhodamine-DHPE (0.01 mol%), which stains the liquid expanded (LE) phase [3], was added to the ternary mixtures for all experiments. Infrared (IR) spectra of the monolayers were recorded in external reflection mode (IRRAS) to investigate the phase behavior of the individual components in the mixture. Microbubbles coated with the same ternary mixtures and a C₄F₁₀ gas core were made by probe sonication as described previously [4,5]. Before sonication the components were either dispersed directly in PBS (*direct method*; for both DSPC and DPPC-based microbubbles), or dissolved in chloroform:methanol (9:1), dried, and then dispersed in PBS (*indirect method*; for DSPC-based microbubbles). In order to visualize the ligand distribution, microbubbles were conjugated with streptavidin-Oregon Green 488, which binds to the biotinylated DSPE-PEG2000 in the coating. High-axial-resolution 4Pi microscopy was used to image the lipid phase and ligand distribution in the microbubble coating.

Results

The Langmuir monolayer experiments showed that pure DPPC transitioned from LE phase to liquid condensed (LC) phase, while pure DSPC was always in LC phase. All ternary mixtures had an additional transition plateau around 12 mN/m. IRRAS experiments confirmed that for the DPPC-based ternary mixture there was one transition due to DPPC (LE to LC) and a second transition at ~ 12 mN/m due to the PEGylated components (mushroom to brush state), whereas for the DSPC-based ternary mixture there was only one transition at ~ 12 mN/m, which was due to the PEGylated components. The morphology of the LC phase domains was different in the monolayers at the air/water interface of DPPC and DSPC ternary mixtures, while this was similar in microbubbles coated with DPPC- and DSPC-based ternary mixtures (Figure 1, top row). The direct DPPC-based microbubbles had the smallest total LC phase area. The ligand distribution was homogenous as illustrated in Figure 1E, which is in concurrence with our previous study [5]. Lipid handling influenced the lipid phase and ligand distribution for DSPC-based microbubbles.

Direct DSPC-based microbubbles had less LC phase area than indirect DSPC-based microbubbles, with less defined ligand distributions varying from heterogeneous (Figure 1F) to homogenous (Figure 1G), and the ligand co-localized with the LE phase area. Indirect DSPC-based microbubbles had the largest LC phase area with homogenous ligand distribution (Figure 1H).

Conclusions

These results indicate that lipid handling prior to microbubble production can affect the lipid phase and ligand distribution in the coating. The indirect method resulted in microbubbles with a more homogenous ligand distribution, which is expected to improve the targeting efficiency. By controlling these features, we can further study the underlying mechanism of targeting microbubbles. This will lead to custom-made microbubble formulations for specific clinical applications.

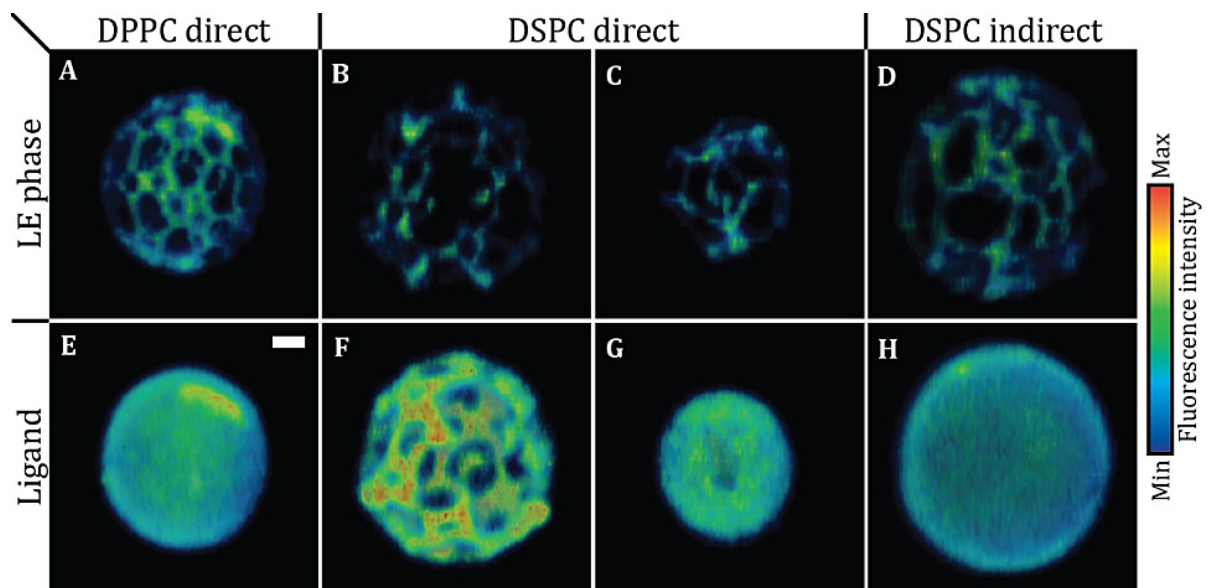


Figure 1. Selected views of 4Pi microscopy z-stacks, 3D rendered using AMIRA software, of direct DPPC (A, E), direct DSPC (B, C, F, G) and indirect DSPC (D, H) microbubbles. Scale bar is 1 μ m. Images show the LE phase (A-D, Rhodamine-DHPE) and ligand distribution (E-H, Oregon Green 488).

Acknowledgements – This project was funded by the Phospholipid Research Center in Heidelberg, Germany.

References

- [1]. Van Rooij T, Daeichin V, Skachkov I, de Jong N, Kooiman K, Targeted ultrasound contrast agents for ultrasound molecular imaging and therapy. *Int. J. Hyperthermia*, 31: 90-106, 2015.
- [2]. Roovers S, Segers G, Lajoinie G, Deprez J, Versluis M, De Smedt SC, Lentacker I, Microbubble dynamics in drug delivery: from microbubble fundamentals to clinical translation. *Langmuir*, 35: 10173-10191, 2019.
- [3]. Baumgart T, Hunt G, Farkas ER, Webb WW, Feigenson GW, Fluorescence probe partitioning between Lo/Ld phases in lipid membranes. *Biochim Biophys Acta*, 1768: 2182-94, 2007.
- [4]. Klivanov AL, Rasche PT, Hughes MS, Wojdyla JK, Galen KP, Wible JH, Brandenburger GH, Detection of Individual Microbubbles of Ultrasound Contrast Agents. *Investigative Radiology*, 39: 187-195, 2004.
- [5]. Kooiman K, Kokhuis TJA, van Rooij T, Skachkov I, Nigg A, Bosch JG, van der Steen AFW, van Cappellen WA, de Jong N, DSPC or DPPC as main shell component influences ligand distribution and binding area of lipid-coated targeted microbubbles. *Eur J Lipid Sci Tech*, 116: 1217-1227, 2014.

Towards clinically relevant therapeutic microbubbles

Nicola Ingram¹, Radwa Abou-Saleh^{2,3}, Steve Evans² and P. Louise Coletta¹

¹ School of Medicine, University of Leeds, Leeds, U.K.

² School of Physics and Astronomy, University of Leeds, Leeds, U.K.

³ Department of Physics, Faculty of Science, Mansoura University, Egypt

Corresponding author: n.ingram@leeds.ac.uk

Introduction

Current architecture for delivery of drugs using microbubbles has traditionally used biotin-avidin linkages to join the liposomally-encapsulated drug to the microbubble. In addition, antibody-targeted microbubbles have also used the biotin-avidin linkage due to the vast array of biotinylated antibodies that can be commercially supplied. However, the use of this linkage is not currently clinically approved and therefore may delay their use in clinical trials. Therefore, the Leeds Microbubble Consortium are creating therapeutic microbubbles using the FDA-approved maleimide-thiol linkage. Here we present very simple chemistry to reduce the amount of time and effort needed to generate targeted microbubbles that retain their functionality. This study determines the efficacy of maleimide-thiol linkages in direct comparison to biotin-avidin linkages in terms of their ability to target an epitope *in vitro* and their imaging and lifetime parameters *in vivo*.

Methods

Traut's reagent is used to thiolate antibodies to generate targeted microfluidically-generated microbubbles. In addition, the linkage of a targeted drug-encapsulating liposome to the microbubble (therapeutic microbubble) was effected using very low levels of TCEP. Both these (targeted microbubbles and therapeutic microbubbles) were tested under flow for their binding properties to cells bearing target receptors.

These microbubbles were intravenously injected into mice and their imaging properties and lifetimes were compared to their biotin-avidin counterparts.

Results

Using Traut's reagent, we show how antibodies can be thiolated and that this thiolation does not disrupt their antigen recognition compared to native antibodies. We also show that these targeted microbubbles perform as well as biotin-avidin microbubbles in flow assays with a specificity of targeting ratio of 2.86 compared to 1.68 for biotin-avidin microbubbles (specificity of targeting = mean number of attached VEGFR2-targeted microbubbles per cell/ mean number of attached isotype-targeted microbubbles per cell). This was maintained when microbubbles carried a liposome encapsulating drug which showed a specificity of targeting ratio of 2.5.

We also show how these microbubbles perform as well as biotin-avidin microbubbles *in vivo* in terms of time-intensity curve parameters and longevity. Maleimide-thiol microbubbles showed similar peak enhancement to biotin-avidin microbubbles, similar longevity (full width of curve (time) at half maximum intensity) and area under the curve parameters. Maleimide-thiol microbubbles showed a slightly faster wash-in rate than biotin-avidin microbubbles.

Conclusions

Maleimide-thiol microbubbles can be simply generated and show slightly better targeting properties *in vitro* than biotin-avidin microbubbles. Their imaging and lifetime parameters *in vivo* are also very similar to biotin-avidin microbubbles. Therefore these microbubbles can be used to similar effect as biotin-avidin microbubbles with the added benefit of FDA-approval of linkages.

Acoustic characterization of antibubbles

Anastasiia Panfilova¹, Peiran Chen¹, Ruud van Sloun¹, Hessel Wijkstra^{1,2}, Michiel Postema³, Albert T. Poortinga¹, Massimo Mischi¹

¹ *Electrical Engineering Department, Eindhoven University of Technology, Eindhoven, The Netherlands*

² *Urology Department, Amsterdam UMC, location AMC, Amsterdam, The Netherlands*

³ *School of Electrical & Information Engineering, University of the Witwatersrand, Johannesburg, Braamfontein, R.S.A*

Corresponding author: A.P.Panfilova@tue.nl

Introduction

Traditional contrast agents are gas bubbles encapsulated by a shell. Their nonlinear behavior is exploited by contrast-specific ultrasound imaging to enhance the contrast-to-tissue ratio for improved analysis of the vasculature. It has been shown that adding a sufficiently large inclusion inside the gas bubble increases its nonlinear behavior [1,2]. Such bubbles with inclusions are named antibubbles. This work investigates the harmonic response of antibubbles compared to corresponding reference bubbles without a inclusion and standard Sonovue contrast agent, when insonified at frequencies of 1 and 2.25 MHz. It also presents a dynamic measurement through a vascular phantom at 3.5 MHz. With this study we aim to evaluate to what extent the nonlinear behavior of antibubbles is enhanced compared to current contrast agents.

Methods

The studied antibubbles and reference bubbles have an average size of 10 microns. Filled with air, their core is composed of ZnO, and their shell is stabilized by silica particles. They were produced in a manner similar to that described in [3].

Static measurements were conducted by positioning a gelatin cuvette with the studied contrast agents in the focal region of a piezoelectric transducer source (Fig. 1. a., Table 1) . A 20-cycle pulse was transmitted to insonify the contrast agent, and a planar piston transducer was used as a receiver in a configuration perpendicular to the source's beam propagation direction. This allowed capturing the signal generated exclusively by the contrast agents, avoiding signals from the primary beam. Several insonifying pressures were used, corresponding to mechanical indexes in the range 0.1-0.3 inside the cuvette, measured by a hydrophone (Precision Acoustics) positioned in the center of the cuvette after the acquisition. Results of 5 experiments were averaged to derive the presented harmonic responses.

Table 1. Sources and receivers used for the harmonic response measurement.

Transmit frequency, MHz	Source (diameter, focal distance, central frequency)	Planar piston receiver (diameter central frequency)
1	V302-SU-F (2.54cm, 6.35cm, 1 MHz), Olympus	C304-SU (2.54cm, 2.25 MHz), Olympus
2.25	V304-SU (2.54cm, 6.55cm, 2.25 MHz), Olympus	V307-SU (2.54cm, 5 MHz), Olympus

The dynamic measurement was performed with a Vanatge system (Versonics) equipped with a linear probe L11-4. A frequency of 3.5 MHz was transmitted, and the signal was recorded in echo-mode utilizing a combination of pulse inversion and amplitude modulation. Water was pumped through a porous vascular phantom, made of tissue mimicking beads (Fig. 1 a). Indicator dilution curves were acquired and compared for their enhancement.

Results

Antibubbles generate stronger harmonic signal compared to the corresponding contrast agents when insonified at 1 MHz and 2.25 MHz. Figure 2 shows the acquired harmonic responses for a mechanical index of 0.23. The dynamic measurement shows that the indicator dilution curves produced by antibubbles are comparable to that of Sonovue, while the reference bubbles demonstrated much lower enhancement.

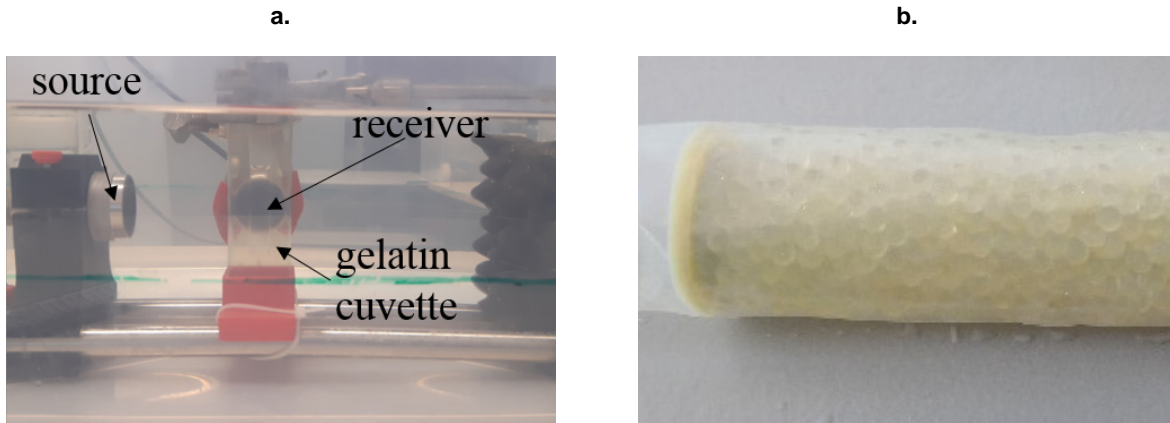


Figure 1. a, Illustration of the set up for the static measurement. b, Illustration of a part of the vascular phantom used for dynamic measurements.

Conclusions

This work demonstrates that antibubbles show strong nonlinear behavior and are therefore suitable contrast agents, especially at low frequencies. At higher frequencies, lower nonlinearity is observed. Further work involves additional experiments, adding more evidence to the current observations.

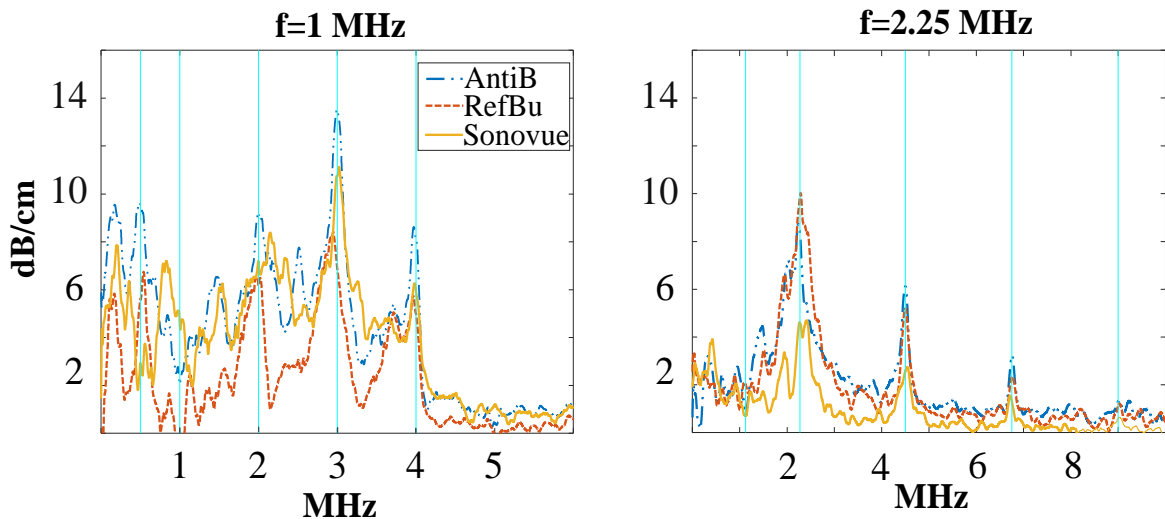


Figure 2. Acoustic response of antibubbles, reference bubbles and Sonovue when insonified at frequencies of 1 and 2.25 MHz, with mechanical index of 0.23.

References

- [1]. Kotopoulos S., Johansen K. et. al., Acta Physica Polonica A, 127: 99-102, 2015.
- [2]. Postema M., Novell A. et. al., Applied Acoustics, 13: 148-150, 2018.
- [3]. Poortinga A.T., Colloids and Surfaces A: Physicochemical and Engineering Aspects, 419: 15-20, 2013.

Theranostics with Lipid Bubbles and Ultrasound

Kazuo Maruyama¹, Tomohiro Osaki², Daiki Omata¹, Ryo Suzuki¹

¹ Faculty of Pharma-Science, Teikyo University

² Veterinary Clinical Medicine, Faculty of Agriculture, Tottori University

Corresponding author: maruyama@pharm.teikyo-u.ac.jp

The combination of microbubble and ultrasound (US) is a good tool for “Theranostics” due to have multi-potency both of imaging with enhanced echo signal from bubble and therapeutics with sonoporation of bubble. We have developed a new lipid bubble suitable for sonoporation. For good storage stability and ease of handling, lipid bubbles were made into freeze-dried formulations. Here we investigate neovascular imaging and enhancement of ERP effect by combination of lipid bubbles and ultrasound and describe a new drug delivery technology.

Methods

Lipid-stabilized bubbles (LB) were prepared by homogenization of a lipid dispersion in the presence of perfluoropropane gas (Figure 1). Doxorubicin (DOX) and LB were administered to osteosarcoma-bearing mice via tail vein. Immediately after injection, linear imaging US was exposed to solid tumor site transdermally to take the neovascular imaging. Then, therapeutic US probe was placed directly on the tumor surface and therapeutic US was exposed (2MHz, 2W/cm²). This treatment was repeated three times, on days 1, 2 and 4. DOXIL® and LB were co-administered to thyroid cancer dog and ultrasound treatment (1MHz, 2W/cm²) was done four times.

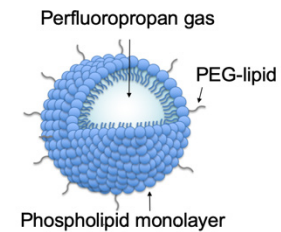


Fig.1 Illustration of lipid stabilized bubble

Results

LBs were in the size range 2-3 μm and could be preserved by freeze-drying and re-constituted by simple addition of water. LBs were well suited for imaging of blood flow in tumor. The US theranostics capabilities of LB for the solid tumor were studied in osteosarcoma-bearing mice. LB was injected to mice via tail vein and linear imaging US was exposed to solid tumor site transdermally. The flow of LB in blood was observed and neovasculature of tumor tissue was imaged clearly. Following, therapeutic US was exposed transdermally over the site of solid tumor tissue. Oscillation and cavitation of LB induced by low intensity US exposure showed transiently open the tumor blood vessels and allowing DOX co-injected with LB was delivered into deep area in the tumor tissue. This system achieved an equivalent antitumor effect at about 1/5 the dose in monotherapy of DOX. A thyroid cancer dog was administered DOXIL® and LB and ultrasonic treatment was performed four times. This cancer is a good experiment for proof of concept because it is close to human cancer from the viewpoint of spontaneous onset. From the CT image, the primary tumor volume was clearly reduced (Figure 2). In contrast, because lung metastases were not irradiated with ultrasound, no reduction was observed. From these results, it was considered that DOXIL® was efficiently delivered to the tumor tissue from the blood circulation by LB and ultrasound.

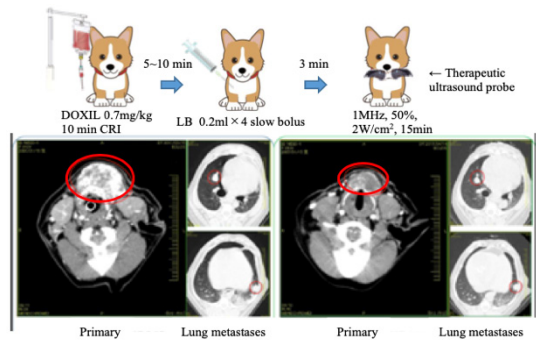


Fig.2 Antitumor effect of DOXIL+LB+US in thyroid cancer dog

Conclusions

Oscillation of LB induced by therapeutic US exposure showed transiently open the neovasculature of tumor tissue and allowing DOX or DOXIL® co-injected with LB was delivered into deep area in the tumor tissue. This new approach by the combination of LB and US could delivery medicines into tumor tissue and work better.

Reference

- [1]. Scale-up production, characterization and toxicity of a freeze-dried lipid-stabilized microbubble formulation for ultrasound imaging and therapy. J. Unga, S. Kageyama, R. Suzuki, D. Omata, K. Maruyama. *J. Liposome Res.* 2019 in press

Ultrasound-targeted microbubble destruction and Photoacoustic Tracking of Mesenchymal Stem Cells in Multiple Myeloma Model

Yajing Liu¹, and Pintong Huang¹

¹ *Department of Ultrasonography, the 2nd Affiliated Hospital of Zhejiang University College of Medicine, Hangzhou 310009, China*

Corresponding author: liuyajingyyyyy@126.com, huangpintong@zju.edu.cn

Introduction

Multiple myeloma (MM) is a disease predominantly of the elderly (median age at diagnosis, 70 years) [1]. It is the second most common hematologic malignancy. It is characterized by the proliferation of malignant plasma cells with clinical features most commonly resulting from end organ damage, including hypercalcemia, renal dysfunction, anemia, or bone lesions. MSCs are multipotent progenitor cells that can differentiate into tissue-specific cell types [2]. They are capable of migrating to tumor regions to participate in angiogenesis and metastasis of these tumors. Because of these remarkable capabilities, MSCs have recently become a platform for the emerging stem cell therapy that seeks to heal damaged tissues, alleviate inflammation responses, and treat cancers. In order to understand the role of stem cells in tumor, continuous monitoring of the distribution of stem cells, as well as interaction of the stem cells with their microenvironment, is essential.

Ultrasound targeted microbubble destruction (UTMD) plays an important role in facilitating antitumor cargo delivery and tumor uptake by microbubble cavitation. To overcome the tumor barriers, UTMD was explored in the delivery of MSCs to multiple myeloma cells. PA imaging detects ultrasound signals generated by thermal expansion of tissue after laser irradiation. By integrating fine optical focusing and advanced scanning techniques, PA microscopy (PAM) is capable of single-organelle and -cell imaging in real-time [3]. PAM is sensitive enough to capture subtle changes of disease microenvironments, including nutrition supply capillaries, drug pharmacokinetics, and local acidity. Specifically, PAM can track functional cellular or subcellular activities such as cell entanglement after labeling with different dyes at unprecedented depth, which cannot be achieved by photo-activated localization microscopy (PALM), stochastic optical reconstruction microscopy (STORM), two-photon microscopy, or confocal microscopy [4]. Herein, we use UTMD technique to facilitate the MSCs delivery and PAM platform for tracking migration of MSCs in MM model.

Methods

Synthesis

All the commercially available chemicals were obtained from J&K Scientific Ltd. The synthesis of CDA was performed following our previous literature [5]. A black precipitate was purified by silica gel column chromatography with a yield of 90%.

In vivo UTMD and PA imaging studies.

All animal studies were performed under the animal use and care regulations approved by the Second Affiliated Hospital of Zhejiang University School of Medicine. Balb/c mice were purchased from Beijing Vital River Laboratory Animal Technology (China). Tumor-bearing animal models were prepared by subcutaneously injecting multiple myeloma cells. Following UTMD, CDA labeled MSCs were intravenously injected and PA imaging was performed over 24 hours.

Results

Compared with representative prominent indocyanine green (ICG), Prussian blue (PB), and gold nanorods (GNR) [5], this probe can produce the strongest photoacoustic signal based on same mass concentration (Figure 1a-b). The results illustrated that MSCs can be monitored with PAM for tumor homing. Under 808 nm laser irradiation, CDA displayed obvious hyperthermia (from 26 to 63°C), inducing the necrosis and apoptosis of tumor cells (Figure 1c). Our result illustrated that CDA was designed as an ideal organic dye with high performing NIR photothermal property and photostability.

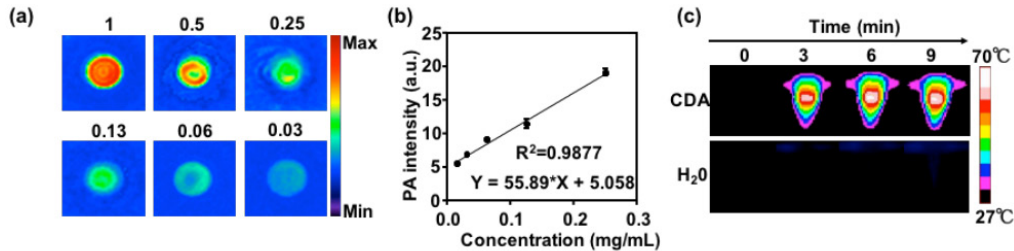


Figure 1. (a) PA imaging of CDA at different concentrations (1, 0.5, 0.25, 0.125, 0.063, 0.031 mg/mL). (b) PA signal intensity as the function of concentration. (c) Photothermal imaging of CDA and water under 808 nm laser (1 W cm⁻², 10 minutes).

Labeling MSCs with CDA for in vitro and in vivo tracking will be based on PAM (Figure 2a). The croconium dye labeled MSCs will be injected intravenously in the MM-bearing mice after UTMD. Then, migration of the MSCs to the MM region will be captured by OR-PAM (Figure 2b). Additionally, the croconium probe can also produce hyperthermia which has huge potential to ablation of tumor. Evaluating the delivery and spatial distribution of NIR dye labeled cells, followed by remote temperature mapping and monitoring, is essential to ensure the optimal therapeutic outcome.

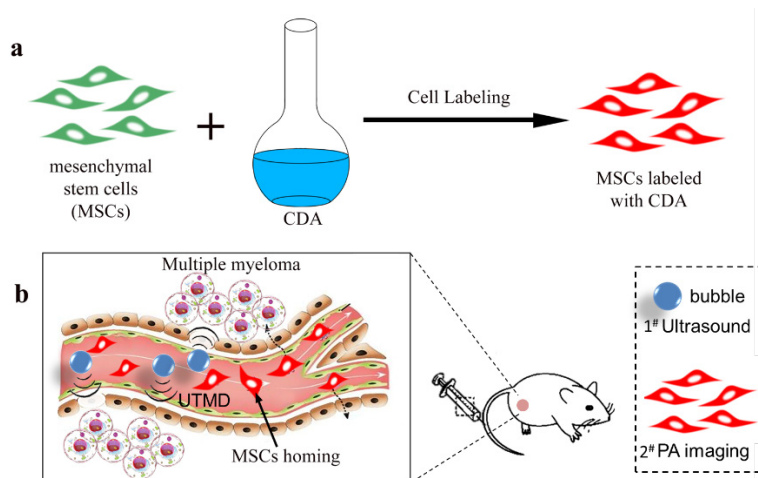


Figure 2. (a) Schematic representation of MSCs labeled with CDA dye. (b) Following ultrasound-targeted microbubble destruction (UTMD), CDA labeled MSCs were intravenously injected and PA imaging was performed.

Conclusions

Continuous tracking of the migration of MSCs is essential to understand their role in cancer. With enhanced photothermal property, effective PA response, and sensitive NIR absorption, CDA plays a very important role in tracking MSCs. Herein, we use UTMD to facilitate the MSCs to overcome the tumor barriers to reach multiple myeloma cells. Ultra-sensitive PAM is used for tracking CDA labeled MSCs at cell level and guiding photothermal therapy. Our findings will provide potential strategies for facilitating MSCs delivery with UTMD and tracking MSCs at cell level with ultra-sensitive PAM.

References

- [1]. Bergin, K., McQuilten, Z., Moore, E., Wood, E. & Spencer, A. Myeloma in the Real World: What Is Really Happening? *Clinical lymphoma, myeloma & leukemia*.
- [2]. Koike, N. et al. Tissue engineering: creation of long-lasting blood vessels. *Nature* 428, 138-139.
- [3]. Nie, L.; Chen, X., Structural and functional photoacoustic molecular tomography aided by emerging contrast agents. *Chemical Society reviews* 2014, 43 (20), 7132-70.
- [4]. Hu, S. & Wang, L. V. Optical-resolution photoacoustic microscopy: auscultation of biological systems at the cellular level. *Biophysical journal* 105, 841-847
- [5]. Liu, Y.; Yang, Y.; Sun, M.; Cui, M.; Fu, Y.; Lin, Y.; Li, Z.; Nie, L., Highly specific noninvasive photoacoustic and positron emission tomography of brain plaque with functionalized croconium dye labeled by a radiotracer. *Chem Sci* 2017, 8 (4), 2710-2716.

Trajectories Analysis before Adhesion of Microbubbles to Endothelial Cells

G. Paradossi, Barbara Cerroni, Flavia Righi Riva, Letizia Oddo, Elisabetta Tortorella, Yosra Toumia, Francesco Brasili, Fabio Domenici

*Department of Chemical Sciences and Technologies, University of Rome Tor Vergata, Rome, Italy
Corresponding author: gaio.paradossi@uniroma2.it*

Introduction

Adhesion is a key process in targeting pathological tissues with microbubbles (MBs) supporting ultrasound imaging and ultrasound mediated drug delivery. A way to target tumors is tethering endothelial cells in the upregulated vascularization of cancer tissues. This can be accomplished by introducing on the surface of MBs, the Arginine-Glycine-Aspartate, RGD, sequence [1]. Such peptide interacts with the receptors of the integrins placed on the membrane of human umbilical vein endothelial cells, HUVEC. Studies on the dynamic behavior of neutrophils or ligand-modified microparticles flowing over substrates characterized by a regular flat surface and a controlled amount and distribution of receptors have been reported in the literature [2]. In this work the stability and the trajectories of RGD modified lipid shelled MBs have been analyzed in vitro by microscopy observation during the flow through HUVEC-coated microchannels, which mimic physiological, blood stream flow conditions and present a roughness comparable to the vascular endothelium. In these conditions, MBs adhesion has dynamic features recalling the motion of neutrophils engaged near the substrate. These findings can be useful for the optimization of in vivo imaging and targeting functions.

Methods

About 10^5 cells were seeded inside the channel (400 μm x 5mm x 5 cm) of the μ -Slides I 0.4 (Ibidi, GE). The slides were turned upside-down in the incubator (HeraCell 150i, Thermo Fisher Scientific) and left in this position overnight in order to allow the cells growth and adhesion on the top side of the chamber slide. Afterwards, cells were washed three times with HEPES-BSS; the slides were then placed in the upright position under an inverted microscope (Nikon Inverted Microscope Eclipse Ti-E) equipped with a 40x long distance objective (Nikon S Plan Fluor, Florence, IT), and connected by silicon tubes (internal diameter 1.6 mm and outer diameter 3.2 mm) with Luer lock adaptors to a syringe filled with a MBs suspension in PBS (about 10^7 MB mL^{-1}) with added 10% (v/v) of the serum free growth medium.

Non-targeted MBs (plain MBs) were prepared following the procedure reported by Schneider et al. [3]. Briefly, DSPC (30 mg), DPPG-Na (30 mg), PA (6 mg) and PEG4000 (2.94 g) were dissolved in *t*BuOH (31 mL) under stirring at 82 °C. After complete dissolution the clear solution was rapidly frozen and lyophilized (freeze dryer Lio 5P, Cinquepascal, Milan, Italy). The obtained cake (25 mg) was introduced in a 10 mL glass vial. The vial was closed with a rubber stopper and SF₆ gas was flushed through a needle. MBs were reconstituted by injecting PBS (5 mL) in the vial with a needle and dispersing the powder by vigorous shaking for 20 seconds. RGD functionalized MBs, RGD-MBs, were prepared by adding the surfactant DSPE-PEG2000-Mal (4.59 mg) (2% by moles of phospholipids) to the PEG/DSPC/DPPG/PA solution in *t*BuOH at 82 °C. The thiol moiety of cyclo-RGD-Cys was coupled with the maleimide group of the new surfactant. Glossary: Palmitic acid (PA); 1,2-distearoyl-*sn*-glycero-3-phosphocolyne (DSPC), 1,2-dipalmitoyl-*sn*-glycero-3-phospho-(1'-*rac*-glycerol) (sodium salt) (DPPG-Na) and 1,2-distearoyl-*sn*-glycero-3-phosphoethanolamine-N-[maleimide(polyethylene glycol)-2000] (ammonium salt) (DSPE-PEG2000-Mal). An estimate of the RGD coupled on the MBs shell is reported in Table 1.

Table 1. RGD surface density on MBs, RGD-MBs.

Sample name	RGD: Maleimide feed ratio	RGD molecules/MB ·10 ⁶	RGD molecules/μm ² ·10 ⁵
plain MB	-	-	-
MB1	1:1	2.5±0.3	0.9±0.1
MB3	1:3	4.0±0.5	1.4±0.2
MB5	1:5	4.7±0.5	1.7±0.2
MB10	1:10	9.0±0.8	3.1±0.3

Plain MBs or RGD-MBs samples were fluxed for 10 min into the channel slide at a constant flow rate of 1.12 mL min⁻¹, corresponding in the μ-Slide I 0.4 IbiTreat chambers to a shear stress of 1 dyne cm⁻². Images of several ROIs (333x333 μm²) were captured with a 40x long distance objective (Nikon S Plan Fluor, Florence, IT). The fraction of unspecific binding by turning upside down and perfusing the microchannel slide for 10 min. with PBS and 10% (v/v) of serum free growth medium. Five different regions of interest (ROIs) were taken in order to compare the average number of adherent bubbles before and after the slide inversion. Tracking: After 90 s from the injection, fast time lapse sequences of MBs in flow were recorded for 3 min at a frequency of 100 frames s⁻¹ (100 fps). Single particle trajectories were studied with particular reference to parameters such as MBs speed, time of adhesion and RGD surface coverage on the shell. We consider MBs to be stationary (steadily or transiently) if their average speed is equal or less than 10 μm s⁻¹. This limit is dictated by the spatial and time resolution of our set up: a MB is considered steady if its velocity is lower than the speed of cells movements and MBs wobbling, i.e. 5 μm s⁻¹.

Results

RGD-MBs have shown a good ability to tether to HUVEC cells under a stream with a shear rate of 144 s⁻¹ (see Figure 1).

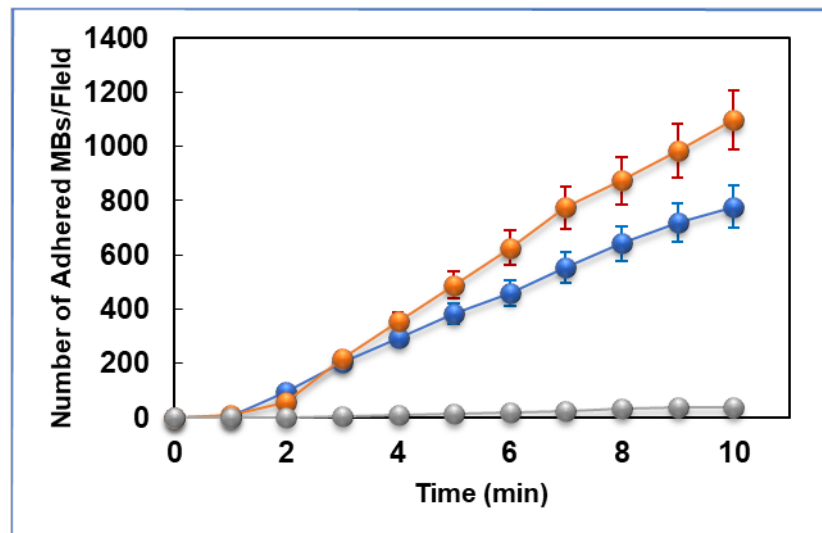


Figure 1. Adhesion of MBs with different RGD coverage (see Table 1) observed in a field 333x333 μm² during ten minutes of flow (shear stress = 1 dyne cm⁻²; hear rate = 144 s⁻¹): red, MB10; blue, MB1; green, plain MBs. MBs concentration: 1·10⁷ MBmL⁻¹

Some characteristic features are found in the dynamic behaviour of RGD-MBs and plain MBs, monitored by single particle tracking as reported in these examples (see Figure 2), when the RGD-MBs are approaching the final arrest:

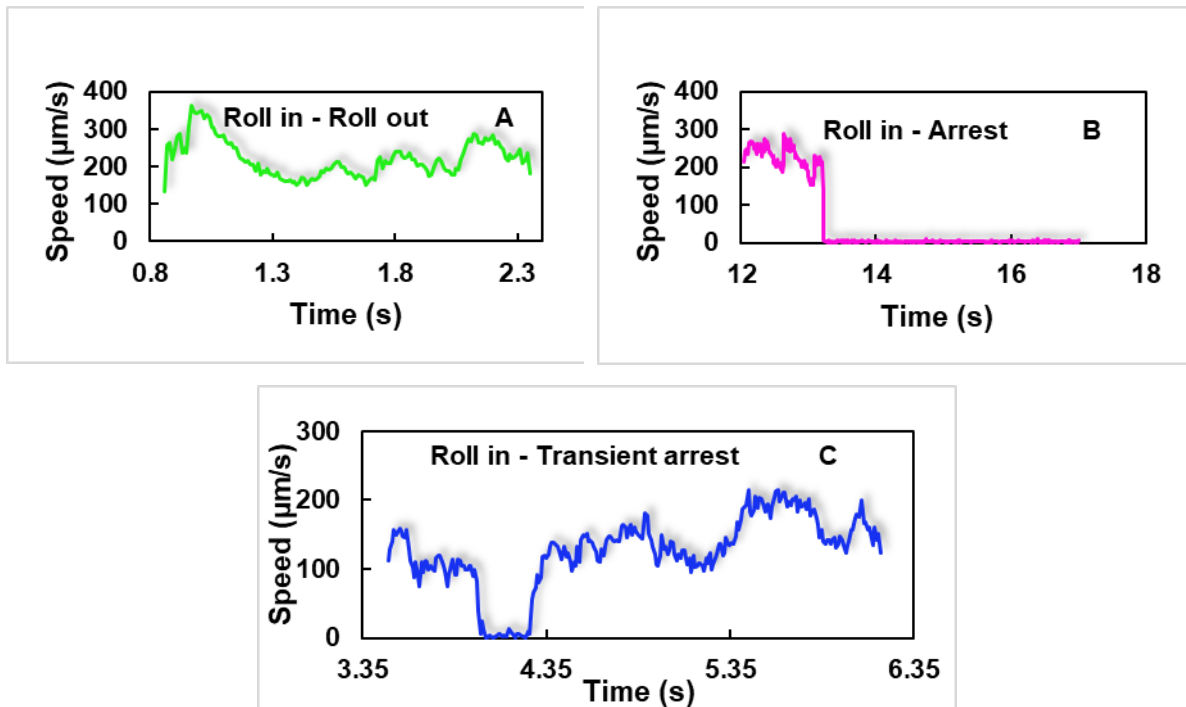


Figure 2. Examples of different trajectories of RGD-MBs in a 333x333 μm^2 field

Similar dynamic behaviour can be found also in Selectin rich neutrophils in the proximity of an artificial substrate containing receptors. The trajectories have been compared between different RGD coverages. It has been found that RGD-MBs tether to cells preferentially for short time (see Figure 3A) and that they move for short distances ($\geq 1 \mu\text{m}$) between two tethers (see Figure 3B). This behaviour is typical of the “rolling” motion found for bioadhesion of neutrophils [4]. Plain MBs interact (unspecific interactions) with the HUVEC layers in a very different way (Figure 3A, 3B).

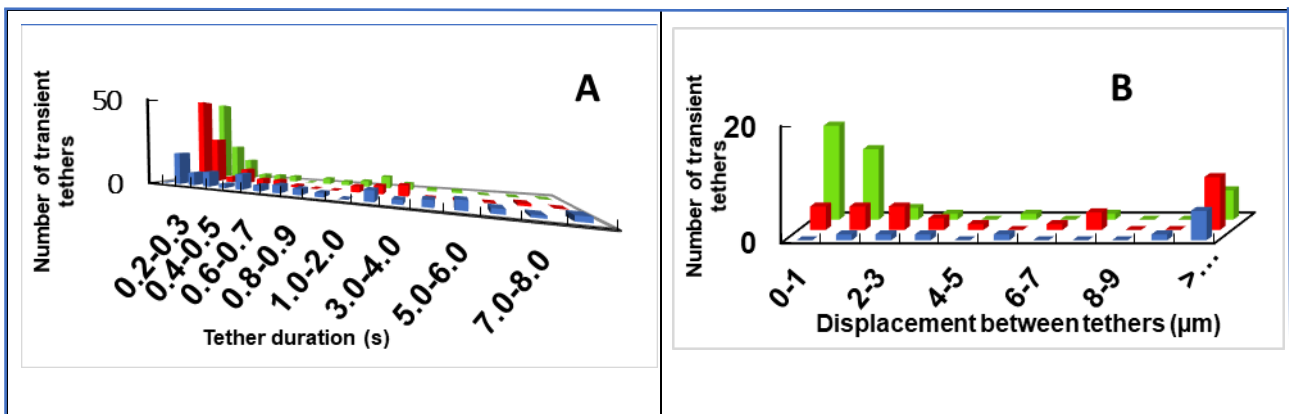


Figure 3. A: number of transient tethers observed in a field of 333x333 μm^2 as a function of the duration of each tether for different RGD surface area: blue columns, plain MBs; red columns, MB1; green columns, MB10; B: displacements separating different tethers blue columns, plain MBs; red columns, MB1; green columns, MB10

Conclusions

The trajectories of RGD-MBs show motion modalities close to a microchannel wall coated with HUVEC layers already found with neutrophils approaching the endothelial cells of a blood post capillary vessel. The findings collected in this study indicate that the adhesion of MBs, and more in general of microparticles and cells occurs with similar modalities.

References

- [1]. Pierschbacher MD, Ruoslahti E, (1984-05-03). Cell attachment activity of fibronectin can be duplicated by small synthetic fragments of the molecule 1984, Nature. 309: 30 -33, 1984.
- [2]. Alon R, Hammer DA, Springer TA, Lifetime of the P-selectin-carbohydrate bond and its response to tensile force in hydrodynamic flow, Nature 1995, 374, 539.
- [3]. Schneider M, Yan F, Lazarus D, Brochot J, Puginier J (Bracco International B.V.), USA 2008/0063603, 2008.
- [4]. Chang KC, Tees DJF, Hammer DA, The state diagram for cell adhesion under flow: Leukocyte rolling and firm adhesion, Proc. Natl. Acad. Sci. 2000, 97, 11262

Cavitation Therapy Monitoring of Commercial Microbubbles with a Clinical Scanner

Sara B. Keller, Noah Matsuyoshi, Michalakis Averkiou

Department of Bioengineering, University of Washington, Seattle, WA, USA

Introduction

Ultrasound-mediated drug delivery using microbubbles is a promising technique that can lead to enhanced local therapeutic effect or macromolecule transport. The biological mechanism is thought to be a result of cavitation events at the site of interest [1]. Depending on the desired therapeutic outcome, different types of cavitation, stable or inertial, may be preferred [2]. Both stable [3] and inertial cavitation [4] have been shown to have therapeutic efficacy; however, inertial cavitation is sometimes avoided due to the likelihood of tissue damage, e.g. when opening the blood brain barrier [5] – [7]. The goal of this work was to investigate and characterize standard microbubble formulations (Optison, Sonovue, Sonazoid, and a custom “Definity-like” agent) and compare the outcome when using the Philips EpiQ with a C5-1 curvilinear probe. We developed a novel methodology for investigating cavitation thresholds that can be used as a standard comparison between contrast agents. We further showed that these characteristics and thresholds are maintained when using a diagnostic ultrasound system for receiving cavitation data. We believe that a systematic evaluation of the frequency response of the cavitation activity of different microbubbles in order to inform real-time therapy monitoring using a clinical ultrasound device could make an immediate clinical impact.

Methods

A 1 MHz focused transducer was used as the source of cavitation excitation. A 5 MHz focused transducer or a C5-1 curvilinear probe on a Philips EpiQ was confocally aligned with the 1 MHz transducer at a 90-degree angle and used to passively acquire scattered signals. Microbubbles were added directly to the degassed water tank after sizing with a Coulter counter at a concentration of 1E4 microbubbles/mL. Waveforms were collected either on an oscilloscope for the single element transducer or RF data was extracted from the EpiQ scanner when using the imaging array.

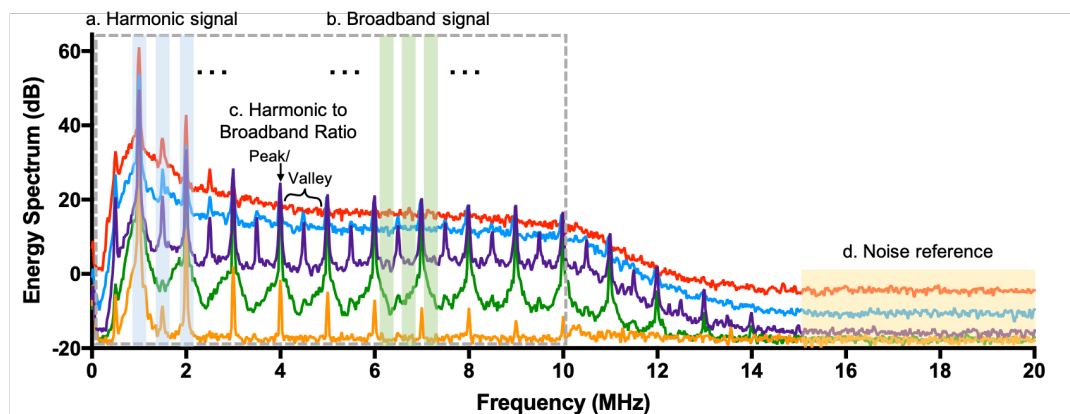


Figure 1: Analysis methods for cavitation detection. (a) average of all harmonics and ultraharmonics; (b) average of all broadband noise; and (c) ratio of harmonic peaks to valleys. The dashed line indicates the analysis frequencies. Both (a) and (b) were compared based to the respective noise references.

Each received echo was cropped and windowed with a Hamming window. A Fast Fourier Transform (FFT) was implemented on each windowed waveform. FFTs from 50 echoes were averaged, resulting in an average spectrum for each transmit pressure setting. Comb and notch filters were designed to isolate stable and inertial cavitation. The energy at these frequencies was averaged and the level above noise in

decibels was calculated. A ratio of harmonic signal to broadband cavitation signal was then calculated. This involved dividing the value of a harmonic peak by the average value of the subsequent valley, excluding any ultraharmonics. An additional requirement was that the harmonic peak be at least 20 dB above the baseline noise level, to ensure sufficient signal to noise. A ratio approaching unity indicated where broadband noise became the dominant signal component.

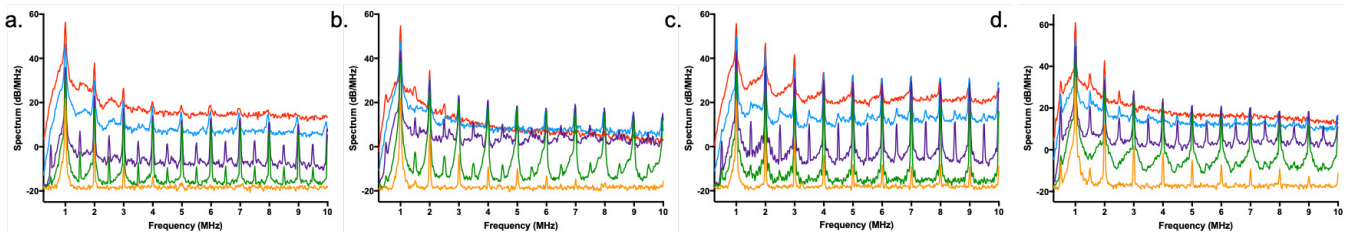
These metrics were then used as the basis for determining cavitation thresholds. Cavitation probability was defined as the number of trials (out of 50) in which the harmonic signal above noise and the broadband signal above noise were above a threshold. Thresholds were determined by fitting an exponential curve to the average data from all agents and finding the point that was a factor of e^{-1} below the plateau of the curve (63% of the peak). To determine the threshold for harmonic to broadband signal ratio, an exponential decay function was fit to the average of all agents, the point that corresponded factor of $1 - e^{-1}$ down from the y-intercept (37% of the y-intercept). A sigmoid curve was fit to the pressure versus probability data to determine the 50% crossing point, which signified the cavitation threshold.

Finally, the same process was repeated on the entire frame of RF data in Matlab. Color-based indicators were created to show stable cavitation and inertial cavitation using the same notch filters and pressure thresholds.

Results

Averaged FFTs of all microbubbles at increasing excitation pressures can be seen in Fig. 5. In (a) – (d) we show data acquired using the C308 single element receiver, while in (e) and (f) we show data acquired using the C5-1. It can be seen that with an increase in pressure, the frequency spectra also increase in magnitude, due to an increase in both harmonic power and broadband noise. Ultraharmonics also appear prominently in several midrange pressures (0.2 – 0.5 MPa) but are less obvious at the highest pressure (1 MPa), likely due to the broadband emissions of inertially cavitating microbubbles.

I. Single Element Receiver



II. Curvilinear Array Receiver

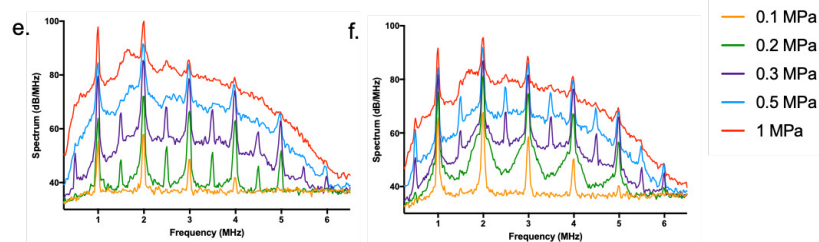


Figure 2: Average FFTs from 50 trials from four agents (a) “Definity-like”, (b) Optison, (c) Sonazoid, and (d) Sonovue taken with the C308 transducer. (e) and (f) show received pulses from the “Definity-like” agent and Sonovue, respectively taken with the C5-1.

Table 1 shows the results from the 50% crossing points calculated from the sigmoid curves. It can be seen that stable cavitation thresholds occur at low excitation pressures (0.1 – 0.2 MPa) and inertial cavitation thresholds at pressures slightly higher (0.25 – 0.35 MPa). The thresholds from the C5-1 transducer are slightly higher due to possibly the differences in frequency response. With the slight variation from the C5-1 as an exception, all thresholds are about the same.

Table 1: Cavitation thresholds of various commercial microbubbles with different receivers

C308			
	Stable Cavitation Threshold	Inertial Cavitation Threshold	Ratio Threshold
“Definity-like”	0.268	0.326	0.204
Optison	0.178	0.274	0.231
Sonovue	0.145	0.259	0.171
Sonazoid	0.186	0.362	0.390
C5-1			
	Stable Cavitation Threshold	Inertial Cavitation Threshold	Ratio Threshold
“Definity-like”	0.291	0.468	0.365
Sonovue	0.266	0.552	0.463

Fig. 3 shows image reconstruction from RF data from Sonovue scatters collected with the C5-1 and the EpiQ for 3 different pressures – 0.1, 0.2, and 1 MPa. 0.1 MPa shows no significant stable or inertial cavitation behavior, 0.2 MPa shows stable cavitation, and 1 MPa shows inertial cavitation. These thresholds are consistent with the cavitation analysis discussed above.

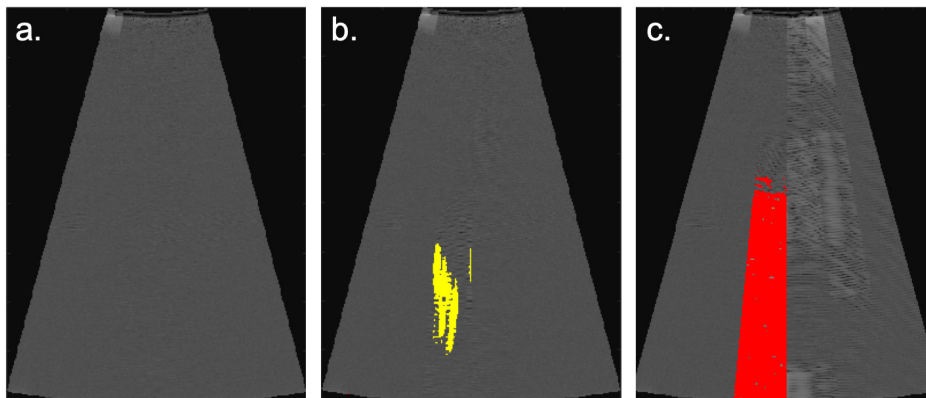


Figure 3: C5-1 data reconstructed and analyzed in Matlab. (a) was from 0.1 MPa, (b) from 0.2 MPa and (c) from 1 MPa. Yellow indicates stable cavitation and red indicates inertial cavitation.

Conclusions

The stable and inertial cavitation thresholds of commercial bubbles were measured with a stringent methodology and with both a clinical scanner and a custom single element transducer. We have shown that common commercial microbubble formulations (Sonovue, Optison, Sonazoid) in bulk solution demonstrated cavitation behavior with similar spectral content. We found that the inertial cavitation threshold of these microbubbles occurs between 0.25-0.35 MPa, consistent with prior findings. The slight variation between formulations may be due to differences in overall particle size, shell properties and dispersity. More importantly, we have shown that a diagnostic ultrasound device may be used as a passive cavitation detector and can identify cavitation behavior in real-time. The use of a commercial scanner as a passive cavitation detection device opens many opportunities in guiding therapeutic ultrasound procedures such as microbubble-mediated drug delivery and thermal ablation. Future work in this area will be to incorporate spatial localization of cavitation signals with a clinical scanner.

References

- [1]. K. Ferrara, R. Pollard, and M. Borden, "Ultrasound Microbubble Contrast Agents: Fundamentals and Application to Gene and Drug Delivery," *Annu. Rev. Biomed. Eng.*, vol. 9, pp. 415–47, 2007
- [2]. I. Lentacker, I. De Cock, R. Deckers, S. C. De Smedt, and C. T. W. Moonen, "Understanding ultrasound induced sonoporation: Definitions and underlying mechanisms," *Adv. Drug Deliv. Rev.*, vol. 72, pp. 49–64, 2014
- [3]. N. McDannold, N. Vykhodtseva, and K. Hynynen, "Targeted disruption of the blood–brain barrier with focused ultrasound: association with cavitation activity," *Phys. Med. Biol.*, vol. 51, no. 4, pp. 793–807, Feb. 2006
- [4]. D. E. Goertz et al., "Antitumor Effects of Combining Docetaxel (Taxotere) with the Antivascular Action of Ultrasound Stimulated Microbubbles," *PLoS One*, vol. 7, no. 12, p. e52307, Dec. 2012
- [5]. Y.-S. Tung, J. J. Choi, B. Baseri, and E. E. Konofagou, "Identifying the Inertial Cavitation Threshold and Skull Effects in a Vessel Phantom Using Focused Ultrasound and Microbubbles," *Ultrasound Med. Biol.*, vol. 36, no. 5, pp. 840–852, May 2010
- [6]. D. McMahon, C. Poon, and K. Hynynen, "Evaluating the safety profile of focused ultrasound and microbubble-mediated treatments to increase blood-brain barrier permeability," *Expert Opin. Drug Deliv.*, vol. 16, no. 2, pp. 129–142, Feb. 2019
- [7]. S. Xu et al., "Correlation Between Brain Tissue Damage and Inertial Cavitation Dose Quantified Using Passive Cavitation Imaging," *Ultrasound Med. Biol.*, vol. 45, no. 10, pp. 2758–2766, Oct. 2019

Cell death dynamics after calcium delivery via sonoporation

Martynas Maciulevicius, Sonam Chopra, Baltramiejus Jakstys, Diana Navickaite, Saulius Satkauskas

*Biophysical Research Group, Vytautas Magnus University, Kaunas, Lithuania
Corresponding author: Martynas.Maciulevicius@vdu.lt*

Introduction

Sonoporation is a biophysical technique, developed with the aim to achieve spatio-temporally controllable therapeutic agent delivery of to cells and tissues. The mechanism behind sonoporation is related to transient cell membrane permeabilisation, facilitated by ultrasound (US) assisted microbubble (MB) cavitation. Increased cell membrane permeability is exploited for the intracellular delivery of membrane impermeable bioactive compounds (anticancer drugs, DNA, RNA). The combination of sonoporation and anticancer drugs has already been successfully applied in clinical practice for the treatment of pancreatic tumours [1]. Recently, intracellular calcium ion (Ca^{2+}) delivery using sonoporation has been suggested to be alternative strategy, compared to anticancer drug use. Calcium in combination with sonoporation may decrease potential side-effects, caused by cytotoxic drugs while sustaining sufficient tumour treatment efficiency.

Calcium ion distribution within the cell interior reservoirs plays a key role in cell response to external stress conditions as well as regulation of cell lethal processes. The significance of calcium has also been already elucidated in membrane pore/ wound resealing after US treatment [2]. Thus, in the current study we aimed to investigate the influence of different CaCl_2 concentration on cell membrane permeability and cell viability after sonoporation.

Methods

Sonovue MB scattered US signals were recorded using passive cavitation detection system in order to provide information about MB sonodestruction dynamics.

Chinese hamster ovary cells were sonoporated with different CaCl_2 concentrations using Sonovue MBs. Propidium iodide (PI) was used as a permeability marker in order to evaluate cell membrane integrity. Cells were sonoporated using 1 MHz central frequency, 1 kHz pulse repetition frequency, 10 % duty cycle (100 μs on), 400 kPa peak negative acoustic pressure US and 6 s exposure duration. The experiments were performed using different CaCl_2 concentrations (0, 1, 5, 10, 20 mM) and different PI administration time after sonoporation (30, 60, 90, 180 min). Cell viability after 6 days was evaluated using cell clonogenic assay.

Results

MB side-scattering signals we used for root mean square (RMS) calculation in different frequency ranges. In all the frequency ranges tested MB side scattering RMS decreases to ~ 0 V background level within 3 s (Fig. 1), indicating complete MB sonodestruction. Thus, the adjusted exposure duration of 6 s is sufficient for maximal sonoporation efficiency.

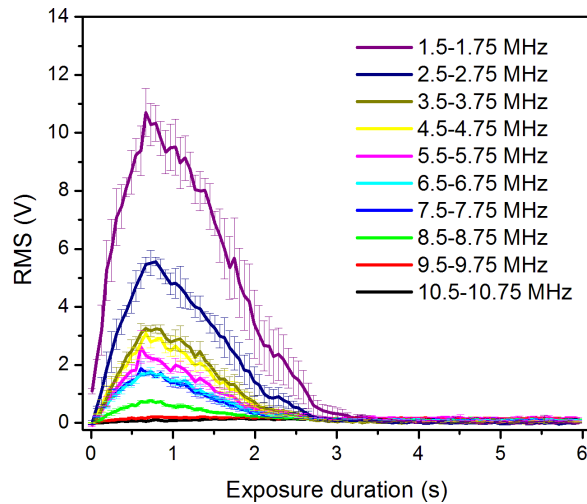


Figure 1. RMS dynamics of Sonovue MB side-scattering signal, evaluated at different frequency ranges

The sonoporation results show that MB without US or MB and Ca^{2+} (20 mM) coadministration without US as well as cell exposure to US in the presence of Ca^{2+} (20 mM) have only insignificant effect to cell membrane permeabilisation (evaluated by PI fluorescence) (Fig. 2). US assisted MB cavitation (0 mM Ca) increases membrane permeabilisation to ~25-46%, while increasing Ca^{2+} concentration to 5 mM leads to ~60% permeabilisation, that is similar at higher Ca^{2+} concentrations. The measurements, performed at different PI administration times, indicate Ca^{2+} -MB-US assisted membrane permeabilisation to reach the state of maximal permeability within 30 min with no significant increase. The latter result suggests rapid distribution of highly diffusible calcium ions within the cell interior eventually leading to directly or indirectly induced cell membrane permeability increase.

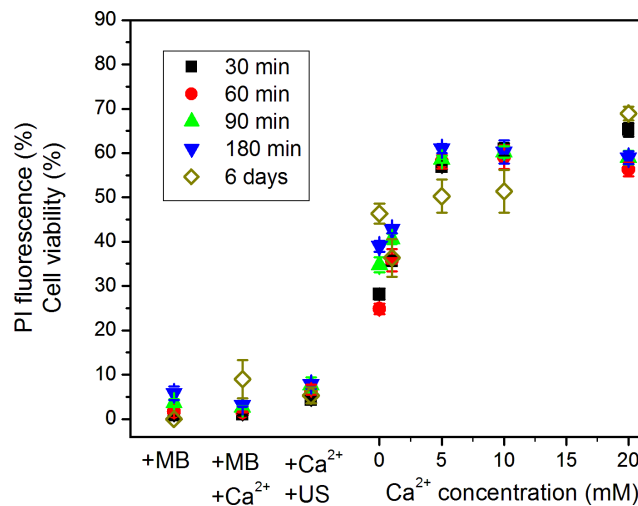


Figure 2. Cell membrane permeability, evaluated at different time after sonoporation, and cell viability for different experimental groups. “+MB” indicates cell exposure to MB without US; “+MB+Ca²⁺” indicates cell exposure to MB and Ca²⁺ (20 mM) without US; “+Ca²⁺+US” indicates cell exposure to US in the presence of Ca²⁺ (20 mM); other points indicate cell exposure to MB and US at different Ca²⁺ concentrations. The first four symbols indicate different PI administration time after sonoporation, the last symbol indicates cell viability results, obtained using cell clonogenic assay.

The results of cell clonogenic assay show that MB-US application with the presence of 1-20 mM Ca concentrations after 6 days leads to cell death of ~50-68 %. This indicates that cells, permeabilised within 30 min, die after 6 days. The latter finding implies instant cell death to be dominant in sonoporation with no additional cell death occurring within 6 days. This phenomenon is in contrast to electroporation, where there is a significant difference between the percentage of instantly permeabilised cells, evaluated using

PI, and dead cells, evaluated using clonogenic assay. Electroporation results indicate significantly higher cell death compared to cell permeabilisation results [3]. Altogether these findings define different mechanisms behind cell permeabilisation/ death after sonoporation and electroporation.

Conclusions

The results, obtained in the current study, indicate instantly occurring cell death after calcium sonoporation (within 30 min) with no additional cell death observed within 6-day period.

Acknowledgements

This work was supported by the grant (DOTSUT – 09.3.3-LMT-K-712-01-0188) from the Research Council of Lithuania.

References

- [1]. Kotopoulos S, Dimcevski G, Gilja OH, Hoem D, Postema M. Treatment of human pancreatic cancer using combined ultrasound, microbubbles, and gemcitabine: a clinical case study. *Medical Physics*, 40: 072902, 2013.
- [2]. Schlicher RK, Radhakrishna H, Tolentino TP, Apkarian RP, Zarnitsyn V, Prausnitz MR. Mechanism of intracellular delivery by acoustic cavitation. *Ultrasound in Medicine and Biology*, 32:915-24, 2006.
- [3]. Jakštys B, Ruzgys P, Tamošiūnas M, Šatkauskas S. Different cell viability assays reveal inconsistent results after bleomycin electrotransfer in vitro. *Journal Membrane Biology*, 248: 857-63, 2015.

An in-vitro study comparing sonothrombolytic efficacy of acoustically activated perflutren nanodroplets with perflutren microbubbles

***S. El Kadi*^{1,2}, *L. Qian*^{2,3}, *P. Zeng*², *J. Lof*², *E. Stolze*², *F. Xie*², *O. Kamp*¹, *A.C. van Rossum*¹, *T. Porter*²**

¹*Department of Cardiology, Amsterdam UMC – Location VUmc, Amsterdam, The Netherlands*

²*Department of Cardiovascular Medicine, University of Nebraska Medical Center, Omaha, United States*

³*Department of Cardiology, the first affiliated hospital of Nanjing Medical University, Nanjing, China*

Corresponding author: tr.porter@unmc.edu

Introduction

Diagnostic ultrasound transducers have been used in combination with commercially available microbubbles to dissolve arterial thrombi. The occurrence of stable and inertial cavitation is thought to create powerful microstreaming and shear stress around the thrombus, resulting in erosion and ultimately sonothrombolysis [1, 2]. Microbubbles serve as cavitation nuclei, lowering the threshold of acoustic pressures needed for the occurrence of both stable and inertial cavitation [3]. Recently, sub-micron sized liquid nanodroplets have gained attention as novel contrast agents. These droplets typically contain liquid perfluorocarbons with low boiling points and can be preserved in a superheated condition without vaporization. When exposed to threshold acoustic pressures, the droplets transform into gaseous microbubbles with 3-5 times the original diameter [4]. This controlled, non-invasive way to create microbubbles has been termed acoustic droplet vaporization (ADV). The small diameter of the nanodroplets can potentially lead to improved thrombus penetration. Local activation of the accumulated nanodroplets within the thrombus and subsequent cavitation may result in better thrombus dissolution. The main aim of this study is to investigate the potential of sonothrombolysis using perfluorocarbon nanodroplets and compare the efficacy with microbubbles, using an established in-vitro experimental set-up.

Methods

Arterial whole blood samples were taken from different pigs and mixed with 2 IU/mL thrombin before injection in T-connectors. A vascular mimicking system was used consisting of an acyclic water-filled tank and tubing with an internal diameter of 2.6 mm. Phosphate-buffered saline (37°C) was pumped through the flow system at a rate of 10ml/min. A T-connector was placed in conjunction with the tubing at the center of the flow system, with one side serving as the thrombosed vessel and the other side as a bypass vessel. A tissue mimicking phantom was placed on top of the T-connector to simulate transthoracic attenuation. A diagnostic ultrasound transducer (S5-1, Philips) was used to emit intermittent high mechanical index impulses in real-time imaging (56-Hz frame rate, 1.3-MHz center frequency, 3.4 MHz received frequency, 3- μ s pulse, ultraharmonic mode or fundamental mode 1.8MHz center frequency and 1.8MHz received frequency).

Three treatment groups were defined: 10% Definity nanodroplets (DND) with intermittent high mechanical index (HMI) ultrasound, 10% Definity microbubbles (DMB) with intermittent HMI ultrasound, and saline only. Preparation of the solution has been described previously [5]. Infusion rate was 1mL/min. In the DMB and DND group, both single pulse harmonic and multipulse fundamental HMI ultrasound were utilized.

Thrombus dissolution was measured by weighing the T-connectors before and after treatment. Change in thrombus mass before and after treatment was analyzed using paired t-testing. ANOVA was used to compare the different treatment strategies.

Results

A total of 18 porcine arterial thrombi were tested, 6 in each group. T-connector weight did not differ between the groups ($p= 0.83$).

Thrombus weight before treatment did not differ significantly between the groups ($p= 0.33$).

Overall, there was significant difference in thrombus dissolution between DND treated thrombi, DMB treated thrombi and control group ($p=0.01$, fig. 1).

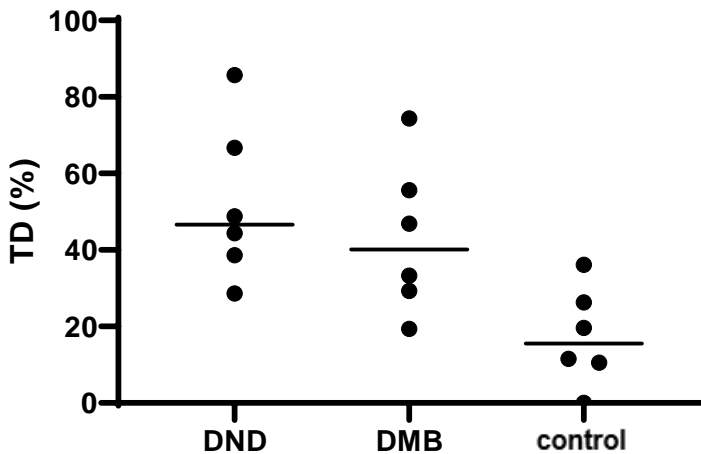


Figure 1: Percentage thrombus dissolution per treatment group

When compared to the control group, the DND with ultrasound treated group had significantly more thrombus dissolution ($p=0.01$). The DMB treated group tended to have better thrombus dissolution compared with control ($p=0.06$). Cross sectional and side view images after treatment with saline and DND are shown in figure 2.

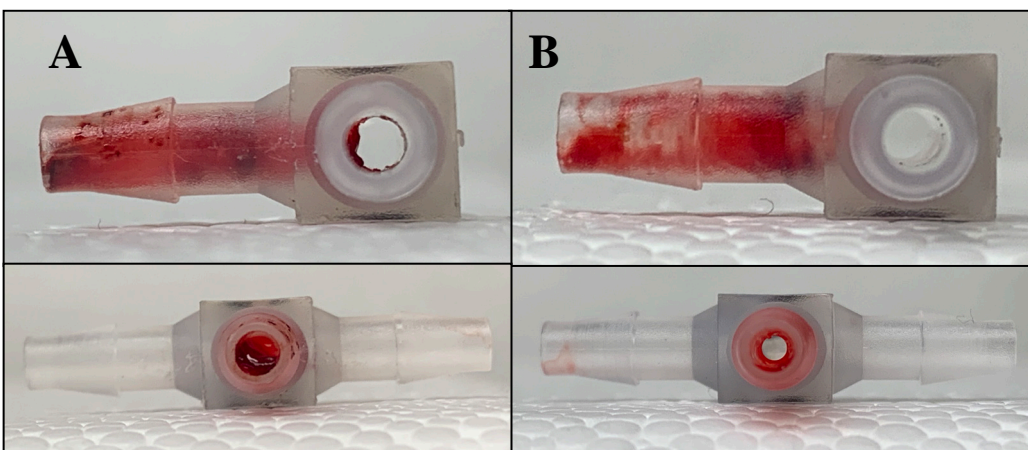


Figure 2: A: T-connector with residual thrombus after control treatment (saline). B: T-connector with residual thrombus after sonothrombolysis with DND.

Conclusions

Acoustically activated Definity nanodroplets with high mechanical index ultrasound is capable of thrombus dissolution. Further work is needed to identify optimal high MI cavitation schemes and whether droplets can permeate thrombus better than microbubbles.

References

- [1]. Weiss, H.L., et al., Mechanical clot damage from cavitation during sonothrombolysis. *J Acoust Soc Am*, 2013. 133(5): p. 3159-75.
- [2]. Chen, X., et al., New insights into mechanisms of sonothrombolysis using ultra-high-speed imaging. *Ultrasound Med Biol*, 2014. 40(1): p. 258-62.
- [3]. Holland, C.K. and R.E. Apfel, Thresholds for transient cavitation produced by pulsed ultrasound in a controlled nuclei environment. *J Acoust Soc Am*, 1990. 88(5): p. 2059-69.
- [4]. Sheeran, P.S., et al., Decafluorobutane as a phase-change contrast agent for low-energy extravascular ultrasonic imaging. *Ultrasound Med Biol*, 2011. 37(9): p. 1518-30.
- [5]. Choudhury, S.A., et al., Selective infarct zone imaging with intravenous acoustically activated droplets. *PLoS One*, 2018. 13(12): p. e0207486.

Signal intensities and velocity estimations of *in vitro* echoPIV measurements in a carotid artery stent

Astrid M. Hoving¹, Jason Voorneveld², Julia Mikhal³, Erik Groot Jebbink⁴, Johan G. Bosch², Cornelis H. Slump¹

¹*University of Twente, TechMed centre, Robotics and Mechatronics group (RaM), Enschede, The Netherlands*

²*Erasmus MC, Department of Biomedical Engineering, Thorax Center, Rotterdam, The Netherlands*

³*University of Twente, TechMed centre, BIOS Lab-on-a-chip group, Enschede, The Netherlands*

⁴*University of Twente, TechMed centre, Multi-modality medical imaging group (M3I), Enschede, The Netherlands*

Corresponding author: a.m.hoving@utwente.nl

Introduction

Patients with symptomatic carotid artery stenosis can be treated by placing a stent inside the narrowed artery. For development of stents and stenting techniques, and for follow up of patients, blood flow imaging in the stented area is useful. High-frame-rate contrast-enhanced ultrasound imaging, followed by particle image velocimetry analysis (echoPIV), enables blood flow pattern analysis inside arteries. The performance of echoPIV in the presence of a stent is not well established. In this study, *in vitro* echoPIV measurements are performed to show the effects on signal intensity and velocity estimations after stent placement.

Methods

A carotid artery stent (Wallstent, Boston Scientific, Marlborough, MA, USA) was placed halfway into a PVA-gel phantom simulating the carotid artery (diameter 7.2 mm). A 0.4 mL bolus of microbubble solution (BR-14, Bracco Imaging SpA, Milan, Italy), provided via Dr. M. Versluis (Physics of Fluids group, University of Twente) was added to 2L of continuously flowing (0.49 L/min) blood-mimicking fluid (aqueous 39mass% glycerine mixture). Five measurements were obtained using ultrafast high-frame-rate (2929 fps) ultrasound acquisitions with a linear transducer (L12-3v) on a Verasonics Vantage 256 system (Verasonics Inc., Kirkland, WA, USA). The protocol consisted of three angled 9 MHz plane wave transmissions, which were coherently compounded after SVD-based filtering. Image intensities in dB were obtained in small regions of interests (ROIs) inside and outside the stent (Figure 1A) and were obtained relative to the maximal intensity per acquisition. Particle image velocimetry (PIV) was applied on the first 100 frames of each measurement, using two iterative interrogation areas of 32×32 pixels and 16×16 pixels with an overlap of 75%. The PIV-results were split in two parts, one region outside the stent and one region in the stent. Expected mean and peak velocity values in the stented region were calculated with the non-stented region as reference value. Velocities were expected to be lower in the stented region, since the vessel diameter was enlarged to 7.8 mm due to the expanding force of the stent.

Results

Five acquisitions, each consisting of 250 frames, were analysed. The mean intensity in the non-stented region was higher (-22.9 dB (SD: 2.8)) than in the stented region (-24.6 dB (SD: 2.9)) (Figure 1, Table 1). Mean velocity in the stented region (22.5 cm/s) was comparable to the expected mean velocity (22.9 cm/s), but peak velocity was higher (34.4 cm/s) than expected (31.5 cm/s) (Table 1). Correlation coefficients were lower in stented regions than in non-stented regions, with mean correlation coefficients of 0.71 and 0.81, respectively (Table 1).

Conclusions

Microbubble signal intensity was lower in the stented than in the non-stented region of the phantom, although this effect was hardly visible in the B-mode images. PIV quality was not severely degraded in stented regions, as indicated by the correlation coefficients, and velocity estimations were consistent. This indicates feasibility of *in vitro* echoPIV measurements in stents. Peak velocity estimations inside the stent were different from our expectation, considering the enlarged vessel diameter, so more research into possible offset of velocity estimation caused by a stent is necessary.

1

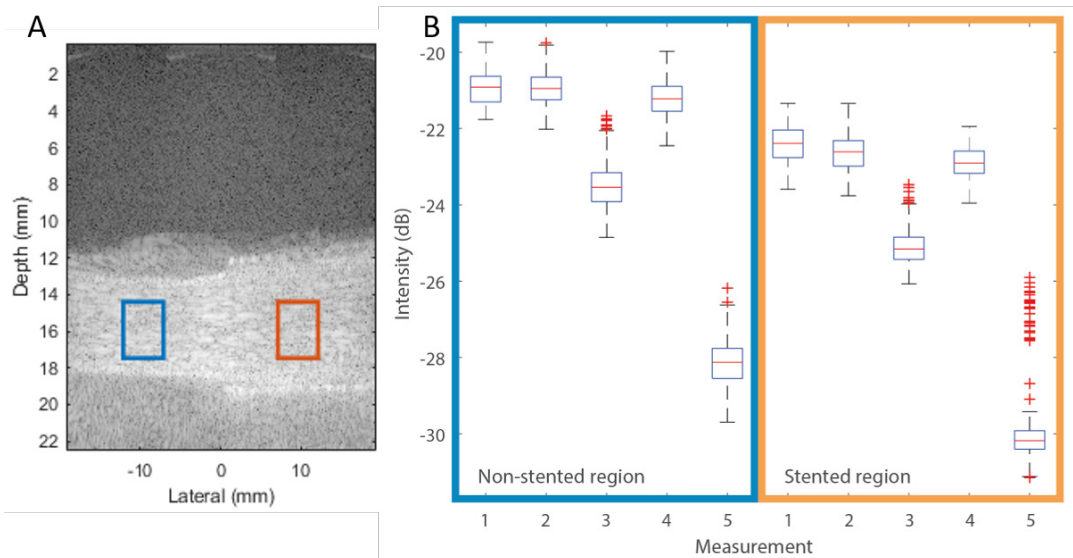


Figure 1. Time-averaged B-mode showing signal intensity in non-stented (blue) and stented (orange) regions (A). Boxplots of the intensities (relative to maximal intensity per acquisition) of non-stented region (left) and stented region (right) (B).

Measurement	Non-stented region				Stented region			
	Intensity (dB) (SD)	Mean velocity (SD) (cm/s)	Peak velocity (SD) (cm/s)	Correlation coefficient (SD)	Intensity (dB) (SD)	Mean velocity (SD) (cm/s)	Peak velocity (SD) (cm/s)	Correlation coefficient (SD)
1	-20.9 (0.4)	26.5 (9.3)	36.5 (1.3)	0.80 (0.07)	-22.4 (0.5)	21.8 (11.0)	34.0 (1.5)	0.71 (0.11)
2	-20.9 (0.4)	27.2 (8.5)	36.3 (1.6)	0.76 (0.07)	-22.6 (0.5)	22.4 (10.6)	33.7 (1.5)	0.67 (0.11)
3	-23.5 (0.7)	26.3 (10.0)	37.2 (1.3)	0.82 (0.06)	-25.1 (0.4)	22.6 (10.9)	35.0 (1.4)	0.73 (0.10)
4	-21.2 (0.5)	27.0 (9.9)	37.8 (1.3)	0.82 (0.06)	-22.9 (0.4)	22.7 (11.0)	35.2 (1.5)	0.71 (0.10)
5	-28.2 (0.6)	27.2 (9.3)	37.2 (1.0)	0.82 (0.06)	-29.9 (1.1)	22.8 (10.6)	34.2 (1.8)	0.70 (0.10)
Expected*						22.9	31.5	
Mean	-22.9 (2.8)	26.9 (9.4)	37.0 (1.4)	0.81 (0.07)	-24.6 (2.9)	22.5 (10.8)	34.4 (1.6)	0.71 (0.10)

Table 1. Intensities, velocity estimations and correlation coefficients of stented and non-stented regions.

*Expected mean and peak velocities in stented region based on the measured velocity values of non-stented region, taking the difference in vessel diameter into account. SD = standard deviation.

Developing a 3D tumor spheroid model for Ultrasound-microbubbles (USMB) mediated delivery of chemotherapy drugs

Rahul Misra¹, Raffi Karshaffian²

*Institute of Bioengineering Science & Technology (iBEST), Keenan Research Centre,
St. Michael's Hospital, Department of Physics, Ryerson University, Toronto, ON, Canada
Corresponding author: rahul.misra@ryerson.ca*

Introduction

In USMB drug delivery, the Ultrasound activated microbubbles can result in several bio-effects for facilitating drug extravasation and the cellular uptake of drugs and can produce therapeutic effects by bursting the microbubble (localized in tumors) under certain ultrasound intensity. 3D tumor spheroid model are well known for accurately reproducing the organization of a microtumor, recapitulating cell-cell and cell-microenvironment interactions. The growing tumor spheroids constitutes a rim of proliferating cells, an intermediate region of quiescent cells and a necrotic core and display a cell heterogeneity similar to microregions of a real tumor. Such spheroids are considered as bridge for filling the gap between 2D in-vitro monolayer cultured cells and animal models.

Methods

We are interested in developing such spheroids as an evaluation model for new anti-cancer strategies using ultrasound and microbubbles. We developed a size-controlled method to design MDA-MB-231 tumor spheroids (500-800 μm) suitable for USMB treatment using "Ultra-low attachment" procedure based on optimized cell density (1000-5000 cells/well) and cell aggregation (scattered, loose or compact aggregates) with real-time monitoring of growth and proliferation of each tumor spheroid through high content imaging system. These actively growing spheroids were exposed to chemo drug with and without combination of USMB. Post treatment, spheroids were imaged using live imaging microscopy and the changes in size and volume of spheroids was recorded over time using a MATLAB digital imaging code. The live and dead regions within the spheroids post-treatment was also studied using a 3D live-dead viability assay and confocal imaging.

Results

The developed 3D spheroid model is capable of showing the structural complexity close to real tumor tumor along with a clear necrotic core and proliferating rim. It highlights the significant difference in drug uptake and penetration with USMB treatment and the resultant cytotoxicity with drug uptake.

Conclusions

Currently, we are using this model to study the penetration and diffusion of drug molecules within the treated spheroids and the significance of ultrasound parameters and size of spheroids on drug diffusion. We believe this model can highlight the distribution of drug molecules within the tumor with USMB treatment and can be helpful in addressing the challenges of delivering the drugs to the necrotic regions of tumor.

References

- [1]. Denekamp J, Hobson B. Endothelial-cell proliferation in experimental tumours. *Br. J. Cancer.* 1982;46:711–720.
- [2]. Huang BW, Gao JQ. Application of 3D cultured multicellular spheroid tumor models in tumor-targeted drug delivery system research. *J Control Release.* 2018 Jan 28;270:246-259.
- [3]. De Cock I. et al, Ultrasound and microbubble mediated drug delivery: Acoustic pressure as a determinant for uptake via membrane pores or endocytosis, *JCR* 197, 2015.

High-Frame-Rate Contrast-Enhanced Ultrasound Particle Image Velocimetry in the Stented Superficial Femoral Artery

Majorie van Helvert^{1,4}, Stefan Engelhard^{1,3,4}, Jason Voorneveld², Guillaume Lajoinie³, Hendrik J. Vos², Nico de Jong², Johan G. Bosch², Erik Groot Jebbink^{1,4}, Michel Versluis³, Michel M.P.J. Reijnen^{1,4}

¹Dept. of Vascular Surgery, Rijnstate Hospital, Arnhem, The Netherlands

²Dept. of Biomedical Engineering, Thorax Center, Erasmus MC, Rotterdam, The Netherlands

³Physics of Fluids group, TechMed Centre, University of Twente, Enschede, The Netherlands

⁴Multi-modality Medical Imaging Group, TechMed Centre, University of Twente, Enschede, The Netherlands

Corresponding author: mvanhelvert@rijnstate.nl

Introduction

The influence of the local arterial microenvironment on atherosclerotic plaque formation has only recently been addressed more extensively[1]. Visualization of blood flow on a local scale could help to understand the role of complex flow patterns on the pathogenesis of vascular diseases. Hence, successful blood flow quantification may provide an important step towards the prediction of atherosclerotic disease progression and the advancement of endovascular treatment on a patient-specific level.

High-frame-rate contrast-enhanced ultrasound (HFR-CEUS) in combination with particle image velocimetry (PIV), or echoPIV, is a recent development in the field of human blood flow quantification. EchoPIV has proven its feasibility in the abdominal aorta and carotid artery in healthy volunteers[2,3]. Its applicability in patients with femoral occlusive disease, and near stented regions, has not been reported yet. Here we present preliminary data of a pilot study on the clinical feasibility of echoPIV near the femoral bifurcation and stented superficial femoral artery (SFA) in patients with femoral occlusive disease.

Methods

HFR-CEUS data was obtained in patients who had recently (<6 weeks) been treated with a stent placement in the SFA, using a linear array transducer connected to a fully programmable research US system (L11-4v transducer; Verasonics Vantage 256, Verasonics, Kirkland WA, USA). The study protocol was approved by an authorized institutional review board in the Netherlands. Patients were included after written informed consent was provided.

Measurements were performed at five different locations near the femoral bifurcation and the stented SFA. Prior to each measurement 0.75 ml of SonoVue was administered as an ultrasound contrast agent. A three-angled plane wave pulse-inversion acquisition scheme was used at 100 frames/s to visualize bubble arrival real-time. When a semi-stable bubble concentration was established, HFR-CEUS measurements were performed using a three-angled plane wave, single cycle pulse, acquisition scheme at a pulse repetition frequency of 6000 Hz. Subsequently, the image frame rate was 2000 frames/s. Images were captured for 2.5 seconds and the transmit frequency was set to 4 MHz. Two different transmitter voltages were used, resulting in mechanical indexes of 0.06 and 0.12 at the depth of interest (20-30 mm).

Vessel visibility and the contrast-to-background ratio (CBR) were evaluated as a measure of image quality. PIV analysis was performed in an iterative manner with progressive grid refinement. Four iterations of blockwise cross-correlations were calculated between each image pair. A final 32x32 (pixel) interrogation window with 75% overlap was used, corresponding to a spatial vector grid of 0.76x0.76 mm². The final correlation maps of five consecutive frames were averaged and the maximum normalized cross-correlation per window was taken to determine the velocity vectors. A 3x3 Gaussian filter was applied for spatial averaging. Finally, the median of the cross-correlation peak value was calculated over 20 consecutive frames during systole and diastole and used as a surrogate metric for the accuracy of the

PIV analysis (in absence of a ground truth). All steps regarding the PIV analysis were performed on one patient with good vessel visibility.

Results

HFR-CEUS data was successfully acquired in nineteen patients (14 male, 70%) with a median age of 71 years (IQR, 62;94). The within-patient variability in data quality and PIV performance becomes clear from Table 1 which presents the CBR and median cross-correlation values of all locations of a single patient. CBR may vary due to differences in bubble concentration, bubble disruption and calcified lesions. In general, the PIV analysis performed best on data acquired at a mechanical index of 0.12 and during diastolic flow. Furthermore, measurements with higher CBR showed higher normalized cross-correlation values.

Figure 1A represents the vector field during systole at the inflow of the stent in the SFA. The flow velocity is highest at the transition between the native and treated vessel. Visually, the contrast can be clearly observed inside the stent (white lines). However, the CBR of this area is lower, 7.6 ± 1.42 dB, compared to the CBR of the native vessel of 14.4 ± 0.5 dB. Both are calculated in contrast to the same background region, highlighted in blue in Figure 1A. The corresponding median cross-correlation value is lower as well, 0.44 compared to 0.62 inside and outside the stent, respectively. Figure 1B gives the average temporal velocity profile near the inflow of the stent in the SFA showing triphasic flow within physiological ranges. This patient showed an irregular heart rhythm which explains the high frequency and differences in peak systolic velocities.

Conclusions

Quantification of local blood flow profiles near the femoral bifurcation and stented SFA using echoPIV was feasible. CBR seems to influence the PIV analysis in terms of normalized cross-correlation values. Blood flow velocity tracking was established within physiological range in HFR-CEUS data with a high CBR. The CBR inside the stented region was lower, however, blood flow velocities could still be tracked with relatively high cross-correlation values. Nevertheless, data of only one patient is shown. All data should be analyzed to draw a thorough conclusion in the future.

Table 1. CBR and cross-correlation values of a single patient during systole and diastole.

Location	CBR (dB)*	xcorr (a.u.)		xcorr (a.u.)	
		systolic, MI = 0.06	diastolic, MI = 0.06	systolic, MI = 0.12	diastolic, MI = 0.12
CFA	8.4 ± 1.3	0.32 (0.22;0.43)	0.41 (0.32;0.51)	0.46 (0.33;0.58)	0.53 (0.40;0.64)
PFA	1.1 ± 0.7	0.10 (0.07;0.15)	0.08 (0.06;0.14)	0.19 (0.09;0.32)	0.14 (0.08;0.28)
Bifurcation	3.9 ± 0.9	0.29 (0.16;0.41)	0.48 (0.37;0.58)	0.29 (0.18;0.42)	0.22 (0.12;0.38)
Inflow stent**	11.6 ± 0.8	0.29 (0.16;0.41)	0.45 (0.34;0.57)	0.48 (0.31;0.60)	0.57 (0.47;0.65)
Outflow stent	11.5 ± 0.8	0.17 (0.10;0.27)	0.37 (0.24;0.49)	0.31 (0.21;0.42)	0.56 (0.48;0.65)

Contrast-to-background ratio (CBR), presented as mean value \pm standard deviation; and cross-correlation values (xcorr), presented as median (inter-quartile range). MI - mechanical index; CFA - common femoral artery; PFA - profunda femoral artery.

* CBR of the full vessel calculated during systole of the measurements performed at an MI of 0.12.

** PIV results of this location are presented in detail in Figure 1.

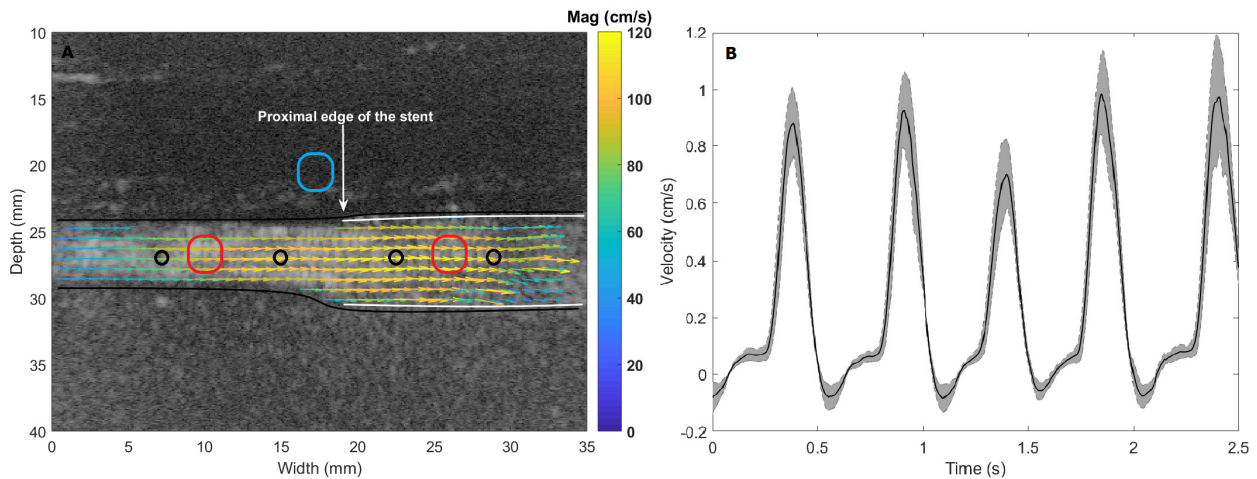


Figure 1. Particle image velocimetry results at the inflow of the stent in the SFA, measured at an MI of 0.12. (A) The velocity vector field during systole. Black lines represent the estimated delineation of the vessel wall, with the inserted stent in white. Color of the arrows represents the magnitude of the velocity vectors. Probed locations (o) of the temporal velocity profiles are given in black. Selected areas to calculate the contrast-to-background ratio are highlighted in red for vessel/contrast outside the stent (left, native vessel) and inside the stent (right, treated vessel) and in blue for tissue. (B) Average temporal velocity profile of the entire HFR-CEUS measurement. Shaded area gives the standard deviation of the measured velocities at the different probed locations.

References

- [1]. Yurdagul, A. et al. The arterial microenvironment: the where and why of atherosclerosis. *Biochemical journal*, 473(10):1281-1295, 2016.
- [2]. Engelhard, S. et al. High-frame-rate contrast-enhanced US particle image velocimetry in the abdominal aorta: first human results. *Radiology*, 289(1):119-125, 2018.
- [3]. Gates, P.E. et al. Measurement of wall shear stress exerted by flowing blood in the human carotid artery: Ultrasound doppler velocimetry and echo particle image velocimetry. *Ultrasound in medicine & biology*, 44(7):1392–1401, 2018.

Contrast-enhanced perfusion imaging in a teleost model organism, rainbow trout (*Oncorhynchus mykiss*)

Una Goncin¹, Ngoc Ton¹, Ashwin Reddy², Ahmed El Kaffas², Markus Brinkmann³, Steven Machtaler¹

¹Department of Medical Imaging, University of Saskatchewan, Saskatoon, Saskatchewan, Canada

²Department of Radiology, Stanford University, School of Medicine, Stanford, California, USA

³School of Environment and Sustainability, Toxicology Centre, University of Saskatchewan, Saskatoon, Canada

Corresponding author: ung039@usask.ca

Introduction

Fish, including zebrafish and rainbow trout, have become attractive models for studying the impact of environmental toxins/pollution on development, tumor formation, reproduction, and overall fish health [1,2]. Currently, this is no real-time, non-lethal tool used in the field to determine the effects of environmental toxins on fish organ health. The aim of this study was to determine if contrast-enhanced ultrasound (CEUS) imaging in fish could provide a real-time, functional measure of organ perfusion in response to a mock-environmental toxin. Microbubbles (MBs) are micron-sized, gas-filled contrast agents used for CEUS that have been well characterized for clinical applications in cardiology, liver, spleen, and kidney perfusion, and for molecular imaging of cancer [3,4]. However, the use of MBs in non-mammalian species has not been well documented, and there are numerous challenges that must be investigated. Fish are ectotherms, therefore all physiological functions including body temperature and heart rate are affected by ambient temperatures, which may affect blood flow and metabolic rates. Most importantly, it is unknown how MBs behave in these conditions *in vivo*, or what “normal” fish liver perfusion looks like. In this study, we investigate CEUS perfusion imaging in rainbow trout liver. Our objectives were to determine whether a reliable CEUS signal can be obtained in the liver and assess whether changes in perfusion could be measured after exposure to a common beta-blocker propranolol. This proof-of-concept study is essential for establishing CEUS as a non-lethal, real-time tool for measuring organ health in fish species in response to environment toxins.

Methods

Rainbow trout (n=6, 250-350 g) were anesthetized by immersing fish in a solution containing Aquacalm (metomidate; 10 mg/L in water, 14°C) and then placed onto an animal holding device. Anesthetic was continuously delivered through the mouth and over the gills for the duration of the imaging session. On a small region of their abdomen, scales were carefully removed. Fish were imaged using non-linear contrast mode on a small animal ultrasound system (Vevo3100; MV250 Transducer). A bolus of MBs (polydisperse, 1-5µm, 2.5x10⁵ MB/g) was administered through the caudal vein over 20 s. Each fish received a total of two consecutive MB boluses in the same imaging session and imaging plane, allowing for MB clearance in between. A small subset of fish (n=3) received a dose of propranolol (β-blocker causing vasodilation; 1 mg/kg) and a third MB bolus 20 minutes post-propranolol administration. A ROI was drawn over the liver lobe and a time-intensity curve (TIC) was generated. This curve was used to determine peak enhancement (PE), repeatability, and estimated blood pool half-life. Following imaging, fish were euthanized, and livers harvested for *ex vivo* histology.

Results

There was clear and uniform perfusion of the rainbow trout livers. High repeatability between the first two sequential boluses (91.4 ± 7.2%) and the average blood pool half-life of MBs was 4.1 ± 0.5 min. The intensity of the response to propranolol varied between fish, where PE increased by 38.6%, 52.9% and 200% (97.2 ± 89.3%) in comparison to the boluses prior to administering propranolol. This is consistent with dilation of vasculature allowing more MBs into the field of view, increasing PE.

Conclusions

CEUS perfusion imaging in fish liver was repeatable and able to visualize and quantify changes in the vasculature. Blood pool half-life and TIC of MBs show similarities to mammals, allowing us to construct a model based on existing perfusion models for fully characterizing fish perfusion. These data also suggest that molecular imaging with targeted MBs will be possible using existing approaches.

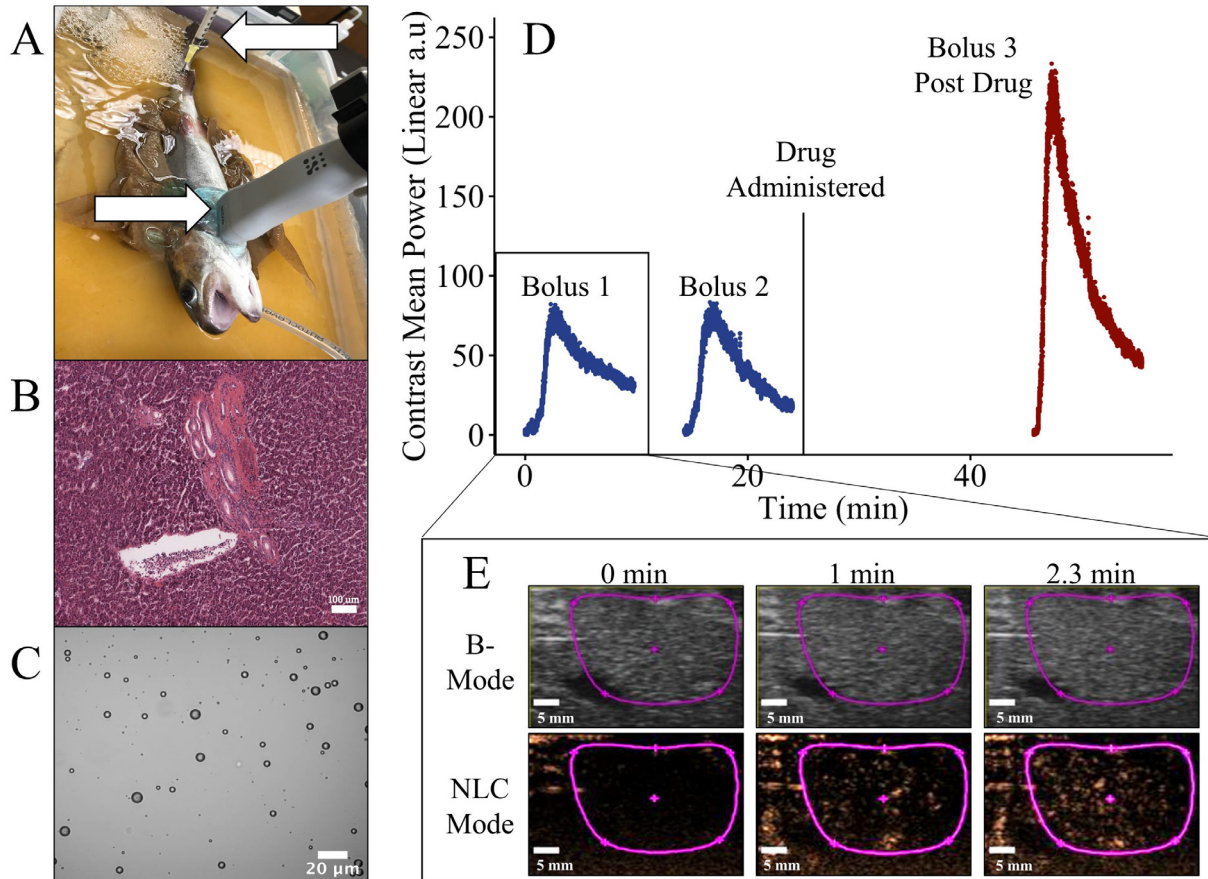


Fig. 1. Contrast-enhanced perfusion imaging of rainbow trout liver. A) Animal holding device containing an anaesthetized rainbow trout. B) H&E staining of trout liver (scale bar = 100 µm). C) Polydisperse microbubbles ranging from 1 – 5 µm in size (scale bar = 20 µm). D) Time Intensity Curve showing injection of two boluses within 30 min followed by a final bolus 20 min post-injection of propranolol (depicted by vertical bar). E) Contrast-enhanced sonographs: B-mode (top) and Non-Linear Contrast (NLC) Mode (bottom; purple ROI within left liver lobe; scale bar = 5 mm) at 0 min (left), 1 min (middle), and 2.3 min (right) post bolus injection.

References

- [1]. Bailey, G.S., Williams, D.E. & Hendricks, J.D. Fish models for environmental carcinogenesis: The rainbow trout. 1996. *Environ Health Persp*, 104, 5-21.
- [2]. Dai, Y.J., et al. Zebrafish as a model system to study toxicology. 2014. *Environ Toxicol Chem*, 33, 11-17.
- [3]. Quايا, E. Microbubble ultrasound contrast agents: an update. 2007. *Eur Radiol*, 17, 1995-2008.
- [4]. Willmann, J.K., et al. Ultrasound Molecular Imaging With BR55 in Patients With Breast and Ovarian Lesions: First-in-Human Results. 2017. *J Clin Oncol*, JCO2016708594.

Cancer therapy by the combination of ultrasound contrast imaging agent mediated sonotherapy and immunotherapy

Ryo Suzuki¹, Daiki Omata¹, Kazuo Maruyama²

¹Laboratory of Drug and Gene Delivery Research, Faculty of Pharma-Science, Teikyo University, Tokyo, Japan

²Laboratory of Theranostics, Faculty of Pharma-Science, Teikyo University, Tokyo, Japan

Corresponding author: r-suzuki@pharm.teikyo-u.ac.jp

Introduction

Microbubbles have various behaviors under ultrasound field such as oscillation and cavitation. Especially, inertial cavitation induces the jet stream and heat generation. This phenomenon can directly induce the damage of tumor cells, it would be applied for cancer therapy. Actually, we showed that the combination of the intratumoral injection of microbubbles and ultrasound exposure for tumor tissue significantly suppressed the tumor growth. In this therapy, we reported that the cellular immunity mainly contributed for the tumor growth suppression [1]. This immune response would be induced by the release of tumor associated antigens from the damaged tumor cells. Therefore, we thought that the injection of dendritic cells (DCs) into the damaged tumor tissue would effectively prime the anti-tumor immune response and result in the enhancement of strong tumor growth suppression. Therefore, in this study, we examined the enhancement of anti-tumor effect by the combination of ultrasound therapy and DC-based immunotherapy.

Methods

Colon-26 cells (mouse colon carcinoma) were inoculated into the backs of mice. After 8 days, microbubbles were intratumorally injected and ultrasound was transdermally exposed toward tumor tissue. DCs were intratumorally immunized on days 9, 10, 11, and 13 after tumor inoculation. The anti-tumor effect was evaluated by measuring tumor volume.

Results

In either ultrasound therapy with microbubbles or DC-based immunotherapy, we obtained only slight anti-tumor effect. On the other hand, the combination of ultrasound therapy with microbubbles and DC-based immunotherapy efficiently suppressed tumor growth (Fig.1).

Conclusion

It seems that ultrasound therapy with microbubbles supports the induction of effective anti-tumor immunity. Therefore, the combination of ultrasound therapy with microbubbles and DC-based immunotherapy would be a useful cancer therapy strategy.

Reference

- [1]. Suzuki R, Oda Y, Omata D, Nishiie N, Koshima R, Shiono Y, Sawaguchi Y, Unga J, Naoi T, Negishi Y, Kawakami S, Hashida M, Maruyama K. Tumor growth suppression by the combination of nanobubbles and ultrasound. *Cancer Sci.* 107(3):217-23.(2016)

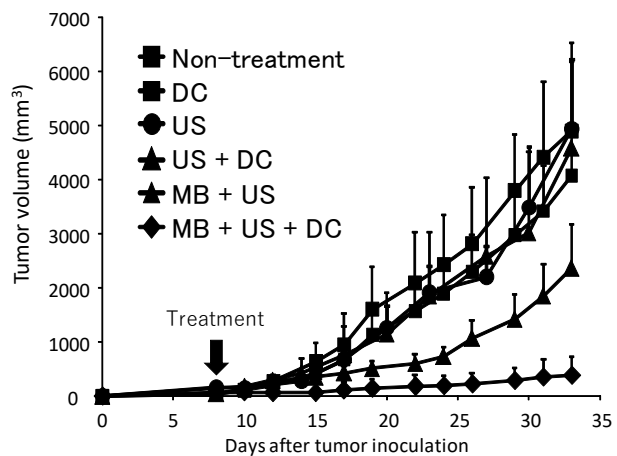


Fig. 1 Tumor growth suppression by the synergic effect with microbubble/US and DC-based immune-therapy.

US: Ultrasound, MB: Microbubble, DC: Dendritic cell

Acoustically-mediated blood-brain barrier opening: investigation of neurophysiological consequences by neurotranscriptomics

Antoine Pesset¹, Sylvie Bodard¹, Edward Oujagir¹, Sylviane Marouillat¹, Frédéric Laumonnier¹, Ayache Bouakaz¹, Lydie Nadal-Desbarats¹, Jean-Michel Escoffre¹

¹UMR 1253, iBrain, Université de Tours, Inserm, Tours, France
Corresponding author: antoine.pesset@univ-tours.fr

Introduction

The blood-brain barrier (BBB) is a highly selective specialized barrier, composed by endothelial cells enhanced by the presence of tight junctions (TJs), a basal membrane and pericytes [1]. More than 99% of therapeutic molecules used for the treatment of neurological diseases do not pass through the BBB, thus causing a major problem for the therapeutic care of these patients [2]. Microbubble-assisted ultrasound can non-invasively disrupt these TJs, thus increasing the extravasation of therapeutic molecules. Nevertheless, if many studies described the BBB opening and the enhancement of the intracerebral biodistribution of drugs using sonoporation but only few reported the long-term bioeffects.

Previous studies reported that the acoustically-mediated BBB opening caused a sterile inflammation response [3,4]. Indeed, microbubble-assisted focused ultrasound induced significant changes in the expression of inflammation- and immunity-associated genes [4]. The activation of NFκB pathway was clearly involved in this neuroinflammation up to 6h after the ultrasound exposure [3,4]. This neuroinflammation was positively correlated with an activation of microglial cells, an infiltration of peripheral immune cell and brain tissues damages [3,4]. If both investigations bring relevant information on neurological consequences of acoustically-mediated BBB opening, they also showed two main limitations: (1) NFκB pathway was the only one signaling pathway investigated in both studies; (2) These investigations did not describe long term effect of acoustically-mediated BBB opening on the neuroinflammation. In this context, we proposed to investigate the neurophysiological consequences of acoustically-mediated BBB opening 3 hours, 48 hours and 1 week after ultrasound exposure using neurotranscriptomics.

Methods

BBB disruption – Anesthetized rats were placed into stereotactic frame. A 1 MHz single element transducer was placed over scalped skull at specific stereotactic coordinates of our region of interest (ROI), the striatum (AP -0.5mm, L ±3.15, VD 5mm). After a bolus injection of BG8758 microbubbles (100 μL at 2.5×10^8 MBs/mL). This ROI was exposed to 1 MHz sinusoidal ultrasound waves for 30 s with a pulse repetition frequency (PRF) of 1 Hz and 10 000 cycles per pulse (10 ms). The peak negative pressure was set to 0.6, 0.8 and 1.2 MPa. To monitor the BBB opening, Evans blue (EB) dye (2% w/v) was intravenously injected at 5 mL/kg. Rats were sacrificed approximately 1 hour after the Evans blue (EB) injection. After the intracardiac perfusion of physiological serum, the brains were collected. The EB extravasation and the intracerebral hemorrhages were qualitatively assessed using a binocular microscope.

Neurotranscriptomics analysis – As previously described, brains were exposed to similar acoustic parameters (*i.e.*, 1 MHz, 1 Hz PRF, 10 000 cycles per pulse, for 30 s) at 0.6 MPa. Then, they were collected 3 hours (3 hrs group), 48 hours (48 hrs group) and 1 week (1 wk group) after sonoporation after an intracardiac perfusion of physiological serum. Insonated and control (*i.e.*, w/o ultrasound treatment) striatum were dissected and mechanically homogenized. Total mRNA were extracted with Direct-zol™ RNA Miniprep. Striata's transcriptome sequenced with HiSeq4000 Illumina. Differential gene expressions were expressed as log₂ fold-change of fragment per kilobase millions (FPKM) of one experimental group compared to control group.

Statistics – All quantitative data are collected for statistical analysis using the t-test. P-values were corrected with a multiple comparison test (Voom transformation that correct gene-by-gene variance), which provided a statistical value called q-value. Thresholds to observe a gene dysregulation was chosen as follows: q-value < 0.1 and |log₂(FC)| > 1.

Results

Effects of acoustic pressure on BBB opening – In the control group (w/o ultrasound exposure), the transducer was placed on scalped skull of rats and a bolus of microbubbles was intravenously administered. It means that the brain tissue is not exposed to ultrasound (*i.e.*, 0 MPa). As described in Figure 1, no EB extravasation and no hemorrhages were observed in these control animals. In agreement with the available literature, the EB extravasation and the number of hemorrhaged sites increased with the acoustic pressure (*i.e.*, 0.6, 0.8 and 1.2 MPa). Based on these results, an acoustic pressure of 0.6 MPa was selected for neurotranscriptomics analysis. Regarding to our previous works, rat skull attenuates the transmitted acoustic pressure of 50%, thus suggesting that the cerebral tissue is exposed to an acoustic pressure of 0.3 MPa.

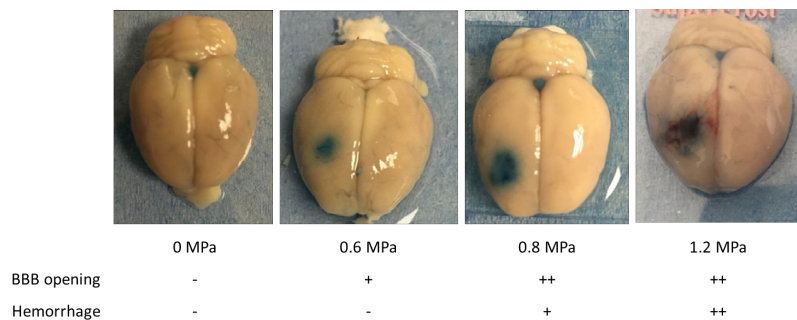


Figure 1: BBB opening and hemorrhage assessment.

Neurotranscriptomics analysis – As described in Figure 2A, the principal component analysis highlighted a heterogeneity of our samples. Transcriptomics analysis revealed that there are 18 over-expressed genes and only 1 under-expressed gene between 3hrs and control groups, as well as 12 overexpressed genes between 1 week and control groups. In addition, comparison between 3hrs groups and 2 days groups brought to light the over-expression of 7 genes and the under-expression of 2 genes (Figure 2B). Bioinformatics analysis allowed to associate relative biological processes to concerned genes. These processes could be associated with each other to reveal putative links between each dysregulated genes. The 3hrs group showed a dysregulation of hypoxia response pathway (upregulation of *Hif3a*), cell cycle (upregulation of *Cdkn1a*), phospholipid (upregulation of *Pla2g3*) and energetic (upregulation of *Pdk4*) metabolism but an activation of immune system (upregulation of *Prr5*, *Cd163* and *Tnfrsf11a*) in comparison to control groups. In the 1 wk group, a dysregulation of calcium signaling pathway and an activation of PKC pathway (upregulation of *Ramp3* and *Prkcd*) were observed in the 1 wk group. These changes in gene expression might have a role in activation of complement (upregulation of *C3*), activation of immune cells, apoptosis and Wnt signaling pathways (upregulation of *Lef1*). The comparative study of 3 and 48 hrs groups revealed the involvement of response of hypoxia stress (upregulation of *Hif3a*), antigen processing process (upregulation of *Zbtb16*), phospholipid metabolism (upregulation of *Gpd1*) and thyroid hormone transport (downregulation of *Slco1c1* expression).

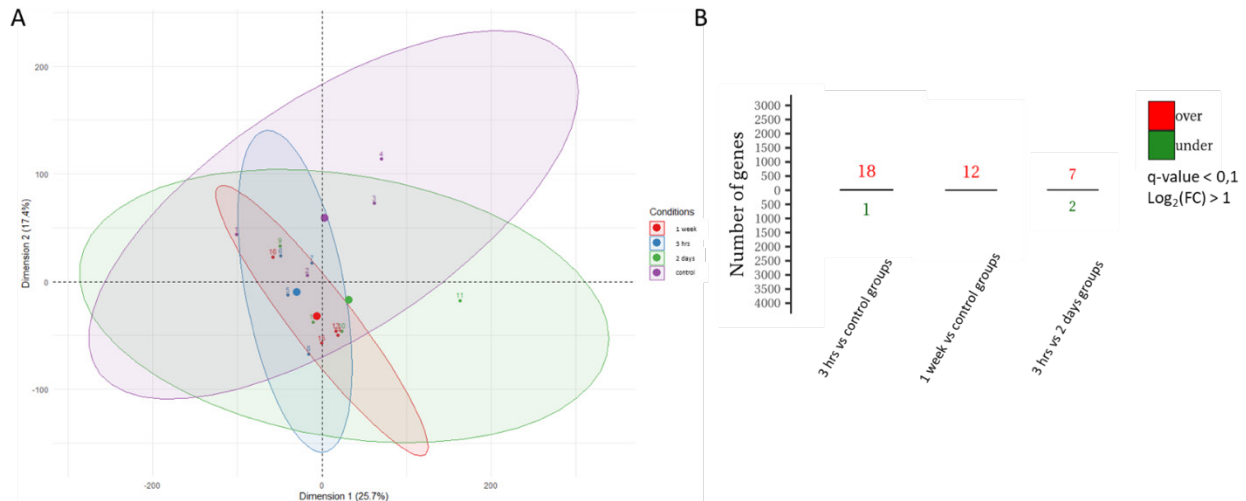


Figure 2: Statistical overview of neurotranscriptomics analysis of sonicated striatum. (A) Principal Component Analysis (PCA) of thousand most variant genes score plot. (B) Summary of dysregulation of genes depending of different groups.

Conclusions

The present study showed that many changes in expression of immunity and inflammation-associated gene were observed within a few hours after the acoustically-mediated BBB opening. In agreement with previous works [3,4], the NFκB pathway (*i.e.*, *Tnfrsf11a*, *Prr5*) might be the signaling pathway involved in this neuroinflammation. In addition, our results demonstrated a significant dysregulation of gene expression involved in calcium (*Ramp3*, *Prkcd*) and hypoxia signaling pathways (*Hif3a*). These results support both hypotheses that suggest that the activation of calcium signaling pathways and hypoxia condition induce the disruption of TJs. Further histological analysis of brain tissues are on-going and should confirm these results.

Acknowledgments

We thank Jean-Yves Tartu (UMR 1253, iBrain, Université de Tours, Inserm, Tours, France) for his technical support and Bracco Suisse, S.A. (Geneva, Switzerland) for supplying the microbubbles. This work is supported by cross-cutting project grant from Inserm UMR 1253 iBrain/University of Tours. Antoine Passet was the recipient of a PhD grant from the President of the University of Tours.

References

- [1]. Abbott, N., Rönnebeck, L. and Hansson, E. (2006). Astrocyte–endothelial interactions at the blood–brain barrier. *Nature Reviews Neuroscience*, 7(1), pp.41-53.
- [2]. Pardridge WM. Blood-brain barrier genomics. *Stroke* 2007; 38:686-90. Kovacs et al. (2016)
- [3]. Kovacs, Z., Kim, S., Jikaria, N., Qureshi, F., Milo, B., Lewis, B., Bresler, M., Burks, S. and Frank, J. (2016). Disrupting the blood–brain barrier by focused ultrasound induces sterile inflammation. *Proceedings of the National Academy of Sciences*, 114(1), pp.E75-E84.
- [4]. McMahon D, Hynynen K. Acute Inflammatory Response Following Increased Blood-Brain Barrier Permeability Induced by Focused Ultrasound is Dependent on Microbubble Dose. *Theranostics* 2017; 7:3989-4000.

Monodisperse microbubbles as a tool to elucidate sonoporation fundamentals

Joke Deprez^{1*}, Benjamin Van Elburg^{2*}, Guillaume Lajoinie², Stefaan C. De Smedt¹, Michel Versluis², Ine Lentacker^{1#}, Tim Segers^{2#}

¹*Ghent Research Group on Nanomedicines, Laboratory of General Biochemistry and Physical Pharmacy, Ghent University, Ghent, Belgium*

²*Physics of Fluidics Group (POF), University of Twente, Enschede, The Netherlands*

Corresponding author: Joke.Deprez@UGent.be

^{*,#} Both authors contributed equally

Introduction

Conventional ultrasound contrast agents (UCA) have been explored thoroughly for sonoporation applications. However, these agents consist of a suspension of polydisperse microbubbles, typically ranging from 1 to 10 μm in diameter. Microbubbles are resonators with a resonance frequency that is inversely proportional to the microbubble size. At resonance, the relative amplitude of oscillation is at maximum. Therefore, it is expected that the efficacy and controllability of theranostic applications that rely on ultrasound-driven volumetric microbubble oscillations, such as drug and gene delivery through sonoporation, can be dramatically increased through the use of resonant monodisperse bubbles. Moreover, due to their uniform acoustic response, monodisperse microbubble populations may potentially solve remaining fundamental questions as to the optimal acoustic parameters required to induce therapeutic effects. Recently, microfluidic flow-focusing devices have been shown to be able to produce highly stable monodisperse lipid-coated microbubble suspensions. The microbubble size can be tuned in such way that the resonance frequency of the microbubble population can either be perfectly matching or mismatching the insonifying ultrasound frequency. Thus, through the use of monodisperse bubble suspensions with different mean sizes and a single insonifying ultrasound frequency, a different microbubble behaviour is evoked which subsequently alters the interaction of microbubbles with cells in close vicinity. Therefore, access to monodisperse microbubbles makes it is possible to study sonoporation fundamentals, e.g., to answer whether monodisperse microbubbles can achieve higher sonoporation rates with a lower toxicity. In this research, the role of different microbubble sizes on sonoporation efficiency was studied and compared to that measured using polydisperse microbubbles. The sonoporation efficiency was characterized through the uptake patterns of FITC-dextran.

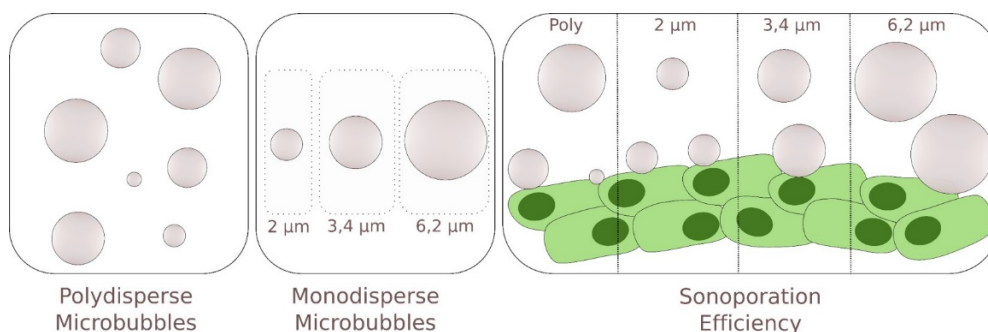


Fig. 1 | Experimental design of sonoporation experiments

Methods

Polydisperse microbubbles, resembling DefinityTM microbubbles, were prepared by shaking a vial filled with C₄F₁₀ and phospholipids dissolved in a propylene glycol:glycerol:water mixture as described in

Roovers *et al* [1]. Monodisperse microbubble suspensions of different mean sizes were produced in a microfluidic flow-focusing device as in Segers, *et al* [2]. The monodisperse bubbles were also C₄F₁₀ – filled. For sonoporation experiments, Bowes Lung Metastasis (BLM) cells were seeded in Lumox dishes. After reaching full confluency, microbubbles (mono or polydisperse) and FITC-dextran (4 kDa or 2 MDa) were added to the cells. Subsequently, lumox dishes were inverted, immersed into a water tank and exposed to the following ultrasound conditions; 1 MHz, 1 MPa or 700 kPa, 1000 cycles, 1 burst. After treatment, the exposed area was cut out of the lumox dish and the cells were harvested. The efficiency of sonoporation was subsequently evaluated using flow cytometry.

Results

Large monodisperse microbubbles with a radius of 4.8 μm showed the highest sonoporation efficiency in the *in vitro* experiment. The FITC-dextran uptake was clearly enhanced for both FITC-dextran sizes and for both employed acoustic pressures amplitudes. Smaller microbubbles (< 3.4 μm in radius) showed no improvement in sonoporation efficiency compared to polydisperse microbubbles. Overall, a gaussian sonoporation efficiency distribution as a function of microbubble size was found, with a maximum at a bubble radius of 4.8 μm . The specific microbubble dynamics that were at play and the reason behind the superiority of 4.8 μm radius microbubbles for sonoporation will be further investigated using supplemental high speed imaging experiments.

Conclusions

Large uniform monodisperse microbubbles show an advantageous effect on sonoporation efficiency compared to polydisperse microbubbles.

References

- [1]. Roovers S, Deprez J, et al. Sonoprinting liposomes on tumor spheroids by microbubbles and ultrasound. *J Control Release*. 316(October), 79–92 (2019).
- [2]. Segers T, Gaud E, et al. High-precision acoustic measurements of the nonlinear dilatational elasticity of phospholipid coated monodisperse microbubbles. *Soft Matter*. 14(47), 9550–61 (2018).

Combined Sonodynamic and Chemoradiotherapy for Pancreatic Cancer

Richard J. Browning^{1,2}, Sarah Able¹, Estelle Beguin², Jia-Ling Ruan¹, Heather Nesbitt³, Sukanta Kamila³, Philip D. Allen¹, Veerle Kersemans¹, Sean Smart¹, Eleanor Stride², Anthony P. McHale³, John F. Callan³, & Katherine A Vallis¹

¹*CRUK/MRC Oxford Institute for Radiation Oncology, Department of Oncology, University of Oxford, Oxford, UK*

²*Institute of Biomedical Engineering, University of Oxford, Oxford, UK*

³*Biomedical Sciences Research Institute, University of Ulster, Coleraine, Northern Ireland, UK*

Corresponding author: richard.browning@eng.ox.ac.uk

Introduction

Pancreatic cancer is a disease with poor prognosis. With a symptomless early progression, the cancer typically presents as a hypoxic, chemo- and radio-resistant tumour with desmoplasia. For non-resectable disease, gemcitabine is the cornerstone of control, but only modestly increases survival, highlighting a clinical need for other therapies.

It has been shown that release of oxygen (O₂) from lipid microbubbles (MBs) can temporarily relieve tumour hypoxia. When combined with gemcitabine and sonodynamic therapy using ultrasound and Rose Bengal (RB), this led to improved survival and tumour growth delay in a murine model of pancreatic cancer[1]. As radiotherapy is also enhanced by O₂ and gemcitabine, further combination therapies were investigated to determine additional additive and synergistic effects of gemcitabine-based chemoradiotherapy (CRT) with either oxygen delivery or sonodynamic therapy.

Methods

Biotinylated RB was prepared and bio-conjugated via an avidin linker to a perfluorobutane, biotinylated-lipid MB produced by sonication. These were sparged with O₂ to form RB-loaded oxygen MB (O₂MB-RB) which could be used as sonodynamic therapy agents under ultrasound. In addition, unloaded oxygen MB (O₂MB) were also created without the biotinylated RB or avidin linkers, which could be used as oxygen delivery agents under ultrasound. Subcutaneous xenograft tumours were established in athymic nude mice using the BxPC-3 or PSN-1 pancreatic cell line. Tumours were treated with gemcitabine and radiotherapy (chemoradiotherapy, CRT) in combination with ultrasound after injection of either O₂MB (O₂ delivery) or O₂MB-RB (sonodynamic therapy). Tumour growth and survival was monitored until endpoint.

Results

As expected, CRT was effective in delaying tumour growth in both tumour types, with increased survival vs untreated control. In both tumour types, the oxygen delivery by O₂MB did not improve CRT. In PSN-1 tumours, the combination of CRT with sonodynamic therapy improved tumour growth delay and survival, however this was not seen in BxPC-3 tumours. In neither tumour type was sonodynamic therapy alone found to be effective. Tumours formed by PSN-1 and BxPC-3 are marked by significantly different vasculature and perfusion, which may explain why therapeutic response was different.

Conclusions

This study helps underline that effective diagnosis and characterisation of a disease is essential for therapy selection, and that sonodynamic therapy may provide an inexpensive and effective addition for management of pancreatic cancer by standard therapy in certain tumours.

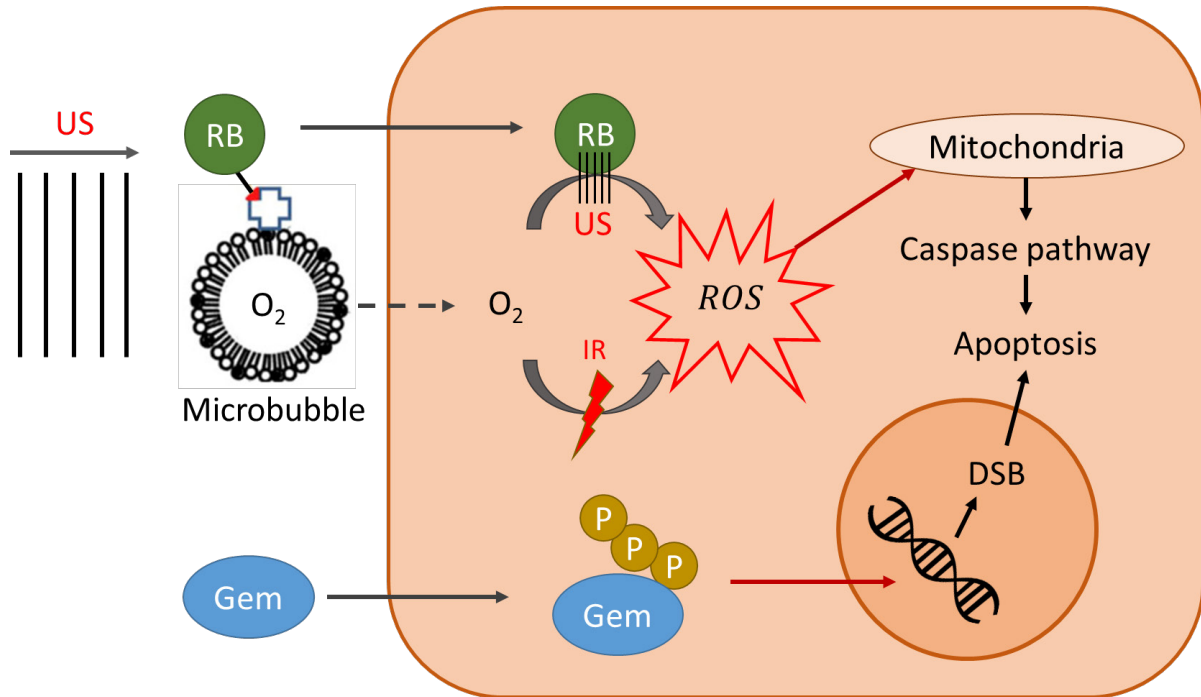


Figure 1. Schematic concept of the proposed combination therapy. Ultrasound (US) causes microbubble release of Rose Bengal (RB) and O₂ in the tumour area. US activation of RB and radiation (IR) convert O₂ to reactive oxygen species (ROS) leading to mitochondrial damage and pro-apoptotic signals. Also, gemcitabine (Gem) enters cells and is phosphorylated (P). This form incorporates into DNA to cause double strand breaks (DSB) leading to apoptosis.

Reference

- [1]. Nesbitt H, Sheng Y, Kamila S, Logan K, Thomas K, Callan B, Taylor MA, Love M, O'Rourke D, Kelly P, Beguin E, Stride E, McHale AP, Callan JF, Gemcitabine loaded microbubbles for targeted chemo-sonodynamic therapy of pancreatic cancer, *Journal of Controlled Release*, 279: 8-16, 2018.

Low-intensity focused ultrasound and microbubbles heighten immune response in pancreatic tumors

Jordan B. Joiner^{1,2}, Philip G. Durham^{1,2}, Nancy P. Kren^{2,3}, Yuliya Pylayeva-Gupta^{2,3}, Paul A. Dayton^{1,3,4}

¹*Pharmaceutical Sciences, Eshelman School of Pharmacy, University of North Carolina at Chapel Hill, Chapel Hill, USA*

²*Department of Genetics, University of North Carolina at Chapel Hill, Chapel Hill, USA*

³*Lineberger Comprehensive Cancer Center, University of North Carolina at Chapel Hill, Chapel Hill, USA*

⁴*Joint Department of Biomedical Engineering, University of North Carolina at Chapel Hill & North Carolina State University, Chapel Hill, USA*

Corresponding author: padayton@email.unc.edu

Introduction

Pancreatic ductal adenocarcinoma (PDA) has a dismal 5-year survival rate as a consequence of late diagnosis and notorious resistance to therapy [1]. Attempts to invigorate anti-tumor immune responses to PDA using checkpoint blockade have been unsuccessful, highlighting the need to understand barriers that impede activity of immunotherapy [2]. Profound immunosuppression, coupled with insufficient antigen presentation capacity as well as desmoplasia-driven compression of tumor vasculature, are thought to account for the failure of cytotoxic T cells to successfully reach and target tumor cells. Non-invasive, low-intensity focused ultrasound (FUS) has emerged as a potential immunomodulatory treatment modality in several cancer types [3]. One of the main consequences of FUS application at the tumor site is a transient increase in vascular permeability and availability of antigens that may boost delivery of therapeutics and augment anti-tumor immune responses. However, lack of knowledge regarding optimized FUS parameters that might achieve such effects precludes its current application in patient care. This effort will inform the optimal design of FUS-directed immunotherapy strategies against PDA.

Methods

To understand how FUS treatment modulates anti-tumor immunity and vascular parameters, we have used murine syngeneic models of pancreatic cancer. 30 female C57Bl/6J mice were subcutaneously injected with 1×10^5 KPC cells in 0.1 mL HBSS in the right flank [4]. Fifteen days after tumor inoculation, mice (n=16) were treated by intravenously infusing decafluorobutane microbubbles (MBs) with a DSPC-PEG2k lipid shell (7×10^7 MBs total) and scanning the tumor with a Philips Therapy and Imaging Probe System (TIPS) [5]. Ultrasound parameters were as follows: 100 Hz PRF, 1 MHz frequency, 0.5 MPa, 10% duty cycle, 0.13 W/cm^2 , and 2 seconds/spot for a total treatment time of 8-10 minutes. Animals were sacrificed at 2 days (n=8) and 14 days (n=8) post-treatment to evaluate tumor growth and immune cell infiltration in the tumor and lymph node (**Figure 1A**). Part of the tumor tissue was analyzed for histology and the rest for flow cytometry. Histology slides were scanned using a Aperio ScanScope XT at UNC's Translational Pathology Lab and flow cytometry data was acquired on LSRII Fortessa (BD Bioscience) at UNC Flow Cytometry Core Facility [6].

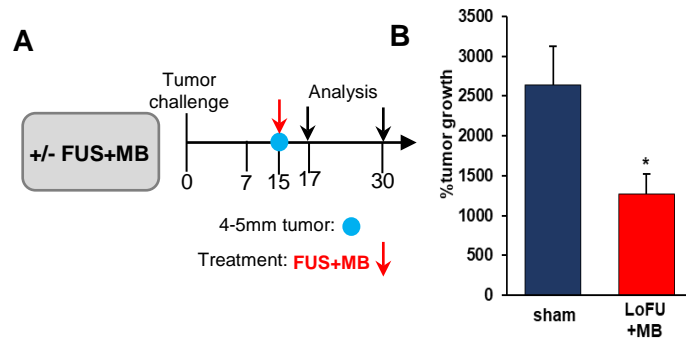


Figure 1. Schema for treatment with FUS+MBs. Decrease in tumor growth rate was evident 2 weeks post-FUS treatment.

Results

Evaluation of tumor growth revealed significant decrease in the rate of tumor growth for PDA tumors treated with FUS+MB (**Figure 1B**). To understand the effects of FUS on functionality of antigen presenting cells, we assessed frequency and functional markers on macrophages and dendritic cells in draining lymph nodes (LN). We observed significant but transient increase in frequency of MHCII⁺ dendritic cells and macrophages of mice treated with FUS+MB (**Figure 2A**). Increase in macrophage frequency was also evident intra-tumorally and persisted through week 2 post-treatment (**Figure 2B**). Furthermore, there was an increase in PD-1^{low} CD8⁺ T cells in LN following FUS+MB treatment, suggesting that ultrasound treatment may increase antigen availability, priming of dendritic cells and/or macrophages, and subsequent expansion of T cells (**Figure 2C**). This was accompanied by increased intratumoral expression and cytoplasmic localization of damage marker HMGB1.

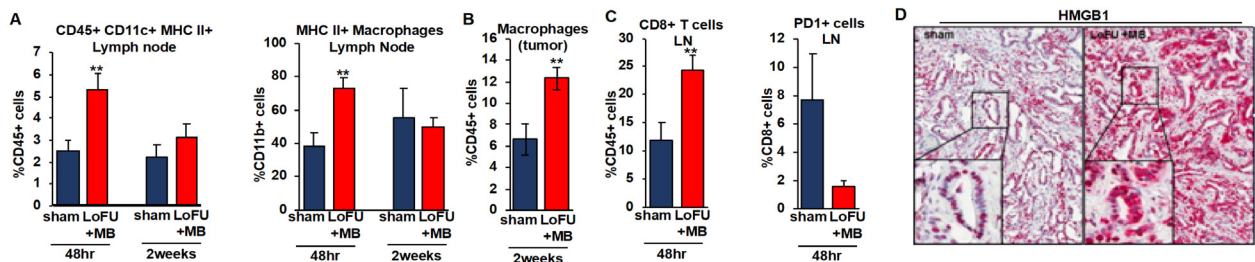


Figure 2. Modulation of immune responses with FUS+MB.

Conclusions

We conclude that low frequency FUS combined with microbubble contrast agent may ameliorate tumor growth by potentiating antigen presentation and priming of myeloid cells. This may result in expansion of PD1-low CD8⁺ T cells, thus allowing us to pursue further studies, which will dissect the mechanism of FUS efficacy and test this modality in combination with a leading immunotherapy agent for PDA.

References

- [1]. Siegel RL, Miller KD, Jemal A. Cancer statistics, 2016. *CA Cancer J Clin.* 2016;66(1):7-30. Epub 2016/01/09. doi: 10.3322/caac.21332. PubMed PMID: 26742998.
- [2]. Royal RE, Levy C, Turner K, Mathur A, Hughes M, Kammula US, Sherry RM, Topalian SL, Yang JC, Lowy I, Rosenberg SA. Phase 2 trial of single agent Ipilimumab (anti-CTLA-4) for locally advanced or metastatic pancreatic adenocarcinoma. *J Immunother.* 2010;33(8):828- 33. Epub 2010/09/16. doi: 10.1097/CJI.0b013e3181eec14c. PubMed PMID: 20842054.
- [3]. Liu, H. L., Hsieh, H. Y., Lu, L. A., Kang, C. W., Wu, M. F., & Lin, C. Y. (2012). Low-pressure pulsed focused ultrasound with microbubbles promotes an anticancer immunological response. *J Transl Med*, 10, 221. <https://doi.org/10.1186/1479-5876-10-221>
- [4]. Pylayeva-Gupta, Y., Das, S., Handler, J. S., Hajdu, C. H., Coffre, M., Koralov, S. B., & Bar-Sagi, D. (2016). IL35-Producing B Cells Promote the Development of Pancreatic Neoplasia. *Cancer Discovery*, 6(3), 247 LP-255. <https://doi.org/10.1158/2159-8290.CD-15-0843>
- [5]. Newsome, I. G., Kierski, T. M., & Dayton, P. A. (2019). Assessment of the Superharmonic Response of Microbubble Contrast Agents for Acoustic Angiography as a Function of Microbubble Parameters. *Ultrasound in Medicine & Biology*, 45(9), 2515–2524. <https://doi.org/https://doi.org/10.1016/j.ultrasmedbio.2019.04.027>
- [6]. Mirlekar, B., Michaud, D., Searcy, R., Greene, K., & Pylayeva-Gupta, Y. (2018). IL-35 hinders endogenous anti-tumor T cell immunity and responsiveness to immunotherapy in pancreatic cancer. *Cancer Immunology Research*, 6(September), canimm.0710.2017. <https://doi.org/10.1158/2326-6066.CIR-17-0710>

Investigation of the effect of orally administered oxygen bubbles upon tumour response to sonodynamic therapy

Joshua Owen^{1,2}, Kieran Logan³, Heather Nesbitt³, Alexandra Vasilyeva¹, Emma Bluemke¹, Sarah Able², Katherine Vallis², Anthony McHale³, John Callan³, Eleanor Stride¹

¹ Oxford Institute of Biomedical Engineering, University of Oxford, Oxford, United Kingdom

² Oxford Institute for Radiation Oncology, University of Oxford, Oxford, United Kingdom

³ Biomedical Sciences Research Institute, Ulster University, Coleraine, Northern Ireland, United Kingdom

Corresponding author: eleanor.stride@eng.ox.ac.uk

Introduction

Hypoxia is a common feature of locally advanced solid tumours; it is caused by disorganized vascular architecture in cancerous tissues and can be further exacerbated by disease- or treatment-associated anaemia [1]. Oxygen imbalance is associated with poor clinical outcomes, especially for therapies that depend on reactive oxygen species production, such as chemo-, radio- and photodynamic therapy [2,3], and alleviating tumour hypoxia has been shown to improve patients' response to these treatments [4]. A wide range of methods has been proposed for controlling oxygen supply or consumption in tumours; however most of them have encountered technical difficulties or significant side effects that have stalled their development [5].

In order to mitigate systemic side effects, a number of stimuli-responsive carriers has been designed for local oxygen delivery. In particular, lipid microbubbles (MBs) have attracted some attention in this field due to their good biocompatibility, high potential for oxygen loading, as well as possibility of local activation and enhanced extravasation upon exposure to ultrasound. Several groups have demonstrated hypoxia reduction by oxygen-loaded MBs *in vitro* and *in vivo* [6-8].

There are, however, limits to the quantity and frequency with which MBs can be given intravenously, and these agents have not yet demonstrated sufficiently low level of side effects in earlier clinical trials. Consequently both intraperitoneal and oral administration of oxygen-loaded bubbles have also been investigated [9,10]. Previous work by the authors demonstrated that an orally delivered suspension of oxygen-filled nanobubbles (NBs) with a mean diameter below 100 nm could produce an increase in tumour oxygen levels comparable to that generated by intravenously injected MBs [10]. The aim of the present study was to determine whether this approach could be used to improve therapeutic response to sonodynamic therapy.

Methods

Bubble solutions were prepared according to Owen et al [10]. NB size distributions were characterized using a nanoparticle tracking analyser (NanosightNS300). Oxygen loading and release was studied in glass vials with an optical oxygen sensor (OxyMini, PreSens).

All animal procedures were carried out in accordance with the UK Animals (Scientific Procedures) Act 1986 and with local ethical committee approval. BxPC3 xenografts were established by subcutaneous injection. For sonodynamic therapy experiments, ultrasound was applied to the tumour using a Sonidel SP100 probe for 3.5 minutes at an intensity of 3.5 W/cm², centre frequency 1 MHz and 30% duty cycle. For oxygenation studies, an oxygen/temperature bare-fibre sensor of tip diameter 350 µm (Oxylite by Oxford Optronix) was inserted into the centre of the tumour.

Results

Nanobubbles and *in vitro* oxygen measurements. NB size distributions were measured before and after oxygen and nitrogen sparging; no significant difference was found between these three conditions. The measurements of oxygen release were consistent with those reported by Owen et al. [10] showing a

rapid elevation in oxygen partial pressure (pO₂) upon injection of either oxygen bubbles or oxygenated water, with the bubble suspension producing a more prolonged change.

Sonodynamic therapy (SDT) experiments with Rose Bengal. A statistically significant difference in the rate of change of tumour volume was seen between the groups receiving SDT only and those receiving both SDT and oxygenated NBs; the bubbles alone had no effect upon tumour growth (Fig. 1). An elevation in tumour oxygen levels and corresponding reduction in HIF-1 α was also observed in murine models after treatment with oxygen-loaded nanobubbles compared to non-oxygenated NBs.

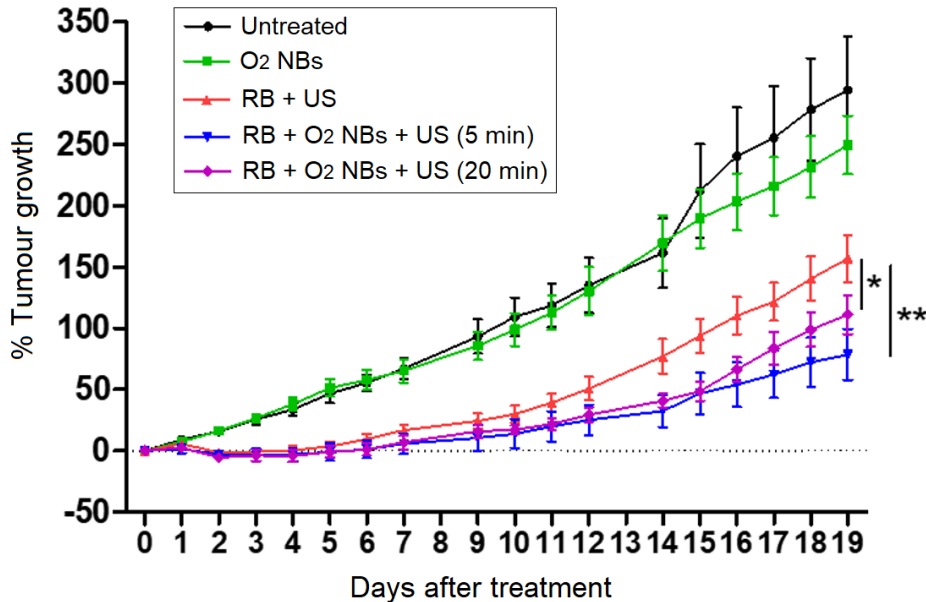


Figure 1. Effect of oral administration of oxygen-loaded nanobubbles upon tumour response to sonodynamic therapy: change in volume of a BxPC-3 pancreatic tumour in a murine model. Treated animals received oxygen bubbles (O₂ NBs) by gavage and/or an intratumoural injection of Rose Bengal (RB) followed by 3.5 minutes exposure to ultrasound at an intensity of 3.5 W/cm², centre frequency 1 MHz and 30% duty cycle. Ultrasound was applied either 5 minutes or 20 minutes after the oxygen bubble gavage. Animals were treated on Days 0, 5, 11 and 15. (* p < 0.05; ** p < 0.01)

Conclusions

The obtained results support the hypothesis that the increase in tumour oxygenation produced by oral administration of oxygen bubbles has the potential to enhance tumour response to SDT. This finding is also consistent with the results of previous studies using intravenously delivered oxygen microbubbles to promote SDT, in which similar changes in tumour oxygen levels and in hypoxia inducible factor expression were measured and found to correlate with therapeutic effect [6,11].

While these results are encouraging, the mechanism of oxygen delivery warrants further discussion. A simple estimate of the amount of oxygen encapsulated in a dose of bubble carriers, even after assuming 100% oxygen transport after ingestion, is not able to account for the rise of oxygen concentration that was observed in the tumours. One possible explanation for this discrepancy is that small lipid structures that pass from the digestive tract into the bloodstream can act as artificial oxygen transporters, i.e. absorb oxygen during their passage through lungs and then release it in the hypoxic tumour region. Such behaviour would explain observed oxygen levels and significant duration of effect; however further investigation is needed to either support this hypothesis or find an alternative explanation for the mechanism of oxygen delivery.

References

- [1]. Vaupel P, Harrison L. Tumor hypoxia: causative factors, compensatory mechanisms, and cellular response. The oncologist. 2004 Nov 1;9(Supplement 5):4-9.

- [2]. Harrison LB, Chadha M, Hill RJ, Hu K, Shasha D. Impact of tumor hypoxia and anemia on radiation therapy outcomes. *The oncologist*. 2002 Dec 1;7(6):492-508.
- [3]. Rebutti M, Michiels C. Molecular aspects of cancer cell resistance to chemotherapy. *Biochemical pharmacology*. 2013 May 1;85(9):1219-26.
- [4]. Overgaard J, Horsman MR. Modification of hypoxia-induced radioresistance in tumors by the use of oxygen and sensitizers. In *Seminars in radiation oncology* 1996 Jan 1 (Vol. 6, No. 1, pp. 10-21). WB Saunders.
- [5]. Yu M, Dai M, Liu Q, Xiu R. Oxygen carriers and cancer chemo- and radiotherapy sensitization: Bench to bedside and back. *Cancer treatment reviews*. 2007 Dec 1;33(8):757-61.
- [6]. McEwan C, Owen J, Stride E, Fowley C, Nesbitt H, Cochrane D, Coussios CC, Borden M, Nomikou N, McHale AP, Callan JF. Oxygen carrying microbubbles for enhanced sonodynamic therapy of hypoxic tumours. *Journal of controlled release*. 2015 Apr 10;203:51-6.
- [7]. Sun J, Yin M, Zhu S, Liu L, Zhu Y, Wang Z, Xu RX, Chang S. Ultrasound-mediated destruction of oxygen and paclitaxel loaded lipid microbubbles for combination therapy in hypoxic ovarian cancer cells. *Ultrasonics sonochemistry*. 2016 Jan 1;28:319-26.
- [8]. Eisenbrey JR, Shraim R, Liu JB, Li J, Stanczak M, Oeffinger B, Leeper DB, Keith SW, Jablonowski LJ, Forsberg F, O'Kane P. Sensitization of hypoxic tumors to radiation therapy using ultrasound-sensitive oxygen microbubbles. *International Journal of Radiation Oncology* Biology* Physics*. 2018 May 1;101(1):88-96.
- [9]. Feshitan JA, Legband ND, Borden MA, Terry BS. Systemic oxygen delivery by peritoneal perfusion of oxygen microbubbles. *Biomaterials*. 2014 Mar 1;35(9):2600-6.
- [10]. Owen J, McEwan C, Nesbitt H, Bovornchutichai P, Averre R, Borden M, McHale AP, Callan JF, Stride E. Reducing tumour hypoxia via oral administration of oxygen nanobubbles. *PloS one*. 2016 Dec 30;11(12):e0168088.
- [11]. McEwan C, Kamila S, Owen J, Nesbitt H, Callan B, Borden M, Nomikou N, Hamoudi RA, Taylor MA, Stride E, McHale AP. Combined sonodynamic and antimetabolite therapy for the improved treatment of pancreatic cancer using oxygen loaded microbubbles as a delivery vehicle. *Biomaterials*. 2016 Feb 1;80:20-32.

Investigating cell membrane modulation by microbubbles and ultrasound using confocal fluorescence microscopy

*Veerle A. Brans*¹, *Michael D. Gray*¹, *Erdinc Sezgin*^{2,3}, *Eleanor P. J. Stride*¹

¹*Department of Engineering Science, Institute of Biomedical Engineering, University of Oxford, OX3 7 DQ Oxford, United Kingdom*

²*MRC Human Immunology Unit and Wolfson Imaging Centre Oxford, Weatherall Institute of Molecular Medicine, Radcliffe Department of Molecular Medicine, University of Oxford, OX3 9DS Oxford, United Kingdom*

³*SciLifeLab, Karolinksa Institutet, 171 77 Stockholm, Sweden*
Corresponding author: eleanor.stride@eng.ox.ac.uk

Introduction

Ultrasound exposure of circulating cavitation agents, such as phospholipid-shelled microbubbles, and/or drug-carrying vehicles, such as liposomes, has been shown to enable the delivery of a therapeutic payload to target locations within the human body [3-4]. Direct transfer of therapeutics from the microbubble shell to cellular membranes via microbubble-cell fusion, microbubble destruction, sonoporation and/or lipid shedding, is a promising candidate mechanism for this enhancement of ultrasound-mediated drug delivery. It has been shown that transfer of shell components between microbubbles and cells can alter cell membrane hydration and lipid order, potentially improving delivery efficiency [2]. Elucidating the underlying mechanisms, however, requires investigation of microbubble-cell interactions, which is the aim of this study.

Methods

CellMask Deep Red stained adenocarcinomic human alveolar basal epithelial cells (A549s) were incubated with two different formulations of microbubbles constituting a fluorescently-tagged synthetic phospholipid and a fluorescently-tagged conical lipid, respectively, which were subsequently insonated using a 0.5 MHz transducer at ~0.18 MPa for 60 continuous seconds, in a custom-built ultrasound set-up. Acoustic emissions were recorded using a passive cavitation detector (PCD). Confocal fluorescence microscopy was performed to both assess the success of microbubble shell labelling as well as to investigate potential transfer, fusion and/or uptake of fluorescently-labelled lipid to the surface cellular membrane. Phospholipid-coated microbubbles of $2.34 \pm 1.37 \mu\text{m}$ and $8.47 \pm 3.55 \mu\text{m}$ in size were used, which are of a slightly larger size than agents clinically used in ultrasound imaging and therapy due to the presence of double bonds in the lipid tails. They were used at a concentration of $1.24 \cdot 10^9$ and $1.11 \cdot 10^7$ bubbles/ml, respectively.

Results

Our previous work provided strong evidence for the transfer of material from microbubble coatings into cell membranes [1-2]. Secondly, those results indicated that transfer of phospholipids alters the organisation of molecules in cell membranes, specifically the molecular ordering. What was not known, however, was the impact of lipid type on this transfer mechanism. The work presented here shows direct lipid transfer and/or microbubble fusion of both the fluorescently-tagged synthetic phospholipid and conical lipid from microbubbles (green) with the target cellular membrane (magenta), a process which is enhanced dramatically by the application of ultrasound. What is particularly striking is the different means of incorporation depending on the lipid type, as clearly demonstrated in figure 1, which could have important implications for therapeutic microbubble engineering.

Conclusions

These findings provide a direct insight into the interactions of microbubbles with target cellular membranes under ultrasound exposure, opening avenues for studying non-invasive delivery of lipids and lipid-conjugates to target cells by means of transfer, fusion or uptake using ultrasound.

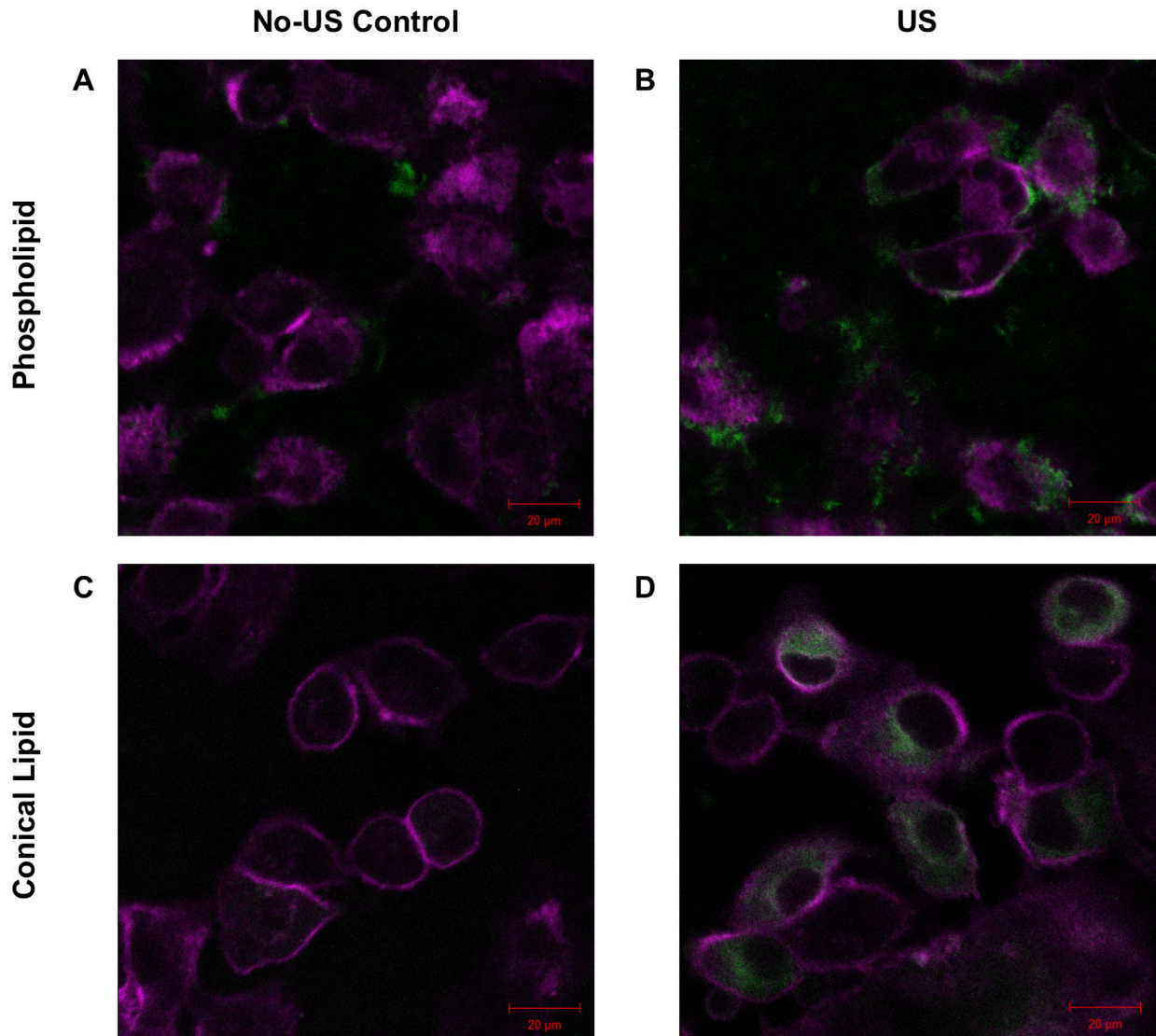


Figure 1. A549s incubated with CellMask Deep Red (magenta) and subsequently with microbubbles with green fluorescently labelled phospholipid (A, B) and conical lipid (C, D). A and C show the control, where cells are incubated with bubbles but not exposed to ultrasound, whereas B and D show the sample exposed to microbubbles and ultrasound.

References

- [1]. Aron, M., Vince, O., Gray, M., Mannaris, C., & Stride, E. (2019). Investigating the Role of Lipid Transfer in Microbubble-Mediated Drug Delivery. *Langmuir*, 35(40), 13205-13215.
- [2]. Carugo, D., Aron, M., Sezgin, E., de la Serna, J. B., Kuimova, M. K., Eggeling, C., & Stride, E. (2017). Modulation of the molecular arrangement in artificial and biological membranes by phospholipid-shelled microbubbles. *Biomaterials*, 113, 105-117.
- [3]. Roovers, S., Segers, T., Lajoinie, G., Deprez, J., Versluis, M., De Smedt, S. C., & Lentacker, I. (2019). The role of ultrasound-driven microbubble dynamics in drug delivery: from microbubble fundamentals to clinical translation. *Langmuir*.
- [4]. Stride, E., & Coussios, C. (2019). Nucleation, mapping and control of cavitation for drug delivery. *Nature Reviews Physics*, 1(8), 495-509.

Vascular disruption and enhanced drug penetration performed in a mouse model of HCC with a clinical scanner

Sara B. Keller, Dingjie Suo, Yak-Nam Wang, Heidi Kenerson, Ally Sestero, Raymond Yeung, Michalakis Averkiou

Department of Bioengineering, University of Washington, Seattle, WA, USA

Introduction

Despite advances in chemotherapeutic drug development, hepatocellular carcinoma (HCC) is still the third leading cause of cancer-related deaths worldwide with a <30% 5-year survival rate [1]. This poor prognosis can be attributed to the fact that HCC most commonly occurs in patients with pre-existing liver conditions, rendering many systemic options too aggressive [2]. Patient survival rates could be improved by a more targeted therapy. Ultrasound and microbubbles can provide a means for overcoming traditional barriers defining drug uptake [3], [4]. The goal of this work was to evaluate preclinical efficacy of image-guided vascular disruption and enhanced doxorubicin (DOX) penetration with ultrasound (US) and microbubbles (MBs) using a Philips EpiQ scanner with an S5-1 probe on a mouse model of HCC.

Methods

Pten^{flox/flox} and *Alb-Cre* mice were crossed, whose progeny have hepatocyte-specific *Pten* deletion. At 40 weeks of age, *Pten*-null mice develop tumors that are physiologically similar to HCC [5]. 20 male mice and 18 female mice with tumors up to 2 cm in diameter were treated with either DOX alone or DOX + MBs + US. A Philips S5-1 probe with modified research settings was used as the focused source. Focused beams for sonoporation were created in pulsed wave (PW) Doppler mode, where a longer focal length beam was chosen in order to provide a larger nearfield insonation area (Fig. 1a). The system was modified to supply an ultrasound dose of 200 cycles at up to 4 MPa with a PRF of 50 Hz for 30s. Application of ultrasound began at 30s post retro-orbital injection, based on preliminary analysis of bolus wash-in kinetics (Fig. 1d). An L12-5 linear array was used to assess bubble delivery pre- and post-treatment using time-intensity curve analysis. Doxorubicin was extracted from frozen tissue samples and analyzed for fluorescent uptake. Tissue samples were qualitatively analyzed for doxorubicin penetration beyond CD31-labelled cells and proliferation was observed in Ki67 labelled cells.

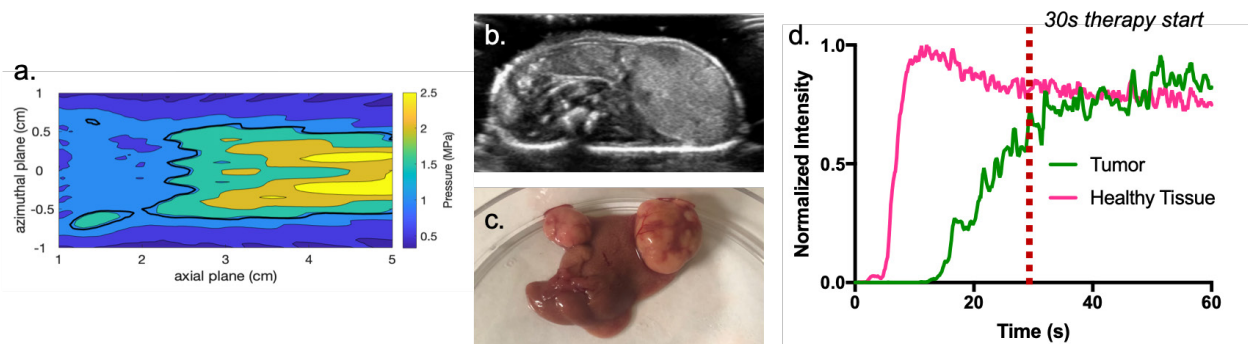


Figure 1: (a) Measured PW Doppler field of the Philips S5-1 in water with 6 dB contour lines shown in black. (b) B-mode image of mouse tumor, also seen after dissection in (c). (d) Time-intensity curve of tumor and healthy tissue wash-in and wash-out, used to inform treatment timing.

Results

Pre- and post-therapy contrast-enhanced ultrasound (CEUS) exams were used to show immediate changes in vascularity following treatment. As shown in the time-matched pre-and post-therapy contrast images in Fig. 2a and b, treated animals show reduction in contrast agent present in the tumor region following treatment, an effect not seen in normal tissue. Furthermore, bolus wash-in rate in tumors shows statistically significant reduction in control versus treated animals, also not seen in healthy tissue (Fig. 2d and e). This implies that the tumor vasculature is inherently susceptible to perfusion changes.

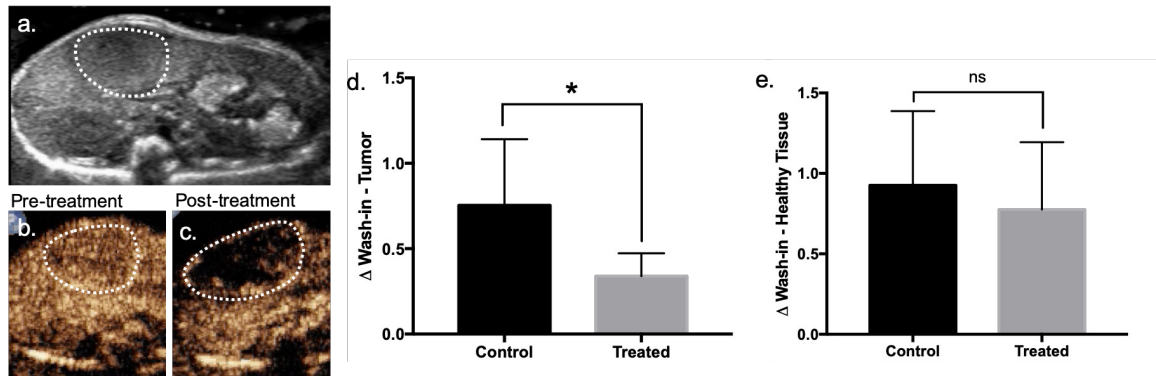


Figure 2: Anatomical B-mode image (a) and time-matched contrast images of pre- (b) and post- CEUS (c) scans of a treated mouse. (d) Significant reduction in bolus wash-in rate in tumors of treated versus control mice ($p < 0.05$). (e) No significant reduction in bolus wash-in rate in healthy liver tissue.

Tissue was analyzed quantitatively for doxorubicin uptake using fluorescence extraction. Shown in Fig. 3a, treated animals had a statistically significant increase in doxorubicin uptake in tumors. Minimal increase in drug was seen in other organs (Fig. 3b).

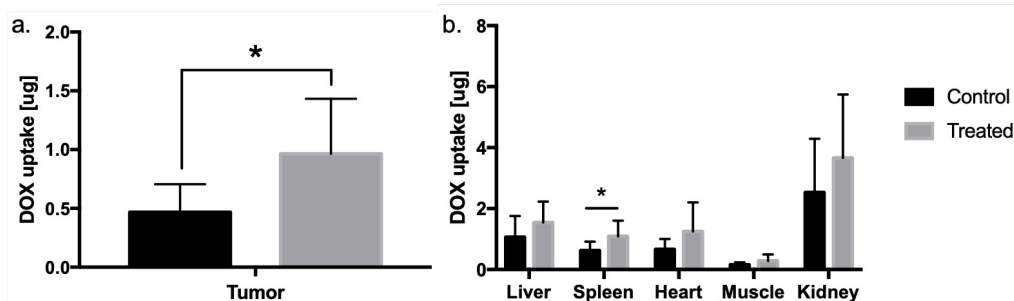


Figure 3: (a) Treated mice showed a significant increase of doxorubicin in tumors. (b) shows doxorubicin in other tissues. Only the spleen, located near the liver, shows a significant increase in treated animals.

5 μ m slices of frozen tissue were evaluated using fluorescence microscopy (Fig. 4a), and were also stained with CD31 to see vascular morphology (Fig. 4b) and Ki67 to show proliferation (Fig. 4c). It can be seen that doxorubicin (red) is present in the outer rim of the tumor, where the proliferating cells are located. Moreover, tumor vasculature is shown to be much more tortuous and chaotic than the surrounding vasculature.

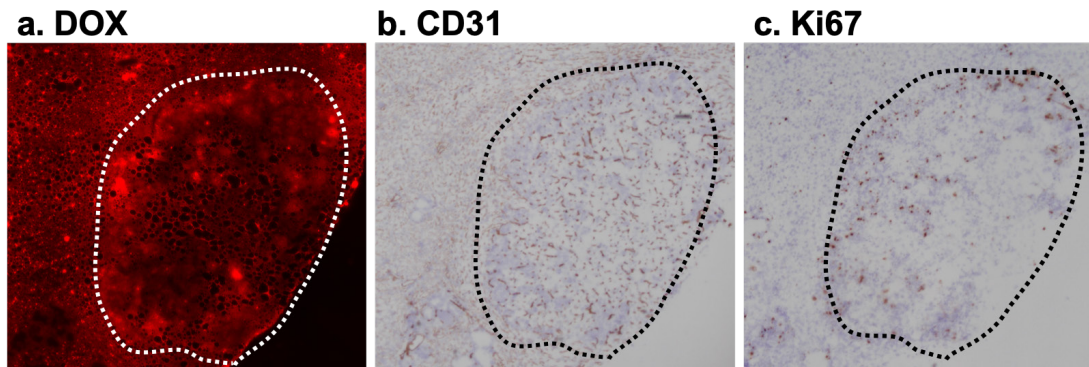


Figure 4: (a) 5 μm tissue slice analyzed qualitatively for fluorescence presence. Notice high accumulation in the outer rim of the tumor. (b) and (c) show CD31 and Ki67 staining, respectively. Note the tortuous vascular structure within the tumor, seen in (b) and the proliferating cells shown on the outer rim of the tumor in (c).

Conclusions

We observed that there was significant and immediate perfusion changes following treatment with ultrasound and microbubbles. This effect was specific to the tumor, implying an inherent vulnerability in the tumor microvasculature that was not seen in healthy tissue. Furthermore, it was shown that there was a statistically significant increase in doxorubicin in tumors in treated versus control animals. From imaging of fluorescent and antibody-labelled slices, it was shown that doxorubicin presence was mainly in the outer, proliferative rim of the tumor, whereas vascular disruption mainly occurred in the center of the tumor. The combination of the vascular disruption effect and enhanced drug penetration may play a synergistic role in successful cancer therapy. This work was performed with a clinical scanner and commercial microbubbles with hopes for clinical translation in the near future.

References

- [1]. H. B. El-Serag and K. L. Rudolph, "Hepatocellular carcinoma: epidemiology and molecular carcinogenesis.," *Gastroenterology*, vol. 132, no. 7, pp. 2557–76, Jun. 2007
- [2]. H. Cao, H. Phan, and L.-X. Yang, "Improved chemotherapy for hepatocellular carcinoma.," *Anticancer Res.*, vol. 32, no. 4, pp. 1379–86, Apr. 2012.
- [3]. D. E. Goertz *et al.*, "Antitumor Effects of Combining Docetaxel (Taxotere) with the Antivascular Action of Ultrasound Stimulated Microbubbles," *PLoS One*, vol. 7, no. 12, p. e52307, Dec. 2012.
- [4]. I. De Cock *et al.*, "Ultrasound and microbubble mediated drug delivery: acoustic pressure as determinant for uptake via membrane pores or endocytosis," *J. Control. Release*, vol. 197, pp. 20–28, 2015.
- [5]. Y. Horie *et al.*, "Hepatocyte-specific Pten deficiency results in steatohepatitis and hepatocellular carcinomas.," *J. Clin. Invest.*, vol. 113, no. 12, pp. 1774–83, Jun. 2004.

Enhanced Heating with Microbubbles in High Intensity Focused Ultrasound Applications

Alicia Clark, Sierra Bonilla, Dingjie Suo, Michalakis Averkiou

Department of Bioengineering, University of Washington, Seattle, USA

Corresponding author: clarka34@uw.edu

Introduction

High intensity focused ultrasound (HIFU) is a noninvasive tool for targeted thermal ablation treatments. HIFU is used clinically for thermal ablation of various cancers and uterine fibroids. Additionally, it has applications in the brain for treatment of essential tremor, Parkinson's disease, and neurological pain. Current HIFU treatments in the brain require very high acoustic intensities for treatment since a large amount of energy is absorbed or reflected by the skull. Additionally, focused ultrasound is only capable of burning very small regions towards the center of the brain. Safely increasing the ablation zone and decreasing the acoustic intensity is necessary to treat a wider range of neurological disorders. Previous research has shown that HIFU in conjunction with gas-filled bubbles can increase ablation regions and shorten acoustic exposures at lower acoustic pressures [1, 2, 3, 4]. Additionally, previous animal studies have shown that microbubbles reduce the amount of acoustic energy needed for thermal treatments [5, 6, 7]. For microbubble-enhanced heating to be clinically relevant, microbubble cavitation must be extensively studied and shown to reproducibly form lesions through well understood mechanisms. This work focuses on enhancing HIFU treatments in the brain by utilizing ultrasound contrast agents to better localize treatments and to decrease the acoustic energy required for thermal ablation.

The main objective of this work was to study microbubble-enhanced heating in an *in vitro* experimental setup under real-time ultrasound image-guidance. We considered a lower frequency than previously explored in the literature due to the intended brain application. Thin-wire thermocouples were inserted into egg white phantoms containing microbubbles at various concentrations to measure the temperature change in the phantom during each HIFU treatment. These measurements were taken both with and without microbubbles to determine the effect of microbubbles on temperature rise. The effect of varying acoustic pressure and microbubble concentration was also studied to explore the interaction between pressure and microbubble concentration on pressure attenuation and lesion formation.

Methods

Fig. 1(a) shows the experimental setup that was developed to understand the effect of microbubbles on heating in HIFU treatments.

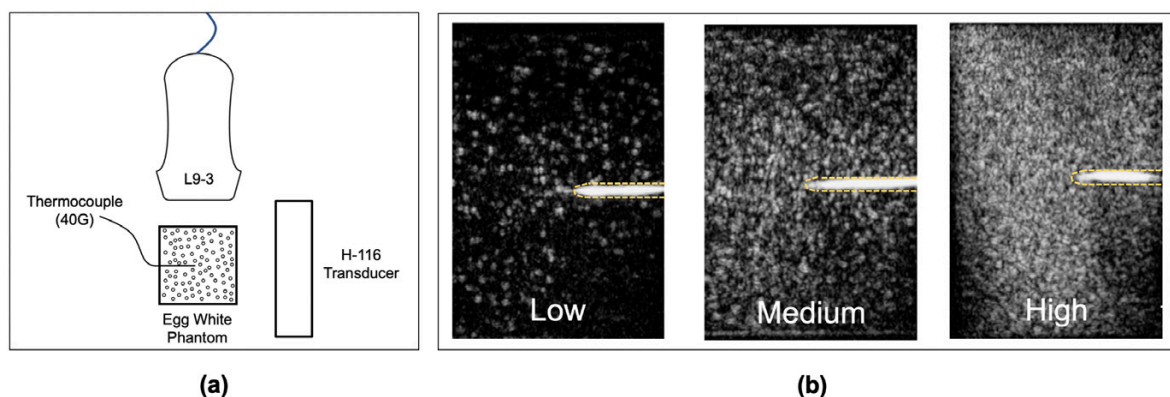


Figure 1. (a) Experiment setup. (b) Ultrasound contrast images showing the dilution of microbubbles in egg white phantoms at three different microbubble concentrations: low, medium, and high. Thermocouples (yellow outline) were inserted into each phantom to measure the temperature rise during each thermal treatment.

A 0.9 MHz focused transducer (H-116, Sonic Concepts, Seattle, USA) was used for this study. An egg white phantom [8] was treated with the H-116 transducer for 30 seconds at an 82% duty cycle to allow ultrasound imaging to be interleaved with therapy. The interleaved imaging (L9-3, Philips, Amsterdam, NL) was used to monitor the behavior of the microbubbles diluted in the phantom and monitor for lesion formation. Additionally, a 40G thermocouple, which was inserted into the back of the egg white phantom along the axis of ultrasound propagation, was used to take temperature measurements at the focus of the transducer. Temperature was recorded during the entire 30 second treatment time and an additional 30 seconds afterwards to monitor the phantom as it cooled.

Results

Experiments were conducted at three different concentrations of microbubbles (low, medium, and high ranging from about 10^2 to 10^4 MBs/mL) and three different pressure amplitudes (0.5 MPa, 2.0 MPa, and 6.0 MPa). Fig. 2 shows ultrasound images taken during the “down time” of the 82% duty cycle of the H-116 transducer for three separate concentrations of microbubbles at 2.0 MPa. Ultrasound from the H-116 propagates from left to right and the imaging probe is at the top. At the low concentration, it is evident that the initial microbubbles were destroyed since the contrast image is dark around the thermocouple. Additionally, the fundamental image shows that larger gas bubbles, shown as a hyperechoic region, are now present in place of the microbubbles. Similar behavior is seen in the phantom with the medium concentration of microbubbles. At this concentration, however, there are less larger gas bubbles post-focally due to nonlinear attenuation of the pressure field from the pre-focal microbubbles. This asymmetry is more noticeable in the high concentration fundamental image. Interestingly, for this concentration, the pre-focal microbubbles were still present in the contrast imaging and were not immediately destroyed, probably due to the larger number of microbubbles present to shield the incoming pressure field.

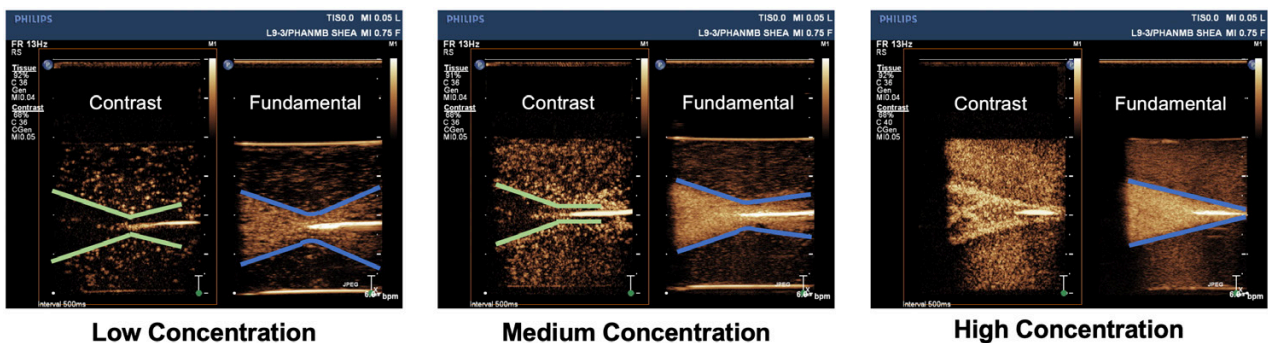


Figure 2. Fundamental and contrast images were taken during the thermal treatment of phantoms with microbubbles at various concentrations. The HIFU field propagates from left to right in the images. The blue lines in the fundamental images outline the region of larger bubble activity and gas formation. At higher concentrations, there is less bubble activity post-focally due to acoustic shadowing. The green lines outline the regions where microbubbles were destroyed in the contrast images.

Fig. 3 shows the temperature rise in egg white phantoms with microbubbles at different concentrations and different pressure amplitudes. At the low concentration of microbubbles, the temperature rise behaves similarly to the phantom without microbubbles (not shown in Fig. 3), with a slight increase in the peak temperature rise measured in comparison to the phantoms without microbubbles. The large oscillations in the temperature measurement at 6.0 MPa are due to inertial cavitation events present in the phantom and confirmed with imaging.

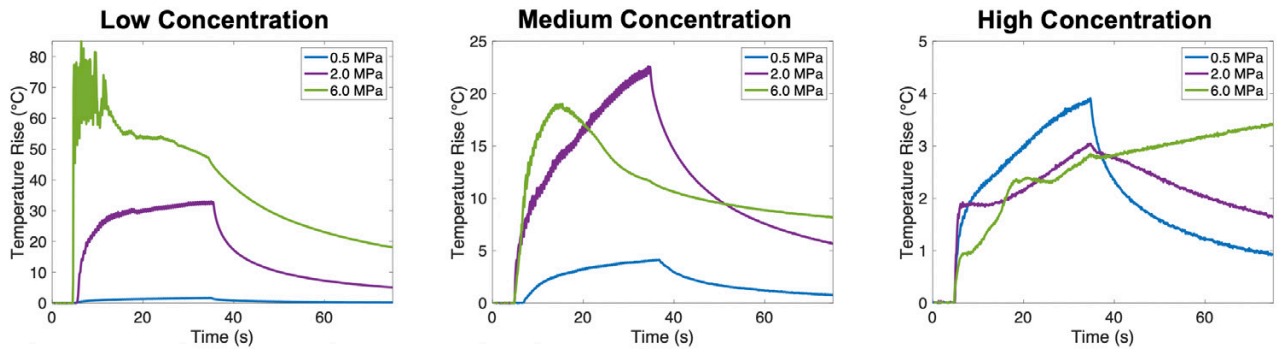


Figure 3. Temperature measurements taken at the focus in the phantom during thermal treatments. Three different concentrations of microbubbles were studied at three separate pressures: 0.5 MPa, 2.0 MPa, and 6.0 MPa. At higher concentrations, the microbubbles largely attenuate the sound field, leading to decreased measured temperature at the focus.

Similar temperature profiles were also observed in the medium concentration phantoms; however, there are two notable differences. First, at 2.0 MPa, the slope of the temperature changes, most likely due to nonlinear attenuation from pre-focal microbubbles. Additionally, there is a noticeable decrease in total temperature rise at 6.0 MPa at this concentration compared to the low concentration measurement; the lesion formation also occurs pre-focally as shown in Fig. 4. Finally, at high concentration of microbubbles, there is no noticeable temperature rise at the focus at 2.0 and 6.0 MPa. This is because the pre-focal microbubbles heavily attenuate the pressure field while propagating in the phantom; a lesion is formed right at the entrance of the phantom at 6.0 MPa.

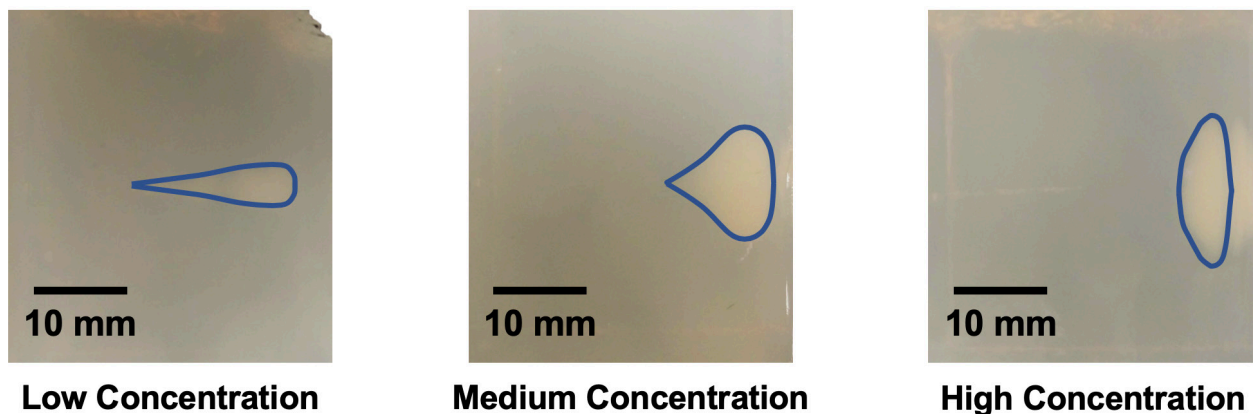


Figure 4. Optical images of lesion formation in the phantoms with 6.0 MPa heating treatments. The lesion shape changes and migrates towards the front face (right edge) of the phantom as the microbubble concentration is increased. The shape of the lesion is seen easier with a blue outline. The HIFU field propagates from right to left in the images.

Conclusions

Microbubble-enhanced heating was studied in egg white phantoms at three different microbubble concentrations and pressure amplitudes. We show that microbubbles increase the temperature in egg white phantoms compared to phantoms without microbubbles. However, the combination of pressure and microbubble concentration is extremely important for microbubble-enhanced heating due to pressure dependent acoustic shadowing. At higher concentrations of microbubbles, the pre-focal microbubbles shield the sound field, making it difficult to accurately localize lesion formation. We have also shown that the location of the formed lesion is highly dependent on the combination of acoustic pressure and microbubble concentration used. Real-time image guidance is therefore essential for microbubble-enhanced heating to observe microbubble dynamics during heating at different pressure amplitudes.

References

- [1]. Chang N, Lu S, Qin D, Xu T, Han M, Wang S, Wan M, Efficient and controllable thermal ablation induced by short-pulsed HIFU sequence assisted with perfluorohexane nanodroplets, *Ultrasonics Sonochemistry*, 45: 57–64, 2018.
- [2]. You Y, Wang Z, Ran H, Zheng Y, Wang D, Xu J, Wang Z, Chen Y, Li P, Nanoparticle-enhanced synergistic HIFU ablation and transarterial chemoembolization for efficient cancer therapy, *Nanoscale*, 8: 4324–4339, 2016.
- [3]. Zhang P, Porter T, An in vitro study of a phase-shift nanoemulsion: A potential nucleation agent for bubble-enhanced HIFU tumor ablation, *Ultrasound in Medicine & Biology*, 36: 1856–1866, 2010.
- [4]. Tung Y, Liu H, Wu C, Ju K, Chen W, Lin W, Contrast-enhanced ultrasound thermal ablation, *Ultrasound in Medicine & Biology*, 32: 1103-1110, 2006.
- [5]. McDannold N, Vykhodtseva N, Hynynen K, Microbubble contrast agent with focused ultrasound to create brain lesions at low power levels: MR imaging and histologic study in rabbits, *Radiology*, 241: 95-106, 2006.
- [6]. Yu T, Wang G, Hu K, Ma P, Bai J, Wang Z, A microbubble agents improves the therapeutic efficiency of high intensity focused ultrasound: A rabbit kidney study, *Urological Research*, 32: 14-19, 2004.
- [7]. Tran BC, Seo J, Hall TL, Fowlkes JB, Cain CA, Microbubble-enhanced cavitation for noninvasive ultrasound surgery, *IEEE Transactions on Ultrasonics, Ferroelectrics, and Frequency Control*, 50: 1296-1304, 2003.
- [8]. Takegami K, Kaneko Y, Watanabe T, Maruyama T, Matsumoto Y, Nagawa H, Polyacrylamide gel containing egg white as new model for irradiation experiments using focused ultrasound, *Ultrasound in Medicine and Biology*, 30: 1419-1422, 2004.

Visualization of Vasculature by Non-Rigid Registration and Segmentation of Subharmonic Ultrasonic Images

H. Neustadter¹, Y. Dan¹, G. Zurakhov¹, S. Kotopoulos², A. Langer³, G.R. de Garibay³,
E. McCormack³, M. Stanczak³, J. Eisenbrey⁴, F. Forsberg⁴, D. Adam¹

¹Dept. of Biomedical Engineering, Technion, Haifa, Israel; ²Haukeland University Hospital, Bergen, Norway; ³CCBIO, University of Bergen, Bergen, Norway; ⁴Dept. of Radiology, TJU, Philadelphia, PA
Corresponding author: Hanni.neus@gmail.com

Introduction

Detection of abnormal vasculature in pancreatic cancer tumors may allow early diagnosis, more effective treatment and improve the survival rates of patients. Contrast-enhanced ultrasound (CEUS) is a commonly used imaging modality that promotes visualization of the vasculature of the tissue and may help detect small morphological changes. Non-rigid registration of images (frames) within a clip may be beneficial to overcome some of the problems inherent to the physiological motion of the observed anatomical structures [1]. Segmentation of different types of tissue within the clip, differentiating the dynamics of noisy background (tissue) from that of flow (vascularization), may further improve the visualization of the vasculature. Herein we present improved visibility of the vasculature by utilizing a two-step method. In the first step, a non-rigid registration is performed of the images in the clip acquired by grayscale imaging, and consequently applying the estimated deformation field to the images obtained by the employment of subharmonic imaging (SHI). In the second step, the registered clip is segmented by analyzing the dynamics of vascular flow, as visualized by SHI.

Methods

Data: Two groups of data were used: *Group 1* - human pancreas with pancreatic tumor; *Group 2* - mice hindlimb with induced tumor. The data were acquired using a curvi-linear transducer with a GE Healthcare research Logiq 9 or E9 system (employing a dual mode of transmissions of 4-MHz for the grayscale imaging and pulse inversion transmission at 2.5-MHz for the SHI, while receiving at 1.25-MHz for SHI) [2]. The pulse-echoes of the fundamental harmonic and subharmonic signals were generated by employing interleaving acquisition mode, and are shown simultaneously. The clips were acquired after a bolus injection (*Group 1*) or continuous injection of contrast agent (UCA) (*Group 2*).

Step I - Registration: The Morphon (i.e. a local phase) registration method was used, by applying directional quadrature filters to the grayscale images and estimating the deformation field from the resultant filtration response [3, 4]. This deformation field, which represents the new position of each pixel in the deformed image is then applied to the SHI clip. The results of registration of the clips are presented, as well as maximum intensity projection (MIP) processing applied to the clips preceding/succeeding the registration.

Step II - Flow Segmentation: Local spatial-temporal feature extraction and block processing were employed: selected regions of interest (ROI's) within the SHI clip were decomposed by wavelet decomposition, for both the noise reduction and the extraction of local spatial-temporal behavior [5]. Since similar tissues have similar properties but may have a shift in phase in the temporal domain, a time-independent discrete cosine transformation (DCT) was performed, followed the spatial-temporal feature extraction. Next, ROI's representing different properties were selected: 1) background tissue - containing a low concentration of UCA, 2) blood vessels - containing high concentrations of UCA, 3) blood vessels containing low concentrations of UCA. The clustering of these areas was applied to segment the SHI clip [6].

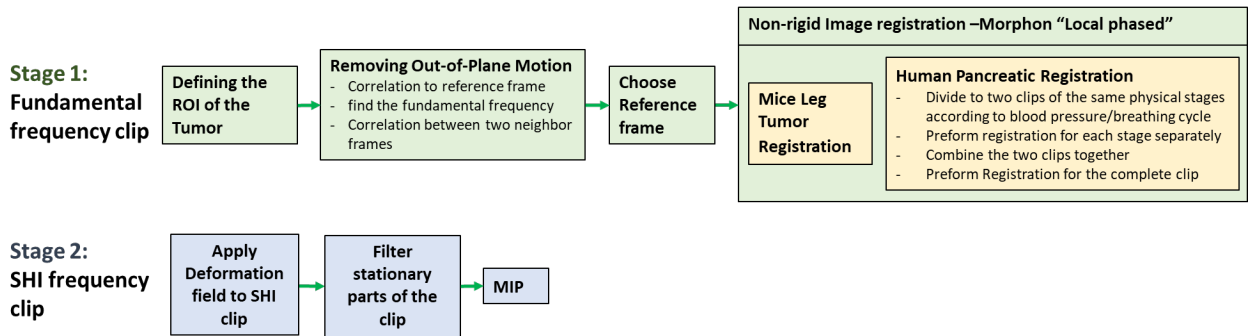


Table 1: Step I - Registration method algorithm

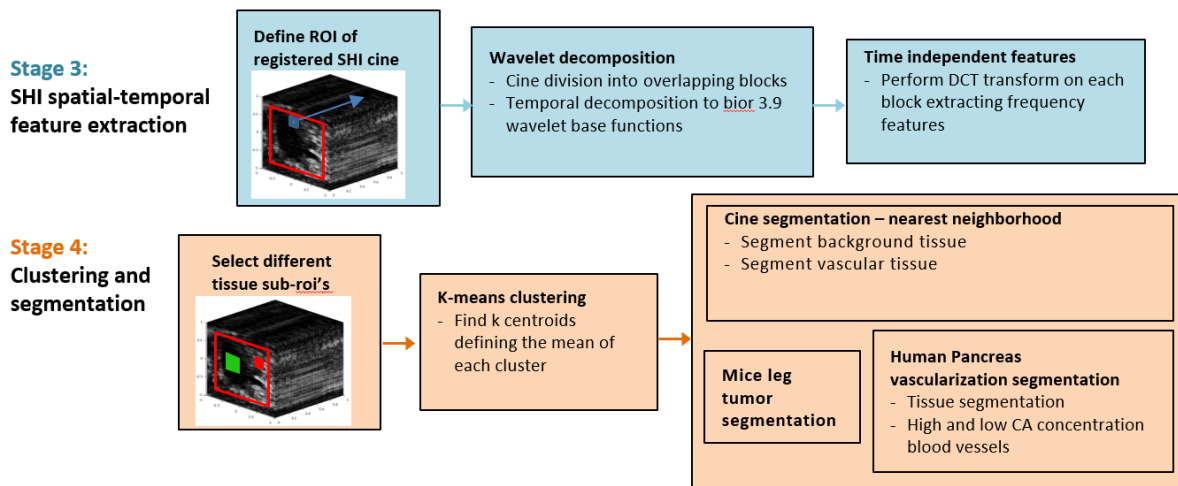


Table 2: Step II - Segmentation method algorithm

Results

The results, best presented as clips, are here presented and validated by depicting the correlation between frames (before and after the registration). Additionally, MIP images are presented, illustrating the total movements of the organ and the vessels.

The examples below (Fig. 1, 3, and 5) demonstrate the increase of the correlation. In group 1, Fig. 1, a significant improvement of the correlation is depicted after performing registration at the end-expiration period. Further improvement is achieved for the registration of a full breathing cycle (Fig. 1(G)). In the MIP images of the unprocessed grayscale and SHI data, Fig. 1(B), 1(D), the edges of the vessel are smudged due to its movement, as opposed to the MIP result after applying the registration data, Fig. 1(C), 1(E). Another example from *Group 1* is given in Fig. 5. An example from *Group 2* is given in Fig. 3., with higher correlations, since there is less movement in the hindleg tumor clips of the mouse.

Results of the segmentation of different flow patterns, as viewed in the respective SHI clips, are depicted for an example from *Group 1* (human pancreas) in Fig. 2, and from *Group 2* (mice tumor) in Fig. 4. In both cases, capillary flow is not marked, while flow in arterioles and venules is marked in red, and rapid flow in blue.

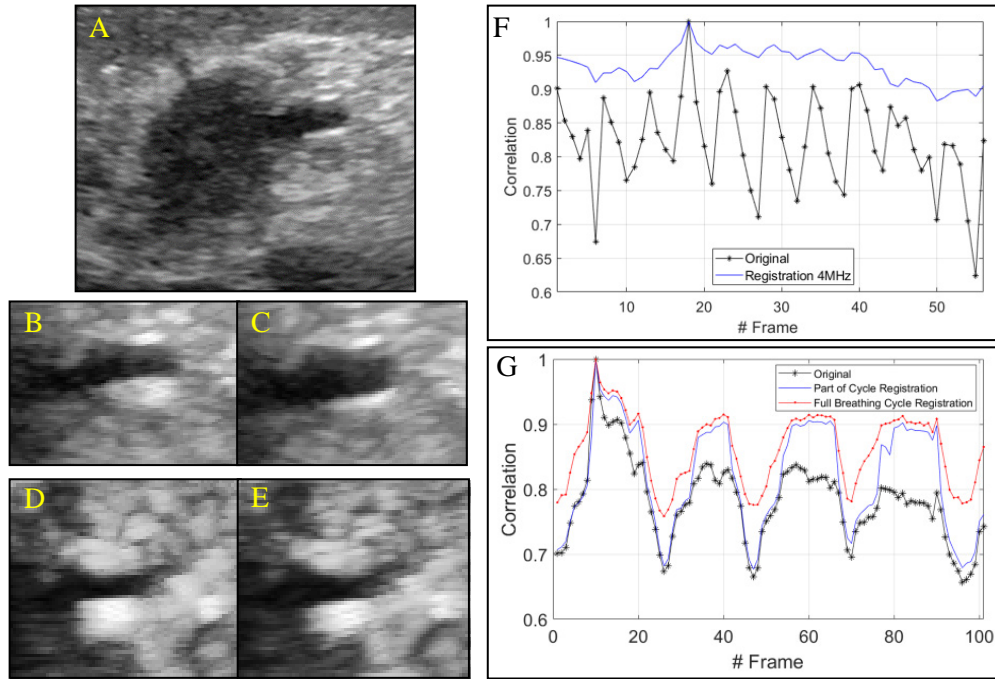


Figure 1. Human pancreas – A) original picture in fundamental frequency; B) MIP picture of unprocessed grayscale images; C) MIP picture of grayscale images after registration; D) MIP picture of unprocessed SHI; E) MIP picture of SHI after registration; F) Correlation graph of the grayscale images before and after registration of part of the breathing cycle. G) Correlation graph of the grayscale images, before and after registration of the full breathing cycle.

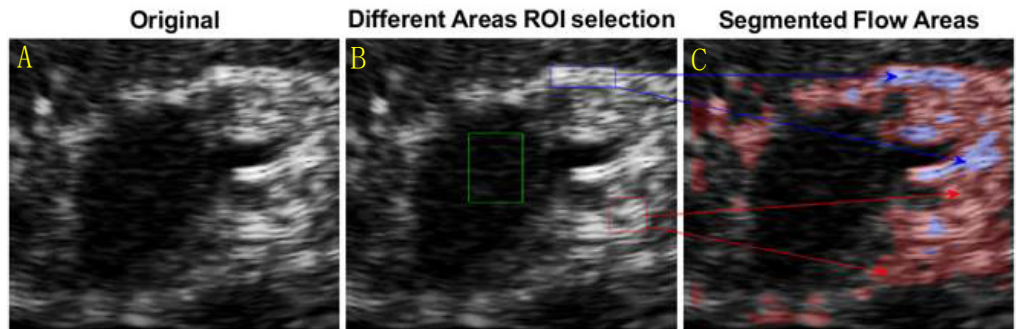


Figure 2. Sub Harmonic
C) Results of the ϵ

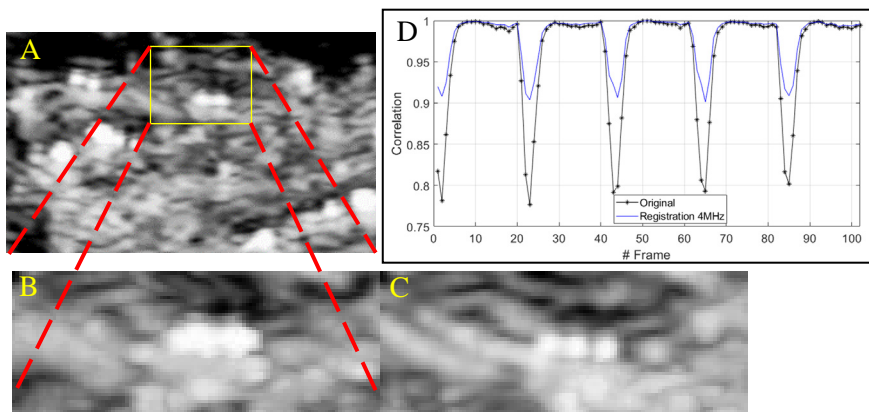


Figure 3. Tumor in mice - A) original picture (fundamental frequency); B) MIP picture of unprocessed SHI, yellow ROI area; C) MIP picture of SHI after registration, yellow ROI area; D) Correlation graph of the grayscale images, before/after registration.

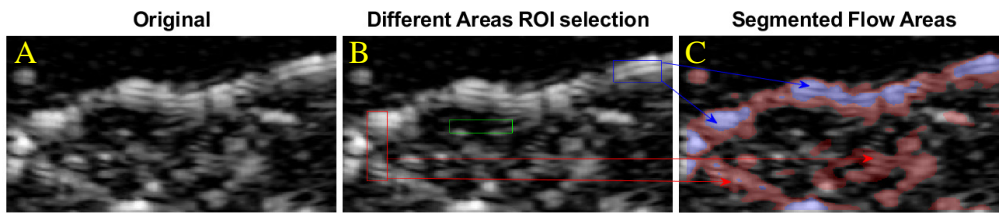


Figure 4. Sub Harmonic Imaging (SHI) of Tumor in mice - A) original SHI; B) 3 ROI's marked with different flow properties; C) Results of the automatic segmentation of the different flow regions. Arrows show matching of segmented areas to ROI's.

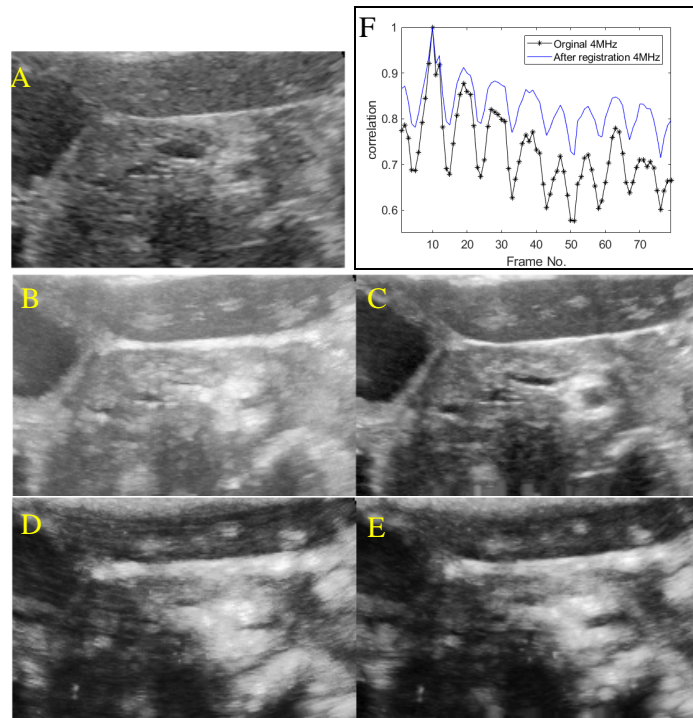


Figure 5. Human pancreas – A) Original picture (fundamental frequency); B) MIP picture of unprocessed fundamental frequency images; C) MIP picture of fundamental frequency images after registration; D) MIP picture of unprocessed SHI; E) MIP picture of SHI after registration; F) Correlation graph of the fundamental frequency images, before and after registration.

Discussion and Conclusions

Both the clinical and the pre-clinical data were acquired under conditions that severely limit the ability to register and process the images. First, the acquisition frame rates were very low (7-8 FPS and 18-20 FPS, respectively) affecting the quality of motion estimation when movements occur. Moreover, the grayscale images and SHI were acquired in an interleaving mode, leading to temporal mismatch due to the time gap between acquisitions, thus affecting the correction. In addition, UCA was infused without employing the flash-replenishment technique, thus the UCA was circulating for a long time and filling up capillaries, which makes the segmentation of the blood vessels more challenging. These shortcomings will not be overcome in the near future. In addition, the grayscale clips of the pancreas suffer from a low SNR and significant clutter noise, which interfere with the pre-processing, registration and segmentation processes.

The correlation between the frames of the SHI clips was improved for both groups, indicating an improved alignment. The visualization of the tissue vasculature was also improved after the registration. Segmentation of the vasculature by their properties further enhanced the visualization. The human

pancreas data, which commonly suffers from large movements and low FPS, benefits from the two-step registration, e.g. registration during the end-expiration followed by the registration of the entire clip. When only small movements are present, as shown in Fig. 3, there is no need for the two stages solution.

The limitation regarding the data should be further investigated in the future. One potential way of overcoming the impact of these shortcomings is preprocessing before registration, where for clips with large movements local registration should first be performed, and only then global registration. Moreover, a post-segmentation process can additionally be performed by utilizing the statistical properties of UCA groups, by removing the regions that were segmented as having large UCA concentration and reprocessing the regions of low UCA concentration for enhancing the visualization of smaller vasculature.

Supported in part by NIH R01 CA199646

References

- [1]. Kibo Nam, John R. Eisenbrey, Maria Stanczak, Anush Sridharan, Adam C. Berger, Tiffany Avery, Juan P. Palazzo, Flemming Forsberg, "Monitoring Neoadjuvant Chemotherapy for Breast Cancer by Using Three-dimensional Subharmonic Aided Pressure Estimation and Imaging with US Contrast Agents: Preliminary Experience", *Radiology*, 2017
- [2]. Forsberg, F., Stanczak, M., Lyschik, A., Loren, D., O'kane, P., Siddiqui, A., Kowalski, T.E., Miller, C., Fox, T., Liu, J.B. and Eisenbrey, J.R., 2018. Subharmonic and Endoscopic Contrast Imaging of Pancreatic Masses: A Pilot Study. *Journal of Ultrasound in Medicine*, 37(1), pp.123-129.
- [3]. Plumat, J., Andersson, M., Janssens, G., Orban de Xivry, J., Knutsson, H. and Macq, B., 2009. Image registration using morphon algorithm: an itk implementation. *Insight Journal*.
- [4]. Forsberg, D., 2013. Robust image registration for improved clinical efficiency: using local structure analysis and model-based processing (Doctoral dissertation, Linköping University Electronic Press).
- [5]. Bar-Zion, A.D., Tremblay-Darveau, C., Yin, M., Adam, D. and Foster, F.S., 2015. Denoising of contrast-enhanced ultrasound cine sequences based on a multiplicative model. *IEEE Transactions on Biomedical Engineering*, 62(8), pp.1969-1980.
- [6]. Angelelli, P., Nylund, K., Gilja, O.H. and Hauser, H., 2011. Interactive visual analysis of contrast-enhanced ultrasound data based on small neighborhood statistics. *Computers & Graphics*, 35(2), pp.218-226.

Investigation of the relationship between microvascular architecture and ultrasound-contrast-agent kinetics by controlled porous media

*P. Chen¹, S. Turco¹, R. J.G. van Sloun¹, A. M.A.O. Pollet², J. M.J. den Toonder²,
H. Wijkstra^{1,3}, M. Misch¹*

¹*Department of Electrical Engineering, Eindhoven University of Technology, Eindhoven, Netherlands*

²*Department of Mechanical Engineering, Eindhoven University of Technology, Eindhoven, Netherlands*

³*Department of Urology, Amsterdam University Medical Centers, Amsterdam, Netherlands*

Corresponding author: p.chen1@tue.nl

Introduction

As a recognized hallmark of cancer, tumor-driven angiogenic microvasculature is characterized by increased microvascular density (MVD), smaller vessel diameter, and higher vessel tortuosity. This irregular microvascular network leads to complex blood flow patterns [1, 2, 3]. To assess the blood flow and further analyze the microvascular architecture, dynamic contrast-enhanced ultrasound (DCE-US) provides real-time analysis of the vasculature by imaging the blood flow with the help of intravenously-injected ultrasound contrast agents (UCAs). The temporal evolution of the UCA concentration is reflected in pixel intensity variations over the DCE-US loops. By collecting these variations, time-intensity curves (TICs) can be obtained at each pixel; their analysis enables the assessment of the underlying blood flow patterns and microvascular architecture, aiding with tumor detection. In the past years, extensive work has shown the value of convective-dispersion modeling for the interpretation of the measured TICs, with promising results for the diagnosis of e.g. prostate cancer [4, 5, 6, 7]. By interpreting the time evolution of the UCA concentration as the result of a convective-dispersion process, the mono-dimensional convective-dispersion equation is employed to model this process [8]. Based on this equation, we have already proposed the modified local density random walk model to assess the microvascular architecture by estimation of a local dispersion parameter [4]. More recently, considering the microvasculature as a dynamic system, we have proposed a method to locally identify the impulse response of the system by input-output analysis of TICs, yielding the separate estimation of velocity and dispersion components [5]. According to the results obtained in the prostate, increased velocity and decreased dispersion are observed in tumor tissue. However, a clear link between the estimated parameters and the underlying microvasculature is still lacking.

In this work, modeling the microvasculature as a porous medium, we developed a set-up including dedicated porous phantoms to investigate this relationship between convective-dispersion parameters and microvascular architecture. These phantoms were realized by packing mono-sized beads in a cylinder tube. The pore size was controlled by tuning the bead diameter, simulating different MVD and vessel diameter. DCE-US was performed to record the UCA flow through the realized phantoms, and velocity and dispersion coefficient were estimated by a model-based deconvolution method [9]. The estimated parameters in different phantoms were then compared to analyze the relationship between microvascular architecture and UCA dynamics. Moreover, in order to validate the experimental results, we also simulated the porous phantoms in-silico, and a preliminary simulation test was performed by combining the simulated phantoms with fluid dynamic simulations of bubble transport.

Methods

Our in-vitro experimental set-up consists of a dedicated perfusion pump [10], UCA injector, porous phantom, and an ultrasound acquisition system, as schematically shown in Fig. 1. In this set-up, the self-designed perfusion pump provided a constant water flow at a rate of 0.22 mL/s. A long tube connected between the pump and the phantom was employed to obtain a fully-developed laminar flow. The UCA

injector was connected to the tube by a three-way tap. The porous phantoms were built by packing 3% alginate beads in a polyurethane tube, whose shape was fixed by two circular nets at the two ends of the phantoms. The chosen bead material has acoustic properties similar to human tissue. The phantoms were gently squeezed and shaken after packing to provide a more homogeneous structure. The length of the phantoms was comparable to the length of the ultrasound transducer. Variable MVD and vessel diameter were realized by packing beads with diameters of 3.1, 2.5, and 1.6 mm, respectively.

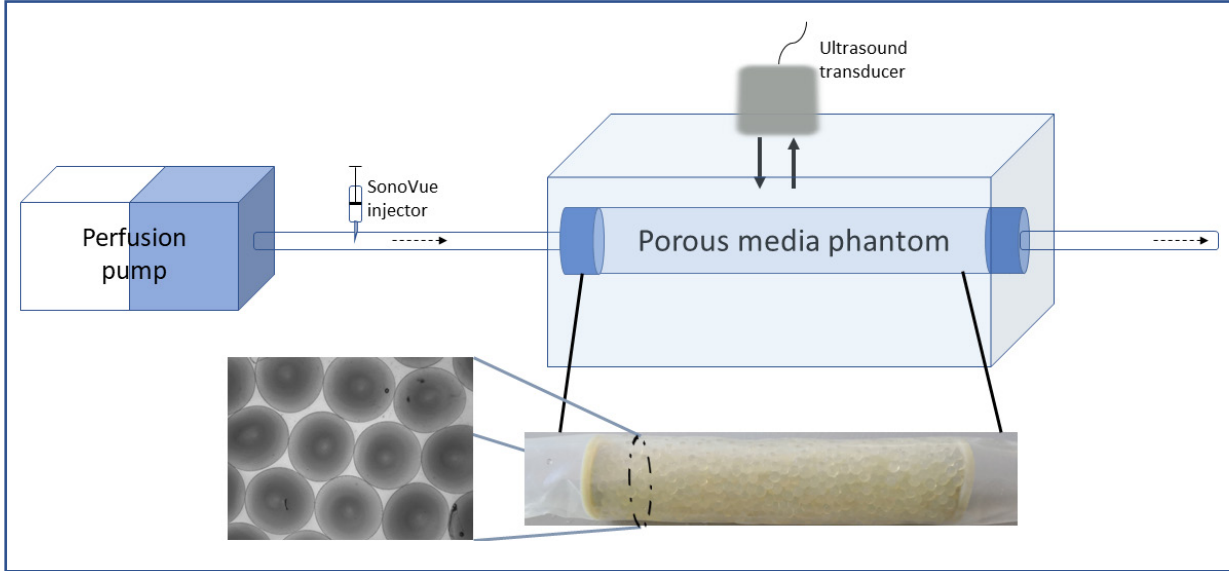


Figure 1. Schematic overview of the in-vitro set-up.

In our experiment, the phantoms were submerged in water for ultrasound imaging, avoiding air interference. A 1-mL SonoVue® bolus (Bracco, Milan, Italy) diluted 1:100 was injected into the fluid dynamic set-up. After the injection, the UCA transport through the porous medium was imaged by DCE-US using a Verasonics ultrasound platform (Vantage 128, Verasonics Inc.) equipped with a L11-4v probe. Imaging was performed in contrast mode by combining pulse inversion and amplitude modulation techniques at a frame rate of 25 Hz for two minutes.

As shown in Fig. 2, the UCA bolus flows through the phantom from its left side to its right side, representing the input and output region of interests (ROIs). TICs extracted from input and output ROIs were linearized prior to the following analysis. To reduce the influence of ROI placement, the estimation was repeated 400 times for each phantom by translating the input-output ROIs axially and laterally, and changing the distance between them.

Considering the microvascular network as a dynamic system, the impulse response of the system could be identified by input-output analysis of TICs. The impulse response was then fitted by the Green's function of the convective-dispersion equation, which describes the UCA transport in the medium as

$$\partial_t C(z, t) = D \partial_z^2 C(z, t) - v \partial_z C(z, t),$$

where $C(z, t)$ is the concentration of UCA at position \mathbf{z} and time t , D is the dispersion coefficient, and v is the convective velocity. Similar to a microvascular network, the dispersion coefficient is mainly determined by the multipath trajectories through the porous medium [11].

The in-silico simulation of porous phantoms was realized using a sphere-packing algorithm. Initially, we defined a cylinder region representing the polyurethane tube, and thousands of mono-sized spheres were uniformly distributed inside this region, allowing overlapping between spheres. Then, an iterative procedure was implemented to separate the spheres until there was no overlapping. During this process,

for each 100 iterations, a random movement was applied to all the spheres to mimic a shaking process. Finally, if needed, a few additional spheres were added to fill those voids that were large enough to contain an individual sphere, using a search algorithm that minimized the distance between the newly added spheres and the existing spheres until they touched each other without overlapping.

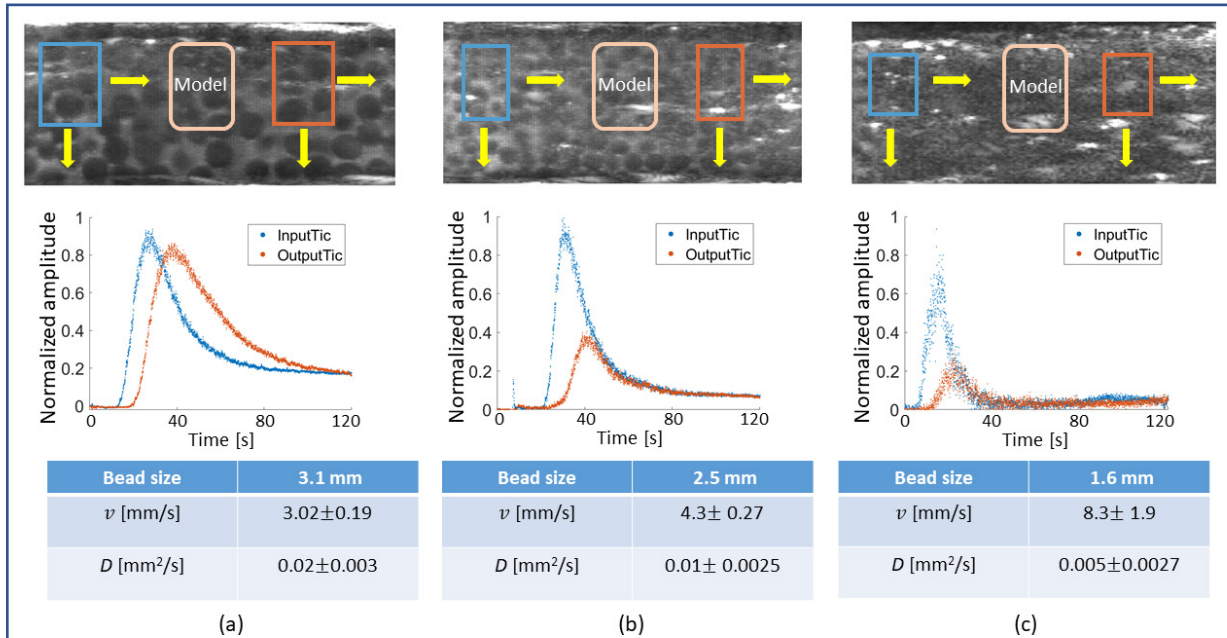


Figure 2. The maximum intensity persistence images of three porous phantoms, their corresponding TICs from input and output ROIs, and the estimated parameters v and D : (a) bead size of 3.1 mm, (b) bead size of 2.5 mm, (c) bead size of 1.6 mm.

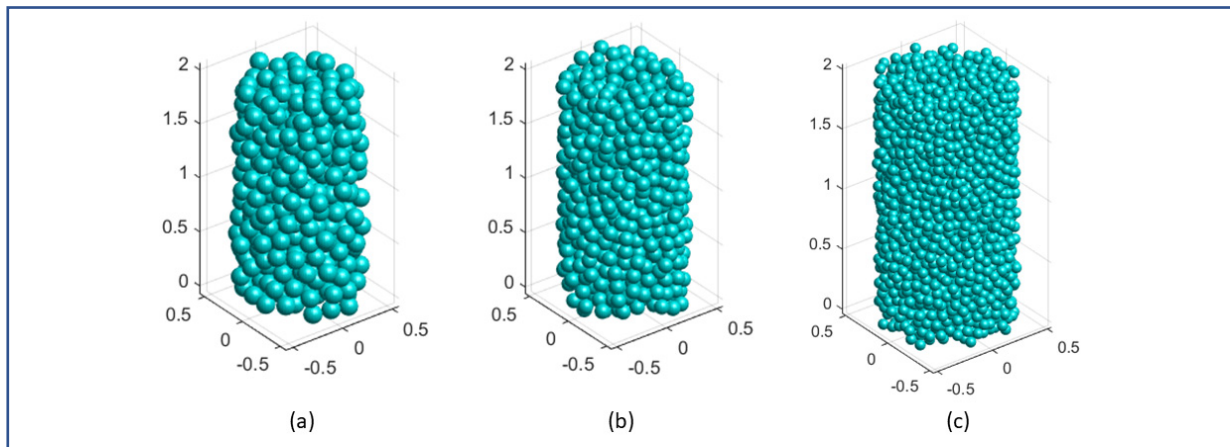


Figure 3. Simulated porous phantoms using a sphere-packing algorithm: the diameters of the spheres are 3.1, 2.5 and 1.6 mm, respectively from (a) to (c). The diameter of the tube is 20 mm and the length of the tube is 40 mm. In this figure, all the dimension is scaled up by a factor of 50.

Results

Figure 2 shows maximum intensity persistence images of three porous phantoms obtained from their DCE-US acquisitions. A decreasing bead size corresponds to an increase in MVD and a decrease in vessel diameter. Input and output TICs corresponding to the three phantoms are also shown in Fig. 2. Qualitatively, the measured TICs become less skewed for smaller bead diameter. Quantitatively, the estimated velocity increases and the dispersion coefficient decreases with decreasing bead size.

Figure 3 demonstrates the simulated porous phantoms with variable pore size. These phantoms are combined with fluid dynamic simulations of bubble transport to replicate the experiment in-silico, enabling further investigation of the relationship between microvascular architecture and UCA dynamics.

Conclusions

In this work, we developed dedicated porous phantoms and investigated the relationship between UCA dynamics and the underlying microvascular architecture. The obtained results are in line with previous in-vivo finding [4, 5], confirming the value of contrast-ultrasound dispersion imaging for quantification of cancer angiogenesis. This investigation also represents a first step in demonstrating the relationship between microvascular architecture and UCA dynamics. In the future, further validation will be performed both in-silico, by combining the simulated porous phantoms with fluid dynamic simulations of bubble transport, and in-vitro, by developing more complex phantoms using beads of polydispersed size.

References

- [1]. Folkman J, Role of angiogenesis in tumor growth and metastasis, *Seminars in Oncology*, 29: 15-18, 2002.
- [2]. Weidner N, Carroll PR, Flax J, Blumenfeld W and Folkman J, Tumor angiogenesis correlates with metastasis in invasive prostate carcinoma, *The American journal of pathology*, 143: 401-409, 1993.
- [3]. Russo G, Mischi M, Scheepens W, de la Rosette JJMCH, Wijkstra H, Angiogenesis in prostate cancer: onset, progression and imaging, *BJU international*, 110: 794-808, 2012.
- [4]. Kuenen MPJ, Mischi M and Wijkstra H, Contrast-enhanced diffusion imaging for localization of prostate cancer, *IEEE Transactions on Medical Imaging*, 30: 1496-1502, 2011.
- [5]. van Sloun RJG, Demi L, Postema AW, de la Rosette JJMCH, Wijkstra H and Mischi M, Ultrasound-contrast-agent dispersion and velocity imaging for prostate cancer localization, *Medical Image Analysis*, 35: 610-619, 2016.
- [6]. Kuenen MPJ, Saidov TA, Wijkstra H and Mischi M, Contrast ultrasound dispersion imaging for prostate cancer localization by improved spatiotemporal similarity analysis, *Ultrasound Med. & Biol.*, 39: 1631-1641, 2013.
- [7]. Kuenen MPJ, Saidov TA, Wijkstra H, de la Rosette JJMCH and Mischi M, Correspondence-spatiotemporal correlation of ultrasound contrast agent dilution curves for angiogenesis localization by dispersion imaging, *IEEE Transactions on Ultrasonics, Ferroelectrics, and Frequency control*, 60: 2665-2669, 2013.
- [8]. Mischi M, Contrast Echocardiography for Cardiac Quantifications, PhD thesis, Jan. 2004.
- [9]. Mischi M, Jansen AHM, Korsten HHM, Identification of cardiovascular dilution system by contrast ultrasound, *Ultrasound Med. & Biol.*, 33: 439-451, 2007.
- [10]. Sammali F, Blank C, Xu L, Huang Y, Kuijsters NPM, Schoot BC and Mischi M, Experimental setup for objective evaluation of uterine motion analysis by ultrasound speckle tracking, *Biomedical Physics & Engineering Express*, 4(035012), 2018.
- [11]. Taylor GI, Dispersion of soluble matter in solvent flowing slowly through a tube, *Proceedings of the Royal Society of London. Series A. Mathematical and Physical Sciences*, 219: 186-203, 1953.

High-speed optical characterization of the acoustic response of protein-and-nanoparticle-stabilized microbubbles

Charlotte L. Nawijn¹, Tim Segers¹, Guillaume Lajoinie¹, Sigrid Berg^{2,3,4}, Sofie Snipstad^{2,3,4}, Michel Versluis¹

¹*Physics of Fluids group, MESA+ Institute for Nanotechnology and Technical Medical (TechMed) Center, University of Twente, Enschede, The Netherlands*

²*Norwegian University of Science and Technology, Trondheim, Norway*

³*SINTEF AS, Trondheim, Norway*

⁴*Cancer Clinic, St. Olav's Hospital, Trondheim, Norway*

Corresponding author: c.l.nawijn@student.utwente.nl

Introduction

Ultrasound-driven microbubbles (MBs) were shown to have great potential for drug delivery applications [1] since they allow for a decreased systemic load of toxic drugs, owing to their ability to locally release the payload at the target site [2]. Encapsulating the cytotoxic drugs in nanoparticles (NPs) loaded in the microbubble shell may further enhance uptake by tumors [3]. NP-loaded MBs can be activated by ultrasound, thereby releasing the NP payload [4]. Understanding in detail the release mechanism and the effects of the ultrasound parameters on the release process is crucial for efficient and controlled release. Several systems have been proposed to load microbubbles with nanoparticles, e.g. through avidin-biotin binding, by click chemistry, or through direct incorporation in a denaturated protein shell. In particular the latter has been little investigated until now. Here, we focus on MBs loaded with polymeric NPs consisting of poly(2-ethyl-butyl cyanoacrylate) (PEBCA) from SINTEF (Trondheim, Norway), fixated in a denaturated casein shell [4], as can be seen in Fig. 1A where the NPs are stained with a fluorescent dye.

The main goal of this research was to characterize the microbubble response as a function of the driving ultrasound pressure and frequency in order to gain a phenomenological understanding of the nanoparticle-loaded protein stabilized microbubble behavior. The acoustic pressure amplitudes were varied over a range from 100 kPa to 1200 kPa and the employed ultrasound frequencies were 1, 2, 3 MHz.

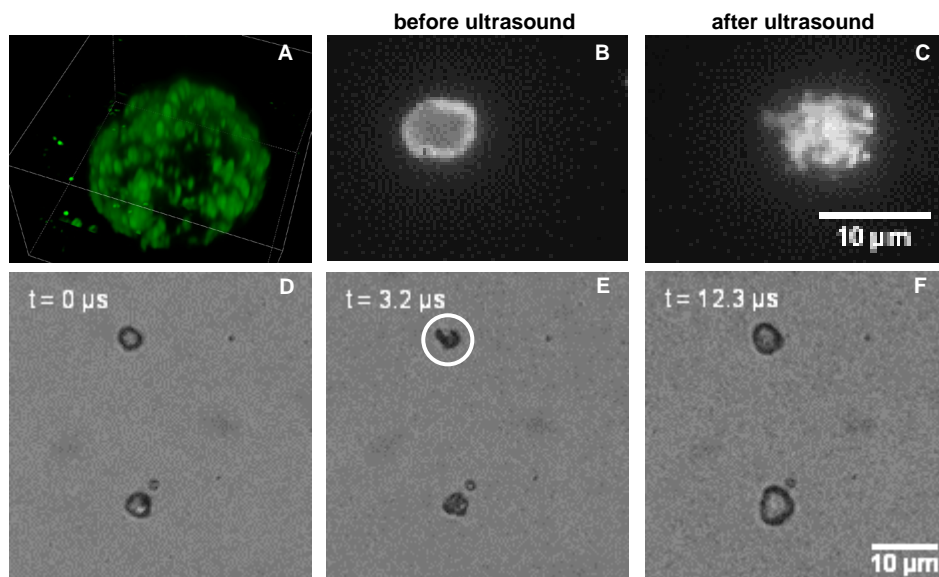


Figure 1. Images of NP-stabilized MBs: (A) 3D image stack taken using confocal microscopy, (B) fluorescence microscopy before, and (C) after sonication at 2 MHz and 500 kPa, (D) bright field microscopy of two NP-stabilized MBs before sonication, (E) after 3.2 μ s of ultrasound exposure (at 1 MHz and 150 kPa), and (F) after 12.3 μ s of ultrasound exposure at 1 MHz up to 1.3 MHz, and 150 kPa).

Experimental setup and results

The NP-stabilized MBs had a C_3F_8 gas core and they were formed by mechanical agitation, as described in [4]. The mean microbubble diameter was $2.4 \pm 0.2 \mu\text{m}$ [5]. First, the delivery of NPs was investigated using high-speed fluorescence microscopy using a laser (5 W, $\lambda = 532 \text{ nm}$; Cohlubri, Lightline, Osnaburg, Germany), and where the dye NR668 was used to stain the NPs [5]. The bubble response was recorded at 500 thousand frames per second (fps). The delivery probability was determined as a function of the initial bubble radius, where delivery was defined as the deposition of the fluorescent shell on the membrane to which the bubbles floated (see Fig. 1C). The delivery probability is plotted in Fig. 2. Note that in general the probability of NP delivery increases with an increase in acoustic driving pressure. Furthermore, higher frequencies require higher acoustic pressures for the same delivery probability. Finally, note that clear resonance behavior is observed, with a shift towards smaller bubble sizes with an increase in driving ultrasound frequency.

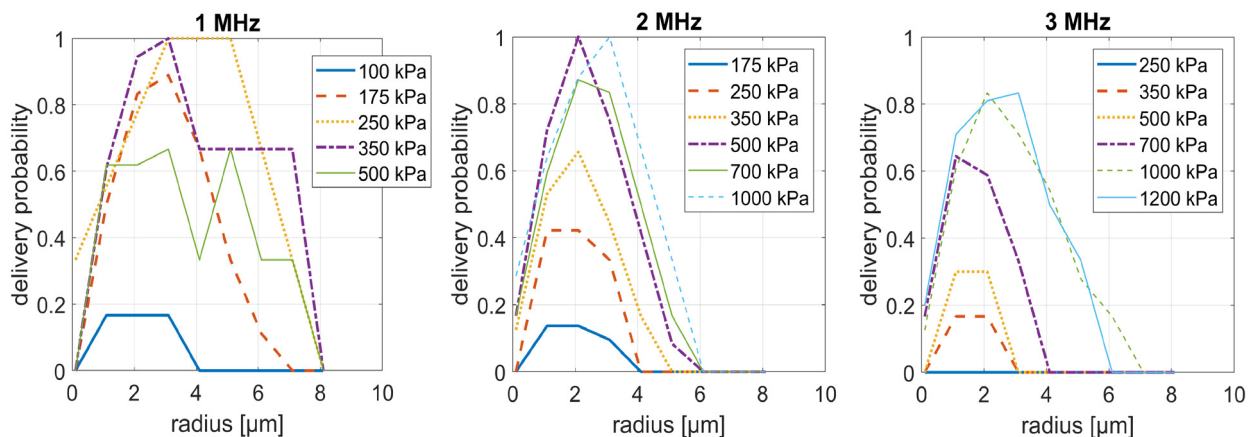


Figure 2. The delivery probability of NPs as a function of the equivalent initial bubble radius for 1 MHz, 2 MHz and 3 MHz (left to right), for a range of acoustic pressures.

A second set of experiments aimed at observing the acoustic microbubble response and shell rupture directly. Therefore, microbubble spectroscopy measurements [6] were performed at 10 million fps using a bright field microscope and a Shimadzu HPV-X2 high speed camera. The driving frequency of 5-cycle ultrasound pulses was increased from 1.0 MHz to 3.1 MHz in steps of 150 kHz, at acoustic pressure amplitudes of 50 kPa, 91 kPa, 150 kPa, and 250 kPa. The shell of the microbubbles was observed to rupture typically after several ultrasound cycles. Upon rupture, the gas core was observed to expand into the surrounding medium thereby forming a free uncoated gas bubble that oscillated at higher amplitudes. Before shell rupture, the bubbles were observed to show only small volumetric oscillations. In Fig. 1D through F, two typical NP-coated MBs are shown as observed before and during ultrasound exposure. Fig. 1E shows buckling for both bubbles and shell rupture for the MB indicated with the white circle. Fig. 1F shows two free gas bubbles that have formed after shell rupture.

Conclusions and outlook

By investigating NP delivery using fluorescence microscopy it was observed that the probability of NP delivery increased by increasing the acoustic pressure. Higher acoustic pressures were needed at higher frequencies to reach an equivalent delivery probability. A pronounced resonance behavior was observed. Future work will focus on elucidating what parameters cause shell rupture, and how rupture of the shell is related to delivery of the NPs. Prospective experiments are outlined to investigate the behavior of the NP-coated MB further. Namely, quasi static experiments will provide insights into the response of the coated bubbles as a function of the applied pressure, and help to understand the mechanical response of the shell. In parallel, additional ultra-high-speed recordings will focus on the response of the bubble at a single frequency to investigate the history effect on the shell rupture.

References

- [1]. Roovers S, Segers T, Lajoinie G, Deprez J, Versluis M, De Smedt, SC, Lentacker I, The role of ultrasound-driven microbubble dynamics in drug delivery: from microbubble fundamentals to clinical translation, *Langmuir*, 2019.
- [2]. Kooiman K, Vos HJ, Versluis M, de Jong N, Acoustic behavior of microbubbles and implications for drug delivery, *Advanced drug delivery reviews*, 72: 28-48, 2014.
- [3]. Snipstad S et al., Ultrasound improves the delivery and therapeutic effect of nanoparticle-stabilized microbubbles in breast cancer xenografts, *Ultrasound in medicine & biology*, 43(11): 2561-2669, 2017.
- [4]. Mørch Ý et al., Nanoparticle-stabilized microbubbles for multimodal imaging and drug delivery, *Contrast media & molecular imaging*, 10(5): 356-366, 2015.
- [5]. Yemane PT et al., Effect of Ultrasound on the Vasculature and Extravasation of Nanoscale Particles Imaged in Real Time, *Ultrasound in medicine & biology*, 45(11): 3028-3041, 2019.
- [6]. Van der Meer SM et al., Microbubble spectroscopy of ultrasound contrast agents, *The Journal of the Acoustical Society of America*, 121(1): 648-656, 2007.

Tunable viscoelastic shell properties of lipid-coated monodisperse microbubbles formed by flow-focusing

Benjamin van Elburg, Kim Bruil, Guillaume Lajoinie, Tim Segers, Michel Versluis

*Physics of Fluids group, TechMed Centre, MESA+ Institute for Nanotechnology, University of Twente,
Postbus 217, 7500 AE Enschede, The Netherlands
Corresponding author: b.vanelburg@utwente.nl*

Introduction

Ultrasound contrast agents (UCA) were shown to have great potential for emerging medical applications of microbubbles and ultrasound including as non-invasive blood pressure measurement [1], drug and gene delivery [2], and molecular- and deep tissue imaging [3]. Recently, the potential of microbubbles for medical applications further increased through the successful synthesis of stable and enriched monodisperse microbubble suspensions by sorting and by flow-focusing [4,5]. Microbubbles are resonators with a characteristic resonance frequency that is inversely proportional to the microbubble size. At resonance, the relative amplitude of oscillation and the nonlinear echo are at maximum. In addition to its dependency on the microbubble size, the acoustic response of a microbubble is also strongly affected by the viscoelastic properties of the lipid shell. The shell stiffness governs the resonance frequency shift due to both bubble compression at an increased ambient pressure, and due to an increased acoustic driving pressure. To date, a wide range of shell stiffness values are reported in the literature, typically ranging from 0.1 N/m up to 3.5 N/m, but questions remain as to how to tune shell stiffness and how shell stiffness changes with different physical parameters. Here, we show that the shell stiffness of lipid-coated microbubbles can be precisely tuned over one order of magnitude with values ranging from 0.5 N/m to 4.5 N/m. Moreover, we obtain insight in the lipid packing density dependent stiffness of the bubble shell for bubbles with a different shell stiffness. To that end, the dilatational shell stiffness was measured as a function of the microbubble surface area by measuring attenuation spectra while the surface dilatation was controlled through the ambient pressure. Furthermore, to gain insight in the acoustic uniformity of monodisperse microbubbles suspensions formed by flow-focusing, the overpressure required to reach the buckling state was measured optically for individual bubbles. The present work therefore allows for both the design of contrast microbubbles for novel applications and for an improved understanding of the nonlinear viscoelastic properties of the lipid shell.

Methods

Monodisperse bubble suspensions were synthesized using a flow-focusing device (Fig. 1A). The C₄F₁₀-filled bubbles were formed at a temperature of 55°C to minimize bubble coalescence [5]. The lipid mixtures comprised DSPC and DPPE-PEG5000 mixed at a molar ratio of 9:1 at a total concentration of 12.5 mg/mL. Palmitic acid (PA) was added up to 80 mol% to investigate its role on the viscoelastic shell properties. The shell properties were characterized acoustically by attenuation measurements at transmit frequencies ranging from 0.5 MHz to 5.5 MHz at a peak negative acoustic driving pressure of 5 kPa while the ambient pressure was controlled from 60 kPa (-300 mmHg) to 135 kPa (262 mmHg). The size distribution of the bubble suspensions was measured using a Coulter counter. The bubble size as a function of the ambient pressure was measured from optical recordings in a flow cell. The viscoelastic properties were obtained by fitting a model [6] to the attenuation spectra.

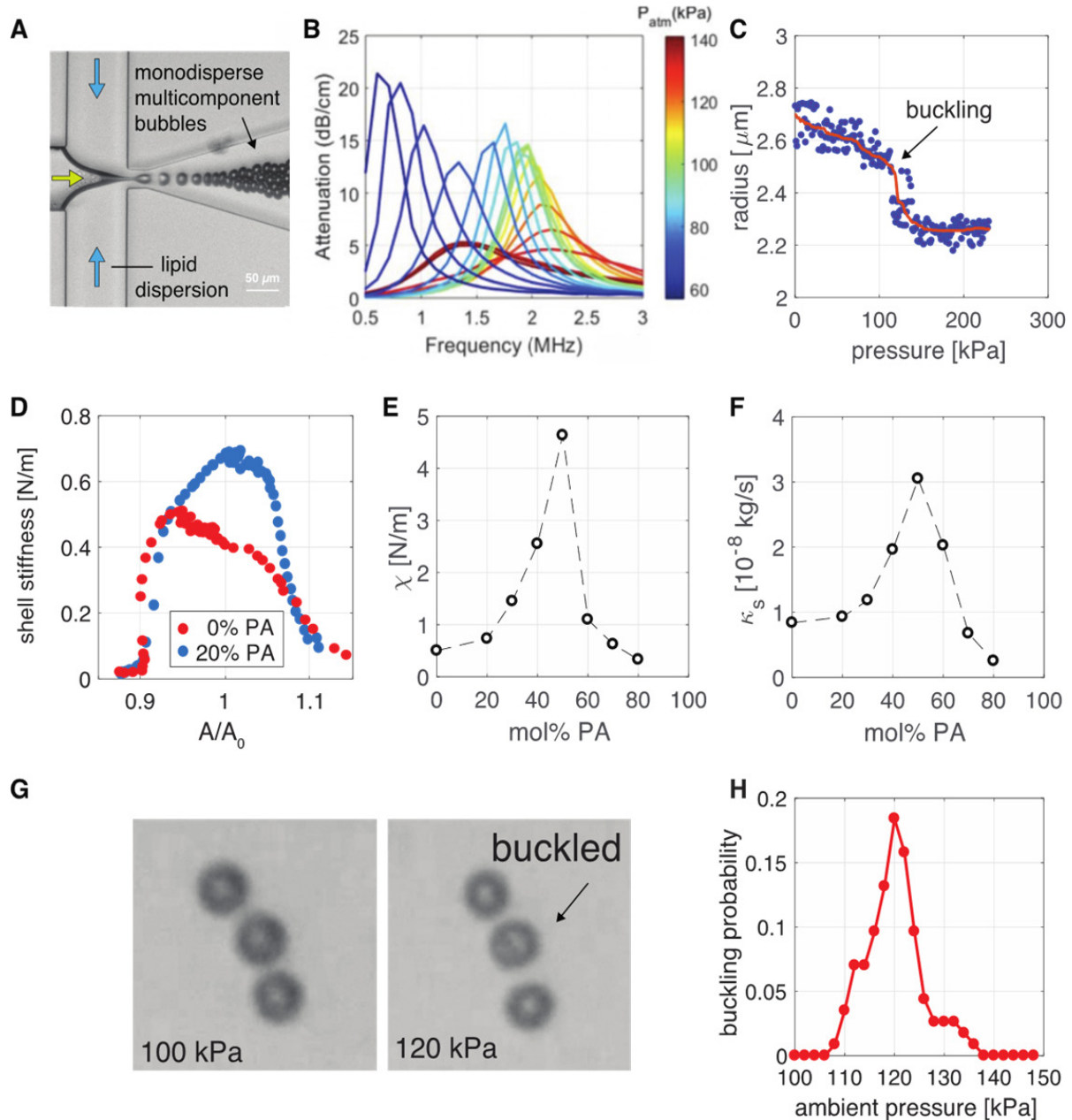


Figure 1 A) The employed microfluidic flow-focusing chip. B) Attenuation spectra measured at different ambient pressures. C) Microbubble radius as a function of the ambient pressure measured from optical recordings. D) Shell stiffness as a function of the microbubble surface area normalized by the surface area at atmospheric pressure E) Shell stiffness as a function of the molar palmitic acid (PA) concentration measured at atmospheric pressure. F) Shell viscosity as a function of the molar palmitic acid concentration measured at atmospheric pressure. G) A non-uniform buckling behaviour was observed for bubbles of the same size. H) Buckling probability versus ambient pressure.

Results

Figure 1B shows a typical example of the ambient pressure-dependent attenuation spectrum of a bubble suspension formed using a lipid mixture of DSPC/DPPE-PEG5k and 40 mol% palmitic acid. The frequency of maximum attenuation shifts dramatically when the ambient pressure is either increased or decreased. The optically measured ambient pressure-dependent bubble radius of a 2.5 μm radius bubble is shown in Fig. 1C.

Shell stiffness as a function of the microbubble surface area was measured from the ambient pressure-dependent attenuation curves through a model fit, see Fig. 1D. The figure shows the shell stiffness curve obtained for a lipid mixture without palmitic acid, and one for a lipid mixture with 20 mol% palmitic acid. Note that not only the maximum value of the shell stiffness increases through the addition of palmitic acid, but that also the shape of the curve changes. The shell stiffness as a function of the molar palmitic acid concentration measured at atmospheric pressure is plotted in Fig. 1E. The shell stiffness increases from 0.5 N/m up to almost 5 N/m when the molar palmitic acid concentration is increased from zero to 50%. At even higher palmitic acid concentrations, the shell stiffness drops to values lower than those for a PA concentration of zero mol%. The shell viscosity as a function of the PA concentration was also obtained from the model fit and it is shown in Fig. 1F. Note that the shell viscosity curve follows the same trend as the shell stiffness curve. Optically, a non-uniform buckling behavior was observed. Figure 1G shows that 3 bubbles of the same size imaged at atmospheric pressure. At an overpressure of 120 kPa, one of the bubbles showed a buckling behavior. The buckling pressure is then defined as the pressure at which the radius suddenly drops, see Fig. 1C. In Fig. 1H, the buckling probability is plotted as a function of the ambient pressure. These preliminary results show that bubbles, monodisperse in terms of size, do not necessarily show a uniform buckling behavior, and that they therefore are likely to show a nonuniform acoustic behavior. In our future work will more systematically focus on the acoustic dispersity of lipid-coated bubbles formed under various physical conditions and using different lipid mixtures.

Conclusions

The shell stiffness of monodisperse lipid-coated microbubbles can be tuned through the addition of palmitic acid. The stiffness varies between 0.5 N/m and 4.5 N/m with its maximum near 50 mol% added palmitic acid. The measured shell viscosity as a function of the molar palmitic acid concentration showed a similar trend as the shell stiffness, with its maximum at 50 mol% PA. We also measured the shell stiffness as a function of ambient pressure, or surface dilatation, to fully reveal the nonlinear dilatational properties of the microbubble shell for bubbles with a different shell stiffness. Furthermore, microbubbles monodisperse in terms of size were observed to show a non-uniform buckling behavior.

References

- [1]. Tremblay-Darveau, Charles, Ross Williams, and Peter N. Burns. "Measuring absolute blood pressure using microbubbles." *Ultrasound in medicine & biology* 40.4 (2014): 775-787.
- [2]. Dewitte, H., Vanderperren, K., Haers, H., Stock, E., Duchateau, L., Hesta, M., ... & Lentacker, I. (2015). Theranostic mRNA-loaded microbubbles in the lymphatics of dogs: implications for drug delivery. *Theranostics*, 5(1), 97.
- [3]. Segers, T., Kruizinga, P., Kok, M. P., Lajoinie, G., De Jong, N., & Versluis, M. (2018). Monodisperse versus polydisperse ultrasound contrast agents: Non-linear response, sensitivity, and deep tissue imaging potential. *Ultrasound in medicine & biology*, 44(7), 1482-1492.
- [4]. Segers, T., Lohse, D., Versluis, M., & Frinking, P. (2017). Universal Equations for the Coalescence Probability and Long-Term Size Stability of Phospholipid-Coated Monodisperse Microbubbles Formed by Flow Focusing. *Langmuir*, 33(39), 10329-10339.
- [5]. Segers, T., Lassus, A., Bussat, P., Gaud, E., & Frinking, P. (2019). Improved coalescence stability of monodisperse phospholipid-coated microbubbles formed by flow-focusing at elevated temperatures. *Lab on a Chip*, 19(1), 158-167.
- [6]. Segers, T., Gaud, E., Versluis, M., & Frinking, P. (2018). High-precision acoustic measurements of the nonlinear dilatational elasticity of phospholipid coated monodisperse microbubbles. *Soft matter*, 14(47), 9550-9561.

Spatial Coherence Volumetric Beamforming of Microbubbles Using a Sparse Array

Luxi Wei¹, Geraldi Wahyulaksana¹, Alessandro Ramalli², Enrico Boni², Piero Tortoli², Nico de Jong^{1,3}, Hendrik J. Vos^{1,3}

¹*Thoraxcenter, Dept Biomedical Engineering, Erasmus University Medical Center, Rotterdam, the Netherlands*

²*MSD Lab, Department of Information Engineering, University of Florence, Florence, Italy*

³*Acoustical Wavefield Imaging, Faculty of Applied Sciences, Delft University of Technology, Delft, the Netherlands*

Corresponding author: l.wei@erasmusmc.nl

Introduction

Volumetric ultrasound imaging of microbubbles enables full visualization of the vasculature without artefacts from out-of-plane motion. Our group has previously manufactured a prototype sparse array with a density-tapered spiral element layout, optimized for volumetric imaging using focused beams [1], [2]. This allowed volumetric imaging with high spatial resolution and low clutter level, but the low volume rate, achieved with standard focused beam acquisition, leads to motion artefacts and makes it unsuitable for flow estimation. The current study explores the feasibility of high volume rate imaging using divergent transmissions for microbubble imaging with the sparse array. As a result of the sparsity of the elements and dynamic beamforming in reception (DAS), high bubble clutter signals originate from multiple side lobes in the contrast signal. This clutter severely degrades image quality and can neither be removed with tissue clutter suppression techniques nor with specific contrast detection schemes (such as amplitude modulation and pulse inversion). Thus, we propose to use the Short Lag Spatial Coherence (SLSC) beamforming method which preserves the coherent bubble signal and reduces incoherent clutter [3]. Phantom experiments show the increase in signal to background ratio by 15 dB in SLSC beamformed volumes compared to conventional DAS beamformed volumes when using divergent transmissions.

Methods

High concentrations of Microbubbles (DefinityTM, MA, USA) were injected with a syringe pump through a 1 mm diameter vessel into a PVA-based tissue-mimicking phantom at a flow rate of 120 $\mu\text{L}/\text{min}$, leading to peak flow velocity of 5.1 mm/s assuming a parabolic flow profile. The prototype 256-element density-tapered spiral array was placed above the vessel at 2 – 4 cm distance, and a Vantage 256 system (Verasonics Inc, Washington, USA) was used for signal transmission and data collection. 3-cycle pulses centered at 5 MHz were transmitted at 20° divergence angle using the center 120 elements at 1 kHz pulse repetition frequency for one second. Radio-frequency data were collected and an singular value decomposition (SVD) filter was applied to remove all stationary signal components stemming from the PVA, as well as reflections from the edges of the phantom. For each volume, appropriate delays were calculated and applied offline using a custom algorithm. Following the concepts laid out in [4], the coherence between the delayed signals of all element pair combinations at each pixel location was then calculated and summed. Only the positive real parts of the coherence coefficients were kept, and then the volumetric images were normalized to between 0 and 1 prior to logarithmic compression. As a comparison, the same data were beamformed using the conventional DAS method by summing the delayed channel data instead of calculating the coherence between channel pairs. Signal to background ratio (SBR) was evaluated as

$$SBR = 20 \times \log_{10} (RMS_{vessel}/RMS_{background}), \quad (1)$$

where the root mean square (RMS) levels were calculated in the vessel and background, respectively, of the linear envelope data. The vessel was segmented based on the full-width-half-maximum of the vessel cross-sections in DAS volumes after averaging 1000 frames, and background was defined as the volume outside of twice the vessel diameter. The diameter estimated from the DAS beamformed volumes was also used to construct segmentation masks in SLSC images even though this biases the contrast towards the DAS results.

Results

The image quality is compared between SLSC and DAS beamformed volumes. Fig. 1 shows an example of rendered volumes using both methods. Only the region where the vessel is visible is chosen for better visualization and comparison. The vessel diameter is estimated to be 1.3 ± 0.1 mm and 1.8 ± 0.2

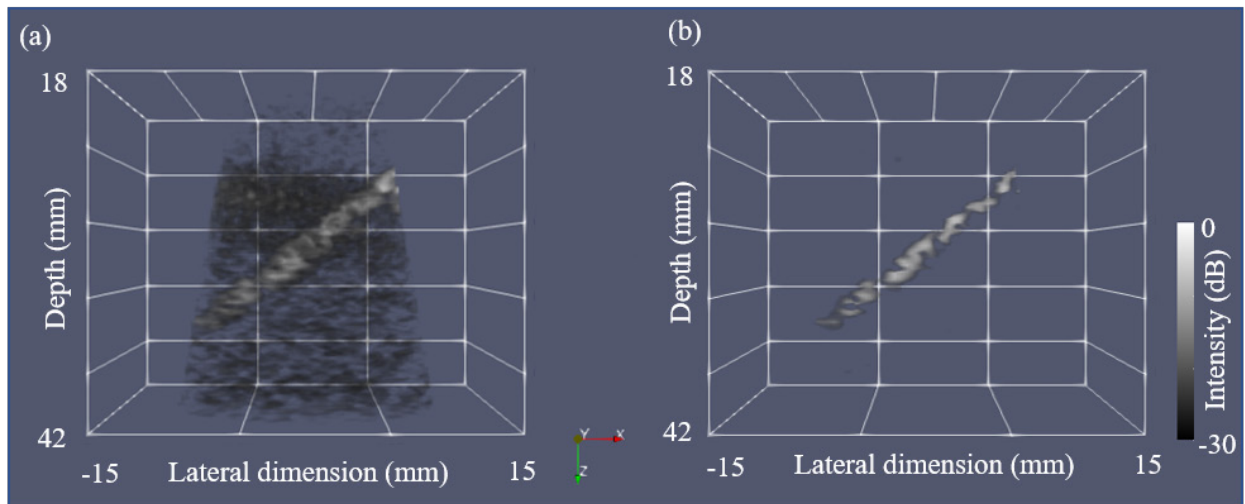


Figure 1: Example single-frame renders of flowing bubbles through a vessel embedded in a tissue mimicking phantom using DAS (a) and SLSC (b) beamforming methods. Both volumes are scaled to 30 dB dynamic range.

mm using the SLSC and DAS beamformers respectively. Using the segmentation mask, the mean SBR and standard deviation is calculated for all frames, 32.0 ± 0.8 dB (SLSC beamformer) and 17.4 ± 0.6 dB (DAS beamformer), respectively. For better comparison, histograms of the vessel and background signals

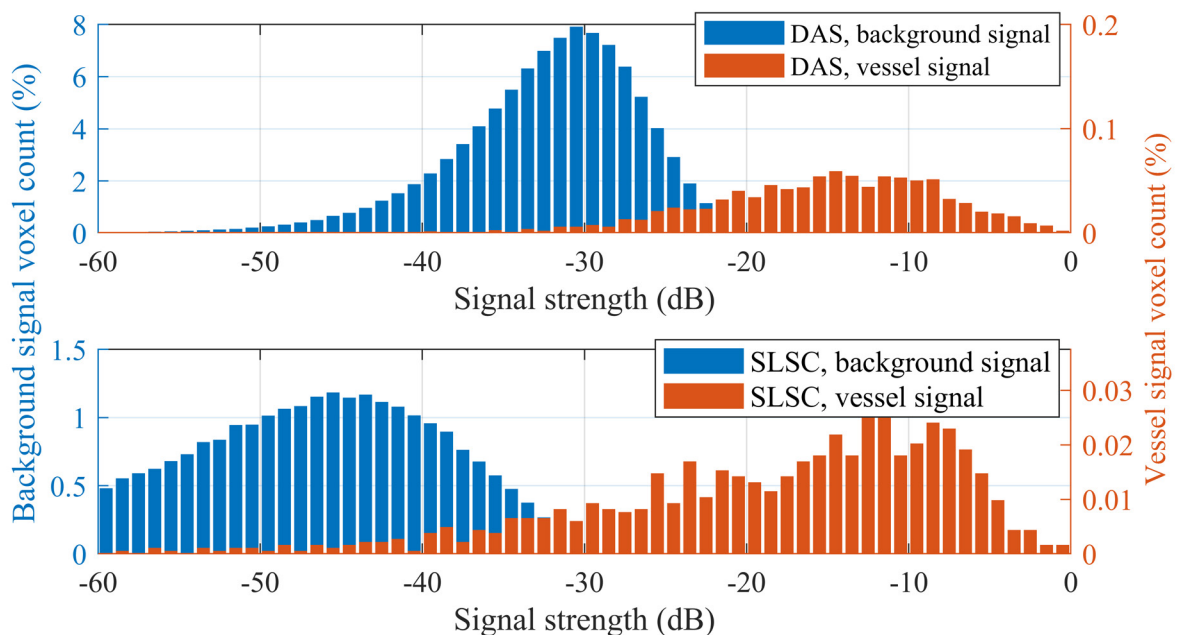


Figure 2: Normalized histograms of segmented vessel and background signal voxels for a volume beamformed using both DAS (a) and SLSC (b) methods. Segmentation of vessel and background are done using the estimated diameters from both methods, and the histograms normalized to the number of voxels in the sum of the vessel and background regions (ie. 100% corresponds to all voxels in the vessel and background regions combined). All voxels lower than -60 dB are not presented in this graph.

are computed (Fig. 2). The background amplitude is significantly lower in the case of SLSC compared to DAS beamformed acquisitions. Furthermore, a clearer separation of the vessel signal and background signal is present in the SLSC beamformed volumes, but not for the DAS beamformed volumes due to relatively high bubble signal clutter levels. The range of voxel signal intensities is larger for SLSC compared to DAS beamformed images. This may indicate decorrelation of the RF signal within the vessel due to high bubble concentrations. Further experiments and analyses are warranted to optimize the concentration and results.

Conclusions

High frame rate volumetric imaging of flowing bubbles in a small vessel is demonstrated using a sparse spiral array. Low signal to background ratio resulting from the sparsity of the transducer elements and the lack of transmit focus can be significantly reduced by 15 dB using the SLSC beamformer.

References

- [1]. E. Boni, A. Ramalli, V. Daeichin, N. de Jong, H. J. Vos, and P. Tortoli, Prototype 3D Real-Time Imaging System Based on a Sparse PZT Spiral Array, 2018 IEEE International Ultrasonics Symposium (IUS), pp. 1-4, 2018.
- [2]. A. Ramalli, E. Boni, A. S. Savoia, and P. Tortoli, Density-tapered spiral arrays for ultrasound 3-D imaging, *IEEE Trans. Ultrason. Ferroelectr. Freq. Control*, 62:1580–1588, 2015.
- [3]. D. Hyun, L. Abou-Elkacem, V. A. Perez, S. M. Chowdhury, J. K. Willmann, and J. J. Dahl., Improved Sensitivity in Ultrasound Molecular Imaging with Coherence-Based Beamforming, *IEEE Trans. Med. Imaging*, 37:241, 2018.
- [4]. D. Hyun, A. L. C. Crowley, and J. J. Dahl, Efficient Strategies for Estimation the Spatial Coherence of Backscatter, *IEEE Trans. Ultrason. Ferroelectr. Freq. Control*, 176:139–148, 2017.

Single particle localization algorithms for Ultrasound Localization Microscopy *in silico* and *in vivo*

A. Chavignon^{1,*}, B. Heiles^{2,*}, V. Hingot¹, O. Couture¹

¹Laboratoire d'Imagerie Biomédicale, Sorbonne Université – Campus des Cordeliers
15 rue de l'École de Médecine, 75006 Paris

²Institute Physics for Medicine, CNRS, INSERM, ESPCI Paris, PSL Research University,
17 rue Moreau, 75012, Paris

*These authors contributed equally

Corresponding author: Arthur.chavignon.pro@gmail.com

Introduction

Ultrasound Localization Microscopy (ULM) has been demonstrated to overcome the penetration/resolution paradigm [1]. It relies on localizing the centre of individual microbubbles and accumulating a large number of echoes to produce micrometric images of in-vitro canals in 2D [2], [3] and in 3D [4]-[6], and in-vivo, rat brain microvasculature [7], [8], tumours [9]. In this study, we introduce a new localization algorithm based on radial symmetry of the system's point spread function. To compare its performance against existing algorithms, we present here a dedicated assessment workflow and associated sets of metrics. Such comparison is performed on both in silico and on in vivo data.

Methods

We first simulated a media comprised of 10 tubes with various geometries and diameters (from 5 to 200 μm) with various complexity : a pseudo double helix, a curved tube with constant diameter and a horseshoe pattern, 3 curved tubes, four spreading tubes (horizontal and vertical).

To simulate moving microbubbles flowing in these tubes, we chose initial random positions in the media and recorded them as a point like scatterer. For each of these positions, a trajectory calculated by Poiseuille's flow was assigned. Using the Verasonics Research Ultrasound Simulator, we simulated radiofrequency and beamformed images of the moving scatterers insonified with 3 tilted plane waves with a 15MHz probe. For each image in the simulation, we added clutter noise modeled by a Gaussian filtered white Gaussian noise post-beamforming

We then built a second dataset on a craniotomized rat brain with IV injection of 0.2 mL of Sonovue (Bracco®) [10]. A 15 MHz probe (Vermon, France) was used to acquire in between 192k images at 20V, with 3 tilted plane waves reaching a framerate of 1kHz. The beamformed images were spatiotemporally filtered using SVD decomposition [11] and then filtered images were used to perform ULM using 7 algorithms : no-shift assumption, cubic, Lanczos or spline interpolation, Gaussian fit, weighted average, radial symmetry based.

In the first case, the error in the two directions, the Root Mean Square Error (RMSE), the cardinality of True Positives (TP), False Positives (FP), and False Negatives (FN) ensembles, Jaccard Index, total number of localizations were calculated. An efficiency index defined as $E = 100 - \sqrt{(100 - JAC)^2 + \alpha^2 RMSE^2}$ was calculated to sum up these different indices.

In the latter case, a measure based on the spatial frequency peak to baseline value was devised to quantify aliasing effects, a computation time factor, and visual analysis of the different ULM renderings was performed

Results

The statistical indices *in silico* confirm that the radial symmetry based localization scheme is more precise than other schemes. This is due to a low localization error ($RMSE_{radial} = 0,12 \times \lambda$), along with a high cardinality of true positives ($Card(TP_{radial}) = 389,000$). As the total number of TP+FN is finite

(706,000), this also means that the sensitivity index is high. For the weighted average scheme, we measure a high precision and high sensitivity although its localization error is the highest among the schemes ($0,17 \times \lambda$). The weighted average and cubic interpolation have almost the same standard deviation $\sigma_{ax} \cong 0,13\lambda$, $\sigma_{lat} \cong 0,12 \lambda$, directional errors and RMSE ($0,17\lambda$). Summing up the Jaccard indices and the RMSE into the efficiency index is helpful to discriminate the algorithms. In the end, the radial symmetry localization algorithm comes out on top with an efficiency twice as high as the second bests ($E = 41,8$). The weighted average fares better than the cubic interpolation because of a higher Jaccard index.

Figure 1.a) presents zoomed-in ULM renderings of the rat brain *in vivo*. The no-interpolation based ULM performs very poorly *in vivo* as expected. The vessels in the cortex suffer from considerable aliasing making their structure disorganized. The cubic interpolation also suffers from aliasing as predicted, however, the weighted average localization-based ULM is in appearance non gridded. The radial symmetry based algorithm seem to deliver more microvessels than the other schemes without suffering from aliasing. The running time of each algorithm with respect to the fastest one (weighted average which runs in under 3 minutes) is presented in figure 1.b). Radial symmetry comes out on top even with more localizations.

A radar chart is presented in figure 1.c) to sum up both the *in silico* and *in vivo* metrics.

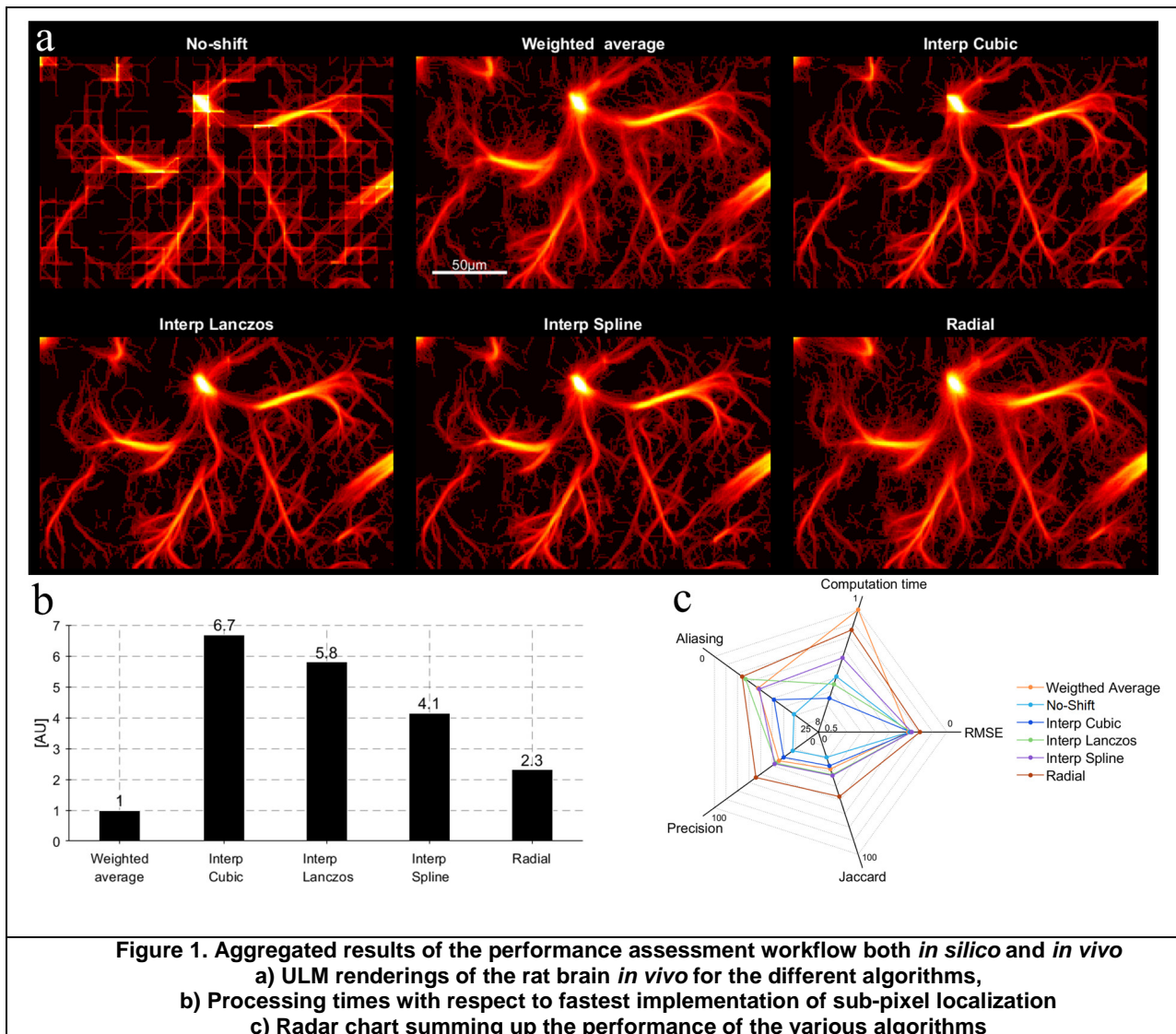


Figure 1. Aggregated results of the performance assessment workflow both *in silico* and *in vivo*
a) ULM renderings of the rat brain *in vivo* for the different algorithms,
b) Processing times with respect to fastest implementation of sub-pixel localization
c) Radar chart summing up the performance of the various algorithms

Conclusions

Two datasets were compiled to assess the performance of existing and new algorithms. The radial symmetry based ULM method appears to be both accurate and fast. This study also provided metrics and a complete workflow to test out and compare the different schemes used in the super-resolution field.

References

- [1]. O. Couture, V. Hingot, B. Heiles, P. Muleki-Seya, and M. Tanter, "Ultrasound localization microscopy and super-resolution: a state-of-the-art," *IEEE Transactions on Ultrasonics, Ferroelectrics, and Frequency Control*, pp. 1–1, 2018.
- [2]. O. Couture, B. Besson, G. Montaldo, M. Fink, and M. Tanter, "Microbubble ultrasound super-localization imaging (MUSLI)," 2011, pp. 1285–1287.
- [3]. O. M. Viessmann, R. J. Eckersley, K. Christensen-Jeffries, M. X. Tang, and C. Dunsby, "Acoustic super-resolution with ultrasound and microbubbles," *Physics in Medicine and Biology*, vol. 58, no. 18, pp. 6447–6458, Sep. 2013.
- [4]. Y. Desailly, O. Couture, M. Fink, and M. Tanter, "Sono-activated ultrasound localization microscopy," *Applied Physics Letters*, vol. 103, no. 17, p. 174107, Oct. 2013.
- [5]. B. Heiles, M. Correia, V. Hingot, M. Pernot, J. Provost, and O. Couture, "Ultrafast 3D Ultrasound Localization Microscopy using a 32x32 Matrix Array," *IEEE Transactions on Medical Imaging*, p. 13, 2019.
- [6]. M. A. O'Reilly and K. Hynynen, "A super-resolution ultrasound method for brain vascular mapping: Super-resolution ultrasound method for brain vascular mapping," *Medical Physics*, vol. 40, no. 11, p. 110701, Oct. 2013.
- [7]. C. Errico et al., "Ultrafast ultrasound localization microscopy for deep super-resolution vascular imaging," *Nature*, vol. 527, no. 7579, pp. 499–502, Nov. 2015.
- [8]. B. Heiles et al., "Volumetric ultrafast Ultrasound Localization Microscopy in vivo," presented at the IEEE International Ultrasound Symposium, Kobe, Japan, 2018.
- [9]. F. Lin, S. E. Shelton, D. Espíndola, J. D. Rojas, G. Pinton, and P. A. Dayton, "3-D Ultrasound Localization Microscopy for Identifying Microvascular Morphology Features of Tumor Angiogenesis at a Resolution Beyond the Diffraction Limit of Conventional Ultrasound," *Theranostics*, vol. 7, no. 1, pp. 196–204, 2017.
- [10]. V. Hingot, C. Errico, B. Heiles, L. Rahal, M. Tanter, and O. Couture, "Microvascular flow dictates the compromise between spatial resolution and acquisition time in Ultrasound Localization Microscopy," *Scientific Reports*, vol. 9, no. 1, Dec. 2019.
- [11]. C. Demene et al., "Spatiotemporal Clutter Filtering of Ultrafast Ultrasound Data Highly Increases Doppler and fUltrasound Sensitivity," *IEEE Transactions on Medical Imaging*, vol. 34, no. 11, pp. 2271–2285, Nov. 2015.

3D flow visualization with locally and acoustically activated nanodroplets and high frame rate imaging using a matrix array

Matthieu Toulemonde¹, Sevan Harput², Thomas Tiennot¹, Xiaowei Zhou¹, Meng-Xing Tang¹

¹Department of Bioengineering, Imperial College London, London, United Kingdom

²Div. of Electrical and Electronic Engineering, London South Bank University, London, UK

Corresponding authors: m.toulemonde@imperial.ac.uk, mengxing.tang@imperial.ac.uk

Introduction

Blood flow visualization and quantification methods with microbubble contrast agents using High-Frame-Rate (HFR) ultrasound have been investigated but the real-time visual feedback can be challenging because of the high computational cost, particularly if in 3D. Nanodroplets have been investigated as an alternative to microbubbles, due to their smaller size and longer half-life. We previously have shown their potential use as a flow indicator in 2D in-vitro and in-vivo acquisitions [1] [2]. This work aims to demonstrate the feasibility of 3D flow visualization in-vitro using a HFR ultrasound acquisition and locally activated nanodroplets.

Methods

A 3D pulsatile flow was generated in a 14%-polyvinyl alcohol (PVA) wall-less vessel phantom. The tube-like PVA phantom had a diameter of 9 mm and an inner diameter of 3.2 mm [3]. The phantom was connected to a pulsatile pump (1407, Harvard Apparatus, Holliston, MA, USA) used at a pulse rate of 60 pulses/min. The circulating fluid was composed of 2.5 ml of decafluorobutane nanodroplets diluted and mixed in 2.5 L of water at 37°C and used as an open circuit (no recirculation).

The 3D HFR flow visualization was performed with a 256-Verasonics platform (Verasonics Inc., Redmond, WA) and a multiplexed 32x32 matrix array (UTA 1024-MUX, Verasonics, WA) with a pitch of 300 μm and a central frequency of 7.81MHz was developed. The experimental setup is shown in Fig 1.a-b.

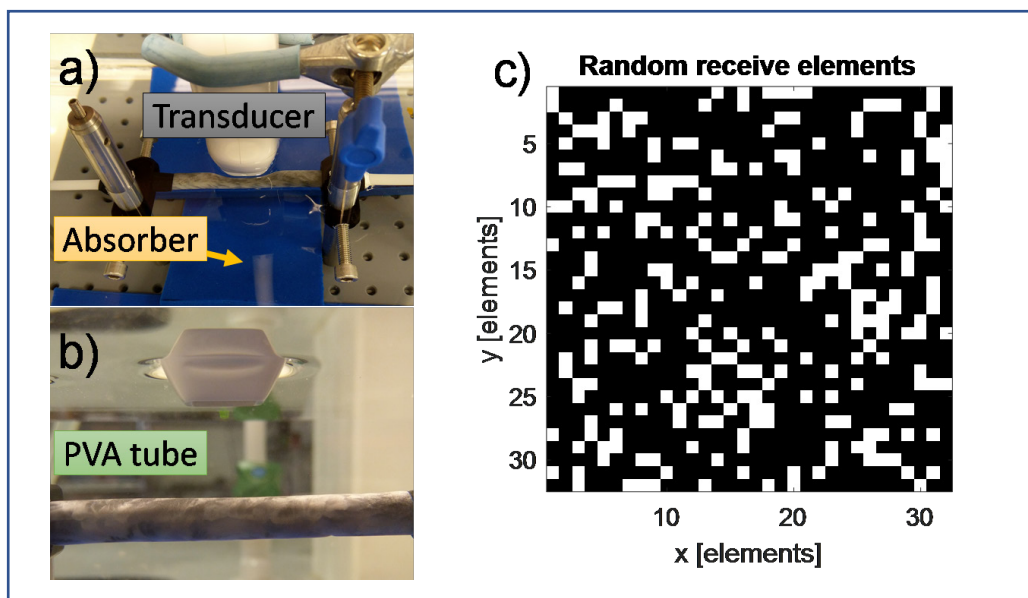


Figure 1. (a, b) Experimental setup and (c) received apodization for 3D HFR acquisition.

Two different transmissions were designed for nanodroplets activation based on standard line by line scanning approach and a 3D HFR imaging for flow visualization. The acquisition sequence used is similar to the one developed for HFR cardiac contrast acquisition as described in [4]. Nanodroplet activation was

achieved by transmitting 10 consecutive focused waves at 22 mm depth and covering 3 mm in the cross-sectional direction inside the vessel. The activation frame rate was 50 Hz (Table 1). The 3D HFR images were generated by coherently compounding five plane wave transmissions using the full matrix array in transmission (Table 1). However, only 256 random elements were used for the receive because of the multiplexing limitation of the probe (Fig 1.c).

Table 1. In-vitro parameters.

Acquisition		Activation	
Parameter	Value	Parameter	Value
Frequency (cycles)	7.81 MHz (3)	Frequency (cycles)	6.5 MHz (10)
Angle range (lateral / elevation)	(15° / 15°)	Focus depth	22 mm
Number of angles	5	Number of transmissions	10
Frame rate	2000 Hz	Frame rate	50 Hz

Results

Fig. 2 (left) shows the nanodroplets before and after the activation inside the vessel. The activation area is highlighted in a yellow in the top-left image. The first frame after activation is plotted in the top-right image, by showing the activated nanodroplets, which are microbubbles, in purple colour. After few milliseconds, the activated nanodroplets are washed out by the flow and the activation and acquisition processes can be repeated in real-time. The Fig. 2 (right) image shows the flow streamlines obtained from the detection of the microbubbles.

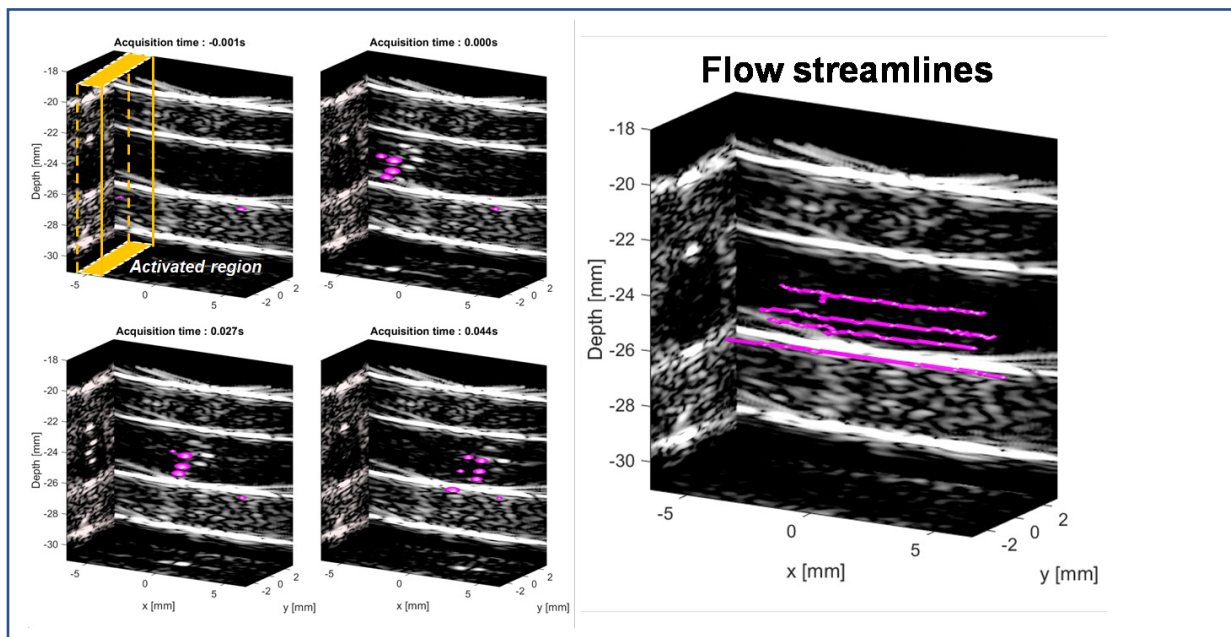


Figure 2. (Left) HFR 3D B-Mode acquisition before and after nanodroplet activation and (Right) flow streamlines of the activated nanodroplets. The activated region is highlighted in the top left image. Images are display with a 20dB dynamic range. Isosurfaces microbubbles and flow streamlines have been magnified for display purpose.

Conclusions

In this work, we showed that locally activated nanodroplets present an opportunity to introduce indicators into 3D flow non-invasively with a high temporal resolution.

Acknowledgements

This work was supported by an Engineering and Physical Sciences Research Council (EPSRC) Impact Acceleration Account EP/R511547/1 and by the British Heart Foundation Centre of Research Excellence grant RE/13/4/30184. We gratefully acknowledge the support of NVIDIA Corporation with the donation of the Titan Xp GPU used for this research.

References

- [1]. M. Toulemonde, G. Zhang, R.J. Eckersley and M.X. Tang, “Flow Visualization through Locally Activated Nanodroplets and High Frame Rate Imaging”, IEEE IUS, Kobe, 2018.
- [2]. M. Toulemonde, G. Zhang, K. Riemer, P.D. Weinberg, and M.X. Tang, “Locally activated nanodroplets and high frame rate imaging for real-time flow visualization – preliminary in-vivo demonstration”, BioMedEng18, ISBN 978-1-9996465-0-9, 2018.
- [3]. X. Zhou, D. A. Kenwright, S. Wang, J.A. Hossack, and P. R. Hoskins, “Fabrication of Two Flow Phantoms for Doppler Ultrasound Imaging”, IEEE Trans. on UFFC, vol. 64, no. 1, pp. 53-65, 2017.
- [4]. M. Toulemonde, et al., “High-Frame-Rate Contrast Echocardiography using diverging waves: initial invitro and in-vivo evaluation”, IEEE Trans. Ultrason. Ferroelectr. Freq. Control., 2018.

Tuning vaporization by interfacial melting in endoskeletal and exoskeletal droplets

Gazendra Shakya¹, Samuel E. Hoff², Shiyi Wang², Hendrik Heinz^{2,3}, Xiaoyun Ding¹, Mark A. Borden^{1,3}

¹Department of Mechanical Engineering, University of Colorado, Boulder, CO, USA

²Department of Chemical and Biological Engineering, University of Colorado, Boulder, CO, USA

³Materials Science and Engineering Program, University of Colorado, Boulder, CO, USA

Corresponding author: Mark.Borden@colorado.edu

Introduction

Perfluorocarbon droplets have been used extensively as phase-change contrast agents for ultrasound imaging and therapy. The phase-change behavior of these droplets is governed by the interplay between intermolecular forces and entropy. Several studies have aimed at understanding the vapor embryo nucleation and vaporization behavior of these droplets. However, these studies largely used high mechanical index, low-boiling species or solid surfaces that pin the vapor/liquid contact line to initiate vaporization. We propose to initiate vaporization through an alternative mechanism: interfacial melting and fluid mixing in an endoskeletal droplet.

Methods

We investigated the synthesis, structure and vaporization behavior of endoskeletal droplets made with liquid/solid structures comprising fluorocarbon/fluorocarbon (FC/FC) or fluorocarbon/hydrocarbon (FC/HC). Perfluoropentane (n-C₅F₁₂) was used as the volatile liquid, and either perfluorododecane (n-C₁₂F₂₆) or solid normal alkane (ranging from 18 to 24 carbon chain length) were used to make endoskeletal (solid-in-liquid) as well as exoskeletal (liquid-in-solid) droplets. Vaporization of these droplets was observed over a range of temperatures both optically and acoustically using a clinical ultrasound scanner.

Results

We show that the presence of an FC skeleton stabilizes C₅F₁₂ against vaporization, even up to 75 °C. Conversely, the presence of an HC skeleton facilitated C₅F₁₂ vaporization at temperatures below its boiling point. Surprisingly, FC/HC endoskeletal droplets vaporized near the melting point of the bulk HC phase. Vaporization temperature could be tuned from 23 °C to 45 °C by the choice of HC species. A thermodynamic and molecular dynamics analyses indicated that interfacial melting and mixing of the FC and HC species within the diffuse fluid interface lowered the spinodal and initiated homogenous nucleation. On the other hand, for FC/FC endoskeletal droplets, mixing of C₁₂F₂₆ into the C₅F₁₂ reinforced intermolecular cohesion and raised the spinodal. These results demonstrate how the interplay between intermolecular forces and entropy can be manipulated to tune vaporization thresholds, a generalizable mechanism that could be used in for a large library of droplet components.

Conclusions

Vaporization of endoskeletal and endoskeletal FC droplets with FC or HC solid components can be tuned by interfacial melting of the solid species to achieve a wide range of vaporization thresholds. Future work will exploit these properties for phase-change contrast ultrasound imaging and therapy.

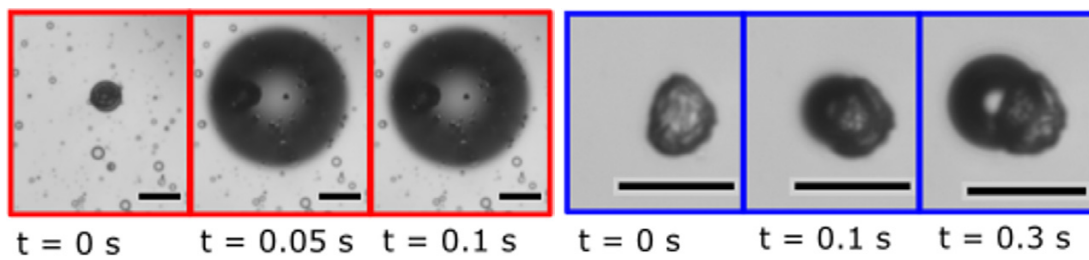


Figure 1. Optical microscopic images of endoskeletal (left) and exoskeletal (right) vaporization. Scale bar = 20 μm .

Determination of Acoustic Droplet Vaporization threshold for various microfluidically formed PFC-nanodroplets

Romain Melich, Philippe Bussat, Alexis Vivien, Emmanuel Gaud, Thierry Bettinger and Samir Cherkaoui*

Bracco Suisse SA, Geneva, Switzerland

**Corresponding author: romain.melich@bracco.com*

Introduction

Phase-change or acoustically activated nanodroplets are receiving increased popularity in both diagnostic and therapeutic delivery. Except the core, often consisting of liquid perfluorocarbons, nanodroplets display similar composition to commercially available gas-filled microbubbles. Thanks to acoustic droplet vaporization (ADV) process, encapsulated droplets are converted into gas bubbles upon exposure to ultrasound energy beyond a vaporization threshold [1]. In fact, ultrasound serve as a remote trigger to promote the vaporization of the droplets in a controllable, non-invasive and also localized manner. Perfluorocarbon nanodroplets (PFC-NDs) present a potential as an extravascular ultrasound contrast agent in a number of theranostic applications [2]. For a more detailed review of acoustically responsive phase-change nanodroplets please see recently published literature [3,4,5]

In this study, we report the use of rapid and controlled microfluidic mixing for the manufacturing of various types of PFC-NDs with different encapsulating shells. In contrast to already published microfluidic methods enabling nanometric size PFC droplets with limited production rate [6], this novel formulation procedure allows for the rapid optimization/preparation of narrowly dispersed NDs at a reliable yield. Then, we acoustically determined the ADV threshold for NDs flowing in a tube setup using echogenicity signals from produced bubbles. Finally, the influence of various formulation parameters on the ADV threshold was investigated related to the PFC type and the encapsulating shell composition (Surfactants, Lipids, Polymers).

Methods

Preparation of PFC nanodroplets:

PFC-NDs were formulated thanks to the use of staggered herringbone (SHB) microfluidic mixer allowing size-controlled self-assemblies (NanoAssemblr™ instrument from Precision Nanosystems). Briefly, an aqueous phase is mixed with an organic phase composed of PFC and coating agent (surfactant, lipid or PLGA polymer) dissolved in an appropriate organic solvent into the microfluidic cartridge (Fig. 1). Microscopic characteristics of the channels are engineered to cause the fluid stream to mingle in a controlled way. The microfluidic process settings namely Total Flow Rate (TFR, in mL/min) and Flow Rate Ratio (FRR), which is the ratio between the aqueous and organic phases, are used to control the NDs characteristics. Then, the obtained ND formulations were systematically characterized in terms of size and polydispersity (PDI) using Dynamic Light Scattering (Zetasizer, Malvern Instruments). The stability of tailored PFC-NDs was also addressed depending on the nature of the molecular constituents.

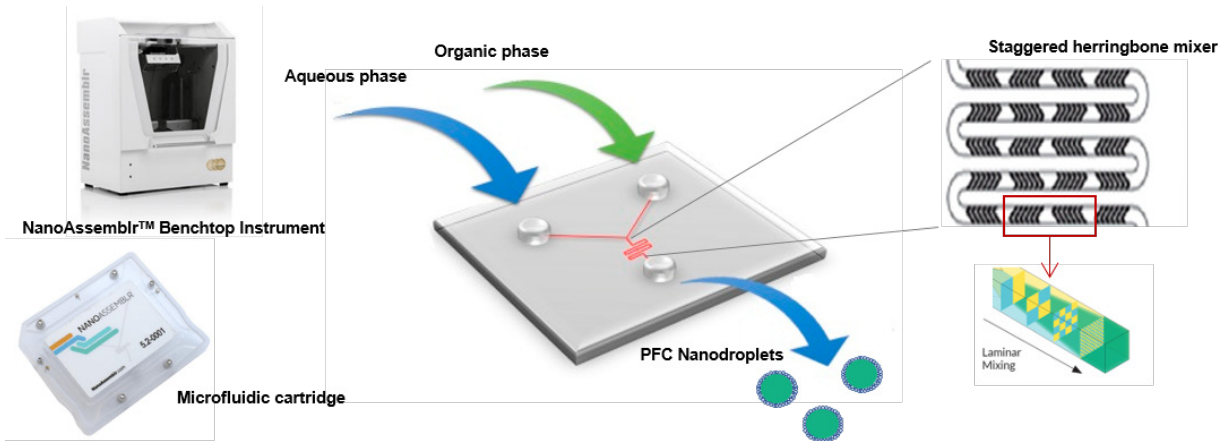


Figure 1: Schematic representation of the production of PFC-NDs using the NanoAssemblr™ Benchtop microfluidic system

Determination of ADV threshold:

A home-made set-up was implemented to study the vaporization of microfluidically produced nanodroplets in acoustic fields (Fig. 2). Specifically, a water tank was used that contained a dialysis tube to circulate the diluted nanodroplets using a peristaltic pump at 4.3 mL/min. ADV experiments were carried out at human body temperature (37 °C) and atmospheric pressure. A linear ultrasonic probe (L11-4V), connected and driven by a Vantage 256 system (Verasonics) was placed above the flow tube to acquire videos by B-mode imaging. The suspension was exposed to ultrasound by a 6.0 MHz single-element transducer (28 mm aperture, Vermon). This transducer, placed at a 90° angle to the imaging plane of the linear array, was used to vaporize nanodroplets. Pulses were emitted in burst mode, 100 cycles per pulse, at a pulse-repetition frequency (PRF) of 10 Hz. The acoustic pressure was increased every 10 seconds until the observation of the NDs vaporization. Before ADV experiments, the transducer was calibrated for its transmitted acoustic pressure using a lipstick hydrophone (Onda Hydrophone). The PFC-ND suspensions were vaporized while passing through the focal zone of the transducer located in the region of interest (ROI) called the “After” area. Then, the echo-power values of each ROI were determined from video images by VueBox™ quantification software (Bracco Suisse SA). Finally, with Matlab (MathWorks Inc., Natick, MA, USA), a sigmoid fit corresponding to the difference in echo-power between two ROIs as a function of the applied acoustic pressure was used to determine the ADV threshold.

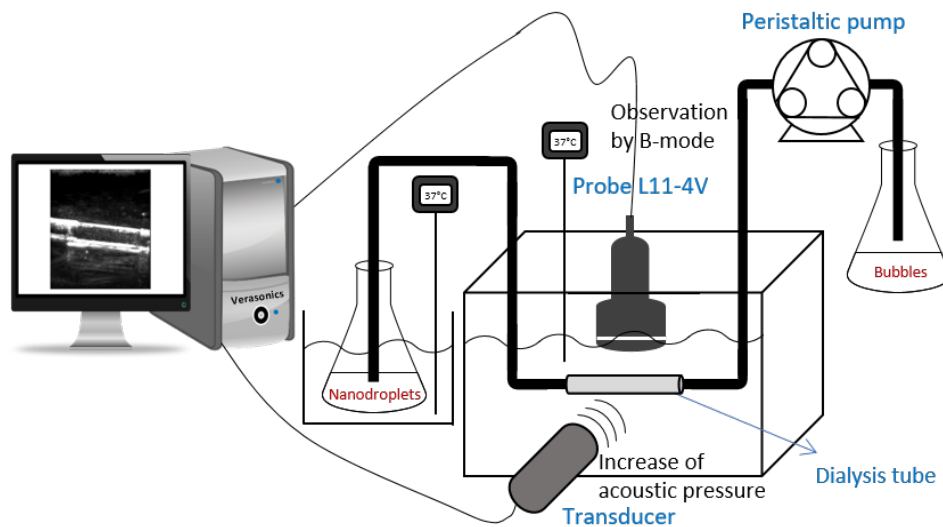


Figure 2: Schematic representation of the set-up to vaporize and determine the ADV threshold

Results

PFC-Nanodroplets formulation:

The size and size distribution (polydispersity) of PFC-NDs formulation, composed of perfluoropentane (PFP) and Zonyl FSO, are shown in Fig. 3. The droplet sizes were in the nanometric range (Z-Ave: 287,1 nm) with a narrower size distribution (PDI: 0.079) and no microdroplets were observed by optical microscopy. Moreover, this PFC-ND suspension was found stable for several weeks upon storage at 5 °C. More importantly, this microfluidic method has shown a high reproducibility in the nanodroplets preparation for various formulations.

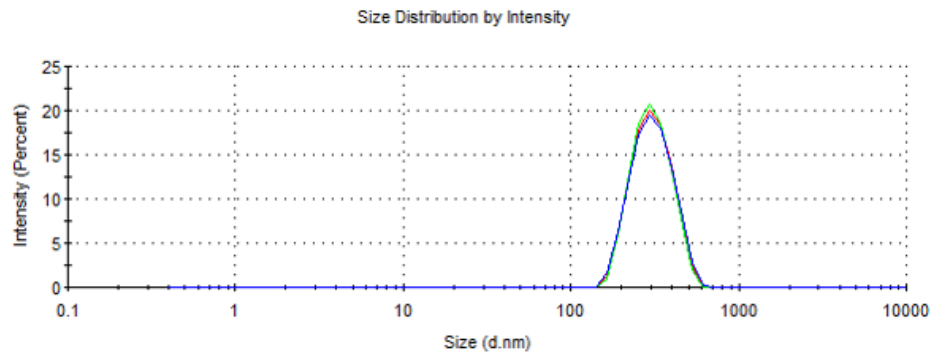


Figure 3: Narrow size distribution of microfluidically formed nanodroplets (PFP@Zonyl FSO) as obtained by Dynamic Light Scattering

PFC-nanodroplets vaporization:

Fig. 4 (left) shows the vaporization of nanodroplets in the tube, as imaged by the linear array in B-mode. When the applied pressure exceeded a threshold, the nanodroplet phase change from liquid (green rectangle) to gas (yellow rectangle). The resulting bubble continued to flow inside the tube, generating a bubble cloud with a highly-echogenic scatters.

Collected data were fitted to a sigmoidal model and the ADV threshold was determined as the intersection of noise level and the fit tangent at the maximum derivative of the sigmoid. The ADV threshold is denoted by a black cross on the fit curve in Fig. 4 (right). For PFP@Zonyl FSO formulation, the average ADV threshold (n=6) obtained was 4.37 ± 0.03 MPa. Similar ADV threshold results were reported for similar PFC nanodroplets in the same size range [6,7,8].

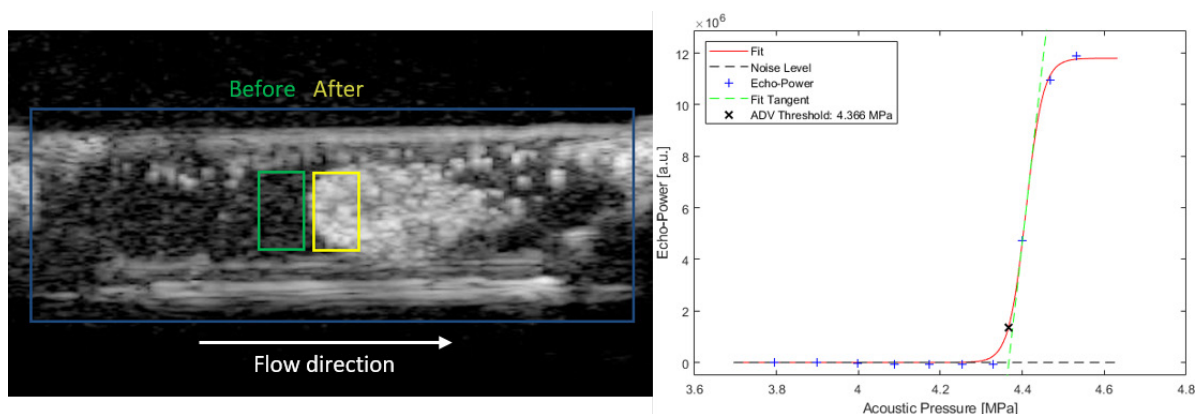


Figure 4: Observation by B-mode of the vaporization of nanodroplets (PFP@Zonyl FSO) flowing in the tube (left) and Echo-power obtained by VueBox™ as function of applied acoustic pressure with the respective fit sigmoid to determine ADV threshold (right)

Conclusions

Overall, these results demonstrate the usefulness of microfluidic technologies to prepare tailored made PFC-NDs systems with different encapsulating shells including surfactants, lipids or polymers. The generated nanodroplets were systematically characterized for size, polydispersity and stability. Ultimately, a home-made set-up was applied to acoustically characterize the NDs in terms of ADV threshold. In this context, VueboxTM software package associated with a sigmoidal fit seems to be a great tool to determine and to assess the influence of formulation parameters on the ADV threshold.

References

- [1]. Kripfgans O. D., Fowlkes J. B., Miller D. L., Eldevik O. P., Carson P. L., Acoustic droplet vaporization for therapeutic and diagnostic applications, *Ultrasound in Medicine & Biology* 26 (7) 1177–1189, 2000.
- [2]. Ho Y. and Yeh C. K., Theranostic performance of acoustic nanodroplet vaporization-generated bubbles in tumor intertissue, *Theranostics*, vol. 7, no. 6, pp. 1477–1488, 2017.
- [3]. Loskutova K., Grishenkov D., Ghorbani M., Review on Acoustic Droplet Vaporization in Ultrasound Diagnostics and Therapeutics. *BioMed Res. Int.* 2019, 1–20, 2019.
- [4]. Lea-Banks, H., O'Reilly, M. A. & Hynnen, K. Ultrasound-responsive droplets for therapy: A review. *J. Controlled Release* 293, 144–154, 2019.
- [5]. Kee, A. L. Y. & Teo, B. M. Biomedical applications of acoustically responsive phase shift nanodroplets: Current status and future directions. *Ultrason. Sonochem.* 56, 37–45, 2019.
- [6]. Martz, T. D., Bardin, D., Sheeran, P. S., Lee, A. P. & Dayton, P. A. Microfluidic Generation of Acoustically Active Nanodroplets. *Small* 8, 1876–1879, 2012.
- [7]. Seo, M., Williams, R. & Matsuura, N. Size reduction of cosolvent-infused microbubbles to form acoustically responsive monodisperse perfluorocarbon nanodroplets. *Lab. Chip* 15, 3581–3590, 2015.
- [8]. Williams, R. et al. Characterization of Submicron Phase-change Perfluorocarbon Droplets for Extravascular Ultrasound Imaging of Cancer. *Ultrasound Med. Biol.* 39, 475–489, 2013.

Preliminary Evaluations of Safety and Efficacy of a Ultra Small Contrast Agent for Contrast-enhanced Ultrasound Imaging

Chung-Hsin Wang¹, Shih-Tsung Kang¹, Winters Fu¹

¹Trust Bio-sonics, Inc., HsinChu City, Taiwan

Corresponding author: chwang@trust-biosonics.com

Introduction

Contrast-enhanced ultrasound (CEUS) has gradually become an essential diagnostic tool for cardiac and abdominal imaging. In the past decade, different kinds of technologies, such as new beam forming and imaging sequence, have been developed to improving the performances of CEUS. Contrast to the elevation of ultrasound technologies, most of the commercialized microbubble products are developed in 1990s. Thus, to keep up with imaging techniques and to overcome the limitation imposed by the commercial microbubbles, a new contrast agent is expected and such development is gaining attention in academia. In this study, a newly developed ultra-small microbubble was evaluated by various animal models for its safety and efficacy.

Methods

TBS-002, the new contrast agent was constructed with perfluorocarbon gas and phospholipid shell. It's mean size is 1.2 μm (with a distribution from 0.7 to 2 μm) and concentration up to 4×10^{10} bubbles/mL. Toxicology and safety pharmacology studies were carried out with rodents and canines under GLP standards. Dose-escalating study was included as well. To answer the major safety concerns of microbubble product, i.e. cardiac reaction under echocardiography¹ and local embolism, two specially designed studies were performed. For the potential risk of cardiac reaction, six healthy dogs were scanned with end-systolic triggering technique under the mechanical indexes (MI) of 0.83 and 1.9 with the Sequoia system (Acuson-Siemens). Diagnostic EKG and physiological monitor were used to identify abnormal events during the scanning period (5 minutes). In an independent canine study, TBS-002 was directly dosed into left ventricular (LV) chamber to evaluate the potential risk of embolism.

The utility of contrast echocardiography and the detection of liver lesions were also tested in rabbit, swine, and canine models. Imaging peak intensity, half-life, and imageable duration in different organs were evaluated and analyzed. Various ultrasound systems were applied in these studies, including CX-50, Epiq from Philips, Sequoia from Siemens, and SSA-660, Aplio 500 from Canon Medical Systems.

Results

All the studies suggested the projected human clinical dose of TBS-002. Under such dose, there was no significant adverse effect found. Furthermore, no abnormal cardiac reaction, such as premature ventricular contraction, was noted in the study with high-MI ultrasound imaging. In the study for observing local embolism, neither physiological nor pathological change was noted, even when the doses is 20 times of the projected human clinical one. As to efficacy, all animals showed clear opacifications. For echocardiography, TBS-002 successfully demonstrated its capability in visualizing both LV and myocardium (shown in Fig. 1). In VX-2 rabbit liver tumor model, TBS-002 showed a typical perfusion pattern of early wash-in and clear wash-out in the tumor areas.

Conclusions

TBS-002 is a new microbubble contrast agent capable of producing robust opacification for cardiac and abdominal imaging. In addition, it is not only safe as per the toxicology and safety pharmacology studies, but also less likely to cause adverse effects such as acute cardiac reaction and local embolism. Future evaluation in human clinical study is required to translate the product into clinical uses. Phase 1 trial is ongoing when this abstract submitted.

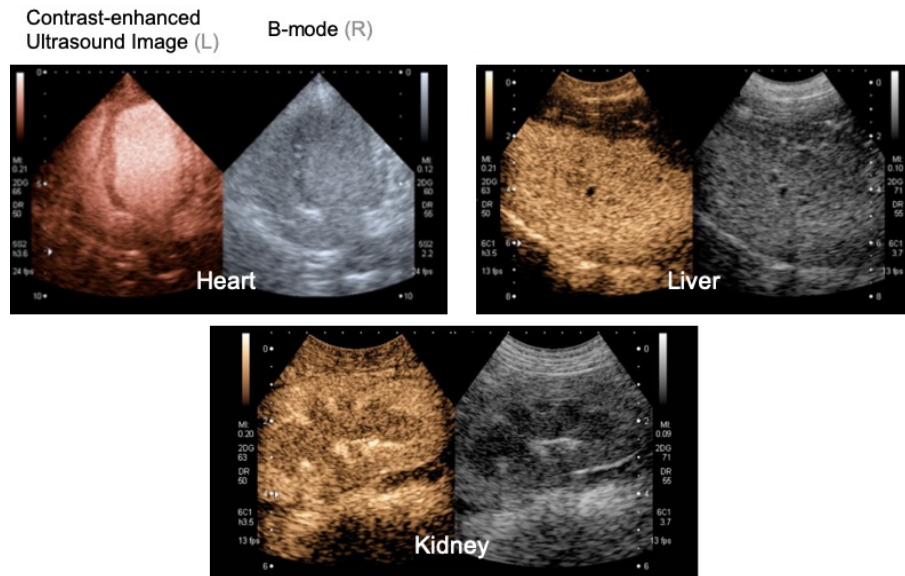


Fig. 1. Representative images of the efficacy evaluation in different organs.

Reference

- [1]. van der Wouw PA, Brauns AC, Bailey SE, Powers JE, Wilde AA, Premature ventricular contractions during triggered imaging with ultrasound contrast, *J Am Soc Echocardiogr*, 13: 288-294, 2000

DODAB-shelled microdroplets, invaluable antitumor carriers

Fabio Domenici, Damiano Palmieri, Elisabetta Tortorella, Letizia Oddo, Francesco Brasili, Daniele Gigante, Yosra Toumia, Gaio Paradossi

*Dipartimento di Scienze e Tecnologie Chimiche, Università degli Studi di Roma "Tor Vergata"
Via della Ricerca Scientifica, 00133 Rome, Italy
Corresponding author: fabio.domenici@uniroma2.it*

Introduction

The introduction of phase-change perfluorocarbon microdroplets (MDs) in the vast theranostic scenario is evaluated through the key opportunity they offer to conjugate drugs cargo capability with echogenicity promoted by acoustic core vaporization [1]. Significant improvement in this respect mainly passes through the optimization of the MDs shell with respect to stability, chemical versatility, and synthesis efficiency.

We present decafluoropentane (DFP) MDs stabilized by a shell of dimethyldioctadecylammonium bromide (DODAB) cationic surfactant. The long saturated hydrocarbon chains, deeply penetrating the hydrophobic core, stabilize the droplet and the drug cargo within, and the high positive ζ -potential favours the colloidal stability of MDs. The biological attractiveness of DODAB shell lies in the ability to bind anionic antigenic proteins, nucleotides or DNA, and nanoparticles, providing in turn, a remarkable immunoadjuvant activity, support for gene therapy, and antitumour action [2,3]. We developed a DODAB-MDs drug delivery vector, promoting the release of anthracyclines (e.g., Doxorubicin) against highly aggressive, invasive and poorly differentiated triple-negative breast cancer cells.

Methods

$3 \cdot 10^{10}$ droplets/ml were readily provided within few seconds by pulsed high-power insonation, resulting in low polydispersed 1 μm sized droplets, exhibiting a ζ -potential of ~ 100 mV. Specifically the MD carrier was prepared under sterile conditions by emulsifying pre-dissolved DFP and DODAB phase in iso-osmolar water solution through a few seconds of pulsed insonation at 20 kHz, 100 W. The MDs size can be easily tuned by varying the insonation conditions. The MDs size, surface charge, and morphology were analyzed by photo correlation (DLS), ζ -potential, confocal laser scanning microscopy (CLSM) and microplate absorbance and fluorescence reader. The effect of ultrasound (US)-induced MDs into microbubbles transition was tested by acoustic attenuation spectroscopy. The DFP core of the MDs was able to embed doxorubicin (Dox), whereas at the water interface the MDs can form complexes with hydrophilic drugs and bind onto the cell phospholipid membrane for combined chemotherapeutic strategies. The loading of Dox in the vector core was obtained by pre-dissolving Dox within the DFP and DODAB mixture. Washings (by centrifugation) and spectrophotometric tests were carried out to ensure the removal of not encapsulated Dox. The potential cytotoxic effect of the MDs was evaluated on the MDA-MB-231 cells (human breast adenocarcinoma, basal-like: estrogen receptor/progesterone receptor/ErbB2-negative) in the proliferative phase by the MTT assay [4]. Viability tests were performed at different drug concentrations (10, 5, 2 nM) and incubation times (24, 48, 72 h); measurements were made with a Tecan multiplate reader and all the results are expressed as average value and standard deviation of 3 replicates.

Results

We obtained DODAB-MDs loaded with Dox (30% of loading efficiency) which remains stably confined within the DFP core (Figure 1, A). Because of their mutual electrostatic repulsion, the MDs maintain both the small size distribution and the high-density dispersion also in physiological conditions. The DODAB-MDs provide a high pharmacological concentration at the interface with MDA-MB-231 tumor cells. According to time-lapse CLSM measurements the MDs show a high affinity of interaction

with the cell membrane and, upon the contact, the overall amount of the drug is promptly released in the cytosol (Figure 1, B). MTT assays reveal (Figure 1, C) the strongest cytotoxic effect which is given by MDs+Dox at nM range of Dox concentration (e.g., MDs dispersion carrying 5 nM Dox decreases the cell viability down to $64 \pm 4\%$ after 24 h, and it is progressively reduced down to $38 \pm 5\%$ after 48 h). Upon acoustic droplet vaporization of the MDs the cytotoxic effect is retained, whereas equivalent concentrations of either free Dox or unloaded MDs do not produce any effect on the cell viability.

Conclusions

We show that DODAB-MDs act as an efficient reservoir system for Dox *in vitro*. Specifically, the droplets shell is able to interact with the cell membrane of epithelial, human breast cancer cells, favouring the drug internalization and the killing of them up to 36% in only 24 h at 5 nM Dox concentration. Remarkably, this concentration is more than one order of magnitude lower than the IC_{50} of the most recent proposed strategies using polymer scaffolds [4]. Moreover, the transition of Dox loaded MDs into microbubbles further modulates the level of the drug penetration maintaining remarkable cytotoxicity. The selectivity of MDs interaction with tumour cells will be also discussed. Our results may be relevant in greatly amplifying the benefit-to-risk ratio of chemotherapeutics against aggressive and highly resistant neoplasms as well as in facilitating real-time monitoring of treatments towards personalised medicine.

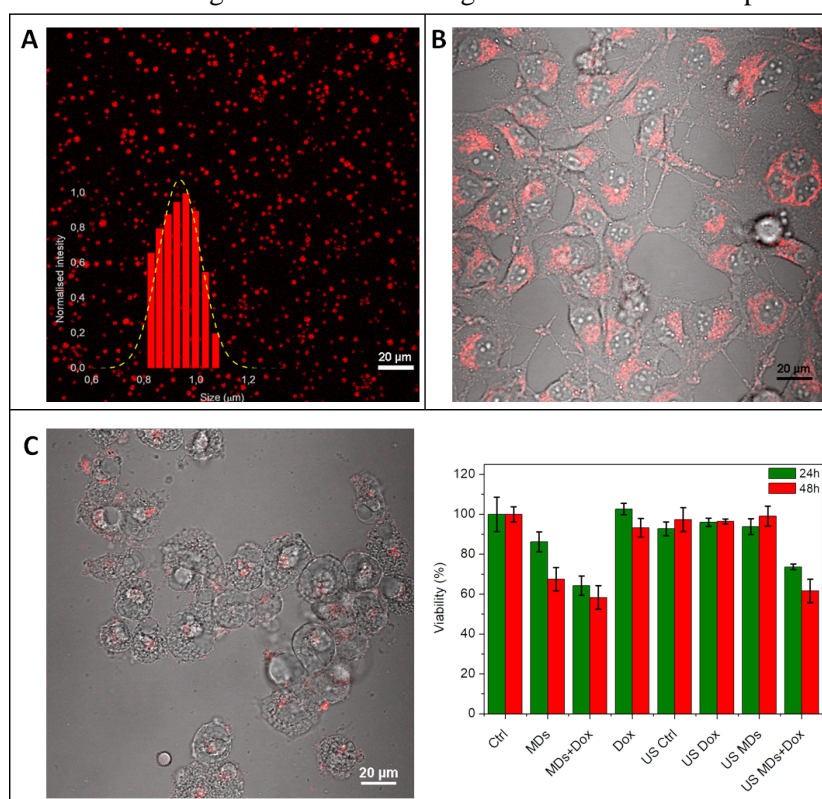


Figure 1. CLSM images representative of DODAB-MDs loaded with red fluorescent Dox (MDs+Dox) together with DLS analysis of the size distribution (A); after being just incubated (B) and after 24 h (C) onto human adenocarcinoma cells. Comparative MTT viability assay after 24 h and 48 h of incubation with 5 nM Dox (C, right side).

References

- [1]. Capece S, Domenici et al, Phys.Chem.Chem.Phys. 18: 8378-8388, 2016.
- [2]. F. Domenici, C. Castellano et al, Colloids Surf.B 88: 432-439, 2011.
- [3]. P.S. Dubey, Srinivasan et al, Sci.Rep. 8: 1-16, 2018.
- [4]. L. Chronopoulou, F. Domenici et al, Colloids Surf.B 180: 495-502, 2019.

Pharmacokinetic modeling of targeted ultrasound nanobubbles to quantify PSMA expression in prostate cancer

Simona Turco¹, Reshani Perera², Elisabetta Peri¹, Hessel Wijkstra^{1,3}, Agata A. Exner², Massimo Mischi¹

¹*Biomedical diagnostics lab, Eindhoven University of Technology, Eindhoven, the Netherlands*

²*Departement of Radiology, Case Western Reserve University, Cleveland OH, United States*

³*Departement of Urology, Amsterdam University Medical Center, Amsterdam, the Netherlands*

Corresponding author: s.turco@tue.nl

Introduction

Prostate cancer is one of the most commonly diagnosed cancer worldwide (7.1% of overall cancer cases) and a leading cause of cancer death among males [1]. Currently, the gold standard for the diagnosis of prostate cancer is the assessment of prostate specific antigen in plasma, followed by a histologic examination of tissue sampled via biopsy [2]. Among the most relevant drawbacks of biopsies, it often results in misclassification of cancer and it cannot provide accurate spatial localization of the tumor, hampering the use of focal therapy as cancer treatment [2, 3]. Novel diagnostics for more reliable detection and localization of prostate cancer are urgently needed.

Although Contrast Enhanced Ultrasound (CEUS) has shown promise for imaging of angiogenesis, a hallmark of cancer growth [4], its value for prostate cancer diagnosis is still debated [5, 6]. Recently, molecular ultrasound imaging of prostate cancer by using novel microbubbles targeted to vascular endothelial growth receptor 2 (VEGFR2) has been proposed, but the detection rate in a first-in-human clinical trial was limited to 65% [7]. The introduction of nanobubbles (NBs) has opened new possibilities for ultrasound molecular imaging. Indeed, thanks to their smaller size (~0.3 μ m compared to 1-10 μ m), NBs can cross the vascular endothelium and reach targets beyond the vessel wall. This is particularly relevant in tumor vasculature, where permeability is typically enhanced [8]. In the context of prostate cancer imaging, NBs targeted to the prostate-specific membrane antigen (PSMA) have been developed and preliminary tested [8], showing prolonged retention and selective accumulation in PSMA-expressing tumors. However, methods for in-vivo quantification of NB extravasation and binding are currently lacking.

In previous work, we proposed pharmacokinetics modeling of NB transport by the simplified reference tissue model and tested its feasibility for assessment of extravasation and binding on one dual-tumor mouse model [9, 10]. In this work, we optimized parameter estimation using a basis-function method and we extended the pre-clinical validation of the proposed method to seven dual-tumor mouse models of prostate cancer.

Methods

Pharmacokinetic modeling framework:

The kinetics of PSMA-targeted NBs can be described by a three-compartment model, including the plasma, the free tissue (where no binding occurs) and the bound tissue (where binding occurs). In fact, PSMA-targeted NBs travel through plasma, they may cross the vascular endothelium, and they may attach to cell membranes that overexpress PSMA. When reference tissue is available i.e., tissue with the same kinetics as the bound tissue but where no binding occurs, the kinetics of targeted NBs can be described as [11]

$$\left\{ \begin{array}{l} \frac{dC_r(t)}{dt} = K_1' C_p(t) - k_2' C_r(t) \\ \frac{dC_f(t)}{dt} = K_1 C_p(t) - k_2 C_r(t) - k_3 C_f(t) + k_4 C_b(t), \\ \frac{dC_b(t)}{dt} = k_3 C_f(t) - k_4 C_b(t) \end{array} \right. \quad (1)$$

where $C_p(t)$, $C_f(t)$, $C_b(t)$, and $C_r(t)$ are the concentrations of NBs in the plasma, free, bound, and reference tissue compartments, respectively; K_1 ($\text{mL} \cdot \text{mL}^{-1} \cdot \text{min}^{-1}$) is the rate constant for transfer from plasma to free compartment; k_2 is the rate constant for transfer from free to plasma compartment (min^{-1}); k_3 is the rate constant for transfer from free to bound compartment (min^{-1}); k_4 is the rate constant for transfer from bound to free compartment; K_1' is the rate constant for transfer from plasma to reference compartment ($\text{mL} \cdot \text{mL}^{-1} \cdot \text{min}^{-1}$); k_2' is the rate constant for transfer from reference to plasma compartment (min^{-1}).

When the kinetics of free and bound compartments are difficult to distinguish, the differential equations can be simplified. Defining the binding potential as $\text{BP} = k_3/k_4$, and the ratio $R_1 = K_1/K_1'$, if the NB concentration in the target and reference tissues can be measured, the solution of the simplified reference tissue model can be obtained as

$$I_t(t) = R_1 I_r(t) + \left(k_2 - \frac{R_1 k_2}{1 + \text{BP}} \right) I_r(t) * e^{-\frac{k_2}{1 + \text{BP}} t}, \quad (2)$$

where $I_t(t) = G \cdot C_t(t)$ and $I_r(t) = G \cdot C_r(t)$ are the linearized acoustic intensity over time in the target and reference tissues, respectively, and G is a multiplicative constant. In fact, although in practice the concentrations $C_t(t)$ and $C_r(t)$ are not available, a linear relationship between the acoustic intensity and the contrast concentration can be assumed, provided that TICs obtained from CEUS loops are properly linearized [10].

CEUS imaging in dual-tumor mice

Seven dual-tumor mouse models were obtained by subcutaneous implantation of PSMA-positive PC3pip cells in one flank of each mouse, and PSMA-negative PC3flu cells in the other flank of six-week old male athymic nude mice. Animal experiments were conducted according to a protocol approved by the Institutional Animal Care and Use Committee (IACUC) at Case Western Reserve University.

CEUS was performed by a 200- μL bolus of either non-targeted NBs or PSMA-targeted NBs. Data was acquired with a Toshiba Scanner (AplioXG SSA-790A, Toshiba Medical Imaging Systems, Otawara-Shi, Japan) with a PLT-1204BT probe working at 12 MHz (MI, 0.1; dynamic range, 65dB; gain, 70dB; imaging frame rate, 0.2 frames/s) placed to visualize both tumors in the same field of view.

The experimental procedure consisted of bolus injection (non-targeted NBs or PSMA-targeted NBs) and imaging acquisition for 30 min, followed by NBs destruction via high-intensity ultrasound flashes to destroy any residual bubble. After waiting about 30 min, the other contrast agent was administered with the same protocol. Regions of interest (ROIs) were drawn on both PSMA-positive and PSMA-negative tumors, and TICs for each ROI were extracted and linearized for further processing. Two mice were

excluded from analysis after visual inspection of TICs, which revealed large artefacts including peak saturation, amplitude distortion, and late start of recording.

Estimation of extravasation and binding

Linearized TICs obtained with both NB types were interpolated by a factor 3 (up to 0.6 frame/s) and filtered by a Savitzky-Golay filter. The TICs obtained from the PSMA- positive tumor (target tissue, i.e., $I_t(t)$ in (2)) were fit by the model in (2), using as reference tissue the TICs obtained from the PSMA-negative tumor, i.e., $I_r(t)$ in (2). The reference TICs were first fit by an analytical function to constrain them to a physiologically feasible shape and filter out noise. For this, a model previously proposed by Orton et al (model 1) in the context of pharmacokinetic modeling of dynamic contrast-enhanced MRI was used [11].

A basis function method was used to increase robustness and decrease computation time of parameter estimation. Equation (2) can in fact be rewritten as [13]

$$I_t(t) = \theta_1 I_r(t) + \theta_2 I_r(t) * e^{-\theta_3 t}, \tag{3}$$

where $\theta_1 = R_1$, $\theta_2 = k_2 - R_1 k_2 / (1 + BP)$, and $\theta_3 = k_2 / (1 + BP)$. Equation (3) is linear in the parameters θ_1 and θ_2 , while the non-linear term can be handled by defining a set of basis functions as

$$B_i(t) = I_r(t) * e^{-\theta_{3i} t}. \tag{4}$$

Setting boundaries for k_2 between 10^{-7} min^{-1} and 10 min^{-1} , and for BP between 0 and 10, resulted in a range for θ_3 between 10^{-8} min^{-1} and 5 min^{-1} , which was spanned for 5000 equally-spaced samples on a logarithmic scale.

Results

Table 1 reports the estimated parameters in all mice included in the analysis. The estimated BP values were larger for PSMA-targeted NBs in three mice, smaller for PSMA-targeted NBs in one mouse, and equal to zero for both NB types in one mouse. Examples of TICs obtained in the target and reference tissues are shown for two mice in Figure 1. Consistent with the estimated high BP value, a steady plateau is observed in the late phase for PSMA-targeted NBs in ‘mouse 5’ (Figure 1(d)). Conversely, a return to baseline intensity is observed in the late phase for both NB types in ‘mouse 3’ (Figure 1(a, c)), which is in line with the estimated BP equal to zero.

Table 1. Estimated parameters in all mice for non-targeted NBs and PSMA-targeted NBs

	Non-targeted NBs		PSMA-targeted NBs	
	$k_2 \text{ (min}^{-1}\text{)}$	BP(-)	$k_2 \text{ (min}^{-1}\text{)}$	BP(-)
mouse1	0.04	0.83	0.31	0.28
mouse2	4.20	0.29	0.06	0.42
mouse3	1.21	0.00	1.85	0.00
mouse4	1.40	0.03	0.26	0.18
mouse5	5.04	0.63	0.04	10.00

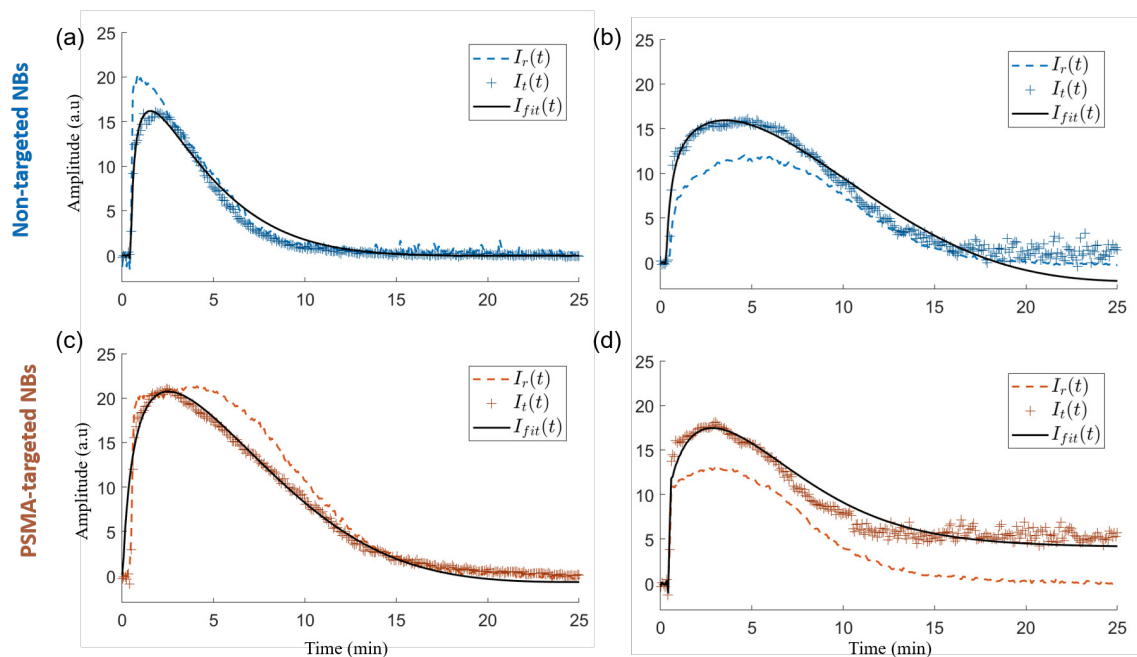


Figure 1. Examples of TICs obtained in ‘mouse3’ (a, c) and ‘mouse5’ (b, d) for non-targeted (a, b) and PSMA-targeted (c, d) NBs. The reference-tissue TICs are plotted as grey circles, the target-tissue TICs as black stars, and the corresponding fit by the reference tissue model as solid black line.

Conclusions

In this work, we proposed pharmacokinetic modeling by the reference tissue model for quantification of extravasation and binding of PSMA-targeted NBs. After optimizing the parameter estimation, the proposed method was tested in 7 dual-tumor mouse model of prostate cancer.

For most of the mice included in the study, the estimated BP was larger for PSMA-targeted NBs compared to non-targeted NBs. This confirms previous findings, demonstrating longer retention and selective accumulation of PSMA-targeted NBs in PSMA-expressing tumors [8]. The non-zero BP values obtained in some cases for non-targeted NBs may result from non-specific binding. This is in line with previous reports, showing that both non-targeted and targeted NBs are seen in ex-vivo tumor tissue, although higher degree of retention is observed for targeted NBs [8]. In one mouse, a smaller BP was estimated for PSMA-targeted NBs compared to non-targeted NBs, suggesting that higher non-specific binding of non-targeted NBs occurred in this mouse compared to the actual binding of PSMA-targeted NBs. Moreover, a BP equal to zero was observed for both NB types in one mouse. Beside possible inaccuracies in the parameter estimation, possible physiological causes for this include heterogeneous vascularity and vascular permeability of these tumors, low NB targeting efficiency, and low PSMA expression in the PSMA-positive tumor.

In the future, sensitivity analysis will be performed to investigate possible correlation between parameters and clarify whether some parameters are weakly identifiable. Moreover, immune-histological quantification of PSMA expression will be performed, which is necessary to confirm the promise of the proposed BP parameter as an in-vivo biomarker of PSMA expression. Finally, more complex pharmacokinetic models will be investigated, which do not require the presence of a reference tissue in the field-of-view. Additional modeling of the contrast plasma concentration could, for instance, provide also assessment of the vascular compartment, meanwhile avoiding the need for measuring the concentration in the reference tissue [10, 14].

References

- [1]. Bray, F., Ferlay, J., Soerjomataram, I., Siegel, R. L., Torre, L. A., & Jemal, A. (2018). Global cancer statistics 2018: GLOBOCAN estimates of incidence and mortality worldwide for 36 cancers in 185 countries. *CA: a cancer journal for clinicians*, 68(6), 394-424.
- [2]. Mottet N, Bellmunt J, Bolla M, et al. "EAU-ESTRO-SIOG Guidelines on Prostate Cancer. Part 1: Screening, Diagnosis, and Local Treatment with Curative Intent ", *Eur Urol*. 2017 Apr;71(4):618-629. doi: 10.1016/j.eururo.2016.08.003. Epub 2016 Aug 25.
- [3]. E. C. Serefoglu, S. Altinova, N. S. Ugras, E. Akincioglu, E. Asil, and M. D. Balbay, "How reliable is 12-core prostate biopsy procedure in the detection of prostate cancer?" *Canadian Urological Association Journal*, vol. 7, no. 5-6, p. E293, 2013
- [4]. Folkman, J. (1995). Angiogenesis in cancer, vascular, rheumatoid and other disease. *Nature medicine*, 1(1), 27.
- [5]. Smeenge, M. , Barentsz, J. , Cosgrove, D. et al. (2012), Role of transrectal ultrasonography (TRUS) in focal therapy of prostate cancer: report from a Consensus Panel. *BJU International*, 110: 942-948. doi:10.1111/j.1464-410X.2012.11072.x
- [6]. Wink, Margot, et al. "Contrast-enhanced ultrasound and prostate cancer; a multicentre European research coordination project." *European urology* 54.5 (2008): 982-993.
- [7]. Smeenge, M., Tranquart, F., Mannaerts, C. K., de Reijke, T. M., van de Vijver, M. J., Laguna, M. P., ... & Wijkstra, H. (2017). First-in-human ultrasound molecular imaging with a VEGFR2-specific ultrasound molecular contrast agent (BR55) in prostate cancer: a safety and feasibility pilot study. *Investigative radiology*, 52(7), 419-427.
- [8]. R. Perera, X. Wang, Y. Wang, G. Ramamurthy, P. Peiris, E. Abenojar, J. P. Basilion, A. A. Exner et al., "Real time ultrasound molecular imaging of prostate cancer with psma-targeted nanobubbles," *bioRxiv*, p. 634444, 2019.
- [9]. Turco, S., Perera, R., Wijkstra, H., Exner, A. A., & Mischi, M. (2019). Pharmacokinetic analysis of targeted nanobubbles for quantitative assessment of PSMA expression in prostate cancer. In *24th European Symposium on Contrast Ultrasound Imaging*.
- [10]. Mischi, M., Turco, S., Soliman, O. I., Folkert, J., Wijkstra, H., & Schoots, I. (2018). Quantification of contrast kinetics in clinical imaging. *Springer*.
- [11]. Lammertsma, Adriaan A., and Susan P. Hume. "Simplified reference tissue model for PET receptor studies." *Neuroimage* 4.3 (1996): 153-158. M.R.Orton, J.A.d'Arcy, S.Walker-Samuel, D.J.Hawkes, D. Atkinson, D. J. Collins, and M. O. Leach, "Computationally efficient vascular input function models for quantitative kinetic modelling using dce-mri," *Physics in Medicine & Biology*, vol. 53, no. 5, p. 1225, 2008.
- [12]. M. R. Orton, J. A. d'Arcy, S.Walker-Samuel, D. J. Hawkes, D. Atkinson, D. J. Collins, and M. O. Leach, "Computationally efficient vascular input function models for quantitative kinetic modelling using DCE-MRI," *Physics in Medicine & Biology*, vol. 53, no. 5, p. 1225, 2008.
- [13]. R. N. Gunn, A. A. Lammertsma, and V. J. Cunningham, "Parametric imaging of ligand-receptor interactions using a reference tissue model and cluster analysis," in *Quantitative functional brain imaging with positron emission tomography*. Elsevier, 1998, pp. 401-406.
- [14]. Turco, S., Tardy, I., Frinking, P., Wijkstra, H., & Mischi, M. (2017). Quantitative ultrasound molecular imaging by modeling the binding kinetics of targeted contrast agent. *Physics in Medicine & Biology*, 62(6), 2449.

Towards Ultrasound-assisted Photon Radiation Dosimetry using Polymeric Phase Change Nanodroplets: A Preliminary Concept Study

Yosra Toumia^{1*}, *Madalina Cociorb*^{1,2}, *Fabio Domenici*¹, *Roberto Miceli*³, *Rolando Maria D'Angelillo*³, *Piero Rossi*⁴, *Letizia Oddo*¹, *Emiliano D'Agostino*², *Sophie V. Heymans*⁵, *Bram Carlier*^{6,7}, *Uwe Himmelreich*⁷, *Koen Van Den Abeele*⁵, *Jan D'Hooge*⁸, *Gaio Paradossi*^{1*}

¹*Department of Chemical Science and Technologies, University of Rome Tor Vergata, Rome, Italy*

²*DoseVue, Hasselt, Belgium*

³*UOC Radiotherapy, Department of Oncology, Policlinico Tor Vergata (PTV), University of Rome Tor Vergata, Italy*

⁴*Department of Experimental Medicine and Surgery, PTV, University of Rome Tor Vergata, Italy*

⁵*Department of Physics, KU Leuven Campus KULAK, Kortrijk, Belgium*

⁶*Department of Oncology, KU Leuven, Leuven, Belgium*

⁷*Molecular Small Animal Imaging Cente KULeuven, Leuven, Belgium*

⁸*Department of Cardiovascular Sciences, KU Leuven, Leuven, Belgium*

Corresponding authors: paradossi@stc.uniroma2.it; Yosra.Toumia@uniroma2.it

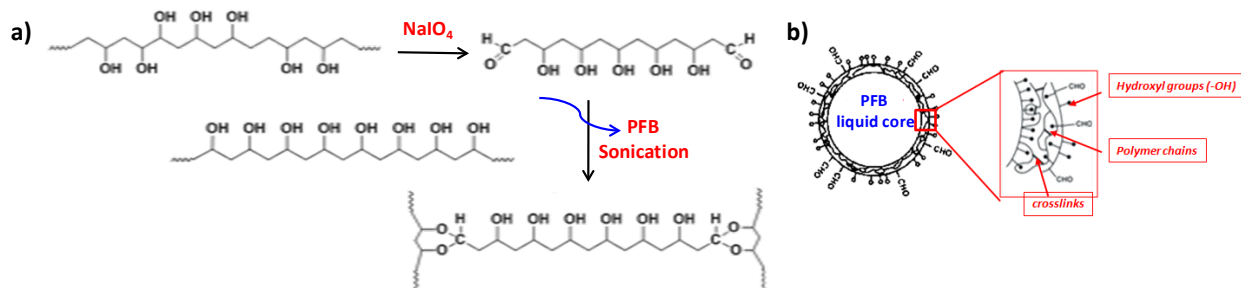
Introduction

Ultrasound imaging (US) is one of the most used diagnostic tools in medicine. Due to the recent advances regarding the US technology, the latter applications are so far expanded to theranostic approaches as well [1]. The use of contrast agents in US was mainly aiming to enhance the diagnostic yield for better and early-detection of anomalies. Phase-change nanodroplets are now considered as the next generation of ultrasound contrast agents due to their ability to extravasate in tumoral tissues. These consist of a lipid/polymer coated perfluorocarbon (PFC) liquid core which can undergo a liquid ↔ gas transition upon acoustic/optical activation [2]. Although in a similar way, vaporization of superheated droplets by ionizing radiation was reported in the literature, such activation of PFC shelled nanodroplets has not been investigated yet [3]. The response of nanodroplets to ionizing radiation, e.g. X-rays, and their detection by ultrasound could further expand the use of US into the radiotherapy dosimetry field. Indeed, current dose verification methods remain rudimentary and generally consist of offline measurements or point verifications on the patient's skin.

In this contribution, we first report on the formulation and the acoustic performance of novel poly(vinyl-alcohol), PVA, shelled perfluorobutane (PFB) nanodroplets. This is followed by a proof-of-concept experiment testing the capability of these nanodroplets to vaporize upon their exposure to X-ray ionizing radiation. The rationale behind the investigation of PVA shelled droplets as a candidate being part of an integrated dosimeter is the enhanced stability with respect to thin lipid counterparts in addition to an easier surface modification for targeting purposes.

Methods

The nanodroplets studied herein consist of a perfluorobutane (PFB) liquid core encapsulated by a crosslinked shell of poly(vinyl-alcohol), PVA. The PFB (b.p. = -2°C) was condensed in liquid nitrogen according to the procedure reported in a previous work [4]. The formulation of nanodroplets as well as the crosslinking of the shell resulted from a sonication process of oxidized PVA aqueous solution at the PFB water interface (see Scheme 1). The colloidal stability of the obtained nanodroplets, i.e. PVA/PFB NDs, was studied over time by dynamic light scattering at 90° (BI-200SM goniometer, Brookhaven Instruments Co.), while the concentration of the PFB core can be estimated by ¹⁹F NMR spectroscopy (Bruker 400 MHz).



Scheme 1. a) Crosslinking reaction and formulation of PVA/PFB NDs ; b) Structural representation of PVA/PFB NDs shell.

The potential of PVA/PFB nandroplets as an ultrasound contrast agent was evaluated *in vitro* by different techniques after triggering an acoustic droplet vaporization (ADV), either in a human serum physiological medium or in tissue mimicking phantoms. In a first step, the ADV upon insonation using a sonoprotator (SP100-1MHz) was investigated by bright field microscopy (inverted eclipse model Ti-E, Nikon Instruments, Japan) and by measuring the ultrasound attenuation before and after activation. The latter was performed by an in-house developed setup equipped with a glass container featuring two opposite openings where 10 MHz emitting and receiving flat transducers (Olympus V311) are connected. The vaporization efficiency of droplets from different size batches, after selective centrifugation, was studied as a function of the applied ultrasound intensity.

In a second step, different tissue-mimicking phantoms designed for *in vitro* ionizing radiation experiments were tested in order to allow for a stable entrapment of the PVA/PFB NDs without inducing their spontaneous vaporization (e.g. ultrasound gel, polyacrylamide (PAM) hydrogels). The phantoms were optimized based on the stability of NDs at 37°C as well as their ability to expand into microbubbles when exposed to a stimulus such as ultrasound. The evaluation of the behavior of NDs and their phase transition in the phantoms was performed using a clinical US system (Mindray DP50, Milan) equipped with a transducer (f_c 7.5 MHz).

A first preliminary X-ray radiation experiment was performed at room temperature. The PVA/PFB NDs nandroplets phantom was brought to the radiotherapy room and placed in a sample holder located at isocenter. The radiation beam was delivered by a linear accelerator (Elekta Precise®) with 6 MV photons within a field size of 10×10 cm². PVA/PFB NDs were irradiated with a total dose of 10 Gy (at a dose rate of 5 Gy/min). A control experiment was performed on non-irradiated PVA/PFB NDs phantoms and on an irradiated phantom without the NDs. In order to assess the radiation effect on the PVA/PFB NDs, the phantoms were imaged pre and post radiation with the clinical US apparatus. All the images were acquired at the same gain under a mechanical index ≤ 0.3 , and subsequently analyzed by measuring the gray value using ImageJ freeware.

Results

A high yield of submicron-sized PFB droplets encapsulated by PVA crosslinked shells can be obtained. The resulting PVA/PFB NDs show a good stability over a period of two weeks with minor spontaneous vaporization events. The NDs demonstrate good vaporization efficiency when triggered by ultrasound and result in a size expansion of about 5-10 fold. The ADV study of both large (average size = 900 nm) and small (average size = 400 nm) PVA/PFB NDs revealed two acoustic attenuation resonance events, i.e. at about 2 MHz and similar to PVA MBs at 10 MHz [5], which could be attributed to two populations of NDs with different shell thickness.

When entrapped into a tissue-mimicking phantom, the stability and phase-change transition response of the NDs is a matter of their dispersion conditions into the phantom matrix and stiffness/softness of the

latter. Herein, the PVA/PFB NDs show a fair stability when entrapped into a commercial ultrasound gel but their homogenous dispersion without creating air bubbles in the medium is hard to achieve. Alternatively, a tissue-mimicking polyacrylamide hydrogel reveals to be a promising candidate as the NDs dispersion matrix. The ultrasound images of PVA/PFB NDs dispersed in the PAM phantom illustrate an almost clear background as the hydrogel is formed at room temperature, and after its incubation at physiological temperature, i.e 37°C (see Figure 1a,b). Moreover, the favorable visco-elastic features of the PAM hydrogel allow for maintaining the NDs ability to expand into microbubbles when exposed to an external energy such as US at mechanical index threshold of 0.4 (see Figure 1c).

The *in vitro* radiation study of PVA/PFB NDs shows an evident response to X-rays after phantom exposure to 10 Gy dose. This confirmed that it is possible to detect vaporization events of NDs triggered by other means than ultrasound or optical stimuli. The quantified gray contrast signals from the recorded post-radiation US images increased by a factor of 3 fold as compared to pre-radiation images.

Conclusions

We investigated the use of novel perfluorobutane nanodroplets coated with crosslinked PVA as an ultrasound contrast agent in the perspective of photon radiation dosimetry where vaporization events can be triggered by ionizing radiation and detected by ultrasound. Although it is too early to claim the efficiency of high-energy X-ray induced vaporization of PVA/PFB NDs, our study demonstrated an evident response of the nanodroplets after radiation exposure. Future work will focus on evaluating the radiation dose effect on the PVA/PFB nanodroplets response in the optimized phantoms at both room and physiological temperatures, as well as exploring lower b.p. perfluorocarbon NDs.

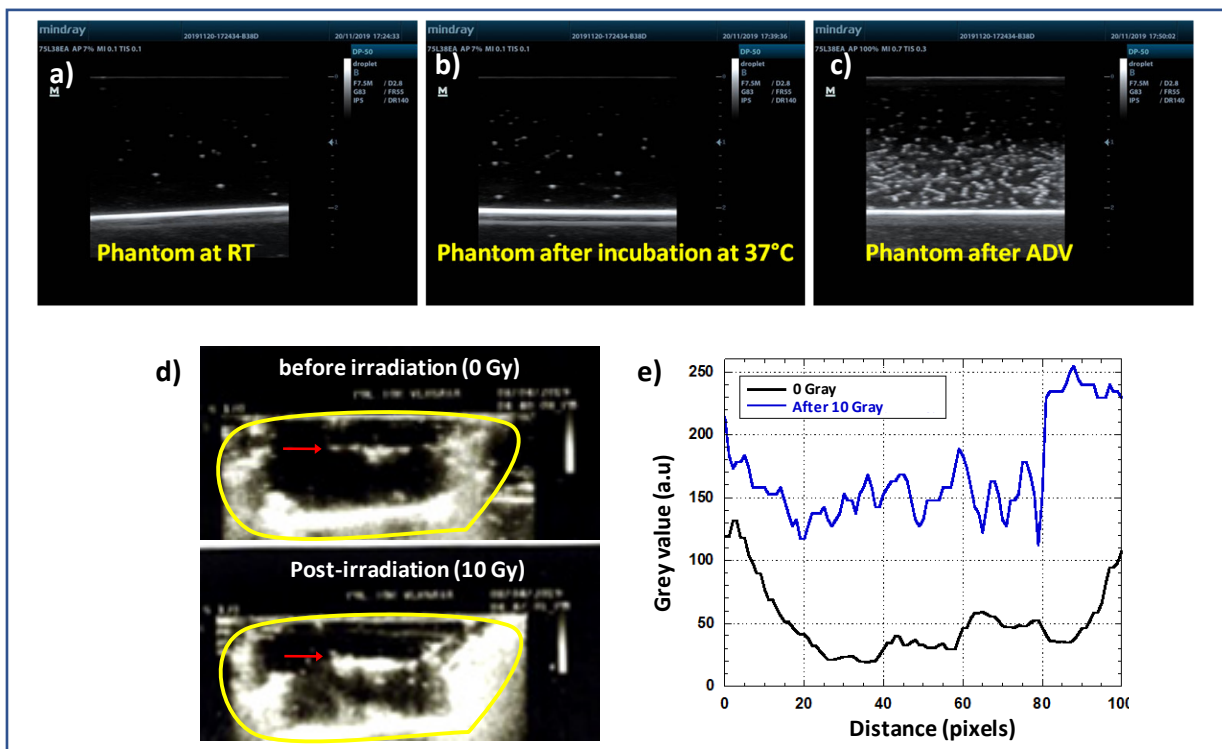


Figure 1. Tissue-mimicking phantom optimization: US images of PVA/PFB NDs in polyacrylamide hydrogel a) as dispersed at room temperature, b) after incubation at 37°C and c) after ADV induced by clinical US transducer (7.5 MHz); d) pre-and post-radiation US images sof PVA/PFB droplets entrapped in ultrasound gel (the red arrows show NDs/MBs accumulation); e) contrast quantification processing of US images of PVA/PFB droplets before and after exposure to 10 Gy radiation. The ROI in US images is delimited by the yellow selection.

References

- [1]. Kiessling F, Fokong S, Koczera P, Lederle W, Lammers T, Ultrasound microbubbles for molecular diagnosis, therapy and theranostics with abstract submission 2014, *The Journal of Nuclear Medicine*, 53: 345-348, 2012.
- [2]. Dove JD, Mountford PA, Murray TW, and Borden MA, Engineering optically triggered droplets for photoacoustic imaging and therapy, *Biomedical Optics Express*, 5(12):4417-4427, 2014.
- [3]. D'Errico F, Radiation dosimetry and spectrometry with superheated emulsions, *Nuclear Instruments and Methods in Physics Research B*, 184: 229-254, 2001.
- [4]. Toumia Y et al., Phase Change Ultrasound Contrast Agents with a Photopolymerized Diacetylene Shell, *Langmuir*, 35:10116–10127, 2019.
- [5]. Toumia Y, Cerroni B, Trochet P, Lacerenza S, Oddo L, Domenici F, Paradossi G, Performances of a Pristine Graphene-Microbubble Hybrid Construct as Dual Imaging Contrast Agent and Assessment of its Biodistribution by Photoacoustic Imaging, *Particle and particle Systems Characterization*, 35: 1800066, 2018.

Acknowledgment

This project has received funding from the European Union's Horizon 2020 research and innovation Programme under grant agreement 766456" (AMPHORA).

Systematic Characterisation of Sub-Micron Ultrasonic Contrast Agents in their Natural Hydrated State

Adeel S. Shafi^{1,2}, Jake McClements¹, Thomas Glen³, Norbert Radacsi¹, Carmel M. Moran², Vasileios Koutsos¹

¹*School of Engineering, Institute for Materials and Processes, The University of Edinburgh, The King's Buildings, Edinburgh EH9 3FB, United Kingdom,*

²*Centre for Cardiovascular Science, Queen's Medical Research Institute, The University of Edinburgh, Edinburgh EH16 4SB, United Kingdom,*

³*School of Engineering, Institute for Condensed Matter and Complex Systems, The University of Edinburgh, The King's Buildings, Edinburgh EH9 3FB, United Kingdom,*

Corresponding author: vasileios.koutsos@ed.ac.uk

Introduction

Ultrasonic contrast agents, known as microbubbles (MBs), have distinct acoustic signatures which significantly enhance visualisation of the vasculature. Research is progressing to develop agents which act as drug/gene delivery vehicles for site-specific therapeutics that can access all regions of the human body. To manufacture clinically translatable theranostic vehicles, it is imperative to understand the mechanical and nanostructural properties of these agents, as once inside the body there are many physiological challenges that they will have to overcome, for drug delivery applications. Consequently quantifying this information, will not only improve design, it will also improve the understanding of how the structural, biophysical and chemical properties of these bubbles impact their functionality. In this study, we manufacture phospholipid-shelled sub-micron bubbles (SMBs) and conduct systematic characterisation using a range of techniques to investigate their nanostructural properties, all whilst these agents are in their natural, hydrated state. We drew upon atomic force microscopy (AFM) and cryo focused-ion-beam scanning electron microscopy (Cryo FIB-SEM) to image SMBs and further the quantification of our previous work on determining the thickness of the phospholipid-shell membrane [1].

Methods

Using state of the art quantitative imaging (QI) mode AFM, which is a force-curve based imaging mode, we acquired high resolution quantitative height images on our SMBs using the Bruker-JPK Nanowizard 4 AFM. This is made possible through the ability to control vertical forces without applying any lateral forces that could damage the structural integrity of the SMBs. We also performed force studies causing significant deformation that led to further quantification of the shell thickness and lipid configuration. Additionally, through QI mode, we acquired adhesion maps to distinguish key interaction events.

To further characterise the morphological properties of our SMBs, cryo imaging, using a CRYO-FIB/SEM (Zeiss Crossbeam 550 with the PP3010 Cryo Preparation system from Quorum Technologies), has been used as it allows for nanoscale resolution of MBs under conditions that keep the MBs in a swollen hydrated state, such as they are when circulating in the bloodstream.

Results

By way of QI mode, we successfully imaged SMBs that were immobilized and in their natural hydrated states. All experiments showed significant deformation of the SMBs when increasing the vertical force applied. This was seen as height profiles of the immobilized SMBs decreased from as high as 600 nm when the lowest forces were used, to less than 300 nm when using higher forces, and was further corroborated by the height images showing significant deformation and ultimately, destruction of the

SMBs. Moreover, adhesion maps further corroborated that the MBs had burst; the bursting of the SMBs allowed the quantification of shell thickness for the first time in aqueous conditions. In this study we show shell materials with height profiles of ~6nm, validating previous values recorded using tapping-mode AFM in air [1].

Our CRYO FIB-SEM work characterising the shell thickness further corroborates the findings from our AFM experiments. As with this work we found shell thickness values within the same range as our AFM investigation. Henceforth, we show comprehensively that MBs are not encapsulated by a monolayer or bilayer as is the current consensus, but in fact by a trilayer of phospholipids.

Conclusions

We have exploited the potential of these two advanced material characterisation techniques (AFM and Cryo-FIB-SEM) and, to the best of our knowledge, are the first to present these powerful techniques for the visualisation of SMBs. Furthermore, this unique possibility of direct visualisation of nanostructural components has led to further quantification of the thickness of MB shells as well as the observation of morphological changes that occur during MB deformation and, ultimately, their destruction. As a result of this work we highlight new and improved methods for MB imaging which can be used to help propel the development of theranostic MBs for site specific drug/gene delivery.

References

- [1]. Shafi, AS, McClements, J., AlBaijan, I., Abou-Saleh, RH., Moran, C and Koutsos, V. 2019. Probing phospholipid microbubbles by atomic force microscopy to quantify bubble mechanics and nanostructural shell properties. *Colloids and Surfaces B: Biointerfaces*, 181, 506-515.
- [2]. Sboros, V., Glynos, E., Ross, JA., Moran, CM., Pye, SD., Butler, M., McDicken, WN. and Koutsos, V. 2010. Probing Microbubble Targeting with Atomic Force Microscopy. *Colloids and Surfaces B: Biointerfaces* 80, 12-17.
- [3]. Santos, EB., Morris, JK., Glynos, E., Sboros, V. and Koutsos, V. 2012. Nanomechanical Properties of Phospholipid Microbubbles. *Langmuir*. 28, 5753-5760.

Novel nanoplatform for ultrasound imaging and theranostic applications using different perfluorocarbons

Maria F. Acosta¹, Emmanuelle J. Meuillet¹, and Evan C. Unger^{1,2}

¹*Microvascular Therapeutics, Tucson Az, USA.*

²*Departments of Radiology and Biomedical Engineering, The University of Arizona, Tucson AZ, USA.*

Corresponding author: e.unger@mvtpharma.com

Introduction

Recently, several investigators have proposed perfluorocarbon (PFC)-based nanodroplets as potential new technology for ultrasound (US) imaging. Currently octafluoropropane (OFP), decafluorobutane (DFB), and dodecafluoropentane (DDFP) or a combination of those PFCs are used for the preparation of nanodroplets. Due to the different boiling points of the gases, OFP nanodroplets are thought to have insufficient stability that limits their biological application. On the other hand, DDFP nanodroplets require a higher mechanical Index (MI) for US imaging.

Methods

The purpose of these studies was to formulate OFP and DDFP nanodroplets, characterize their physical and chemical properties, and test them in a variety of applications in *in vitro* models. By extensive characterization of the different nanodroplets, it can be decided which ones can be used to detect and/or treat different diseases. Different techniques were employed to characterize the nanodroplets. Particle size was measured using a particle size analyzer. The morphology and the size of the nanodroplets were also visualized by Transmission Electron Microscopy (TEM). Raman spectroscopy and gas chromatography were used to confirm the content of the gas in the nanodroplets.

Results

Particle size distribution showed that the size of the droplets was in the nano scale. TEM images validated spherical and stable nanodroplets on both OFP (figure A and B) and DDFP (figure C and D) nanodroplets. Raman results confirmed the PFC gas content. Finally, in order to validate the therapeutic use of the nanodroplets, we have functionalized some of these nanodroplets for the detection of tau aggregates and fibrin clots for the detection and treatment of Alzheimer and cardiovascular diseases, respectively. We present preliminary results regarding the nanodroplets effects on these protein aggregates upon ultrasound activation.

Conclusions

In conclusion, we have developed a strong multifunctional nanoplatform using a novel methodology. These results show promising applicability for enhanced theranostic applications of the phase change ultrasound contrast agents.

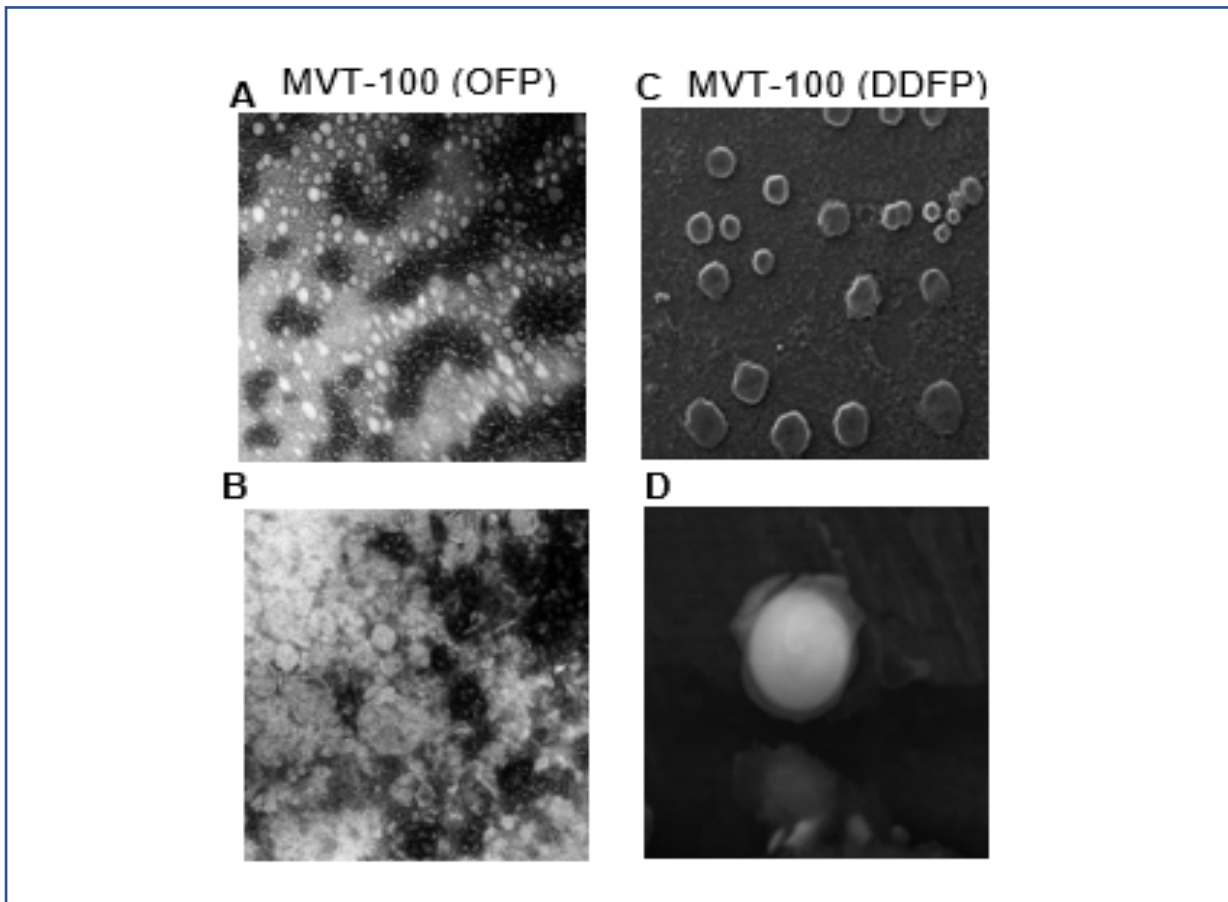


Figure 1. TEM micrographs of MVT-100 nanodroplets with different gases.

References

- [1]. US 9,801,959 B2 “Phospholipid composition and microbubbles and emulsions formed using same” Unger, EC and Evans, DC
- [2]. US 9,427,410 B2 “Formulation of acoustically activable particles having low vaporization energy and methods for using same” Dayton, PA; Sheeran, PS; Matsunaga, TO and Borden, MA.
- [3]. PCT/US2019/024713 “Composition and methods detecting and treating Alzheimer’s disease”

Financial interest Statement: “All of the authors have a direct or indirect financial interest in the products under investigation or subject matter discussed in the manuscript. A separate statement will be attached that details this proprietary interest. The authors grant permission to publish this information or an appropriate summary thereof with the abstract.”

Targeted Hydrodynamic Cavitating Flows via Ultrasound Waves via Pickering Stabilized Perfluorodroplets

Morteza Ghorbani^{1,2}, Anna Justina Svagan³, Dmitry Grishenlov¹

1Department of Biomedical Engineering and Health Systems, KTH Royal Institute of Technology, Stockholm, Sweden

2Sabanci University Nanotechnology Research and Application Center, 34956 Tuzla, Istanbul, Turkey

3Department of Fibre and Polymer technology, KTH Royal Institute of Technology, SE-100 44 Stockholm, Sweden

Corresponding author: dmitryg@kth.se

Introduction

Acoustic Droplet Vaporization (ADV) is a phase change phenomenon in which the liquid state, in the form of droplets, is converted to gas as a result of bursts in the excited ultrasound field. Having a wide range of medical applications, ADV has drawn considerable attention in imaging [1], diagnosis and critical medical treatment [2]. Therefore, benefitting from its broad potentials, with the consideration of its capability in localized noninvasive energy exposure, it is possible to utilize its effect in different medical applications from targeted drug delivery [3] to embolotherapy [4].

Recently, it was shown that the generation of cavitation bubbles and collapse of the bubbles are affected by thermophysical properties of the working fluids as well as the surface topology of the channels inside the microfluidic device [5]. In this regard, we investigate the potential of particle-stabilized perfluoropentane (PFC5) droplets as cavitation intensifiers. The PFC5 droplets are stabilized by cellulose nanofibers at the Oil/Water (O/W) interface via a Pickering mechanism [6]. Such particle-stabilized droplets are much more stable compared to a surfactant stabilized droplet, because the particles do not easily detach from the O/W interface. This makes particle-stabilized PFC5 droplets promising with the respect to storage stability, because droplets will not merge together into bigger droplets with time. In other words, it is possible to facilitate a device, where energy can be stored and then released “on demand” in the form of heat.

In this study, a new type of pickering stabilized perfluorodroplets (PFC) was examined under the effect of the different acoustic parameters to evaluate its potential in the acoustic droplet vaporization process. The potential of the ADV activated microbubbles is used in a combination with hydrodynamic cavitation in microfluidic devices to be used in the cell sorting based studies.

Methods

Materials and emulsion preparation

Perfluoropentane (PFC5) was purchased from Apollo Scientific (City, U.K.). Bleached sulfite pulp (from Nordic Paper Seffle AB, Sweden) was used in the production of the cationic cellulose nanofibers (CNFs). The CNF suspension (1.32 wt%) were prepared as described previously [7]. The CNFs had a dimension of 3.9 ± 0.8 nm in width and a length in the micrometer range. The amount of cationic groups was 0.13 mmol per g fiber, obtained from conductometric titration [7]. A suspension of CNF (0.28 wt%) was prepared by diluting the stock CNF with MilliQ-water (pH of diluted CNF suspension was 9.5). The suspension was treated with ultra-sonication at amplitude of 90% for 180 s (Sonics, Vibracell W750). The suspension was brought to room temperature. An amount of 36 g of the 0.28 wt% CNF suspension was mixed with 1 g of PFC5. The mixture was sonicated for 60s at an amplitude of 80% (under ice-cooling) to obtain the CNF-stabilized PFC5 droplets.

The protocol for the acoustic tests

100 μ L of CNF-stabilized PFC5 droplets were added to 1900 μ L of deionized water in order to prepare the solution which were exposed to the ultrasound waves. The droplet sample, diluted 1:19 in distilled

water was introduced to the Opticell® and the acoustic waves at a fixed frequency and different powers were applied to the targeted area inside the Opticell® which is located inside a water bath. The ultrasound triggered sample then was placed under a 20X magnification objective of upright transmitted light microscope (ECLIPSE Ci-S, Nikon, Tokyo, Japan).

The acoustic tests were performed using high-power tone burst pulser-receiver (SNAP Mark IV, Ritec, Inc., Warwick, RI, USA) equipped with a transducer (V382-SU Olympus NDT, Waltham, MA) operating at the frequency of 3.5 MHz. The emulsion of CNF-stabilized PFC5 droplets were exposed to the power range which has the ascending trend from -30 to 0 dB at the given frequency. To investigate the droplet size variations at each power between, the droplets were collected inside the Opticell® and the droplet diameter was measured with the aid of the ImageJ software (version 1.50b, National institutes of health, USA) to determine the concentration and size distribution. The Gaussian distribution is plotted with mean value and standard deviation recover from the experimental data. An in-house image edge detection MATLAB™ script (MathWorks Inc., Natick, MA) were applied to analyze the images obtained from the microscope and provides the size and volume distributions.

Results

The results (Figure 1) show a significant increase on the size distribution even on the surface of the counting chamber. The droplets have already experienced transition in their core due to the temperature variations and further increase in the size after the ultrasound exposure is due to the effect of the shell and the interaction between the bubble, droplet and the materials existed on the perimeter of the shell. As a result, the interaction between microbubbles and ultrasound waves is the most important parameter in the bubbles size variations. It is shown that while the average diameter of the droplets is around 5 μm, the generated bubbles, as a result of the ADV, reaches up to 30 μm at the highest possible power. The droplet emulsion exhibited in NO US in Figures 1 and 2, which shows the regular view and distribution range of the CNF-stabilized PFC5 droplets at the room temperature, experiences ADV process with the diameter rise of about 6 times at the highest power when the frequency is fixed at 3.5 MHz.

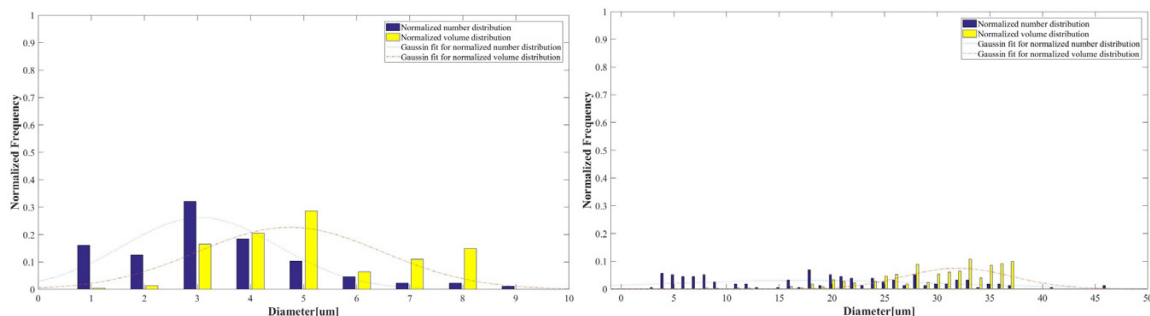


Figure 1. Size distributions for (a) No US (b) 0 dB

The images below (Figure 2) are captured with using opticell®. As it is shown, some bubbles are interestingly emerged after US exposure with different frequency even with naked eyes. The same area was observed under microscope and as it is illustrated there are lots of droplets which might be of the potential to reach to the bigger size after some time.

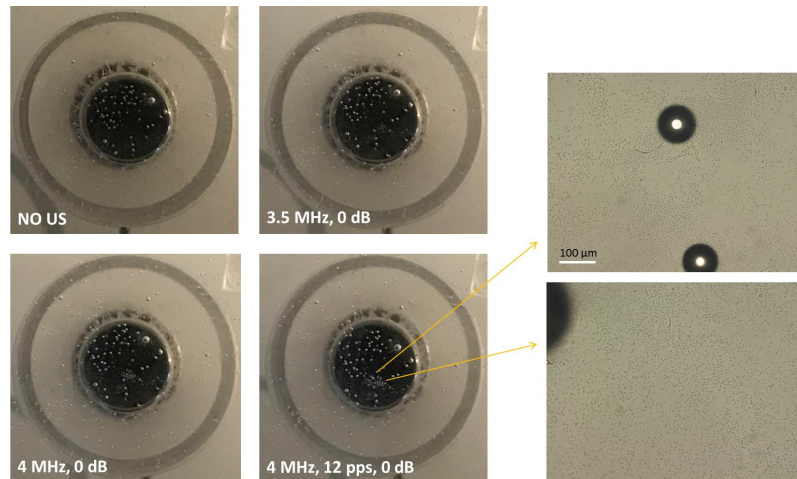


Figure 2. Size variations after exposing the sample to US at different frequencies

Furthermore, the potential of the hydrodynamic cavitation is increasingly utilized in the biomedical applications. It was recently proved that hydrodynamic cavitation would be a powerful alternative for ultrasound cavitation in the fragmentation of the abnormal tissues such as prostate. Our preliminary results [8,9] indicate that the cavitation inception occurs with the formation of a cavitation cloud, which is limited to the inlet of the nozzle for a surface roughened channel. With a further increase in downstream pressure, while the upstream pressure is constant or vice versa, the flow pattern shifts to developed cavitation, where a rapid growth in cavitation zone volume is apparent (Figure 3).

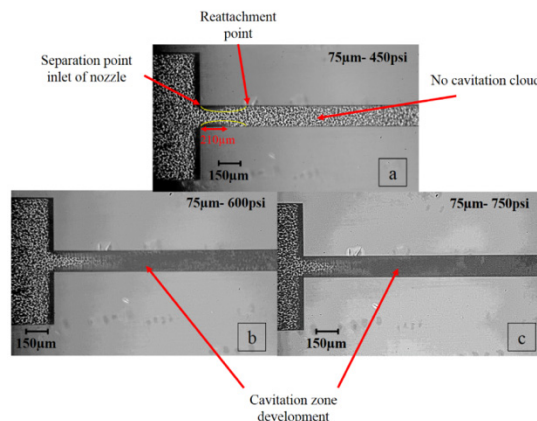


Figure 3. a) The cavitation inception b) developed cavitation flow pattern in the microchannel c) Super cavitation flow in the nozzle with hydraulic diameter of 75 μm

Based on the obtained results from the bubble generation due to the ADV and bubbly flow generation due to the hydrodynamic cavitation, a microfluidic-based ADV Cell Sorting technique that rely on the specific binding of target cells to microdroplets conjugated with specific antibodies on their surface for continuous cell separation using ultrasonic standing wave is suggested for the future studies. In acoustophoresis, cells being positive acoustic contrast particles migrate to pressure nodes. On the contrary, air-filled polymer-shelled microbubbles being strong negative acoustic contrast particles migrate to pressure antinodes and can be used to selectively migrate target cells. The schematic (Figure 4) illustrates the introduction of the droplet solution conjugated with different cells into the microchannel using a syringe pump. The flow inside the microchannel is affected by hydrodynamic cavitation at the entrance of the restrictive element and also by transducer along the channel.

The combination of the hydrodynamic and ultrasonic cavitation would provide a static pressure reduction together with the phase transition of the microdroplets to microbubbles following a size raise of the particles. This study would reveal the collapse behavior of the microbubbles affected by the cavitation beside the potential of the suggested system in cell sorting.

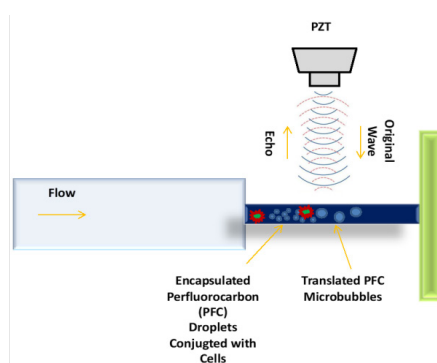


Figure 4. Schematic illustrating the effect of combination of hydrodynamic and ultrasonic cavitation on collapse of ADV activated droplet to be used in cell sorting

Conclusions

The results show that there is appreciable rise on the size of the droplets after ultrasound waves exposure at a fixed frequency. Acoustic droplet vaporization (ADV) was illustrated at different powers for CNF-stabilized PFC5 droplets as a new class of pickering stabilized perfluorodroplets with the increase in the size of the droplets and following phase transition to bubbles. Diameter increase of 6 times were obtained after the ultrasound exposure indicating the efficiency of the suggested droplets for the ADV process and therapeutic applications. The potential of the ADV activated microbubbles is believed to be utilized as a strong working fluid in mitigation of the bubbly flow generated by hydrodynamic cavitation to be used in the cell sorting studies.

References

- [1]. Arena CB, Novell A, Sheeran PS, Puett C, Moyer LC, Dayton PA, Dual-Frequency Acoustic Droplet Vaporization Detection for Medical Imaging 2015, IEEE Transactions on Ultrasonics, Ferroelectrics and Frequency Control, 62: 9.
- [2]. Kripfgans OD, Fowlkes JB, Miller DL, Eldevik OP, Carson PL, Acoustic droplet vaporization for therapeutic and diagnostic applications 2000, Ultrasound Med. Biol, 26:1177–1189.
- [3]. Kang ST, Yeh CK, Intracellular Acoustic Droplet Vaporization in a Single Peritoneal Macrophage for Drug Delivery Applications 2011, Langmuir, 27:13183–13188.
- [4]. Zhu M, Jiang L, Fabiilli ML, Zhang A, Fowlkes JB, Xu LX, Treatment of murine tumors using acoustic droplet vaporization-enhanced high intensity focused 2013, Ultrasound Phys. Med. Biol, 58:6179–6191.
- [5]. Ghorbani M, Sadaghiani AK, Villanueva LG, Koşar A, Hydrodynamic cavitation in microfluidic devices with roughened surfaces 2018, J. Micromechanics Microengineering. 28:75016.
- [6]. Ghorbani M, Olofsson K, Benjamins JW, Loskutova K, Wiklund M, Grishenkov D, Svagan AH, Unraveling the Acoustic and Thermal Responses of Perfluorocarbon Liquid Droplets Stabilized with Cellulose Nanofibers 2019, Langmuir. Under review 35:13090-13099.
- [7]. Svagan AJ, Benjamins JW, Al-Ansari Z, Shalom DB, Müllertz A, Wågberg L, Löbmann K, Solid cellulose nanofiber based foams—towards facile design of sustained drug delivery systems 2016, J. Control Release, 244:74–82 (Part A).
- [8]. Ghorbani M, Chen H, Villanueva LG, Grishenkov D, Koşar A, Intensifying cavitating flows in microfluidic devices with poly (vinyl alcohol)(PVA) microbubbles 2018, Phys. Fluids. 30:102001.
- [9]. Ghorbani M, Aghdam AS, Gevari MT, Koşar A, Cebeci FÇ, Grishenkov D, Svagan AJ, Facile hydrodynamic cavitation ON CHIP via cellulose nanofibers stabilized perfluorodroplets inside layer-by-layer assembled SLIPS surfaces 2020, Chemical Engineering Journal, 15:382:122809.

A model-guided optimization of contrast pulse sequence for polyvinyl alcohol microbubbles

H. Chen¹, W. Löffler¹, D. Grishenkov¹

¹*Department of Biomedical Engineering and Health Systems, KTH Royal Institute of Technology, Stockholm, Sweden*

Corresponding author: hongjian@kth.se

Introduction

In the current study, a novel contrast pulse sequence, CPS4, that combines sub-harmonic (SH), ultra-harmonic (UH) and pulse inverse imaging was further optimized for the use with thick-shelled polyvinyl alcohol microbubbles (PVA MBs). First a linear oscillator model adapted from Hoff and Church[1, 2] was built for single PVA MB. The attenuation and phase velocity of a PVA MB suspension were obtained to calibrate the linear oscillator. The model was used to estimate the resonance frequency, f_0 , of the MBs. The transmitting frequency of CPS4 for ultra-harmonic, $\frac{f_0}{5}$, and sub-harmonic, f_0 , was set at four frequency points around the resonance frequency. The performance of the contrast pulse sequence was evaluated in water and blood mimicking fluid solution.

Methods

The PVA MBs fabrication and the morphology test were described previously in detailed elsewhere [3, 4]. The size distribution of the isolated MBs is $3.86 \pm 0.79 \mu\text{m}$ and the MBs concentration of PVA MBs was 10^6 mL^{-1} in both water and artificial blood experiments.

Estimation of the resonance frequency

The theoretical model that predicts the resonance frequency was adapted from Hoff and Church[1, 2]. The equation of motion of the bubble surface can be written as (1)

$$M\ddot{\xi} + R\dot{\xi} + S\xi = -4\pi a_2^2 p_i \quad (1)$$

With the following components of the harmonic oscillator:

$$M = 4\pi a_2^2 \rho_L + \pi(a_2^2 - a_1^2)\rho_S \quad (2)$$

$$S = 12\pi a_2 \kappa p_e + 48\pi G_s d_s \quad (3)$$

$$R = 4\pi a_2^2 (\rho_L c_w (k_c a_2)^2) + 4 \left[\rho_S a_1^2 \left(1 + \frac{\rho_L - \rho_S}{\rho_S} \frac{a_1}{a_2}\right) \right]^{-1} \cdot (M a_1^3 \eta_L \omega_0 + m V_s \eta_S \omega) \quad (4)$$

where a_2 is the outer radius of MB, a_1 is the inner radius of MBs, ξ is the displacement, ρ_L is density of surrounding liquid, ρ_S is the density of the shell, κ is polytrophic gas exponent equals to 1, p_e is equilibrium pressure, G_s is the shear modulus of the shell, d_s is the shell thickness, c_w is the speed of sound in water, k_c is the wave number of, η_L is the shear viscosity of liquid, η_S is the shear viscosity of shell, ω_0 is the angular resonance frequency, $V_s = a_2^3 - a_1^3$.

The dispersion of a wave propagating through the MBs suspension is defined in Eq.5

$$\left(\frac{c_w}{c_c}\right)^2 = (u + jv)^2 = 1 - 4\pi c_w^2 \int_0^\infty \frac{a_2}{\omega_0} \frac{1}{\left(\frac{\omega}{\omega_0}\right)^2 - 1 - j \frac{\omega R}{\omega_0^2 M}} n(a_2) da_2 \quad (5)$$

Where c_c is a complex frequency dependent phase velocity and $n(a_2)$ is the number of the MBs with a radius of a_2 .

By solving Eq.5 the attenuation and phase velocity and can be determined as

$$\alpha(\omega) = \frac{\omega \nu}{c_w} \quad (6)$$

$$c(\omega) = \frac{u}{c_w} \quad (7)$$

The experimental data on attenuation and phase velocity of MB suspension were obtained at a broad frequency span from 1 to 15 MHz using 5 single crystal transducers with overlapping bandwidth. By varying viscoelastic parameters, i.e. shear modulus, G_s , and viscosity, η_s , it was possible to fit theoretical estimation to the experimental data and identify the resonance frequency, f_0 . The rank-based algorithm [5] was used to identify the best fit between experimental data and theoretical prediction. Two cases for the shell thickness, d_s , were considered: 1. Constant shell thickness that is the same for all MBs in the suspension; 2. The shell thickness that is proportional to the MB radius.

Visualization using CPS4

A tissue-mimicking phantom (Model 524 Peripheral Vascular Doppler Flow Phantom, ATS Laboratories) with 2 wall-less channels of a diameter 6 and 8 mm, respectively, was used to mimic in vivo environment. Two groups of samples, i.e. MBs aqueous suspension vs water and artificial blood with MBs vs artificial blood; were loaded into the phantom by a peristaltic pump.

The filtering frequency of CPS4, and corresponding UH and SH transmitting frequency are presented in Table 1. The US images of CPS4 with different filtering frequencies were obtained and repeated for five times for each sample pair.

Table 1. The transmitting frequency and filtering frequency considered in the study

Filtering frequency (MHz)	Transmitting frequency of UH (MHz)	Transmitting frequency of SH (MHz)
4.5 _s	3	9
5	3.33	10
5.63	3.91	11.25
6.43	4.29	12.86

The performance of the novel optimized contrast pulse sequence, CPS4, were assessed using Contrast-to-tissue ratio (CTR) and calculated as (6)

$$CTR = 20 \log_{10} \frac{\langle I_S \rangle}{\langle I_T \rangle} \quad (6)$$

where, $\langle I_S \rangle$ is mean pixel intensity in MBs channel, $\langle I_T \rangle$ is mean pixel intensity of tissue-mimicking material. Figure 1 is an example of the sonogram obtained with marked region of interest used for CTR calculation.

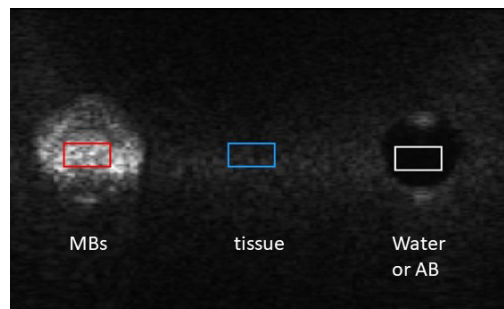


Figure 1. Example of the ultrasound image

Results

The sets of optimized parameters for both cases of the shell thickness assumption were found and listed in Table 2.

Table 2. The set of optimized parameters

Shell Thickness	d_s	η_s	G_s
d_s constant	360 nm	0.325 Pa·s	16.5 MPa
d_s proportional	0.16*outer radius	0.322 Pa·s	14.5 MPa

The shell thickness of PVA MBs found by other studies[7] using the experimental methods is in the range of 200 to 500 nm, which correlates well with our results.

The simulated attenuation and phase velocity curves have a high agreement with the experimental results especially at the high frequency range typically above 5 MHz; see Fig. 2. However, at the low frequency range i.e. 2 to 5 MHz, the simulation result deviates substantially from them. The major cause of this deviation is attributed to the assumption on the frequency independent viscoelastic modulus that is not accounting for the molecular relaxation mechanisms at a broad frequency range.

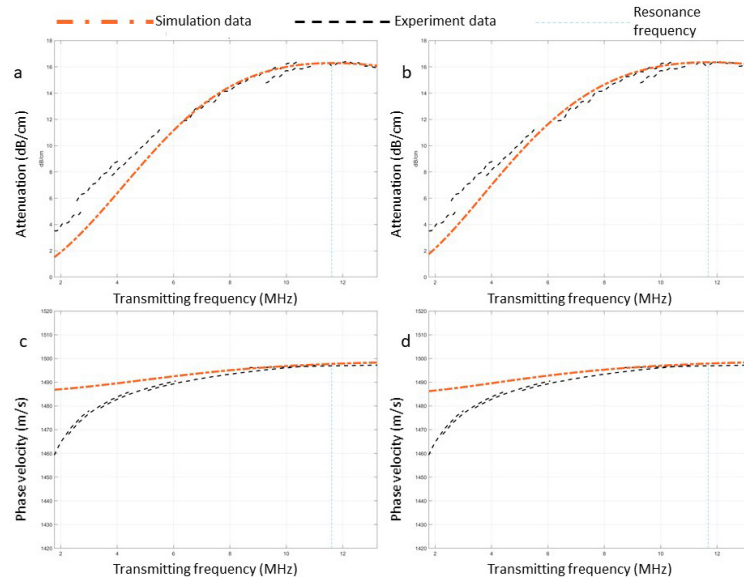


Figure. 2 Measured and simulated attenuation [(a),(b)] and phase velocity [(c),(d)]. On the left side, shell thickness is fixed [(a),(c)], on the right side shell thickness is a fixed proportion of the MB radius[(b),(d)].

By introducing the actual size distribution of the isolated PVA MBs, used in US imaging, into the model, the resonance frequency of the MBs was estimated as 10.85 and 11.15 MHz for constant thickness and proportional thickness assumption, respectively.

Following Katiyar et al. [8] that evaluated the threshold for subharmonic generation, the filtering frequency for CPS4 were set to cover the bandwidth around half the resonance frequency, i.e. 5.43 (constant thickness) or 5.58 MHz (proportional thickness).

The mean CTR of CPS4 at four filtering frequencies with MBs aqueous suspension and MBs in artificial blood is showed in Fig. 3.

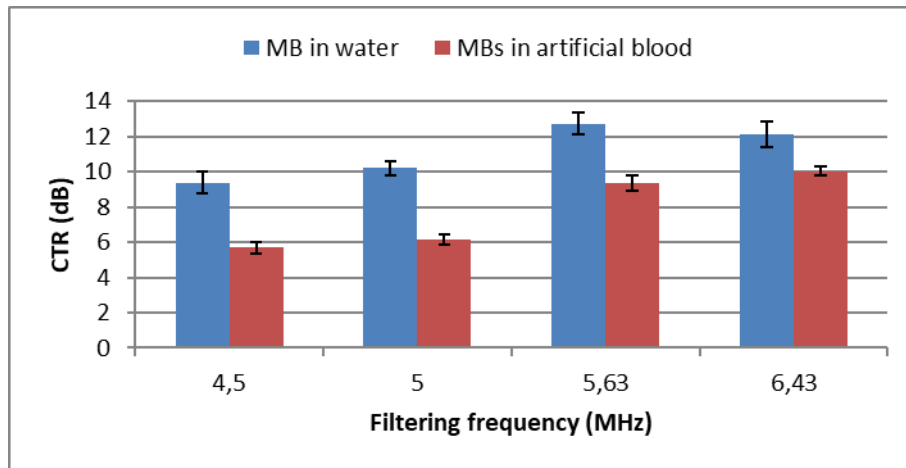


Figure 3. Mean CTR of CPS4 with MBs aqueous suspension and MBs in artificial blood over frequency

The CTR of CPS4 with MBs aqueous suspension increases from 9.4 dB to 12.8 dB when the filtering frequency increases from 4.5 MHz to 5.63 MHz and drops to 12.1 dB when the filtering frequency further increases to 6.43 MHz. This suggests that the peak performance of the CPS4 with the PVA MBs aqueous suspension used in the current study could happen at the filtering frequency around 5.63 MHz, which agrees with the simulation results.

The CTR of CPS4 with MBs in artificial blood increases monotonously from 5.7 dB to 10 dB as the filtering frequency increases from 4.5 MHz to 6.43 MHz. At all filtering frequency, the CTR decreases when the water is replaced by the artificial blood. This might be caused by higher damping due to the high liquid viscosity and scattering effect of the small particle in artificial blood. Future work is needed to understand the underlying mechanism of this reduction effect.

Conclusions

In this study, a model of PVA MBs was built and calibrated. The model was used to predict the resonance frequency of the MBs population, at 10.85 and 11.15 MHz for fixed thickness and fixed proportion assumption. The simulation result was utilized to guide the optimization of CPS4. The performance of CPS4 at different frequencies with MBs aqueous suspension and MBs in artificial blood were evaluated. The best performance of CPS4 is achieved at frequency 5.63 and 6.43 MHz for the MBs aqueous suspension and MBs in artificial blood, respectively. The frequency-dependent performance of CPS4 with MBs aqueous suspension showed a good correlation with the simulation works.

References

- [1]. L. Hoff, *Acoustic characterization of contrast agents for medical ultrasound imaging*. Springer Science & Business Media, 2001.
- [2]. C. C. J. T. J. o. t. A. S. o. A. Church, "The effects of an elastic solid surface layer on the radial pulsations of gas bubbles," vol. 97, no. 3, pp. 1510-1521, 1995.
- [3]. F. Cavalieri, A. El Hamassi, E. Chiessi, G. Paradossi, R. Villa, and N. Zaffaroni, "Tethering functional ligands onto shell of ultrasound active polymeric microbubbles," *Biomacromolecules*, vol. 7, no. 2, pp. 604-611, 2006.
- [4]. M. Zheng, "Ultrasound contrast agents: fabrication, size distribution and visualization," ed, 2011.
- [5]. A. Saranlı and M. J. P. R. Demirekler, "A statistical unified framework for rank-based multiple classifier decision combination," vol. 34, no. 4, pp. 865-884, 2001.
- [6]. J. A. Feshitan, C. C. Chen, J. J. Kwan, and M. A. Borden, "Microbubble size isolation by differential centrifugation," *Journal of colloid and interface science*, vol. 329, no. 2, pp. 316-324, 2009.
- [7]. M. Poehlmann et al., "On the interplay of shell structure with low-and high-frequency mechanics of multifunctional magnetic microbubbles," *Soft Matter*, vol. 10, no. 1, pp. 214-226, 2014.
- [8]. A. Katiyar and K. J. T. J. o. t. A. S. o. A. Sarkar, "Excitation threshold for subharmonic generation from contrast microbubbles," vol. 130, no. 5, pp. 3137-3147, 2011.

A physical model to investigate the acoustic behaviour of microbubbles within a bone fracture

S. Ferri^{1,2}, A. Polydorou^{1,2}, J.P. May^{1,2}, Q. Wu³, E. Stride³, N.D. Evans^{1,2}, D. Carugo^{1,2}

¹*MiNaTher, Faculty of Engineering and Physical Sciences, University of Southampton, Southampton, UK*

²*Bone&Joint, Faculty of Medicine, University of Southampton, Southampton, UK*

³*Department of Engineering Science, University of Oxford, Oxford, UK*

Corresponding author: S.Ferri@soton.ac.uk

Introduction

Impaired fracture healing is a major financial burden for healthcare services; 5-10% of bone fractures result in costly and debilitating conditions such as delayed or non-union, where the bone fails to heal properly [1]. Common treatments are invasive and rely on the immobilisation of the fracture site, with a significant impact on a patient's quality of life. Currently, there is no clinically approved systemic therapy for the treatment of bone fractures. In this study, we aim to overcome this limitation by using acoustically-stimulated microbubbles (MBs) [2] as non-invasive ultrasound (US) responsive vehicles for the targeted delivery of osteogenic compounds.

The therapeutic efficacy of MBs is likely to be influenced by their acoustic responsiveness at the fracture site. In this study, a microscope-compatible water-tank incorporating a passive cavitation detector (PCD) was developed to study the acoustic behaviour of MBs. We tested the hypotheses that: (i) the microscope-compatible tank could provide a uniform acoustic stimulation at the fracture site; (ii) the presence/absence of MBs and their response to US could be detected in the tank thanks to the embedded PCD; (iii) the presence/absence of a bone could impact on the acoustic field at the fracture site and consequently on the acoustic response of MBs.

Methods

A microscope-compatible water-tank incorporating a passive cavitation detector (PCD), shown in Figures 1a and 1b, was developed to study the acoustic behaviour of MBs and to quantify their cavitation activity upon US stimulation [3]. The device was designed using SOLIDWORKS (Solidworks Applications Limited, Oldbury, West Midlands, UK), evaluated using COMSOL Multiphysics (COMSOL Inc., Burlington, MA, USA), and tested *in-vitro*. The apparatus was employed to investigate the behaviour of MBs when embedded in a 2% agarose gel, which was injected within physical models of bone fracture of different geometry. The model was composed of a PDMS manifold accommodating two fragments of bone and a chamber in the gap, which keeps the sample of MBs in place, as presented in Figure 1c. Bone was modelled using a material with comparable acoustic impedance ($Z = 5.41 \times 10^6 \text{ kg/m}^2\text{s}$, Sawbones, Washington, USA). Different fracture gaps (3.5-5.5 mm), thicknesses (2 and 4 mm), and inclination angles (45° and 90°) were evaluated. Ultrasound stimulation experiments were performed at either 1 or 2 MHz US frequency, duty cycle of 1-5%, acoustic pressure of 0.06-0.33 MPa, and exposure time of 30 s. A PCD was used to detect the signal emitted, and a frequency-domain analysis (i.e. Fast Fourier Transform, FFT) was performed to extract the content in frequency of the detected signal.

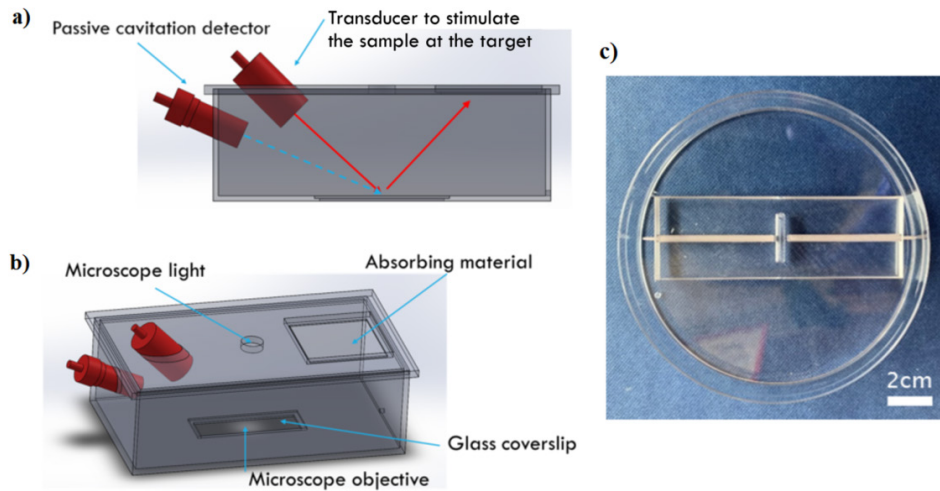


Figure 1. a,b) Microscope-compatible water tank incorporating a passive cavitation detector (PCD) to acoustically characterise MBs in a fracture model. c) PDMS manifold accommodating two fragments of bone in the lateral channels and the sample of MBs in the central chamber.

Results

Numerical simulations showed that the developed experimental set-up generated an acoustic pressure field at the target plane (that also corresponds to the optical focal plane of the microscope) characterised by the presence of standing waves (Figure 2a). The inclusion of a fracture model caused perturbations to the acoustic field, which were dependent on the architecture of the fracture (i.e. relative to the incident US field), as shown in Figures 2b and 2c. US wave reflection at the inner edges of the fracture gap resulted in the generation of a standing wave field, with ‘hotspots’ of higher acoustic pressure located within the fracture gap.

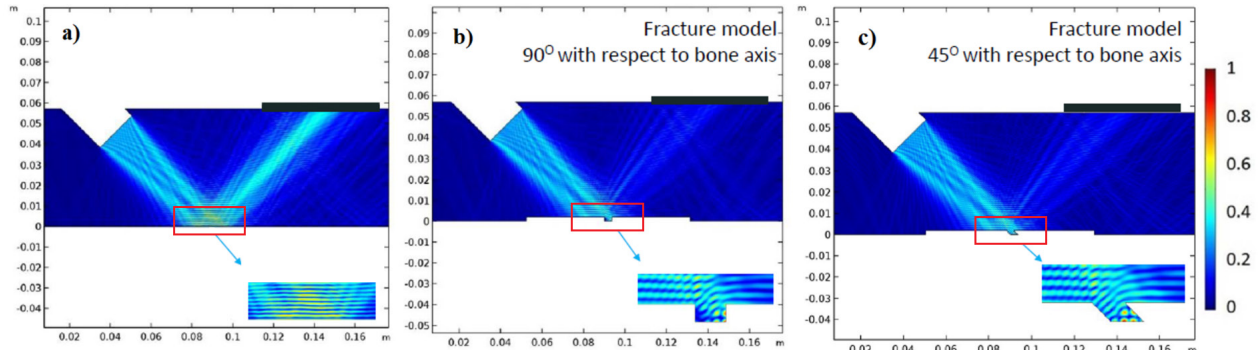


Figure 2. Numerical simulations showing the acoustic pressure field developed in the setup following a stimulation at 1 MHz. The values have been normalised to the maximum value detected. a) Apparatus without fracture; b) Apparatus with a 90° fracture; c) Apparatus with a 45° fracture.

Experiments were performed to investigate the acoustic behaviour of MBs within fracture models. The transducer was operated at 1 MHz and the signal was recorded by a PCD either in the presence or absence of MBs. FFT spectra presented in Figure 3 show that the addition of MBs generated harmonics, subharmonics and ultraharmonics, likely corresponding to MB oscillations.

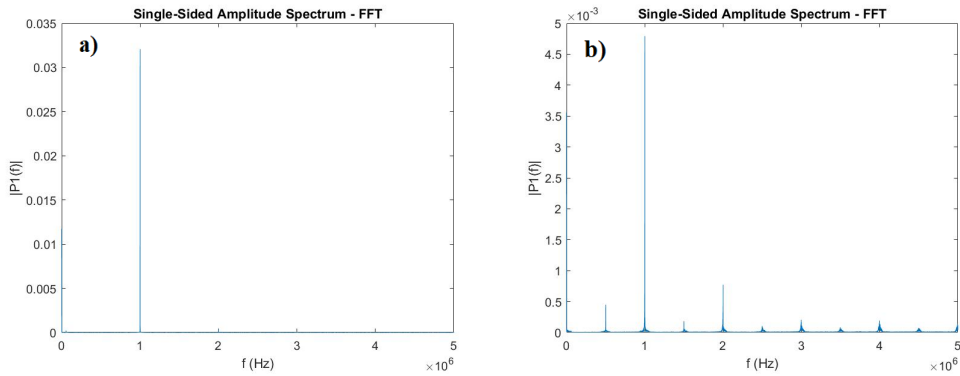


Figure 3. FFT of the signal recorded by the PCD. **a)** Apparatus containing the fracture model, where the fracture gap was filled with a 2% agarose gel (without MBs). **b)** Apparatus with MBs embedded in a 2% agarose gel and placed in a PDMS mold at the target.

When the bone fracture model was added to the apparatus, it was still possible to detect MB behaviour through the presence of harmonics and sub/ultraharmonics. As shown in Figure 4, the presence of the bone led to higher FFT amplitudes at the harmonics and ultraharmonics analysed. This increased response is likely due to the higher acoustic pressure developed in the hotspots present in the fracture gap.

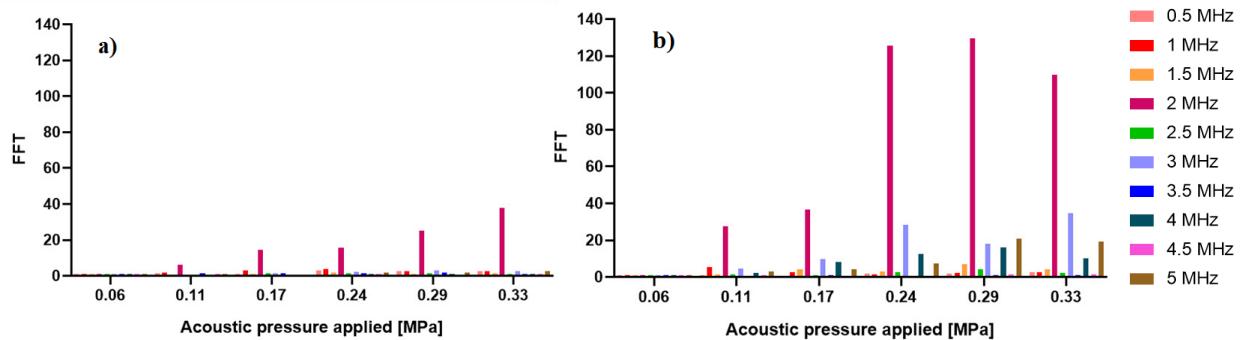


Figure 4. FFT amplitude values at specific frequencies (subharmonic, harmonics, ultraharmonics). Every acoustic pressure tested has been normalized with respect to the lowest one of the control case (no microbubbles and no bone). **a)** MBs in 2% agarose gel. **b)** MBs in 2% agarose gel and bone.

Conclusion

The developed setup allowed the generation of a relatively uniform acoustic field at the target plane; and revealed perturbations and hotspots generated in the fracture gap when a bone fracture model was tested. When MBs were added to the model, the FFT spectra showed harmonics, subharmonics and ultraharmonics; their intensity increased when tested in the bone fracture. These peaks likely correspond to ultrasound-induced MB oscillations.

Future work will focus on characterising the acoustic response of nanodroplets within physical models of bone fractures, and its relationship with the release of biologically active compounds.

References

- [1]. Corrarino JE. Fracture repair: Mechanisms and management. *The Journal for Nurse Practitioners*, vol. 11, no. 10, pp. 960-967, 2015.
- [2]. Sirsi SR and Borden MA, State-of-the-art materials for ultrasound-triggered drug delivery. *Advanced Drug Delivery Reviews*, no 72, pp. 3-14, 2014.
- [3]. King DA, Malloy MJ, Roberts AC, Haak A, Yoder CC and O'Brien WD, Determination of postexcitation thresholds for single ultrasound contrast agent microbubbles using double passive cavitation detection. *The Journal of the Acoustical Society of America*, vol. 127, no. 6, pp. 3449-3455, 2010.

Single microbubble-induced tissue deformation to estimate tissue properties

James H. Bezer¹, Hasan Koruk², Christopher J. Rowlands¹, James J. Choi¹

¹Department of Bioengineering, Imperial College London, UK

²Department of Mechanical Engineering, MEF University, Istanbul, Turkey

Corresponding author: j.choi@imperial.ac.uk

Introduction

When exposed to ultrasound, microbubbles experience a primary radiation force in the direction of wave propagation [1]. In a previous study, the cumulative radiation force of a cloud of microbubbles was shown to be large enough to reversibly deform soft materials [2]. This directional force could potentially be used for therapeutic or diagnostic purposes, such as to improve the contrast of ultrasound elasticity imaging. However, using a microbubble cloud has limited scope, because it cannot improve the resolution of elasticity imaging and may not be relevant to therapeutic techniques, which use very dilute microbubble concentrations. This study aimed to investigate whether a single bubble could deform a tissue boundary and assess its dynamics and reproducibility. The indentation curve of the bubble was also analysed to infer the radiation force on the bubble and the properties of the gel.

Methods

Dilute populations of microbubbles in wall-less channels in soft gel were exposed to ultrasound, and the degree of deformation was compared with predictions. In-house manufactured microbubbles were introduced into a 100 μ m diameter wall-less channel in polyacrylamide gel (4% acrylamide, $G=3\pm 1.5$ kPa rheometer: 1 Hz and shear strains of 0.1-10%). The samples were exposed to an ultrasound pulse (pulse length: 10 ms, peak rarefactional pressure: 200 kPa, centre frequency: 1 MHz) using a focussed immersion transducer (Olympus). Images of bubble dynamics were obtained using a high-speed camera (Chronos 1.4, Krontech, CA) linked to an Olympus 40x water immersion lens. Most images were obtained at a frame rate of 4,858 frames per second (FPS), although some images of single bubbles were taken at 31,191 FPS, to track the shape of the deformation curve. Bubble motion was tracked in Matlab using an arbitrary threshold model combined with a Hough transform. Bubble displacements were predicted using a viscoelastic model of a bubble penetrating a tissue interface [3]. The shear modulus of the gel used in the predictions was measured via nanoindentation and rheometry. The primary radiation force on the bubble was predicted using a Rayleigh-Plesset model [4]. These force values were then time averaged to provide a full nonlinear estimate of average force.

Results

Single microbubbles can reversibly deform tissue-mimicking materials. The simple model gives good estimates of the magnitude of tissue deformation induced by a bubble, although there is significant variation in displacement amplitude for apparently identical bubbles. At this frequency, the maximum indentation amplitudes are due to resonant bubbles. The results agree well with the model, although there is significant variation. This may be due to micron-scale inhomogeneities in the gel structure; uncertainty in measuring bubble radius; variation in acoustic properties between similarly sized bubbles; variation in the local acoustic field; or bubble expansion. Typical forces on bubbles were estimated to be of the order of one hundred nanonewtons. Gel viscosity was estimated from the bubble dynamics at approx 0.6-1 Pa s.

Conclusions

Tissue deformations induced by the primary radiation force on a microbubble can be reliably produced at low ultrasound pressures, and their typical magnitudes can be predicted accurately. This method is able to estimate the shear modulus and viscosity of soft materials. Further research is underway to refine the amplitude of deformation and replicate these experiments *in vitro* in live brain slices.

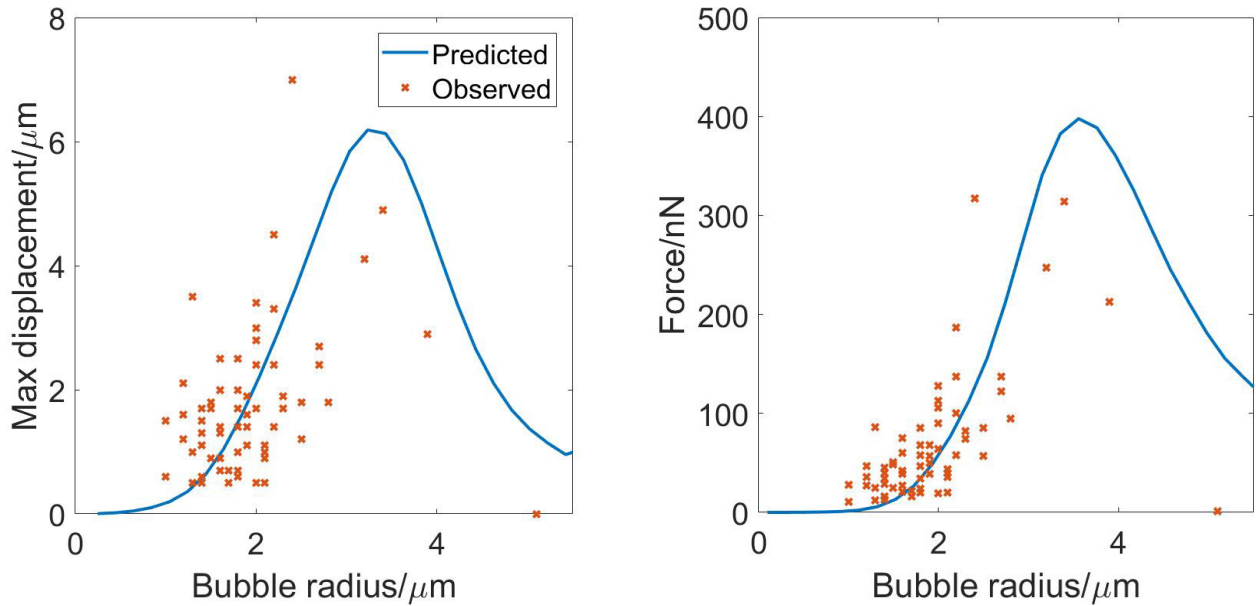


Figure 1. Left: Maximum wall deformation versus bubble radius for 62 microbubbles exposed to an acoustic pulse (pulse length: 10 ms, centre frequency: 1 MHz, peak rarefactional pressure: 200 kPa). Right: Radiation force versus bubble radius. Plots are of predicted values (line) and values inferred from observations

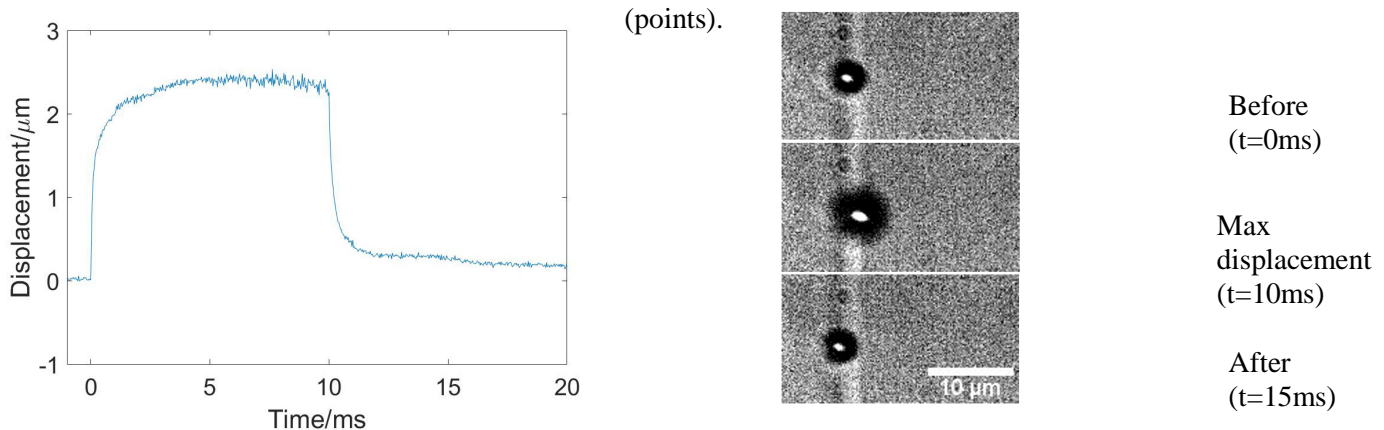


Figure 2. Left: Wall deformation curve for a 1.2 μm radius bubble impacting a gel boundary imaged at 31,191 FPS, during a 10ms pulse. Right: Example image of bubble movement during pulse.

References

[1]. Dayton, P.A., Allen, J.S. and Ferrara, K.W., 2002. The magnitude of radiation force on ultrasound contrast agents. *The Journal of the Acoustical Society of America*, 112(5), pp.2183-2192.

[2]. Koruk, H., El Ghamrawy, A., Pouliopoulos, A.N. and Choi, J.J., 2015. Acoustic particle palpation for measuring tissue elasticity. *Applied physics letters*, 107(22), p.223701.

[3]. Koruk, H. and Choi, J.J., 2019. Displacement of a bubble located at a fluid-viscoelastic medium interface. *The Journal of the Acoustical Society of America*, 145(5), pp.EL410-EL416.

[4]. Marmottant, P., Van Der Meer, S., Emmer, M., Versluis, M., De Jong, N., Hilgenfeldt, S. and Lohse, D., 2005. A model for large amplitude oscillations of coated bubbles accounting for buckling and rupture. *The Journal of the Acoustical Society of America*, 118(6), pp.3499-3505.

Different experimental patterns of microstreaming observed around acoustically excited microbubbles

Sarah Cleve^{1,*}, Gabriel Regnault¹, Cyril Mauger¹, Claude Inserra², Philippe Blanc-Benon¹

¹Univ Lyon, École Centrale de Lyon, INSA de Lyon, CNRS, LMFA UMR 5509, F-69134 Écully CEDEX, France

²Univ Lyon, Université Lyon 1, Centre Léon Bérard, INSERM, LabTAU, F-69003 Lyon, France

**now at: Physics of Fluids group, MESA+ Institute for Nanotechnology and Technical Medical (TechMed) Center, University of Twente, P.O. Box 217, 7500 AE, Enschede, The Netherlands*

Corresponding author: s.cleve@utwente.nl

Introduction

The use of bubbles in combination with ultrasound is known to significantly enhance both, the imaging contrast and the efficacy of therapeutic approaches such as sonoporation and blood-brain-barrier opening. Both, inertially cavitating and stably oscillating bubbles can cause these effects [1,2]. Stably oscillating bubbles are argued to be more controllable [3] and to lead to more repairable sonoporation. In this context, the microstreaming generated around acoustically excited bubbles and the subsequent shear stress induced to the cell membranes are assumed to play a major role. The exact mechanisms are, however, not yet fully understood. In particular, there have been little fundamental studies on the streaming patterns that also take into account the detailed temporal bubble dynamics or bubble deformations (in particular surface modes). Here, we show the different microstreaming patterns arising around a single microbubble and successfully correlate them to the microbubble dynamics on the timescales of the oscillations. To ensure the free-field behaviour, we acoustically trap the bubble far from any solid boundary. We drive the bubbles into stable, non-inertial oscillations, and tune the acoustic pressure and the bubble size to trigger specific surface modes. The method provides direct insight into the role of the surface modes in the generated streaming patterns.

Methods

Experiments were conducted in a cubic water tank in which a standing wave is generated by an ultrasound transducer driven at 31 kHz. The ultrasound field allows to simultaneously trap the bubble at a pressure antinode and to drive its radial oscillations. We then ‘trigger’ surface modes by inducing the coalescence of two bubbles of chosen size at a specific acoustic pressure [4]. The bubble dynamics is recorded using a high speed camera, and the fluid motion around the bubble is imaged in fluorescence by means of tracer particles passing through a laser sheet (see example in Figure 1). The combined approach allows to correlate liquid flow, velocity field and bubble dynamics [5].

Results

A large collection of streaming patterns was observed [5]. In particular, we can classify two classes of streaming patterns with a different outreach: (i) patterns consisting of multiple lobes closely confined around the bubble and (ii) cross-shaped patterns leading to streaming further away from the bubble. From the direct correlation with the bubble dynamics, we can identify parameters linked to the exact shape of the streaming patterns. As expected, different mode numbers will lead to different streaming patterns, but a further distinction between large patterns and lobe-shaped patterns can be achieved through the bubble size (relating to the resonance of the shape modes). Furthermore, a closer look on the modal analysis reveals differences in the amplitudes and phase behavior of the modal content. A recent theoretical approach [6,7] supports many of our experimental observations.

Discussion

Even though in the clinical application of ultrasound contrast agents, the microbubbles are exposed to a more complicated environment, the present findings are a first step towards understanding the exact role of microstreaming in applications such as sonoporation. In particular, the size of the streaming patterns is interesting to take into account. Furthermore, from the measured velocity fields, it is possible to directly deduce the induced shear stress acting on membranes and cells.

Conclusion

We show for the first time a detailed study on different streaming patterns that are induced by acoustically trapped bubbles oscillating on surface modes. A large variety of patterns is observed for which a first classification according to mode numbers and bubble sizes (relating to the resonance of the shape modes) is possible.

Acknowledgements

This work was performed within the framework of the Labex CeLyA of the Université de Lyon, within the programme ‘Investissements d’Avenir’ (ANR-10-LABX-0060/ANR-11-IDEX-0007) operated by the French National Research Agency (ANR).

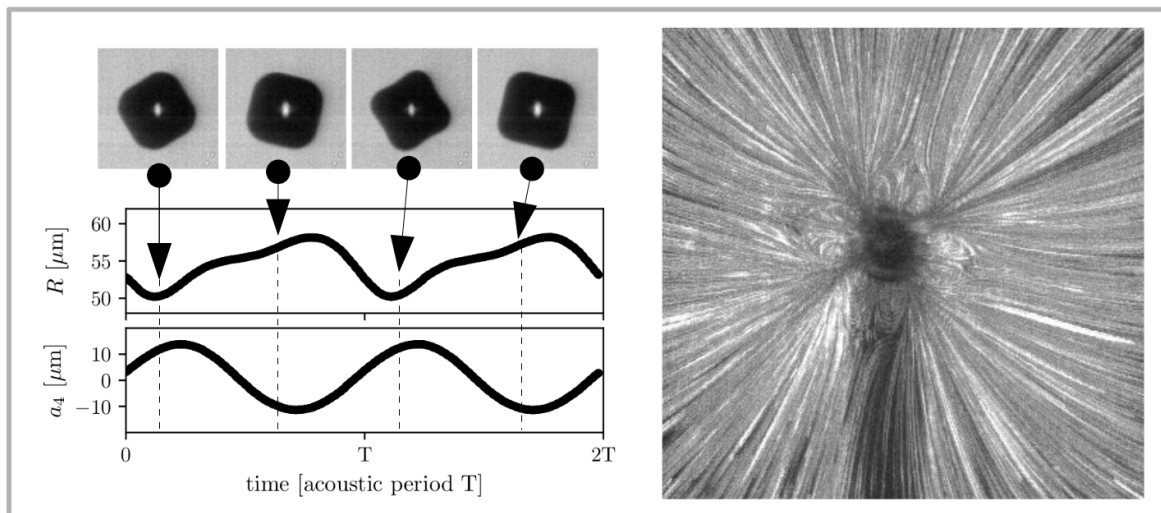


Figure 1. *Upper left:* Snapshot series of a bubble of about $53 \mu\text{m}$ radius oscillating on a surface mode 4; *lower left:* temporal evolution of the radial mode and the mode 4 with respect to the time (expressed in acoustic periods $T=0.032\text{ms}$); *right:* the resulting microstreaming (visualization of the particle trajectories by streak photography, that means superposition of all images taken during 1 s of recording is shown, the bubble is visible in the center).

References

- [1]. Lentacker I, De Cock I, Deckers R, De Smedt S, Moonen C, Understanding ultrasound induced sonoporation: definitions and underlying mechanisms, *Advanced drug delivery reviews*, 72, 49–64, 2014.
- [2]. Kooiman K, Vos HJ, Versluis M, de Jong N, Acoustic behavior of microbubbles and implications for drug delivery, *Advanced Drug Delivery Reviews*, 72, 28-48, 2014.
- [3]. Marmottant P, Hilgenfeldt S, Controlled vesicle deformation and lysis by single oscillating bubbles, *Nature* 423.6936,153–156, 2003.
- [4]. Cleve S, Guédra M, Mauger C, Insera C, Blanc-Benon P, Surface modes with controlled axisymmetry triggered by bubble coalescence in a high-amplitude acoustic field, *Physical Review E*, 98, 033115 2018.
- [5]. Cleve S, Guédra M, Mauger C, Insera C, Blanc-Benon P, Microstreaming induced by acoustically trapped, non-spherically oscillating microbubbles, *Journal of Fluid Mechanics*, 875, 597-621, 2019.
- [6]. Doinikov AA, Cleve S, Regnault G, Mauger C, Insera C, Acoustic microstreaming produced by nonspherical oscillations of a gas bubble. I. Case of modes 0 and m, *Physical Review E*, 100, 033104, 2019.
- [7]. Doinikov AA, Cleve S, Regnault G, Mauger C, Insera C, Acoustic microstreaming produced by nonspherical oscillations of a gas bubble. II. Case of modes 1 and m, *Physical Review E*, 100, 033105, 2019.

Controlling microbubble diameters from a flow focusing microfluidics device

Yanjun Xie, Adam J. Dixon, Rudy Montayre, John A. Hossack

Biomedical Engineering Department, University of Virginia,
Charlottesville, VA 22908, USA

Corresponding author: jh7fj@virginia.edu

Introduction

Flow focusing microfluidic devices (FFMDs) have been investigated over recent years as a means for producing a stream of microbubbles (MBs) for imaging or drug delivery. MBs from FFMDs, especially those possessing a relatively large diameter (15-25 μm) and short-term stability, have been shown to be optimal for catheter-based (i.e. *in situ* generation) sonothrombolysis applications [1]. In FFMDs, a gas stream is focused by two liquid flows and monodisperse MBs are released from an outlet port. Both the liquid flow-rate and the input gas pressure can be controlled by electronic devices. By varying gas pressure or flow-rates, the size and count of MBs are adjustable. It is critical to monitor and control MB count and diameter to ensure clinical safety and, we presume, to address probable regulatory requirements. A previous design of FFMD with an integrated micro Coulter Particle Counter (μCPC) enabled MB counting and sizing based on Coulter principle [2]. In this work, we present a real-time feedback control system on MB diameter.

Methods

A benchtop FFMD was fabricated with a μCPC by plasma-bonding a PDMS microfluidic channel with an electrode-deposited glass wafer. The μCPC detected impedance changes induced by passages of non-conducting MBs and the impedance changes were detected using a Wheatstone bridge paired to a low-noise instrumentation amplifier. The consequent voltage changes were mapped to estimated diameter in real time. The monitoring of MB diameter was included in a feedback control loop to regulate the input gas pressure (Fig. 1a) and a proportional-integral (PI) controller was implemented to control MB diameter and update the gas pressure every 200 ms. The parameters of the PI controller were: proportional gain $K_c = 0.045$, integral time $T_i = 3.3$ s.

Results

MBs were produced between 13 and 26 μm at production rate up to $140 \times 10^3/\text{s}$. A cubic diameter-voltage relation was calculated using simultaneously captured electrical signals and high-speed camera images resulting in $R^2 = 0.99$ for our data. Based on the electrically determined diameter, a PI controller was implemented.

The PI controller stabilized MB diameter at 22 μm (Fig. 1b). After 120 seconds, we disabled the PI controller so the input gas pressure remained unchanged for another 120 s. While the gas pressure and flow rate were constant, the MB diameter started to diverge from nominal as shown in Fig 1b.

Conclusions

The output voltage of the detection circuit exhibits a cubic relationship with MB diameter. The electrical-based method can measure the MB diameter in real-time. By using this measurement, a feedback control system achieves control over MB diameter. Results of enabling and disabling the controller suggests that using fixed parameters of input flow rate and gas pressure does not guarantee a stable MB diameter. The pressure required to maintain a preselected MB diameter of FFMDs is dynamic. This necessitates the use of some type of feedback control system in practical uses such as those considered above.

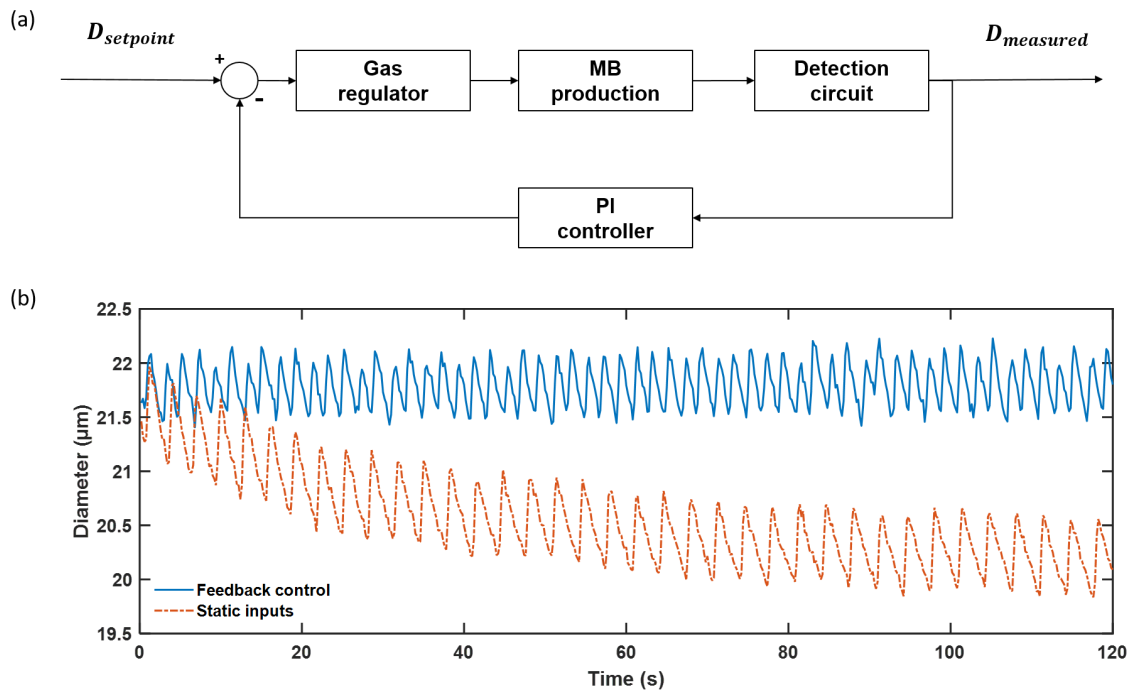


Figure 1. (a) Schematic of feedback control system in a benchtop FFMD. (b) Electrically determined diameters starting at 22 μm .

References

- [1]. Dixon AJ, Li J, Rickel JM, Klibanov AL, Zuo Z, Hossack JA, Annals of biomedical engineering, 2019, 47(4):1012-22.
- [2]. Rickel JR, Dixon AJ, Klibanov AL, Hossack JA, Lab on a Chip, 2018, 18(17):2653-64.

Experimental investigation of frequency-dependent shape modes of a bubble cluster under a sound field

Yuta Hatano¹, Takeshi Okada¹, Naohiro Sugita¹, Toshihiko Sugiura¹

¹*Mechanical Engineering, Keio University, Yokohama, Japan
Corresponding author: mitama0905@keio.jp*

Introduction

It is known that in the presence of multiple bubbles, the bubbles interact and attract each other to form one system called a bubble cluster, whose behavior is complicated and unclear compared with single bubbles. In this study, we observed a phenomenon of a bubble cluster similar to the shape oscillation of a single bubble in a sound field. The shape oscillation behavior of a bubble cluster was observed experimentally, and the relationship with its volume vibration was compared with the theory of single bubbles.

Theory

When a single bubble with an equilibrium radius R deviates from the sphere due to an external force, it generates a shape oscillation expressed by Eq. (1) with the gravity direction as the axis of symmetry [1].

$$r(\theta, t) = R + Y_n \sin(\omega_n t + \beta) \quad (1)$$

$$Y_n = a_n P_n(\cos\theta)$$

$$P_n(x) = (2^n n!)^{-1} [d^n/dx^n] (x^2 - 1)^n \quad (2)$$

Where Y_n is the n th-order spherical harmonic function consisting of Legendre polynomials, β is the phase, and ω_n is the natural frequency of the n th-order shape oscillation mode. When the frequency of the bubble volume oscillation is close to twice ω_n , the shape oscillation amplitude a_n of the n th-order mode can be increased by parametric excitation [2]. Here ω_n is expressed by the following equation [3].

$$\omega_n^2 = (n + 1)(n - 1)(n + 2) \sigma / \rho_l R^3 \quad (3)$$

As an example, Figure 1 shows the outline of the process of shape oscillation in each mode.

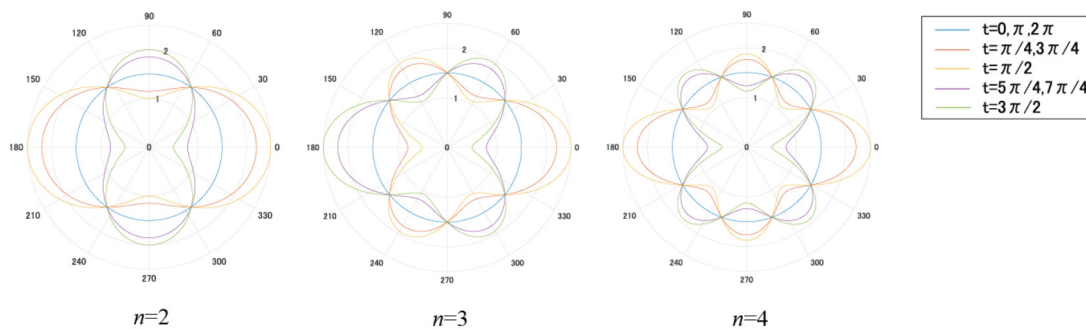


Figure 1. Processes of shape deformation in 2nd, 3rd and 4th oscillation modes.

Experiment

Figure 2 (a) and (b) show a schematic diagram of our experimental apparatus as seen from the side and top. In this experiment, water was placed in an acrylic container with an inner dimension of 50 mm width, depth 50 mm, height 100 mm and thickness 5 mm, and the container was fixed to an oscillator (513-BS / Z08, EMIC). The internal pressure was reduced to 5 kPa with a vacuum pump, and oscillation was applied in the vertical direction at an excitation acceleration of 5 m/s². By reducing the pressure, bubbles can be with a size of several millimeters, and the natural frequency of their volume oscillation can be reduced by about three orders of magnitude compared to those with a few μm. Therefore, they respond sufficiently to

the frequency of several hundred Hz in this experiment. Frames per second of the camera (FATCAMSA-X2, Photoron) were set to 20 000 to 70 000 fps.

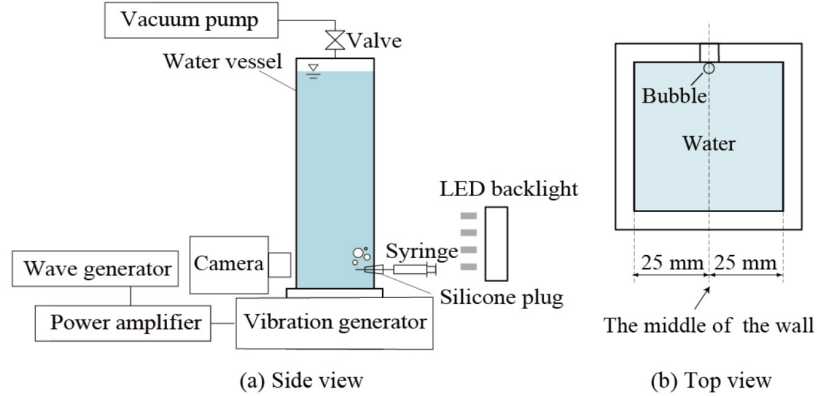


Figure 2. Experimental setup.

Results

Figure 3 shows the results of plotting the relationship between the equilibrium radius R_0 and the input frequency f of the bubble cluster for each shape oscillation mode observed. Based on the theory of single bubbles, curves representing the excitation conditions of the second and third modes are also drawn. Experimental results of both the modes agree well with the single-bubble theoretical curves respectively. Two different sequences of recorded images showing bubble-cluster oscillation are shown in Figure 4. Figure 4 (a) shows the shape oscillation of $n=2$ at half the input frequency f , which is parametrically excited through the volume oscillation at the input frequency f . On the other hand, Figure 4 (b) shows only the volume oscillation at the input frequency f without any shape oscillation. Furthermore, time histories of the volume oscillation of bubble clusters were obtained by image analyses. Figure 5 shows a time history and its FFT result of the volume oscillation of a bubble cluster showing the second-mode shape oscillation as well, while Figure 6 shows results without any shape oscillation. In Figure 5, it can be found that the frequency component at half the input frequency is large, which is considered to be due to the shape oscillation having half of the volume oscillation frequency.

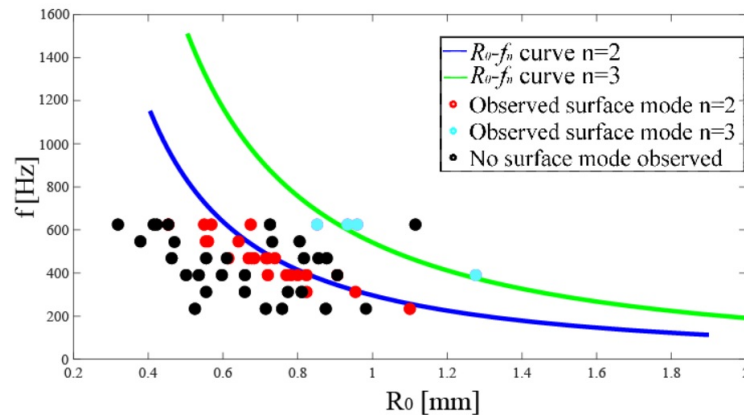


Figure 3. Comparison between experimental plots and theoretical curves showing input frequencies exciting 2nd- or 3rd-mode shape oscillation for equilibrium radii.

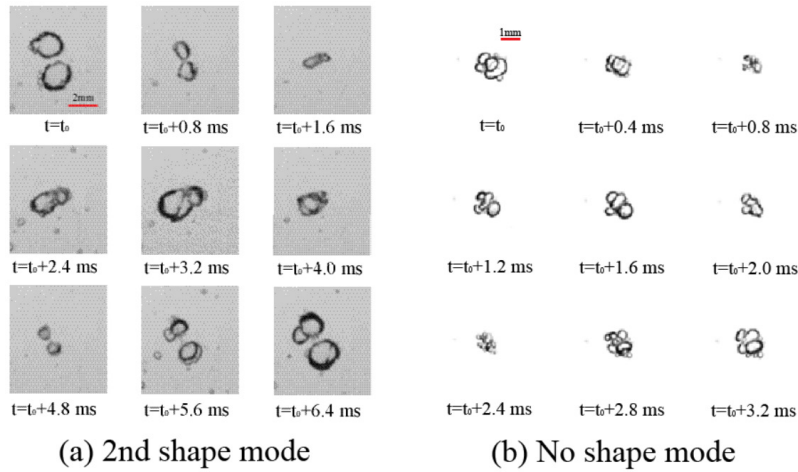


Figure 4. Sequences of recorded images showing bubble-cluster oscillation.

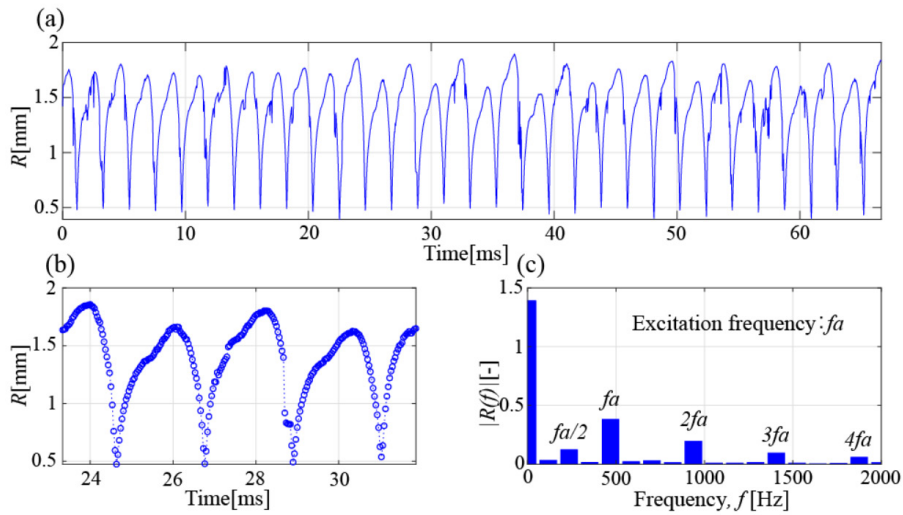


Figure 5. Results obtained by image analysis of bubble cluster oscillation including 2nd shape mode. (a) Time history, (b) Time history curve(enlarged) and (c) its Fourier spectrum.

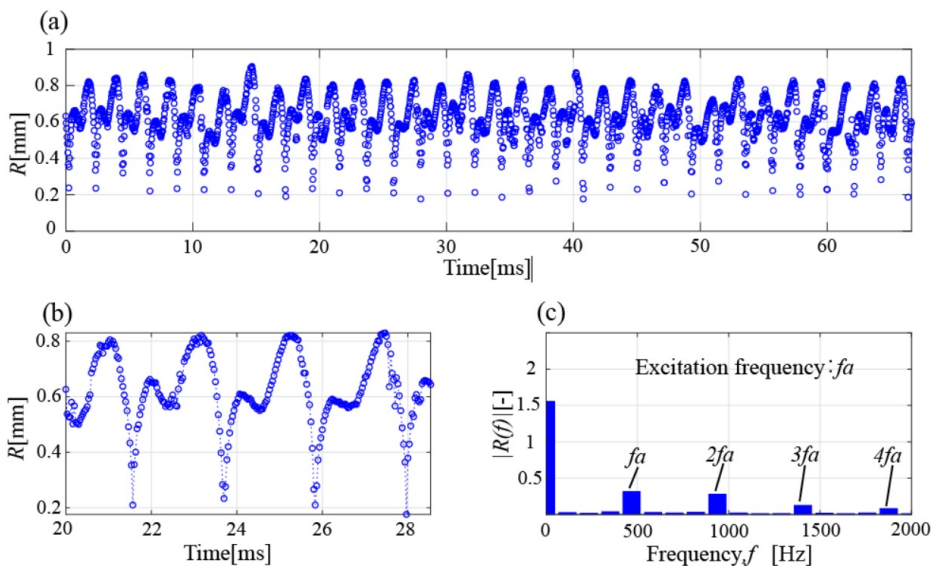


Figure 6. Results obtained by image analysis of bubble cluster oscillation without shape mode. (a) Time history, (b) Time history curve(enlarged) and (c) its Fourier spectrum.

Conclusions

In this study, it was experimentally confirmed that the relationship between the frequency of volume oscillation that generates the second or third mode of the shape oscillation and the equilibrium radius of a bubble cluster in the sound field agrees with the relationship based on the theory of a single bubble. In the FFT results of bubble clusters' volume oscillation obtained from image analyses, the frequency component of half the volume-oscillation frequency appears only when shape oscillation is observed.

References

- [1]. Ashgriz N, Handbook of atomization and sprays theory and applications, Springer Science: 125-129, 2011.
- [2]. Versluis M, Goertz DE, Microbubble shape oscillations excited through ultrasonic parametric driving, Physical Review E, 82: 026321-3, 2010.
- [3]. Brennen CE, Cavitation and bubble dynamics, Cambridge University Press: 95-109, 2013.

A 3D Printed Chamber for Microbubble Acoustic Characterisation

Elliott Smith¹, Luzhen Nie¹, James McLaughlan^{1,2}, Harry Clegg¹, Stephen Evans³, Thomas Carpenter¹, David Cowell¹, Steven Freear¹

¹*School of Electronic and Electrical Engineering, University of Leeds, Leeds, LS2 9JT, U.K.*

²*Leeds Institute of Medical Research, University of Leeds, Leeds, LS9 7TF, U.K.*

³*Molecular and Nanoscale Physics Group, School of Physics and Astronomy, University of Leeds, Leeds LS2 9JT, U.K.*

Corresponding author: e.i.j.smith@leeds.ac.uk and s.freear@leeds.ac.uk

Introduction

Microbubbles are used as contrast agents because they oscillate in the presence of an ultrasound pressure wave. The scattering power of these oscillating bubbles, at a given ultrasound excitation frequency, is dependant on the characteristics of the gas, the encapsulating shell and bubble radius [1]. Microbubbles can undergo linear or non-linear oscillations depending on the magnitude of the pressure wave they are exposed to [2]. The non-linear oscillations of microbubbles are exploited in a number of imaging modalities including second harmonic imaging [3], subharmonic imaging [4] and pulse inversion imaging [5]. At higher acoustic pressures, destruction can occur by fragmentation of the bubble or diffusion of the gas [6]. Destruction can be exploited for targeted drug delivery or perfusion imaging. All of these applications benefit from knowledge of the behaviour of microbubble populations in the presence of an acoustic field and hence require robust acoustic characterisation.

Acoustic characterisation of microbubbles typically consists of attenuation and scattering measurements. The basic experimental setup used to characterise a population of microbubbles acoustically is presented in [7] and is shown in Figure 1. Although most experiments for characterising populations of microbubbles share this basic setup, variations inevitably occur across different research groups. Variations in the parameters of the transducers, excitation signals, setup geometry, environment and procedure can make comparison between different research groups challenging. In addition, no standardised universal set of metrics has been adopted. One acoustic metric that has been proposed to describe the effectiveness of a contrast agent is the scattering-to-attenuation ratio (STAR) [8].

A novel design for the acoustic characterisation of populations of microbubbles is presented. This design consists of 3D printed parts to keep manufacturing costs low and so that the design can be easily reproduced by different groups. The microbubble acoustic characterisation chamber (MACC) overcomes some of the limitations of the setup illustrated in Figure 1. By constraining the geometry of the setup, the MACC makes direct comparison across research groups easier. Results from an initial experiment are presented to prove the efficacy of the design for acoustic measurements of populations of microbubbles.

Methods

In the setup shown in Figure 1, a vessel with acoustically transparent windows is used to constrain the solution of microbubbles in the far field of the transducers. Transducers are placed in line with each other for attenuation measurements. Scattering can be measured by the transmit transducer or by a third transducer placed orthogonal to the transmit transducer. The transmitter is typically excited with a sharp broadband pulse or a linear frequency modulated (LFM) pulse to obtain a broadband frequency response. Measurements are taken with degassed water in the vessel to obtain a reference. Measurements are then taken with a known dilution of microbubbles. The microbubble solution is normally agitated with a magnetic stirrer to replenish the microbubbles in the path of the transducers.

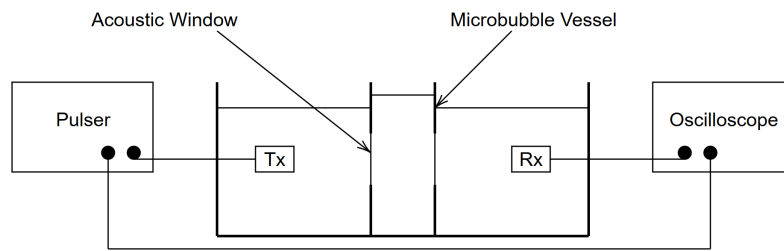


Figure 1. Traditional setup for acoustic experiments with populations of microbubbles

The setup described in Figure 1 has a number of limitations. Firstly, using a second vessel to constrain the bubbles places barriers in the path of the acoustic wave which can cause unwanted reflection. Secondly, a large volume of microbubble solution is required to fill the vessel but only a small subset of the bubbles are in the path of the transducers. In addition, the bubble chamber must be refilled with a fresh sample of bubbles regularly for different measurements and experiment repetitions. This leads to large quantities of bubbles required to perform an experiment. Due to the volume of bubbles used in this type of experiment, excitation signals are typically limited to sharp broadband pulses or LFM pulses to obtain acoustic information for a broad range of frequencies in a short time. Thirdly, due to limitations in transmit and receive electronics of the laboratory equipment used, as well as limitations with the microbubble vessel geometry, this experiment is usually performed with only two matched transducers. Occasionally more transducers are used through multiplexing schemes. When more transducers are used, they are normally placed in parallel with each other to interrogate a different region of the sample chamber. This makes it difficult to obtain scattering information for a broad range of frequencies from a single excitation because the immersion transducers used typically have a 60 percent bandwidth. Finally, the geometry for the experimental setup is not tightly constrained. This leads to difficulties with transducer alignment, difficulties in recreating the experiment and ultimately leads to a large degree of uncertainty in the measurements taken.

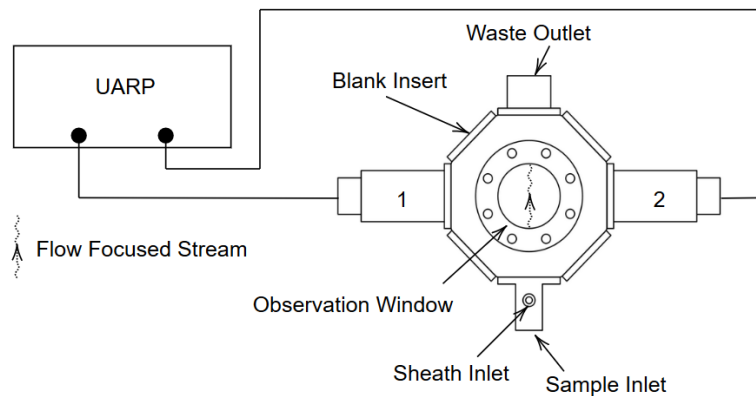


Figure 2. MACC setup for acoustic experiments with populations of microbubbles

The experimental setup used for the MACC is shown in Figure 2. This setup utilises a 16 channel variant of the University of Leeds Ultrasound Array Research Platform II (UARP-II-16) system. This open platform allows the connection of 16 single element transducers and can transmit and receive on all 16 channels simultaneously. Housings have been designed to accommodate upto 6 immersion transducers (V323, V384, V310, Olympus Industrial, Essex, UK) with centre frequencies of 2.25, 3.5 and 5 MHz. The transducers are aligned towards the centre of the chamber allowing scattering to be recorded on 5 transducers at a time over a range of frequencies and attenuation to be recorded on 1 transducer. The geometry of the chamber and alignment of these transducers is fixed allowing experiments to be recreated

easily. In addition, the MACC has an inlet and an outlet housing. The inlet housing consists of two coaxially aligned nozzles and two inlets. This allows a flow focused stream of microbubbles, constrained to the far field of the transducers, by careful control of a sample flow and sheath flow. This scheme does not introduce any barriers in the paths of the transducers and ensures the volume of bubbles required to perform the experiment is kept to a minimum. The assembled MACC is shown in Figure 3.

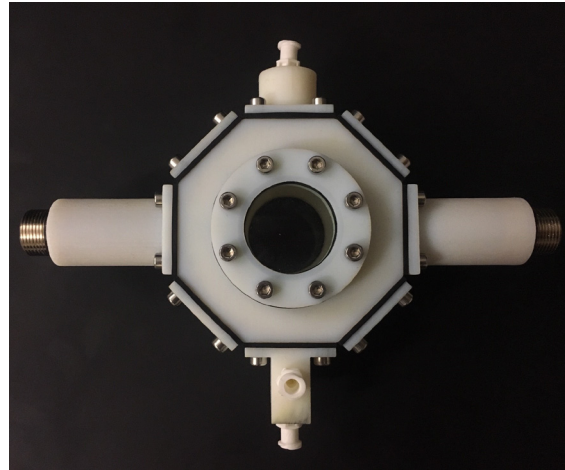


Figure 3. Microbubble Acoustic Characterisation Chamber assembled with 2 transducers in positions 1 (left) and 2 (right)

To prove the efficacy of the MACC for microbubble acoustic measurements, an experiment was performed using two unfocused 2.25 MHz transducers in position 1 and 2 in Figure 2. Blank inserts were used in place of all other transducer positions. The flow rate for the sheath flow was chosen to be 22 ml per minute, the flow rate for the sample flow was chosen to be 7 ml per minute. This resulted in the sample constrained to a stream approximately 1 mm wide in the centre of the chamber. A 10 μ s, stepped frequency sine wave excitation was used ranging from 1.7-2.9 MHz at increments of 0.2 MHz. The pulse repetition frequency (PRF) for the experiment was chosen to be 500 Hz and each frequency was repeated 225 times. This was repeated for two scans, one in which position 1 was used as the transmitter, and one in which position 2 was used. The total time taken to perform the experiment and download the data was 30 seconds. A switched excitation scheme [9] with a maximum switching level of ± 24 V was used and the transmitted pulse was pre-distorted to obtain a uniform pressure over the range of frequencies used. The corresponding pressure wave generated did not exceed 100 kPa. A 1:1000 dilution of SonoVue (Bracco, Milan, Italy) was used and the experiment was repeated 8 times with a fresh dilution of SonoVue and 8 times with degassed water to provide a reference. The choice between repeating the experiment with a reference solution and repeating the experiment with SonoVue was selected randomly to assess the null hypothesis: ‘The introduction of microbubbles into the path of transducer X has no effect on the signal received by transducer Y’. The data was collected and post-processed using MATLAB. This post-processing consisted of windowing the data and averaging in the frequency domain.

Results

Figure 4 shows the attenuation and backscatter frequency spectrum plots for the reference data and the measured data as well as the attenuation and gain measured for the microbubble solution. The two scans do not show close agreement in terms of attenuation or scattering. In this experiment, pre-distortion was used to obtain a more uniform pressure across the range of frequencies. Because the first transducer and the second transducer had different transmit sensitivities, the pressure wave at the centre of the chamber from each scan was different. This may be the reason for the differences seen in the attenuation and scattering profile for each scan. Calibration of the whole system to obtain pressure values is the subject of future work.

Table 1 shows the p-values of a one tailed t-test for both scans in terms of attenuation and backscatter. All of the frequencies for attenuation data in both scans reject the null hypothesis outlined previously at the 5% significance level. For backscatter, all but one frequency reject the null hypothesis for scan 1 and all but two reject the null hypothesis for scan 2. It is believed that further experiment repeats and more recordings per experiment should allow the null hypothesis to be rejected for the three outstanding cases.

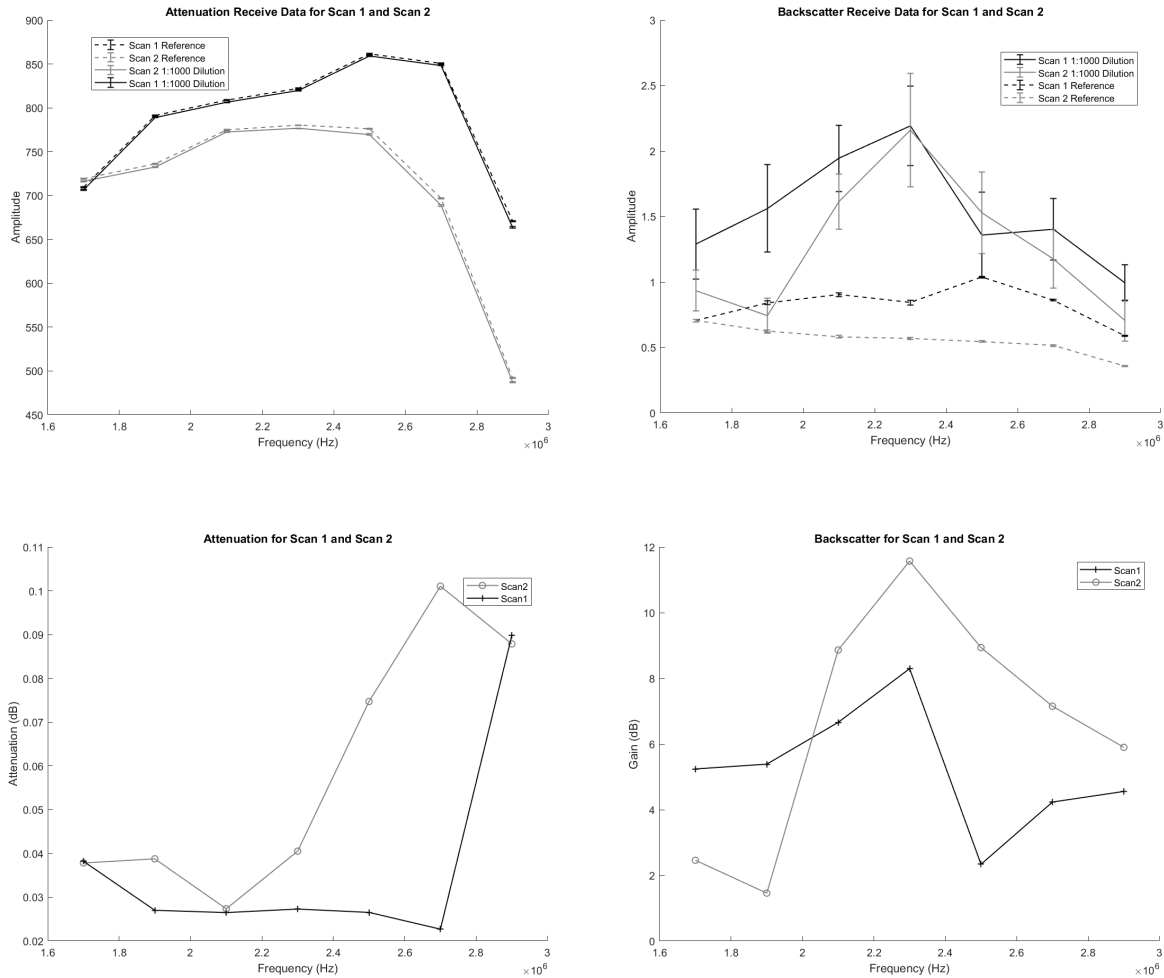


Figure 4. Attenuation and scattering frequency spectrum plots for the reference and microbubble solutions and calculated attenuation and gain plots.

Table 1. T-test p-values for attenuation and backscatter data

	1.7 MHz	1.9 MHz	2.1 MHz	2.3 MHz	2.5 MHz	2.7 MHz	2.9 MHz
Scan 1 Attenuation	1.4e-4	4.3e-3	1.9e-3	1.9e-3	2.3e-3	4.9e-3	2.7e-5
Scan 2 Attenuation	3.3e-4	1.9e-3	1.6e-3	2.2e-4	2.7e-5	2.0e-5	1.1e-5
Scan 1 Backscatter	0.033	0.033	2.2e-3	1.5e-3	0.18	0.028	0.010

Scan Backscatter	2	0.091	0.21	8.7e-4	3.9e-3	8.2e-3	0.010	0.032
-------------------------	----------	-------	------	--------	--------	--------	-------	-------

Conclusions

In this study, a 3D printed chamber for the acoustic characterisation of microbubbles was presented. The chamber presented is designed to overcome some of the limitations with existing acoustic characterisation experiments and to provide a framework for better comparison between groups. An initial experiment was performed with the chamber to prove its suitability in acoustic measurements of microbubbles. Further refinement of the experimental procedure and calibration is required to obtain accurate pressure values.

Acknowledgments

The author would like to acknowledge EPSRC for funding (EP/P023266/1) this work and thank the Microbubble Consortium at the University of Leeds.

References

- [1]. H. Medwin, "Counting bubbles acoustically: a review," *Ultrasonics*, 1977.
- [2]. D. L. Miller, "Frequency relationships for ultrasonic activation of free microbubbles, encapsulated microbubbles, and gas-filled micropores," *J. Acoust. Soc. Am.*, vol. 104, no. 4, pp. 2498–2505, 1998.
- [3]. B. A. Schrope and V. L. Newhouse, "Second harmonic ultrasonic blood perfusion measurement," *Ultrasound Med. Biol.*, 1993.
- [4]. F. Forsberg, W. T. Shi, and B. B. Goldberg, "Subharmonic imaging of contrast agents," *Ultrasonics*, 2000.
- [5]. D. H. Simpson, C. T. Chin, and P. N. Burns, "Pulse inversion Doppler: a new method for detecting nonlinear echoes from microbubble contrast agents," *IEEE Trans. Ultrason. Ferroelectr. Freq. Control*, vol. 46, no. 2, pp. 372–382, 1999.
- [6]. J. E. Chômas, P. Dayton, J. Alien, K. Morgan, and K. W. Ferrara, "Mechanisms of contrast agent destruction," *IEEE Trans. Ultrason. Ferroelectr. Freq. Control*, vol. 48, no. 1, pp. 232–248, 2001.
- [7]. C. Cachard, A. Bouakkaz, and G. Gimenez, "In vitro evaluation of acoustic properties of ultrasound contrast agents: Experimental set-up and signal processing," *Ultrasonics*, 1996.
- [8]. A. Bouakaz, N. De Jong, and C. Cachard, "Standard properties of ultrasound contrast agents," *Ultrasound Med. Biol.*, 1998.
- [9]. D. Cowell, S. Freear "Quinary excitation method for pulse compression ultrasound measurements," *Ultrasonics*, vol. 48, pp.98-108. 2008.

Ultrasound Localization Microscopy *in vivo*: characterization, modelization and limits in various tissues

V. Hingot¹, B. Heiles¹, O. Couture²

¹Institute Physics for Medicine Paris, Inserm U1273, CNRS FRE 2031, PSL University, Paris, France

²Laboratoire d'Imagerie Biomedicale, Sorbonne Université, CNRS, Inserm, F-75006, Paris, France

Corresponding author: Vincent Hingot, vincenthingot@gmail.com

Introduction

Until recently, vascular imaging in ultrasound was limited to the biggest vessels. The use of contrast agents enabled measurements of perfusion in organs but the imaging of the microvasculature itself was not possible. The detection, localization and tracking of individual flowing microbubbles enables the mapping of vessels with a resolution finer than the diffraction limit (1,2). For moving tissues, various methods for motion correction, microbubble localization and tracking have been introduced (3). As of today, tools to describe imaging performances were thoroughly described and used (4).

In this study, we demonstrate the efficiency of a general affine method for motion correction in a variety of *in vivo* situations: brain, kidney, pancreas and tumors. Moreover, we introduce metrics and models to characterize image quality in Ultrasound Localization Microscopy (ULM) that may serve as tools to determine spatial resolution and acquisition times and validate motion correction strategies.

Methods

ULM was performed in various rodent organs, mainly brain, kidney, pancreas, and tumors. For each acquisition, 200 - 400 μ L of Sonovue microbubbles were injected in the tail or jugular vein as a bolus or an infusion while ultrasound images were acquired for several minutes by blocs of 800 compounded frames (-5° , 0° , 5°) at 1000 Hz. Microbubbles signals were filtered using a combination of high pass Butterworth and Singular Value Decomposition filters, localized using a radial symmetry based algorithm and tracked using the Hungarian method for assignment. Density images were reconstructed on a 10 μ m grid. An iterative gradient descent was used to estimate the affine transformation matrix for each image before the transformation could be applied back to correct motions.

Results

A method based on the calculation of the Fourier Ring Correlation was used to estimate the spatial resolution of ULM images. As the quality of the image relies not only on spatial precision but also on sufficient microbubbles positions accumulation, saturation methods were used to estimate image completion. A model for the acquisition time is proposed as a function of the vascular microbubble concentration, the reconstructed pixel size and the microvascular flow. Using this model, we were able to estimate microbubbles' concentration using two different methods. In the rat's brain and during the constant injection of Sonovue, we estimate the vascular concentration of microbubbles to be $2 \cdot 10^5$ MB.ml⁻¹, the spatial resolution to be 10 μ m and the temporal resolution to 5 minutes. In the other tissues, such as the tumor, the vascular network is less populated due to motion, along with lower physiological perfusion and a visible chaotic organisation.

Conclusions

We propose a general paradigm for ULM *in vivo* to produce images with motion correction, characterization of both spatial and temporal resolutions as well as vascular microbubbles concentration. The introduction of resolution metrics can also allow the comparison between various ULM approaches.

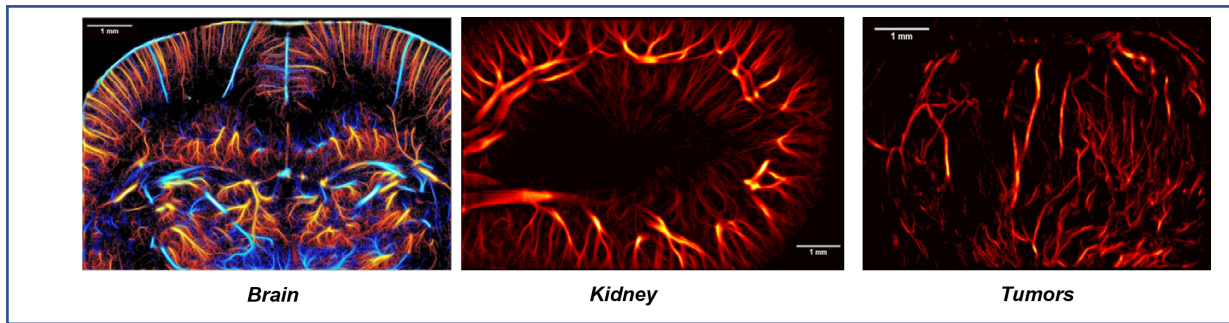


Figure 1. Ultrasound Localization Microscopy in various organs in rodents enable microvascular imaging with sub millimetric resolution in under 5 minutes

References

- [1]. Errico C, et al, Ultrafast Ultrasound Localization Microscopy for deep super-resolution vascular imaging 2015, Nature, Nov 26;527(7579):499-502, 2015
- [2]. Couture O, et al, Ultrasound Localization Microscopy and Super Resolution: A state of the art. 2018, IEEE TUFFS, 2018 Aug;65(8):1304-1320, 2018
- [3]. Hingot V, et al, Subwavelength motion correction for ultrafast Ultrasound Localization Microscopy 2017, Ultrasonics, May;77:17-21, 2017
- [4]. Hingot V, et al, Microvascular flow drives the tradeoff between spatial resolution and acquisition time in Ultrasound Localization Microscopy 2019, Sci Rep 9, 2456, 2019

Developing a microbubble-based contrast agent for X-ray phase contrast imaging

Ngoc Ton¹, Una Goncin¹, Arash Panahifar³, M. Adam Webb³, Dean Chapman^{1,2,3}, Sheldon Wiebe¹, Steven Machtaler¹

¹Medical Imaging Department, University of Saskatchewan, Saskatoon, Canada

²Anatomy, Physiology and Pharmacology Department, University of Saskatchewan, Saskatoon, Canada

³Canadian Light Source, Saskatoon, Canada

Corresponding author: nmt281@mail.usask.ca

Introduction

X-ray phase contrast (XPC) imaging is an emerging modality that generates contrast from X-rays that slightly change direction as they pass through objects, generating exquisite soft tissue resolution with a reduced radiation dose [1]. This has potential to be an excellent alternative to traditional mammography [2]. Nonetheless, XPC imaging still focuses on visualizing anatomical structures, similar to traditional mammography. Our goal is to develop a contrast agent for XPC imaging, based on ultrasound microbubbles (MBs), to be used for XPC-molecular imaging of breast cancer.

There are two promising XPC techniques that may be suitable to use with ultrasound microbubbles: In-line phase contrast imaging (PCI) and Diffraction enhanced imaging (DEI). PCI has the simplest setup without any crystals or analyzers between an object and a detector. The intensity variation of the phase shift is quantified when moving the micron pixel-size detector a distance from the object [3]. This method is a robust approach which has been used clinically [4-6]. DEI is another promising X-ray phase contrast approach that generates high soft tissue contrast with a low absorbed radiation dose [1]. In DEI, a crystal analyser is placed between an object and a detector, working as a filter to allow only X-rays having a similar Bragg angle with the atomic planes of the crystal [3]. In contrast to other X-ray phase contrast imaging approaches, these data can be easily separated into three images: absorption, refraction and X-ray scattering [7]. DEI also has a moderately large field of view [8] and has been successfully used in breast imaging with synchrotron radiation [4, 9, 10]. There is currently a need in the field to develop a contrast agent for these imaging approaches.

Microbubbles are micron-sized spheres with a core, made from a high-molecular weight gas, protected by a shell [4, 11, 12]. The gaseous core, which has a refractive index different from the biological fluid environment in the living subjects, can change both the direction and phase of the wavefront to form bright boundaries and can substantially promote the image contrast [3]. Therefore, we aim to determine the optimal microbubble to generate contrast using PCI and DEI through a systemic assessment of microbubble composition, including size, shell material, shell coating and concentrations.

Methods

MBs were constructed from two different shell materials: phospholipids (lipid) and polyvinyl alcohol (PVA). Polydisperse perfluorobutane-core, lipid MBs were created by solubilizing two lipids (DSPC and PE-PEG2000) in water and sonicating for 30 seconds at 40C. MBs were collected and size separated using centrifugation [13]. PVA microbubbles were constructed by oxidizing a solubilized PVA solution at 800C, cooling to 220C and inserting a tissue homogenizer running at 8000 RPM for 2 hours. We used two different homogenizers which gave us MBs with two different size distributions: 2-3 um and 3-4 um. To a subset of PVA-MBs (3-4 um), their surface was coated with alternating layers of polymers (PEI, PSS and PAH) coating the outmost layer in 1 or 4 layers of 3 nm iron oxide nanoparticles (SPIONs) [14]. PVA-MBs with SPIONs integrated into their shells were created by adding a SPIONs solution during MB construction. After synthesis process, we had five groups of lipid MBs isolated by size and seven groups of PVA MBs varied by size and shell coatings. MBs were embedded in 0.5% agar at 370C, allowing

uniform MB distribution throughout the cuvettes, at three different concentrations, 5x10⁷, 5x10⁶, 5x10⁵ MBs/ml. In total, 37 samples including the negative control – agar, were tested.

PCI was performed at BMIT-BM beamline of the Canadian Light Source with white beam X-ray combined micro-computed tomography (uCT) and following parameters: detector voxels: 3.57 μm^3 , field of view: 9.2 mm x 9.2 mm, energy range: 15-40 KeV, projections: 1800, exposure time: 150ms, sample to detector distance: 45 cm and source to sample distance: 26 m. The CT reconstruction was done by using TomoVIEWER and UFO-KIT software to generate XY slices. Reconstructed slices were grouped into 10-slice stacks and converted into minimum and maximum intensity projections using ImageJ. The number of x-ray phase contrast objects (microbubbles) in a cylindrical-shaped region of interest with a volume of 56 mm³ was counted and averaged from five experimental repeats. This cylinder had a radius of 3.1 mm and a height of about 1.85 mm which was made of 52 minimum intensity projections.

DEI was also conducted at BMIT-BM beamline of the Canadian Light Source with a monochromatic beam and a silicon analyzer (2,2,0). The pixel size was 25 μm , the field of view was 0.5 cm x 10 cm and the energy was 30 KeV. The reflectivity curve width was 1 mm and 14 images were scanned along 4 mm. Three images of absorption, refraction and ultra-small angle x-ray scattering (USAXS) were generated using Multiple Imaging Radiography and analysed by ImageJ. After reconstruction, the contrast signal was assessed by mean pixel value (MPV), measured in a rectangular area of 1.25 x 7.5 mm² in the middle of scattering images, and averaged from six experimental repeats.

Results

In PCI, lipid MBs, 6-10 μm generated the greatest contrast enhancement which was decreased when the microbubble size decreased, with both positive contrast (from the bright shell) and negative contrast (from the dark core) after image reconstruction (**Figure 1A**). At the highest MB concentration, 5 x10⁷ MBs/ml, lipid microbubbles from 6-10 μm and 4-6 μm were detectable (**Figure 1B**: 927,418 MBs detected/56 mm³ and 904,026 MBs detected/56 mm³ respectively). Uncoated PVA microbubbles were not detectable (3,169/56 mm³: 2-3 μm , and 4,671/56 mm³: 3-4 μm), nor polymer-coated PVA-MBs (8,811/56 mm³). Polymer coated MBs tend to form loose clusters in solution. These clusters were detectable in XPC imaging (aggregated polymer-coated PVA-MBs: 61,283/56 mm³, and 4-layer SPION-coated PVA-MBs: 87,048/56 mm³).

With DEI, lipid MBs 6-10 μm with the highest concentration, showed the highest and clearest signal in 8-bit USAXS images (MPV: 184/255) which dropped to background intensity levels at lower concentrations (**Figure 1C-III**) and in all other lipid MB samples (MPV: < 100/255) (**Figure 1D**). The largest lipid MBs showed a reduction in X-ray absorption, presenting as darker signal in the absorption image (**Figure 1C-I**). In refraction image, because the pixel size, 25 μm , was much larger than the sizes of 6-10 μm microbubbles, the phase contrast generated from MBs was barely detected (**Figure 1C-II**). Moreover, there was no visible signal from either smaller lipid microbubbles or all types of PVA microbubbles (**Figure 1D**).

Conclusions

These data suggest that with the minimum concentration of 5x10⁷ MBs/ml, lipid-shelled MBs larger than 4 μm are a candidate for PCI while lipid-shelled MBs larger than 6 μm are a candidate for DEI XPC-molecular imaging of breast cancer. These PCI data suggest that MBs in close proximity (aggregated PVA-MBs) to each other may increase detectability. This may be optimal for molecular imaging, since MBs will accumulate on target vessels in close proximity to each other, while individual circulating MBs will generate a lower signal. With DEI, the size of microbubbles possibly plays a key role in generating the contrast from the deviated X-rays or X-ray scatterings whereas both shell material and shell coating may have less impact on the scattering-based contrast.

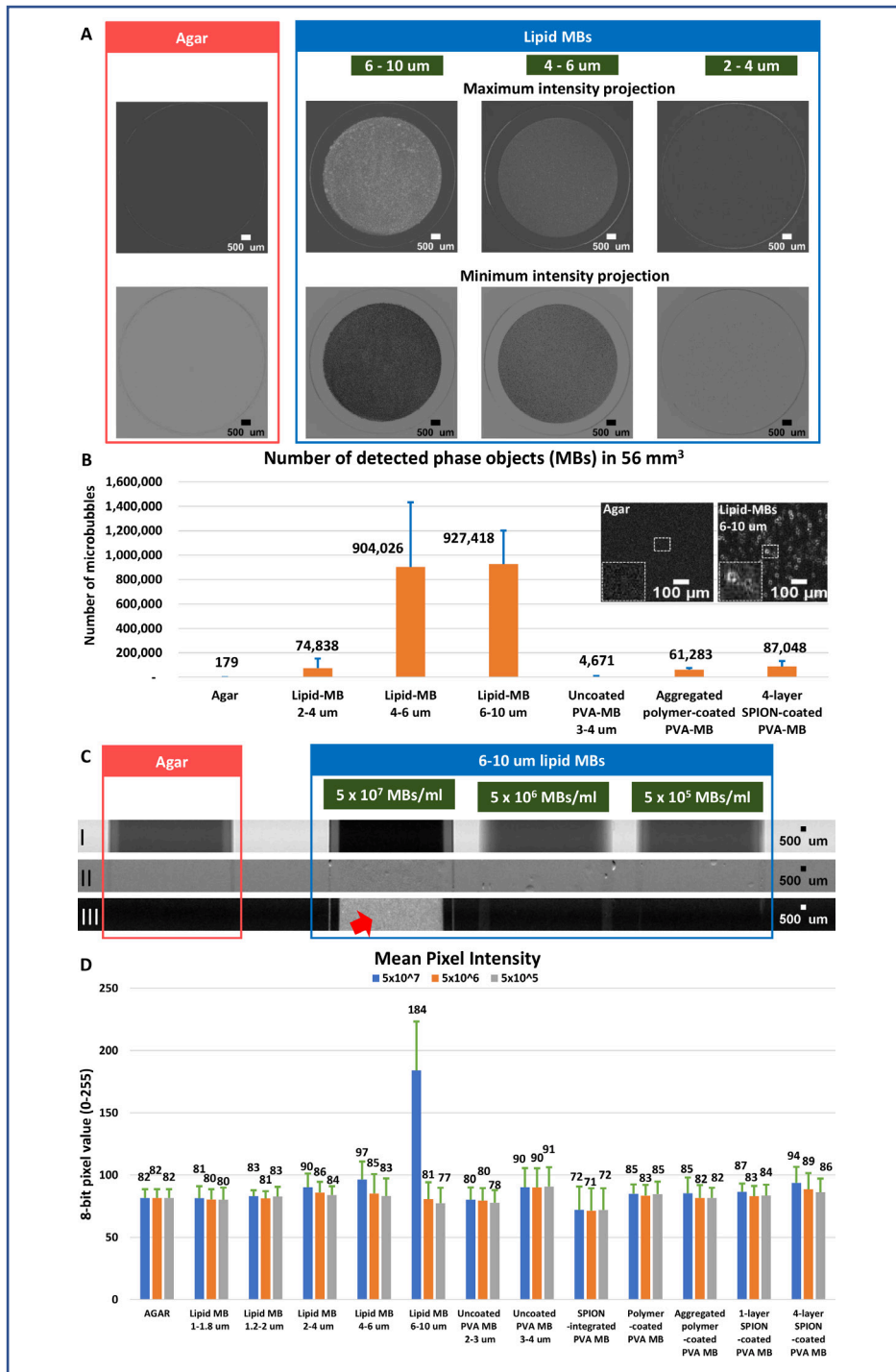


Figure 1: In-line Phase Contrast Imaging (A-B) and Diffraction Enhanced Imaging (C-D) of microbubbles. A) Maximum (top) and Minimum (bottom) intensity projections generated from a 520-slice stack from lipid microbubbles. B) Number of PCI objects observed in each sample with the highest concentration. C) Three images of separate absorption (I), refraction (II) and ultra-small angle X-ray scattering (III) were extracted from DEI where lipid MBs 6-10 um showed the remarkable signal in the scattering image. D) Mean pixel intensity of objects observed in each sample, with the highest signal going to the highest concentration of the largest lipid MBs 6-10 um.

References

- [1]. Chapman, D., et al., Diffraction enhanced x-ray imaging. *Phys Med Biol*, 1997. 42(11): p. 2015-25.
- [2]. Bravin, A., S. Fiedler, and W.C. Thomlinson. Very low dose mammography: New perspectives in Diffraction Enhanced Imaging (DEI) mammography. 2002. San Diego, CA, United states: SPIE.
- [3]. Alberto, B., C. Paola, and S. Pekka, X-ray phase-contrast imaging: from pre-clinical applications towards clinics. *Physics in Medicine & Biology*, 2013. 58(1): p. R1.
- [4]. Arfelli, F., L. Rigon, and R.H. Menk, Microbubbles as x-ray scattering contrast agents using analyzer-based imaging. *Physics in Medicine & Biology*, 2010. 55(6): p. 1643.
- [5]. Castelli, E., et al., Mammography with Synchrotron Radiation: First Clinical Experience with Phase-Detection Technique. *Radiology*, 2011. 259(3): p. 684-694.
- [6]. Fedon, C., et al., Dose and diagnostic performance comparison between phase-contrast mammography with synchrotron radiation and digital mammography: a clinical study report. *Journal of medical imaging (Bellingham, Wash.)*, 2018. 5(1): p. 013503-013503.
- [7]. Auweter, S.D., et al., X-ray phase-contrast imaging of the breast—advances towards clinical implementation. *The British Journal of Radiology*, 2014. 87(1034): p. 20130606.
- [8]. Velroyen, A., et al., Ex Vivo Perfusion-Simulation Measurements of Microbubbles as a Scattering Contrast Agent for Grating-Based X-Ray Dark-Field Imaging. *PLOS ONE*, 2015. 10(7): p. e0129512.
- [9]. Hasnah, M.O., et al., Diffraction enhanced imaging contrast mechanisms in breast cancer specimens. *Medical Physics*, 2002. 29(10): p. 2216-2221.
- [10]. Keyriläinen, J., et al., Phase-contrast X-ray imaging of breast. *Acta Radiologica*, 2010. 51(8): p. 866-884.
- [11]. Velroyen, A., et al., Microbubbles as a scattering contrast agent for grating-based x-ray dark-field imaging. *Physics in Medicine & Biology*, 2013. 58(4): p. N37.
- [12]. Xi, Y., et al., Microbubbles as contrast agent for in-line x-ray phase-contrast imaging. *Applied Physics Letters*, 2011. 99(1): p. 011101.
- [13]. Feshitan, J.A., et al., Microbubble size isolation by differential centrifugation. *Journal of Colloid and Interface Science*, 2009. 329(2): p. 316-324.
- [14]. Barrefelt, Å., et al., Biodistribution, kinetics, and biological fate of SPION microbubbles in the rat. *International journal of nanomedicine*, 2013. 8: p. 3241-3254.
- [15]. ImageJ (<http://rsb.info.nih.gov/ij/>)

On the importance of sensor placement when recording a microbubble cloud's acoustic emissions

K. Sujarittam¹, J. J. Choi¹

¹ *Noninvasive Surgery and Biopsy Laboratory, Department of Bioengineering, Imperial College London, London, UK*

Corresponding author: j.choi@imperial.ac.uk

Introduction

Microbubbles driven by ultrasound have been studied for several therapeutic applications.; Potential treatments include drug delivery to the brain, the dissolution of blood clots, and drug delivery across cell membranes. During these treatments, microbubbles oscillate in the acoustic field to produce the therapeutic action. The same oscillations also produce unique acoustic emissions, which are used to monitor the bubbles' actions to confirm or control the treatment's efficacy and safety. Common methods used to interpret these emissions include temporal and frequency domain analysis. For example, the energy of harmonic and broadband signals are being used to categorise microbubble activities. However, this technique has been performed in many different spatial orientations with the sensor (i.e., passive cavitation detector (PCD)) placed at different angles relative to the direction of wave propagation and bubble cloud. Here, we hypothesised that the location of the sensor would influence the temporal and frequency content of the recorded acoustic emissions from the microbubble cloud.

Methods

A simulation and in vitro experiments were used to evaluate the effect of sensor placement. We simulated 128 randomly distributed polydisperse microbubbles in a 0.56mm-diameter, 10.2mm-long tubular space, oriented 45-degree clockwise to the direction of primary sonication. The simulated excitation pulse had a waveform similar to that generated by the transducer used in the validation experiments. Each bubble's response was simulated using the modified Rayleigh-Plesset-Marmottant model. The acoustic emission of each bubble was simulated from their radial dynamics. Two 2-mm circular sensor surfaces were simulated. One sensor was placed 45-degree counter-clockwise to the tube axis; another 135-degree clockwise to it.

Validation experiments employed the same arrangements and dimensions as the simulation. We sonicated a microbubble suspension that flowed through a wall-less polyacrylamide gel channel, (0.27-0.48MPa; 0.5MHz; 5-cycle excitation pulses) and recorded the bubbles' acoustic emissions using two receivers: a 2mm needle hydrophone – placed at the two positions in subsequent experiments – and a focused PCD always arranged concentrically with the transducer. The PCD recordings were used to confirm that the cavitation signals measured at a fixed position was similar for both needle positions – that any difference in the needle's signals were due solely to its position. We subtracted each bubble data with the average of ten corresponding control data, acquired by sonicating pure water under identical conditions. This deleted the background signal, leaving only recordings of bubbles' acoustic emissions.

Results

Both the simulation and the experiments showed that the position of the sensor had a substantial influence on the recordings of bubbles' acoustic emissions. The 45-degree placement produced signals with a lower centre frequency whereas the 135-degree placement captured broadband signals (Figure 1). Stationary PCD recordings showed similar signals for both cases, implying that the differences were solely due to the placement of the needle hydrophone and not due to the statistical variation of bubble activities.

Conclusions

We demonstrated that when monitoring a bubble cloud's acoustic emissions at therapeutically-relevant acoustic pressures, placement of the acoustic sensor will affect the signal's temporal and frequency contents. Sensor placement should thus be carefully considered when interpreting a microbubbles' emissions during microbubble-mediated therapies.

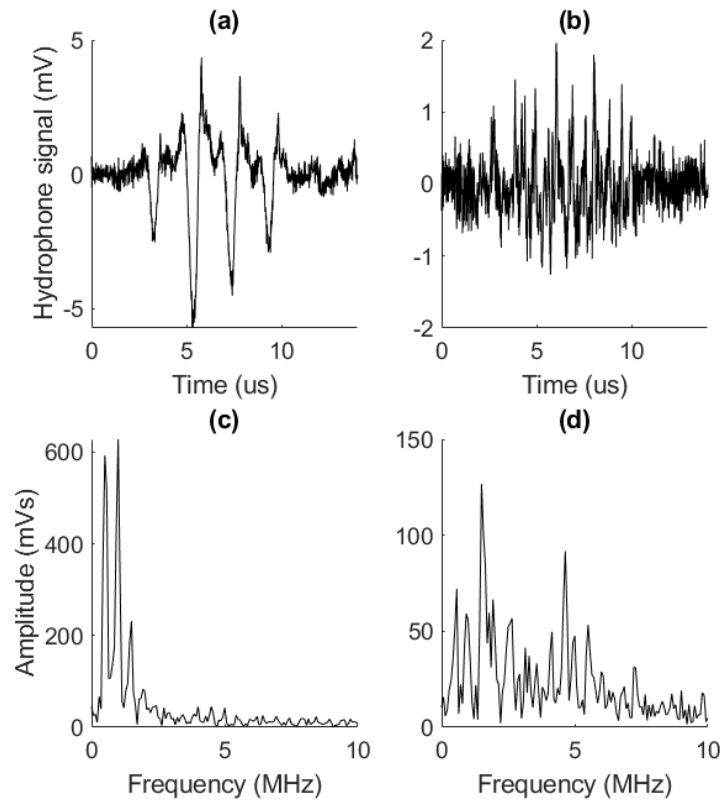


Figure 1. Comparison of readings made by a hydrophone placed at the two different positions under 0.27-MPa sonication: a) 45-degree hydrophone reading, and c) its Fourier magnitude spectrum; b) 135-degree hydrophone reading, and d) its Fourier magnitude spectrum.

The screenshot shows the Live Media website interface. At the top left is the 'LIVE MEDIA' logo. To its right is a search bar with the placeholder text 'Search videos, photos and events...'. Below the search bar are four navigation buttons: 'CONGRESSES' (red), 'COURSES' (blue), 'EVENTS' (green), and 'WEBTV' (purple). The main content area is titled 'Congresses | The 25th European symposium on Ultrasound Contrast Imaging'. Below this, the event details are displayed: 'The 25th European symposium on Ultrasound Contrast Imaging' in large text, followed by '16-17 January 2020 - Hilton Hotel Rotterdam, The Netherlands' and 'An ICUS Conference'. A central image collage includes a diagram of a network, ultrasound contrast images, and a grid of small images. Below the collage, the organizers and scientific board members are listed: 'Organised by: Nico de Jong, Folkert ten Cate, Rik Vos, Klazina Kooiman, Annemien van den Bosch, and Arend Schinkel' and 'Scientific board: Mike Averkiou, Mark Borden, Paolo Colonna, Olivier Couture, Beat Kaufmann, and Eleanor Stride'.

WEBCASTING

Introducing exciting news for our friends who are not able to join the 25th European symposium on Ultrasound Contrast Imaging in Rotterdam! To learn from the best in the world even if travel is not an option, you can join the Symposium through worldwide live streaming by the WEB CONFERENCE CHANNEL, through Livemedia <https://www.livemedia.com/25symposium>
For info of the the previous symposium check <https://www.livemedia.com/24symposium>

Videos will remain hosted on Livemedia indefinitely and available for on demand viewing. Once registered, remote participants will receive log in credentials that will allow them access and will monitor the viewing time. GAIN ONLINE ACCESS to the well known 25th European symposium on Ultrasound Contrast Imaging.

Please register here: <https://www.livemedia.com/25symposium>. For any inquiries please contact Irene Syraki irene@livemedia.gr or the symposium secretariat.



The 25th European Symposium on Ultrasound Contrast Imaging Rotterdam is sponsored by:

Bracco Suisse SA

Marco Graf, Senior
Communication Events Manager
Manno, Switzerland

Mindray Innovation Center

Glen McLaughlin, president
San Jose, USA

Erasmus University MC - Thorax Center

Prof.dr. Felix Zijlstra,
Head of the department
Rotterdam
The Netherlands

Siemens Healthineers

Helen Cleminson
SHS US IN ADGI
United Kingdom

GE Healthcare

Julie Hillsdon
Marketing & Compliance Co-
Ordinator
United Kingdom

Samsung Electronics Benelux

Luc van Dalen, Business
Development Manager
Health Medical Equipment
The Netherlands

Philips Healthcare

Radjen Ganpat
Senior Field Marketing
General Imaging Ultrasound
Eindhoven, The Netherlands

TIDE Microfluidics BV

Wouter Bolt
Sales manager
Enschede, The Netherlands

Oldelft Ultrasound

Stefan Roggeveen
Commercial Manager
Delft, the Netherlands

Fujifilm VisualSonics

Adrie Gubbels
Amsterdam, the Netherlands

Nederlandse Hartstichting

Rebecca Abma-Schouten
Manager Research Dept.
Den Haag, The Netherlands

Mindray Medical Germany GmbH

Hongbo Zhu
Marketing Ultrasound
Europe
Darmstadt, Germany

FIRST ANNOUNCEMENT 2021

**26th EUROPEAN SYMPOSIUM ON
ULTRASOUND CONTRAST IMAGING**

14-15 JANUARY 2021

ROTTERDAM, THE NETHERLANDS

Information on the 26th EUROPEAN SYMPOSIUM ON ULTRASOUND CONTRAST
IMAGING: Sharon Sewell, s.sewell-albert@erasmusmc.nl

sponsors:

Golden sponsor



GE Healthcare



PHILIPS

SAMSUNG



mindray
healthcare within reach

Erasmus MC



SIEMENS
Healthineers

Silver sponsor



 **Oldelft**
Ultrasound

FUJIFILM
VISUALSONICS



The 25th European Symposium on Ultrasound Contrast Imaging, Rotterdam is sponsored by:



GE Healthcare



PHILIPS

Erasmus MC



SAMSUNG



FUJIFILM
VISUALSONICS